AR TARGET SHEET

The following document was too large to scan as one unit, therefore, it has been broken down into sections.

EDMC#:	0056409
SECTION:	3 of 4
DOCUMENT #:	RPP-7884, REV 000
TITLE:	Field Investigation Report for WMA S-SX

then fit to the data from 6005 eV to the end of the data (approximately 6350 eV). A third-order spline with two regions was used to fit this region of the spectrum, with a k^4 weighting. The normalization point for the edge jump was set at 6025 eV. The data were normalized on the 6025 eV spline point and output into an ASCII format. The pre-edge features of these normalized spectra were then analyzed using the program Grams/32, where a maximum search was performed, yielding the pre-edge peak height and position. The percent Cr(VI) was then calculated using these peak height values and the equations below from beamline-specific calibration curves:

$$\text{BL 11-2: } \%\text{Cr(VI)} = 102.83(\text{height}) - 12.80$$

$$\text{BL 4-3: } \%\text{Cr(VI)} = 128.64(\text{height}) - 12.77$$

A plot of the beamline 11-2 calibration curve with the Cr(VI) percentage 95% prediction intervals is shown in Figure D.4.1.1. The prediction interval includes, with 95% confidence, any future Cr(VI) percentages calculated from the Cr pre-edge peak height using the above linear regression equation. The calibration curve properly predicted the Cr(VI) percentages of three unknown samples that were used to test the calibration process.

The normalized Cr K-XANES spectra of the eight Hanford borehole samples are shown in Figure D.4.1.2, and the results of the Cr(VI) determination are shown in Table D.4.1.1.

D.4.1.3 Chromium Speciation Mapping and Micro-XANES Spectroscopic Analyses of Thin Sections

D.4.1.3.1 Experimental Procedure and Data Analysis. We examined four subsurface samples obtained from the Hanford S and SX tank farms using XAFS spectroscopy and X-ray microprobe elemental mapping at the Advanced Photon Source (GeoSoilEnviroCARS Sector 13; Newville et al. 1999). These consisted of different portions of the same two samples from the SX-108 slant borehole (samples SX-108-7A and SX-108-8A) and the same two samples from borehole 41-09-39 (samples 41-09-39-6AB and 41-09-39-7ABC) that were examined at SSRL. Prior to examination, these samples were placed in an Al-tube and impregnated with epoxy at PNNL. Once the epoxy had hardened, the samples were cut in cross section and polished to produce 0.1-mm-thick wafers. Each wafer was glued to a SiO_2-glass plate, sealed with Kapton™ film, and sent to the Advanced Photon Source (APS) for micro-XRF and micro-XAFS analysis. Once at the APS, the samples were placed into acrylic sample holders and sealed with a second Kapton™ film.

This undulator-based instrument uses a Si(111) cryogenic, double-crystal, scannable monochromator. The x-ray micro-beam was produced using Kirkpatrick-Baez (KB) micro-focusing mirrors (Eng et al. 1999). The KB system consisted of two mirrors (100 mm length), one in the horizontal plane and one in the vertical plane, which focused the x-ray beam from 350 μm down to approximately 5 μm. The mirrors are made of single-crystal silicon coated with several hundred Å of Rh, and the flat surfaces were dynamically bent to elliptical shapes using mechanical benders. The "double-bounce" focusing system provided excellent harmonic rejection capabilities for micro-XAFS applications. Samples were placed on an x-y-z stepping motor stage (0.1 μm resolution, positioned at 45° to the incident beam) allowing the analysis point of interest to be positioned in the monochromatic x-ray beam. An optical microscope, consisting of a 5x Mitutoya, long-working-distance objective lens mounted to an Optem motor-driven focus/zoom transport tube and equipped with a CCD camera, was used to view the samples at high resolution. The position of the x-ray beam was determined using a luminescent phosphor (YAG) mounted to the sample stage. The position stability of the beam on the sample was of the order 0.1 °m. Micro-XRF and micro x-ray absorption fine structure (XAFS) spectra were collected in fluorescence mode using a 16-element Ge solid-state detector (Canberra) positioned at 90° to the incident beam and in the horizontal, polarization plane of the synchrotron (position of minimum scattered background radiation). The electron current of the APS storage ring ranged from 60 to 100 mA at an energy of 7 GeV.

Initially, x-ray fluorescence spectra were collected on representative areas of the four core samples. Each sample was moved through the beam over a 300 µm × 300 µm area in 10 µm steps, in order to determine the elemental associations of Fe, Cr, Mn, K, Ca, and Ti. XANES spectra were collected at the Cr K-edge on selected spots in each sample and along linear transects of each sample. In general, high Cr spots were selected for single analysis spots, but the line scans also sampled lower Cr material. XANES spectra were also collected from the model compounds, Na_2CrO_4, $BaCrO_4$, and Na_2CrO_3. Additionally, the focused beam was kept on the Cr(VI)-containing models and on Cr(VI)-rich regions of the samples for 1 hour to evaluate the potential for x-ray-induced reduction of Cr(VI). No such reduction was observed in this time frame.

The fraction of total Cr present as Cr(VI) in each sample spot was determined by comparing the area of the pre-edge peak for the unknown samples to that of Na_2CrO_4 and $BaCrO_4$. The Cr XANES spectra were normalized to an edge jump defined by the difference of pre-edge background and the height of the spline at 6030 eV as described above (Peterson et al. 1997a) (Figure D.4.1.5). The area of the pre-edge peak was determined by fitting this peak with mixed Gaussian and Lorentzian functions using the program Grams/32.

D.4.1.4 Results

The spatial distribution of each element within each sample was found to be highly heterogeneous even in an area as small as 300 µm × 300 µm. Figure D.4.1.3 shows the element maps of two samples as examples. Qualitative correlations between certain elements are visible in the maps (e.g., Cr and Mn from Figure D.4.1.3a). Using the data provided from the element maps for the four samples, scatter plots (Figure D.4.1.4) were generated to further investigate the elemental associations. While sample 41-09-39-6AB shows a moderately strong association between chromium and both manganese and iron, the other samples show a weaker correlation. Samples SX-108-07A, 41-09-39-7ABC, and SX-108-8A (shown in Figure D.4.1.4) have weak linear associations, and the shape of their scatter plots suggests a possible weak quadratic association. A filter was applied to the chromium matrix in order to look for correlations with other elements at spatial positions where there are high chromium concentrations (greater than 75th quantile) and low chromium concentrations (less than 25th quantile). This data treatment did not significantly improve the correlations between chromium and any other element. Plotting some of the data using a quadratic relationship also showed no significant improvement in the correlation between chemical elements.

Figure D.4.1.2. Normalized Cr K-Edge XANES Spectra of the SX-108 Contaminated Sediment Samples: (a) 41-09-39-6AB, (b) 41-09-39-7ABC, (c) SX-108-6A, (d) SX-108-7A, (e) SX-108-8A, (f) SX-108-9A, (g) SX-108-13A, (h) SX-108-14A.

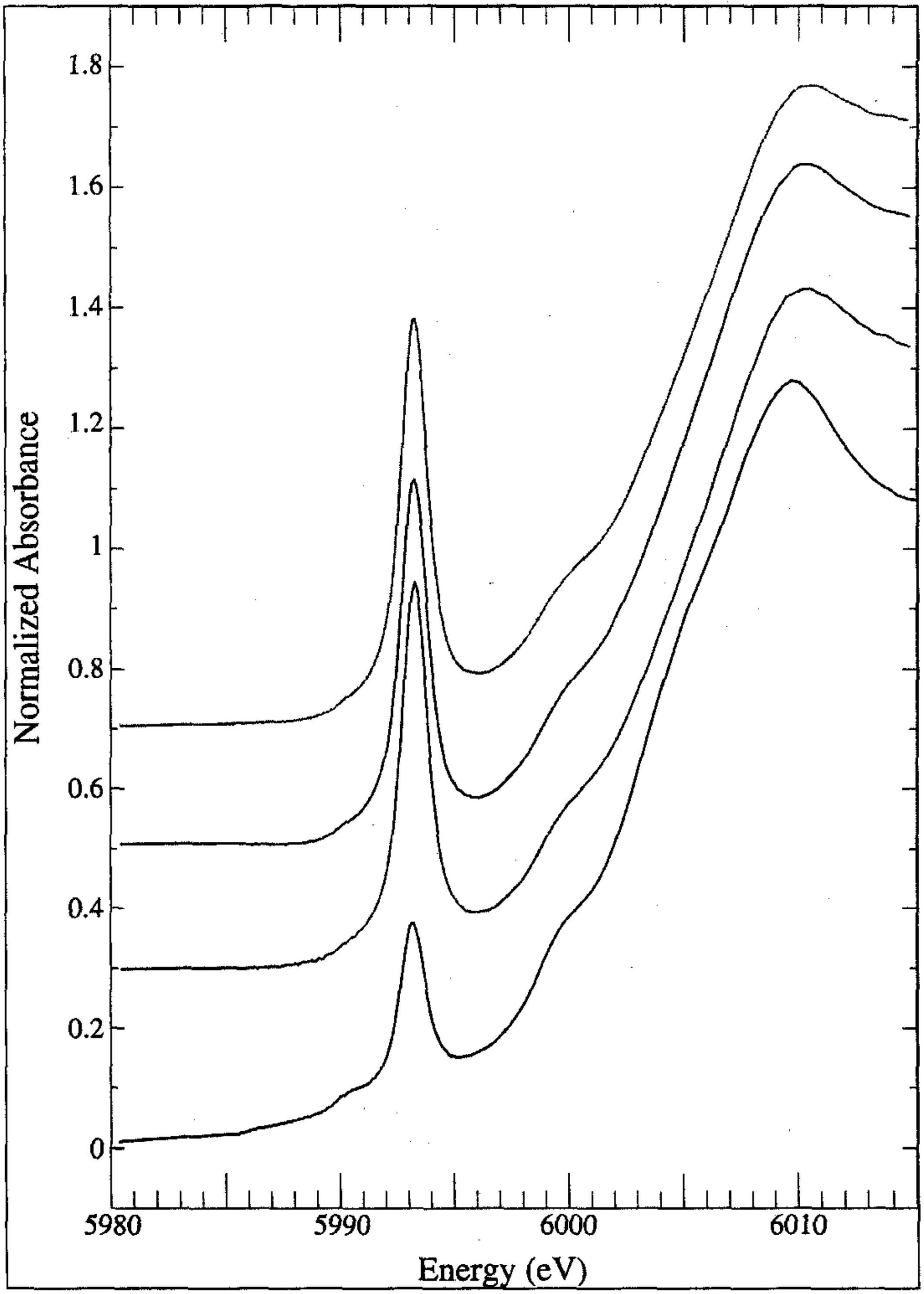

Figure D.4.1.3. Element Maps of Selected Areas From a) Sample 41-09-39-6AB and b) Sample SX-108-8A.

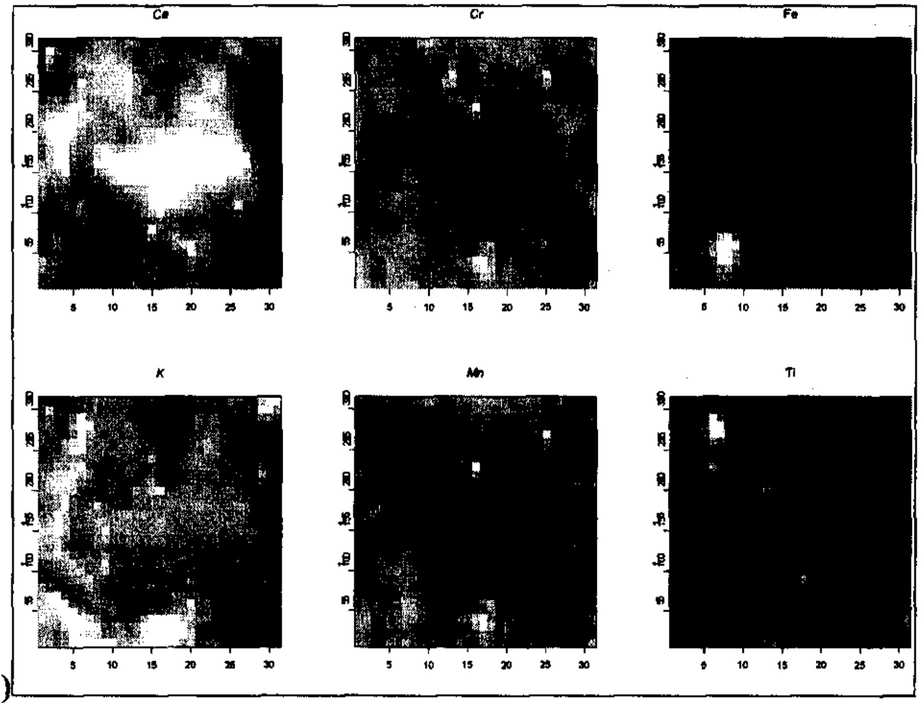

a)

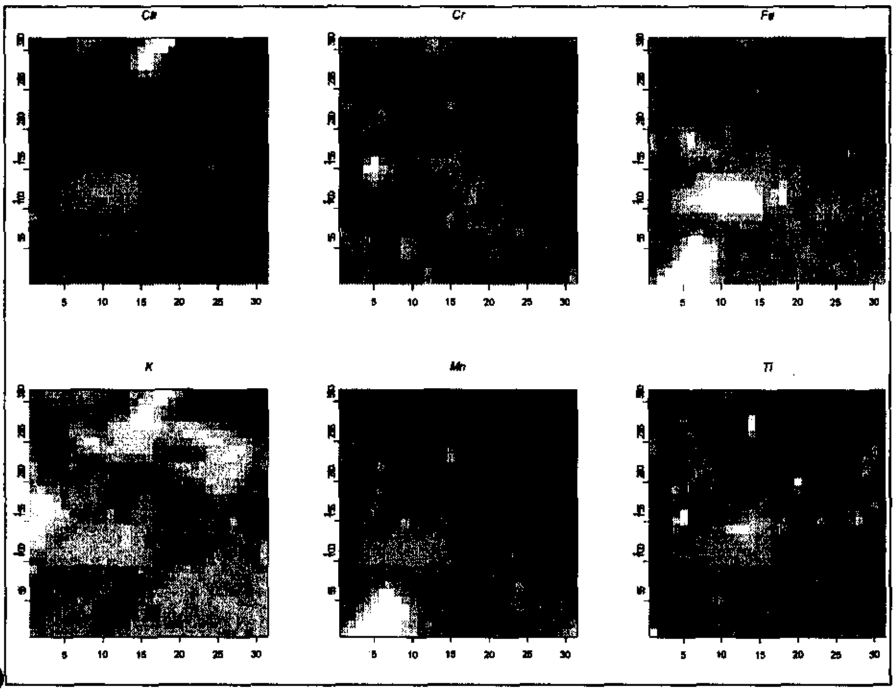

b)

Note: Total Dimensions of the Scanned Image are 300µm × 300 µm and Each Pixel Element is 10 µm x 10 µm. Light Areas Have the Highest Concentrations and Dark Areas Have the Lowest.

Figure D.4.1.4. Scatter Plots Between Cr, Mn, Fe, and Ti for Sample SX-108-8A.

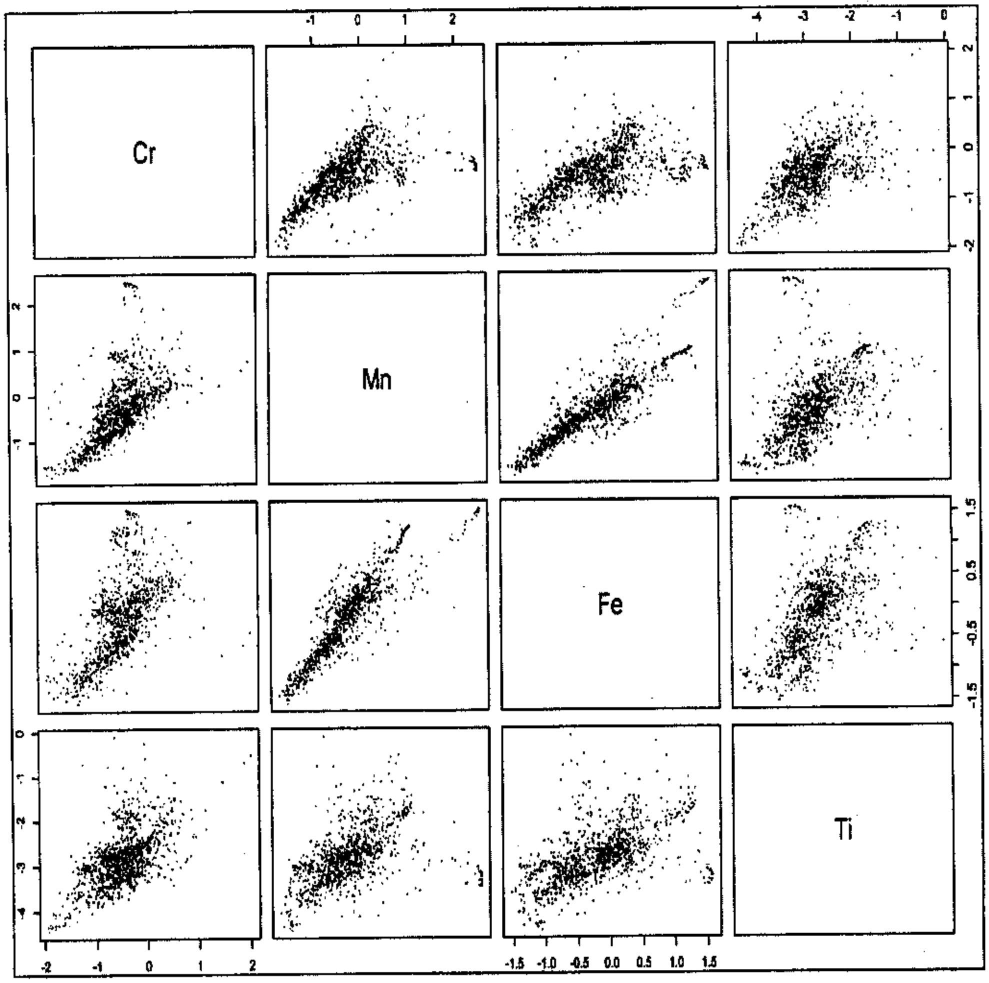

Note: The Plots in the Same Row as the Elements have that Element's Normalized Fluorescence Intensity Plotted Along the x-Axis. The y-Axis of That Plot Corresponds to the Element in the Column.

Figure D.4.1.5. Selected Cr K-XANES Spectra Collected From Sample SX-108-8A. Normalized Absorbance is Plotted on the Vertical Axis.

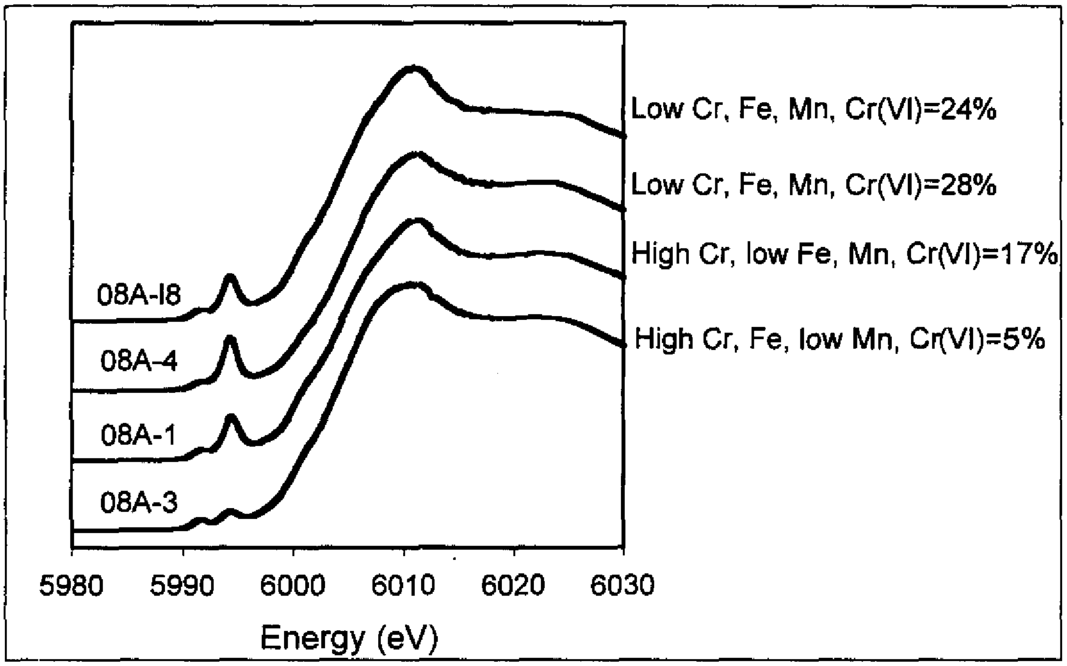

Correlation coefficients were calculated in order to estimate the linear dependence between pairs of elements in the samples. The log correlation matrices for the four samples are shown in Table D.4.1.2. As expected there is a strong association between manganese and iron in all of the core samples and a very weak association between calcium and all other elements except potassium. Sample 41-09-39-6AB also shows a strong correlation between chromium and manganese (0.94) and iron (0.81). However, this strong association with chromium is not repeated in the other samples, with their correlation coefficients ranging between 0.46 and 0.60 for manganese and between 0.32 and 0.59 for iron. The correlation coefficient for chromium and titanium ranged from 0.29 to 0.58 for the four samples. The lack of strong correlations between Cr, Fe, and Mn suggests that sorption reactions between Cr and Fe- or Mn-oxide particles are limited. There is also evidence that such reactions occur to varying degrees in the samples.

The analyses of Cr micro-XANES spectra taken at 53 spots on the four thin sections yielded average Cr(VI) percentages of 13%, 28%, 23%, and 12% for SX-108-7A, SX-108-8A, 41-09-39-6AB, and 41-09-39-7ABC, respectively (Table D.4.1.3). All spots analyzed but two contained mixtures of Cr(III) and Cr(IV). Of the two end member spots, one was Cr(III) and the other was Cr(VI). These results indicate that, in general, the two species are intermixed at the 10 μm scale (approximate analysis scale).

Table D.4.1.2. Log Correlation Matrices for Ca, Cr, Fe, K, Mn, and Ti in the Four Core Sample Thin Sections.

Sample 41-09-39-6AB

	Ca	Cr	Fe	K	Mn	Ti
Ca	1.00	-0.30	-0.32	0.65	-0.29	-0.22
Cr	-0.30	1.00	0.81	0.16	0.94	0.58
Fe	-0.32	0.81	1.00	0.16	0.86	0.54
K	0.65	0.16	0.16	1.00	0.16	0.23
Mn	-0.29	0.94	0.86	0.16	1.00	0.58
Ti	-0.22	0.58	0.54	0.23	0.58	1.00

Sample 41-09-39-7ABC

	Ca	Cr	Fe	K	Mn	Ti
Ca	1.00	-0.02	0.15	0.83	0.17	0.02
Cr	-0.02	1.00	0.32	0.13	0.46	0.29
Fe	0.15	0.32	1.00	0.27	0.96	0.66
K	0.83	0.13	0.27	1.00	0.29	0.34
Mn	0.17	0.46	0.96	0.29	1.00	0.64
Ti	0.02	0.29	0.66	0.34	0.64	1.00

Sample SX108-07A

	Ca	Cr	Fe	K	Mn	Ti
Ca	1.00	-0.16	-0.30	0.75	-0.14	0.03
Cr	-0.16	1.00	0.53	0.04	0.56	0.31
Fe	-0.30	0.53	1.00	-0.14	0.83	0.24
K	0.75	0.04	-0.14	1.00	-0.04	0.34
Mn	-0.14	0.56	0.83	-0.04	1.00	0.19
Ti	0.03	0.31	0.24	0.34	0.19	1.00

Sample SX-108-8A

	Ca	Cr	Fe	K	Mn	Ti
Ca	1.00	0.31	0.34	0.38	0.36	0.31
Cr	0.31	1.00	0.59	0.09	0.60	0.58
Fe	0.34	0.59	1.00	0.11	0.90	0.54
K	0.38	0.09	0.11	1.00	0.07	0.38
Mn	0.36	0.60	0.90	0.07	1.00	0.43
Ti	0.31	0.58	0.54	0.38	0.43	1.00

Table D.4.1.3. Percent of Total Cr as Cr(VI) From Micro-XANES Analysis.

Core SX-108	Sample Spot*	Cr(VI) content (%)	Core 41-09-39	Sample Spot*	Cr(VI) content (%)
SX-108-07A			**41-09-39-6AB**		
	1	1		1	22
	2	12		2	6
	3	25		4	35
	L1	17		5	38
	L2	24		6	39
	L3	8		8	43
	L4	10		10	17
	L5	8		12	10
	L6	11		13	20
	L7	11		L1	14
		Avg. = 13		L2	16
				L3	17
SX-108-08A				L4	28
	1	20			Avg. = 23
	2	11			
	3	6	**41-09-39-7ABC**		
	4	27		1	10
	5	42		2	10
	6	46		3	17
	7	48		L1	8
	L1	16		L2	12
	L2	14		L3	17
	L3	18		L4	11
	L4	15		L5	11
	L5	16		L6	10
	L6	19		L7	13
	L7	24		L8	10
	L8	25		L9	9
	L9	100		L10	11
		Avg. = 28		L11	12
					Avg. = 12

*XANES spectra collected from 10 μm × 10 μm spots. Data from regions with an "L" designation were collected during a "line-scan" across a Cr-rich region of each sample.

Thus, the micro-XANES results showed more reduced chromium than the bulk XANES measurements. The cause of this difference is not fully understood but there are several possible explanations. One possibility is that the original sample aliquots had different oxidation states, but this seems unlikely since the samples were derived from the same parent material. The fact that all four sectioned samples yielded more reduced Cr suggests that Cr reduction may have occurred subsequent to borehole sampling. Reduction of Cr(VI) by the x-ray beam was ruled out – changes in redox state were not observed for the model compounds or in sample regions that were illuminated for up to 1 hour. Thus, photochemical reduction of Cr(VI) was negligible over the time scales of the XANES measurements. Another possibility is that the thin section preparation process, involving epoxy impregnation, slicing, and grinding, may have resulted in Cr reduction.

To investigate possible redox changes introduced by thin section preparation, we epoxy-impregnated Na_2CrO_4 and measured Cr K XANES spectra on beam line 4-3 at the Stanford Synchrotron Radiation Laboratory. These Cr K-XANES spectra showed no Cr(III) suggesting that the Cr oxidation state is unaltered by the epoxy used in sample preparation (although admittedly, there may be significant differences in the behavior of the model compound and the soils during such treatment). To further evaluate possible Cr reduction due to thin section preparation, bulk XANES measurements were carried out on two of the thin sections (41-09-39-6AB and 41-09-39-7ABC) and two thin sections adjacent in the core to those analyzed at the APS (SX-108-7B and SX-108-8B) on beamline 4-3 at SSRL. The procedures used were identical to those described in Section II. The bulk XANES of the thin sections showed a good agreement with the micro-XANES measurement of the Cr(VI) content of the samples, and both showed significant deviation from the bulk XANES of the untreated samples (Table D.4.1.4). These results suggest that the method of thin section preparation employed caused a significant decrease in the Cr(VI):Cr(III) ratio in the samples. A number of scenarios during thin section preparation could have caused this decrease, including epoxy replacement of Cr(VI)-bearing porewater, epoxy-induced dissolution and mobilization of Fe(II) from Fe(II)-bearing minerals, causing Cr(VI) reduction by Fe(II), or direct reduction of Cr(VI) by the epoxy. While no direct reduction of Cr(VI) in solid Na_2CrO_4 by the epoxy was observed, as noted above, Cr(VI) in the samples would occur (presumably) as aqueous, adsorbed, or possibly precipitated CrO_4^{2-}. The prior two forms may show a much higher propensity for reduction by epoxy than the solid form.

Table D.4.1.4. Comparison of % Cr(VI) Content of the Original and Thin Sectioned Samples.

Sample	%Cr(VI) from bulk XANES	%Cr(VI) from micro-XANES of thin section	%Cr(VI) from bulk XANES of thin section
41-09-39-6AB	51	23	36
41-09-39-7ABC	58	12	9
SX-108-7B	25	13	11
SX-108-8B	53	28	16

D.4.1.5 Conclusions

Seven of the eight samples from boreholes drilled at the Hanford S and SX tank farms contain 51-71% Cr(VI), whereas the fourth sample (SX-108-7B) contains 25% Cr(VI). These data suggest that while significant reduction of chromium has occurred, most likely via abiotic pathways due to the lack of significant numbers of microorganisms in the Hanford vadose zone, it has not been complete, assuming that the bulk of Cr introduced into the Hanford vadose zone was Cr(VI). Possible reasons for this include (1) insufficient reductants in the vadose zone, (2) the presence of nonconductive carbonate coatings on Fe(II)-bearing minerals, (3) the build-up of nonconducting Cr(III)-hydroxide coatings on reductant surfaces, which can quickly stop the electron transfer process necessary for the Cr(VI) to Cr(III) reduction reaction, or (4) some other process that has inhibited the transfer of electrons from reductants to Cr(VI).

Micro-fluorescence elemental mapping of Cr, Fe, Mn, Ti, Ca, and K at 10 μm x 10 μm spatial resolution in 300 μm × 300 μm areas on thin sections of four of the borehole samples showed that they are highly heterogeneous with respect to these elements, with Cr(III) hot-spots (diameters of several 100 μm^2) occurring, presumably as a result of the precipitation of Cr(III)-hydroxides or chromite or sorption of Cr on Fe(III)-hydroxides. Trivalent and hexavalent chromium are intermixed on a very fine scale (less than 10 μm). The spatial correlation between Cr and Fe-bearing minerals, which are likely reductants for Cr(VI), is strong in only one of the four thin sections, indicating that such reactions are limited and occur to varying degrees in these materials.

A comparison of the Cr speciation data from the bulk XANES analysis of the untreated samples and thin sections conducted at SSRL and the micro-XANES analysis of the thin sections conducted at the APS indicates major differences in Cr(VI) concentrations, with the thin section results showing average Cr(VI) percentages of 9-36%. We conclude, however, that the untreated sample results are more representative of the true average Cr speciation in the eight borehole samples examined. This conclusion is based on the significant differences in the Cr(VI):Cr(III) ratios between the untreated samples and the thin sections.

D.4.1.6 Acknowledgments

We wish to thank John Bargar and Joe Rodgers (SSRL) for their technical support on BL 11-2 prior to data collection at SSRL. We also wish to thank Ian Evans, Ray Russ, and Carol Morris of the SLAC ES&H staff for their help in the safe handling of the radioactive samples from Hanford. We thank Steve Heald (University of Washington) and James McKinley (PNNL) for their efforts in sample mounting, handling, and shipping of thin sections to the APS. These studies were supported in part by DOE-EMSP grants DE-FG07-99ER15022 (Traina, Brown, and Ainsworth) and DE-FG07-99ER15024 (Zachara and Brown). SSRL is supported by the Department of Energy-Basic Energy Sciences (Chemical Sciences and Materials Science Divisions) and the National Institutes of Health. The GSECARS sector is supported by the National Science Foundation (Earth Sciences Instrumentation and Facilities Program) and the Department of Energy-Basic Energy Sciences (Geosciences Program).

D.4.1.7 References

Abbasi, S. A., and R. Soni, 1984, "Teratogenic Effects of Chromium (VI) in the Environment as Evidenced by the Impact of larvae of Amphibian *Rand tigrina*: Implications in the Environmental Management of Chromium," *International Journal of Environmental Studies*, Vol. 23:31-137.

Baes, C. F., Jr., and R. E. Mesmer, 1986, "*The Hydrolysis of Cations,*" Robert F. Krieger Publishing Co., Malabar, Florida, pp. 489.

Bargar, J. R., G. E. Brown, Jr., I. Evans, T. Rabedeau, M. Rowen, and J. Rogers, 2001, "A New Hard X-ray XAFS Spectroscopy Facility for Environmental Samples, Including Actinides, at the Stanford Synchrotron Radiation Laboratory," *Proc. 2nd Euroconference and NEA Workshop on Speciation, Techniques, and Facilities for Radioactive Materials at Synchrotron Light Sources*, (In press).

Bish, D. L., S. J. Chipera, and P. Snow, 2000, "Mineralogic Studies of Uncontaminated 200-Area tank farm Sediments: Interim Report (PO #401924)," In: *Reports of the Representative Site Workshop on High Level Waste Contaminated Sediments*, Pacific Northwest National Laboratory, Richland, Washington.

Brigatti, M. F., G. Franchini, C. Lugli, L. Medici, L. Poppi, and E. Turci, 2000a, "Interaction Between Aqueous Chromium Solutions and Layer Silicates," *Applied Geochemistry,* Vol. 15:1307-1316.

Brigatti, M. F., C. Lugli, G. Cibin, A. Marcelli, G. Biuli, E. Paris, A. Mottana, and Z. Wu, 2000b, "Reduction and Sorption of Chromium by Fe(II)-Bearing Phyllosilicates: Chemical Treatments and X-ray Absorption Spectroscopy (XAS) Studies," *Clays and Clay Minerals*, Vol. 48:272-281.

Brown, G. E., Jr., G. Calas, G. A. Waychunas, and J. Petiau, 1988, X-ray Absorption Spectroscopy and its Applications in Mineralogy and Geochemistry," In: *Spectroscopic Methods in Mineralogy and Geology* (F. Hawthorne, ed.), *Reviews in Mineralogy*, Vol. 18, p. 431-512, Mineralogical Society of America, Washington, D.C.

Brown, G. E., Jr., S. A. Chambers, J. E. Amonette, J. R. Rustad, T. Kendelewicz, P. Liu, C. S. Doyle, D. Grolimund, N. S. Foster-Mills, S. A. Joyce, and S. Thevuthasan, 2000, "Interaction of Water and Aqueous Chromium Ions with Iron Oxide Surfaces," In: *American Chemical Society Symposium Series 778, Nuclear Site Remediation - First Accomplishments of the Environmental Management Science Program*, (P. G. Eller and W. R. Heineman, eds.), p. 212-246, American Chemical Society, Columbus, Ohio.

Doyle, C. S., T. Kendelewicz, G. E. Brown, Jr., S. A. Chambers, J. M. Zachara, and C. M. Eggleston, Jr., 2000, "The Effect of Carbonate Coatings on the Reduction of Cr(VI) on the (111) Surface of Magnetite," *Journal of Conference Abstracts*, Vol. 5(2): Goldschmidt Conference, Oxford, United Kingdom.

Eary, L. E., and D. Rai, 1989, "Kinetics of Chromate Reduction by Ferrous Iron Derived from Hematite and Biotite at 25 °C," *America Journal of Science,* Vol. 289:180-213.

Eng, P. J., M. Newville, M. L. Rivers, and S. R. Sutton, 1999, "Dynamically Figured Kirkpatrick Baez X-ray Micro-Focusing Optics," In: *X-Ray Microfocusing: Applications and Technique* (I. McNulty, ed.), *SPIE Proc.* 3449, p. 145.

Fendorf, S. E., and G. Li, 1996, "Kinetics of Chromate Reduction by Ferrous Iron," *Environmental Science and Technology,* Vol. 30:1614-1617.

Fendorf, S., B. W. Wielinga, and C. M. Hansel, 2000, "Chromium Transformations in Natural Environments: The Role of Biological and Abiological Processes in Chromium(VI) Reduction," *International Geology,* Vol. 42:691-701.

Fredickson, J., S.-M. Li, and D. Kennedy, 2000, "Microbiological Analysis of Hanford SX-108 Tank Vadose Sediments," In: *Reports of the Representative Site Workshop on High Level Waste Contaminated Sediments*, Pacific Northwest National Laboratory, Richland, Washington.

George, G. N., and I. J. Pickering, 1993, "EXAFSPAK," Stanford Synchrotron Radiation Laboratory Report.

Ilton, E. S., and D. R. Veblen, 1994, "Chromium Sorption by Phlogopite and Biotite in Acidic Solutions at 25 °C: Insights From X-ray Photoelectron Spectroscopy and Electron Microscopy," *Geochimica et Cosmochimica Acta,* Vol. 58:2777-2788.

Ilton, E. S., D. R. Veblen, C. O. Moses, and S. P. Raeburn, 1997, "The Catalytic Effect of Sodium and Lithium Ions on Coupled Sorption-Reduction of Chromate at the Biotite Edge-Fluid Interface," *Geochimica et Cosmochimica Acta,* Vol. 61:3543-3563.

Kendelewicz, T., P. Liu, C. S. Doyle, and G. E. Brown, Jr., 2000, "Spectroscopic Study of the Reaction of $Cr(VI)_{aqueous}$ with Fe_3O_4 (111) Surfaces," *Surface Science,* Vol. 469:144-163.

Lytle, F. W., R. B. Greegor, D. R. Sandstrom, E. C. Marques, J. Wong, C. L. Spiro, G. P. Huffman, and F. E. Huggins, 1984, "Measurement of Soft X-ray Absorption Spectra with a Fluorescent Ion Chamber Detector," *Nuclear Instrument and Methods,* Vol. 226:542-548.

Newville, M., S. R. Sutton, M. L. Rivers, and P. J. Eng, 1999 "Micro-Beam X-ray Absorption and Fluorescence Spectroscopies at GSECARS: APS Beam Line 13 ID," *Journal of Synchrotron Radiation,* Vol. 6:353-355.

Ono, B. I., 1988, "Genetic Approaches in the Study of Chromium Toxicity and Resistance in Yeast and Bacteria," In: *Chromium in the Natural and Human Environment* (J. O. Nriagu and E. Nieboer, eds.), p. 351-368, John Wiley & Sons, New York.

Paschin, Y. V., V. I. Kozachenko, and L. E. Sal'nikova, 1983, "Differential Mutagenic Response at the HGPRT Locus in V-79 and CHO Cells After Treatment with Chromate," *Mutat. Research,* Vol. 122:361-365.

Peterson, M. L., G. E. Brown, Jr., and G. A. Parks, 1996, "Direct XAFS Evidence for Heterogeneous Redox at the Aqueous Chromium/Magnetite Interface," *Colloids and Surfaces*, Vol. 107:77-88.

Peterson, M. L., G. E. Brown, Jr., G. A. Parks, and C. L. Stein, 1997a, "Differential Redox and Sorption of Cr(III/VI) on Natural Silicate and Oxide Minerals: EXAFS and XANES Results," *Geochimica et Cosmochimica Acta*, Vol. 61:3399-3412.

Peterson, M. L., A. F. White, G. E. Brown, Jr., and G. A. Parks, 1997b, "Surface Passivation of Magnetite (Fe_3O_4) by Reaction with Aqueous Cr(VI): XAFS and TEM Results," *Environmental Science and Technology,* Vol. 31:1573-1576.

Richard, F. C. and A. C. M. Bourg, 1991, "Aqueous Geochemistry of Chromium: A Review," *Water Research,* Vol. 25:807-816.

Serne, R. J., G. V. Last, G. W. Gee, H. T. Schaef, D. C. Lanigan, C. W. Lindenmeier, R. E. Clayton, V. L. LeGore, R. D. Orr, M. J. O'Hara, C. F. Brown, D. B. Burke, A. T. Owen, I. V. Kutnyakov, and T. C. Wilson, 2001a, *Geologic and Geochemical Data Collected from Vadose Zone Sediments from Borehole SX 41-09-39 in the S/SX Waste Management Area and Preliminary Interpretations*, PNNL-2001-2, Pacific Northwest National Laboratory, Richland, Washington.

Serne, R. J., H. T. Schaef, G. V. Last, D. C. Lanigan, C. W. Lindenmeier, R. E. Clayton, V. L. LeGore, M. J. O'Hara, C. F. Brown, R. D. Orr, I. V. Kutnyakov, T. C. Wilson, D. B. Burke, B. A. Williams, and B. N. Bjornstad, 2001b, *Geologic and Geochemical Data Collected from Vadose Zone Sediments from the Slant Borehole under SX-108 in the S/SX Waste Management Area and Preliminary Interpretations*, PNNL-2001-4, Pacific Northwest National Laboratory, Richland, Washington.

D.4.2 DESORPTION AND LEACHING OF CR FROM WMA S-SX SEDIMENTS

Calvin C. Ainsworth[1], Odeta S. Qafoku[1], Steven C. Smith[1], Steve Heald[1,2], James P. McKinley[1], and John M. Zachara[1]

[1]Pacific Northwest National Laboratory, Richland, Washington 99352

[2]Argonne National Laboratory, Argonne, Illinois 60439

D.4.2.1 Introduction

Hexavalent chromium [chromate; $Cr(VI)O_4^{2-}$] is a highly mobile contaminant in the unconfined aquifer underlying the Hanford reservation. The retardation of Cr(VI), in the absence of reduction to the more stable Cr(III) species, has been shown to result from interactions at mineral-water interface (Ainsworth et al. 1989; Zachara et al. 1989). This interaction is dependent on a number of factors: (1) the nature of the surface (surface charge and its variation with pH, number of sorption sites etc.), (2) the presence of grain coatings, (3) the pH and ionic strength of aqueous phase in contact with geologic material, (4) the mode of adsorption (inner-sphere vs. outer-sphere), and (5) the effect of other surface complexants (Brown et al. 1998). As an anion, $Cr(VI)O_4^{2-}$ will sorb most strongly within the pH range below a sorbent's point of net zero charge where the surface is positively charged; for most Fe oxide minerals that means slightly basic to acidic conditions (Cornell and Schwertmann 1996). Because of the slightly basic pH of Hanford groundwater, chromate is not expected to be substantially retarded; in fact, it is considered a highly mobile species.

The sediments directly below the WMA S-SX and above groundwater consist primarily of the Hanford formation. These sediments (Pleistocene-age flood deposits) are a complex association of mineral phases, including unstable primary phases (e.g., feldspars, micas, etc.), and more stable secondary phases (e.g., Al and Fe oxides, poorly crystalline SiO_2, and smectites). Because of the harsh nature of tank leaked fluids (high base, high Na concentrations, etc.) from the SX tanks. Sediments inundated by these fluids may have undergone substantial dissolution and precipitation of secondary mineral phases (see Section D.2.0). Chromate associated with these leak events has moved into the vadose zone in significant concentration (Jones et al. 2000). Chromate interactions with Hanford sediments are being studied as part of groundwater transport studies, remedial actions, and demonstrations, but there is only a limited understanding of chromate behavior in contaminated WMA S-SX sediments.

Here we report on new studies of Cr desorption from WMA S-SX sediments under tank SX-108 (SX-108 slant borehole and 41-09-39). These studies investigated Cr desorption in batch and small columns designed to address two main issues. First, the high pH and $NaNO_3$ concentrations associated with the leaked materials should enhance the Cr(VI) anion's mobility in the affected sediments. Second, accelerated weathering of minerals should cause substantial secondary oxide formation capable of retarding Cr(VI) mobility. These two issues are fundamentally opposing views. By investigating the mobility of Cr(VI) using contaminated sediments and in conjunction with other, linked studies a more complete understanding will evolve regarding Cr behavior below the WMA S-SX.

D.4.2.2 Experimental Procedures

D.4.2.2.1 Sediment Collection and Analysis. Collection and preliminary analyses of sediments from the SX-108 slant and 41-09-39 boreholes are discussed elsewhere (Serne et al. 2001a, b). Materials used in these investigations were SX-108 sediments 7A and 8A and 41-09-39 sediments 6AB and 7ABC. Subsamples of the field moist material were air-dried to a constant weight and sieved to pass a 2 mm mesh. Gravels greater than 2 mm were removed from the air-dried material during the sieving process. The sieved material was thoroughly mixed to obtain a homogeneous sample. Total chemical composition of triplicate subsamples of the homogenized, dried sediments was determined by X-ray fluorescence spectroscopy (XRF). Chromium speciation [Cr(VI)/Cr(III)] in the aforementioned sediments was determined by X-ray absorption spectroscopy (XAS); sample preparation and procedures of these measurements are described elsewhere (Section D.4.1).

D.4.2.2.2 Time-Dependent Cr Desorption with Ammonium Oxalate $(NH_4)_2C_2O_4$. Batch-type desorption experiments were performed in duplicate by suspending approximately 0.5 g of sediment (SX-108 7A and 41-09-39 7ABC) in 5 g of 0.25 mol/L $(NH_4)_2C_2O_4$ in Oak Ridge centrifuge tubes. Tubes were sealed and agitated at 25 °C. At prescribed time intervals (0.1, 0.4, 2, 8, 32, and 64 days) tubes were centrifuged (5000 rcf for 30 minutes). The supernate was carefully transferred to a plastic syringe fitted with a 0.2 μm filter. The first 1-mL of filtrate was discarded and the remaining filtrate collected in a plastic tube. The filtrate was analyzed for metals of interest (e.g., Fe, Al, Ba, Ca, Cr, K, Mg, Na, and Si) using ICP-OES.

D.4.2.2.3 Cr Leaching from Columns. Two sets of column experiments were conducted to determine Cr(VI) release from WMA S-SX sediments. Approximately 2g of air-dried sediments from each sample (SX-108 7A, SX-108 8A, 41-09-39 6AB, and 41-09-39 7ABC) were packed into 3.1 cm length by 0.78 cm diameter polypropylene columns. The columns were then connected to a peristaltic pump on one side and a fraction collector on the other. Before columns were connected to a leaching solution, approximately 10 mL pure CO_2 gas was injected through the columns to displace air from sediment pore space. A uniform movement of the leaching solution through the packed air-dried sediments was observed.

In the first leaching experiment, the sediments were continually leached with 0.5 mol/L $NaNO_3$ solution for about 20 to 25 pore volumes at a flow rate of 0.1 mL/min. This flow rate gave an approximate residence time of 6 minutes. At this time, a stop-flow method was applied for 19 hours and then leached for another 10 pore volumes. In a second study, two sediments (SX-108 7A and 41-09-39 7AB) were used. These sediments were leached with 0.5 mol/L KNO_3 solution during the first 25 pore volumes, then followed with 0.25 mol/L $(NH_4)_2C_2O_4$ solution for the next 25 pore volumes at a flow rate of 0.1 mL/min. After all the leachates were collected, columns were flushed at 0.1 mL/min with 1.0 mol/L $NaNO_3$ or KNO_3 and the electrical conductivity monitored to estimate conservative tracer breakthrough. This procedure was followed by flushing the columns with deionized water, then weighing the columns, and determining the pore space as the difference between wet and air-dried sediments.

Sediment leachates were collected every 6 minutes and the mass of solutions determined to better estimate flow rate. After all the leachates were collected, packed columns were flushed with deionized water, weighted, and sediment pore space determined as a difference of wet and air-dried sediment. The $NaNO_3$ or KNO_3 leachates were analyzed for Cr(VI) using the diphenylcarbizide colorimetric method (540 nm) (Bartlett and James 1996). In the presence of $(NH_4)_2C_2O_4$, Cr(VI) could not be measured by colorimetry; therefore, liquids containing the oxalate matrix were analyzed for total Cr with ICP-OEC.

D.4.2.3 Results

The sediments used in these studies have variable concentrations of total Cr, Fe, Na, and Cr(VI) and Cr(III); Si and Al content were similar in all four sediments (Table D.4.2.1). The Cr and Na observed in the sediments were the result of tank waste. The Fe, Al, and Si content were a reflection of the sediments' mineralogic assemblage, although Al has been reported to be a major component of the leaked fluids as the $Al(OH)_4^-$ anion (at concentrations as high as 1.3 mol/L). While XRD and SEM examination of cored sediments did not find evidence of significant Al oxide precipitation, it is likely that Al precipitated soon after entering the soil leaving substantially less Al in solution as it percolated through the sediment column.

Table D.4.2.1. Total Concentration of Selected Elements and Total Concentration of Cr(VI) and Cr(III) in 4 WMA S-SX Sediments.

Sediment	Al	Fe	Si	Na	Cr(VI)	Cr(III)	Cr Total	Cr(VI) %
	%				µg/g			
SX-108								
7A	6.45	3.65	29.46	4.37	324	973	1297	25
8A	6.68	3.16	30.49	4.65	1112	986	2098	53
41-09-39								
6AB	6.78	3.02	31.38	3.14	605	581	1186	51
7ABC	6.56	5.40	30.30	2.69	1212	878	2090	58

The Fe content of these sediments was variable (Table D.4.2.1) and likely a consequence of the natural heterogeneity of the Hanford formation. The source of the Fe (and native Al and Si) is determined by the primary and secondary minerals present in the sediments. Iron oxide content in pristine Hanford sediments is minor; hematite (0.2 wt%) and magnetite (0.4 wt%) are the most abundant Fe oxides. Sediments exposed to simulated tank-leaked wastes (high base, high saline) do show significant decreases in chlorite and smectite, and alteration of micas with slight, concomitant increases in hematite content (Section D.1.1).

Scanning electron microscopy examination of biotite isolated from pristine sediments and laboratory, base-treated bulk sediments show the potential changes that may occur with sediment exposure to high pH solutions similar to tank-leaked fluids (Figure D.4.2.1). The pristine biotite specimen (Figure D.4.2.1a) exhibits only limited Fe oxide precipitation on its surface, whereas the base-treated biotite surface is covered with secondary precipitates (Figure D.4.2.1b). The appearance of the reacted biotite is similar to that observed under SEM examination of the SX-108 3A sediment, which was probably the most intensely weathered sediment examined from the slant borehole (Section D.1.1). With depth away from the tank, observable alterations of sediment minerals and accumulation of surface precipitates compared to pristine sediments becomes less obvious under SEM examination (Section D.1.1). While mica specimens from 3A show similar impact as those seen in Figure D.4.2.1b, sediment 7A appears only moderately altered, 8A shows only limited surface precipitates, and sediments below this appear pristine. Unfortunately, no comparable examination has yet been performed for the 41-09-39 sediments.

Figure D.4.2.1. Scanning Electron Micrographs of Biotite Grains Showing Fe-Oxides on the Surface, a) From Uncontaminated 200-Area Tank Farm Sediments, and b) From the Same Sediments Reacted with Hyperalkaline (1 M NaOH) Solutions for 24 Days.

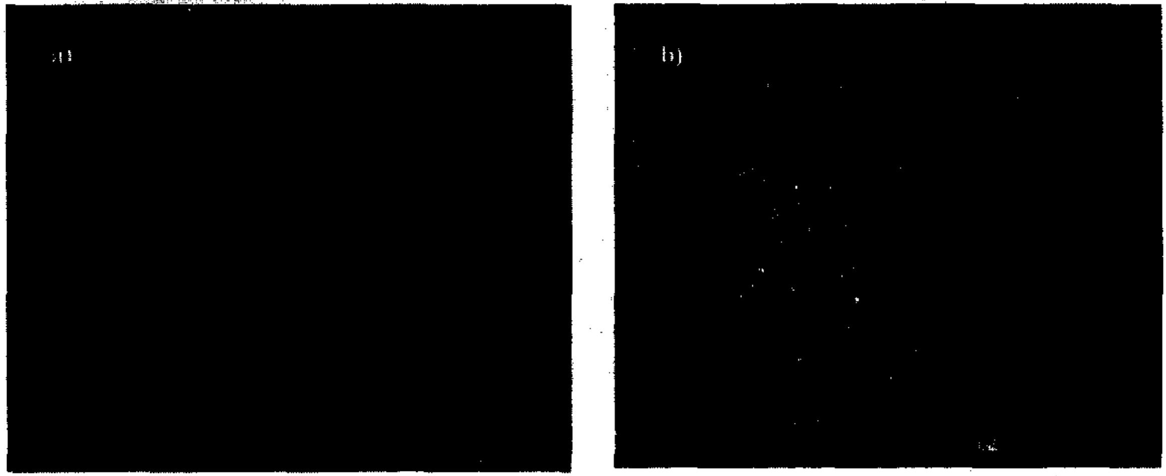

Two points relevant to the present Cr discussion need to be made. First, high base fluids contacting Hanford sediment tend to dissolve/alter the smectite and mica fractions. This leads to the precipitation of secondary Fe and Al oxides and zeolites (D.2), but does not change the total Fe content of the sediment. Second, the oxides precipitated on the biotite surface (Figure D.4.2.1b) are suggested to be Ti substituted Fe oxides or perhaps an ilmenite phase ($FeTiO_4$) (Section D.1.1). The potential for Ti substitution in secondary Fe oxides results from the dissolution of Ti containing smectites and micas. Isomorphic substitution of Ti(IV) for Fe(III) in the Fe oxide structure can impart a permanent positive charge component to the oxide and significantly increase the point of net zero charge of the oxide (Cornell and Schwertmann 1996). This could affect the strength of the chromate-oxide surface interaction at the pH levels observed in these sediments.

The total Cr content and the Cr(VI)/Cr(III) ratio varied in the four sediments studied (Table D.4.2.1). The possible reasons for these variations may be related to: (1) the sediment's position relative to the waste-fluid flow path, (2) the residence time of the fluid, and (3) the nature, rate, and extent of reactions leading to the retardation of the Cr(VI). The first two hypothesized reasons are difficult to access since no spatial distribution information is available other than the two collected cores. The latter aspect of reactivity is being addressed under several EMSP projects and is discussed in several sections of this report (Sections D.4.1, D.4.3, and D.4.4). While there is a small quantity of native Cr present in the Hanford sediments (approximately 60 to 100 μg/g sediment; Serne et al. 2001c) the vast majority of the Cr found under the S and SX tank farms originated from tank leaks. The contaminant ion in the waste supernate was undoubtedly the $Cr(VI)O_4^{2-}$ anion (Lichtner 2001; this report), while the Cr(III) observed in the sediments (Section D.4.1) resulted from the in situ reduction of Cr(VI). Research by S&T Program and EMSP investigators observe, in laboratory studies, the reduction of Cr(VI) by Fe(II) released from the base dissolution of biotite and by the Fe(II) in magnetite (a mixed valance Fe oxide) (Sections D.4.3 and D.4.4).

Using epoxy-impregnated, 0.1-mm-thick sections of different sediments, Heald (at the APS, Argonne National Laboratory) measured selected regions of SX-108 3A and 7A thin-sections for the distribution of Cr by micro X-ray fluorescence spectroscopy. Figure D.4.2.2 shows the results of such an analysis for sediment 7A as a series of elemental maps for Cr, K, Fe, Mn, and Ti. The bright spots (red/yellow) on the Cr map (Figure D.4.2.2) matched the bright spots associated with K, Fe, Mn, and Ti. These Cr "hot spots" were examined by XAFS spectroscopy and were shown to be Cr(III) (spectra not shown). Five regions in the 7A sediment thin section and two regions in the 3A sediment thin section were interrogated in a similar manner. In every case but one, the Cr species identified was Cr(III). Only one Cr "hot spot" showed the possible presence of both Cr(III) and Cr(VI).

Figure D.4.2.2. A Slice of the SX-108 7A Sediment Thin Section Delineating Region 1 and the Results of the Elemental Micro-Mapping Performed on Region 1; the Colored Bar Shows, Qualitatively, the Concentration of a Given Element (Intensity Increases From Blue to Red).

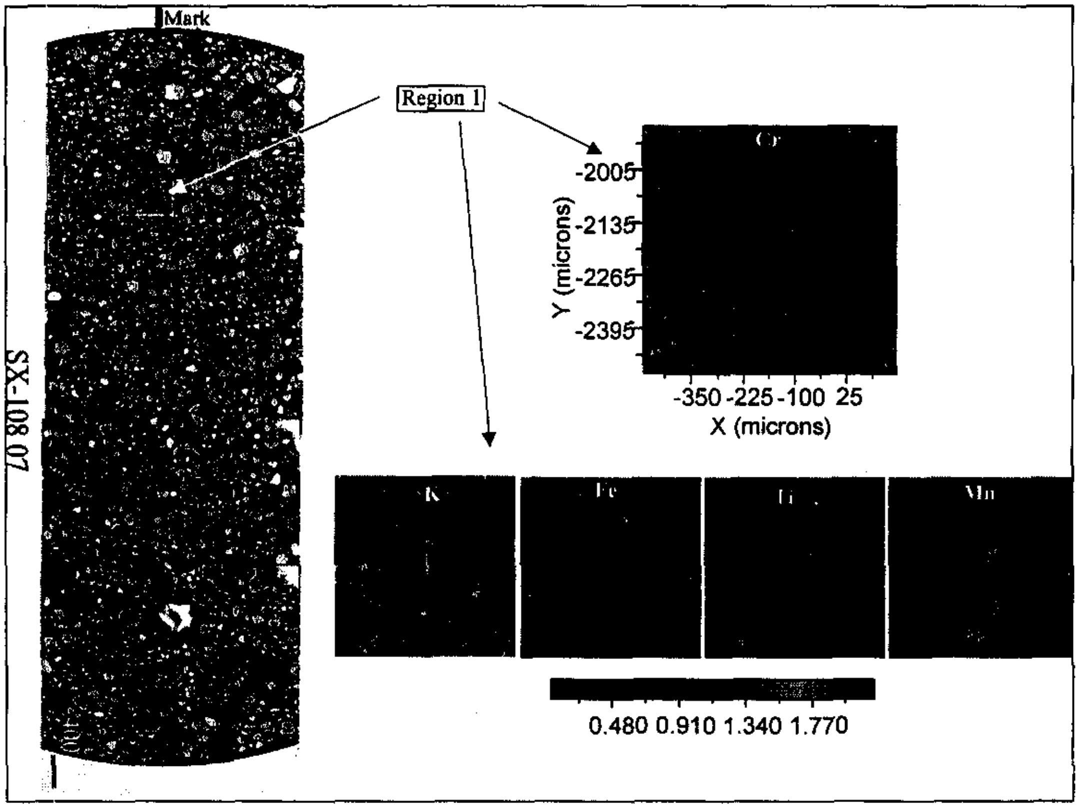

The "hot spot" in the center of the Cr map (Figure D.4.2.2) was coincident with those of Mn, Fe, and Ti. A SEM of region 1 is shown in Figure D.4.2.3 (bottom micrograph). The bright, circled image was indicative of a titanomagnetite or ilmenite phase (as determined by energy-dispersive spectroscopy). Overlaying the Cr map from region 1 showed that the Cr intensity was associated with titanomagnetite or ilmenite particle, and was Cr(III). This relationship between Cr(III), Fe, Mn, and Ti with a titanomagnetite or ilmenite surface is understandable. Ferrous iron is a common component of titanomagnetite and ilmenite; isomorphic substitution of Mn for Fe^{2+} is also common in these oxide minerals. It is suspected that heterogeneous reduction of Cr(VI) by Fe(II) and Mn(II) occurs at the surface of these oxide minerals with the reduced Cr forming mixed metal (Fe, Mn, and Ti) oxides. It is unclear at this time whether the Fe(II) is dissolved from the titanomagnetite and then reduces Cr(VI), or if Cr(VI) is initially sorbed and subsequently reduced. Similarly, the dissolution of biotite and concomitant solubilization of Fe(II) is thought to affect the reduction of Cr(VI) proximal to the point of Fe(II) release.
The two bright spots just below the circle in Figure D.4.2.3 correlate well with a K bright spot in Figure D.4.2.2. The underlying mineral is suspected to be a biotite mica flake. These results complement the findings of Catalano et al. as reported in Section D.4.1. That is, Cr(III) tends to be heterogeneous distributed and isolated to a number of Cr "hot spots," whereas, Cr(VI) is more uniformly distributed throughout the sediment.

Figure D.4.2.3. SEM Image of Region One of a Thin Section of Sediment SX-108 7A with a Biotite Flake Highlighted and the Cr Micro-Map Overlayed.

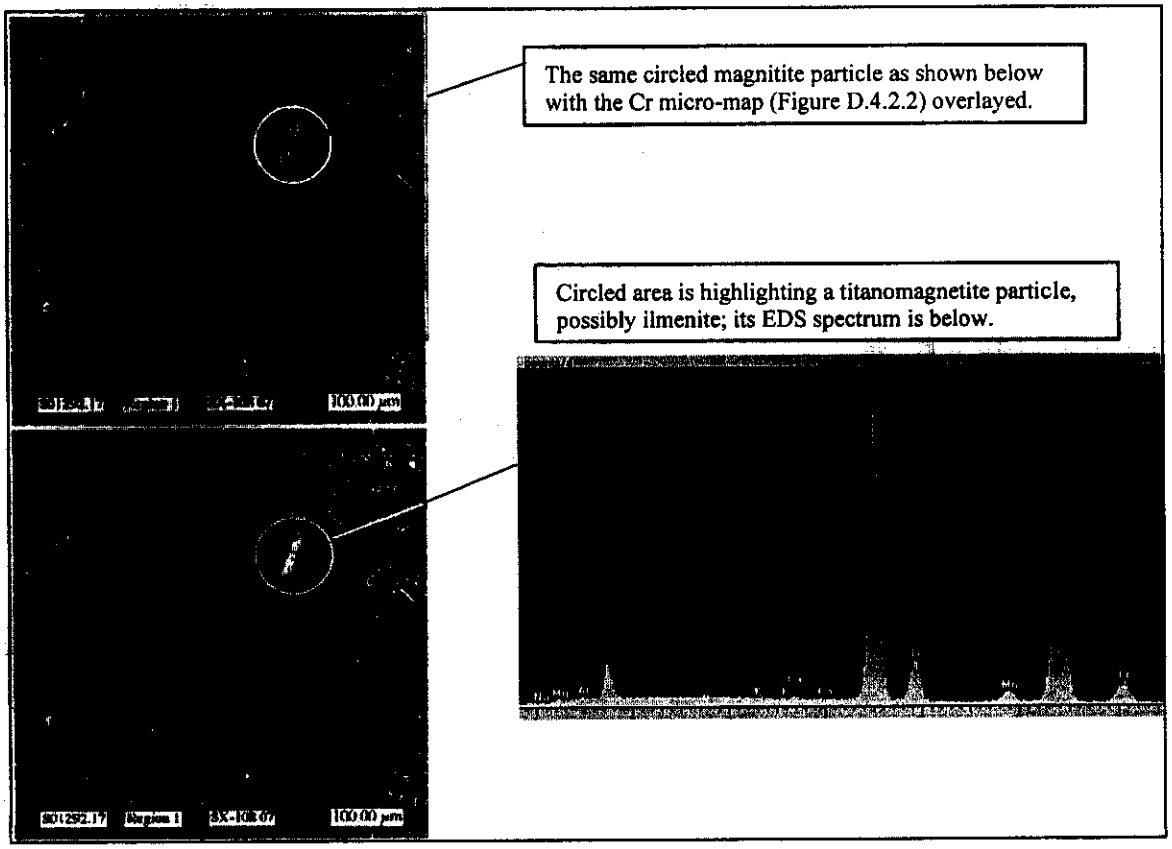

The same circled magnitite particle as shown below with the Cr micro-map (Figure D.4.2.2) overlayed.

Circled area is highlighting a titanomagnetite particle, possibly ilmenite; its EDS spectrum is below.

Chromium was rapidly leached from contaminated S-SX sediments, presumably as the CrO_4^{2-} ion (Figure D.4.2.4, Table D.4.2.2). The initial pulse of Cr(VI) (1 to 4 pore volumes) accounted for 48%, 48%, 67%, and 113% of the Cr(VI) leached from 7A, 8A, 6AB, and 7ABC, respectively. An additional 15%, 8%, 12%, and 14% of the Cr(VI) was leached from 7A, 8A, 6AB, and 7ABC, respectively, after the first 4 pore volumes. While much of the Cr(VI) was leached from the sediments (Table D.4.2.2), 127% of the Cr(VI) was removed from 7ABC. This result reflects variation between subsamples of the same sediment rather than Cr(III) oxidation. It is unlikely that Cr(III) will oxidize under the conditions of these studies (James and Bartlett 1983). The variable release of Cr(VI) from the four sediments studied may result from pH, Fe oxide content, and/or the ionic strength of the solution.

Figure D.4.2.4. Column Effluent Cr(VI) Profiles of WMA S-SX Sediments Leached with 0.5 M/L $NaNO_3$.

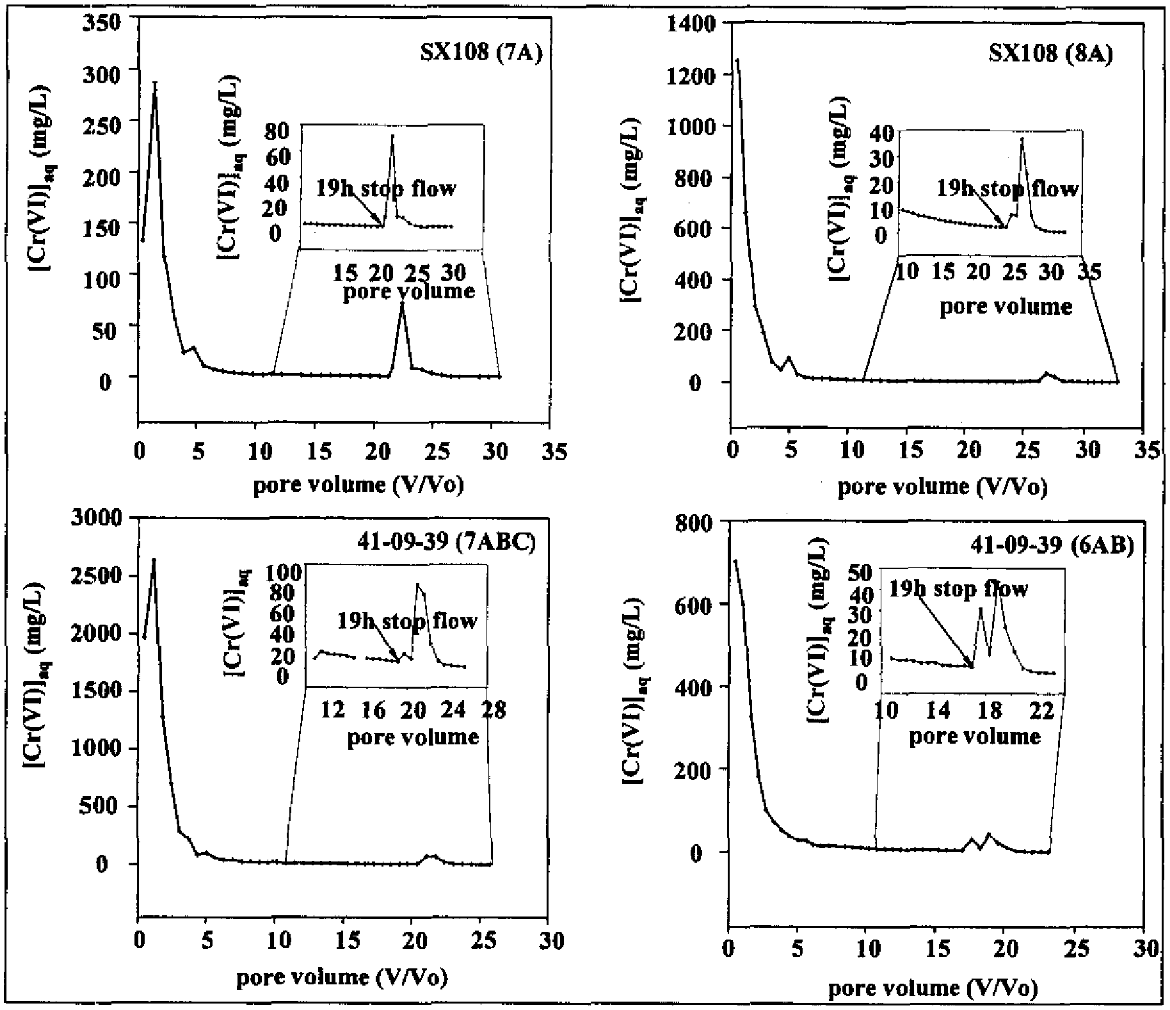

Table D.4.2.2. Initial and Cumulative Cr(VI) Concentrations From Column Effluents Associated with WMA S-SX Sediments Leached with 0.5 M/L $NaNO_3$.

Sediment	Cr in sediment			Cr (VI) leached from column experiments			
	Total	Cr (VI)	Cr (III)	Total	Initial[b]	Total	Initial
	μg/g					%[b]	
SX-108							
7A	1297	324	973	206	156	64	48
8A	2098	1112	986	629	537	57	48
41-09-39							
6AB	1186	605	581	480	405	78	67
7ABC	2090	1212	878	1542	1374	127	113

[a] First four pore volumes
[b] Versus total Cr (VI) in sediment

Sodium nitrate, probably present as a solid in these sediments, was in substantial excess of the leaching solution. The $NaNO_{3\,(s)}$ was solubilized as the sediment was wetted; hence, the initial $NaNO_{3\,(aq)}$ concentrations were at least (and possibly higher than) 3.6 mol/L, 3.1 mol/L, 2.1 mol/L, and 0.84 mol/L for 7A, 8A, 6AB, and 7ABC, respectively. These values are based on water extracts performed as part of the initial characterization of the sediments (Serne et al. 2001a, b). pH and electrolyte concentration can affect the retention of an oxyanion such as CrO_4^{2-} that forms weak outer-sphere complexes at the surfaces of Al and Fe oxides (Ainsworth et al. 1989; Zachara et al. 1989; Kent et al. 1995) and layer Al silicate edges (e.g., kaolinite; Zachara et al. 1988). At pH values observed in the sediments (9.6 [7A], 8.7 [7ABC], 8.3 [6AB], and 7.8 [8A]), the variable charge surfaces that bind Cr(VI) will manifest neutral to negatively charged surfaces, limiting the formation of outer-sphere complexes involved in sorption. In addition, at the aforementioned ionic strengths, the NO_3^- ion could compete with Cr(VI)O_4^{2-} for adsorption sites.

Early, preliminary modeling efforts of the Cr(VI) column data (Figure D.4.2.4) have involved several approaches to identify hypotheses regarding mechanisms controlling the rate of Cr(VI) leaching from the sediments. All initial modeling approaches have assumed one-dimensional saturated transport (i.e., wetting was not included) with one or two reactions to describe CrO_4^{2-} solid-liquid partitioning: (1) no reaction (i.e., tracer breakthrough), (2) fast (i.e., equilibrium) desorption/ dissolution with a single reaction, (3) a single kinetic desorption reaction (first-order), (4) a single kinetic desorption reaction with a limited total mass (i.e., second-order reaction), and (5) two dissolution reactions (each written as pseudo-1st-order). Parameters that are well known (velocity, dispersivity) were fixed during simulations. Hydrodynamic dispersion was determined from tracer data. In these studies, tracer experiments were conducted in each column after CrO_4^{2-} leaching.

Initial modeling results indicated that the initial pulse of soluble CrO_4^{2-} (first 4 pore volumes) could be accounted for by a single first-order kinetic reaction with a small K_d value (less than 0.02 cm^3/g) and fairly fast rate (approximately 8 to 19 minutes $t_{1/2}$). These parameters are consistent with chromate-salt dissolution (fast), or desorption of a weakly adsorbed species in the face of strong competition. The elution of additional chromate mass in the next 30 pore volumes could not be accounted for by one or two simple pseudo-1st-order reactions, but could be accounted for by a slow fractional order chemical reaction or diffusion process. These latter parameters are consistent with those expected for dissolution of a salt with limited solubility.

The leaching and modeling results indicate that there are multiple species of Cr(VI) in the sediment. The largest fraction (represented by the first 4 pore volumes) is only weakly held against transport. Whether this fraction is a fast-dissolving chromate salt (i.e., Na_2CrO_4) or a weakly bound outer-sphere complex cannot be discerned from these studies. However, there was a second, smaller pool of Cr(VI), defined as the Cr(VI) released beyond 4 pore volumes, which exhibited greater retardation than expected for Cr(VI) in the Hanford sediments.
At present, we hypothesize that the second pool of Cr(VI) is represented by CrO_4^{2-} sorbed to secondary Fe oxides. For those sediments most affected by tank-leaked fluids (3A, 7A, and to a lesser extent 8A), the Fe oxides present may exhibit surface properties common to Ti-substituted Fe oxides and present a very different CrO_4^{2-} adsorption potential than typically observed for soil oxides; yielding a larger K_d than expected. Typically, K_d values for CrO_4^{2-} in Hanford aquifers are low; probably below those estimated for the first 4 pore volumes (Jim Szecsody, personal communication).

Batch Cr solubilization studies with $(NH_4)_2C_2O_4$ were performed in conjunction with Cs release studies using sediments SX-108 3A and 7A, and 4109-39 7ABC and 9ABC. Only the results from the 7A and 7ABC studies will be shown here as data is lacking for Cr speciation in the other sediments. Over a period of 32 days, the aqueous concentration of Fe, Al, and Cr (total) increased in a curvilinear fashion (Figure D.4.2.5). While the rate of increase slowed over time, the metal concentrations had not attained aqueous phase steady-state conditions in 32 days. After 32 days, the $(NH_4)_2C_2O_4$ had extracted 1537 μg/g Cr from 7ABC [107% of the estimated Cr(VI) or 75% of total Cr] and 778 μg/g Cr from 7A [219% of the estimated Cr(VI) or 60% of the total Cr]. It is difficult to rationalize the Cr concentrations observed in the extracts given the XAS results and previously discussed column studies without concluding that the $(NH_4)_2C_2O_4$ solubilized at least some of the Cr(III) in these sediments.

Figure D.4.2.5. Al, Fe, and Cr Solubilization as a Function of Time for Two WMA S-SX Sediments, a) SX-108 7A, and b) 41-09-39 7ABC by 0.25 M/L $(NH_4)_2C_2O_4$.

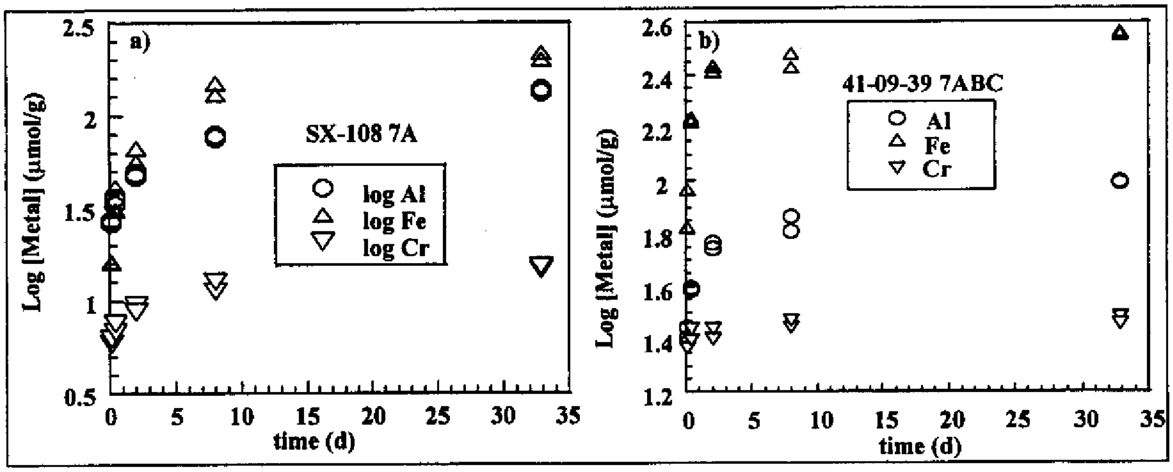

The solubility of pure amorphous $Cr(OH)_3$ (log $K_{sp} = 5.62$) supports about 10^{-3} M Cr(III) in solution at pH 3 to 4 (Rai et al. 1986). In the present sediments, however, Cr(III) is suggested to be present as mixed metal oxides (or hydroxides) rather than a pure Cr phase. Amorphous $Fe,Cr(OH)_3$ solids do form at ambient temperatures and tend to form solid solutions whose Cr(III) solubility decreases from that observed for $Cr(OH)_3$ depending on the mole fraction of Cr in the solid (Rai et al. 1986). At low mole fractions expected in geologic environments, Rai et al. reported that the equilibrium aqueous Cr(III) concentration would be 1 to 3 orders of magnitude lower than that expected from $Cr(OH)_3$. In the present case, at pH 3 to 4), that would still support substantial $Cr(III)_{aq}$ concentrations. However, the time required to reach equilibrium $[Cr(III)]_{aq}$ is a function of its solid solution mole fraction. Rai et al. (1986) found that equilibrium conditions were obtained only after 7 to 90 days depending on the mole fraction of Cr. James and Bartlett (1983) demonstrated that Cr(III) solubilization and oxidation in soils could be enhanced in the presence of citrate, presumably by complexation; although the rate of Cr(III) oxidation was dependent on Cr(III) form. If as suspected from the XAS investigations reported here and by Catalano et al. (Section D.4.1), Cr and Fe are well correlated, then solubilization of Fe oxides by the Tamm's reagent (Loeppert and Inskeep 1996) could facilitate Cr(III) solubilization. Clearly, there is a potential for Cr(III) solubilization in 0.25 M $(NH_4)_2C_2O_4$ at pH 3 to 4 (by the end of the study the pH had shifted slightly in all sediments to 3.5 to 4.1). At this time, however, the rate of Cr(III) solubilization and its concentration in these suspensions is not known.

A regression comparison of extract Fe or Al concentrations versus aqueous Cr concentration yield linear relationships with high correlation coefficients (Figure D.4.2.6). The r^2 values for Fe and Al versus Cr extract concentrations are 0.98 and 0.93 and 0.94 and 0.95 for sediment 3A and 7A, respectively. The Al correlation coefficients for these sediments probably reflect the substitution of Al (and other metals) for Fe in all Fe oxides (Connell and Schwertmann 1996) or the presence of poorly crystalline Al oxide phases. An additional source of Al (and Si) may be the slow acid dissolution of layer silicate minerals. While the dissolution rate of layer silicates is slow at pH 3 and 4, the dissolved solids reported in Section D.3.6 (Table D.3.6.2) shows that after 33 days between 1.73 and 2.77% of the sediment mass had been solubilized (based on Fe, Al, and Si analysis and expressed as oxides). Regardless of the speciation of Cr [Cr(III) and/or Cr(VI)] in these extracts, there is a clear relationship between Cr and sediment Al and Fe oxides.

Figure D.4.2.6. Relationship Between 0.25 M/L $(NH_4)_2C_2O_4$ Solubilized Fe or Al with Cr as a Function of Time for Two WMA S-SX Sediments, a) SX-108 7A, and b) 41-09-39 7ABC.

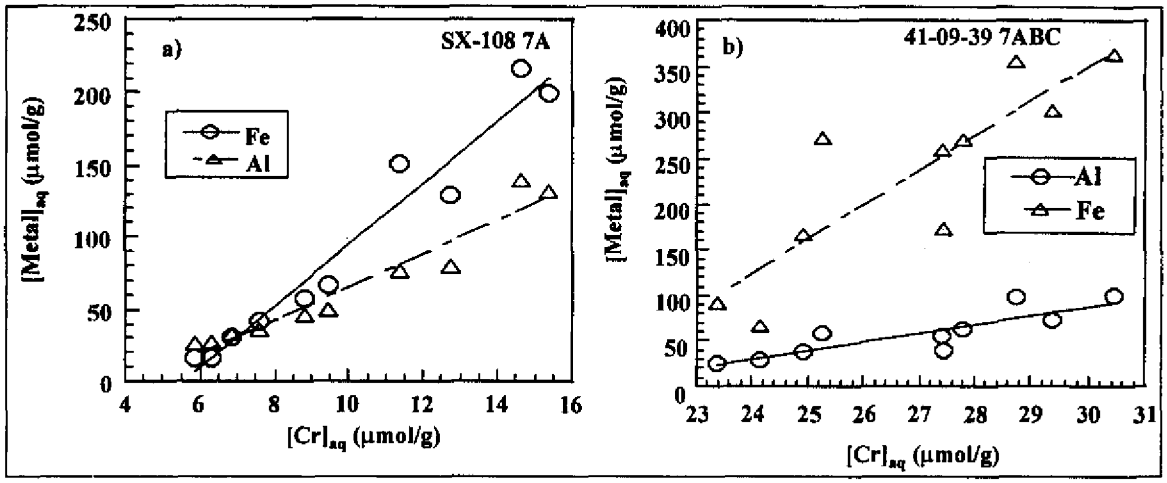

To further investigate the potential relationship between Fe, Al oxides, and Cr in the sediments associated with the WMA S-SX sediments two additional column experiments were performed. These were similar to the previous column studies except 0.5 mol/L KNO_3 was used to elute Cr(VI) for the first 21 pore volumes, followed by 0.25 mol/L $(NH_4)_2C_2O_4$ for approximately 25 pore volumes. Similar to the $NaNO_3$ eluted columns, KNO_3 eluted large quantities of Cr(VI) in the first 4 pore volumes (Figure D.4.2.7; Table D.4.2.3). The initial Cr(VI) concentration eluted from sediment 7ABC was about 2 times less than the previous column results (558 μg/g versus 1374 μg/g), while 7A elution increased slightly (235 μg/g from 156 μg/g). The variation in these data and in relation to the assumed total Cr and Cr(VI) is related to the variability between samples and is a natural consequence of studying actual sediments. Yet, even with the observed variations, the same precipitous decrease in effluent concentration and cumulative Cr(VI) elution over the initial pore volumes was not significantly changed between the two experiments.

Figure D.4.2.7. Column Effluent Cr(VI) Profiles of WMA S-SX Sediments Leached with 0.5 M/L KNO_3 Followed by 0.25 M/L $(NH_4)_2C_2O_4$.

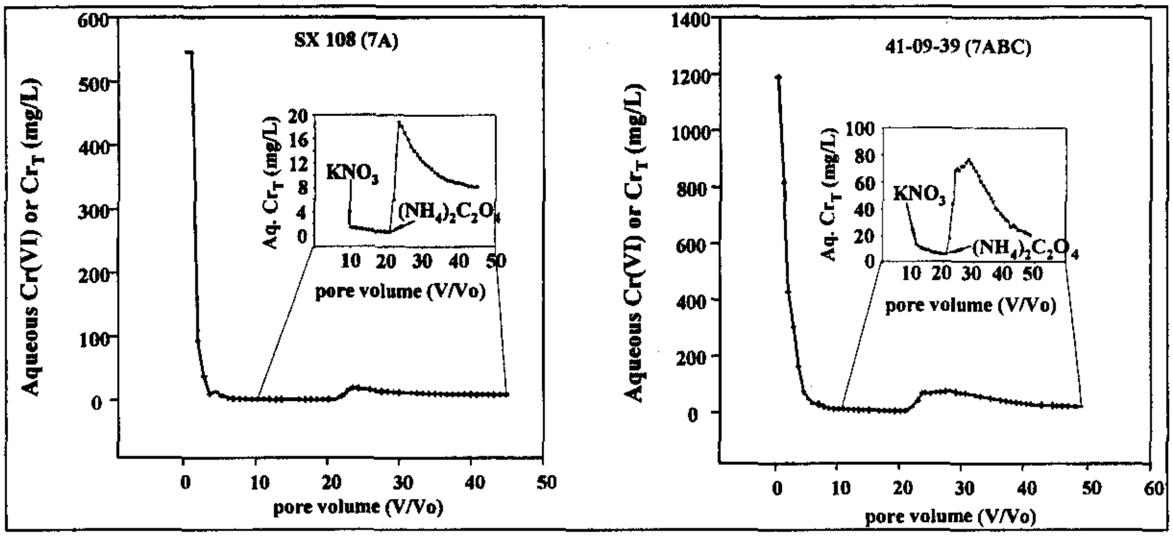

Table D.4.2.3. Initial and Cumulative Cr(VI) Concentrations in Column Effluents From WMA S-SX Sediments Leached with 0.5 M/L KNO_3 Followed by 0.25 M/L $(NH_4)_2C_2O_4$.

Sediment	Cr in sediment			Cr leached from columns			
	Total	Cr (VI)	Cr (III)	Total	Initial[a]	KNO_3[b]	Ox.[c]
	µg/g						
SX108							
7A	1297	324	973	325	235	243	82
41-09-39							
7ABC	2090	1212	878	1015	558	644	371

[a] Initial = sum of Cr(VI) in first 4 pore volumes.

[b] KNO_3 = [Cr(VI)] leached in the first 21 pore volumes by 0.5 mol/L KNO_3 solution.

[c] Ox = [Cr] leached by $(NH_4)_2C_2O_4$ beyond 21 pore volumes.

After the initial flush of Cr(VI), its elution from the sediments slowed markedly. After 21 pore volumes, the shift to 0.25 mol/L $(NH_4)_2C_2O_4$ leaching solution resulted in an immediate increase in Cr elution (see inserts Figure D.4.2.7; Table D.4.2.3). The increase in Cr release from the sediment was substantially greater and long lasting than that observed from a simple stopped-flow as in the previous column studies. While we do not know the speciation of Cr in the oxalate effluents, it was interesting to note that oxalate extracted only a limited amount of Cr and the total Cr leached from the columns did not exceed the expected total sediment Cr(VI) concentration. We are currently attempting to use ion chromatography to determine the Cr speciation.

In addition to the rising Cr concentration, Fe and Al increased concomitantly and the Fe to Cr ratio was stable in both sediments (Figure D.4.2.8). Iron solubilization by the $(NH_4)_2C_2O_4$ for sediment 7ABC was substantially different from 7A in both magnitude and profile. This may be a reflection of the greater Fe content found in 7ABC compared to the other sediments studied (see Table D.4.2.1). It was interesting that the Al solubilization magnitude and profile are similar between the two sediments. This suggests that Al plays a bigger role in the 7A sediment, as discrete, poorly crystalline Al oxide or Al substituted Fe oxides, than 7ABC. Whether this is related to the leaked fluids from tank SX-108, reported to have high $Al(OH)_4^-$ concentration, it is difficult to surmise. Yet, in both sediments (and in the batch studies) the aqueous Cr concentrations are well correlated to solubilized Fe and Al levels.

Figure D.4.2.8. Profile of Al, Fe, and Cr Concentrations in Column Effluent After Switching Eluents From 0.5 M/L KNO_3 to 0.25 M/L $(NH_4)_2C_2O_4$ at Pore Volume 21 (Only Even Numbered Pore Volumes are Shown for Clarity).

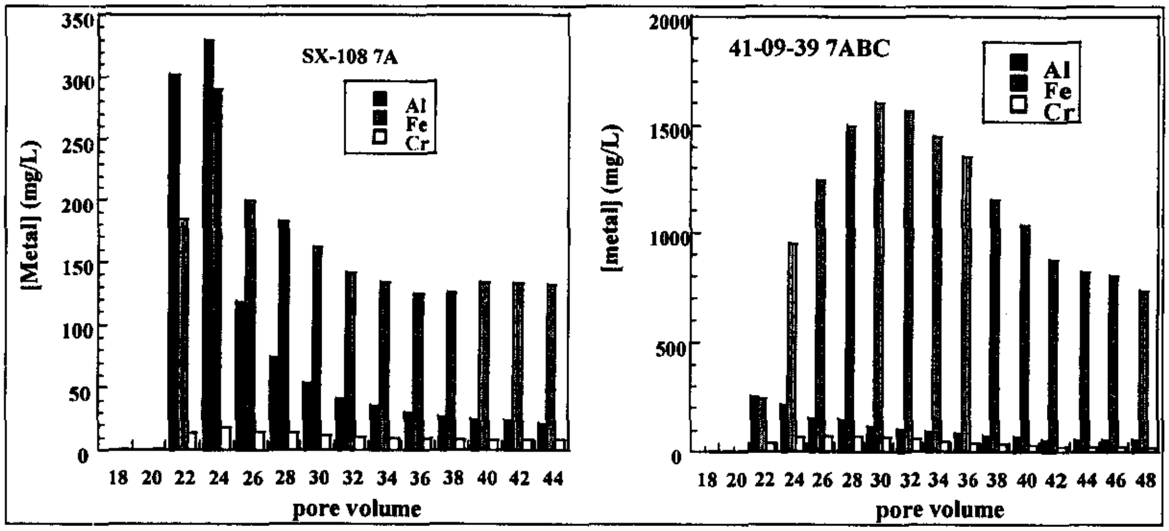

D.4.2.4 Conclusions

These studies, in conjunction with the XAS studies discussed here and by Catalano et al. (Section D.4.1), yields a picture of Cr(VI) dispersed throughout the sediments studied rather than in isolated, highly heterogeneous concentrations as is the case for Cr(III). There appear to be two pools of Cr(VI) in the contaminated sediments studied to date. The largest pool is released rapidly with limited or no retardation. The residual $NaNO_3$ from tank-leaked fluids appears to assist in the mobilization of this pool of Cr(VI). The second pool of Cr(VI) is more strongly bound to the sediments (albeit only slightly). However, it is unclear at this time whether this division into two pools is an artifact of the high ionic strength of the first few pore volumes or related to (1) the presence of a soluble Cr salt (probably Na based) versus a smaller pool of Cr weakly bound as outer-sphere complexes at oxide surfaces, or (2) different pools of Cr(VI) exhibiting different surface binding strengths. The later time periods of the batch study and particularly the $(NH_4)_2C_2O_4$ leaching clearly showed that the "second pool" of Cr(VI) is associated with the Fe, Al oxide fraction of the sediments. As such, it is subject to competition from the soluble salts found in the sediments. Regardless of the Cr(VI) pool, the majority of the

Cr(VI) currently in the vadose zone is extremely mobile and its retardation, from the results of column studies, appears minimal.

D.4.2.5 References

Ainsworth, C. C., D. C. Girvin, J. M. Zachara, and S. C. Smith, 1989, "CrO_4^{2-} Adsorption on Goethite: Effects of Aluminum Substitution," *Soil Science Society of America Journal*, Vol. 53:411-418.

Bartlett, R. J., and B. R. James, 1996, "Chromium," *In* D. L. Sparks et al. (ed.), *Methods of Soil Analysis; Part 3—Chemical Methods*, pp. 683-701, SSSA Book Series: 5, Soil Science Society of America, Inc., Madison, Wisconsin.

Brown, G. E. Jr., V. E. Henrich, W. H. Casey, D. L. Clark, C. Eggleston, A. R. Felmy, D. W. Goodman, M. Gratzel, G. Machiel, M. I. McCarthy, K. H. Nealson, D. A. Sverjensky, M. F. Toney, and J. M. Zachara, 1998, "Metal Oxide Surfaces and Their Interactions with Aqueous Solutions and Microbial Organisms," *Chemical Reviews*, Vol. 99/1:77-174.

Cornell, R. M., and U. Schwertmann, 1996, "The Iron Oxides. Structure, Properties, Reactions, Occurrence and Uses," BCH Verlagsgesellschaft mbH, D-69451, Weinheim (Federal Republic of Germany).

James, B. R., and R. J. Bartlett, 1983, "Behavior of Chromium in Soils. VI. Interactions Between Oxidation-Reduction and Organic Complexation," *Journal of Environmental Quality*, Vol. 12/2:173-176.

Jones, T. E., R. A. Watrous, and G. T. Maclean, 2000, "Inventory Estimates for Single-Shell Tank Leaks in S and SX Tank Farms," RPP-6285, Rev. 0, CH2M HILL Hanford Group, Inc., Richland, Washington.

Kent, D. B., J. A. Davis, L. C. D. Anderson, and B. A. Rea, 1995, "Transport of Chromium and Selenium in a Pristine Sand and Gravel Aquifer: Role of Adsorption Processes," *Water Resources Research*, Vol. 31:1041-1050.

Lichtner, P. C., 2001, *Estimating Tank Supernatant Liquid Compositions*, LA-UR-01-1403, Los Alamos National Laboratory, Los Alamos, New Mexico.

Loeppert, R. L., and W. P. Inskeep, 1996, "Iron," *In* D. L. Sparks et al. (ed.), *Methods of Soil Analysis; Part 3 – Chemical Methods*, pp. 639-644, SSSA Book Series: 5, Soil Science Society of America, Inc., Madison, Wisconsin.

Rai, D., J. M. Zachara, L. E. Eary, D. C. Girvin, D. A. Moore, C. T. Resch, B. M. Sass, and R. L. Schimdt, 1986, "Geochemical Behavior of Chromium Species," *EA-4544*, Electric Power Research Institute, Palo Alto, California.

Serne, R. J., G. V. Last, G. W. Gee, H. T. Schaef, D. C. Lanigan, C. W. Lindenmeier, R. E. Clayton, V. L. LeGore, R. D. Orr, M. J. O'Hara, C. F. Brown, D. B. Burke, A. T. Owen, I. V. Kutnyakov, and T. C. Wilson, 2001a, *Geologic and Geochemical Data Collected from Vadose Zone Sediments from Borehole SX 41-09-39 in the S/SX Waste Management Area and Preliminary Interpretations*, PNNL-2001-2, Pacific Northwest National Laboratory, Richland, Washington.

Serne, R. J., H. T. Schaef, G. V. Last, D. C. Lanigan, C. W. Lindenmeier, R. E. Clayton, V. L. LeGore, M. J. O'Hara, C. F. Brown, R. D. Orr, I. V. Kutnyakov, T. C. Wilson, D. B. Burke, B. A. Williams and B. N. Bjornstad, 2001b, *Geologic and Geochemical Data Collected from Vadose Zone Sediments from the Slant Borehole under SX-108 in the S/SX Waste Management Area and Preliminary Interpretations*, PNNL-2001-4, Pacific Northwest National Laboratory, Richland, Washington.

Serne, R. J., H. T. Schaef, B. N. Bjornstad, B. A. Williams, D. C. Lanigan, D. G. Horton, R. E. Clayton, V. L. LeGore, M. J. O'Hara, C. F. Brown, K. E. Parker, I. V. Kutnyakov, J. N. Serne, A. V. Mitroshkov, G. V. Last, S. C. Smith, C. W. Lindenmeier, J. M. Zachara, and D. B. Burke, 2001c, *Characterization of Uncontaminated Sediments from the Hanford Reservation-RCRA Borehole Core and Composite Samples*, PNNL-2001-1, Pacific Northwest National Laboratory, Richland, Washington.

Zachara, J. M., C. C. Ainsworth, C. E. Cowan, and C. T. Resch, 1989, "Adsorption of Chromate by Subsurface Soil Horizons," *Soil Science Society of America Journal*, Vol. 53/2:418-428.

Zachara, J. M., C. E. Cowan, R. L. Schmidt, and C. C. Ainsworth, 1988, "Chromate Adsorption by Kaolinite," *Clay and Clay Minerals,* Vol. 36:317-326.

D.4.3 FATE AND TRANSPORT OF CR(VI) IN HANFORD SEDIMENTS TREATED WITH AL-RICH, ALKALINE AND SALINE SOLUTIONS

Nikolla P. Qafoku[1], Calvin C. Ainsworth[1], and James E. Szecsody[1]

[1]Pacific Northwest National Laboratory, Richland, Washington 99352

D.4.3.1 Introduction

Hexavalent chromium should be highly mobile in Hanford vadose zone sediments under alkaline conditions. Amphoteric mineral sorbents will generally be deprotonated, exhibiting negative charge density, and tank waste anions including NO_3^- and OH^- will strongly compete for the few sites with favorable complexation properties. However, recent observations of Cr transport in the S and SX tank farms indicate that the movement of Cr was retarded (Serne et al. 2001d). We have speculated, in our EMSP research, that REDOX waste-sediment reaction has induced conditions favorable to Cr(VI) retardation. Since the hypothesized processes are not well known, the objective of this investigation was to study the mechanisms that control the fate of Cr(VI) in the Hanford sediments treated with Al-rich, alkaline and saline solutions similar to REDOX tank wastes.

D.4.3.2 Experimental Procedure

Saturated one-dimensional miscible displacement experiments to study retardation reactions of Cr(VI) in Hanford sediments were performed under alkaline and high-ionic strength conditions. For this purpose, three columns were packed to similar bulk densities (1.50, 1.47, and 1.53 g/cm, respectively) with Hanford sediments. A high-performance liquid chromatographic (HPLC) pump was connected to the columns that were oriented vertically inside a water bath at 50 °C. The leaching solutions were injected at the bottom of the columns to eliminate gravity settling. The leaching solutions were prepared in a CO_2 and O_2 free glove box and were kept inside sealed 3 L plastic bottles. The atmosphere above the leaching solution was continuously saturated with helium gas. The column effluent was collected in sealed 60 mL plastic bottles. Approximately 20 mL of degassed deionized-water was added immediately to each sample to dilute the effluent and avoid precipitation upon cooling. Prior to leaching experiments, the soil columns were slowly saturated and leached with degassed deionized-water for approximately 5 pore volumes.

The first column experiment was performed with a pH neutral, 10 mg/L $Na_2CrO_4 \bullet 4H_2O$ solution to evaluate the reactive transport of CrO_4^{2-} in the absence of REDOX waste simulants. When the Cr(VI) breakthrough curve (BTC) was completed, indicated by equal input and output Cr(VI) concentrations, the leaching solution was changed to one containing 1M NaOH, 1M $NaNO_3$, 0.055 M $Al(NO_3)_3 \bullet 9H_2O$, and 10 mg L^{-1} Cr(VI) as $Na_2CrO_4 \bullet 4H_2O$, hereafter referred to as the alkaline solution. This solution was considered to be a representative of REDOX tank wastes. The second and the third columns were leached from the beginning with the alkaline solution. The fluid residence time in the first, second, and third columns were 8.05, 9.35, and 35.69 hours, respectively.

When chemical steady-state was established in the second column, the flow interruption method (Brusseau et al. 1997) was used to evaluate the Cr(VI) removal rate. Following the termination of each displacement experiment, the columns were dismantled, and the soil was sliced in 3 cm long sections and washed twice with DI-water. Total amounts of Al, Si, K, Mg, Ca, Ba, Cr, Mn, and Fe contents were determined in column effluents and solid sediments using ICP and Energy Dispersive X-ray Fluorescence Spectroscopy (EDXRF), respectively. A UV spectrophotometer was used to measure Cr(VI) in columns effluents. The CXTFIT computer program (Toride et al. 1999) was used to determine transport constants from the soil column Cr(VI) BTC, using the conventional single-region flow concept. The value of the mean pore water velocity (0.01596 cm min^{-1}) was calculated from experimental data, and was used in the program to determine the values of the two other constants of the convection-dispersion equation, namely dispersion coefficient (D) and retardation coefficient (R).

D.4.3.3 Results

In the absence of REDOX waste simulants, Cr(VI) showed no retardation in the Hanford sediment (Figure D.4.3.1). Although the Cr(VI) BTC exhibited tailing in the upper section where Cr(VI) concentrations were smaller than that in the input solution (10 mg/L), the retardation coefficient calculated with the CXTFIT computer program was less than one (R = 0.94). The adsorption of CrO_4 was nonexistent under these conditions. However, when the leaching solution was switched to the alkaline solution, the Cr(VI) concentration in the column effluent decreased steadily and reached the steady-state concentration after approximately 15 pore volumes, which was about 22% less than concentration in the input solution (Figure D.4.3.2). By 100 hours (14 pore volume), 1.75 mg/L chromate was being continuously removed from the aqueous phase. This rate, which continued to the end of the experiment (additional 100 hours), is equivalent to a first-order half-life of 29 hours. It should be noted that the initial Cr(VI) breakthrough was unretarded and removal was gradual, as observed in other columns, suggesting that the removal process was slow or kinetically constrained.

Figure D.4.3.1. Cr Breakthrough Curve in the Hanford Sediments Leached with a Na_2CrO_4 (10 mg/L Cr) Solution.

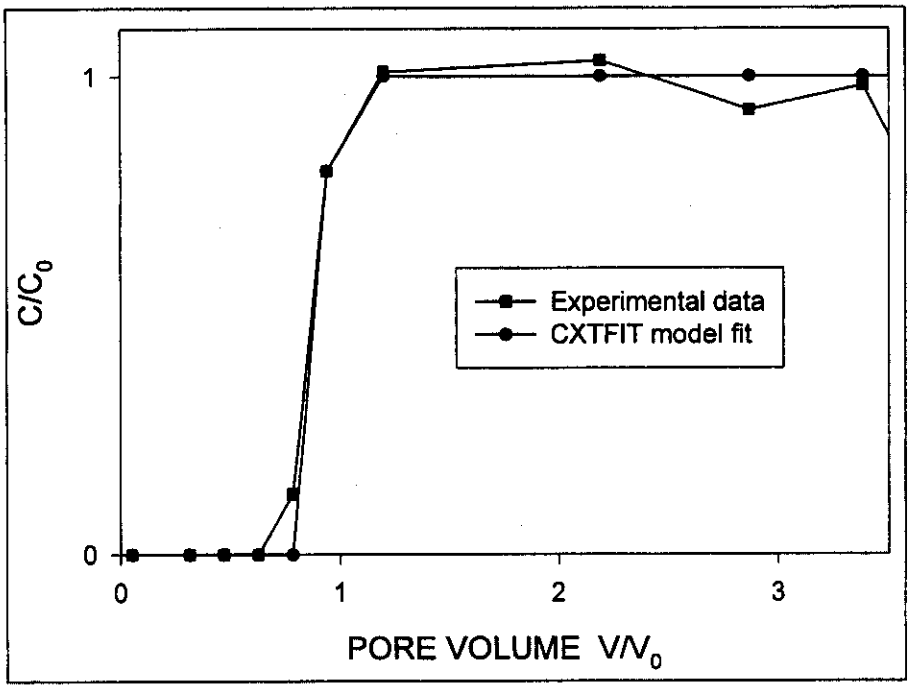

Figure D.4.3.2. Changes in Cr Concentration in the First Column During Leaching with a Na_2CrO_4 (10 mg/L Cr) Solution, and then with a Solution Containing 1M NaOH, 1M $NaNO_3$, 0.055 M $Al(NO_3)_3$, and Na_2CrO_4 (10 mg/L Cr) (residence time of 8.05 hours).

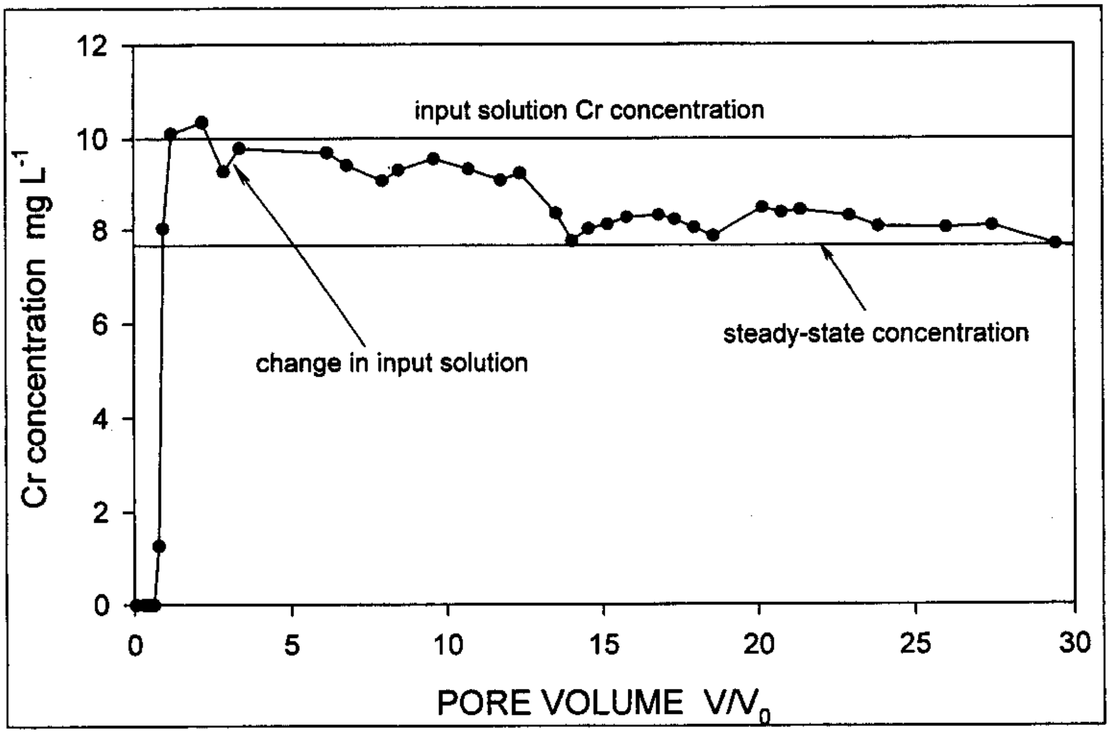

Cr(VI) transport was also retarded in the second column, which was leached from the beginning with the alkaline solution (Figure D.4.3.3). A steady-state concentration was reached after approximately 13 pore volumes, and that concentration was 27% smaller than the influent concentration, and 5% smaller than the steady-state concentration observed in the first column. In this column, 2.6-mg/L chromate was being continuously removed by 140 hours (15 pore volume), representing a first-order half life of 21.5 hours (slightly faster than that observed in the first column). Again, achieving this chromate removal rate was a gradual process. A strong relationship was found between total Cr and Cr(VI) in the column effluents (Figure D.4.3.4). This confirmed that only Cr(VI) was coming out in the column effluents.

Figure D.4.3.3. Changes in Cr(VI) Concentration in the Second Column During Leaching with a Solution Containing 1M NaOH, 1M $NaNO_3$, 0.055 M $Al(NO_3)_3$, and 10 mg/L Cr (residence time of 9.35 hours).

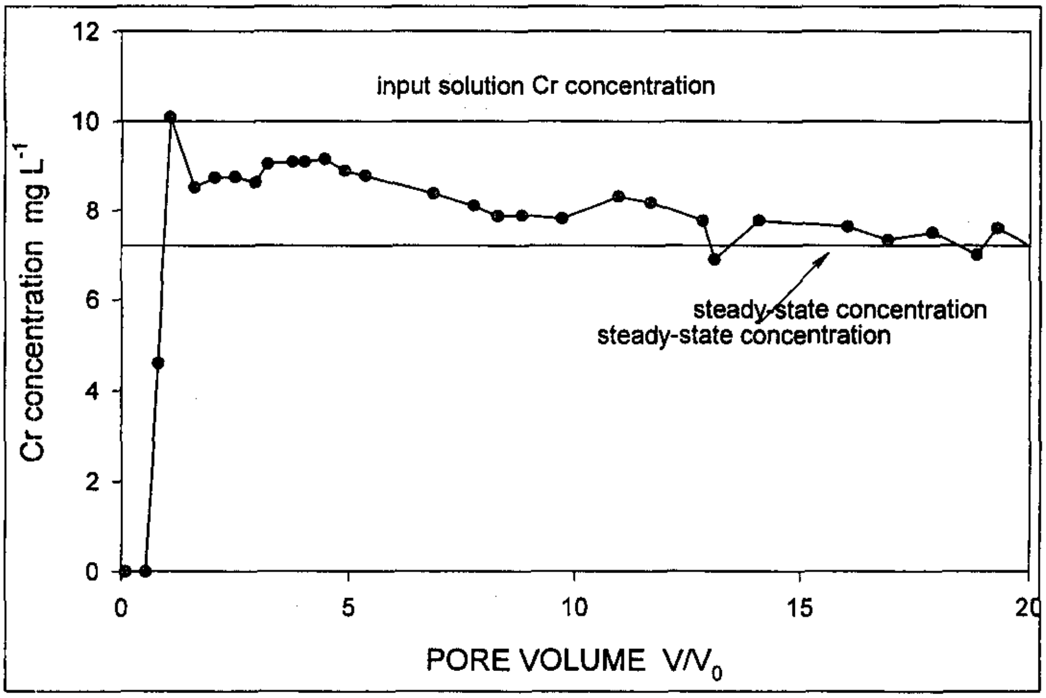

Figure D.4.3.4. Cr(VI) versus Total Cr Measured in the Column Effluent.

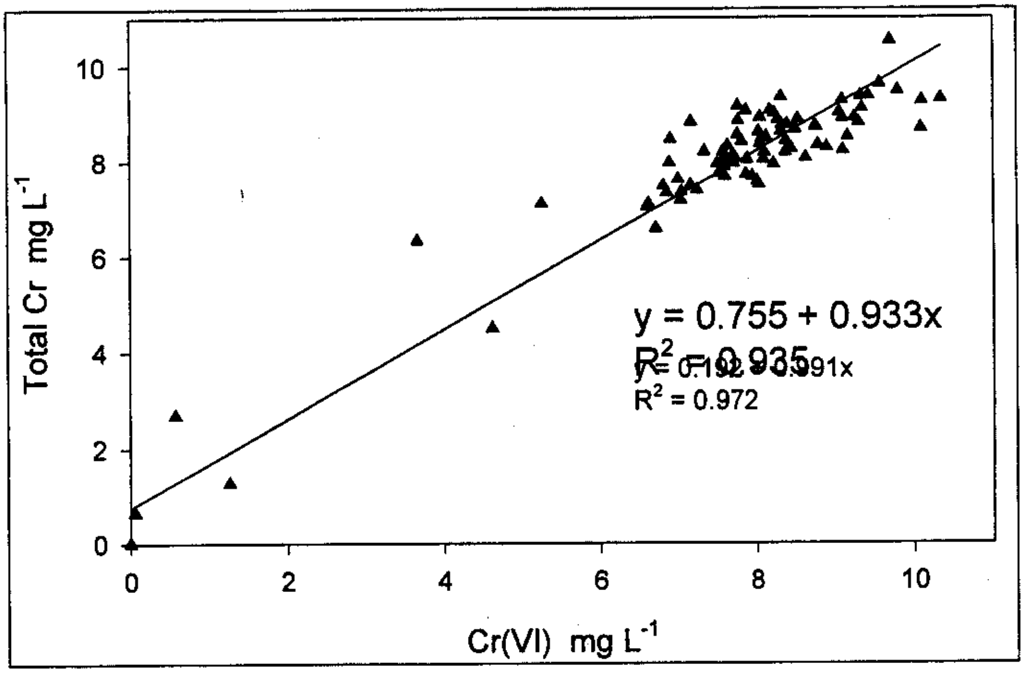

The time required to establish chromate removal was more clearly shown from the results of the third experiment, in which the fluid residence time (35.69 hours) was higher than that in the first and the second column (8.05 and 9.35 hours, respectively) (Figure D.4.3.5). The decrease in the Cr(VI) concentration in the column effluent was quite significant in this experiment, which was conducted for a greater time period (about 1000 hours). As with the first two columns, initial, nearly unretarded chromate breakthrough was observed (less than 1.2 pore volume) followed by a gradual decrease in the effluent chromate concentration. A steady-state chromate concentration took about 400 hours (11 pore volume) to achieve, during which time step decreases in chromate concentration were observed (i.e., 1 to 11 pore volumes). Pseudo-first order Cr(VI) removal rates were calculated at these step concentrations, and illustrated the gradual increase in the removal rate: (1) half-life of 110 hours by 140 hours or 4 pore volume, (2) half-life of 32 hours by 210 hours or 6 pore volume, (3) half life of 17 hours by 300 hours or 8.5 pore volume, and (4) half-life greater than 9.6 hours by 400 hours or 11 pore volume (Figure D.4.3.5).

Figure D.4.3.5. Changes in Cr(VI) Concentration in the Third Column During Leaching with a Solution Containing 1M NaOH, 1M $NaNO_3$, 0.055 M $Al(NO_3)_3$, and 10 mg/L Cr (residence time of 35.69 hours).

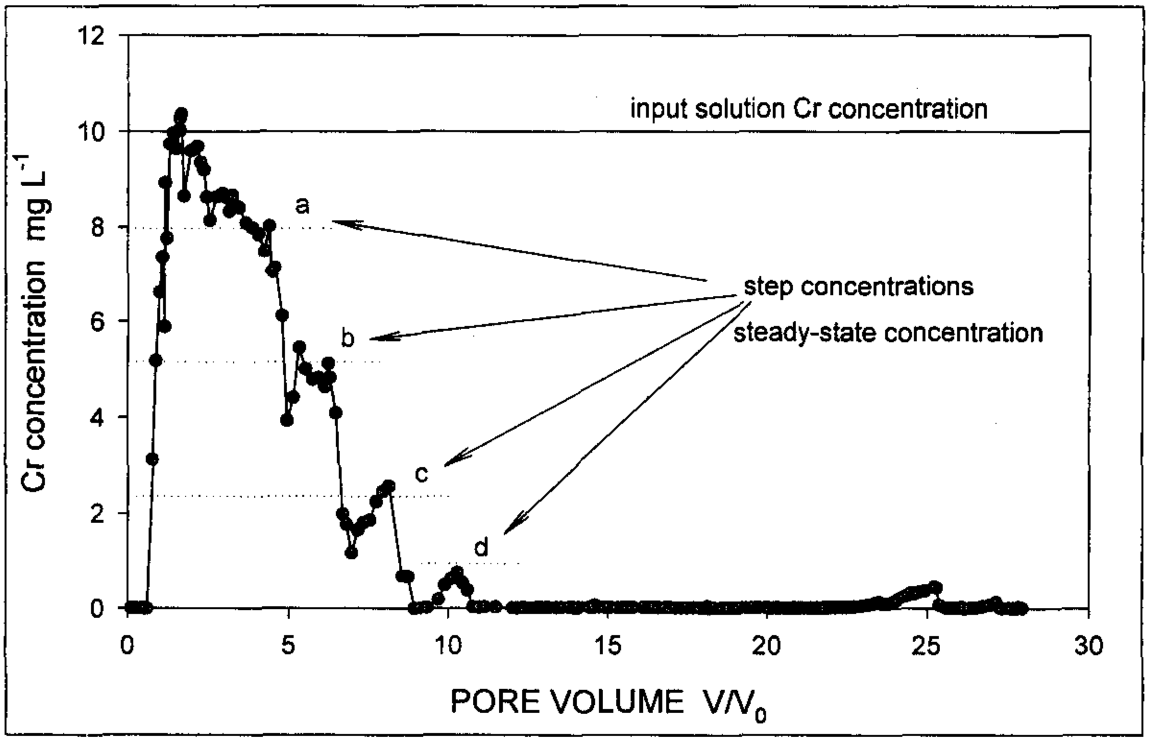

The Cr(VI) concentration in the effluent of the third column decreased to zero after approximately 11 pore volumes, and remained at this level for the rest of experiment (Figure D.4.3.5). In fact, by 900 hours (25 pore volume), the chromate removal rate had still a half-life of greater than 8 hours. Approximately 83% of the total amount of Cr(VI) that entered in the column with the leaching solution was retained in the sediments under this column's flow conditions.

The 24 hours flow interruption method applied in the second column (Figure D.4.3.6) indicated nonequilibrium chemical conditions in the system. When nonequilibrium exists, flow interruption may result in a drop in the effluent solute concentration, similar to the one observed in this experiment. The Cr(VI) concentration decreased to nearly zero when flow interruption was applied. Points A and B in the magnified section of Figure D.4.3.6 correspond to the pre- and post-interrupt Cr(VI) effluent concentrations, respectively. The dip in the Cr(VI) BTC showed that under this experiment's flow conditions (fluid residence time of 9.35 hours); the Cr(VI) removal from the aqueous phase was a rate-limited. The Cr(VI) removal continued to proceed during flow-interruption, decreasing, as a result, the Cr(VI) concentration in the aqueous phase. Assuming the 21.5 hours chromate removal rate calculated from the steady state concentration before the stop-flow event, a 24 hours stop flow should have resulted in the removal of an additional 4.6 mg/L chromate, and the Cr(VI) concentration in the effluent after the 24 hour stop-flow event should have not been smaller than 2.8 mg/L. However, the actual chromate concentration observed after the 24 hour stop-flow event was nearly zero, which indicated a somewhat faster chromate removal rate. It is likely, therefore, that other processes augmented the rate of Cr(VI) removal from the aqueous phase. The Cr(VI) breakthrough front reestablished the Cr(VI) steady-state concentration upon recommencing flow (Figure D.4.3.6).

Elevated Cr levels were found in the sediments at the end of experiments, which provides evidence for Cr incorporation in solid phases. The results from the EDXRF analyses conducted in the sediments of the second column at the end of experiment indicated that the Cr content varied from 45 μg/g in the untreated sediment, to 50 and 68 μg/g in the 3-cm-thick layers near the column inlet and outlet, respectively. The fact that the Cr content in the sediments near the column outlet was the largest, indicated, again, that Cr(VI) removal from the aqueous phase was a kinetically controlled process.

As a result of mineral dissolution, the Fe concentration in the effluent of the second column increased to a maximum of about 3.2 mg/L (Figure D.4.3.7). It then decreased toward a steady-state concentration of 0.9 mg/L. In contrast to what was presented above for Cr(VI), the 24-hour flow interruption resulted in an increase in Fe concentration in the aqueous phase, which more than doubled when the stop-flow was applied (magnified section in Figure D.4.3.7). It appeared that dissolution of Fe-bearing minerals continued during the duration of experiment, and that Fe was continuously released into the soil solution. The Fe front reestablished the steady-state concentration (0.9 mg/L) upon recommencing flow (Figure D.4.3.7).

Aluminum concentrations in the effluent of the second column reached a maximum of 1100 mg/L and then decreased to 200 mg/L (Figure D.4.3.8). Since the Al concentration in the input solution was about 1400 mg/L, the significant decrease in Al concentration indicated Al precipitation. This mass loss reaction was more evident when the stop flow was applied (magnified section in Figure D.4.3.7). The Al concentration in the post-interrupt effluents decreased considerably from 600 mg/L to 70 mg/L, and Al breakthrough front reestablished the value of Al concentration after more than 3 pore volumes upon recommencing flow (magnified section in Figure D.4.3.8).

Figure D.4.3.6. Changes in Cr(VI) Concentration in the Second Column During Leaching with a Solution Containing 1M NaOH, 1M $NaNO_3$, 0.055 M $Al(NO_3)_3$, and 10 mg/L Cr.

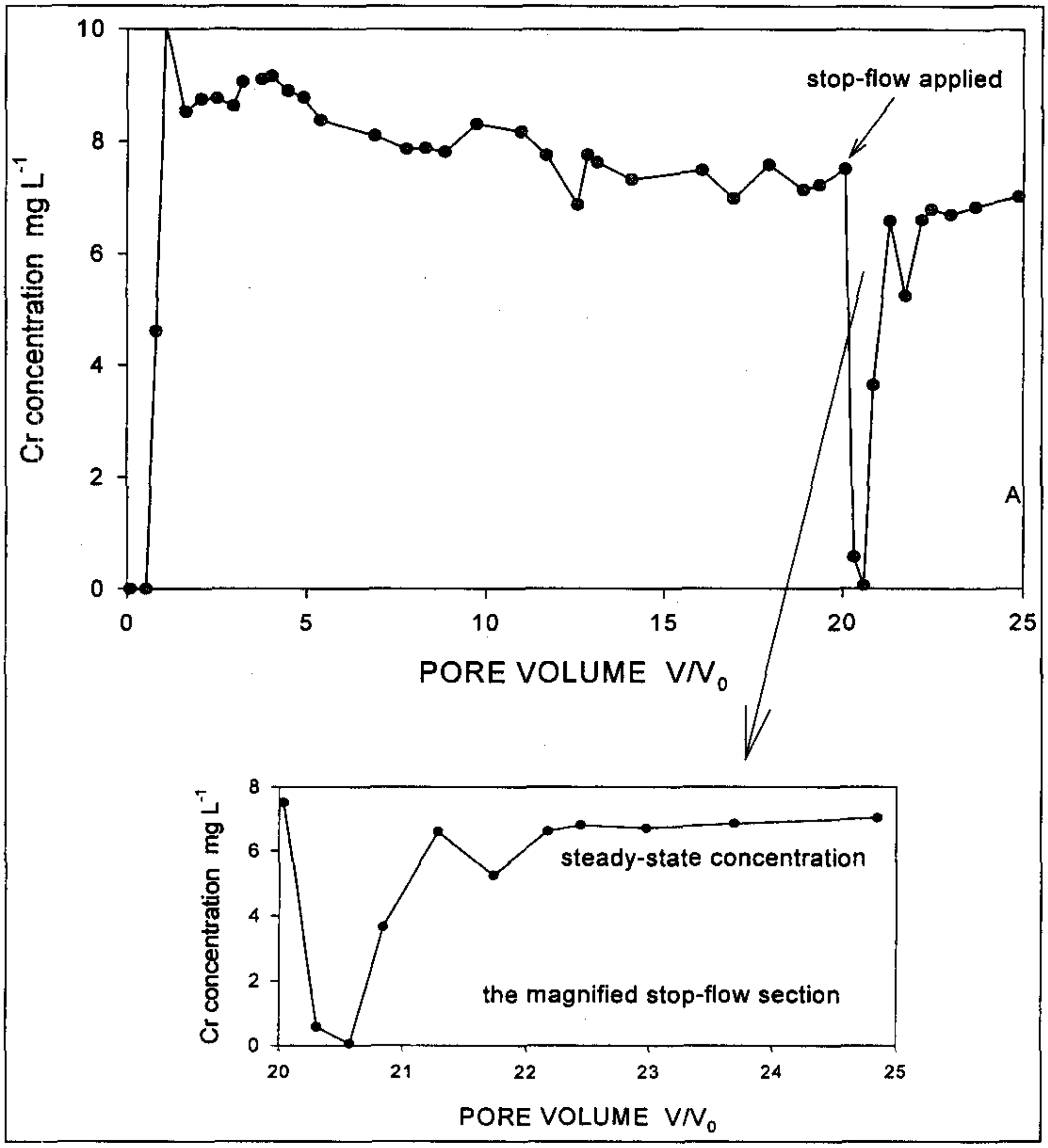

Figure D.4.3.7. Changes in Fe Concentration in the Second Column During Leaching with a Solution Containing 1M NaOH, 1M $NaNO_3$, 0.055 M $Al(NO_3)_3$, and 10 mg/L Cr.

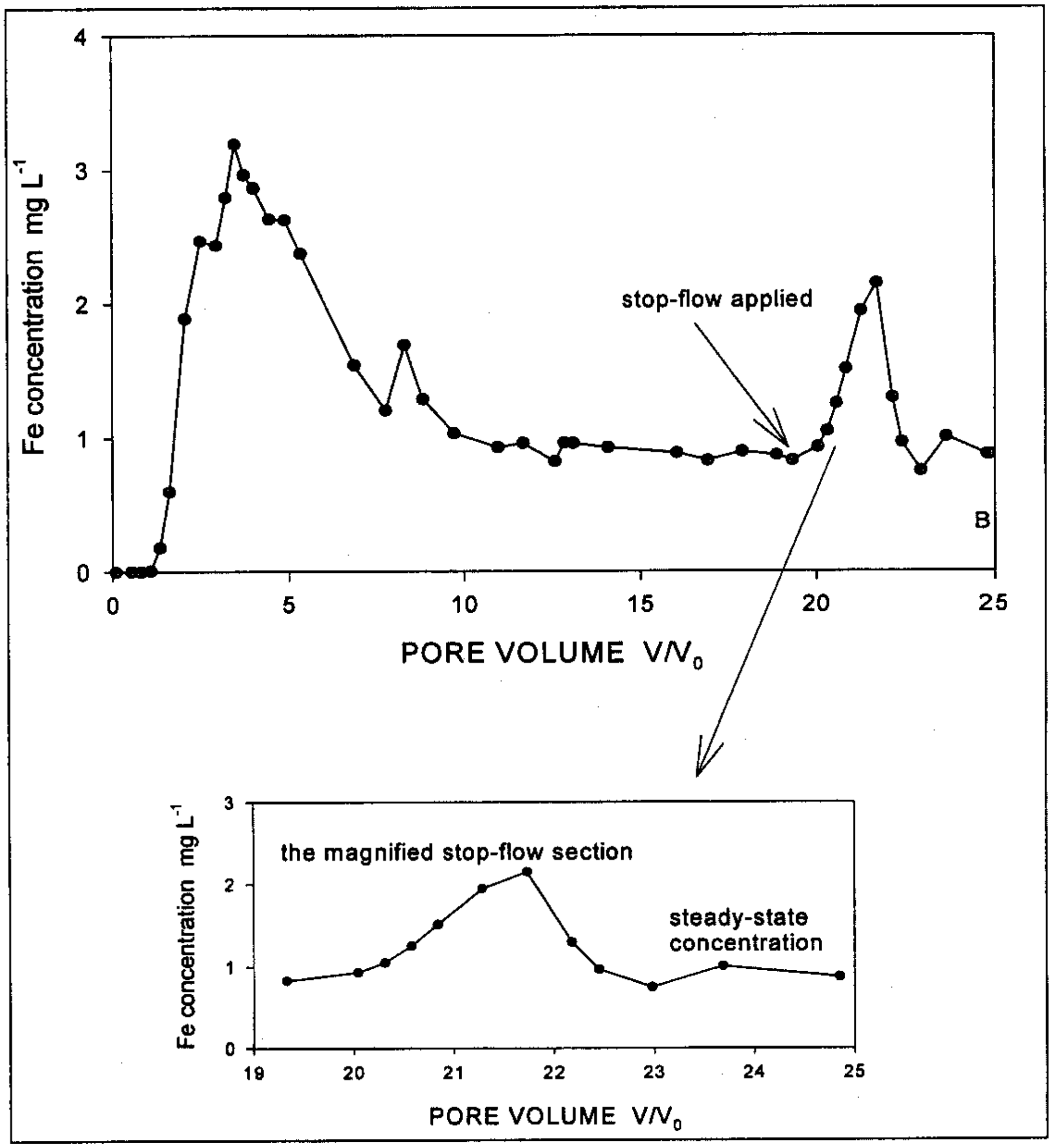

Figure D.4.3.8. Changes in Al Concentration in the Second Column During Leaching with a Solution Containing 1M NaOH, 1M $NaNO_3$, 0.055 M $Al(NO_3)_3$, and 10 mg/L Cr.

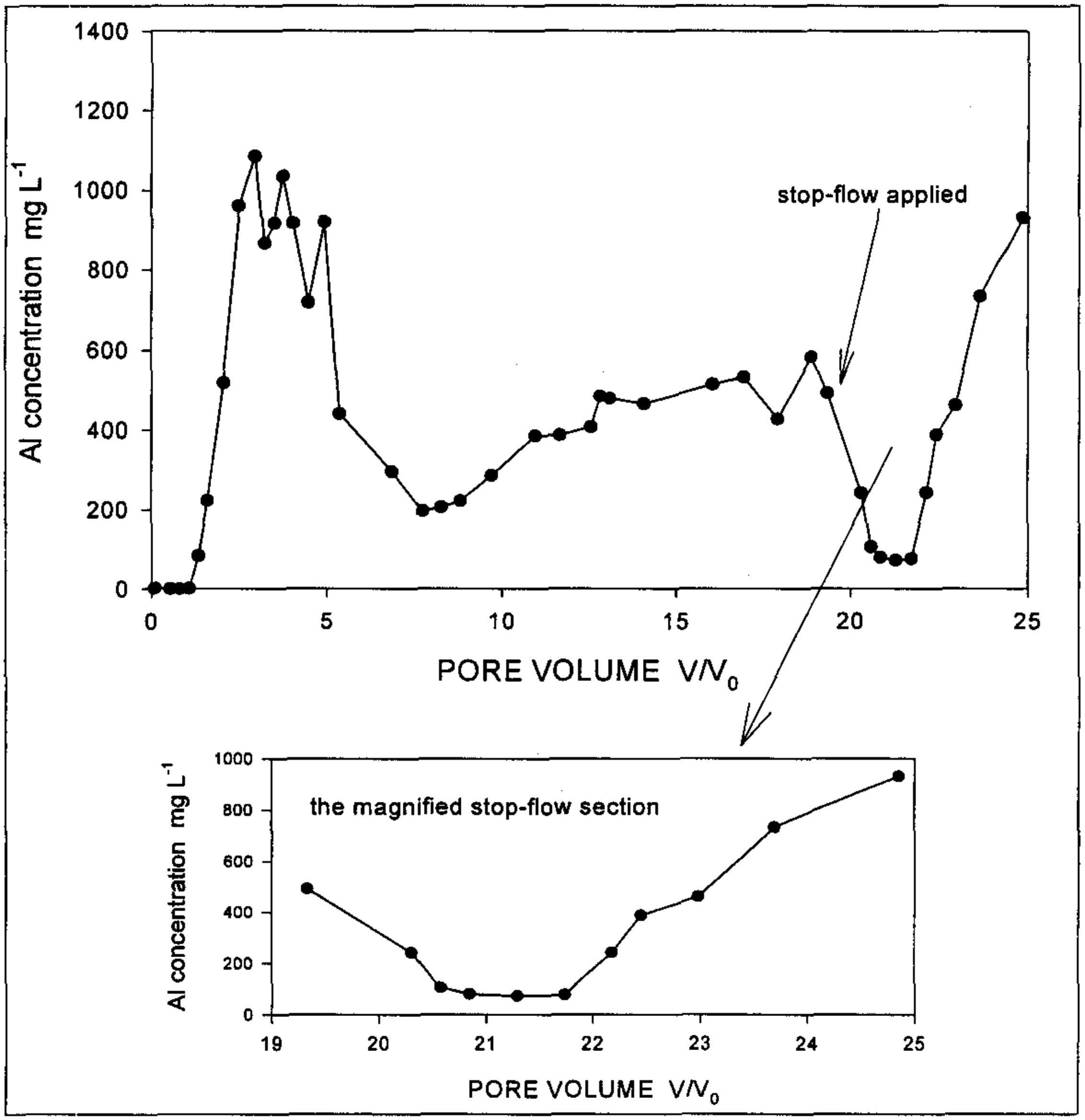

D.4.3.4 Conclusions and Implications

The experimental results presented above demonstrated that Cr(VI) transport in the Hanford sediments was not retarded when sediments are treated with neutral solutions, but undergoes retardation after contact with alkaline and saline solutions similar to REDOX tank waste.

The most likely mechanism causing Cr(VI) retardation in the base-reacted sediments was Fe(II) induced reduction to Cr(III) (Rai and Zachara 1986; Eary and Rai 1989; Fendorf and Li 1996; Sedlak and Chan 1997; Pettine et al. 1998; Fendorf et al. 2000). The reaction of alkaline and saline fluids with the soil matrix caused dissolution of Fe(II)-bearing soil minerals, like biotite and chlorite, and the release of $Fe(II)_{(aq)}$. Fe(II) promotes the reduction of Cr(VI), and less soluble, less mobile Cr(III) species may be formed. Because Cr(III) tends to occur in octahedral coordination with oxygen (Peterson et al. 1997), it may also co-precipitate with Fe(III) to form (Fe, Cr) solid solutions, and/or with Al to form hydrotalcite-like soil minerals (Rai and Zachara 1986). Al precipitates were definitely formed during these experiments.

Our results implied that Cr(VI) reduction was a kinetic process controlled by the rate of Fe(II) release upon dissolution, as metered by other competing reactions like ion exchange, adsorption, and precipitation that may act to lower the aqueous phase Fe(II) activity. The observation that Cr(VI) concentrations in the effluents decreased gradually indicated that the Fe(II) mineral dissolution rate and its subsequent reactivity with other aqueous and solid species were important determinants of the Cr(VI) reduction rate. Although we are unaware of reported Cr(VI) reduction rates under alkaline conditions, we suspect it to be rapid because this rate appears to increase at higher pH (Fendorf and Guangchao 1996; Sedlak and Chan 1997; Pettine et al. 1998).

The steady-state Cr(VI) removal rates observed in the different column experiments were likely the balanced effect of mineral dissolution and precipitation reactions involving Fe(II), the reductant, and Fe(III), the oxidized product. However, a mass balance analysis of the Cr and Fe concentrations indicated that most of the Fe(II) that was evolved by base-induced dissolution remained in the column as Fe(II) phases (solid or adsorbed) or oxidized Fe(III) products (Fe(III) oxides). The sediment exhibited a reddish hue at experiment termination indicating Fe(III) oxide formation. A red color was also quite visible in the Hanford sediments after treatment with a 4 M NaOH, 1 M $NaNO_3$ and 0.88 M $Al(NO_3)_3$ solution for 7 days in a batch experiment. These results experimentally confirm observations made with Cr^- contaminated sediments from the SX-108 slant borehole. Cr migration is partially retarded by $Fe(II)_{aq}$ induced reduction of Cr(VI) to Cr(III). The reaction/reduction extent is dependent on the base (OH^-) induced dissolution rate of Fe(II) bearing minerals, which is effected by column residence time and OH^- concentration. These results suggest that the in situ reduction of Cr(VI) to Cr(III) may no longer be operative in the Cr-contaminated SX-108 sediments.

D.4.3.5 Acknowledgment

These studies were supported by the U. S. DOE Environmental Management Sciences Program (EMSP) through a FY 1999 funded project: "Immobilization of radionuclides in the Hanford vadose zone by incorporation in solid phases" (Traina, Brown, and Ainsworth).

D.4.3.6 References

Brusseau, M. L., Q. H. Hu, and R. Srivastava, 1997, "Using Flow Interruption to Identify Factors Causing Nonideal Contaminant Transport," *Journal of Contaminant Hydrology*, Vol. 14:39-54.

Eary, L. E. and D. Rai, 1989, "Kinetics of Chromate Reduction by Ferrous Ions Derived From Hematite and Biotite at 25 °C," *American Journal of Science*, Vol. 289:180.

Fendorf, S. E. and G. Li, 1996, "Kinetics of Chromate Reduction by Ferrous Iron," *Environmental Science and Technology,* Vol. 30:1614-1617.

Fendorf, S. E., B. W. Wielinga, and C. M. Hansel, 2000, "Chromium Transformations in Natural Environments: The Role of Biological and Abiological Processes in Chromium(VI) Reduction," *International Geology Review*, Vol. 42:691-701.

Peterson, M. L., A. F. White, G. E. Brown, Jr., and G. A. Parks, 1997, "Surface Passivation of Magnetite by Reaction with Aqueous Cr(VI): XFAS and TEM Results," *Environmental Science and Technology*, Vol. 31:1573-1576.

Pettine, M., L. D'Ottone, L. Campanella, F. J. Millero, and R. Passino, 1998, "The Reduction of Cr(VI) by Iron (II) in Aqueous Solutions," *Geochimica et Cosmochimica Acta*, 1509-1519.

Rai, D., and J. M. Zachara, 1986, "Geochemical Behavior of Chromium Species," *EA-4544, Research Project 2485-3*, Pacific Northwest National Laboratory, Richland, Washington.

Schwertmann, U., J. Friedl, and H. Stanjek, 1999, "From Fe(III) Ions to Ferrihydrite and then Hematite," *Journal of Colloid Interface Science*, Vol. 209:215-223.

Sedlak, D. L., and P. G. Chan, 1997, "Reduction of Hexavalent Chromium by Ferrous Iron," *Geochimica et Cosmochimica Acta*, 2185-2192.

Toride, N., F. J. Leij, and M. Th. van Genuchten, 1999, "The CXTFIT Code for Estimating Transport Parameters From Laboratory or Field Tracer Experiments," *Research Report No. 137*, U.S. Salinity Laboratory, USDA.

D.4.4 CHROMIUM(VI) REDUCTION IN HOMOGENOUS AND HETEROGENEOUS FE(II) SYSTEMS UNDER ALKALINE CONDITIONS AT 50 °C

Yongtian He[1], and Samuel J. Traina[1,2]

[1]The Environmental Science Graduate Program, The Ohio State University, Columbus, Ohio 43210

[2]The School of Natural Resources, The Ohio State University, Columbus, Ohio 43210

D.4.4.1 Introduction

The objective of this EMSP research was to examine the adsorption and reduction of Cr(VI) on specimen biotite, and in homogeneous Fe(II) solutions at high pH, high ionic strength, and 50 °C. These conditions are thought to be representative of field conditions that may have existed during the intrusion of tank SX-108 fluids into the underlying vadose zone.

D.4.4.2 Experimental Procedures

Specimen biotite collected in North Carolina, was obtained from the mineral collection of the OSU School of Natural Resources. The specimen biotite was ground to less than 56 μm with an agate mortar and pestle. This well-studied and characterized biotite sample was used as a precursor to planned studies with weathered biotites isolated from the Hanford and Ringold geologic formations.

The experiments conducted with biotite were prepared as follows. Samples were composed of 40 mL of the model solutions described in Table D.4.4.1 and 0.1 g of the biotite. All samples were prepared in an argon-filled glove box in polyethylene containers and then moved to 50 °C incubator for a reaction time of 1 week.

Table D.4.4.1. Reactant Composition in Cr(VI) Reduction by Biotite Studies.

Sample treatment	Reactant fluid composition
1	1 mol/L NaOH
2	1 mol/L NaOH, and 1 mmol/L Na_2CrO_4
3	1 mol/L NaOH, 3 mol/L $NaNO_3$ and 1 mmol/L Na_2CrO_4
4	5 mol/L NaOH, 1 mol/L $Al(NO_3)_3$
5	5 mol/L NaOH, 1 mol/L $Al(NO_3)_3$ and 1 mmol/L Na_2CrO_4
6	5 mol/L NaOH, 1 mol/L $Al(NO_3)_3$ and 100 μmol/L Na_2CrO_4
7	5 mol/L NaOH, 1 mol/L $Al(NO_3)_3$ and 10 μmol/L Na_2CrO_4
8	5 mol/L NaOH, 1 mol/L $Al(NO_3)_3$ and 1 μmol/L Na_2CrO_4
9	5 mol/L NaOH, 1 mol/L $Al(NO_3)_3$ and 0.1 μmol/L Na_2CrO_4

The homogeneous reduction of Cr(VI) was examined in the solutions described in Table D.4.4.2. These samples were again prepared in an Ar-filled glove box, in polyethylene tubes and aged for 1 week at 50 °C.

Table D.4.4.2. Reactant Composition in Homogeneous Cr(VI) Reduction Fe(II).

Sample treatment	Reactant fluid composition
1	1 mol/L NaOH
2	1 mol/L NaOH, and 3 mmol/L $FeCl_2$
3	1 mol/L NaOH, and 1 mmol/L Na_2CrO_4
4	1 mol/L NaOH, 1 mmol/L $FeCl_2$ and 1 mmol/L Na_2CrO_4
5	1 mol/L NaOH, 2 mmol/L $FeCl_2$ and 1 mmol/L Na_2CrO_4
6	1 mol/L NaOH, 3 mmol/L $FeCl_2$ and 1 mmol/L Na_2CrO_4
7	1 mol/L NaOH, 1 mol/L $NaNO_3$ and 3 mmol/L $FeCl_2$
8	1 mol/L NaOH, 1 mol/L $NaNO_3$, 3 mmol/L $FeCl_2$ and 1 mmol/L Na_2CrO_4
9	1 mol/L NaOH, 1 mol/L $NaNO_3$, 3 mmol/L $FeCl_2$, 1 mmol/L Na_2CrO_4, and 1 mmol/L Na_2CO_3
10	1 mol/L NaOH, 1 mol/L $NaNO_3$, 3 mmol/L $FeCl_2$, 1 mmol/L Na_2CrO_4, and 10 mmol/L Na_2CO_3

After 1 week the solids from the heterogeneous experiments were separated by centrifugation and the supernates saved for analyses. The solids were washed with deionized water to remove excess salts. A fraction of the washed solids were kept moist in sealed containers and the remainder of the material was freeze-dried. Freeze-dried materials were examined with scanning electron microscopy (SEM) and X-ray Diffraction (XRD). X-ray absorption near edge structure spectra (XANES) were collected on the moist solids at beam line 11-2 of SSRL as described elsewhere in this report.

Solution analyses was conducted with a Perkin-Elmer Optical Emission ICP and/or by a Perkin-Elmer graphite furnace AA equipped with Zeeman background correction to quantitate total Cr, Si, Al, Fe and K. UV-visible spectroscopy was used to distinguish between dissolved Cr(III) and Cr(VI).

D.4.4.3 Results and Discussion

D.4.4.3.1 Homogeneous Reduction Experiments. Past studies have shown that the reduction of Cr(VI) by Fe(II) involves three, one-electron transfer steps, with the rate of reaction increasing at acidic pH: Fe(II) + Cr(II) = Fe(III) + Cr(V); Fe(II) + Cr(V) = Fe(III) + Cr(IV); Fe(II) + Cr(IV) = Fe(III) + Cr(III); and the overall reaction can be written as: Cr(VI)(aq) + 3Fe(II)(aq) = Cr(III)(aq) + 3Fe(III)(aq). The pH of the aqueous system will affect both the amount of Cr(VI) reduced to Cr(III) and the partitioning of Cr(III) between aqueous and adsorbed species.

In our high pH experiments some Cr(VI) was apparently reduced by Fe(II) very quickly and formed red-brown precipitates within seconds after mixing of the initial solutions. However, after 1 week of reaction there was still some Cr left in solution (Table D.4.4.3). UV-vis spectroscopy indicated that this was all in the form of Cr(VI). The quantity of Cr(VI) removal from solution increased with increased initial concentrations of Fe(II). In the absence of Cr(VI) all of the initial Fe(II) remained in solution. However, addition of 1 mmol/L Na_2CrO_4 resulted in complete removal of all detectable Fe from solution. The addition of 1 mol/L $NaNO_3$ and 0.01 mol/L Na_2CO_3 did not have a significant effect on Cr(VI) reduction.

Table D.4.4.3. Final Solution Composition From Homogeneous Reduction Studies.

Sample treatment	[Cr] μmol/L	%[a] change in [Cr]	[Fe] mmol/L
1	n.a.[b]	n.a.	n.a.
2	n.a.	n.a.	b.d[c]
3	966.2	-3	n.a.
4	786.4	-21	b.d
5	622.9	-38	b.d
6	452.1	-55	b.d
7	n.a.	n.a.	b.d
8	487.0	-51	b.d
9	441.6	-56	b.d
10	442.5	-56	b.d

[a] % change from initial composition
[b] Not applicable
[c] Below detection

Buerge and Hug (1999) showed that in homogeneous aqueous solutions of Cr(VI) and Fe(II), the precipitation of finely dispersed, x-ray amorphous colloids with a chemical composition of $Fe_{0.75}Cr_{0.25}(OH)_3(s)$ were observed. Chromium(III) hydroxide, including $Cr(OH)_3(s)$ and the solid solutions $(Cr,Fe)\ (OH)_3(s)$, have been observed to precipitate rapidly in moderately acidic to alkaline solutions and expected to be the important solubility-controlling solids for dissolved Cr(III) for a wide range of pH. In the present study, powder XRD measurements of the precipitates in the homogeneous reduction experiments failed to detect any crystalline phases.

D.4.4.3.2 Heterogeneous Experiments. Biotite is a common Fe(II) containing mica in Hanford formation sediments (D.2). Table D.4.4.4 shows the release of K, Si, and Al due to the dissolution of specimen biotite at high pH conditions. In treatments without $Al(NO_3)_3$, there was no detectable Al released from the biotite. The concentration of dissolved Si was about 10 times greater in the absence of dissolved in Al than $Al(NO_3)_3$-free treatments. There was no detectable Fe in any of the solutions from the heterogeneous experiments.

Table D.4.4.4. Final Solution Composition From the Heterogeneous Reduction Studies.

Sample treatment	[Cr] µmol/L	%[a] change in [Cr]	[Al] mmol/L	% change in [Al]	[Si] µmol/L	[K] mmol/L	pH
1	n.a.[b]	n.a.	b.d	0	2459.3	0.49	13.75
2	0.0	-100	b.d	0	2330.1	0.78	13.56
3	0.0	-100	b.d	0	2376.4	1.36	13.56
4	n.a.	n.a.	265.5	-73	256.7	1.10	13.93
5	765.4	-23	182.9	-82	206.2	0.74	13.78
6	58.1	-94	250.2	-75	284.1	1.00	13.92
7	2.7	-99	266.9	-73	304.8	1.05	13.92
8	b.d[c]	-100	274.6	-72	256.4	1.34	13.93
9	b.d	-100	259.8	-74	288.8	1.68	13.92

[a] % change from initial composition
[b] Not applicable
[c] Below detection

Reduction of Cr(VI) directly by structural Fe(II) in minerals is a possible mechanism of Cr(VI) reduction. Peterson and coworkers (1996) provided evidence for Cr(VI) reduction at magnetite surfaces. It has been shown that Cr(VI) directly reacted with a Fe(II)-containing smectite, formed precipitates on the smectite surface. Ilton and Veblen (1994) demonstrated that Cr(VI) can be sorbed and reduced to Cr(III) at the biotite edge-fluid interface by structural Fe(II).

Eary and Rai (1989) suggested that chromate is not adsorbed to biotite at high pH and Zachara and others (1988 and 1989) have shown that chromate is not adsorbed onto iron oxides at pH values greater than 11.5 to 12. However in the present study, reaction with biotite removed from 20 to 100% of the initial Cr from solution (Table D.4.4.4). Figure D.4.4.1 shows Cr, K-edge XANES from treatments 6 and 7 (a and b). The lack of any detectable pre-edge peak clearly indicates the conversion of Cr(VI) to Cr(III). No Cr(VI) reduction was observed in the biotite-free control. During these experiments, we observed that the bottom of the reaction vessels turned red-brown in treatments with initial Cr(VI) concentration less than or equal to 10^{-5} mol/L; this might have been due to the precipitation of an Fe(hydr)oxide as Fe originating from biotite dissolution and was oxidized by Cr(VI). Interestingly, in treatments with greater initial Cr(VI) concentration, there was no visible red-brown precipitates.

Figure D.4.4.1. Cr K-Edge Spectra of Biotite Samples Reacted with Either (a) 1 mmol/L Na_2CrO_4 or (b) 100 µmol/L Na_2CrO_4, in the Presence of 5 mol/L NaOH, and 1 mol/L $Al(NO_3)_3$.

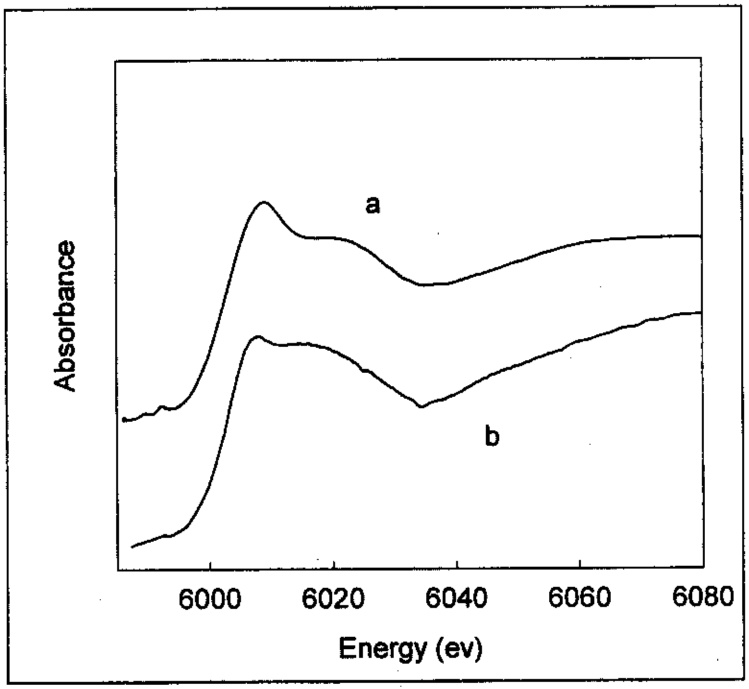

Note: Absence of any Pre-Edge Peak Indicates that all Cr is Present as Cr(III).

It is apparent in the present study that Cr(VI) reduction by biotite did occur at the elevated pH values used. In companion preliminary experiments, we have observed similar patterns of Cr(VI) reduction (in the presence of 1 to 4 mol/L NaOH) in heterogeneous systems containing synthetic magnetite, a magnetic fraction separated from sediments obtained from the Hanford Site and a nonmagnetic, less than 200 µm size fraction of sedimentary material, also obtained from the Hanford Site. Apparently alkaline-induced dissolution of Fe(II) containing solids can indeed result in Cr(VI) reduction.

The capacity of clays to reduce Cr(VI) is correlated with their ferrous iron content (Taylor et al. 2000). Eary and Rai (1989) found that ferrous iron-bearing minerals such as hematite and biotite reduced hexavalent chromium as the minerals underwent dissolution; the rate of reduction was limited by the rate of Fe(II) release from the minerals. They found that the initial rate of chromate reduction is dependent on the dissolution rates of the ferrous iron contents of these minerals. However, the study of Peterson et al. (1997) suggests that reductive sorption of chromate on iron bearing minerals and "zero-valent" iron in the subsurface is a self-limiting process as iron (II) is consumed on the surface, and Cr(III)-oxyhydroxide builds up on the surface. The insulating nature of these layers prevents electron transfer from deep layers, thus bringing redox processes to a halt. The extent to which this occurs in hyperalkaline solutions is not yet known.

Ilton and Veblen (1994) used XPS and SEM to study the reaction of biotites with Cr(VI) solutions they found that Cr is strongly sorbed by the edges of mica books relative to the basal plane. In fact, much of the chromium associated with the basal plane is sorbed by steps and layer edges. In the present study, SEM images of biotite basal planes and edges did not show Cr-rich precipitates (data not shown).

D.4.4.4 Conclusions and Implications

It is evident from the present study that reduction of Cr(VI) by Fe(II)-containing solids can occur. While not discussed above, the reaction rates appear to increase with increasing NaOH concentration (data not shown). This may be due to base-induced dissolution of the Fe(II)-containing silicates, leading to release of Fe(II) to solution. However, it is not clear why increases in NaOH concentration would accelerate the reduction of Cr(VI) by magnetite (Fe_3O_4) yet our initial experiments suggest that this can indeed occur. The extent to which this happens in field environments (e.g., the Hanford vadose zone) is not clear, but it seems likely that Cr(VI) reduction would occur if sufficient NaOH were available for reaction with Fe(II)-containing solids. Indeed the reduced Cr was identified in field samples from the SX-108 slant borehole discussed elsewhere in this report, and it is worth noting that the most extensive reduction of Cr was found in field samples that had the greatest pH. Thus, the most critical factor in the in situ reduction Cr(VI) to Cr(III) by sedimentary Fe(II) may have been the presence of and persistence of hyper-alkaline solutions in the Hanford vadose zone.

D.4.4.5 Acknowledgment

These studies were supported by the U. S. DOE Environmental Management Sciences Program (EMSP) through a FY 1999 funded project: "Immobilization of radionuclides in the Hanford vadose zone by incorporation in solid phases,"(Traina, Brown, and Ainsworth).

D.4.4.6 References

Buerge, I. J., and S. J. Hug, 1999, "Influence of Mineral Surfaces on Chromium(VI) Reduction by Iron(II)," *Environmental Science and Technology,* Vol. 33:44,285-44,291.

Eary, L. E. and D. Rai, 1989, "Kinetics of Chromate Reduction by Ferrous Ions Derived from Hematite and Biotite at 25 °C," *American Journal of Science*, Vol. 289:180-213.

Eary, L. E. and D. Rai, 1988, "Chromate Removal from Aqueous Wastes by Reduction with Ferrous Iron," *Environmental Science and Technology,* Vol. 22:972-977.

Ilton, E. S. and D. R. Veblen, 1994, "Chromium Sorption by Phlogopite and Biotite in Acidic Solutions at 25 °C: Insights from X-ray Photoelectron Spectroscopy and Electron Microscopy," *Geochimica et Cosmochimica Acta,* Vol. 58:2777-2788.

Ilton, E. S., D. R. Veblen, C. O. Moses, and S. P. Raeburn, 1997, "The Catalytic Effect of Sodium and Lithium Ions on Coupled Sorption-Reduction of Chromate at the Biotite Edge-Fluid Interface," *Geochimica et Cosmochimica Acta,* Vol. 61:3543-3563.

Malmstrom, M. and S. Banwart, 1997, "Biotite Dissolution at 25 °C: The pH Dependence of Dissolution Rate and Stoichiometry," *Geochimica et Cosmochimica Acta,* Vol. 61:2779-2799.

Peterson, M. L., G. E. Brown, Jr., and G. A. Parks, 1996, "Direct XAFS Evidence for Heterogeneous Redox at the Aqueous Chromium/Magnetite Interface," *Colloids and Surfaces,* Vol. 107:77-88.

Peterson, M. L., A. F. White, G. E. Brown, Jr., and G. A. Parks, 1997, "Surface Passivation of Magnetite (Fe_3O_4) by Reaction with Aqueous Cr(VI): XAFS and TEM Results," *Environmental Science Technology,* Vol. 31:1573-1576.

Sylvester et al. 2000, "Ferrate Treatment for Removing Chromium from High-Level Radioactive Tank Waste," *Environmental Science and Technology.*

Taylor, R. W., S. Shen, W. F. Bleam, and S. I. Shu, 2000, "Chromate Removal by Dithionite-Reduced Clays: Evidence from Direct X-ray Absorption Near Edge Spectroscopy (XANES) of Chromate Reduction at Clay Surfaces," *Clays and Clay Minerals*, Vol. 48:648-654.

Zachara, J. M., D. C. Girvin, R. L. Schmidt, and C. T. Resch, 1987, "Chromate Adsorption on Amorphous Iron Oxyhydroxide in the Presence of Major Groundwater Ions," *Environmental Science and Technology*, Vol. 21:589-94.

D.4.5 CONCLUSIONS OF S&T INVESTIGATIONS OF GEOCHEMISTRY AND REACTIVE TRANSPORT BEHAVIOR OF CR

To determine the potential for the in-ground inventory of Cr to migrate as a result of future meteoric recharge or spills from tank sluicing operations, it is important to understand where it is, what are the predominate geochemical species, and what are the reactions that lead to its speciation and distribution. The studies to date by Hanford S&T and U.S. DOE EMSP investigators have developed information, much of which is reported here, that has led to a framework of a conceptual model of Cr reactive transport in the Hanford vadose zone.

From the few WMA S-SX sediments that have been studied, Cr is present as the reduced, cationic Cr(III) and anionic Cr(VI) species. The spatial distribution of the Cr(III) species is heterogeneously dispersed as small "hot spots." These loci of Cr(III) concentrations are often well correlated with the presence of Fe and Mn; and in several instances have been shown to be associated with biotite mica flakes, and titano-magnetite (or ilmenite). Presumably, the Cr(III) has formed a mixed metal oxide. Chromate, on the other hand, appears to be more uniformly dispersed throughout the sediments. Extraction of Cr concomitant with Fe and Al yields reasonable correlations suggesting that the CrO_4^{2-} anion is associated with Fe and Al oxides; presumably present as weak outer-sphere surface complexes.

Assuming that the Cr loss to the vadose zone from tank leaks was initially Cr(VI), reduction of Cr(VI) occurred as the fluid was transported away from the leak source. The source of electrons for the reduction of Cr(VI) to Cr(III) is suspected to originate from several sources; the reduced Fe(II) present in the mixed valance mineral magnetite, and the reduced Fe(II) and Mn(II) in 2:1 layer-aluminosilicate minerals such as chlorite and biotite mica. All three of these minerals are present in the Hanford formation sediments; with biotite having the greatest abundance. Under the high pH, high salt, and elevated temperature conditions suspected of REDOX leaked wastes, the homogeneous reduction of Cr(VI) by $Fe(II)_{(aq)}$ is very fast, almost instantaneous. In heterogeneous systems, with biotite or magnetite as the only source of reductant, the rate of Cr reduction is slowed, and follows biotite > magnetite. In column studies with Hanford sediments, residence time has been shown to an important element in the retardation of Cr(VI) influent; presumably because of reduction. Hence, one must surmise that the rate-controlling step in the reduction of Cr(VI) is the dissolution of Fe(II) and Mn(II) containing minerals. The reduction is followed by the rapid precipitation of mixed metal oxides, essentially at or near the source of reductant release. This hypothesis is supported by the abundance of reduced Cr(III) and its highly heterogeneous distribution as "hot spots" of Cr(III) observed by XAS.

The high pH and elevated temperature of the tank-leaked fluids appears key to the magnitude of the Cr(VI) reduction. Under these conditions, the rate of layer aluminosilicate dissolution is substantially increased, as is the rate Fe(II) reduction of Cr. A question of a sediments reductive power, or potential, is still to be addressed. From X-ray diffraction analysis of sediments impacted by these fluids, it is clear that biotite is still present [as is Cr(VI)]; although there is a substantial decrease in smectite clays and chlorite. The apparent precipitation of REDOX products at or near the source of reductant release suggests that these surfaces may become passivated with time even in the presence of high OH concentrations. Hence, there appears to be a limit to the reduction potential that is well below the concentration of reductant.

Chromate is retained, only slightly if at all, by weak adsorption to secondary Al and Fe oxides at pH and ionic strength conditions of the tank-leaked fluids. Even under neutral pH conditions, the retardation of Cr(VI) was minimal at best (an $R_f < 1$). As fluid flow slowed and eventually stopped the Cr(VI) was held in place. Because of the elevated temperatures, water content decreased, and potentially, Cr(VI) fell out of solution as a soluble Na salt. Either way, one is left with a fairly uniform distribution of Cr(VI) in the sediments.

Hence, one is left with a substantial in-ground inventory of Cr in the S-SX vadose zone sediments. The stability Cr(III) oxides and its limited toxicity minimizes concern for its presence. Cause for concern, however, lies with the inventory of Cr(VI). It is unlikely that the rate of reduction will continue with meteoric recharge as the pH has moderated over time because of the aforementioned dissolution reactions and recarbonization of the high pH fluids by CO_2. The pH of all sediments is at or below 9.5 and below about sediment SX-108 7A depth (~84 ft bgs) the pH is between 7.2 and 8.3 (typical pH values for the Hanford formation sediments). While mineral dissolution will continue, its rate will be substantially slower and Cr(VI) will have to compete with O_2 oxidation of Fe(II) and Mn(II) released. Other sources of Cr(VI) reduction (e.g., magnetite) will continue but its abundance is limited. Therefore, it must be assumed that the reactions that led to substantial reduction of Cr(VI) will be of limited value in retarding Cr(VI) in the future.

The majority of the Cr(VI) currently in the vadose zone is extremely mobile and its retardation, from the results of column studies, appears minimal. There appears to be two pools of Cr(VI) in the contaminated sediments studied to date. The largest pool is released rapidly with limited or no retardation. The residual $NaNO_3$ from tank-leaked fluids appears to assist in the mobilization of this pool of Cr(VI). The second pool of Cr(VI) is more strongly bound to the sediments (albeit only slightly). However, it is unclear at this time whether this division into two pools is an artifact of the high ionic strength of the first few pore volumes or related to (1) the presence of a soluble Cr salt (probably Na based) versus a smaller pool of Cr weakly bound as outer-sphere complexes at oxide surfaces, or (2) different pools of Cr(VI) exhibiting different surface binding strengths.

The implications of the above discussion are clear. There is a large mobile pool of Cr(VI) that will transport with meteoric recharge or because of spills during proposed sluicing operations. It's retardation by uncontaminated sediments below will be minimal and the potential for the Cr(VI) to reach groundwater must be considered reasonable.

D.5.0 MICROBIOLOGY

D.5.1 MICROBIOLOGICAL ANALYSIS OF HANFORD TANK SX-108 VADOSE SEDIMENTS

Jim Fredrickson[1], Shu-mei Li[1], Heather Kostandarithes[1], David Balkwill[1], and Dave Kennedy[1]

[1]Pacific Northwest National Laboratory, Richland, Washington 99352

[2]Florida State University, Tallahassee, Florida 32306-4470

D.5.1.1 Introduction

Microorganisms in terrestrial subsurface environments have a major role in the cycling of elements, weathering of rocks and sediments, and on the geochemical properties of groundwater (Fredrickson and Onstatt 2001). They also influence the fate and transport of organic and inorganic contaminants. For example, microorganisms are capable of degrading the various organic compounds present in gasoline and petroleum that may leak from underground storage tanks. Scientists and engineers have taken advantage of these processes and have used bioremediation to eliminate organic contaminants, in situ, from soils and sediments. In addition to the degradation of organic compounds, microorganisms can influence the chemistry of inorganic elements via a number of mechanisms including oxidation-reduction reactions, complexation with cell components or biogenic ligands such as siderophores, or general system-level geochemical changes (e.g., pH, pe) as a result of their concerted metabolism. For example, the activity of dissimilatory metal-reducing bacteria can result in the reductive dissolution of Fe and Mn oxides (Lovley 1995) and the reductive precipitation of U (Fredrickson et al. 2000b) and Tc (Wildung et al. 2000). Such reactions can have a profound impact on the fate and transport of these elements.

While the vadose zone is a relatively harsh environment for microbial life, particularly in arid regions, there have been numerous verifications of the presence of viable microbes in the unsaturated zones in both arid and relatively humid climates (see Kieft and Brockman [2001] for a review on this topic). Water potentials in the vadose zone generally do not directly restrict microbial activity *per se*; many microorganisms are relatively tolerant to the matrix water potentials typical of vadose sediments (Kieft et al. 1993). Rather, it is relatively thin, discontinuous water films that retard the transport of solutes and microorganisms. This, in turn, limits microbial access to nutrients and leads to starvation conditions. Our experience with Hanford Site vadose zone sediments is consistent with these general observations. Viable microorganisms are present at low population densities but in regions where there is evidence of artificial moisture recharge, the size and activity of microbial populations can be significantly higher relative to pristine sediments (Fredrickson et al. 1993; Brockman et al. 1992). Although the physical and chemical properties of the waste that leaked from tank SX-108 would be considered toxic to most life forms, microorganisms have a remarkable capacity for thriving in environments with extremes in pH, temperature, salinity, radiation, and nutrient flux. While certain properties of the waste might be expected to inhibit or even kill indigenous microorganisms, some components could potentially serve as nutrients and possibly stimulate growth and activity. Hence, it is not possible to predict with any degree of certainty the impact of the tank waste on the microbiology of the vadose sediments beneath tank SX-108 and, in turn, whether microorganisms, if present, could have any impact on contaminant fate and behavior.

The main objectives of this research were to

- obtain preliminary information regarding the microbiological properties of tank SX-108 sediment samples in terms of microbial population size and distribution
- assess relationships between sediment chemical and physical properties to gain insight into possible factors controlling microbial presence and distribution
- characterize microorganisms cultured from tank SX-108 to assess their potential for activities that may influence contaminant fate and behavior
- determine whether nitrate respiring bacteria reduce nitrate to N_2O or N_2 via nitrite or to ammonium; the latter has implications for the fate of radioactive Cs^+.

D.5.1.2 Experimental Procedures

During late July and early August of 2000, core samples were collected from the vadose zone beneath tank SX-108 of the 200 West SX tank farm on DOE's Hanford Site. SX-108 cores were sampled at the 337 Building in accordance with RADCON guidelines and requirements. Due to these requirements, it was not possible to use completely aseptic methods in processing these samples. However, staff with extensive experience in aseptic techniques processed all samples, and we are confident that contamination during sample processing would have been minimal.

Due to complications and costs associated with working with highly contaminated sediments samples, we restricted our initial analyses to methods based on culturing. We recognize the limitations in basing analyses only on culturing in that typically 1% or less of the total population will grow on typical laboratory media. However, a major benefit of culturing is that organisms are available for subsequent analyses to assess whether they have activities that could impact contaminant behavior and fate.

Samples were subjected to a variety of microbiological culturing methods to determine whether microorganisms were present in these samples and, if so, the types of biogeochemical reactions they may potentially catalyze as a result of their metabolism. To this end, a range of microbiological agar and broth media were inoculated with each of 16 sediment samples collected from the SX-108 slant borehole. Targeted microbial functional groups included aerobic heterotrophic bacteria, ammonia- and nitrite-oxidizing autotrophic bacteria, denitrifying bacteria, fermentative bacteria, Fe(III)-reducing bacteria, and sulfate-reducing bacteria. Detailed methods for these analyses have been reported elsewhere (McKinley et al. 1997; Fredrickson and Balkwill 1998). Briefly, both dilution plate counting and broth enrichment approaches were used. Liquid medium was inoculated directly with a standard volume of sediment sampled directly from the cores. For dilution plates, sediment was suspended in the sterile pyrophosphate buffer and mixed vigorously prior to dilution and spread plating on agar medium. Media were incubated at room temperature except where noted as being different.

Agar plates were examined periodically over a period of several months and the number of bacterial colonies determined at several points. Distinct colony types, based on color, size, and morphology, arising on agar plates inoculated with the various samples were noted, picked, and streaked for isolation onto fresh medium. In some instances there was no observed bacterial growth on agar plates as indicated by the lack of bacterial colonies but growth was observed in broth enrichments. In these situations, a small volume of broth enrichment was transferred to fresh medium, including agar plates, in an attempt to isolate additional microorganisms. In this manner, approximately 50 bacterial cultures have been obtained to date from the various core samples. These cultures have been preserved at -80 °C in our laboratories at PNNL and have been deposited in the DOE Subsurface Microbial Culture Collection (SMCC) at Florida State University where they have also been preserved.

A subset of cultures (isolates) was subjected to phylogenetic analysis by sequencing the 16 S rRNA gene. Phylogenetic analysis is a measure of the genetic relatedness of the subsurface isolates to other isolates, many of which have been well described and for which considerable physiological information can be available. Thus, phylogenetic typing can provide insights into the types of metabolic functions associated with the individual cultures. In addition to the phylogenetic analysis, select physiological properties are being conducted on a subset of the cultured organisms. These include resistance to ionizing radiation and desiccation (Mattimore and Battista 1996) and ability to reduce Tc(VII), U(VI), and Cr(VI) (Fredrickson et al. 2000a).

D.5.1.3 Results

D.5.1.3.1 Sediment Microbial Populations. In general, the populations of aerobic heterotrophic bacteria, as determined by dilution plate counts, were quite variable, ranging from below detection to greater than 10^4 colony-forming units (CFU) per gram of sediment (Table D.5.1.1). There were no obvious trends regarding the presence or population size of heterotrophic bacteria in relation depth, radioactivity (^{137}Cs), or volumetric water content. In fact, several sediment samples with relatively low water contents and high radioactivity (54.48, 71.51, and 84.13 m, for example) also contained some of the highest populations of heterotrophic bacteria. Two of the samples, 54.48 and 143.99, contained remarkably high populations for vadose sediments. The factors controlling the presence and size of these populations are currently unclear. Modeling efforts to define the historical thermal regime indicate that sediments beneath tank SX-108 were exposed to temperatures in excess of 100 °C to depths as great as 70 feet beneath the tank for as long as 10 years. This heating and associated desiccation would likely have had a negative impact on the viability of vegetative cells. Additional scrutiny of sediment chemical and physical properties may provide additional insights into the controlling factors. Tank waste constituents, depending on their chemical properties and reactivity with sediments, can migrate at different rates through the sediments. Although some constituents may be toxic to microorganisms, others may have little or no impact while a few, such as nitrogen, carbon, or phosphorous-containing compounds may stimulate the growth and metabolism of endogenous vadose microorganisms. Due to the chemical and radiological characteristics of wastes associated with the Hanford tanks, they would not be expected to support microbial populations. However, because of the ability of microorganisms to survive and even thrive under conditions considered uninhabitable by higher life forms, their presence within the tanks cannot be ruled out (Stevens and Fredrickson 1990). To our knowledge, no microbiological analysis of tank wastes has ever been conducted.

Table D.5.1.1. Populations of Aerobic Heterotrophic Bacteria in Vadose Samples From Beneath SX-108.

Sample ID	Depth feet	^{137}Cs pCi/g	Water content %	PTYG[a]	Viable counts R2A[b]	(log CFU/g) Actino[c]
1a	54.48	3.06E+06	4.3	4.0	4.0	4.0
3a	67.27	1.95E+07	2.8	bd[d]	bd	bd
4a	71.51	1.38E+06	2.8	3.7	bd	2.9
5a	75.73	6.52E+06	4.7	bd	bd	bd
6a	79.94	5.31E+07	3.7	bd	bd	bd
7a	84.13	2.14E+07	6.2	3.2	3.1	3.2
8a	88.32	5.55E+05	6.0	bd	bd	bd
9a	92.48	1.71E+02	2.4	2.6	bd	bd
10a	96.64	4.51E+02	1.9	bd	1.8	bd
11a	101.04	9.12E+02	3.2	bd	bd	bd
12a	104.92	3.37E+02	21.4	2.7	2.7	2.7
13a	113.14	5.21E+02	7.6	bd	bd	bd
14a	121.30	8.37E+02	12.0	bd	bd	bd
15a	129.44	5.92E+02	17.4	bd	1.8	bd
16a	137.54	9.79E+01	7.5	3.3	1.5	bd
17a	143.99	1.75E+02	19.7	>4.3	>4.3	>4.3

[a] PTYG = peptone-tryptone-yeast extract glucose medium.
[b] R2A = commercially available (Difco Laboratories) medium formulated for culturing aerobic heterotrophic bacteria.
[c] Actino = Difco medium formulated for culturing actinomycetes.
[d] bd = below detection or less than 1.8 log colony forming units (CFU)/g.

Denitrifying bacteria are able to grow with O_2 as a terminal electron acceptor but, in its absence, can utilize NO_3^- as an alternative acceptor for energy and growth. As a result of this metabolism, denitrifying bacteria reduce NO_3^- to NO_2^- and then to N_2O or N_2 or, alternatively, to NH_4^+ depending upon the microorganism and associated biochemical pathway. Because NO_3^- is a common tank waste constituent, we initiated enrichments for denitrifying bacteria. Core samples 12A and 17A are the only samples where the presence of denitrifying bacteria was confirmed. At issue is whether these organisms dissimilate nitrate to N_2O/N_2 or to NH_4^+. No sulfate-reducing or fermentative bacteria were cultured from any of the samples.

Results from previous microbiological analyses of vadose sediments from the Hanford formation are summarized in Table D.5.1.2 to provide a basis for comparison with the tank SX-108 results. All of the samples reported in this table are either from a borehole located near the Yakima Barricade or from boreholes drilled in the 200 West Area of the Hanford Site. All of these samples are geologically comparable to the SX-108 vadose samples. The Yakima Barricade is located several miles west of the 200 West Area; this site is pristine in that it has not been impacted by site-related activities. The conclusions from these previous studies indicate that pristine Hanford formation vadose sediments contain few or no culturable aerobic heterotrophic bacteria; 10 of 12 Hanford formation sediments samples did not contain detectable levels of viable aerobic bacteria. One (W15, 31.4m) of the two samples that contained culturable bacteria was impacted by artificial recharge and contamination associated with wastewater released to the surface in the Hanford 200 West Area (Fredrickson et al. 1993). It was hypothesized that the observed culturable populations were the result of stimulation of dormant endogenous bacteria by recharge waters and, possibly, associated nutrients. Additional support for this hypothesis was provided by Kieft et al. (1993) who observed bacterial cells, by direct microscopy, in the range of 10^6 to 10^7 cells/g in pristine Hanford formation sediments. Also, studies by our laboratory (Fredrickson et al. 1995; Brockman et al. 1998) and others (Haldeman et al. 1994) have indicated that populations of viable aerobic heterotrophic bacteria in vadose sediments increase with increasing post-sampling time, sometimes by as much as 6 orders of magnitude, within a period of 10 to 80 days. Post-sampling increases in viable microbial populations in vadose sediments are likely due to stimulation of dormant cells via a variety of possible mechanisms. These mechanisms may include the redistribution of cells and solid-phase associated nutrients by sample mixing or disturbance during coring, by increasing gaseous exchange or by facilitating movement of moisture via evaporation or condensation to generate microscale chemical gradients at surfaces. It should be noted that the time elapsed between coring and inoculation of medium with SX-108 vadose core samples was approximately 30 days.

Table D.5.1.2. Microbiological Properties of Hanford Formation Vadose Sediments From Previous Sampling Efforts.

Borehole	Depth (meters)	Viable counts (log CFU/g)	% H_2O	Reference
Yakima Barricade	Surface	6.9	1.6	(Fredrickson et al. 1993)
Yakima Barricade	30.3	2.3	3.9	(Kieft et al. 1993)
Yakima Barricade	31.1	bd[a]	2.2	(Kieft et al. 1993)
Yakima Barricade	31.6	Bd	4.2	(Kieft et al. 1993)
Yakima Barricade	31.8	Bd	7.7	(Fredrickson et al. 1993)
Yakima Barricade	45.8	Bd	2.5	(Kieft et al. 1993)
Yakima Barricade	47.0	Bd	16.1	(Fredrickson et al. 1993)
Yakima Barricade	53.0a	Bd	3.4	(Fredrickson et al. 1993)
Yakima Barricade	53.0b	Bd	1.7	(Kieft et al. 1993)
W18	24.4	Bd	4.5	(Fredrickson et al. 1993)
W18	24.6	Bd	2.9	(Kieft et al. 1993)
W15	31.3[b]	Bd	11.7	(Kieft et al. 1993)
W15	31.4[b]	3.1	7.0	(Kieft et al. 1993)

[a] bd = below detection or less than 2.0 log colony forming units (CFU)/g.

[b] sediments subjected to artificial recharge, contamination by past site activities (Fredrickson et al. 1993).

D.5.1.3.2 Isolate Phylogeny. Approximately 50 cultures of aerobic heterotrophic bacteria have been isolated and purified from the various enrichments and dilution plates. These isolates have been preserved by freezing in glycerol at -80 °C and have been shipped to the SMCC at Florida State University for archiving and phylogenetic analysis based on 16S rRNA gene sequence. The phylogeny of the isolates is, for the most part, unremarkable. The genera represented are typical soil and sediment inhabitants. Interestingly, members of the genus *Arthrobacter* were the most common isolates with 5 of 15 isolates being assigned to this genus (Table D.5.1.3). Members of the genus *Arthrobacter* were also found to represent approximately one-third of the aerobic chemoheterotrophic bacteria isolated from pristine Ringold Formation sediments obtained from the Hanford Site Yakima Barricade borehole (Balkwill et al. 1997), drilled as part of DOE's Subsurface Science Program. These strains of *Arthrobacter* appear to represent novel species within the genus (Crocker et al. 2000). Additional genera found as part of this research that were also found in the previous study by Balkwill et al. include *Rhodococcus*, *Staphylococcus*, *Nocaroides*, *Blastobacter*, *Nocardioides*, and *Sphingomonas*. Hence, it appears that the organisms isolated as part of this study are largely common inhabitants of suprabasalt subsurface sediments on the Hanford Site. The isolates characterized to date, except for *Pseudomonas*, *Sphingomonas*, and *Blastobacter*, are predominantly Gram-positive bacteria. Gram-positive bacteria appear to be dominant in many vadose zone environments (Kieft and Brockman 2001), possibly because they are better adapted for survival under low moisture and nutrient starvation conditions. Although some strains of *Staphylococcus* are known to be human pathogens, the isolate identified as a member of this genus, 4b-2, is most closely related to a strain obtained from an environmental sample of unknown origin and is not known to be a human pathogen. In addition, *Staphylococcus* members represented 20 of 169 isolates cultured from the Yakima Barricade Ringold sediment samples (Balkwill et al. 1997) and thus appears to be a normal component of the vadose zone microbiota on the Site.

Perhaps the most intriguing finding of this research is the isolation of a strain, 7b-1, that is closely related to *Deinococcus radiodurans* (Table D.5.1.3). *Deinococcus radiodurans* is the most radiation-resistant organism discovered to date, exhibiting the ability to withstand doses of ionizing radiation to 15,000 Gy without lethality (Daly et al. 1994). Interestingly, the sediment sample that this bacterium was isolated from had one of the highest levels of radiation (Table D.5.1.1) of any of the samples examined. This is the first isolation, that we are aware of, of a strain of *D. radiodurans* from a radionuclide-contaminated environment. In addition to 7b-1, there are several additional strains isolated from highly contaminated samples that also appear to be members of *Deinococcus*, based on their distinct morphology (Figure D.5.1.1). These strains have recently been submitted to the SMCC and are being sequenced (16S) for phylogenetic analysis.

Table D.5.1.3. Phylogeny of Select Aerobic Heterotrophic Isolates From SX-108 Sediment Samples Base on 16S rRNA Gene Sequence Analysis.

Isolate ID [a]	Phylogeny	GenBank Accession Number
1b-1	*Arthrobacter globiformus*	M23411
1c-1	*Arthrobacter oxydans*	AJ243423
4a-4	*Rhodococcus corynebacteroides*	X80615
4b-2	*Staphylococcus warneri*	AJ223451
4b-3	*Nocardioides plantarum*	Z78211
7b-1	*Deinococcus radiodurans*	Y11332
9c-3	*Blastobacter* sp. str. BF10	AJ223453
10c-2	*Sphingomonas* sp. str. Koll-1	AJ224938
12a-1	*Pseudomonas* sp. str. BRW3	AF025351
12b-1	*Pseudomonas* sp. str. BRW3	AF025351
15a-1	*Terrabacter tumescens*	X83812
17a-1	*Arthrobacter aurescens*	X83405
17a-2	*Arthrobacter oxydans*	AJ243423
17a-3	*Pseudomonas* sp. str. BRW3	AF025351
17b-1	*Arthrobacter pascens*	X80740

[a] The first two digits of the isolated ID refer to the sample from which the culture was isolated.

Figure D.5.1.1. Scanning Electron Microscopic (left) and Transmission Electron Microscopic Image of *D. radiodurans* 7b-1 Cells.

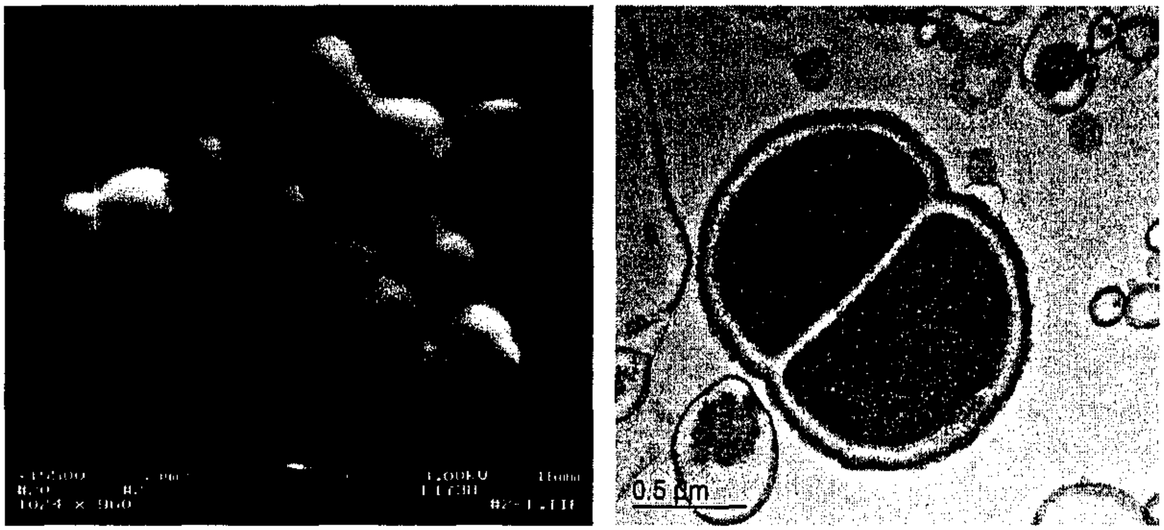

D.5.1.3.3 Characterization of *Deinococcus radiodurans* 7b-1. *D. radiodurans*, at this dose of radiation, incurs a large number of double-stranded DNA breaks, 130 per chromosome (Daly et al. 1994). Extremely efficient DNA repair mechanisms in operation during recovery in the absence of radiation are responsible for the extreme radiation resistance observed in this organism (Daly and Minton 1995, 1996; Minton 1996). We evaluated the resistance of strains 7b-1 and 7c-1 along with *Deinococcus radiodurans* R1, the type strain, to acute doses of ionizing radiation from a ^{60}Co source. The results from this experiment indicate that strains 7b-1 and 7c-1 (not shown) are equally or slightly more resistant to ionizing radiation than *D. radiodurans* R1, the type strain (Figure D.5.1.2). At a dose of 1 MRad, there was no apparent impact on cell growth of either R1, 7b-1, or 7c-1. At a dose of 2 MRad, approximately 0.2% of the cells survived and grew whereas at 3 MRad there was no detectable survival or growth. Resistance to such high levels of ionizing radiation may not represent a direct adaptation response since there are no natural terrestrial environments that generate such high fluxes of ionizing radiation (Minton 1996). It is more likely that the efficient DNA repair system in this bacterium represents an adaptation to prolonged desiccation as dehydration of cells results in DNA damage (double-stranded DNA breaks) similar to that resulting from exposure to ionizing radiation (Mattimore and Battista 1996). It is possible that *Deinococcus* is an indigenous inhabitant of Hanford soils and that the combination of contamination, heating, and drying of sediments led to conditions that only highly stress-tolerant organisms such as *Deinococcus* could survive.

Recently, we demonstrated that *D. radiodurans* R1 was capable of reducing Fe(III) when complexed with nitrilotriacetic acid (NTA), Cr(VI), U(VI), and Tc(VII) and anaerobic conditions with lactate or pyruvate as an electron donor (Fredrickson et al. 2000). Prior to this, *D. radiodurans* was believed to have a strictly aerobic metabolism. These previous findings coupled with the metal and radionuclide contaminants associated with the SX-108 vadose samples (Cr, Tc, U, among others) prompted investigation into the potential for the SX-108 isolates to reduce metals and radionuclides. Our results demonstrate that, similar to *D. radiodurans* R1, 7b-1 also reduced Tc and U under anaerobic conditions but only in the presence of anthraquinone-2,6-disulfonate (AQDS) (Figure D.5.1.3a, b), an organic compound that can function as an electron acceptor and shuttle electrons between cells and metals external to the cell surface. In contrast, 7b-1 was able to reduce Cr(VI) under both aerobic and anaerobic conditions and in the absence of AQDS. The reason for the requirement for AQDS for the reduction of Tc and U but not Cr by *D. radiodurans* are unclear but we previously speculated that it may be due to the inaccessibility of Tc and U to electron transfer enzymes associated with the cells (Fredrickson et al. 2000). In contrast, Cr and AQDS would have access to enzymes that the Tc and U do not. Also similar to *D. radiodurans* R1, 7b-1 was able to reduce Fe(III)-NTA coupled to pyruvate oxidation (Figure D.5.1.4a) and could reduce ferrihydrite only in the presence of pyruvate with AQDS as an electron shuttle (Figure D.5.1.4b).

Figure D.5.1.2. Resistance to Acute Doses of Ionizing Radiation as Measured by the Percentage of Cells Surviving and Growing on Tryptone-Yeast Extract-Glucose Agar Medium Following Exposure to Acute Doses of Gamma Radiation From a ^{60}Co-Source.

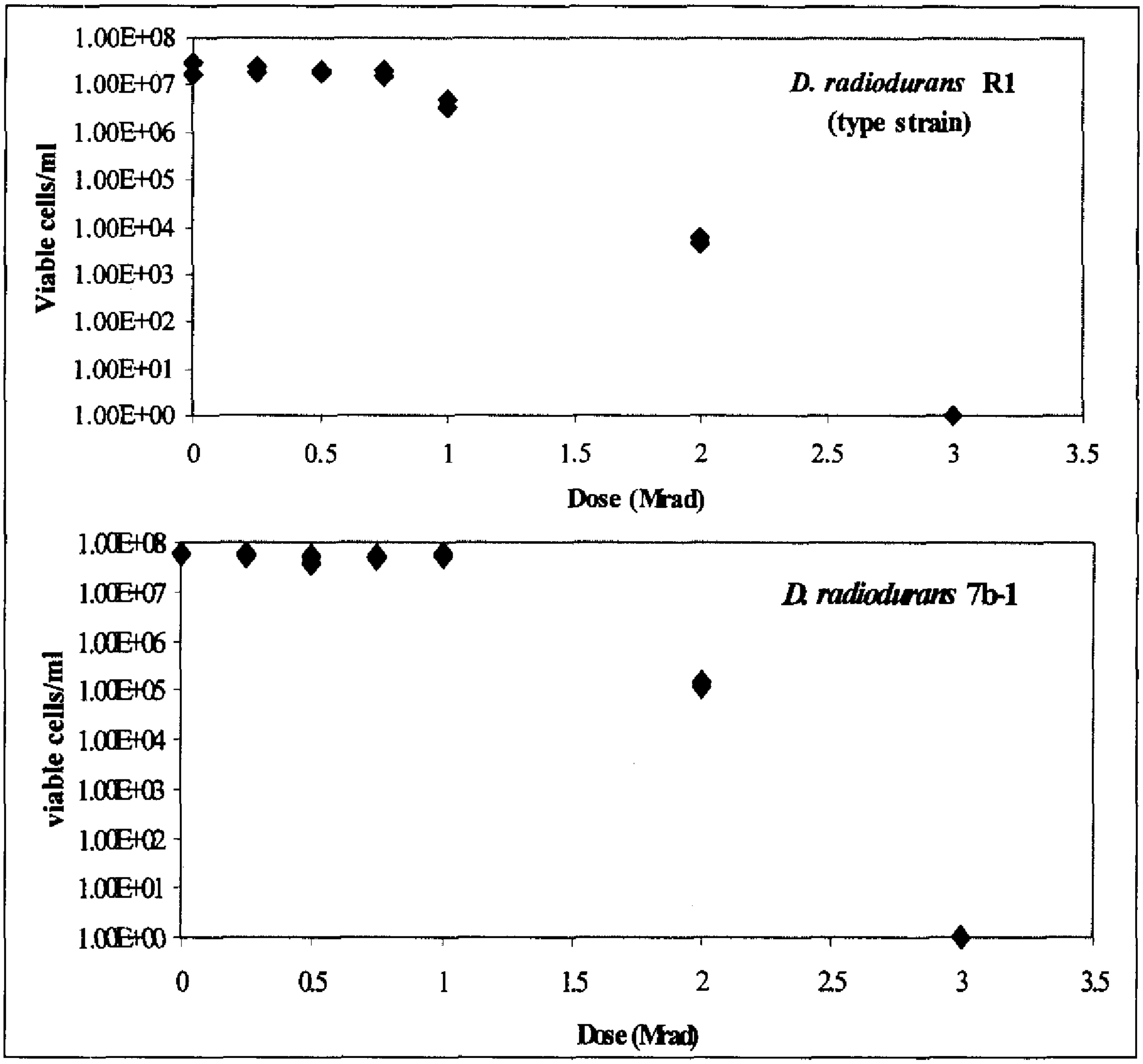

Figure D.5.1.3. Reduction of U(VI) (a), Tc(VII) (b), and Cr(VI) (c) by *D. radiodurans* 7b-1 in TYG for U and Tc and in a pH 7 Bicarbonate-Buffered Medium for the Cr Experiment. AQDS, when Present, was Added a Concentration of 100 μM.

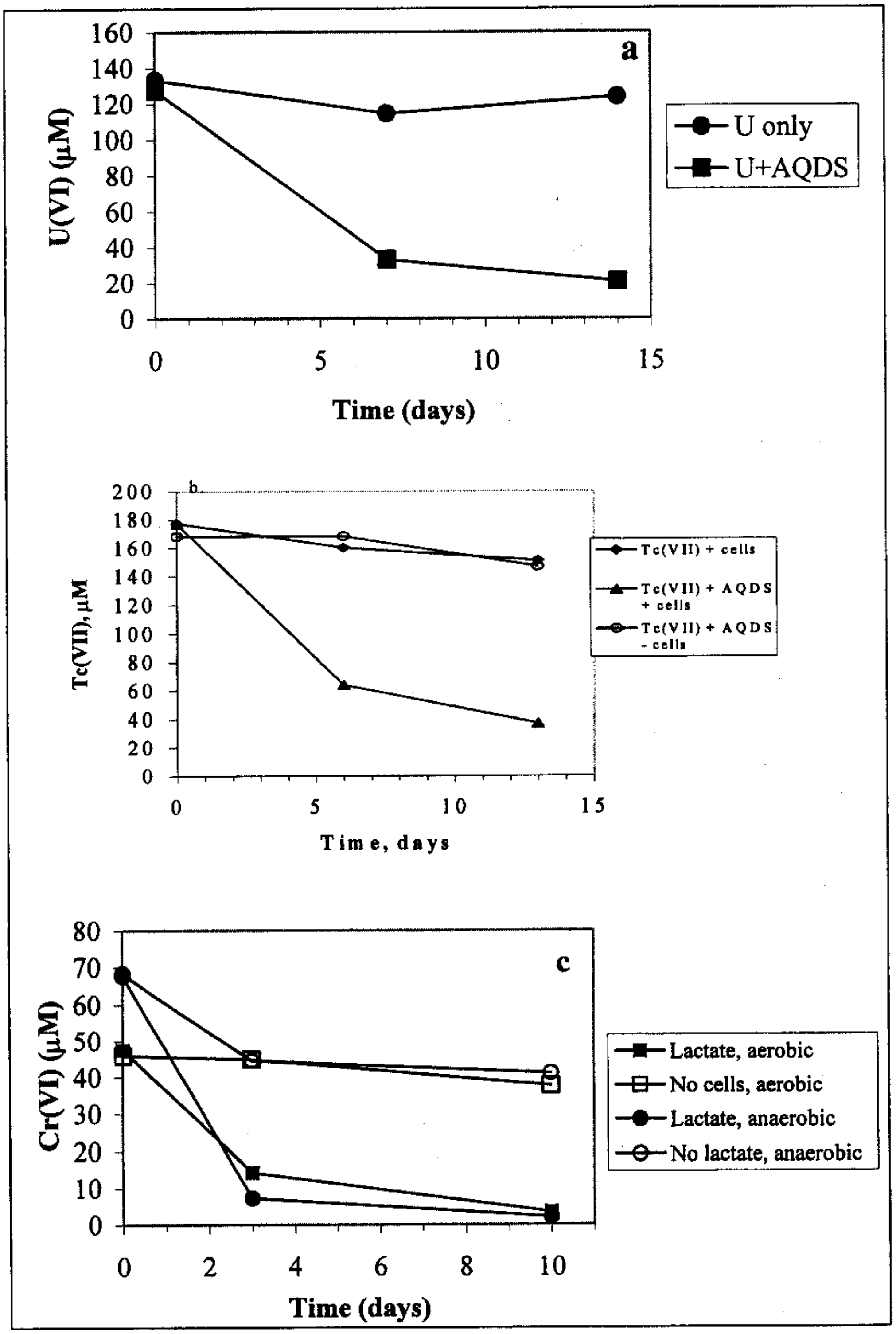

Figure D.5.1.4. Reduction of Fe(III)-NTA in Bicarbonate-Buffered Medium (a) and Ferrihydrite (b) by *D. radiodurans* 7b-1.

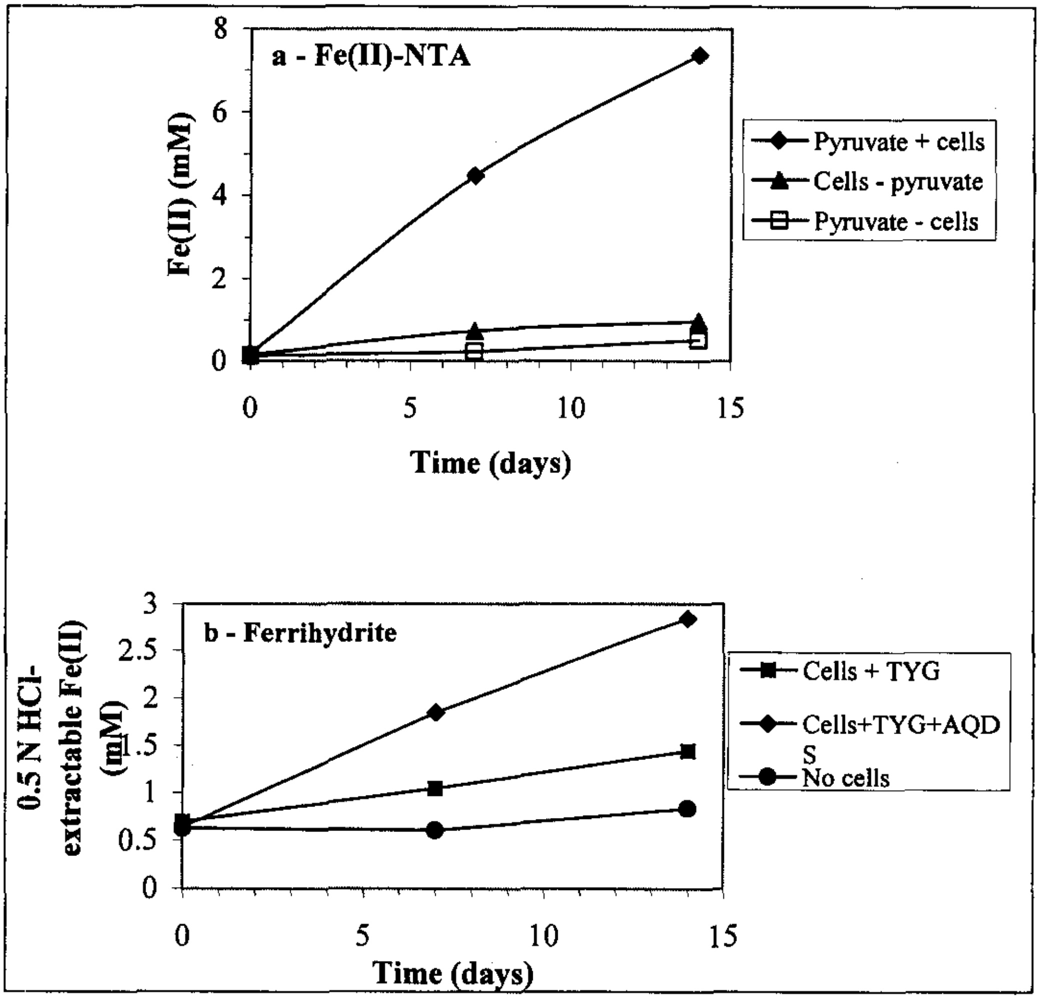

D.5.1.4 Conclusions and Implications

Although the factors influencing the microbiological characteristics of the SX-108 vadose sediments are unclear at this time, the finding of significant populations of aerobic heterotrophic bacteria may have important implications for the fate and transport of waste-associated contaminants. Microorganisms, in general, have the capacity for a wide range of biogeochemical transformations including reactions with waste constituents. For example, microorganisms are capable of degrading a wide range of organic compounds, oxidizing and reducing multivalent metals and radionuclides such as U or Tc, oxidizing ammonium to nitrite and nitrate and reducing nitrate or nitrite to ammonium or N_2 and for sorption and/or assimilation of a range of cations, including Cs and Sr. An important consideration is whether the denitrifying bacteria that were cultured can dissimilate nitrate or nitrite, in the absence of O_2, to ammonium or gaseous end products such as N_2O or N_2. Ammonium effectively competes with Cs for cation exchange sites on soil and sediment particles and has been used to effectively extract exchangeable Cs from soils. The implications would be that the potential exists for the in situ microbiological production of NH_4^+ that could compete with Cs^+ for exchange sites on sediment particles.

As a result of this research, we have confirmed the presence of microorganisms in highly contaminated sediments beneath tank SX-108 and that some of these organisms can utilize nitrate as an electron acceptor in the absence of O_2 while others can reduce several of the contaminating metals and radionuclides to poorly soluble species. The culturable microbiota is composed predominantly of aerobic chemoheterotrophic bacteria, mainly Gram-positive bacteria. These bacteria are generally well adapted to survival under low moisture and low nutrient conditions.

The most remarkable result was the isolation of several ionizing radiation-resistant bacteria closely related to *Deinococcus radiodurans* from one of the most highly contaminated core samples that was collected. This is the first time that *D. radiodurans* has been isolated from a radionuclide-contaminated environment to our knowledge. These organisms were able to reduce U(VII) and Tc(VIII) to poorly soluble species in the presence of an electron-shuttling quinone under anoxic conditions. In contrast, these strains were able to reduce Cr(VI) under anaerobic and aerobic conditions with a suitable electron donor. It is unlikely, in our opinion, that metal reduction has or would be occurring in situ for several reasons including the fact cell populations were relatively low, a few tens or hundreds of cells per gram and that the low moisture content would restrict metabolic activity by limiting nutrient flux. However, the possibility of microsites with higher bacterial populations and levels of metabolic activity cannot be ruled out. The presence of such sites could contribute to the reduction of contaminants such as Cr(VI) or NO_3^-, that are easily reduced relative to U and Tc. Reduction of Cr(VI) to relatively insoluble Cr(III) would limit the mobility of this important contaminant in the subsurface.

Additional investigations are required to determine the phylogeny of the remaining isolates and the metabolic capabilities of these organisms that may influence contaminant fate and transport in the vadose zone. Microbial processes may have an even greater impact on contaminant fate and transport in the subsurface under other leaking tanks at Hanford, such as at the B and BX tank farms, where the concentration of organic complexing agents associated with the tanks wastes was much higher than at SX tank farm. Many of the organics associated with the waste, such as citric and tartaric acids, are readily metabolized by a wide range of microorganisms.

The microbial degradation of these organic complexing agents could have a major impact on the migration of contaminants in the vadose zone.

D.5.1.5 References

Balkwill, D. L., R. H. Reeves, G. R. Drake, J. Y. Reeves, F. H. Crocker, M. Baldwin-King, and D. R. Boone, 1997, "Phylogenetic Characterization of Bacteria in the Subsurface Microbial Culture Collection," *FEMS Microbiology Reviews*, Vol. 20: 201-216.

Brockman, F. J., T. L. Kieft, J. K. Fredrickson, B. N. Bjornstad, S. W. Li, W. Spangenburg, and P. E. Long, 1992, "Microbiology of Vadose Zone Paleosols in South-Central Washington State," *Microbial Ecology*, Vol. 23: 279-301.

Brockman, F. J., S. W. Li, J. K. Fredrickson, D. B. Ringelberg, T. L. Kieft, C. M. Spadoni, J. P. McKinley and D. C. White, 1998, "Post-Sampling Changes in Microbial Community Structure and Activity in a Subsurface Paleosol," *Microbial Ecology*, Vol. 36: 152-164.

Crocker, F. H., J. K. Fredrickson, D. C. White, D. B. Ringelberg, and D. L. Balkwill, 2000, "Phylogenetic and Physiological Diversity of *Arthrobacter* Strains Isolated From Unconsolidated Subsurface Sediments," *Microbiology*, Vol. 146: 1295-1310.

Daly, M. J., and K. W. Minton, 1995, "Interchromosomal Recombination in the Extremely Radioresistant Bacterium *Deinococcus radiodurans*," *Journal of Bacteriology*, Vol. 177: 5495-5505.

Daly, M. J. and K. W. Minton, 1996, "An Alternative Pathway of Recombination of Chromosomal Fragments Precedes recA-dependent Recombination in the Radioresistant Bacterium *Deinococcus radiodurans*," *Journal of Bacteriology*, Vol. 178: 4461-4471.

Daly, M. J., L. Ouyang, P. Fuchs, and K. W. Minton, 1994, "*In vivo* Damage and *rec*A-Dependent Repair of Plasmid and Chromosomal DNA in the Radiation-Resistant Bacterium *Deinococcus radiodurans*," *Journal of Bacteriology*, Vol. 176: 3508-3517.

Fredrickson, J. K. and D. L. Balkwill, 1998, *Sampling and Enumeration Techniques: Techniques in Microbial Ecology*, R. S. Burlage, R. Atlas, D. Stahl, G. Geesey, and G. Sayler, eds, Oxford University Press, New York, 239-254.

Fredrickson, J. K., F. J. Brockman, B. N. Bjornstad, P. E. Long, S. W. Li, J. P. McKinley, J. V. Wright, J. L. Conca, T. L. Kieft and D. L. Balkwill, 1993, "Microbiological Characteristics of Pristine and Contaminated Deep Vadose Sediments From an Arid Region," *Geomicrobiology Journal*, Vol. 11: 95-107.

Fredrickson, J. K., H. M. Kostandarithes, S. W. Li, A. E. Plymale, and M. J. Daly, 2000a, "Reduction of Fe(III), Cr(V), U(VI), and Tc(VII) by *Deinococcus radiodurans* R1," *Applied and Environmental Microbiology*, Vol. 66: 2006-2011.

Fredrickson, J. K., J. M. Zachara, D. W. Kennedy, M. C. Duff, Y. A. Gorby, S. W. Li, and K. M. Krupka, 2000b, "Reduction of U(VI) in Goethite (α-FeOOH) Suspensions by a Dissimilatory Metal-Reducing Bacterium," *Geochimica et Cosmochimica Acta,* Vol. 64: 3085-3098.

Fredrickson, J. K., S. W. Li, F. J. Brockman, D. L. Haldeman, P. S. Amy, and D. L. Balkwill, 1995, "Time-Dependent Changes in Viable Numbers and Activities of Aerobic Heterotrophic Bacteria in Subsurface Samples," *Journal of Microbiological Methods,* Vol. 21: 253-265.

Fredrickson, J. K., and T. C. Onstott, 2001, "Biogeochemical and Geological Significance of Subsurface Microbiology," *Subsurface Microbiology and Biogeochemistry,* J. K. Fredrickson and M. Fletcher, Wiley-LISS Inc., New York, pp. 3-38.

Haldeman, D. L., P. S. Amy, D. C. White, and D. B. Ringelberg, 1994, "Changes in Bacteria Recoverable From Subsurface Volcanic Rock Samples During Storage at 4 °C," *Applied and Environmental Microbiology*, Vol. 60: 2697-2703.

Kieft, T. L., P. S. Amy, F. J. Brockman, J. K. Fredrickson, B. N. Bjornstad, and L. L. Rosacker, 1993, "Microbial Abundance and Activities in Relation to Water Potential in the Vadose Zones of Arid and Semiarid Sites," *Microbial Ecology*, Vol. 26: 59-78.

Kieft, T. L. and F. J. Brockman, 2001, "Vadose Zone Microbiology," *Subsurface Microbiology and Biogeochemistry*, J. K. Fredrickson and M. Fletcher, Wiley-LISS Inc., New York, 141-169.

Lovley, D. R., 1995, "Microbial Reduction of Iron, Manganese, and Other Metals," *Advances in Agronomy,* Vol. 54: 175-231.

Mattimore, V. and J. R. Battista, 1996, "Radioresistance of *Deinococcus radiodurans*: Functions Necessary to Survive Ionizing Radiation are also Necessary to Survive Prolonged Desiccation," *Journal of Bacteriology*, Vol. 178: 633-637.

McKinley, J. P., T. O. Stevens, J. K. Fredrickson, J. M. Zachara, F. S. Colwell, K. B. Wagnon, S. A. Rawson, and B. N. Bjornstad, 1997, "The Biogeochemistry of Anaerobic Lacustrine and Paleosol Sediments within an Aerobic Unconfined Aquifer," *Geomicrobiology Journal*, Vol. 14: 23-39.

Minton, K. W., 1996, "Repair of Ionizing-Radiation Damage in the Radiation Resistant Bacterium *Deinococcus radiodurans*," *Mutation Research*, Vol. 363: 1-7.

Stevens, T. O., and J. K. Fredrickson, 1990, "Potential for Microbial Gas Generation in High-Level Radioactive Waste Storage Tanks," Pacific Northwest National Laboratory, Richland, Washington.

Wildung, R. E., Y. A. Gorby, K. M. Krupka, N. J. Hess, S. W. Li, A. E. Plymale, J. P. McKinley, and J. K. Fredrickson, 2000, "Effect of Electron Donor and Solution Chemistry on the Products of the Dissimilatory Reduction of Technetium by *Shewanella putrefaciens*," *Applied and Environmental Microbiology*, Vol. 66: 2451-2460.

D.6.0 TRANSPORT MECHANISMS INFERRED BY ISOTOPE GEOCHEMISTRY

John C. Evans[1], P. Evan Dresel[1], Orville T. Farmer[1], Mark S. Conrad[2], and Donald J. DePaolo[2]

[1]Pacific Northwest National Laboratory, Richland, Washington 99352

[2]Lawrence Berkeley National Laboratory, Berkeley, California 94720

Mass spectrometric methods for determination of stable and long-lived radiological isotope concentrations and concentration ratios have long been used for a wide range of geotechnical investigations including such diverse applications as age dating, paleotemperature measurement, tracking of groundwater and seawater movement, mineral exploration, and chemical source attribution. In spite of such widespread use within the research community, stable isotope methods tend to be very specialized and have found limited use for routine application on environmental investigations. For the past 4 years, researchers at the Lawrence Berkeley National Laboratory (LBNL) Center for Isotope Geochemistry and Pacific Northwest National Laboratory (PNNL) have been experimenting with a suite of mass spectrometric methods aimed at applying powerful stable and long-lived radiological isotope analysis techniques to obtain a better understanding of sources and sinks for water and contaminant movement in the vadose zone and groundwater at DOE sites. In the past 2 years the principal focus of that work has been the Hanford Site. Most recently, under Hanford S&T Program support, uncontaminated and tank leak contaminated core samples from the SX tank farm environs have been subjected to detailed analysis for the isotopes of H, O, Sr, Cs, Mo, I, Se, and U using several different mass spectrometric procedures. Results of those studies are discussed below for three specific topic areas: (1) fission product isotopic fingerprints of waste movement measured in SX tank farm boreholes, (2) horizontal transport of chemical waste inferred from isotopic and chemical measurements of core samples from B8812 clean borehole, and (3) vertical distribution $^{86}Sr/^{87}Sr$ isotopic ratios measured in B8812 core and implications to water infiltration near the SX tank farm. The first topic discusses work performed at several PNNL labs. The second represents a collaborative effort between LBNL and PNNL, while the Sr isotope work was performed entirely at LBNL.

D.6.1 FISSION PRODUCT ISOTOPIC FINGERPRINTS OF WASTE MOVEMENT MEASURED IN SX TANK FARM BOREHOLES; IMPLICATIONS TO MOBILE CONTAMINANTS

D.6.1.1 Introduction

While waste tank leaks at Hanford have been recognized since at least the late 1950s, a relatively limited amount of research has been directed toward obtaining a detailed understanding of the geochemical behavior of the diverse collection of contaminants released by tank leaks. In the past few years, a greatly increased level of effort has been undertaken to improve our overall understanding of contaminant movement in the vadose zone and, in particular, the potential for groundwater impact from the more mobile constituents. The recent recognition of groundwater impacts at several tank farms (Johnson and Chou 1998; Narbutovskih 1998; Hodges 1998; Hodges and Chou 2000) has added a degree of urgency to this effort. Recent drilling efforts in the vicinity of the SX tank farm have yielded good quality research materials from cores collected at locations associated with leaks believed to be originating from tanks SX-115, SX-109, and SX-108. All three boreholes were found to be contaminated with tank leak material to some degree. The SX-108 borehole was drilled on a 30–degree slant providing material from the heart of the contaminant plume itself for the first time at Hanford. The SX-108 slant borehole thus represents an ideal source of research materials and has consequently become the central theme of a wide range of focused and detailed research efforts supported by DOE/EMSP and augmented by the Hanford S&T Program. All three cores have been managed and intensively studied by a project supported by the Office of River Protection and implemented at PNNL. Results of those studies are discussed in detail elsewhere in this report and in dedicated individual topical reports for each borehole (Serne et al. 2001a, b, c). Materials and data generated by that effort were used in planning and implementing the work described below.

In order to correctly interpret contaminant distributions in these cores with regard to geological and geochemical controls, it is first necessary to understand the temporal and spatial history of the leaks. For example, essentially all contaminants observed in the SX-108 core show two or more concentration maxima. The multiple peaks can be interpreted as resulting from geologic effects (stratification, grain size), geochemical effects (sorption, precipitation, REDOX), or differences in chemical speciation (valence states, ligand complexation). Alternatively, multiple leak events representing different points in time and volumes of liquid may be responsible for affecting the vertical distribution of contaminants. The effect of multiple events will inevitably be superimposed on top of other effects of more fundamental interest and must be unfolded. Separate leak events originating either from different tanks or separate fillings of the same tank should be resolvable through differences in materials containing internal isotopic signatures. Suitable systems, which have been identified in this work, include the fission-derived isotopes of Cs, Mo, Se, and I. The ^{127}I to ^{129}I ratio of waste is particularly diagnostic. Isotopes of Pu and U also form ideal tank signatures, possessing in principle at least, distinctive fingerprints. Neither element has been observed in significant quantity associated with tank leaks in the SX tank farm, however, because of essentially 100% association of those species with the solid phase in those tanks with correspondingly negligible concentrations found in the leaked supernate. Both Pu and U have been observed in tank leaks from other farms (e.g., tank T-106) and are thus expected to be of great value in future investigations. Alternatively, the ratios of various chemical species with little or no retardation following release from a tank into the vadose zone can also be useful as indicators of different source compositions. Species, which are used for that purpose here, include Cl, N, S, and ^{99}Tc. More detailed discussion on the considerations affecting each will be discussed separately below.

An additional goal of this work is the identification and baseline characterization of isotopic fingerprints, which may be used for source attribution of groundwater plumes. Association of groundwater contaminants with specific waste management units is typically very difficult at Hanford because of the close spacing of tank farms, cribs, trenches, ponds, operational spills, and other methods for waste to enter the subsurface. Isotopic fingerprinting techniques can provide a means to distinguish between crib waste and tank waste by providing a better definition of the isotopic composition of distinct waste sources than can be inferred from direct measurement. The SX tank farm coring program provides the first real opportunity to obtain some of that information in a suitable form.

Extensive experimentation is currently underway to better understand the mobility of ^{137}Cs in the subsurface. Sorption effects on the surfaces of clay minerals dominate transport of Cs. Since sorption of ^{137}Cs must compete with other chemical forms of Cs including stable ^{133}Cs and the very long-lived ^{135}Cs ($T_{1/2}$ = 2.3 million years), both of which are themselves high-yield fission products, it is important to know the total Cs content of the system in order to properly conduct and interpret Cs sorption studies and utilize that data in transport models. Cs isotopic studies reported here combined with nuclear modeling calculations performed in association with that work address the issue of competitive Cs sorption.

D.6.1.2 Experimental Procedures

D.6.1.2.1 ICP/MS Analysis. All analyses were performed on either 1:1 water or strong nitric acid extracts of the sediment samples. Extraction was performed by PNNL/ORP staff in the 3720 Building prior to performance of comprehensive analysis on those extracts. Analyses routinely performed on the water and acid extracts included trace metals by ICP–OES and ICP/MS, common anions by ion chromatography, as well as radiological measurement for ^{137}Cs, tritium, ^{90}Sr, ^{99}Tc, and actinides. Details on the experimental protocols used and the results obtained are reported elsewhere in a series of topical reports (Serne et al. 2001a, b, c) and summarized in the main body of this report. Following completion of that work, the remaining extracts and associated blanks, each typically only a few milliliters, were transferred to the 329 Building for more detailed mass spectrometry. Since the samples were highly radioactive, transfer of the samples required appropriate shipping and monitoring protocols for radioactive transfers and all work in the 329 Building was performed under the protocols specified in a Radiation Work Procedure (RWP) specific to that job. A "hot" ICP/MS instrument was dedicated to this activity. Since the "hot" machine was an older instrument with reduced sensitivity (VG PlasmaQuad), some modification of the instrument ion source and vacuum system were required prior to running the samples in order to obtain the requisite instrument sensitivity. Prior to detailed analysis, all samples were screened in the mass range from 91 to 139 and 200 to 243 amu to evaluate potential mass interferences and required dilution factors. Following the screening and determination of appropriate dilution factors, chemical separations were performed on aliquots of the leachates to remove interfering species. ICP/MS analysis was then performed using time resolved ion chromatography/ICP/MS.

D.6.1.2.2 Nuclear Modeling. As an aid to better understanding isotopic ratio measurements, a simple nuclear model was developed to calculate expected ratios of fission-produced Cs, Tc, and Mo. The method employed is very similar to that used in an earlier PNNL study performed for the Nuclear Regulatory Commission (NRC). Details of the FORTRAN-based computer code developed for the NRC work are described in two publications (Evans 1983). A streamlined version of the calculational method used for the NRC study was adapted to a simple Excel spreadsheet. Input data included neutron flux and thermalization parameters for a production reactor, fission and neutron capture cross sections and resonance integrals, fission yields from ^{235}U and ^{239}Pu, and ^{235}U composition for typical production reactor fuel (0.71% ^{235}U). The spreadsheet performed a series of neutron capture and fission event calculations on 0.1-day intervals for up to 150 days to simulate a typical production reactor irradiation during the REDOX Process era at Hanford. Minor adjustments were made to reactor parameters in order to match expected ^{239}Pu/^{240}Pu composition at the end of the irradiation period as well calculating reasonable values for ^{235}U burnup and ^{239}Pu accumulation. An average plutonium composition taken from the Best Basis Inventory documents on tanks SX-108 and SX-109 was used to estimate the expected plutonium composition at the end of irradiation (4.5% ^{240}Pu). ORIGEN2 calculations performed by Watrous and Wootan (1997) were also reconciled as a cross-check for accuracy.

Calculated fission product ratios for Mo and Tc proved to be relatively insensitive to reactor parameters and should thus be reasonably reliable indicators of expected ratios to be compared with the measured values. Table D.6.1.1 lists the expected Cs, Tc, and Mo composition on a relative basis in the reactor fuel at the end of a 110-day irradiation producing plutonium containing 4.5% ^{240}Pu. All results are normalized to ^{99}Tc and assume no chemical fractionation effects. Relative ^{137}Cs values shown in Table D.6.1.1 were corrected for decay assuming a 40-year age for the waste based on the tank leak history for tank SX-108 (WHC 1992). The greatly reduced amount of ^{135}Cs shown in Table D.6.1.1 relative to other similar high-yield fission products is the result of burnup of its parent on the beta decay chain, ^{135}Xe. ^{135}Xe has an exceptionally high neutron capture cross-section, 2.65 million barns. The half-life of ^{135}Xe, 9.1 hours, is long enough that in a high flux reactor burnup is actually favored over decay. Because of this situation, the amount of ^{135}Cs produced is extremely sensitive to reactor flux conditions. The measured values of ^{135}Cs and ^{137}Cs can thus be used to tightly constrain input parameters for the model. The extreme sensitivity of the Cs isotope ratios to reactor conditions also suggests that some source related variability can be expected.

Table D.6.1.1. Results of Nuclear Model Calculation.

Isotope	Relative concentration
^{99}Tc	1.000
^{95}Mo	0.994
^{97}Mo	0.938
^{98}Mo	0.923
^{100}Mo	1.014
^{133}Cs	1.078
^{135}Cs	0.33
^{137}Cs*	0.40

*Corrected for 42 year decay period

D.6.1.3 Results

D.6.1.3.1 Cesium Isotopes. The ^{137}Cs distribution in the SX-108 slant borehole is shown in Figure D.6.1.1. The plot is based on gamma counting data as reported by Serne et al. (2001c). As a point of comparison, the ^{99}Tc concentrations measured in this study on water leach samples from the same core are plotted on the second axis. Both distributions clearly show two peaks with the unretarded ^{99}Tc penetrating much deeper and with more vertical dispersion evident.

Figure D.6.1.1. Vertical Distributions of ^{137}Ce and ^{99}Tc in SX-108 Slant Borehole.

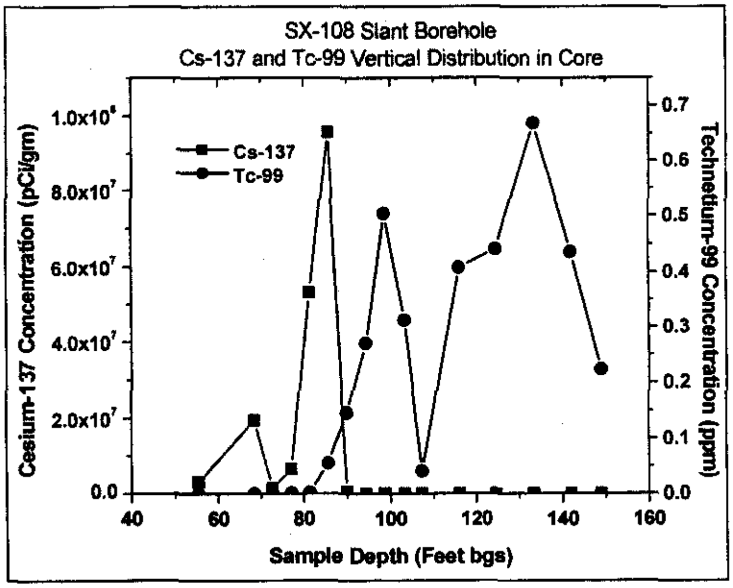

Cs isotopes were measured by ICP/MS on selected water and acid leach samples near the two peaks in the ^{137}Cs vertical distribution. The results of those measurements are shown in Table D.6.1.2. Only data with relative errors of order 10% or less as determined by replicate analysis are included in the table. It is clear that, as expected, the acid extracts resulted in the dissolution of a large amount of native Cs from the mineral matrix of the host sediment. ^{133}Cs results from the acid extracts are thus of little value; however, the ratio of ^{137}Cs to ^{135}Cs is of interest because the ratio can be determined in the acid extracts with very good precision and is unaffected by interferences. The ratio appears to be relatively constant across both peaks. The water leach data does show a small difference between the two peaks but it is unclear if that is significant as it may be an artifact of the larger measurement error on the water leach samples. The Cs data is inconclusive with respect to the issue of separate sources for the two peaks. Additional data from different sources is needed to fully understand the dynamics of this isotopic system.

Additional Cs isotopic measurements were also performed on three samples associated with a series of leaching experiments described in more detail elsewhere in this report. Two of the samples were from the two respective Cs maxima in the SX-108 slant borehole while the third was from the ^{137}Cs maximum in the borehole associated with the SX-109 tank leak (41-09-39). The sediment samples were contacted with a very concentrated electrolyte (5 M $NaNO_3$) for 31 days prior to sampling for Cs isotopics. The measured total Cs to ^{137}Cs ratio in these samples is on average essentially identical to that seen in the water leaches from tank SX-108. These data (Table D.6.1.3) show no significant difference at all between the two SX-108 tank peaks and only a very small (about 5%) difference for the SX-109 tank event. It appears that based on this very limited information, REDOX waste does not exhibit a very large range of variation in the rate of ^{135}Cs production in spite of the high dependence on reactor conditions found in the nuclear modeling work. The measured concentration ratio of total Cs to ^{137}Cs shown in the table (4.75 ± 0.18) may be used with a high degree of confidence for interpreting Cs sorption experiments with respect to competitive chemical sorption of Cs.

Table D.6.1.2. Cesium Isotopic Measurements in SX-108 Slant Borehole Water and Acid Leaches.

Sample	Vertical Depth Feet BGS	Total Cs-137 pCi/gm	Cs-133 Abundance	RSD %	Cs-135 Abundance	RSD %	Cs-137 Abundance	RSD %	Cs-137/ Cs-135	Total Cesium/ Cesium137
Acid Extracts										
S0070-01-AE	55.4	3.06E+06	0.932	0.1	0.0287	0.8	0.0392	2.3	1.37	25
S0070-01-AE-Dup	55.4	3.06E+06	0.939	0.03	0.0251	0.3	0.0357	1.1	1.43	28
S0070-03-AE	68.4	1.95E+07	0.741	0.2	0.108	0.3	0.152	0.9	1.41	6.6
S0070-04-AE	72.7	1.38E+06	0.984	0.1	0.0063	2.8	0.0093	8.0	1.48	108
S0070-05-AE	77.1	6.52E+06	0.808	0.1	0.0798	0.7	0.112	0.1	1.41	8.9
S0070-06-AE	81.4	5.31E+07	0.766	0.1	0.097	0.8	0.137	0.2	1.41	7.3
S0070-07-AE	85.7	9.57E+07	0.744	0.1	0.107	0.8	0.149	0.2	1.40	6.7
S0070-08-AE	90.0	5.55E+05	0.995	0.04	0.002	10.0	0.0032	10.7	1.48	316
Water Extracts										
S0070-03-WE	68.4		0.656	2.6	0.151	1.7	0.193	10.3	1.27	5.18
S0070-03-WE-Rep	68.4		0.638	2.2	0.155	8.1	0.206	2.6	1.33	4.85
S0070-06-WE	81.4		0.627	1	0.150	5.3	0.223	6.1	1.49	4.49
S0070-07-WE	85.7		0.622	0.6	0.157	1.6	0.222	1.1	1.42	4.51
Model Prediction									1.21	4.52

Table D.6.1.3. Cesium Isotopic Measurements on Samples From Long-Term Electrolyte Leaching Experiments.

Sample ID	Sample Name	Cs-133 Ug/L	Cs-133 Abundance	Cs-135 Abundance	Cs-137 Abundance	Cs-137/ Cs-135 Ratio	Cesium/ Cs-137 Ratio
57487-35-3	SX-108-07A	5.95	0.634	0.152	0.214	1.403	4.68
57487-38-3	SX-108 03A	3.50	0.655	0.144	0.202	1.403	4.96
57487-41-3	41-09-39 7A/B/C	3.68	0.636	0.148	0.216	1.467	4.62

D.6.1.3.2 Molybdenum Isotopes. Mo is one of the more isotope rich elements in the periodic table with a total of seven stable isotopes amenable to mass spectrometric analysis (92, 94, 95, 96, 97, 98, and 100). Four of those isotopes are fission products resulting from beta decay of neutron rich high-yield parent isotopes (95, 97, 98, and 100). The other three can be produced in very low yields as direct fission products, but since all three are blocked from the beta chain by stable isotopes of Zr, cumulative fission yields are negligible. Mo isotopes at masses 92, 94, and 96 can be regarded as essentially invariant in composition and representative of naturally occurring Mo. ^{95}Mo is an intermediate case since it has two radioactive precursors with moderately long half-lives, ^{95}Zr (64.02 days) and ^{95}Nb (34.97 days). ^{95}Zr, in particular, is likely to have survived the cool-off period in sufficient quantity prior to REDOX processing to be significant. Thus, some degree of chemical separation is likely to have perturbed the isotope ratio to a lower value than that shown in Table D.6.1.1. This effect provides a means to discriminate between different sources because compositions will depend on the inevitable variations in cool-off time and processing chemistry. Measured Mo isotope ratios from water leaches on SX-108 core material support that premise. Table D.6.1.4 lists the measured isotopic compositions of the water leach samples. Measurements were also performed on the acid leach samples; however, it was clear from the screening results that the large quantity of naturally occurring Mo leached out of the sediment obscured the fission product signal. By contrast, the Mo in the water leaches was dominated by a fission-derived component accounting for up to 96% of the total Mo at the maximum concentration. Table D.6.1.4 shows the composition of natural and purely fission derived Mo compositions across the top two rows for comparison.

Figure D.6.1.2 shows two different representations of the distribution of Mo isotopes in the S-X108 core as a percentage derived from fission. The top plot compares the total Mo concentration measured by ICP-OES with the mass spectrometric determination of fission-derived ^{100}Mo expressed as a percentage associated with fission. The bottom plot shows the same calculation for all four fission-derived isotopes. It is quite clear that the effect of separate events is more readily discernable using the fission-derived isotopes. Three fission-containing peaks are clearly evident with maxima at 68 feet, 90 feet, and 116 feet. The shallowest and deepest peaks contain much less total fission Mo so the percent fission component is somewhat less, however, the fission component still represents more than 80% of the total Mo even in the smaller peaks.

Table D.6.1.4. Molybdenum Isotopic Composition in Water Extracts From SX-108 Slant Borehole Core Segments.

Sample ID	Vertical Depth in Core Feet BGS	Mo-92 0.148 0.000 Abund.	Mo-94 0.0925 0.000 Abund.	Mo-95 0.159 0.255 Abund.	Mo-96 0.167 0.000 Abund.	Mo-97 0.0955 0.243 Abund.	Mo-98 0.241 0.239 Abund.	Mo-100 0.0963 0.263 Abund.	Natural *Fission*
S0070-01 A	55.4	0.141	0.087	0.163	0.162	0.103	0.245	0.099	
S0070-01 A DUP	55.4	0.140	0.087	0.165	0.159	0.102	0.243	0.105	
S0070-03 A	68.4	0.040	0.025	0.225	0.046	0.203	0.244	0.217	
S0070-04 A	72.7	0.090	0.055	0.197	0.100	0.155	0.241	0.161	
S0070-05 A	77.1	0.043	0.026	0.226	0.047	0.202	0.243	0.213	
S0070-06 A	81.4	0.017	0.008	0.242	0.014	0.229	0.244	0.246	
S0070-07 A	85.7	0.015	0.008	0.243	0.014	0.231	0.243	0.246	
S0070-08 A	90.0	0.026	0.008	0.243	0.014	0.230	0.240	0.240	
S0070-09 A	94.4	0.108	0.013	0.217	0.021	0.204	0.222	0.213	
S0070-10 A	98.7	0.408	0.049	0.120	0.085	0.086	0.163	0.089	
S0070-11 A	103.3	0.148	0.092	0.160	0.165	0.096	0.239	0.099	
S0070-12 A	107.3	0.150	0.093	0.163	0.167	0.094	0.239	0.094	
S0070-13 A	116.0	0.090	0.022	0.218	0.039	0.196	0.229	0.206	
S0070-14 A	124.7	0.288	0.062	0.143	0.110	0.100	0.196	0.101	
S0070-14 DUP A	124.7	0.312	0.056	0.140	0.100	0.100	0.188	0.104	
S0070-15 A	133.3	0.359	0.069	0.121	0.122	0.072	0.182	0.074	
S0070-16 A	142.0	0.154	0.094	0.164	0.162	0.096	0.235	0.094	
S0070-17 A	148.9	0.159	0.094	0.163	0.164	0.095	0.235	0.090	

Figure D.6.1.2. Fraction of Total Molybdenum Derived from Fission.

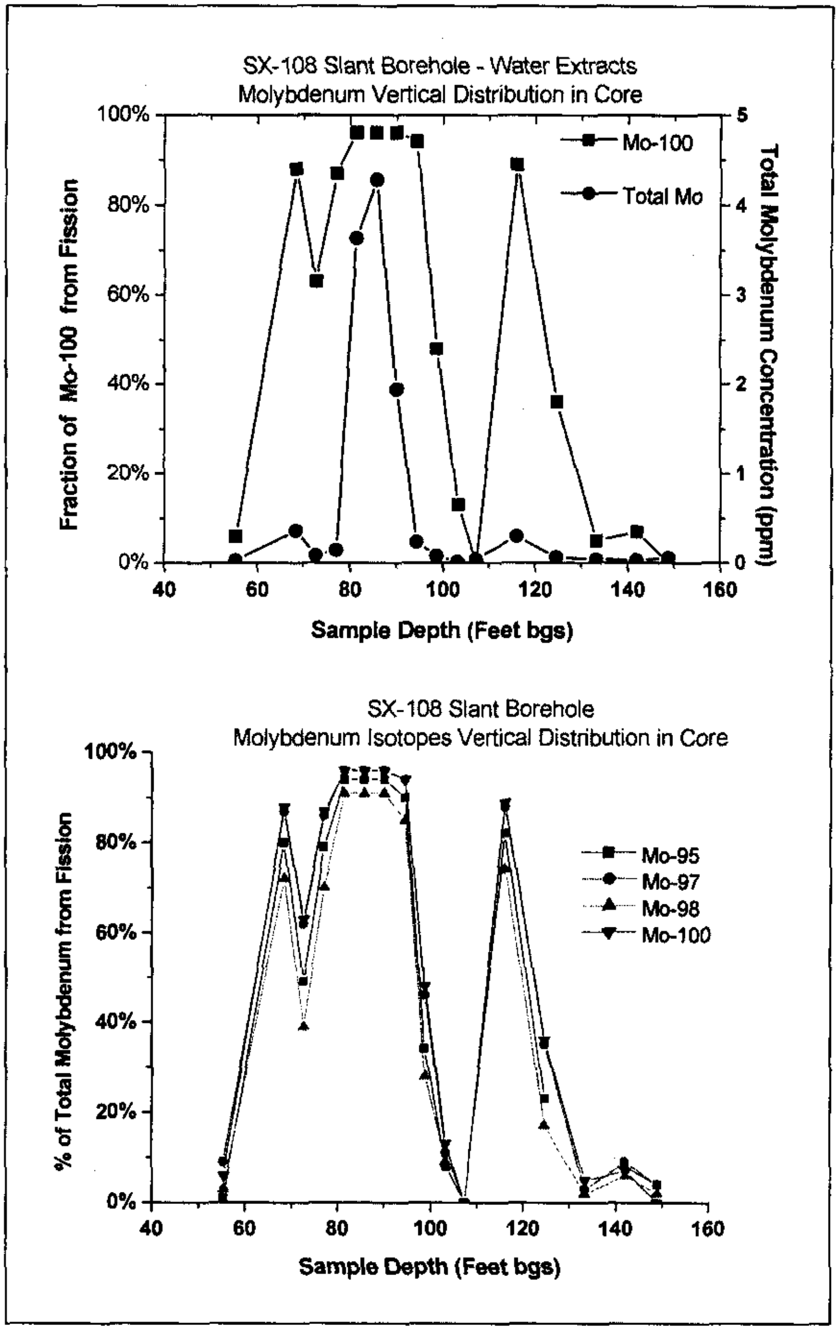

SX-108 Slant Borehole - Water Extracts
Molybdenum Vertical Distribution in Core

SX-108 Slant Borehole
Molybdenum Isotopes Vertical Distribution in Core

Since both peaks are heavily dominated by a fission component, it is possible to use the non-fission derived isotopes (92, 94, and 96) to correct for the natural component present in each core segment leachate and calculate a composition for the purely fission-derived components. Table D.6.1.5 lists the calculated isotopic ratios for the fission-only component for the three peaks with the contribution from naturally abundant Mo stripped out. Isotopic ratio precision is typically around 1% relative or less; however, only the middle peak was wide enough to calculate a relative error directly on multiple segments. These data indicate three distinctly different sources of fission product containing waste.

Table D.6.1.5. Molybdenum Isotope Ratios (Fission Only) for Maximum Concentrations in SX-108 Slant Borehole Core Segments.

Depth (feet)	100/98	97/98	95/98
68	1.096	0.997	0.715
81 to 90	1.078	0.997	0.917
+/-	0.008	0.009	0.011
%RSD	0.7%	0.9%	1.2%
116	1.083	1.012	0.758
Model	**1.100**	**1.010**	**1.06**

Mo is almost certainly present in tank supernate as the Mo oxyanion. Mo falls beneath Cr in the periodic table and should function in a geochemical system as a surrogate for hexavalent Cr with the primary chemical difference being that hexavalent Mo is less easily reduced to the trivalent form than is the case for hexavalent Cr. Figure D.6.1.3 shows a comparison between Cr and Mo measured in the core water extracts by ICP-OES (Serne et al. 2001c). As demonstrated above, the Mo in the water leaches is dominated by a fission component originating from tank supernate while the Cr is associated with chemical additives from the REDOX process found in major quantities in tank supernate. Both species show evidence of three separate events with the three Mo peaks retarded relative to the three corresponding Cr peaks.

Figure D.6.1.3. Fraction of Total Chromium and Molybdenum in SX-108 Water Extracts.

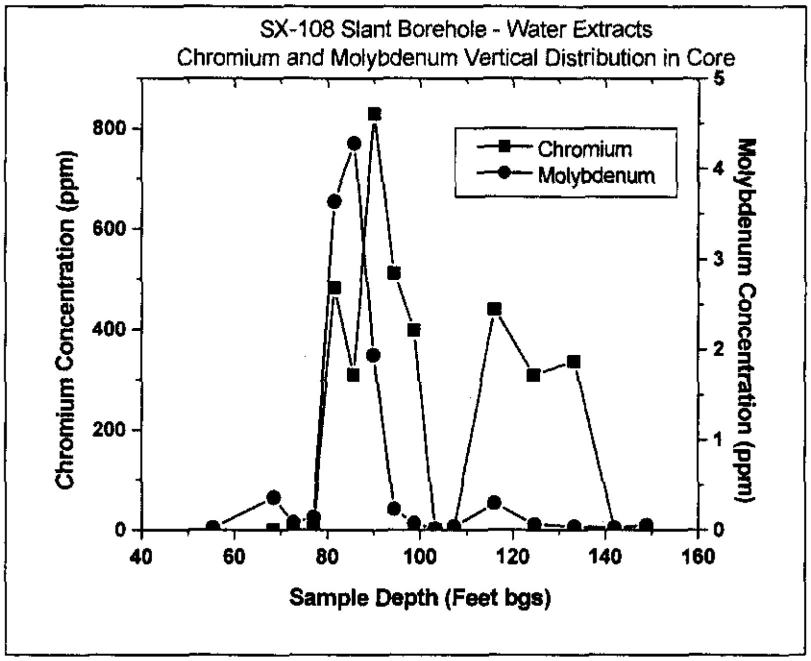

Cr itself appears to be significantly retarded in its vertical transport relative to Tc. Tc along with chloride, nitrate, sulfate, and tritium functions as a purely conservative, unretarded tracer in this system. Figure D.6.1.4 compares the distribution of Cr and ^{99}Tc in water extracts with the Cr peaks clearly shifted to shallower depths. The retardation of both Cr and Mo appears to be associated with either sorption or precipitation on a solid phase. Figure D.6.1.5 shows the comparison between water and acid extracts for Cr. A substantial fraction of the total Cr is unavailable for extraction by water. While it was not possible to perform the same experiment directly for Mo because of the substantial natural component in the acid extracts, it is reasonable to infer that an even larger fraction of the Mo is tied up in a solid phase based on the greatly reduced peak height for the lower fission peak at the116 feet depth. Except for differences in peak height and minor differences in retardation, the Cr and Mo appear to behave similarly. It is likely that the loss of water–extractable Cr is not a REDOX effect because Mo is less easily reduced than Cr. The loss is more probably associated with co-precipitation with an indeterminate solid phase.

Figure D.6.1.4. ^{99}Tc and Cr in Water Extracts From SX-108 Core.

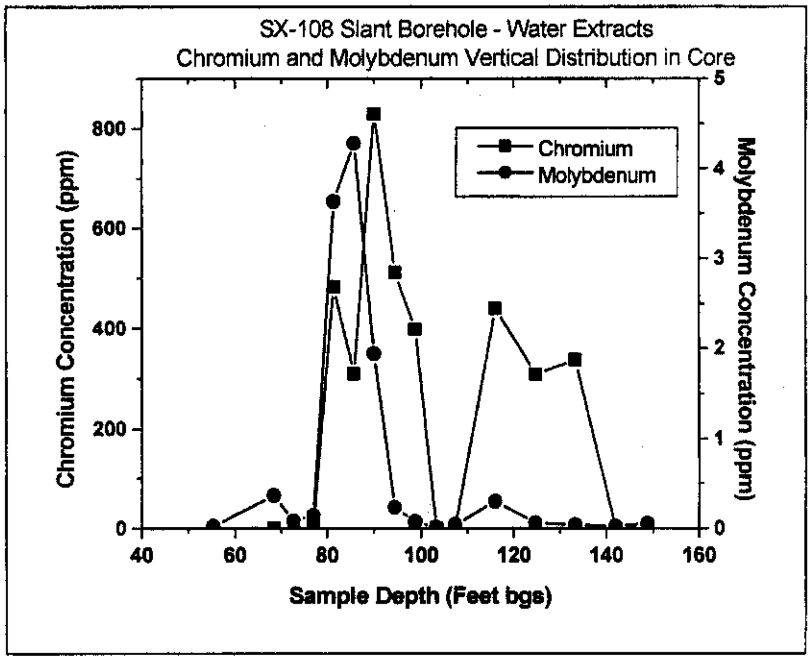

Figure D.6.1.5. Chromium in Water and Acid Extracts From SX-108 Core.

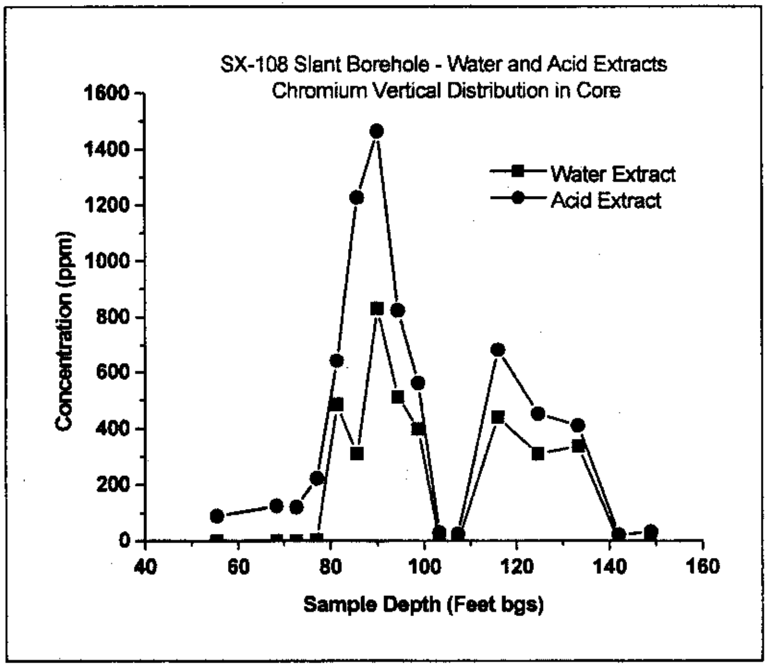

D.6.1.3.3 Iodine Isotopes. ^{129}I is a fission product with a medium yield (0.54%). A great deal of attention has been focused on the two radioactive isotopes of I (131 and 129) in recent years because of their tendency to accumulate in the thyroid. Radio-iodine is thus considered a very hazardous substance when released to the environment with correspondingly stringent regulatory limits (drinking water standard = 1 pCi/L for ^{129}I). Because it is typically present in anionic form as iodide, I also tends to exhibit high environmental mobility although some minor retardation is possible under some conditions (Kaplan and Serne 1995). Under the strongly oxidizing conditions present during fuel dissolution, I is generally believed to be released as elemental I. During operation of REDOX, it thus tended to partition heavily into the vapor phase where it was either released as stack emissions, collected on silver vapor traps, or accumulated in process condensate for eventual release through the groundwater pathway. Very little ^{129}I is thus expected to be present in tank waste; however, any residual fission-derived I disposed to tanks is likely to be found almost exclusively in the supernate and available to be released in association with leaks. Stable I (^{127}I) also should be present in nuclear waste to some degree either through use of I as a reducing agent in REDOX or simply as a chemical impurity. In any case, irrespective of its chemical source, the ^{127}I to ^{129}I ratio in tank waste is likely to be very widely variable constituting an ideal signature for individual waste streams.

^{127}I and ^{129}I measurements on the water extracts from the SX-108 cores are reported in Table D.6.1.6. The depth profiles for the two I isotopes are plotted in Figure D.6.1.6. Two peaks are clearly discernable in the vertical depth profile with a very large difference in the relative amounts of ^{127}I vs. ^{129}I in the two peaks. On a relative basis, the peak at lesser depth has almost twice as much stability I as does the peak lower in the core. These two peaks unquestionably represent material from different sources.

Figure D.6.1.6. Iodine Isotopic Distribution in Water Extracts From SX-108 Core.

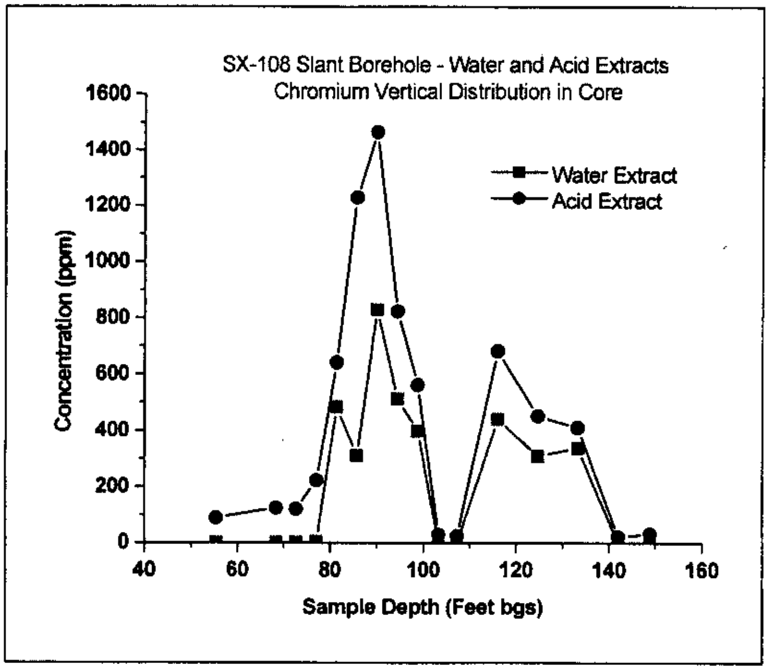

Table D.6.1.6. ^{127}I and ^{129}I in Water Extracts From SX-108 Core.

Sample ID	Vertical Depth in Core (Feet BGS)	^{129}I µg/L	^{127}I µg/L
S0070-01 A	55.4	< 0.17	12.6
S0070-01 A DUP	55.4	< 0.21	14.0
S0070-03 A	68.4	0.39	11.6
S0070-04 A	72.7	0.39	9.2
S0070-05 A	77.1	1.20	23.1
S0070-06 A	81.4	8.70	62.5
S0070-07 A	85.7	14.3	194
S0070-08 A	90.0	14.5	211
S0070-09 A	94.4	15.9	89.8
S0070-10 A	98.7	24.1	122
S0070-11 A	103.3	1.07	18.0
S0070-12 A	107.3	1.30	31.5
S0070-13 A	116.0	15.8	74.1
S0070-14 A	124.7	15.0	90.9
S0070-14 DUP A	124.7	16.5	101
S0070-15 A	133.3	21.2	179
S0070-16 A	142.0	1.48	27.9
S0070-17 A	148.9	0.72	13.5

Figure D.6.1.7 shows a comparison between the concentrations of ^{129}I and ^{99}Tc as measured in the same water leachate samples. The ^{129}I data plotted on the figure has been renormalized by the ratio of fission yields between ^{99}Tc (6.1%) and ^{129}I (0.54%). When plotted in that way, it is possible to make a direct estimate of I losses during REDOX chemical processing for the two peaks. A simple comparison of the two plotting axes reveals that more than 98% of the I was lost relative to the Tc. However, both peaks look otherwise similar when viewed in that way. In order to convincingly demonstrate that two sources are present, it is necessary to include the ^{127}I, which forms a kind of internal tracer showing the major difference in composition between the two peaks. It should also be noted that Figure D.6.1.7 demonstrates that I does exhibit some minor retardation relative to unretarded ^{99}Tc.

Figure D.6.1.7. Iodine and ^{99}Tc Comparison in Water Extracts From SX-108 Core.

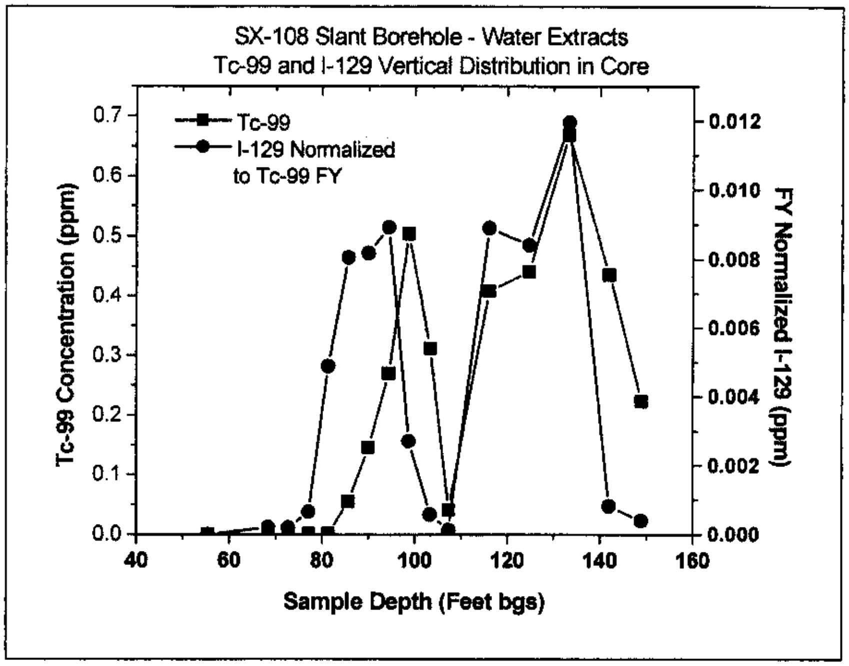

D.6.1.3.4 Selenium Isotopes. Like ^{129}I, ^{79}Se is also formed as a medium yield fission product with a potentially high environmental mobility. The half-life of ^{79}Se has seldom been measured, with the currently accepted value of 1.13 million years based on a recent determination involving accelerator mass spectrometry combined with liquid scintillation counting performed in the Peoples Republic of China (Songsheng et al. 1997). Because of analytical difficulties associated with routine direct measurement of ^{79}Se, little is known about its distribution in the environment. Se can form an oxyanion, selenate, which is likely to be highly mobile. ^{79}Se is often cited as one of the critical path long-lived radionuclides used for performance assessment of tank waste removal and for risk assessment of tank leaks. ^{79}Se and other naturally occurring and fission-produced isotopes (74, 76, 77, 78, 80, and 82 amu) can in principle be measured by ICP/MS; however, measurement of the full suite of isotopes is rendered difficult by an abundance of interferences in that mass region. Because of time and budget constraints associated with issuance of this report, the needed development work could not be completed. However, it is possible to estimate the mobility of fission-derived Se using one of the other fission-produced stable isotopes of Se. Stable ^{82}Se is produced with a fission yield about 5 times higher than that of ^{79}Se. Since ^{82}Se also represents 8.7% of naturally occurring Se, conclusions derived from ^{82}Se alone must be considered as tentative. Figure D.6.1.8 shows the measured ^{82}Se in water leaches from the SX-108 core compared to ^{99}Tc measured on the same samples. The Se data plotted on the figure has been renormalized to the ^{99}Tc fission yield and plotted on the same axis. When plotted in that way it is clear that the two species behave essentially in an identical manner and are completely unretarded. The low baseline at the shallower depths indicates that there is very little natural Se leached out of the core material in the water extracts. The shape of the profile requires that the observed Se originates from the tank and its close agreement to the ^{99}Tc levels after correction for fission yield suggests this is almost certainly fission derived material. An identical situation was also observed in the 41-09-39 borehole associated with the tank SX-109 leak.

Figure D.6.1.8. ^{82}Se and ^{99}Tc Comparison in Water Extracts From SX-108 Core.

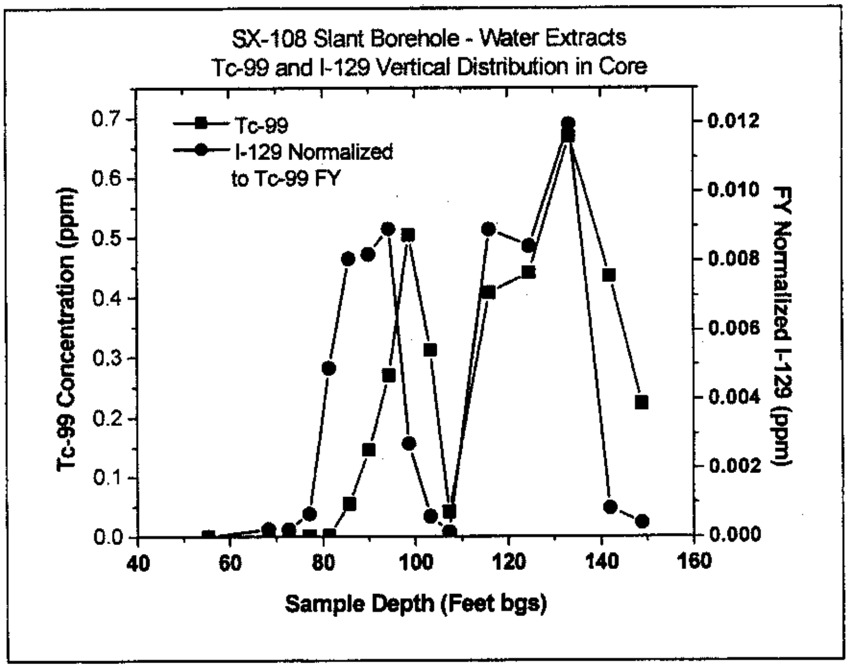

The ^{79}Se concentrations in the water extract samples can be inferred from the ^{82}Se, assuming no natural contribution to the ^{82}Se, by using the ratio of the ^{235}U fission yields. Table D.6.1.7 shows the inferred concentration of ^{79}Se in the water extract samples as well as the concentration converted to pCi/L of extract (using a specific activity of 4.01E-3 Ci/g).

Table D.6.1.7. ^{79}Se Concentrations Inferred From Stable Fission Derived ^{82}Se in Water Extracts from the SX-108 Core.

Sample #	Depth(ft) Vertical	mg/L ICP/MS ^{82}Se	mg/L Inferred ^{79}Se	pCi/L Inferred ^{79}Se
S0070-01A	55	0.000	0.0000	0
S0070-03A	68	0.051	0.0072	28709
S0070-04A	73	0.050	0.0070	28194
S0070-05A	77	0.007	0.0010	3835
S0070-06A	81	0.048	0.0067	26915
S0070-07A	86	0.061	0.0085	34263
S0070-08A	90	0.149	0.0210	84029
S0070-09A	94	0.132	0.0185	74289
S0070-10A	99	0.165	0.0231	92781
S0070-11A	103	0.121	0.0170	68261
S0070-12A	107	0.008	0.0011	4510
S0070-13A	116	0.243	0.0342	137017
S0070-14A	125	0.233	0.0328	131595
S0070-15A	133	0.411	0.0578	231766
S0070-16A	142	0.031	0.0044	17729
S0070-17A	149	0.014	0.0019	7664

D.6.1.3.5 Chloride, Nitrate, Sulfate, and Technetium. Isotopic data can provide the most definitive basis for source attribution since no assumptions are needed with respect to chemical effects. However, a number of species are known or believed to migrate in the vadose zone in an almost purely unretarded fashion. Under those conditions, concentration ratios of species with similar or identical geochemical behavior can also be an effective means for identifying sources. Species well suited to that purpose include chloride, nitrate, sulfate, and ^{99}Tc. Data for the common anions discussed here were taken from the work of Serne et al. (2001c), while the ^{99}Tc measurements were made on samples from the same leachates provided by that group.
Figure D.6.1.9 shows the distribution of nitrate and chloride in the SX-108 slant borehole core. It is clear that these two distributions are markedly different. It is interesting to note that nitrate exhibits a small degree of retardation in the upper peak. That behavior is unexpected and the cause is not obvious.

Figure D.6.1.9. Nitrate and Chloride Vertical Distributions in Water Extracts From SX-108 Slant Borehole Core Segments.

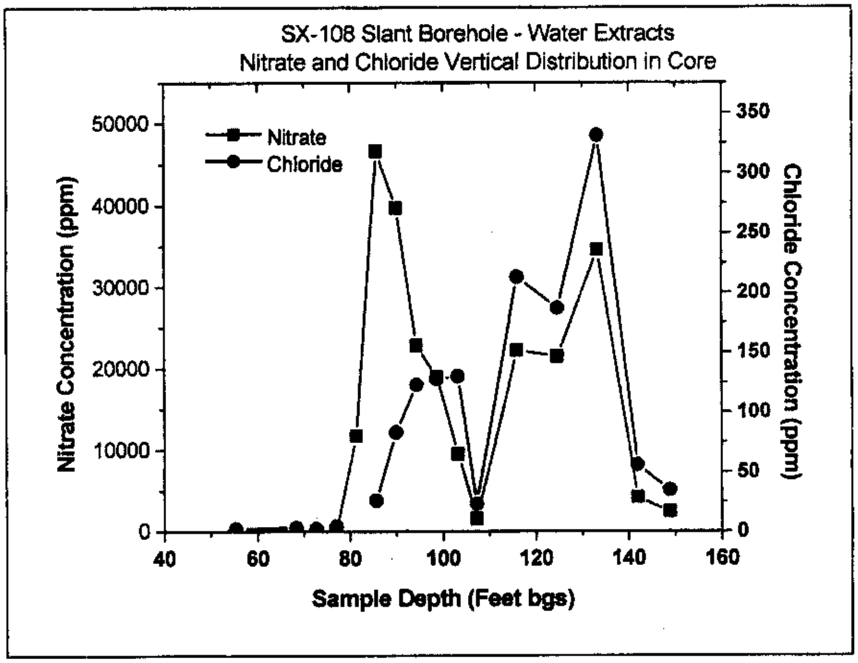

Figure D.6.1.10 shows the same type of presentation for nitrate and Tc. Again the two distributions are clearly different with nitrate showing retardation relative to Tc. Other combinations can be plotted such as chloride versus sulfate, which show a similar pattern.

Figure D.6.1.10. Nitrate and ^{99}Tc Vertical Distributions in Water Extracts From SX-108 Slant Borehole Core Segments.

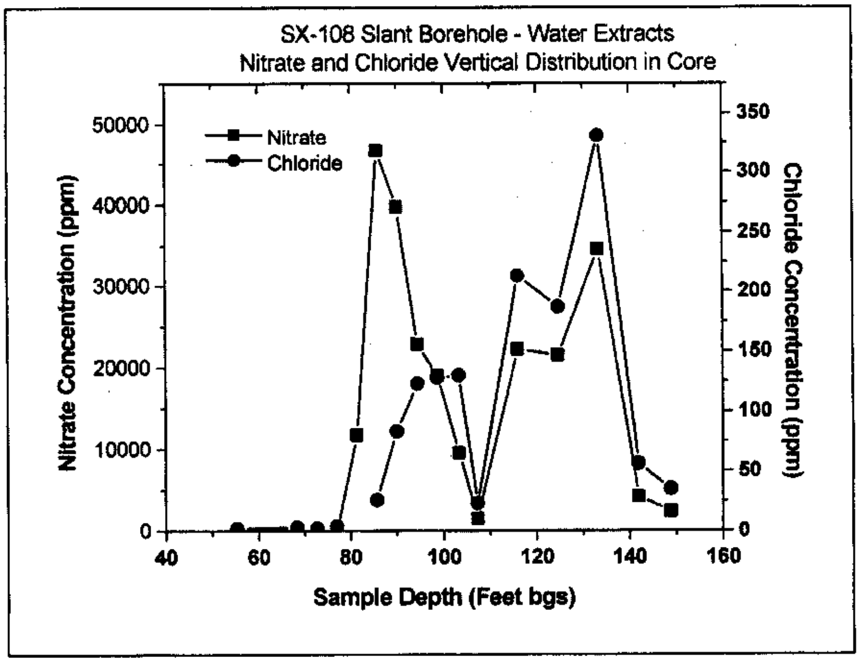

D.6.1.4 Conclusions and Implications

Tank SX-108 was placed in service in late 1955 for disposal of REDOX Process high-level waste. The tank began self-boiling in mid-1956 and was completely filled with self-boiling waste by early 1959. The first evidence of unaccounted volume loss and other indications of a potential leak were first noted in the third quarter of 1962 (WHC 1992). Contaminants found in the deepest part of the SX-108 slant borehole thus presumably date from some time prior to that date. The tank was emptied in 1962 and left dry for about a year. Prior to refilling, condensate from another tank was used to recover sodium nitrate salt cake from tank SX-108. It is now considered quite likely that the leak which had self-healed reopened as a result of dissolution of the salt plug at that time. Tank SX-108 was then filled with another round of fresh REDOX waste from mid–1963 through the end of 1964. Because of concerns raised by increasing activity in lateral wells in November 1965, an isolation cooler was added to the tank which was then shifted to total reflux operation in order to stabilize the liquid level. Stable behavior was subsequently noted suggesting that the leak had again self-healed. Estimates of the volume of leaked material vary widely. The best estimate based on ^{137}Cs data is around 2,400 gallons (Raymond and Shdo 1966) with an upper bound in the range of 35,000 gallons. There is good evidence from the historical record that a significant volume of material representing two different fills was leaked over a relatively long period of time at that location. Measurements conducted on recovered materials from the SX-108 slant borehole, drilled through the heart of the leak plume show evidence to support that scenario.

The best evidence for multiple leak events is visible in the ^{129}I data, which shows a very large difference in isotopic composition of I isotopes between the two concentration maxima in the core. The ^{127}I to ^{129}I ratio thus appears to be an excellent fingerprinting tool for determining source attribution. ICP/MS proved in this study to be a very powerful tool for rapid and low-cost analysis of ^{129}I and ^{127}I on radioactive samples.

The slight sorption of ^{129}I implied by the comparison of the ^{129}I profile to that of ^{99}Tc is in at least general agreement with experimental results (Kaplan and Serne 1995). Application of the experimental results is complicated by the widely varying K_D values reported. This variability may be related to a strong nonlinearity in the sorption isotherm. Because iodide is an anion, the sorption may be controlled by a small number of positively charged sites on the edges of clays and on I and Al oxide surfaces. Thus, the sorption sites may be easily saturated. Competition with other anions may also be a factor.

Mo isotopic analysis also looks promising as an isotopic fingerprinting tool. Variability in the ^{95}Mo to ^{98}Mo ratio from tank to tank provides an excellent means for distinguishing separate sources. Three separate sources of material are indicated in the SX-108 slant borehole corresponding in all likelihood to the first filling in the early 1950s, the second filling in the 1962 to 1964 time frame, and possibly a later leak which occurred in the late 1960s. Mo isotopes also look promising as tracers of tank leak material into groundwater where such impacts are known or suspected, however, because of the high background of naturally occurring stable Mo normally found in groundwater, high precision mass spectrometric techniques would be needed. Recent advances in the development of multicollector ICP/MS instruments make the approach very practical.

Se appears to be essentially unretarded under conditions within the Hanford sediments of the SX tank farm. Although early experimental evidence indicated that the K_D value is near zero under anoxic as well as oxic conditions and at both low and high ionic strengths (Kaplan and Serne 1995), more recent experiments showed a measurable K_D for Se in Hanford formation sediments from the 200 East Area. Kaplan et al. (1998) obtained Se K_D values of 6.73 with a standard deviation of 1.9 using ^{75}Se spiked, uncontaminated Hanford groundwater. Under the study conditions, no sorption was seen for ^{99}Tc. Kaplan et al. (1998) also studied the effect of high ionic strength and high pH on Se sorption to 200 East Area sediment. They found that increasing ionic strength increased sorption of Se from a K_D of 3.31 mL/g in 0.05 M $NaClO_4$ to 4.49 in 0.10 M $NaClO_4$ and 4.11 in 1 M $NaClO_4$. Increasing pH from 8.1 to 9.9 decreased the Se K_D from 5.78 mL/g to 0.29 mL/g and the value decreased further to 0.04 mL/g at pH 11.9. It is important to note, however, that in these experiments the K_D for ^{99}Tc increased from -0.02 mL/g at pH 8.1 to 1.04 to 1.07 mL/g at pH 9.9 and above.

The increasing Se K_D but decreasing Tc K_D seen with increasing pH in the Kaplan et al. experiments suggests that the pH effect does not explain the Se mobility at the SX tank farm. The correlation between ^{82}Se and ^{99}Tc at the tank farm would most likely not continue as contaminants moved to greater depths and lower pH. More work is needed to understand this discrepancy between field and experimental data. Until this is better understood, caution should be used in applying the experimental results in contaminant transport and risk calculations. Because of the long half-life and high mobility, the presence of ^{79}Se should be considered in long-term risk calculations for the tank farms. ^{79}Se activities are only approximately 0.01 to 0.02 times the ^{99}Tc activity in the most concentrated water extracts, however biological uptake of Se may affect the relative risk.

Se isotopes show promise as contaminant tracers because fission–produced ^{82}Se associated with tanks leaks from SX-108 and SX-109 was found to be completely unretarded with mobility identical to that of ^{99}Tc. Some additional improvements in ICP/MS methodology are needed to measure the radioactive species, ^{79}Se, directly.

The Cs isotopes showed remarkably constant isotopic composition on water and electrolyte leaches. The presence of separate leak sources clearly visible from several other lines of evidence was not discernable from the Cs data in spite of an expected large variability in ^{135}Cs concentration predicted from nuclear modeling considerations. A more extensive series of Cs measurements is needed to better define the range of variability. Very minor amounts of naturally occurring Cs at most were leached by month-long exposures to concentrated sodium nitrate solutions. The observed ^{135}Cs in the leachates was attributable to an essentially pure fission component. Those data can be used to correctly assess the total Cs loading in sorption experiments and transport calculations.

An example of the use of fingerprinting techniques is shown in Table D.6.1.8. The table contains comparisons of the ratios of several different unretarded species. Data in the table are taken from (Serne et al. 2001a, b, c) as well as employing the I and Tc data reported above. The two SX-108 columns represent the two different peak maxima with SX-108-A associated with the earlier leak (deeper in core) and SX-108-B the more recent one. The SX-109 column refers to measurements made on the 41-09-39 borehole. Well 299-W23-19 is a Hanford groundwater well completed from the B8809 borehole drilled to measure contaminants associated with the tank SX-115 leak. Contamination by even the most mobile constituents in the recovered core from the borehole tails off more than 50 feet above the surface of the water table; however, substantial contamination indicative of presumptive tank leak material was observed in groundwater at the completed well. ^{99}Tc in this well is extremely high at 72,300 pCi/L as measured in December 2000. Unfortunately, Table D.6.1.8 contains several key data gaps since ^{129}I was not measured in the borehole samples. While ^{129}I was measured by a gamma counting method on a sample from the well, the method does not yield an isotope ratio. Nevertheless, even from the limited data set available, it is clear that each of the sources is distinct from each other. For example, while the nitrate to Tc ratio is very similar in both the well and borehole, the nitrate to chloride ratio is very different. This suggests that the groundwater impact observed at well 299-W23-19 is not associated with the tank SX-115 leak itself but rather a leak from one of the other SX tank farm sources conveyed by some type of preferential pathway to that location. Similarly, the three ratios measured in the groundwater sample are also a poor match to the SX-108 and SX-109 samples. In order for fingerprinting techniques to achieve their full potential, more comprehensive analyses need to be performed on a wider suite of samples.

Table D.6.1.8. Contaminant Fingerprints in Water Extracts and Groundwater.

	SX-108-A	SX-108-B	SX-109	299-W23-19	B8809
NO_3/Cl	104	360	118	37	121
Tc-99/I-129	56	57		134	
NO_3/Tc-99	50,934	92,547	60,381	158,991	169,526
I-127/I-129	13.8	24.4			

D.6.1.5 References

Evans, J. C., E. A. Lepel, R. W. Sanders, C. W. Thomas, and D. E. Roberts, 1988, "Long-Lived Activation Products in Light-Water Reactor Construction Materials: Implications for Decommissioning," *Radioactive Waste Management and the Nuclear Fuel Cycle*, Vol. 11:1-39.

Evans, J. C., E. A. Lepel, R. W. Sanders, C. L. Wilkerson, W. Silker, C. W. Thomas, K. H. Abel, and D. R. Robertson, 1983, *Long-Lived Activation Products in Reactor Materials*, NUREG/CR-3474, PNL-4824, National Technical Information Service, Springfield, Virginia, p. 131.

Hodges, F. N., 1998, *Results of Phase I Groundwater Quality Assessment for Single-Shell Tank Waste Management Areas T and TX-TY at the Hanford Site*, PNNL-11809, Pacific Northwest National Laboratory, Richland, Washington.

Hodges, F. N., and C. J. Chou, 2000, *Groundwater Quality Assessment for Waste Management Area U; First Determination*, PNNL-13282, Pacific Northwest National Laboratory, Richland, Washington.

Johnson, V. G., and C. J. Chou, 1998, *Results of Phase I Groundwater Quality Assessment for Single-Shell Tank Waste Management Areas S-SX at the Hanford Site*, PNNL-11810, Pacific Northwest National Laboratory, Richland, Washington.

Kaplan, D. I., K. E. Parker, and I. V. Kutynakov, 1998, *Radionuclide Distribution Coefficients for Sediments Collected from Borehole 299-E17-21: Final Report for Subtask 1a*, PNNL-11966, Pacific Northwest National Laboratory, Richland, Washington.

Kaplan, D. I. and R. J. Serne, 1995, *Distribution Coefficient Values Describing Iodine, Neptunium, Selenium, Tc and Uranium Sorption to Hanford Sediments*, PNL-10379, Pacific Northwest National Laboratory, Richland, Washington.

Narbutovskih, S. M., 1998, *Results of Phase I Groundwater Quality Assessment for Single-Shell Tank Waste Management Areas B-BX-BY at the Hanford Site*, PNNL-11826, Pacific Northwest National Laboratory, Richland, Washington.

Raymond, J. R., and E. G. Shdo, 1966, *Characterization of Subsurface Contamination in the SX Tank Farm*, BNWL, CC-701, Battelle-Northwest, Richland, Washington.

Serne, R. J., G. V. Last, G. W. Gee, H. T. Schaef, D. C. Lanigan, C. W. Lindenmeier, R. E. Clayton, V. L. LeGore, R. D. Orr, M. J. O'Hara, C. F. Brown, D. B. Burke, A. T. Owen, I. V. Kutnyakov, and T. C. Wilson, 2001a, *Geologic and Geochemical Data Collected from Vadose Zone Sediments from Borehole SX 41-09-39 in the S/SX Waste Management Area and Preliminary Interpretations,* PNNL-2001-2, Pacific Northwest National Laboratory, Richland, Washington.

Serne, R. J., H. T. Schaef, B. N. Bjornstad, D. C. Lanigan, G. W. Gee, C. W. Lindenmeier, R. E. Clayton, V. L. LeGore, M. J. O'Hara, C. F. Brown, R. D. Orr, G. V. Last, I. V. Kutnyakov, D. B. Burke, T. C. Wilson, and B. A. Williams, 2001b, *Geologic and Geochemical Data Collected from Vadose Zone Sediments from Borehole 299 W23-19 [SX -115] in the S/SX Waste Management Area and Preliminary Interpretations*, PNNL-2001-3, Pacific Northwest National Laboratory, Richland, Washington.

Serne, R. J., H. T. Schaef, G. V. Last, D. C. Lanigan, C. W. Lindenmeier, R. E. Clayton, V. L. LeGore, M. J. O'Hara, C. F. Brown, R. D. Orr, I. V. Kutnyakov, T. C. Wilson, D. B. Burke, B. A. Williams and B. N. Bjornstad, 2001c, *Geologic and Geochemical Data Collected from Vadose Zone Sediments from the Slant Borehole under SX-108 in the S/SX Waste Management Area and Preliminary Interpretations,* PNNL-2001-4, Pacific Northwest National Laboratory, Richland, Washington.

Songsheng, J., G. Jingru, J. Shan, L. Chunsheng, C. Anzhi, H. Ming, W. Shaoyong, and L. Shilin, 1997, *Nuclear Instrumental Methods in Physical Research B.*, Vol. 123:405-409.

Watrous, R. A. and D. W. Wootan, 1997, *Activity of Fuel Batches Processed Through Hanford Separations Plants, 1944 Through 1989*, HNF-SD-WM-TI-794, Lockheed Martin Hanford Corporation, Richland, Washington.

WHC, 1992, *Tank 241-SX-108 Leak Assessment*, WHC-MR-0300, Westinghouse Hanford Company, Richland, Washington.

D.6.2 HORIZONTAL TRANSPORT OF CHEMICAL WASTE INFERRED FROM ISOTOPIC AND CHEMICAL MEASUREMENTS OF CORE SAMPLES FROM B8812 CLEAN BOREHOLE

D.6.2.1 Introduction

Understanding the mechanisms and pathways of water movement through the vadose zone at Hanford is clearly necessary for evaluating the potential for contaminant transport at the Site. To address this issue for the S and SX tank farms, an isotopic and chemical study of porewater samples from the B8812 "clean" borehole was undertaken.

The stable oxygen ($\delta^{18}O$) and hydrogen (δD) isotopic compositions of water provide natural labels for water (e.g., Epstein and Mayeda 1953; Friedman 1953; Craig 1961). In addition, evaporation modifies the isotopic signature of water, producing a distinctive signal that can be used to track the affected fluids (e.g., Gat et al. 1969; Gaye and Edmunds 1996). In the area of the S and SX tank farms, the potential inputs to the vadose zone porewaters (local precipitation, process waters derived from the Columbia River) have $\delta^{18}O$ and δD values in the same range as the groundwater. However, evaporation appears to have significantly affected most of the vadose zone waters in the area.

D.6.2.2 Experimental Procedures

The B8812 borehole was drilled in October 1999 and the cores were stored at 4 °C in sealed sleeves to prevent evaporation until they could be sampled for isotopic analyses. During January 2000, 32 samples were collected from the core. The porewaters were extracted from these samples by vacuum distillation at the Center for Isotope Geochemistry (CIG) at LBNL. The amount of water in each of the samples was determined gravimetrically. The $\delta 1^{8}O$ values of the porewaters were analyzed using the automated H_2O-CO_2 equilibration system on CIG's VG Prism Series II Isotope Ratio Mass Spectrometer. The δD values of the porewater samples were measured by reducing the water to H_2 gas with zinc metal and analyzing the isotope ratio of the resulting gas with Prism (Vennemann and O'Neil 1993). Chemical analyses of the porewaters were done using 1:1 deionized water leaches of the core material.

D.6.2.3 Results

D.6.2.3.1 Isotope Data. The $\delta^{18}O$ values of the porewaters are plotted versus their δD values on Figure D.6.2.1. Also plotted on this figure are isotope data for Hanford groundwater samples analyzed in this laboratory, the Global Meteoric Water Line, the Local Meteoric Water Line determined by Hearn et al. (1989), and a characteristic trend for evaporated water. The groundwater samples cluster around the Local Meteoric Water Line. With several notable exceptions, the porewater samples are all shifted to the right of the Local Meteoric Water Line, indicating that these waters have undergone significant evaporation.

Figure D.6.2.1. Plot of δD vs. δ^{18}O Values for Pore Water Distilled From Samples of the B8812 Core (black circles) and Groundwater Samples From Across the Hanford Site (open circles).

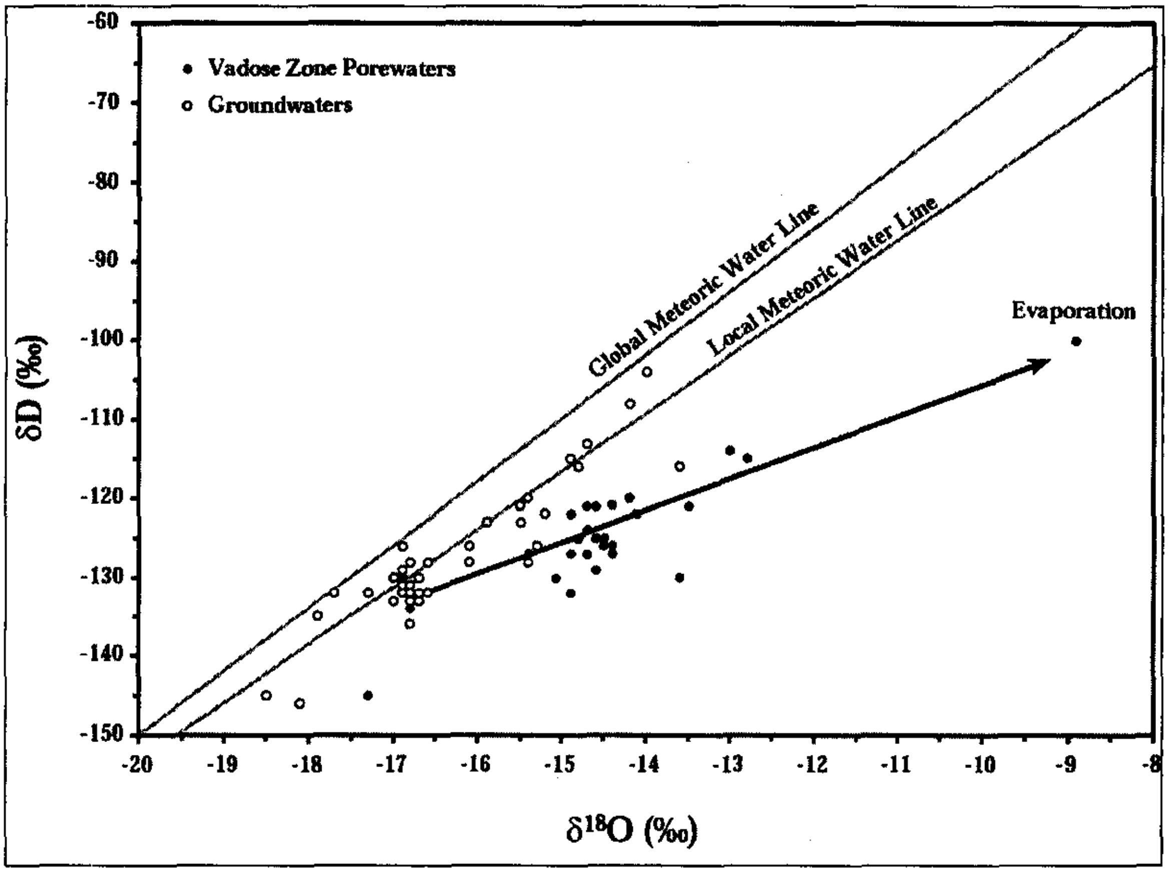

Note: Also shown are the Global Meteoric Water Line, the Local Meteoric Water Line (Hearn et al. 1989) and a Characteristic Evaporation Trend.

The oxygen isotope data for the porewaters are plotted versus depth in Figure D.6.2.2. The δ^{18}O value of the shallowest sample (taken at approximately 0.5 m depth) is much higher than either local precipitation or process water derived from the Columbia River (the two potential sources of surface water), signifying that it is strongly evaporated. This is typical of near-surface soil waters, especially in arid and semiarid environments. At 2 m depth, however, the δ^{18}O value of the porewater is equal to the average value of precipitation/Columbia River water. Beneath 2 m, most of the porewaters are shifted to higher δ^{18}O values, implying that they have also been evaporated. There were two porewater samples from the deeper part of the core that did not have an evaporated signal (the 44.7 and 71.8 m samples). The deeper sample is from the saturated zone and essentially reflects the isotopic composition of the groundwater. The other sample is from a perched water zone above the caliche layer in the core.

Figure D.6.2.2. Variation with Depth of the $\delta^{18}O$ Values of the Pore Water Samples Distilled From the B8812 Core.

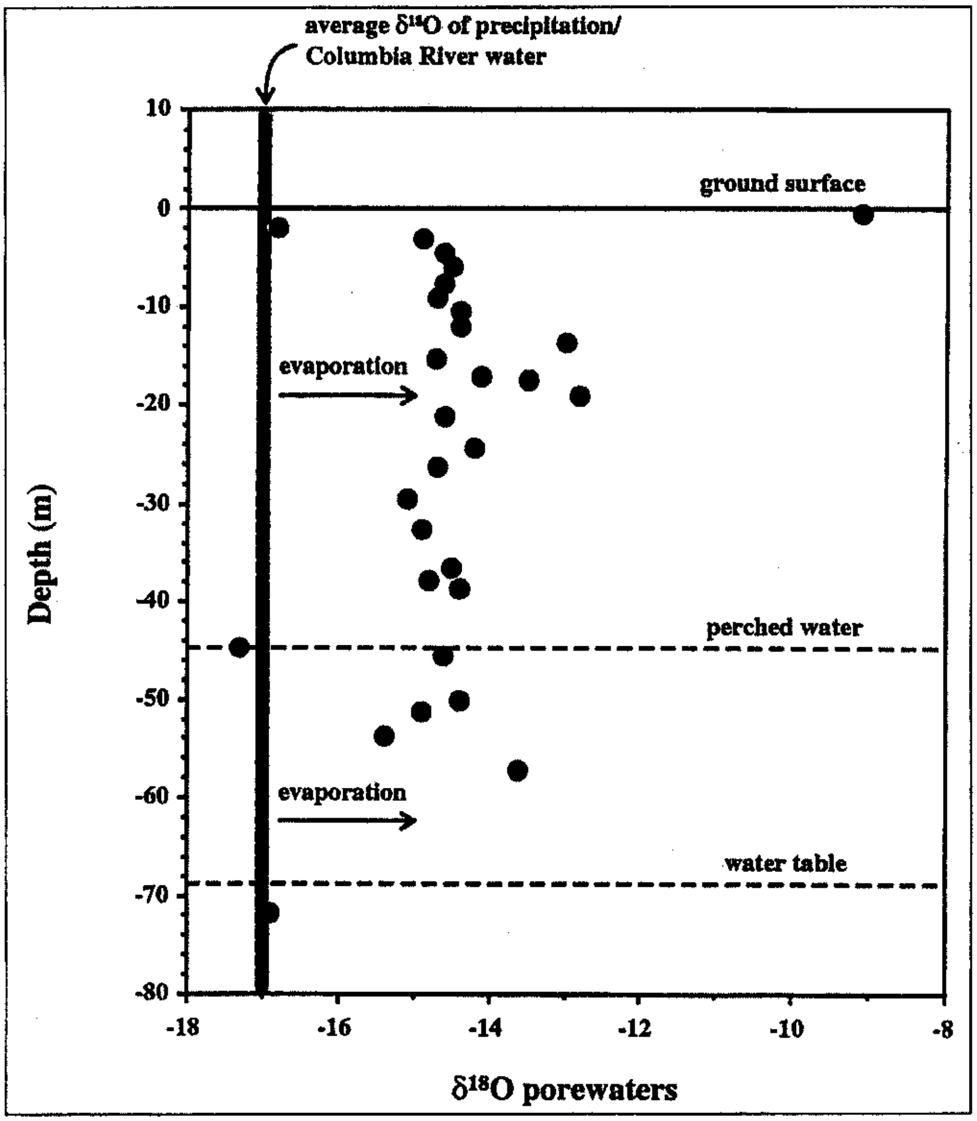

Note: Also shown are the approximate depths of the Perched Water Horizon (underlain by a 60-cm-thick caliche layer) and Groundwater.

D.6.2.3.2 Chemical Data. Chemical measurements by ion chromatography and ICP/MS performed on water leachates from the B8812 core also showed a signature associated with perched water layer at the Plio-Pleistocene boundary. Figure D.6.2.3 shows a plot of nitrate and sulfate concentrations in 1:1 water leaches compared with the associated $\delta^{18}O$ values for the same core horizons.

Figure D.6.2.3. Oxygen Isotopics and Anion Concentrations in B8812 Core.

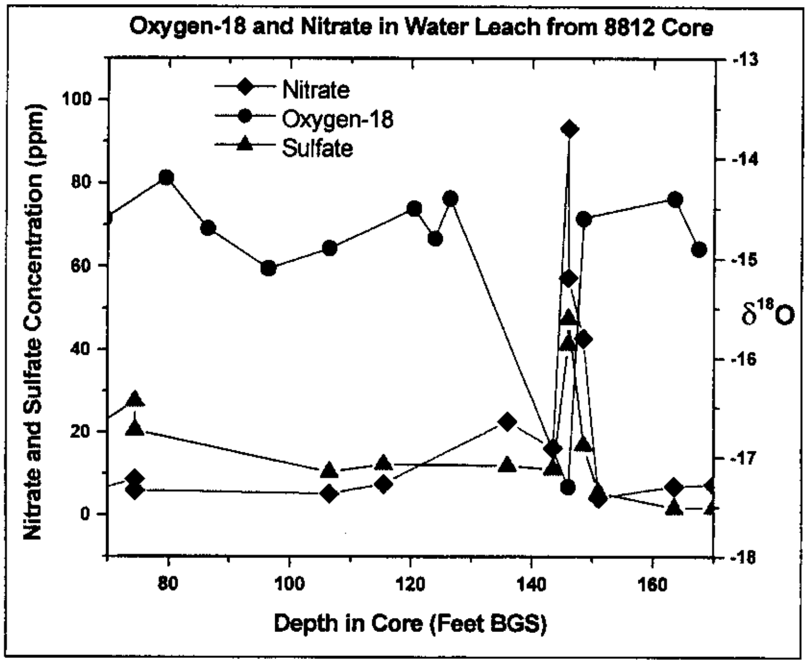

Both Se and Mo also show strong signatures at the same horizon with evidence of mobile Cr and U as well. A comparison of those data are shown on Figure D.6.2.4. Isotopic analyses for the ^{236}U and fission-derived isotopes of Mo showed no evidence of a nuclear production associated signature, however.

Figure D.6.2.4. Uranium, Chromium, Selenium, and Molybdenum Concentrations in Water Leaches From B8812 Core.

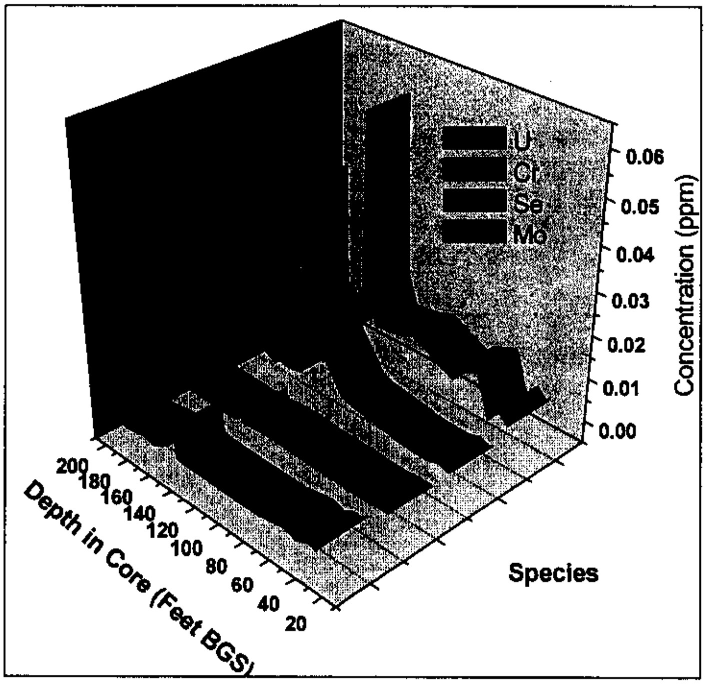

D.6.2.4 Conclusions and Implications

D.6.2.4.1 Near-Surface Samples. The isotopic compositions of the two shallowest samples (0.5 and 2.0 m depth) are significantly different than the deeper samples. The 0.5 m sample is strongly evaporated, whereas the 2 m sample is essentially equal to unevaporated groundwater/ precipitation/Columbia River water. This pattern is similar to the results observed in other studies of shallow, unsaturated soils (Komor and Emerson 1994; Phillips 1995; Melayah et al. 1996; Barnes and Allison 1988). In essence, the thickness of the isotopically enriched zone is a function of the amount of infiltration and the evaporation rate. What is unique about this data set is that the samples at greater than 2 m depth also show evidence of evaporation. This implies that the upper 2 m have been impacted by a period of anomalously high infiltration that allowed unevaporated water to reach that depth. It is unlikely that this was the result of the annual precipitation cycles (wet in the winter, dry in the summer); the upper 2 m of soil contains approximately 30 cm of water and the average rainfall for this area is less than 25 cm/yr. Alternatively, it is possible that some process water was dumped on the surface at this site. B8812 borehole was drilled outside of the contaminated area, but there is anecdotal information suggesting that there was an infiltration pond for clean process waters in the vicinity (Evan Dresel, personal communication). Although there is no direct record of this activity, it is also supported by the Sr isotope ratios of the porewaters, which are in the same general range as Columbia River water (see Section D.6.3 of this report).

D.6.2.4.2 Evaporation of the Deep Vadose Zone Porewaters. At greater than 2 m depth, the isotopic compositions of all of the vadose zone porewaters (except for the perched water sample) reflect a significant degree of evaporation. The $\delta^{18}O$ values have been enriched by 2 to 4%, indicating that they have undergone 20 to 35% vaporization. Similar evaporated signatures were also observed for vadose zone porewaters collected in conjunction with tracer tests performed at the Vadose Zone Test Facility located near the 200 West Area. This implies that the Hanford vadose zone porewaters are generally evaporated.

Due to the difficulties associated with sample collection and extraction of the porewaters, there is limited data on the isotopic composition of deep vadose zone porewaters in arid and semiarid environments. Most studies on vadose zone soils have been restricted to the top few meters of the soil. In these studies, the impact of evaporation is generally limited to a thin zone (less than or equal to 0.5 m) near the surface (e.g., Komor and Emerson 1994; Melayah et al. 1996). The effect of evaporation from the surface cannot penetrate much deeper than 0.5 m because increased tension induces upward flow to balance evaporation and a steady-state isotopic profile is reached. However, if infiltration occurs normally by relatively few events (e.g., one per year penetrating to a depth of ca. 0.5 m), which then can be affected by evaporation over several months, the evaporation signature can be preserved as the water is displaced downward by succeeding infiltration events. No detailed model is available for translating the average $\delta^{18}O$ shift to an infiltration flux. However, to first order it can be reasoned that if the infiltration is episodic as suggested here, then the annual infiltration distance must be less than about 20 to 50 cm in order to produce average vadose zone water with a $\delta^{18}O$ shift of 2 to 4%. Assuming an average soil water content of 12%, this annual infiltration distance corresponds to an infiltration flux of less than 2.5 to 6 cm/yr.

D.6.2.4.3 Perched Water. The data measured for the perched water sample are of great significance for the goals of this project. Clearly, the perched water is not derived from direct, vertical infiltration in the vicinity of the borehole. The O and H_2O isotopic signatures of the porewaters above and below this horizon are distinct from the perched water. Further, the elevated levels of nitrate, sulfate, U, Mo, Se, Cr and Tc in the perched water imply that this water was derived (at least partially) from Hanford operations. The most likely candidate for the source of this water is the 216-S-3 cribs located approximately 50 m west-northwest of the borehole, although it is also possible that there could be some input from the 241-S tank farm. Understanding how these fluids reached the perched water and migrated to the location of the B8812 borehole is key to understanding how contaminants might migrate through the vadose zone.

The stable isotope data can also be used to constrain the age of the perched water. The ca. 1-m-thick perched water layer has an $\delta^{18}O$ value identical to that of Columbia River water and about 2 to 3 % different from the surrounding waters. Isotopic redistribution by combined liquid and vapor phase diffusion will dissipate this isotopic anomaly on a time scale (L^2/D) of roughly 25 years. So this perched water is almost certainly introduced recently. More detailed modeling could potentially constrain the age further.

D.6.2.4.4 Groundwater. The groundwater sample extracted from the deepest sample is also isotopically distinct from the vadose zone porewaters. As with the perched water, it is clear that natural infiltration of water through the vadose zone sediments is not a significant source of recharge. Unlike the perched water, however, there is no evidence that any contamination related to the Hanford activity has reached the groundwater at this point.

D.6.2.5 Summary

This work was restricted to uncontaminated core samples from the vicinity of the S and SX tank farms, but has some significant findings regarding the potential for contaminant transport in the area:

- Natural, vertical infiltration of water through the vadose zone, as evidenced by the pervasive evaporation of the vadose zone porewaters, is limited to less than a few centimeters per year

- Contaminants can and do migrate laterally along perched water horizons.

Analyses of the ^3H (tritium) and ^{36}Cl concentrations of the porewaters and deionized water leaches from these samples could significantly enhance the results of this study. Both tritium and ^{36}Cl would help confirm whether or not the shallow porewaters and perched water were derived from Hanford process waters. ^{36}Cl data for the unaffected samples could be used to estimate vertical recharge rates in this area (e.g., Murphy et al. 1996).

D.6.2.6 References

Barnes, C. J., and G. B. Allison, 1988, "Water Movement in the Unsaturated Zone Using Stable Isotopes of Hydrogen and Oxygen," *Journal of Hydrology*, Vol. 100:143-176.

Craig, H., 1961, "Isotopic Variations in Meteoric Waters," *Science*, Vol. 133: 1702-1703.

Epstein, S., and T. Mayeda, 1953, "Variations of O18 Content of Waters from Natural Sources," *Geochimica et Cosmochimica Acta*, Vol. 4:213-224.

Friedman, I., 1953, "Deuterium Content of Natural Water and Other Substances," *Geochimica et Cosmochimica Acta*, Vol. 4:89-103.

Gat, J. R., E. Mazor, and Y. Tzur, 1969, "The Stable Isotope Composition of Mineral Waters in the Jordan Rift Valley," *Journal of Hydrology*, Vol. 7:334-352.

Gaye, C. B., and W. M. Edmunds, 1996, "Groundwater Recharge Estimation Using Chloride, Stable Isotopes and Tritium Profiles in the Sands of Northwestern Senegal," *Environmental Geology*, Vol. 27: 246-251.

Hearn, P. P., W. C. Steinkampf, D. G. Horton, G. C. Solomon, L. D. White, and J. R. Evans, 1989, "Oxygen-Isotope Composition of Ground Water and Secondary Minerals in Columbia Plateau Basalts: Implications for the Paleohydrology of the Pasco Basin," *Geology*, Vol. 17:606-610.

Komor, S. C., and D. G. Emerson, 1994, "Movements of Water, Solutes, and Stable Isotopes in the Unsaturated Zones of Two Sand Plains in the Upper Midwest," *Water Resources Research*, Vol. 30:253-267.

Melayah, A., L. Bruckler, and T. Bariac, 1996, "Modeling the Transport of Water Stable Isotopes in Unsaturated Soils Under Natural Conditions: 2. Comparison with Field Experiments," *Water Resources Research*, Vol. 32:2055-2065.

Murphy, E. M., T. R. Ginn, and J. L. Phillips, 1996, "Geochemical Estimates of Paleorecharge in the Pasco Basin: Evaluation of the Chloride Mass Balance Technique," *Water Resources Research*, Vol. 32:2853-2868.

Phillips, F. M., 1995, "The Use of Isotopes and Environmental Tracers in Subsurface Hydrology," *Reviews of Geophysics*, Vol. 33:1029-1033.

Vennemann, T. W., and J. R. O'Neil, 1993, "A Simple and Inexpensive Method of Hydrogen Isotope and Water Analyses of Minerals and Rocks Based on Zinc Reagent," *Chemical Geology*, Vol. 103:227-234.

D.6.3 VERTICAL DISTRIBUTION OF ^{86}SR/^{87}SR ISOTOPIC RATIOS MEASURED IN B8812 CORE AND IMPLICATIONS TO WATER INFILTRATION NEAR THE SX TANK FARM

D.6.3.1 Introduction

Recent published work shows that in many instances the Sr isotopic composition of groundwater can be used to infer flow velocity and infiltration flux. This approach has been applied to groundwater at the Lawrence Berkeley National Laboratory (Johnson and DePaolo 1997a, b) at INEEL to infer locations of especially fast groundwater flow in the Snake River Plain aquifer (Johnson et al. 2000), and at Yucca Mountain to estimate infiltration flux (Marshall et al. and DePaolo et al., unpublished). The method is useful for obtaining infiltration flux estimates in situations where fluxes are small and difficult to quantify by other means, such as at LBNL and Yucca Mountain. It is also useful for establishing relative flow velocities in situations where the fluxes are very high and therefore difficult to quantify because the head gradients are very small (as at INEEL). Application of the technique requires measurements of Sr concentrations and ^{87}Sr/^{86}Sr ratios in fluid samples (or distilled water leaches of cores) and in rock or soil samples.

D.6.3.2 Experimental Procedures

Following the vacuum water extraction for stable isotope analysis of O and deuterium (see Section D.6.3.1), 32 soil core samples were prepared for Sr isotopic analysis. The samples were first rinsed in an amount of deionized water equal to the dry weight of the samples. The Sr contained in the rinse water is assumed to be that which was originally dissolved in the pore fluid plus any readily exchangeable Sr on the solid phases. The rinsed samples were subsequently leached with warm 8M HNO_3 and the leachate analyzed. Both the water rinse and HNO_3 leach were done according to the procedure described by ASA (1996), page 420. The Sr isotopic measurements were performed on a VG354 multi-collector thermal ionization mass spectrometer at the University of California, Berkeley; the results are listed in Table D.6.3.1.

D.6.3.3 Results

The distilled water rinse samples show a systematic down-hole shift in ^{87}Sr/^{86}Sr values from a high of 0.721 at a depth of 15 feet to a value of 0.712 at a depth of 185 feet. The trend of decreasing ^{87}Sr/^{86}Sr continues down to the local groundwater value of 0.710. There is a significant spike toward high ^{87}Sr/^{86}Sr at 136 feet, and smaller spikes at 56 feet and 170 feet. The Sr concentrations calculated for the porewaters are in the range 0.1 to 3.7 ppm, with the typical values being the range 1 to 2 ppm and the average value 1.4 ppm. These concentrations are higher than the typical groundwater concentration values of around 0.1 to 0.3 ppm (average of 80 samples from the 200 area is 0.24 ppm; DePaolo and Conrad, unpublished). The calculated concentrations in the vadose zone are likely to be affected by leaching of some adsorbed Sr. It is inferred therefore that the average amount of readily exchangeable Sr in the soils is about 6 times the amount dissolved in the pore water, although the range is from 1 to 20.

Table D.6.3.1. Sr Concentration and Isotopic Results for Core Samples From Borehole 299-W22-48.

Interval (ft)	Depth (ft) Assigned	DI rinse $^{87}Sr/^{86}Sr$ [a]	DI rinse Sr/g soil (ppb) [b]	HNO_3 leach $^{87}Sr/^{86}Sr$ [a]	HNO_3 leach Sr/g soil (ppm) [b]
1.0-1.5	1.25	0.71447	664.7	0.71272	31.1
6.0-6.5	6.25	0.71529	75.0	0.71628	42.0
9.5-10.0	9.75	0.72052	41.1	0.71914	29.5
14.5-15.0	14.75	0.72098	7.7	0.71651	30.4
19.5-20.0	19.74	0.71913	37.1	0.71654	29.7
24.5-25.0	24.74	0.71913	23.9	0.71086	21.3
29.5-30.0	29.74	0.71996	41.3	0.71348	29.5
34.5-35.0	34.74	0.71817	26.4	0.71086	25.2
39.5-40.0	39.74	0.71778	75.0	0.71288	30.7
44.5-45.0	44.74	0.71767	33.7	0.71235	21.6
50.0-50.5	50.24	0.71792	69.4	0.71372	21.3
56.0-56.5A	56.24	0.71771	67.9	0.71416	23.6
56.0-56.5B	56.24	0.71930	72.7	0.71401	28.0
57.5-58.0	57.74	0.71778	70.7	0.71477	24.7
62.0-62.5	62.23	0.71755	38.3	0.71412	22.8
69.5-70.0	69.73	0.71648	20.3	0.71488	25.4
79.5-80.0	79.73	0.71648	75.0	0.71393	27.9
86.5	86.48	0.71529	52.4	0.71379	28.0
96.5	96.48	0.71495	90.5	0.71470	31.6
106.5-107.5	106.97	0.71451	49.8	0.71306	27.9
120.5	120.47	0.71567	53.6	0.71140	30.5
124.0-125.0	124.47	0.71421	42.9	0.71230	31.2
126.5-127.5	126.97	0.71774	108.0	0.71267	29.3
146.0-147.0	146.46	0.71449	134.0	0.71059	197.4
148.5-149.5	148.96	0.71529	75.0		
151.0-152.0	151.46	0.71381	100.1	0.71326	25.7
163.5-164.5	163.96	0.71374	52.7	0.71290	18.0
167.5-168.5	167.96	0.71529	71.7	0.71315	22.4
170.0-171.0	170.46	0.71312	31.2	0.71638	17.4
176.0-177.0	176.45	0.71312	31.2	0.71585	12.0
187.0-188.0	187.45	0.71225	17.1	0.71351	12.2
235.0-236.0	235.44	0.71021	13.0	0.71307	18.1

[a] Uncertainty is ± 0.00002; measured value for NBS987 standard is 0.71028.
[b] Uncertainty ± 0.5% of the value

The uppermost 2 samples, at depths of 1 and 6 feet, have relatively low $^{87}Sr/^{86}Sr$ of about 0.715. The shallowest sample also has a very high Sr concentration, about 10 times the average for the rest of the core samples. The $^{87}Sr/^{86}Sr$ value of the shallowest sample is similar to Columbia River water, so the interpretation of the low $^{87}Sr/^{86}Sr$ values in the shallowest samples is that they reflect river water dumped on the surface that has been highly evaporated. The $\delta^{18}O$ data also indicate that the water was strongly evaporated. However, whereas the extreme evaporation effect is only present in the shallowest sample for $\delta^{18}O$, the two shallowest samples show the effect for Sr. This is expected because the high Sr concentration of the shallow water causes a small contribution from the surficial water to disproportionately shift the $^{87}Sr/^{86}Sr$ value of the underlying level.

The $^{87}Sr/^{86}Sr$ values of the nitric acid leachates are consistently lower than the values in the distilled water rinses between the depths of 10 and 165 feet. The nitric acid leaches do not represent just "exchangeable" Sr. About 5 to 10% of the total soil Sr was removed by the leaching (based on an estimated whole soil Sr concentration of 325 ppm). The strong nitric leach probably did dissolve some silicate mineral framework Sr as well as soluble phases like carbonate. The whole rock values of $^{87}Sr/^{86}Sr$ are therefore probably similar to or lower than the values in the nitric acid leaches, at least down to 165 feet, which is the approximate depth of the base of the Hanford formation. It would be desirable to measure several more analyses of nitric acid leaches nearer the bottom of the hole in the Ringold Formation. In the future, it would be more useful to treat the samples with pH-neutralized sodium acetate to determine the total exchangeable Sr content. However, even this procedure can dissolve carbonate and cause an overestimate of the exchangeable Sr content of the soils.

D.6.3.4 Model for Sr Isotopes

The overall decrease of pore fluid $^{87}Sr/^{86}Sr$ with depth in the core between 10 feet and 165 feet must be a consequence of downward percolation of pore fluids. If the pore fluid starts out at the surface with high $^{87}Sr/^{86}Sr$, then as it exchanges Sr with the soil during downward travel, it will gradually decrease in $^{87}Sr/^{86}Sr$. The rate of release of soil Sr to the pore fluid is effectively the mean rate of primary silicate mineral weathering, weighted by the Sr concentration and $^{87}Sr/^{86}Sr$ of the minerals (Johnson and DePaolo 1994).

If the Sr profile represents a steady-state condition, then the differential form for the depth dependence of the pore fluid $^{87}Sr/^{86}Sr$ (denoted $r_f(z)$), is:

$$\frac{dr_f(z)}{dz} = \left[r_s(z) - r_f(z)\right]\frac{R_s[Sr]_s}{v_f[Sr]_f} \qquad \text{(D.6.3.1)}$$

In this expression $r_s(z)$ is the bulk $^{87}Sr/^{86}Sr$ ratio in the solid at depth z, R_s is the bulk dissolution (weathering) rate of the soil at depth z, v_f is the pore velocity of the fluid at depth z, [Sr]s is the total concentration of Sr in the soil at depth z, and [Sr]f is the Sr concentration in the pore fluid plus readily exchangeable Sr at depth z. This model can be applied to the data to estimate R_s/v_f as function of depth (ratio of the dissolution rate to the fluid velocity). For this calculation, $[Sr]_{soil}$ is assumed to be a constant value of 325 ppm, based on the average values measured from about six samples of core (J. Serne, personal communication). The fluid Sr concentration is taken to be the value measured for the distilled water rinse. The $^{87}Sr/^{86}Sr$ of the nitric acid leaches is tentatively taken to be representative of the isotopic composition of soil Sr that is released from primary weathering of the silicates and incorporated into the pore fluid as it percolates downward. The bulk soil $^{87}Sr/^{86}Sr$ may be somewhat lower than the acid leach values (analyses to check this are underway).

One question is why the fluid starts out near the surface with such high $^{87}Sr/^{86}Sr$ values. Rainwater, which has a very low concentration of Sr, probably dissolves Sr from caliche near the surface and hence initially acquires the isotopic composition of whatever is dissolved first. The Sr in the caliche may be either of aeolian origin or derived from the local soils. The shallow soil Sr can also be dominated by contributions from the weathering of biotite, which has particularly high $^{87}Sr/^{86}Sr$ (Blum and Erel 1997).

The equation above assumes that the vadose zone column is at steady state with respect to Sr isotopes. Transient disturbances to the isotope profile propagate through the section at a velocity that is equal to the fluid velocity divided by a retardation factor (1 + me/mf), where me is the mass of exchangeable Sr per unit volume, and mf is the mass of dissolved (fluid) Sr per unit volume (Johnson and DePaolo 1997a). Based on the data and typical groundwater Sr concentrations, this isotopic retardation factor is estimated to be about 7 ± 3 averaged through the 70-meter soils column. Other estimates of Sr retardation factors in Hanford soils are in the range 20 to 60 for natural fluids (based on K_d values of 5 to 15; PNNL-13037). The isotopic retardation factor can be different from the K_d-based value, because the former depends on the amount of exchangeable Sr present in the rocks, which is different from the amount that can be adsorbed in a single experiment at equilibrium.

The implication of the retardation factor is that the pore fluid Sr isotope profile represented by the deionized (DI) rinses must be a feature that dates from before Hanford operations. For a nominal pore velocity of 30 cm/yr, the transit time for perturbations through the ca. 70-meter section is greater than 1000 years for a retardation factor of 7. The exception to the steady-state assumption for the Sr profile is the upper 6 to 8 feet. Water put on the ground since 1945, if it had the signature of Columbia River water, could have caused a transient isotopic signal to propagate down section by about 5 feet. The soil column Sr isotopic ratios can however be disturbed quite easily if pre-evaporated process water is released to the ground. Since the Sr concentration in pre-evaporated water is much higher than that of river water, concentrated water can overwhelm the budget of adsorbed Sr in the soils, reducing the effective retardation to a value close to unity.

D.6.3.5 Estimates of Infiltration Flux

The available data were fit using a simple finite difference model with the equation given above (Figure D.6.3.1). The ratio R_s/v_f was taken as unknown and adjusted by trial-and-error to match the DI rinse isotopic data. The best fit was done by eye and does not attempt to reproduce every data point, but instead it represents the values of R_s/v_f that match the slope over the length scales of 10 to 40 feet. As shown in the figure, the best-fit values for R_s/v_f are in the range 0.35 to 1.2×10^{-5} m^{-1}. This range of values could change somewhat, probably toward slightly lower values, if the bulk soil $^{87}Sr/^{86}Sr$ ratios are significantly different from those of the nitric acid leachates.

Figure D.6.3.1. (left) Plot of $^{87}Sr/^{86}Sr$ of DI Rinses (open circles) and Nitric Acid Leachates (solid squares) versus Depth.

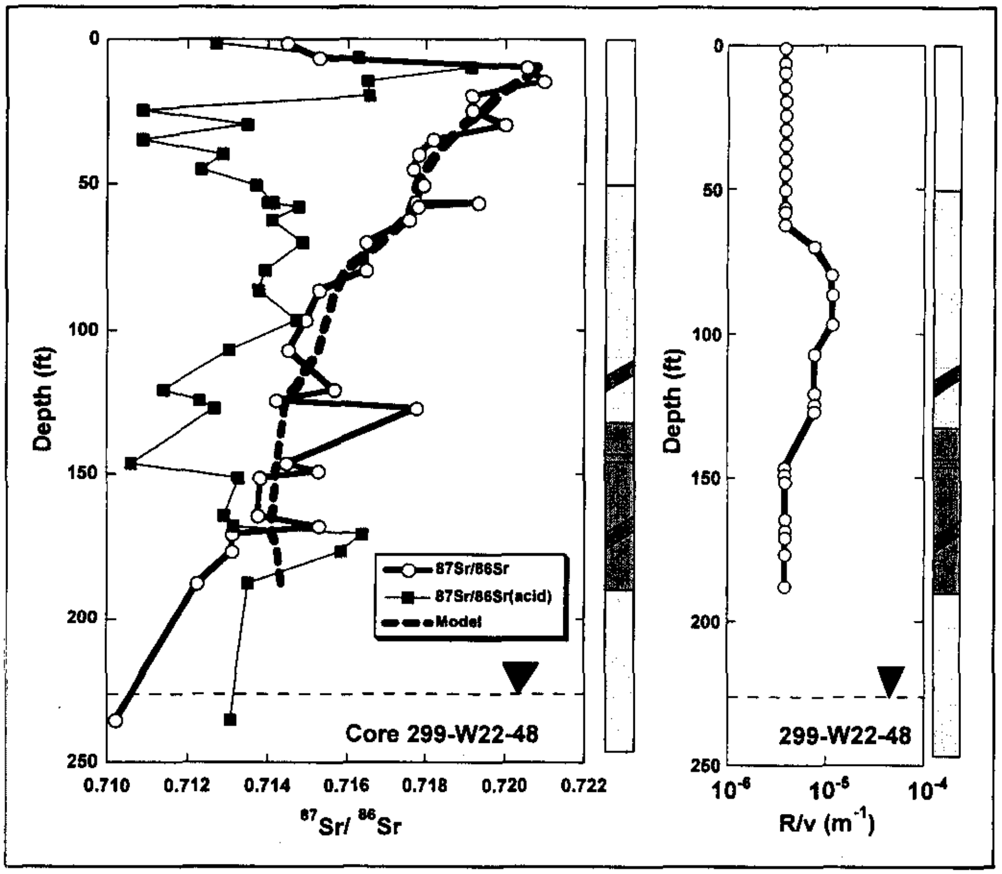

Note: The dashed line is the best-fit trajectory for the model. The simplified lithologic column shown on the right depicts casing (white), Hanford sand (yellow), Hanford silty sand and silt (green), Ringold silty, sandy gravel (pink), clastic dikes (brown) and caliche (blue). (right) Plot of model-derived values of R_s/v_f for the best-fit model is 0.4 -1.2 × 10^{-5} m^{-1}. If the derived R_s/v_f values are changed by as much a factor of 2 in either direction, the model curve will grossly misfit the data. The model does not fit the data in the Ringold Formation or at depths below 170 feet. This misfit may be a consequence of preferential dissolution of particular minerals by the nitric acid procedure, or evidence of non-steady-state conditions.

The infiltration velocity, v_f, can be calculated if the weathering rate (R_s) can be estimated. The bulk weathering rate may be measurable using uranium isotopes, but has not yet been attempted. The rate can be estimated using studies of weathering rates of soils derived from granitic terrains in California (White et al. 1996). White et al. studied soils varying in age from 10 ka to 3000 ka. The bulk weathering rates calculated from their data, and weighted for Sr concentration are 2 to 3 × 10^{-6} yr^{-1}, for soils of ages 40, 130, and 250 ka. (The bulk rate for Sr is approximately the same as the plagioclase weathering rate.) There is a slight trend of higher rates for younger soils, but there is also a trend of lower rates for deeper soil horizons, so values between 1 and 3 × 10^{-6} yr-1 are likely to be applicable to the Hanford vadose zone. This range of values also fits with data obtained on other soils in other studies, but the White et al. (1996) results are more comprehensive, and are most comparable to Hanford because both the mineralogy and climate are similar.

The range of R_s/v_f values of 0.4 to 1.2×10^{-5} yr^{-1}, and $R_s = 2 \pm 1 \times 10^{-6}$ yr-1, gives the estimated downward water velocity of 25 ± 17 cm/yr. The average water content of the soils is about 12 volume percent, so the quoted range of velocity corresponds to an infiltration flux ($v_f\Theta$) of 3 ± 2 cm/yr. This value should be an average value applicable to the past 100 to 1000 years, and is not affected by any recent changes in climate or Hanford operations.

D.6.3.6 Conclusions and Implications

The objective of this study was to obtain an estimate of the average natural infiltration flux at a relatively unmodified site in the Hanford 200 Area. The Sr isotope data obtained are systematic and indicate that the infiltration flux is 3 ± 2 cm/yr. The inferred flux is an average value that applies to infiltration over the past 100 to 1000 years. The implied vadose zone transit time for infiltrating waters is 300 ± 200 years for a 70-m-thick unsaturated zone with 12% average water content. This transit time applies to mobile contaminants and can be used to infer the transit time of other nuclides that are less mobile, and other areas where the vadose zone is a different thickness. The result suggests that natural infiltration is significant for moving mobile species toward the water table over hundreds of years. Similar data sets from other areas of the Hanford Site would be desirable to establish the generality of the results presented here.

D.6.3.7 References

Blum, J. D., and Y. Erel, 1997, "Rb-Sr Isotope Systematics of a Granitic Soil Chronosequence: The Importance of Biotite Weathering," *Geochimica et Cosmochimica Acta*, Vol. 61:3193-3204.

Johnson, T. M., and D. J. DePaolo, 1994, "Interpretation of Isotopic Data in Groundwater-Rock Systems: Model Development and Application to Sr Isotopic Data from Yucca Mountain," *Water Resources Research*, Vol. 30:1571-1587.

Johnson, T. M., and D. J. DePaolo, 1997a, "Rapid Exchange Effects on Isotope Ratios in Groundwater Systems, 1. Development of a Transport-Dissolution-Exchange Model," *Water Resources Research*, Vol. 33:187-195.

Johnson, T. M., and D. J. DePaolo, 1997b, "Rapid Exchange Effects on Isotope Ratios in Groundwater Systems, 2. Flow Investigation Using Sr Isotope Ratios," *Water Resources Research*, Vol. 33:197-205.

Johnson, T., R. C. Roback, T. L. McLing, T. D. Bullen, D. J. DePaolo, C. Doughty, R. J. Hunt, R. W. Smith, L. D. Cecil, and M. T. Murrell, 2000, "Groundwater "Fast-Paths" in the Snake River Plain Aquifer: Radiogenic Isotope Ratios as Natural Groundwater Tracers," *Geology*, Vol. 28:871-874.

White, A. F., A. E. Blum, M. S. Schulz, T. D. Bullen, J. W. Harden, and M. L. Peterson, 1996, "Chemical Weathering Rates of a Soil Chronosequence on Granitic Alluvium: I. Quantification of Mineralogical and Surface Area Changes and Calculation of Primary Silicate Reaction Rates," *Geochimica et Cosmochimica Acta*, Vol. 60:2533-2550.

D.6.4 CONCLUSIONS OF S&T INVESTIGATIONS OF ISOTOPE GEOCHEMISTRY S-SX SEDIMENTS

A series of isotope ratio techniques were employed to investigate the premise that multiple contaminant maxima in the core represent different source materials. The best evidence for multiple leak events associated with tank SX-108 is visible in the ^{129}I data which shows a very large difference in isotopic composition of iodine isotopes between the two concentration maxima in the core. The ^{127}I to ^{129}I ratio thus appears to be an excellent fingerprinting tool for determining source attribution. ICP/MS proved in this study to be a very powerful tool for rapid and low cost analysis of ^{129}I and ^{127}I on radioactive samples.

The slight sorption of ^{129}I implied by the comparison of the ^{129}I profile to that of ^{99}Tc is in at least general agreement with previously reported experimental results. Application of the experimental results is complicated by the widely varying K_D values reported. This variability may be related to a strong non-linearity in the sorption isotherm. Because iodide is an anion, the sorption may be controlled by a small number of positively charged sites on the edges of clays and on iron and aluminum oxide surfaces. Thus the sorption sites may be easily saturated. Competition with other anions may also be a factor.

Variability in the ^{95}Mo to ^{98}Mo ratio provides an excellent means for distinguishing separate sources through isotopic fingering. Three separate sources of molybdenum are indicated in the SX-108 slant borehole, likely corresponding to the first filling in the early 1950s, the second filling in the 1963 to 1964 time frame, and possibly a later leak which occurred in the late 1960s. Molybdenum isotopes also appear to work well as tracers of tank leak material into groundwater where such impacts are known or suspected. However, because of the high background of naturally occurring stable molybdenum typically found in groundwater, high precision mass spectrometric techniques may be needed; recent advances in the development of ICP/MS instruments make the approach very practical.

The Cs isotopes showed remarkably constant isotopic composition on water and electrolyte leaches. The presence of separate leak sources clearly visible from several other lines of evidence was not discernable from the Cs data in spite of an expected large variability in ^{135}Cs concentration predicted from nuclear modeling considerations. A more extensive series of Cs measurements on other tanks is needed to better define the range of variability. Very minor amounts of naturally occurring Cs were leached by month-long exposures to concentrated sodium nitrate solutions. The observed ^{133}Cs in the leachates was attributable to an essentially pure fission component. Those data can be used to correctly assess the total Cs loading in sorption experiments and transport calculations.

The fingerprinting technique was also applied to core and groundwater data from several locations in the SX tank farm. Samples included a borehole near leaking tanks SX-109 and SX-115 as well as groundwater from well 299-W23-19 near SX-115. Although only a limited data set is available, it is clear that each of the tank leak sources is distinct from each other. For example, while the nitrate to Tc ratio is very similar in both the well and borehole, the nitrate to chloride ratio is very different. This suggests that the groundwater impact observed at well 299-W23-19 is not associated with the tank SX-115 leak itself but rather a leak from one of the other SX tank farm sources conveyed by some type of preferential pathway to that location.

Similarly, the three ratios measured in the groundwater sample are also a poor match to the SX-108 and SX-109 samples. In order for fingerprinting techniques to achieve their full potential, more comprehensive analyses need to be performed on a wider suite of samples.

An assessment of the $^{87}Sr/^{86}Sr$ isotopic ratios in the B8812 core indicated an average water infiltration flux of 30 ±20 mm/yr to the vadose zone over the past 100 to 1000 years. In contrast, infiltration estimates for the S and SX tank farms based on a method that uses winter precipitation and surface soil texture data, calibrated by 20 years of Hanford lysimeter data, place the average value at 56 mm/yr with a range of 20 to more than 150 mm/yr, depending on climatic conditions. Regardless of precise value, these results suggest that natural infiltration and drainage is significant for moving mobile species (e.g., NO_3, Cr, ^{99}Tc, $^{127/129}I$, $^{79/82}Se$) toward groundwater over time periods of decades to hundreds of years. The estimated vadose transit time for meteoric waters in the S and SX tank farms range from 60 to 500 years depending on assumptions and model.

D.7.0 SIMULATION OF MULTIPHASE FLUID FLOW AND REACTIVE TRANSPORT AT THE SX TANK FARM

Critical decisions on the management of wastes in the S and SX tank farms will be based on predictions of contaminant transport in the Hanford Site vadose zone. Several of these decisions will be made in the next three to five years:

- barriers to control recharge at the ground surface
- procedures for retrieval and stabilization of tank waste
- remediation of contaminated sediments.

Confidence in the model predictions is built on defensible justifications for the selection of process representations, parameters for those representations, initial and boundary conditions, as well as a demonstrated ability to capture known behaviors. Building this level of trust in the models requires a program of activities that begins with fundamental and simplified analyses that eventually lead to more comprehensive and detailed models. This section describes preliminary modeling analyses performed by the S&T Vadose Zone Modeling team to identify appropriately detailed process models for Hanford Site assessments and provide technical defensibility for their use in predicting long-term behavior of contaminants.

The S&T Vadose Zone Transport Modeling Team is part of an integrated effort to develop the understanding of contaminant behavior in the Hanford vadose zone necessary for waste management decisions. The modeling is dependent on historical data as well as ongoing studies to characterize site-specific processes and properties. These data have been or are being developed by other entities (e.g., EMSP, S&T Program, site contractors) for a variety of purposes and, in most cases, have not been examined in a comprehensive modeling framework for consistency. An important role of the modeling effort, therefore, is to identify inconsistencies between the observations and the process-level understanding, and prioritize areas that merit additional investigation.

The Modeling Team targeted the Hanford SX tank farm from three principal perspectives: (1) nonisothermal multiphase fluid flow resulting from the known temperature history of boiling waste tanks, (2) speciation of high-ionic strength tank fluids, and (3) cesium migration as a function of competitive ion exchange on Hanford sediments.

D.7.1 FLUID FLOW, HEAT TRANSFER, AND SOLUTE TRANSPORT AT TANK SX-108; A SUMMARY REPORT ON MODELING STUDIES

Karsten Pruess[1], Steve B. Yabusaki[2], Carl I. Steefel[3], and Peter C. Lichtner[4]

[1]Lawrence Berkeley National Laboratory, Berkeley, California 94720

[2]Pacific Northwest National Laboratory, Richland, Washington 99352

[3]Lawrence Livermore National Laboratory, Livermore, California 94550

[4]Los Alamos National Laboratory, Los Alamos, New Mexico 87545

D.7.1.1 Introduction

Of 15 single-shell tanks at the 241-SX tank farm, 10 are known leakers (Ward et al. 1997). Fluid flow and solute transport in the unsaturated zone surrounding the tanks is affected by radioactive decay heat and by chemical interactions between fluids and sediments. Multiphase processes near the tanks include flow of aqueous and gaseous phases, boiling and condensation, migration of solutes, precipitation and dissolution, and vapor-liquid counterflow. Additional effects arise from variable solute concentrations in the aqueous phase, heat generation from leaked radioactive fluids, interference between the heat load and fluid leaks of different tanks, and from suspected but poorly constrained water line leaks.

From an environmental management perspective, important issues at the SX tank farm include past, present, and future distribution and migration of contaminants for a "no action" scenario, as well as for various remedial measures that may be considered (such as placing covers to reduce net infiltration, or removing tank contents through sluicing). A key task for performance assessment is to predict the future rates at which different contaminants may be expected to reach the water table and enter the groundwater system. The complexity and intrinsic variability of hydrogeologic conditions and processes is such that a strictly deterministic description is not possible. Performance assessment must adopt simplified models and representations, which must be complemented by stochastic representations of uncertainties. In order to be credible and acceptable, the simplifications and approximations made in performance assessment models must be based on a sound scientific understanding of the underlying processes.

The purpose of the studies reported here is to develop a better understanding of the unique hydrogeologic system created by the Hanford tanks through detailed mechanistic modeling of fluid flow, heat transfer, and mass transport. Our aim is to provide support and guidance for performance assessment, field characterization, and decision making on remedial measures. We focus especially on tank SX-108, which is one of the highest heat load tanks in the 241-SX tank farm, and is a known leaker. A realistic quantitative model of mass and energy transport near the tanks requires

- comprehensive treatment of all significant physical and chemical processes
- accurate representation of hydrogeologic conditions at the site
- realistic parameters for fluids and sediments and for temperature and leak history of the tanks.

These are ambitious goals that can only be achieved through a process of iterative refinement, starting from relatively simple models. The initial emphasis of the work reported here is on process issues, focusing on the extent to which various multiphase and nonisothermal processes may impact the migration of moisture and aqueous solutes. We have attempted to represent significant hydrogeologic features of the Hanford sediments in a reasonably approximate way, but we have made only limited efforts to capture detailed hydrogeologic conditions at a specific tank. We have investigated a series of models that probe different processes and mechanisms, in order to determine what processes are important for contaminant behavior, and how they can be modeled effectively. The present write-up is a summary of work-in-progress; a more detailed report on our thermo-hydrologic modeling is in preparation.

D.7.1.2 Tank Effects

Emplacement of the tanks led to large changes in the hydrogeological conditions at the site. The following effects may be distinguished.

- Sediments down to approximately 16 m depth were removed during construction and backfilled after tank emplacement, altering the hydrogeologic properties of the material.
- A layer of gravel and coarse sand of approximately 2 m thickness was placed on top of the tanks. This will allow precipitation to migrate more rapidly to greater depth, greatly increasing net infiltration by reducing the fraction of infiltration that can be removed by evapotranspiration.
- The "umbrella" effect of the tanks will cause infiltrating water to pond atop the tanks and be diverted sideways, with much increased water fluxes around the perimeter of the tanks.
- Due to the radioactive decay heat, temperatures in several tanks rose to well above the nominal boiling point of 100 °C, in one case up to 160 °C, for extended time periods. This caused elevated formation temperatures with vaporization-condensation effects and associated redistribution of moisture and solutes.
- Tank leaks can introduce hot and highly saline aqueous fluids into the subsurface, whose thermophysical properties and flow behavior may be quite different from pure water. Further changes in flow behavior could result from chemical alteration of the sediments due to reactions with the fluids.

D.7.1.3 Modeling Approach

Modeling of fluid flow, heat transfer, and mass transport at the Hanford tanks is complicated by intrinsic variability of the geologic media, and by the complex forcing of the system from natural and man-made perturbations. Important processes include water seepage from infiltration, umbrella effect and heat output of the tanks, and leakage of fluids with high ionic strength and internal heat generation. Our modeling approach borrows from techniques developed in petroleum and geothermal reservoir engineering, and mining engineering. Several different numerical simulators were used and occasionally enhanced as needed. Specific results reported here were obtained with TOUGH2 (Pruess et al. 1999).

We have simulated different cases to explore mechanisms and sensitivities. As a convenient starting point for introducing and comparing more complete process descriptions we have investigated an "isothermal reference case," using a Richards' (1931) equation approximation in which only the liquid (aqueous) phase is active, while the gas phase is considered a passive bystander at constant pressure. An alternative model, dubbed "nonisothermal base case," includes tank heat effects and a comprehensive treatment of multiphase processes, including boiling and condensation, two-phase flow, and diffusion in aqueous and gas phases. Some simulations were performed to explore special effects, such as moisture tension-dependent anisotropy, and moisture redistribution from vapor diffusion that is driven by reduced vapor pressure of more saline fluids.

Each simulation case requires several (typically two) modeling segments to describe changes in boundary conditions, formation properties, and sinks and sources from tank construction and from storage and leakage of waste fluids. The modeling process begins with the calculation of a "natural state" that corresponds to hydrogeologic conditions prior to tank construction.
The natural state entails steady flow (gravity-capillary equilibrium) under conditions of uniform and time-independent infiltration at a rate of 1 cm/yr at the land surface. Subsequent emplacement of tanks was modeled by using the previously calculated steady state conditions as initial conditions, and making the following changes in the model:

- modify hydrogeologic parameters in the regions occupied by tank and backfill
- alter evapotranspiration conditions at the land surface to a net infiltration of typically 10 cm/yr (Gee et al. 1992)
- introduce appropriate time-dependent sources of heat and saline fluid to model radioactive decay heat and fluid leakage from the tanks.

The starting time of the tank simulations is 1955 (1955.82 to be precise), which is the beginning of monitoring data for tank SX-108. Land surface infiltration at a rate of 10 cm/yr includes a small amount of conservative solute tracer, arbitrarily modeled as 0.1 wt% NaCl, which was added to facilitate monitoring the downward advance of infiltration. Heat generation from the tank is modeled by specifying actual measured tank temperatures as time-dependent boundary conditions on the tank surface. A tank leak was also investigated, see below.

The 241-SX tank farm includes 15 single-shell tanks that are placed in a regular pattern in 5 rows and 3 columns (Conway et al. 1997; see Figure D.7.1.1) with 30.4 m spacing between tank centers (Piepho 1999). To simplify the analysis we consider the vertical planes that bisect the lines between tank centers as planes of symmetry. This will only be approximately valid even for the centrally located tank SX-108, because of different heat loads from different tanks and intrinsic variability in hydrogeologic properties. However, this simplification is appropriate for a study that focuses on coupled multiphase fluid and heat flow effects. It greatly facilitates the analysis, because it is only necessary to model the shaded region in Figure D.7.1.1, with "no flow" conditions applied at the lateral boundaries. For this initial study we make a further approximation and replace the rectangular model domain by a cylinder with radius chosen in such a way as to preserve the cross-sectional area, i.e., $\pi R^2 = 30.4 * 30.4\ m^2$, so that R = 17.15 m. The simulation model then simplifies to a two-dimensional R-Z section (radius-depth).

Geometric parameters used in the model were obtained from a construction diagram of tank SX-108.

Figure D.7.1.1. Plan View of the 241-SX Tank Farm, After Conway et al. (1977).

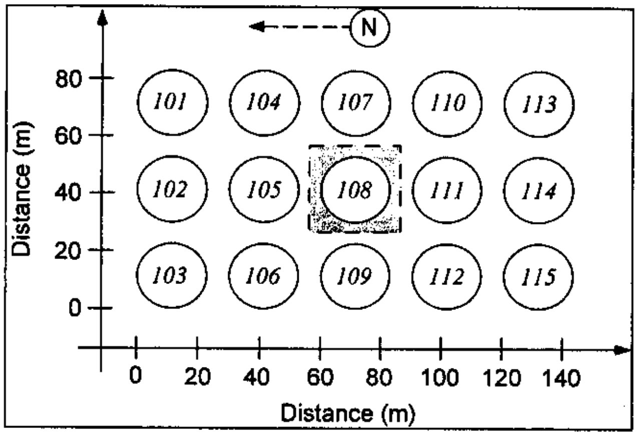

Note: The shaded region around tank SX-108 indicates an approximate symmetry domain.

The dominant hydrogeologic feature at the Hanford Site is the layered structure of the sediments, which is due to the depositional history from a series of cataclysmic floods. However, texture, permeability, and porosity of the individual hydrogeologic units is far from uniform. An intensive program of field sampling and testing, and laboratory analysis, has revealed considerable heterogeneity within individual hydrogeologic units, with permeabilities of bench-scale specimen typically varying over 3 to 4 orders of magnitude (Khaleel and Freeman 1995; Khaleel et al. 1995; Khaleel and Relyea 1997; Smoot and Lu 1994; Rockhold 1999; Khaleel et al. 2000). The predominant large-scale layered structure of the Hanford sediments is significantly disturbed on a local scale; for example, a sloping layer of coarser material has been identified beneath tanks SX-108 and SX-109 (Price and Fecht 1976; Khaleel et al. 2000). Additional complications arise from the presence of clastic dikes. These form extensive networks of sub-vertical structures that could play a role in generating localized preferential flow.

The approach taken in this work is to start from a simplified representation of hydrogeologic structure that honors large-scale layering. In the initial phase of this project our emphasis is primarily on a systematic exploration of process-related issues, e.g., coupling between fluid flow, heat transfer, solute transport, and chemical changes. As our understanding of process-related issues and applicable parameters improves, we intend to introduce more specific hydrogeologic features known to exist near tank SX-108 in step-wise fashion. In the present work, the formation is modeled with "layer-cake" stratigraphy, as shown in Table D.7.1.1 and Figure D.7.1.2. A summary of parameters used for the reference case is shown in Table D.7.1.2. Additional parameter specifications needed for two-phase nonisothermal effects and mass transport are given in the full report (Pruess et al. in preparation). Work is ongoing to explore parameter sensitivities and to implement more site-specific hydrogeologic detail.

Table D.7.1.1. Stratigraphic Sequence at 241-SX Tank Farm, After Ward et al. (1996).

Unit	Thickness	To depth
Backfill	15.4 m	15.4 m
Hanford fine sand	23.6 m	39 m
Plio-Pleistocene	6 m	45 m
Upper Ringold	3 m	48 m
Middle Ringold	20 m	68 m

Figure D.7.1.2. Model Domain Showing Stratigraphic Units (a) and Computational Grid (b).

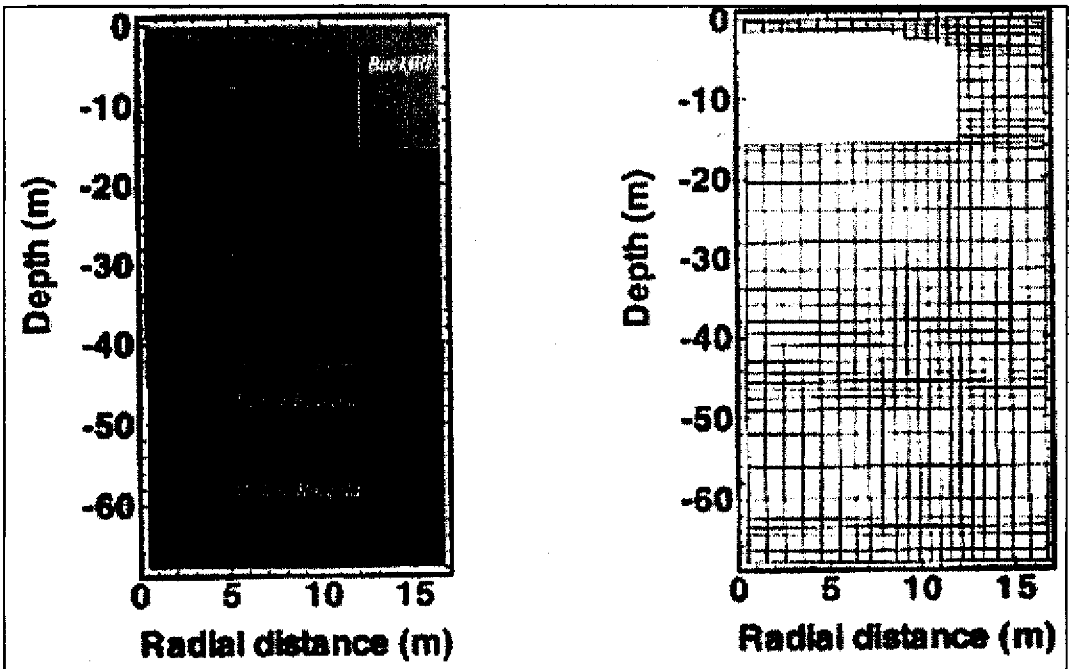
0
-10
-20
-30
-40
-50
-60
Depth (m)
Backfill
0
5
10
15
Radial distance (m)
0
-10
-20
-30
-40
-50
-60
Depth (m)
0
5
10
15
Radial distance (m)

(a)

(b)

Table D.7.1.2. Formation Parameters for Reference Case (Richards' Equation).

Formation parameter		Backfill	Hanford	Plio-Pleistocene	Upper Ringold	Middle Ringold
Permeability (m^2)	hor. vert.	2.48e-12 1.24e-12	3.70e-13 1.23e-13	4.10e-14 1.37e-14	1.58e-13 0.53e-13	2.20e-13 0.73e-13
Porosity		0.2585	0.3586	0.4223	0.2625	0.1643
Liquid rel. perm.	m S_{lr}	0.658 0.0774	0.469 0.0837	0.456 0.2595	0.386 0.2130	0.392 0.0609
Cap. pressure (1/Pa)	$\alpha/\rho g$	10.08e-4	9.394e-5	6.841e-5	2.961e-5	6.331e-5

The computational grid as shown in Figure D.7.1.2 has 22 blocks in R-direction and 44 layers, for a total of 968 grid blocks. The entire tank volume is included in the discretization domain but is omitted from Figure D.7.1.2b. The region occupied by the tank is assigned zero permeability in the simulations, except of course in the natural state (pre-emplacement) simulations where it is given properties identical to the backfill domain. Radial grid increments are $\Delta R = 1$ m near the tank center, decrease to 0.53 m near the perimeter of the tank, and then increase to 0.98 m at the outer boundary of the model domain. Vertical thickness of grid layers varies from 0.33 to 4 m. Finer gridding is used near the land surface, near the bottom of the tank, and at lithologic contacts.

For the pre-emplacement state we adopt boundary conditions of 1 cm/yr net infiltration at the top, and a water pressure of 1.405 bar at the bottom of the model (68 m depth), so that the water table will be at approximately 64 m depth. Initial water saturation does not affect the eventual steady state and was chosen as an arbitrary 60%. Although temperature remains constant during the simulation, its value matters as it determines water density and viscosity. Temperature boundary conditions are a mean land surface temperature of 12.8 °C, and a temperature of 17.26 °C at 68 m depth, which is (linearly) extrapolated from the value of 17 °C at 64 m depth given by Piepho (1999). For the Richards' equation approximation we use an average temperature of 15 °C for the 68 m thick domain modeled.

D.7.1.4 Results

D.7.1.4.1 Modeling and Thermal Regime. Simulation results include cross-sections of temperatures, water saturations, and fluid salinities at different times, as well as time series of various parameters at specified locations (Figure D.7.1.3). In this space it is possible to give only a brief summary of the main phenomena observed in the simulations.

Figure D.7.1.3. Locations for Monitoring Temporal Changes.

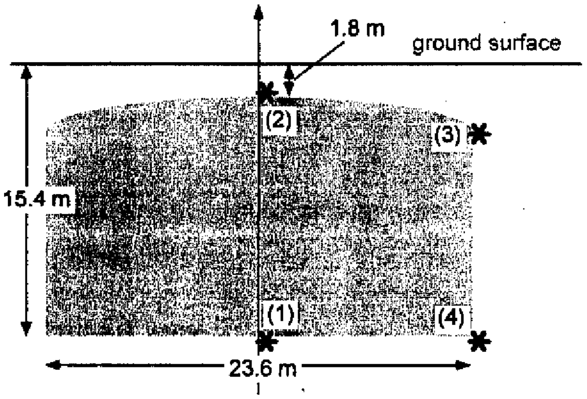

Note: (1) 30 cm below tank, 0.5 m from centerline; (2) 16.5 cm above tank, 0.5 m from centerline; (3) 4.1 depth, 29 cm from sidewall; (4) 30 cm below tank, 29 cm from sidewall.

The highly elevated temperatures in the early period, up to 1967, give rise to boiling near the tank and partial formation dryout. Formation temperatures near the tank rise to above 120 °C, and an extensive zone with temperatures near the ambient boiling temperature of 100 °C develops (see Figure D.7.1.4). This is a "heat pipe" region in which very efficient heat transport takes place by means of vapor-liquid counterflow (Eastman 1968; Doughty and Pruess 1988). The vapor generated near the tank is driven away from the heat source by pressure gradients, and subsequently condenses in cooler regions, releasing its latent heat. Water saturations near the tank are reduced, establishing a capillary pressure gradient that draws liquid water back toward the tank. This vapor-liquid counterflow system rapidly distributes the heat released from the tank over a much greater formation volume than could be accessed by heat conduction alone.

Figure D.7.1.4. Time Dependence of Temperatures at Selected Locations.

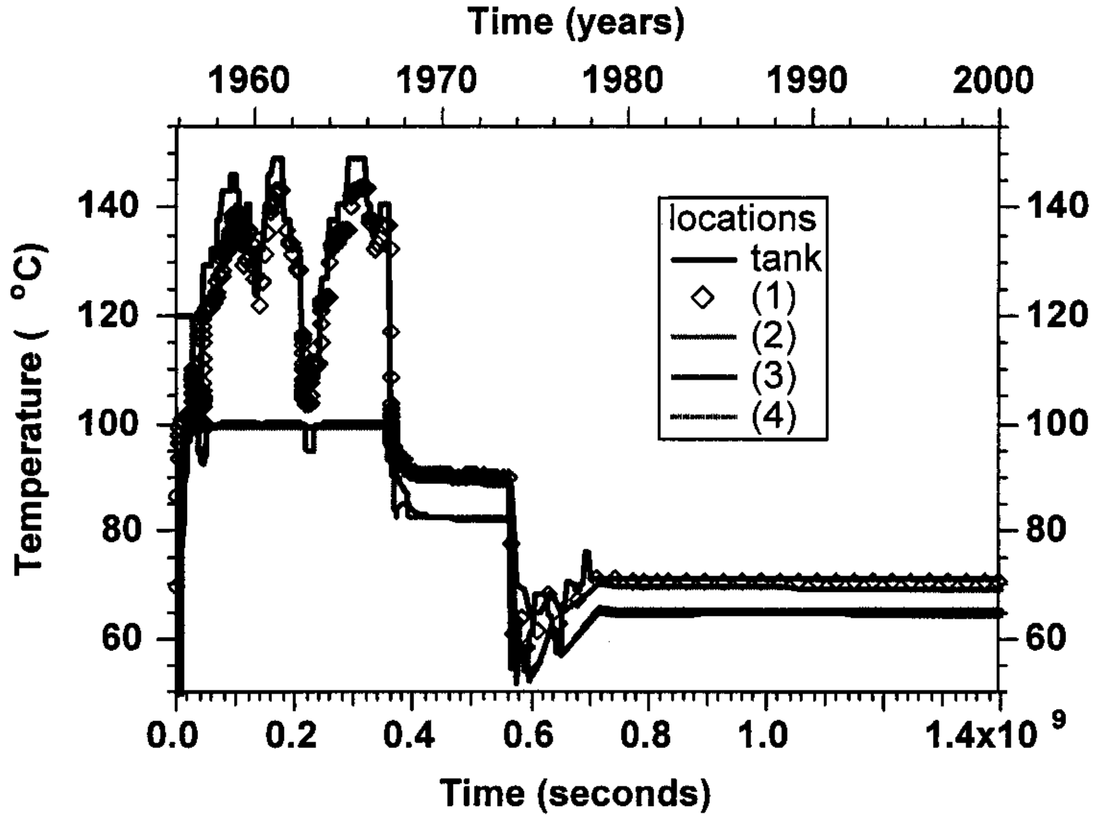

The vapor-liquid counterflow system gives rise to persistent solute transport towards the heat source, which causes solutes to become highly concentrated and even precipitate in the boiling region. Figure D.7.1.5 shows contour diagrams of the aqueous phase mass fraction of infiltrated fluid at three different times. The inventory of infiltrated fluid seems rather small in 1965.91, which is explained by noting that a large fraction of infiltrated solute tracer actually precipitates in the hot region near the tank, reducing the amount available in the aqueous phase. At time 1965.91 precipitated salt amounts to 55.3% of all NaCl that was infiltrated at the land surface. This amount of precipitation is very large, especially when considering that the infiltrating fluid is quite dilute (0.1 wt% NaCl), and highlights the remarkable capacity of the heat pipe system to concentrate solutes near the heat source. As temperatures decline the region near the tank is rewetted, both from capillary-driven liquid flow and from vapor condensation. By the end of 1974 all previously precipitated tracer is redissolved.

Figure D.7.1.5. Distribution of an Environmental Tracer Infiltrating at the Land Surface at Different Times.

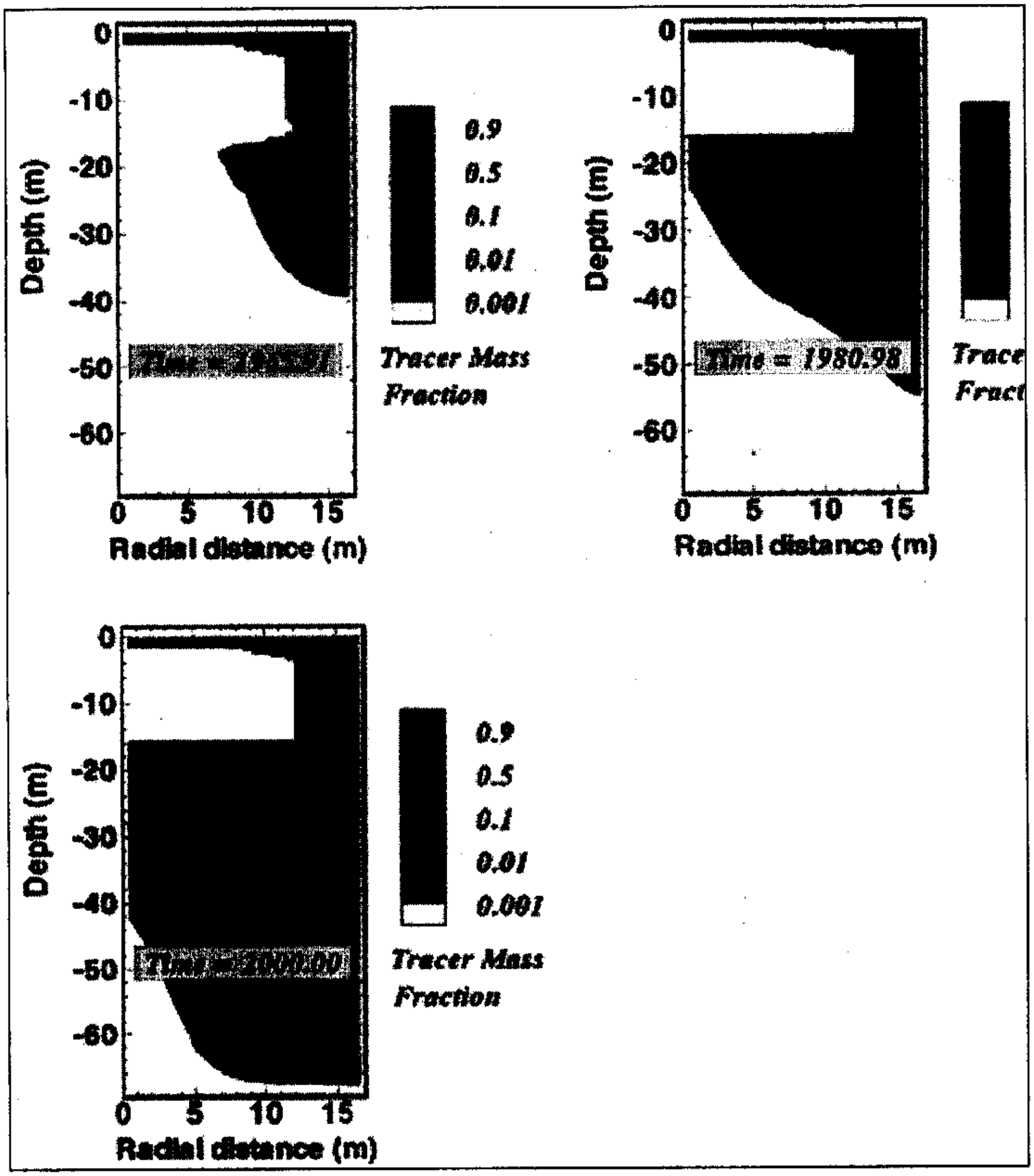

The solute tracer in the infiltrating water was arbitrarily modeled as NaCl, but it can represent any conservative, non-sorbing solute. Tracer breakthrough curves at different horizons are given for the thermal and isothermal cases in Figure D.7.1.6 on a log scale. These curves were obtained by summing all tracer fluxes that cross a horizon at a certain depth, then dividing this by the total liquid flux across that same horizon, and normalizing with respect to tracer concentration in infiltrated fluid. It is seen that early arrivals of tracer are somewhat enhanced from the tank heat, but thermal effects on aggregated tracer migration are generally modest, except at the 16 m horizon right beneath the tank.

Figure D.7.1.6. Tracer Breakthrough Curves at Different Depths.

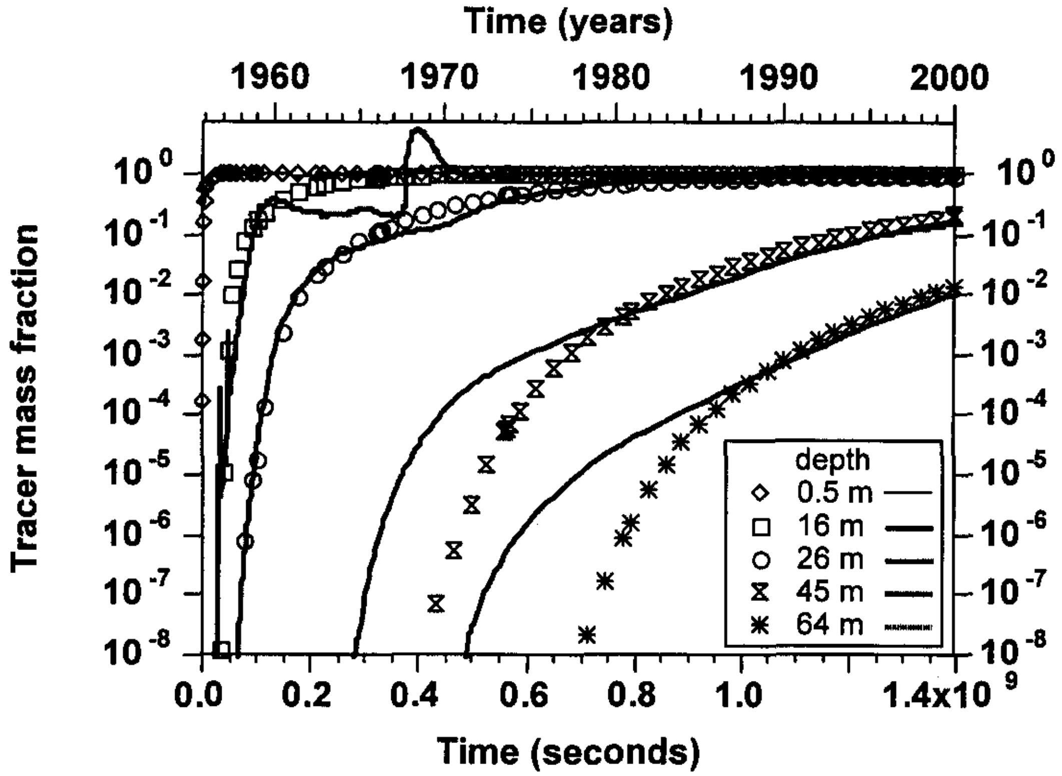

Note: Symbols are for the isothermal reference case, while lines are for the base case with tank heat.

Diffusive vapor fluxes are highest near the tank, and decrease rapidly due to condensation as the land surface is approached. During high-temperature periods vapor diffusion at 0.5 m depth amounts to approximately 10% of net infiltration, while at the land surface itself the effect is less than 4% of net infiltration.

In Figure D.7.1.7 we compare simulated temperatures with appropriately corrected measurements in 41-09-39 borehole, which is a vertical hole centrally located between tanks SX-108, SX-109, SX-111, and SX-112. There is fair overall agreement between the profiles, with some significant discrepancies. It appears that tank temperatures used in the simulation may have been unrealistically high for some period of time prior to the year 2000. The elevated temperatures observed in 41-09-39 borehole below 20 m depth may be attributed to local heating from radioactive decay in fluid leaked from the tanks. This effect will be explored in future simulations and may help to better constrain the magnitude of the leak.

Figure D.7.1.7. Comparison Between Simulated Temperatures and Observations in Hole 41-09-39.

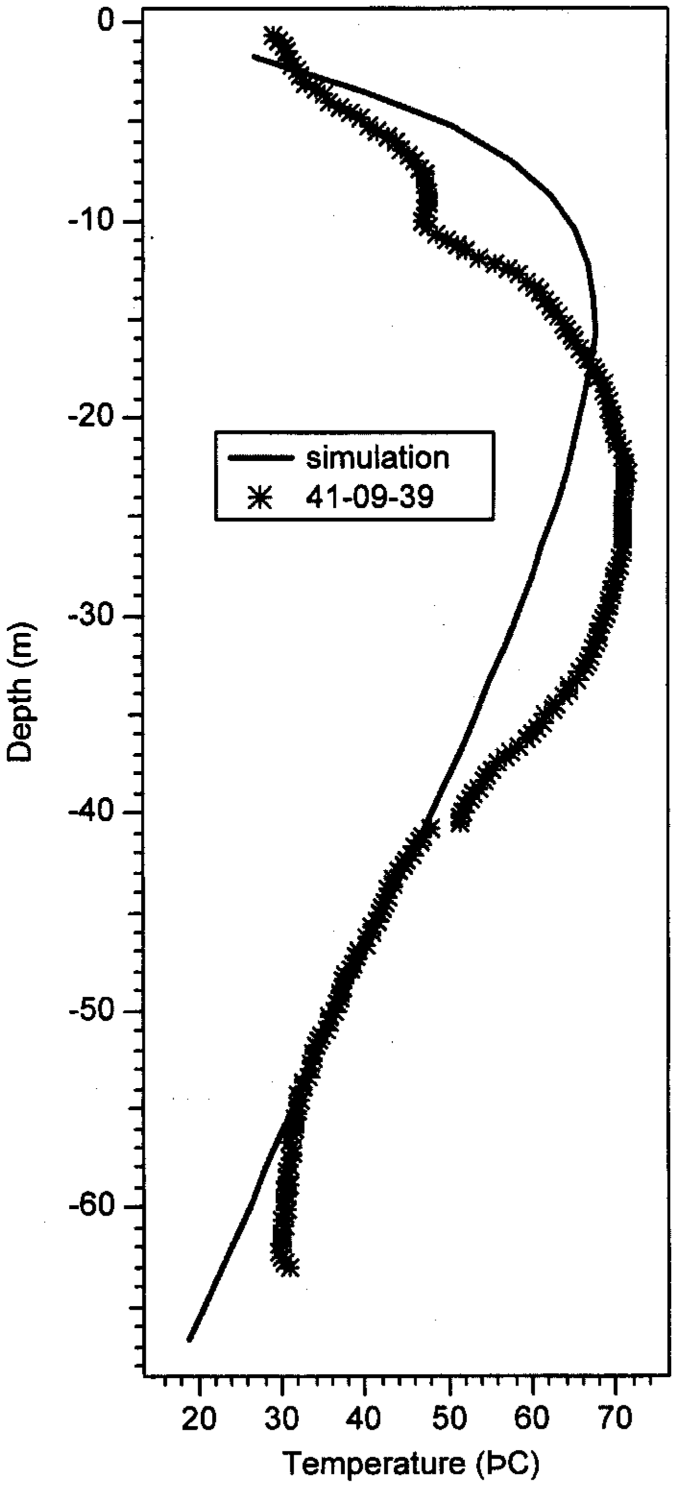

Note: The curve labeled "Simulation" corresponds to a distance of 16 m from the center of tank SX-108 at the beginning of Year 2000.

D.7.1.4.2 Tank Leak Simulations. Separate simulations were performed to investigate the behavior of a tank leak. Reliable information on location, timing, and magnitude of leaks is not available. For tank SX-108 it has been estimated that a leak occurred in the 1966 to 1968 time frame during which approximately 50,000 gallons (= 189.27 m^3) of fluid were discharged into the unsaturated zone (T. Jones private communication 2000). We assume here that the leak occurred over a one-year period during 1966, so that average volumetric leak rate is 5.998e-6 m^3/s. The leaked fluid had high ionic strength and correspondingly large density. The predominant solute in the tank fluid is $NaNO_3$; however, the leak was modeled here as involving a solution of 10 wt% NaCl. This was done because a fluid property description for NaCl solutions was readily available for the temperature conditions of interest (Battistelli et al. 1997). A fluid property package for aqueous solutions of $NaNO_3$ is being developed as part of this research, but experimental data for this system appear to be limited to temperatures below 55 °C (Isono 1984; Mahiuddin and Ismail 1996; Apelblat and Korin 1998). While not quantitatively accurate, substitution of NaCl is expected to provide a reasonably approximate outlook on system behavior. Another limitation arises from the radial symmetry of our current model, which forces tank leaks to be radially symmetric also.

Our simulation includes most but not all effects of salinity on thermodynamic and transport properties of the leaked fluid. Specifically, we include salinity effects on density, viscosity, enthalpy, and vapor pressure of the aqueous phase. Vapor pressure lowering from salinity will induce vapor diffusion towards more saline regions, where subsequent vapor condensation will cause water saturations to increase. Fluid salinity is known to affect surface tension; for example, a saturated NaCl solution at T = 20 °C has approximately 10% larger surface tension than pure water (Adamson 1990). This effect should cause capillary pressures to be somewhat stronger in regions of higher salinity, while the decrease of surface tension with increasing temperatures would weaken capillary pressures in warmer regions. In the present simulation both these effects were neglected.

Breakthrough curves at different horizons are shown in Figure D.7.1.8. Flowing leaked fluid mass fractions at different depths were calculated as the ratio of total solute flow rate to total aqueous phase flow rate, and normalized to the solute concentration in leaked fluid (10 wt%). It is seen that inclusion of thermal effects has negligible impact on the breakthrough time of leaked fluid at 26 m depth, although the concentration of leaked fluid remains lower in the thermal case for an extended time period of approximately 20 years. At deeper horizons, thermal effects are seen to retard and weaken breakthrough of leaked fluids. A comparison case that neglects all salinity effects except solubility constraints produces very similar breakthrough curves, although there are considerable differences in details of thermohydrologic behavior. For example, at t = 1973.66 the simulation with simplified salinity effects predicts almost twice as much solid precipitate in the inner portion of the leakage plume beneath the center of the tank. It is expected that solute transport behavior may depend strongly on the location of the leak, being very different in the infiltration shadow beneath the center of the tank than in the region of enhanced seepage fluxes around the tank perimeter.

Figure D.7.1.8. Breakthrough Curves of Leaked Fluid Released Beneath Tank Center at Different Horizons.

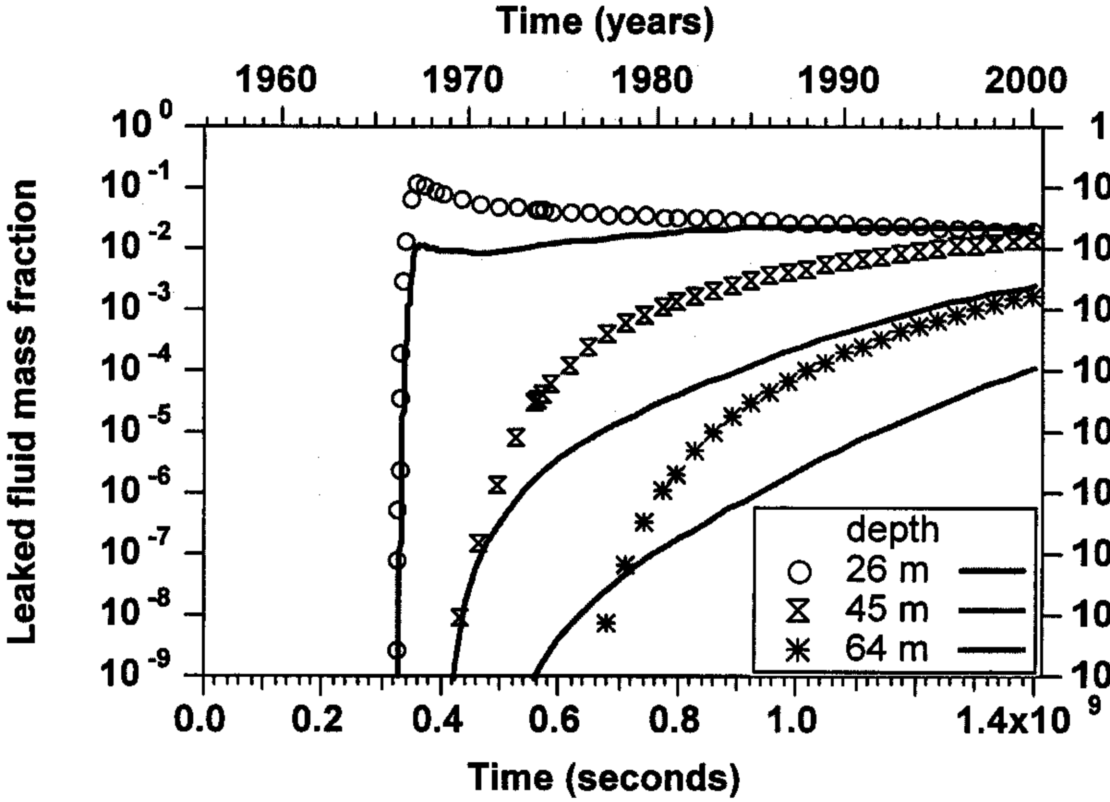

Note: Symbols are for the isothermal reference case, while lines are for the base case with tank heat.

There is much evidence from field and laboratory studies that permeability in sedimentary formations tends to be anisotropic. Depending on moisture tension conditions, permeability in the horizontal direction may exceed vertical permeability by factors of from 3 to 10 or more. The physical condition that causes this anisotropy is the predominantly horizontal layering of sediments, where horizontal and vertical flow proceed via "conductors in parallel" and "conductors in series," respectively. We have made an initial assessment of moisture tension-dependent anisotropy, using a novel two-layer (fine-coarse) model to resolve sub-grid scale heterogeneity. For the isothermal reference case, Figure D.7.1.9 compares pre-emplacement saturation distributions for static anisotropy with those for weak and strong "dynamic" (moisture tension-dependent) anisotropy. Breakthrough curves at different horizons are shown in Figure D.7.1.10. Breakthrough is seen to generally occur more slowly in the anisotropic case, as expected, but more complex behavior is noted in details.

Figure D.7.1.9. Steady-State Water Saturation Profiles for 1 cm/yr Net Infiltration. Two Cases with Dynamic Anisotropy are Shown.

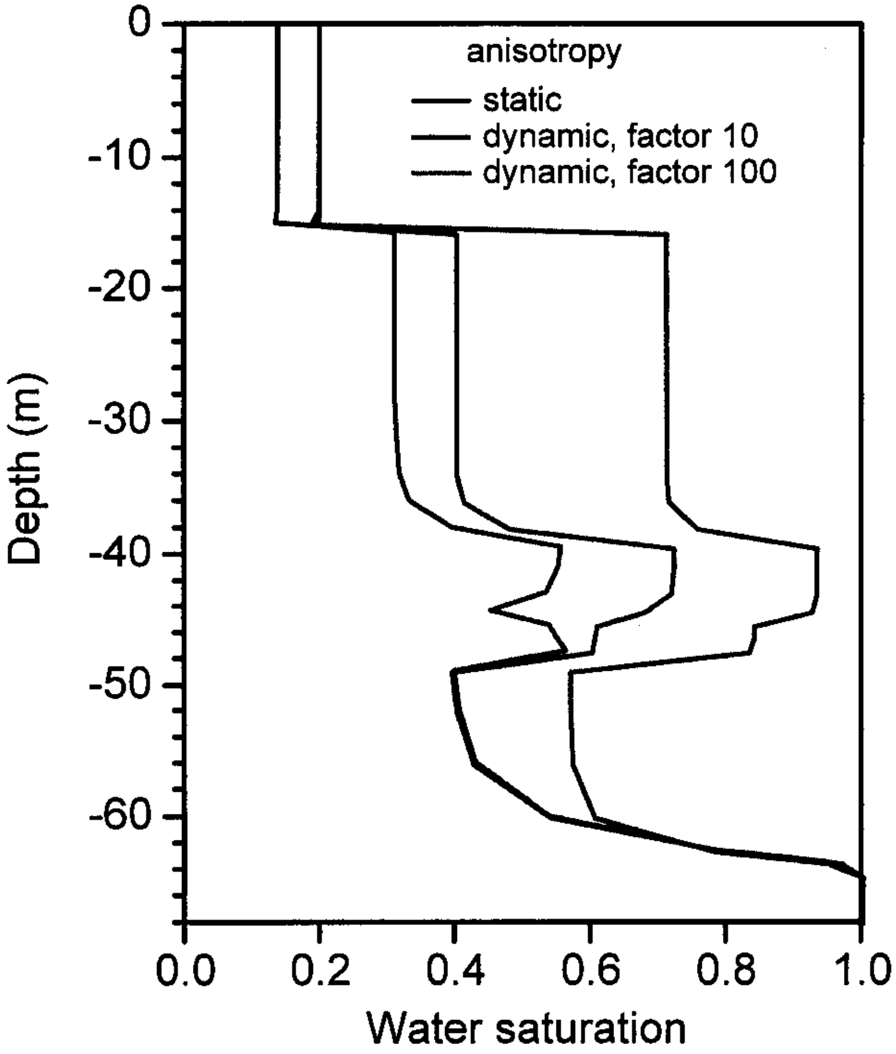

Note: The line labeled "Static" corresponds to the reference case with a tension-independent anisotropy factor of 3 (2 for backfill).

Figure D.7.1.10. Breakthrough Curves of Leaked Fluid Released Beneath the Tank Center on Logarithmic (top) and Linear Scale (bottom).

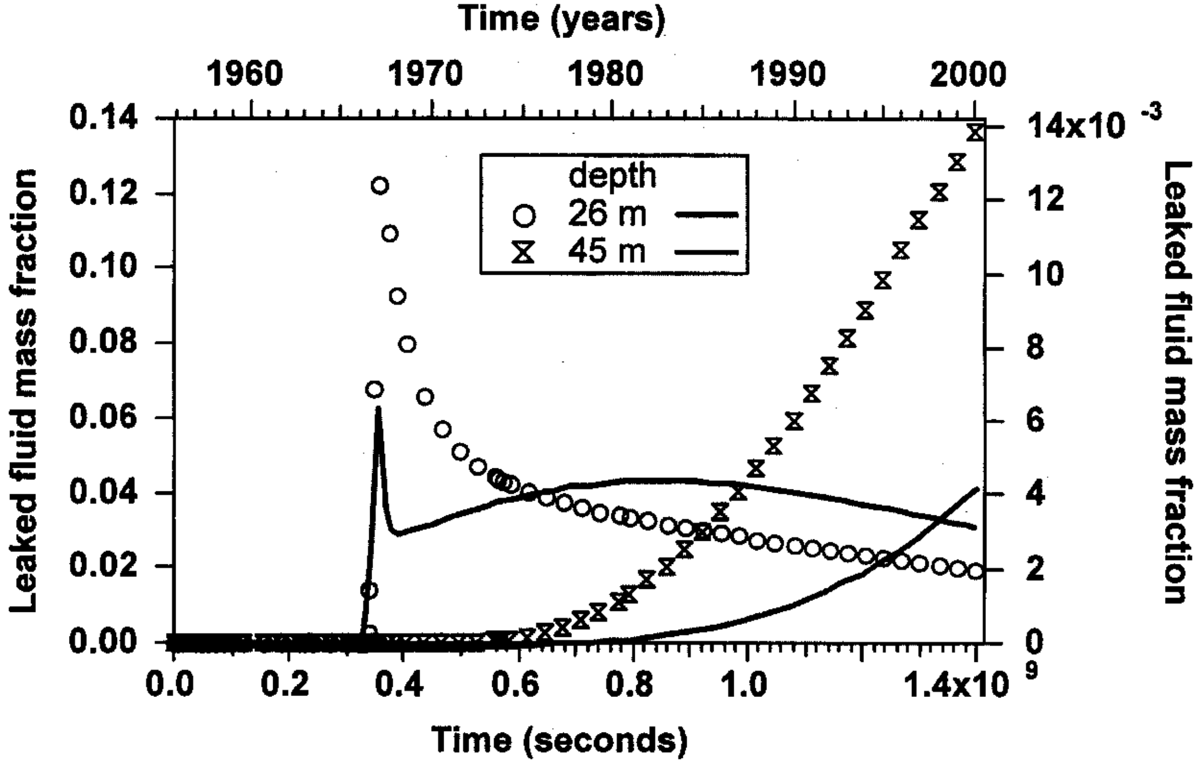

Note: Symbols are for the isothermal reference case, and lines are for the case of "Strong" anisotropy. The data at 26 m depth refer to the left axis, the 45 m data to the right.

D.7.1.5 Conclusions and Implications

Moisture distribution, fluid flow, and solute transport beneath tank SX-108 were strongly affected by tank heat, salinity of leaked fluids, and multiphase processes that include boiling and condensation, partitioning of species among phases, and multiphase flow and transport. A sound assessment of solute behavior must include all of the important physical and chemical processes, and must employ realistic parameters for the different flow and transport processes and for hydrogeologic conditions. In this report we have presented preliminary simulations that have focused primarily on thermo-hydrologic effects, and have adopted a simplified layer-cake stratigraphy. Our simulations show that during the period of above-boiling tank temperatures, the fluid flow and heat transfer regime in the region surrounding the tank is dominated by vapor-liquid counterflow effects. Vapor-liquid counterflow provides a very efficient heat transfer mechanism known as "heat pipe," that rapidly dissipates tank heat over a large volume. The heat pipe system is also very efficient at concentrating dissolved solutes near the heat source, where precipitation of solids occurs as aqueous concentrations in boiling regions exceed solubility limits even for solutes whose initial concentrations in formation waters are small.

Exploratory calculations were performed to study the behavior of tank leaks, and to investigate effects of layering anisotropy. Thermal effects were found to generally retard and reduce downward migration of solutes released from beneath the tank. However, only leaks beneath the center of the tank have been investigated so far. The observed trends may be specific to leak location, and different behavior may be expected for leaks near the tank perimeter. Some of the simulations presented here include a comprehensive treatment of salinity effects on density, viscosity, enthalpy, and vapor pressure of the aqueous phase. These effects were found to partially compensate one another, so that in some cases approximations that neglect most salinity effects may be justified. Salinity effects have so far been modeled by using NaCl as dissolved solid. This was done because for aqueous NaCl the required thermophysical data were available over the entire temperature range of interest. Work is ongoing to develop a thermophysical properties package for $NaNO_3$ solutions, which would provide a better representation of leaked fluids.

A new model was developed to investigate effects of sub-grid scale anisotropy on unsaturated flow and transport in the layered sediments at Hanford. Formation anisotropy was found to be capable of considerably slowing the downward migration of solutes.

Among the issues that remain to be addressed in future work, perhaps the most important ones are (1) comparison with field data on temperatures, moisture content, and solute distributions, and (2) more detailed three-dimensional representation of hydrogeologic conditions at tank SX-108. Additional topics for future work include parameter sensitivities (absolute permeability, characteristic curves, small-scale layering, dependence of thermal conductivity on moisture status, dependence of capillary pressure strength on temperature and salinity), thermal effects of leaked fluid, interference between tanks, and couplings between thermal, hydrologic, and chemical processes. We also plan to explore multi-region effects on solute transport, and to investigate future solute transport behavior under "no action" conditions, as well as for scenarios that involve placing infiltration covers over the tanks, and fluid losses during possible future sluicing operations to remove tank wastes.

D.7.1.6 Acknowledgement

This work was supported, in part, by the U.S. Department of Energy under Contract No. DE-AC03-76SF00098 through Memorandum Purchase Order 248861-A-B2 between Pacific Northwest National Laboratory and Lawrence Berkeley National Laboratory.

D.7.1.7 References

Adamson, A. W., 1990, *Physical Chemistry of Surfaces,* John Wiley & Sons, New York.

Apelblat, A., and E. Korin, 1998, "The Vapour Pressures of Saturated Aqueous Solutions of Sodium Chloride, Sodium Bromide, Sodium Nitrate, Sodium Nitrite, Potassium Iodide, and Rubidium Chloride at Temperatures from 227 K to 323 K," *Journal of Chemical Thermodynamics,* Vol. 30:59-71.

Battistelli, A., C. Calore, and K. Pruess, 1997, "The Simulator TOUGH2/EWASG for Modeling Geothermal Reservoirs with Brines and Non-Condensible Gas," *Geothermics*, Vol. 26: 437-464.

Conway, J. G., R. J. Luxmoore, J. M. Matuszek, and R. O. Patt, 1997, *TWRS Vadose Zone Contamination Issue Expert Panel Status Report,* DOE/RL-RL-49, Rev. 0, U.S. Department of Energy, Richland Operations Office, Richland, Washington.

Doughty, C., and K. Pruess, 1988, "A Semi-Analytical Solution for Heat Pipe Effects Near High Level Nuclear Waste Packages Buried in Partially Saturated Geologic Media," *Int. Journal of Heat and Mass Transfer*, Vol. 31: 79-90.

Eastman, G. Y., 1968, "The Heat Pipe," *Scientific American*, Vol. 218:38-46.

Gee, G. W., M. J. Fayer, M. L. Rockhold, and M. D. Campbell, 1992, "Variations in Recharge at the Hanford Site," *Northwest Science,* Vol. 60:237-250.

Isono, T., 1984, "Density, Viscosity, and Electrolytic Conductivity of Concentrated Aqueous Electrolyte Solutions at Several Temperatures, Alkaline-Earth Chlorides, $LaCl_3$, Na_2SO_4, $NaNO_3$, NaBr, KNO_3, KBr, and $Cd(NO_3)_2$," *Journal of Chemical Engineering Data,* Vol. 29:45-52.

Khaleel, R., and E. J. Freeman, 1995, *Variability and Scaling of Hydraulic Properties for 200 Area Soils, Hanford Site*, WHC-EP-0883, Westinghouse Hanford Company, Richland, Washington.

Khaleel, R., J. F. Relyea, and J. L. Conca, 1995, "Evaluation of van Genuchten - Mualem Relationships to Estimate Unsaturated Hydraulic Conductivity at Low Water Contents," *Water Resources Research,* Vol. 31:2659-2668.

Khaleel, R., and J. F. Relyea, 1997, "Correcting Laboratory-Measured Moisture Retention Data for Gravels," *Water Resources Research,* Vol. 33:1875-1878.

Khaleel, R., T. E. Jones, A. J. Knepp, F. M. Mann, D. A. Myers, P. M. Rogers, R. J. Serne, and M. I. Wood, 2000, *Modeling Data Package for S-SX Field Investigation Report (FIR), River Protection Program,* RPP-6296, Rev. 0, CH2M HILL Hanford Group, Inc., Richland, Washington.

Mahiuddin, S., and K. Ismail, 1996, "Temperature and Concentration Dependence of the Viscosity of Aqueous Sodium Nitrate and Sodium Thiosulphate Electrolytic Systems," *Fluid Phase Equilibrium,* Vol. 123:231-243.

Piepho, M. G., 1999, *SX Tank Farm Vadose Zone Temperature Sensitivity Study*, HNF-4744, Rev. 0, Fluor Daniel Northwest, Inc., Richland, Washington.

Price, W. H., and K. R. Fecht, 1976, *Geology of the 241-SX Tank Farm*, ARH-LD-134, Atlantic Richfield Hanford Company, Richland, Washington.

Pruess, K., C. Oldenburg, and G. Moridis, 1999, *TOUGH2 User's Guide, Version 2.0*, LBNL-43134, Lawrence Berkeley National Laboratory, Berkeley, California.

Richards, L. A., 1931, "Capillary Conduction of Liquids Through Porous Mediums," *Physics*, Vol. 1:318-333.

Rockhold, M. L., 1999, "Parameterizing Flow and Transport Models for Field-Scale Applications in Heterogeneous, Unsaturated Soils," *Assessment of Non-Point Source Pollution in the Vadose Zone,* Geophysical Monograph 108, pp. 243 - 260, American Geophysical Union, Washington, DC.

Smoot, J. L., and A. H. Lu, 1994, "Interpretation and Modeling of a Subsurface Injection Test, 200 East Area, Hanford, Washington," *In-Situ Remediation: Scientific Basis for Current and Future Technologies,* G. W. Gee and N. R. Wing (eds.), Battelle Press, Richland, Washington.

Ward, A. L., G. W. Gee, and M. D. White, 1997, *A Comprehensive Analysis of Contaminant Transport in the Vadose Zone Beneath Tank SX-109*, PNNL-11463, Pacific Northwest National Laboratory, Richland, Washington.

D.7.2 NONISOTHERMAL MULTIPHASE FLUID FLOW AND TRANSPORT: MULTITANK MODELING IN THE SX TANK FARM

Mark D. White[1], Steve B. Yabusaki[1], and Karsten Pruess[2]

[1]Pacific Northwest National Laboratory, Richland, Washington 99352

[2]Lawrence Berkeley National Laboratory, Berkeley, California 94720

D.7.2.1 Introduction

The objective of this numerical investigation was to contribute to the understanding of the thermal and multifluid environment surrounding the single-shell tanks within the WMA S-SX on the Hanford Site, near Richland, Washington. In particular, this investigation considered the thermal and hydrogeologic environment surrounding the westing row of tanks in the center of the WMA S-SX (i.e., tanks SX-107, SX-108 and SX-109) and its effects on the transport of a conservative radionuclide to the WMA border. This row of tanks was selected because tanks SX-108 and SX-109 had histories of high heat loads and elevated temperatures, and tank SX-108 was known to have leaked radionuclides and other contaminants into the subsurface. This study used numerical simulation to investigate the coupled processes of multifluid flow, heat transfer, and solute transport in a heterogeneous geologic environment surrounding the subject row of single-shell tanks. Ancillary investigations of solute transport from the WMA S-SX (White et al. 2001) demonstrated that two-dimensional cross-sectional simulations could be used without introducing significant errors to model the three-dimensional subsurface environment surrounding the single-shell tanks.

Accurate hydrologic modeling of the WMA S-SX requires a comprehensive description of the site hydrogeology, tank thermal and leak histories, hydrologic conditions at the ground surface and water table, and their variability. The hydrogeologic description of the WMA S-SX implemented in this investigation was a modified version of the data package (Khaleel et al. 2000) provided for a complementary study of solute transport under isothermal conditions.

All simulations reported herein were executed with the STOMP simulator (White and Oostrom 2000 a, b), using the Water Operational Mode for isothermal simulations and the Water-Air-Energy Operational Mode for the nonisothermal simulations. All simulations considered the transport of the solute ^{99}Tc from known distributions in the year 2000, as specified in the modeling data package (MDP) (Khaleel et al. 2000). Grid resolutions for all simulations were 0.5334 m (1.75 ft) horizontally and 0.4572 m (1.5 ft) vertically. The isothermal simulations use the assumption of a passive gas phase, where the gas phase is assumed to have a constant pressure of 101325.0 Pa (1 atm). Transport of phase components (i.e., water and air) and solutes are neglected under the passive gas assumption. Gas entrapment by the wetting phase (i.e., aqueous phase) was neglected for both the isothermal and nonisothermal simulations. The nonisothermal simulations use the assumption of an active gas phase; however, ^{99}Tc transport was only considered in the aqueous phase. The numerical modeling of this investigation does not consider chemical interactions with the porous media, nor does it consider heat generated through chemical reaction or radiological decay. The transported solute is assumed to be “infinitely dilute” with respect to altering the properties of the transporting medium. For example the aqueous-phase density was assumed to be dependent on temperature and pressure, but independent of the dissolved-solute concentration. A more comprehensive analysis would consider the heat contribution from radioactive decay, chemical interactions with the porous media, including dissolution and precipitation, which may significantly alter local hydrologic properties and fluid property dependence on solute concentration. The modeling analysis described in this report should be considered preliminary to a more comprehensive representation of the hydrologic flow and transport processes which occurred and continue to proceed in the subsurface environment surrounding the single-shell tanks at the Hanford Site WMAs.

D.7.2.2 Modeling Procedures

The simulations executed for this investigation followed the specifications of the Base Case scenario for the cross-section through tanks SX-107, SX-108, and SX-109 of the modeling data package (Khaleel et al. 2000). This scenario involved simulating flow and transport considering natural infiltration only, with no water line leaks, no tank leaks, no interim surface barrier, a closure barrier by the year 2040, and a uniform distribution of initial solute inventory. For the isothermal simulation aqueous flow was considered and for the nonisothermal simulation, coupled aqueous and gas flow and heat transfer was considered. For both simulations only the transport of the solute ^{99}Tc was investigated. Isothermal simulation results for all case scenarios and solute species described in the MDP (Khaleel et al. 2000) are reported separately (White et al. 2001).

The geology of the subject cross-section was a modified version of the WMA S-SX Cross-Section D-D' reported by Price and Fecht (1976) as specified in the MDP (Khaleel et al. 2000). The Khaleel modifications principally involved combining like soil types, yielding five different strata: (1) backfill, (2) sand, (3) gravelly sand/sandy gravel, (4) Plio-Pleistocene (including caliche), and (5) sandy gravel. Because the dominant geologic feature at the Hanford site is a layered structure of depositional sediments, the soil units are commonly referred to as strata. The geology for the subject cross section is generally layered (see Figure D.7.2.1), except for the sloping layer of material identified as gravelly sand/sandy gravel that extends from just underneath tank SX-107, sloping downward toward the west beneath tanks SX-108 and SX-109. The other anomaly to the layered system is the trench of backfill material near the ground surface, which surrounds the tanks. Not included in this simplified geology is the 2 m of gravel and coarse sand placed on top of the tanks, the layer of compacted material placed beneath the tanks, pinched-off sublayers identified in the original geologic interpretations, and known clastic dikes.

Figure D.7.2.1. Geology for Cross-Section Through Tanks SX-107, SX-108, SX-109.

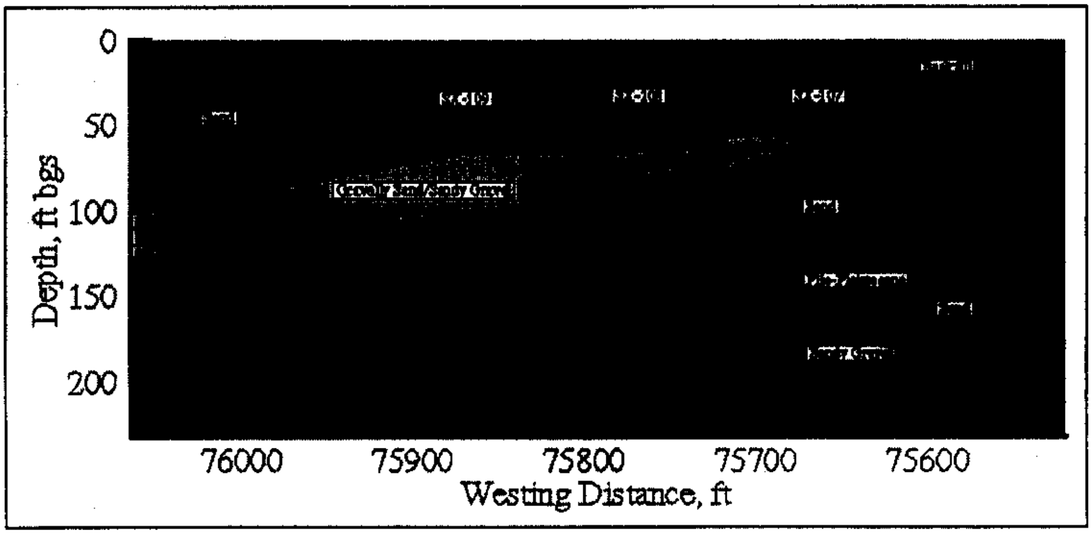

Hydrogeologic properties include functions and/or parameters that define a soil's porosity, intrinsic permeability, tortuosity, bulk density, thermal conductivity, soil-moisture retention characteristics, and phase relative permeability. Hydrogeologic properties for the isothermal and nonisothermal simulations were obtained from the MDP (Khaleel et al. 2000), except for the aqueous- and gas-phase relative permeability functions, which were changed from the Mualem porosity distribution function (Mualem 1976) with Polmann anisotropy (Polmann 1990) to the Corey function (Corey 1954). The Corey aqueous- and gas-phase relative permeability functions are defined according to Equations D.7.2.1 and D.7.2.2, respectively

$$k_{r\ell} = (\bar{s}_\ell)^4 \qquad \text{(D.7.2.1)}$$

$$k_{rg} = (1-\bar{s}_\ell)^2\left(1-(\bar{s}_\ell)^2\right) \qquad \text{(D.7.2.2)}$$

where $k_{r\ell}$ is the aqueous-phase relative permeability, k_{rg} is the gas-phase relative permeability, and $\bar{s}_\ell$ is the effective aqueous saturation. The hydrogeologic properties for each of the five defined soil types are summarized in Table D.7.2.1.

Table D.7.2.1. Hydrogeologic Properties.

Soil/Property	Backfill	Sand	Gravelly Sand	Plio-Pleistocene	Sandy Gravel
Porosity	0.138	0.382	0.213	0.435	0.138
Residual saturation	0.0725	0.116	0.0151	0.153	0.0725
Saturation function	van Genuchten [1980]	van Genuchten [1980]	van Genuchten [1980]	van Genuchten [1980]	van Genuchten [1980]
van Genuchten α, 1/cm	0.021	0.0117	0.0141	0.0085	0.021
van Genuchten	1.3740	1.6162	1.3730	1.8512	1.3740
Vertical hydraulic conductivity, cm/s	5.60×10^{-4}	9.88×10^{-5}	2.62×10^{-4}	2.40×10^{-4}	5.60×10^{-4}
Horizontal hydraulic conductivity, cm/s	5.60×10^{-3}	9.88×10^{-4}	2.62×10^{-3}	2.40×10^{-3}	5.60×10^{-3}
Particle density, kg/m^3	2650.	2650.	2650.	2650.	2650.
Dry thermal conductivity, W/m K	0.25	0.25	0.25	0.25	0.25
Wet thermal conductivity, W/m K	2.0	2.0	2.0	2.0	2.0
Thermal conductivity model	Somerton et al. [1973]	Somerton et al. [1973]	Somerton et al. [1973]	Somerton et al. [1973]	Somerton et al. [1973]
Particle specific heat, J/kg K	750.	750.	750.	750.	750.
Longitudinal dispersivity, cm	150	150	100	50	150
Transverse dispersivity, cm	15	15	10	5	15
Tortuosity model	Millington and Quirk [1961]	Millington and Quirk [1961]	Millington and Quirk [1961]	Millington and Quirk [1961]	Millington and Quirk [1961]

Boundary conditions for the isothermal and nonisothermal simulations ignored the temporal fluctuations in meteoric recharge, atmospheric relative humidity, ground-surface temperature, water table elevation and cross-flow gradient, and aquifer temperature. Changes in meteoric recharge were considered for changes in surface barriers. Heat generation in tanks SX-108 and SX-109 were modeled by specifying tank surface temperatures as a function of time.

The boiling temperature of the subject tanks has been estimated as 112 °C(a), whereas sludge temperatures at the bottom of the tank have been measured in excess of 140 °C. With these guidelines, tank surface temperatures assignments were binned into two categories: (1) tank vertical walls and top and (2) tank bottom. Tank vertical wall and top surfaces were assigned a temperature equal to the minimum of 112 °C and the reported tank temperature history (Agnew and Corbin 1998). Tank bottom surfaces were assigned a temperature equal to those reported for the tank. S and SX tank farms were covered with gravel and coarse sands to prevent vegetative growth and provide radiation shielding. Bare gravel, however, significantly reduces the amount of meteoric moisture that is returned to the atmosphere through evaporation and plant transpiration. Drainage from bare sands has been estimated at 70 mm/yr under Hanford climatic conditions (Ward et al. 1997). No direct measurements have been made for tank-farm gravels; however, earlier studies have suggested recharge rates of 130 mm/yr for gravel-covered waste sites (Gee et al. 1992). Meteoric recharge for these investigations was assumed to follow the values shown in Table D.7.2.2. The ground-surface temperature and relative humidity were held at 12.8 °C and 30%. The 30% relative humidity condition was used to reflect Hanford climatic conditions. The bottom of the computational domain (71.32 m-bgs) was modeled as a no flux boundary for aqueous- and gas-phase flow with a held temperature of 17.26 °C. The lowest 5.944 m on the vertical sides of the domain were modeled as constant aqueous pressure conditions, where a hydrostatic variation in pressure was used vertically. These boundary conditions created a water table at 65.46 m-bgs on the left side and 65.68 m-bgs on the right side resulting in a cross-flow hydraulic gradient of 1.3×10^{-3}. Temperatures on these sections of vertical boundaries were held at 17.26 °C.

(a) Tom Jones, U.S. Department of Energy, Richland, Washington (private communications).

Table D.7.2.2. Recharge Boundary Condition.

Condition	Recharge (mm/yr)
No Barrier [1955.82-2010]	100.
Interim Barrier [2010-2040]	0.5
Closure Barrier [2040-2540]	0.1
Degraded Barrier [2540-3000]	3.5

Time dependent boundary conditions for the tank SX-108 and SX-109 surfaces are shown in Figure D.7.2.2. The surfaces of tank SX-107 were treated as impermeable to aqueous and gas flow and adiabatic to heat transfer. The adiabatic thermal boundary condition ignores material inside the tank and heat transfer across the tank surfaces. This approach yields unlikely temperature contours around tank SX-107, which could be corrected if additional information about the temperatures inside the tank or content histories were incorporated into the simulation.

Figure D.7.2.2. Temperature Histories for Tanks SX-108 and SX-109.

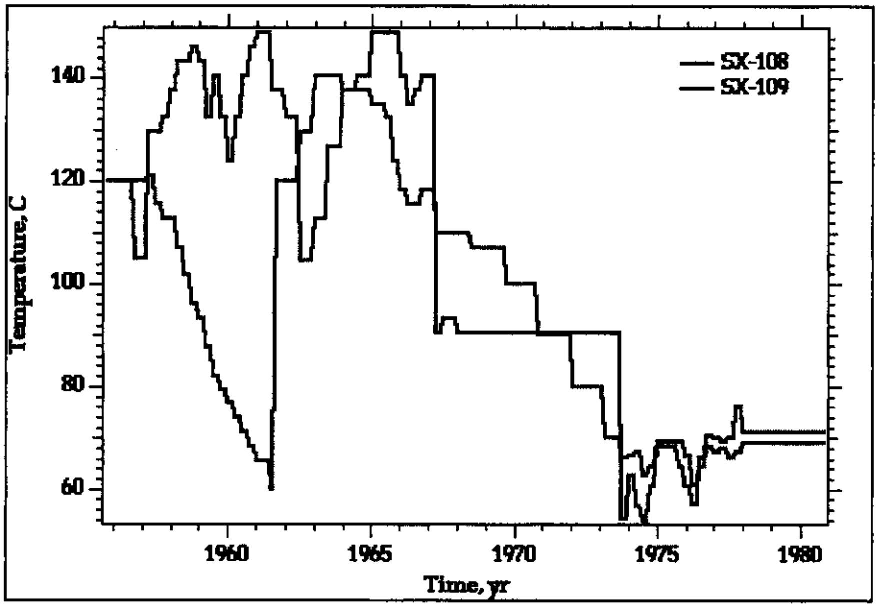

D.7.2.3 Results

D.7.2.3.1 Historical Thermal Regime. The thermal response of the hydrogeologic environmental surrounding tanks SX-107, SX-108 and SX-109, as predicted by the numerical simulation, is shown as a series of color-scaled contour plots for specified times in Figures D.7.2.3 through D.7.2.13. The hydrologic response is shown as a series of color-scaled contour plots of saturation differential in Figures D.7.2.14 through D.7.2.24. For these figures saturation differential refers to the change in saturation from the initial steady-flow condition. The thermal response begins as a linear gradient in temperature from the water table at 17.2 °C to the ground surface at 12.8 °C. From this point, starting at 1955.82, the surface temperatures of tanks SX-108 and SX-109 rise above ambient conditions as they are used for storage of heat-generating liquid waste, where the surface temperatures followed the histories shown if Figure D.7.2.5. After 0.1 years, the soil immediately surrounding the heated tanks begins to increase in temperature (Figure D.7.2.3) reaching a maximum temperature of 103.3 °C. After 0.5 years, the temperature beneath the heated tanks increases to 106.5 °C (Figure D.7.2.4) and dryout of the soils at this point begins to occur (Figure D.7.2.15). The maximum change in saturation is a decrease of 0.24. Water displacement occurs by evaporation, migration and recondensation of water vapor through the gas phase. Because of its higher permeability, water vapor transport away from the heated tanks generally occurs along the sloped gravely sand layer, yielding higher water saturations in this strata. This progression of increasing temperature and soil dryout continues to 2 years (Figures D.7.2.5 to D.7.2.8 and D.7.2.16 to D.7.2.17).

Figure D.7.2.3. Temperature Profile at 1955.92 (+0.1 yr).

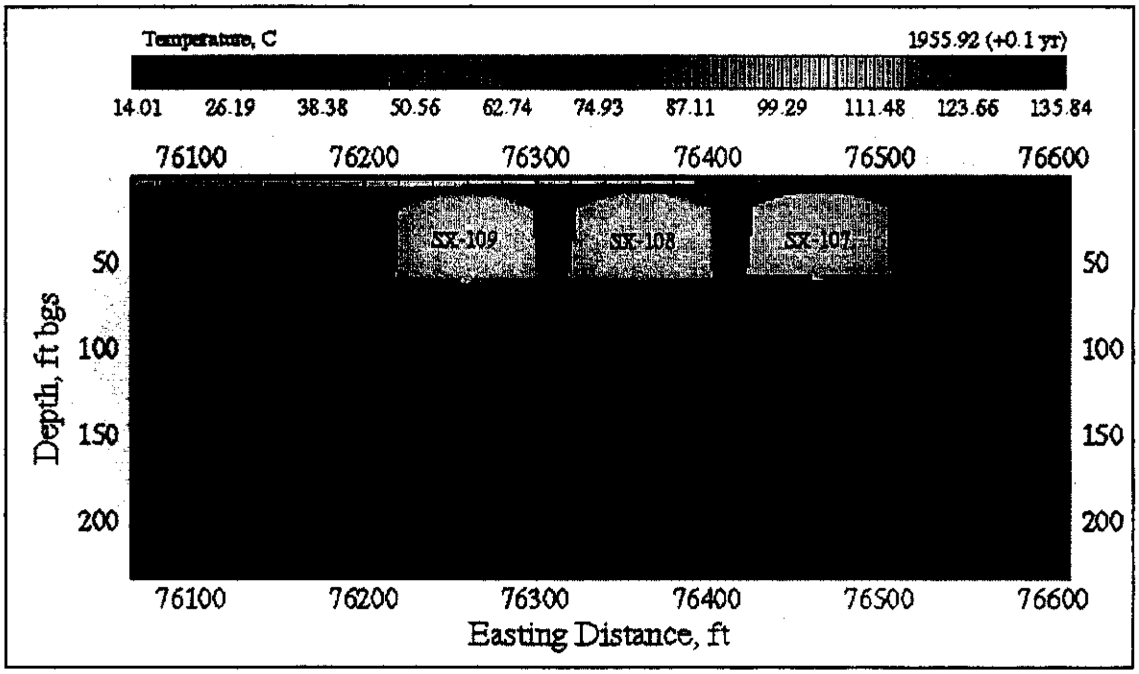

Figure D.7.2.4. Temperature Profile at 1956.32 (+0.5 yr).

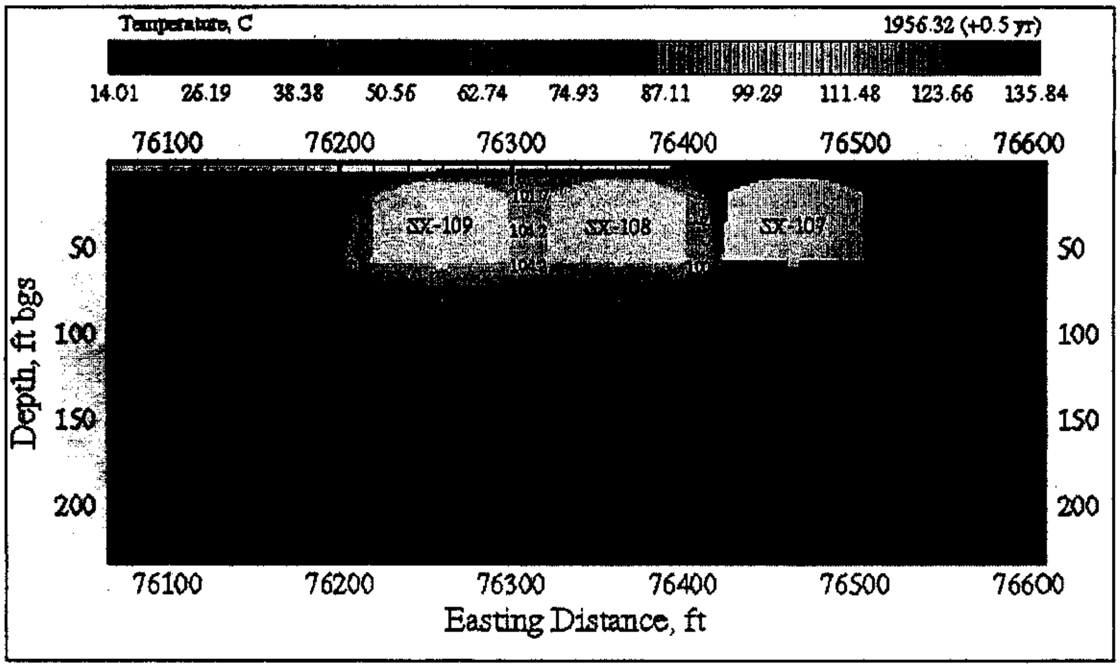

Figure D.7.2.5. Temperature Profile at 1956.82 (+1 yr).

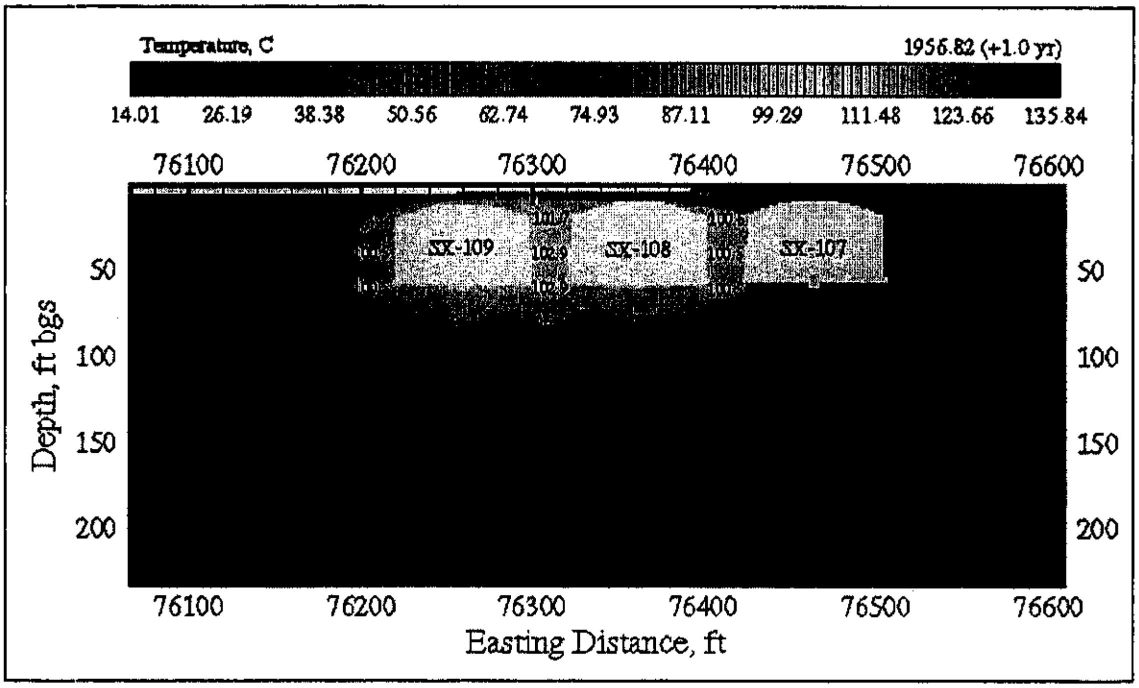

Figure D.7.2.6. Temperature Profile at 1957.82 (+2 yr).

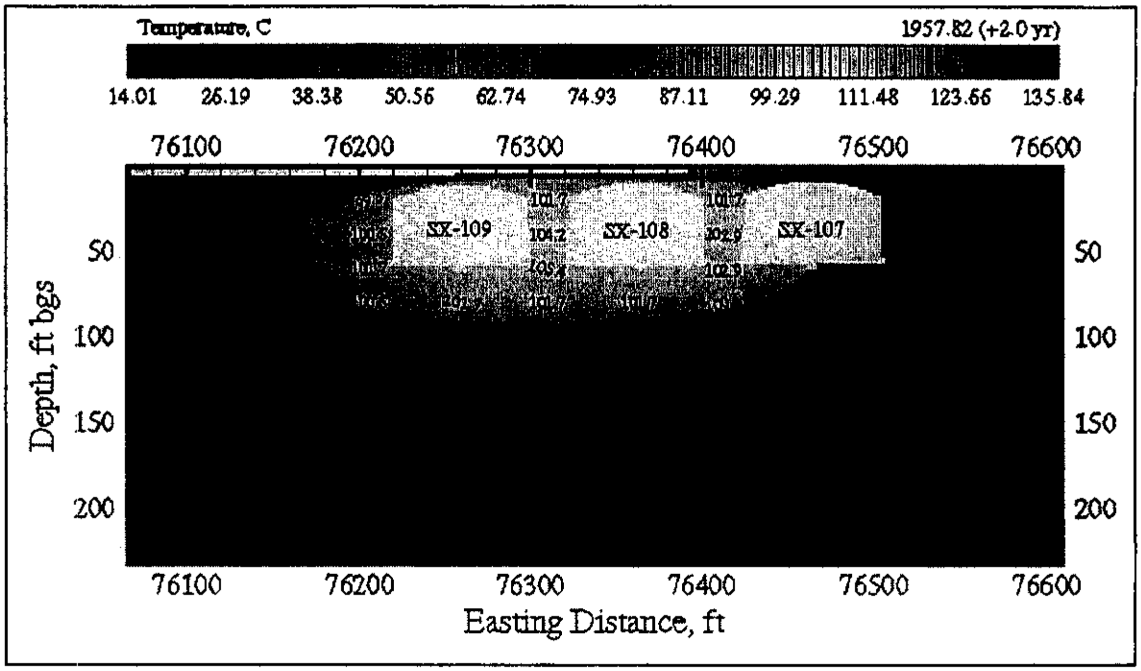

Figure D.7.2.7. Temperature Profile at 1960.82 (+5 yr).

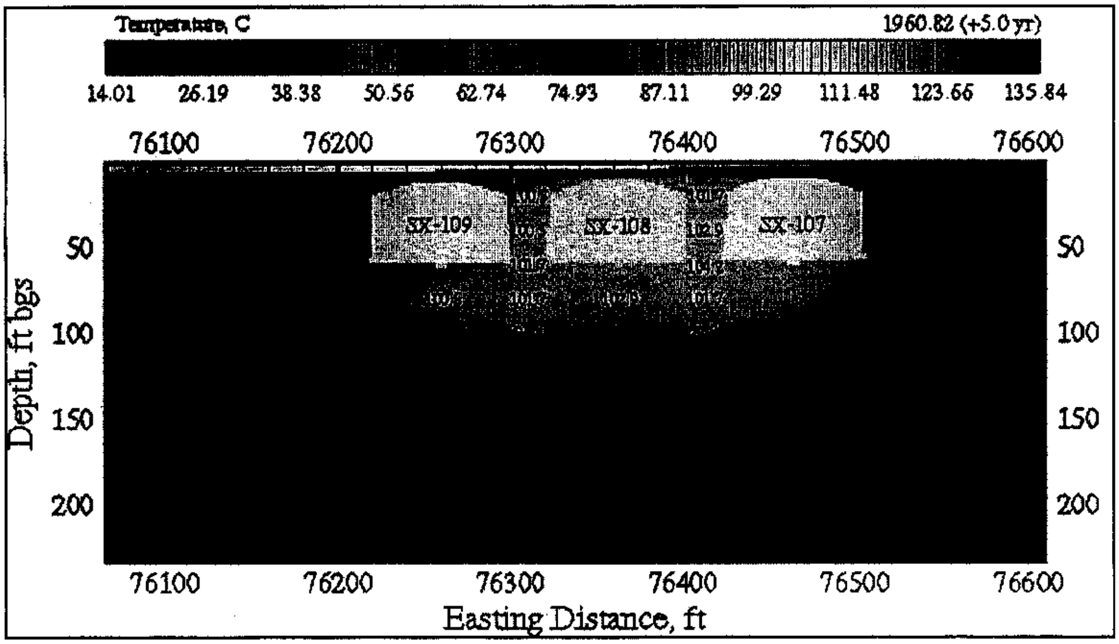

Figure D.7.2.8. Temperature Profile at 1965.82 (+10 yr).

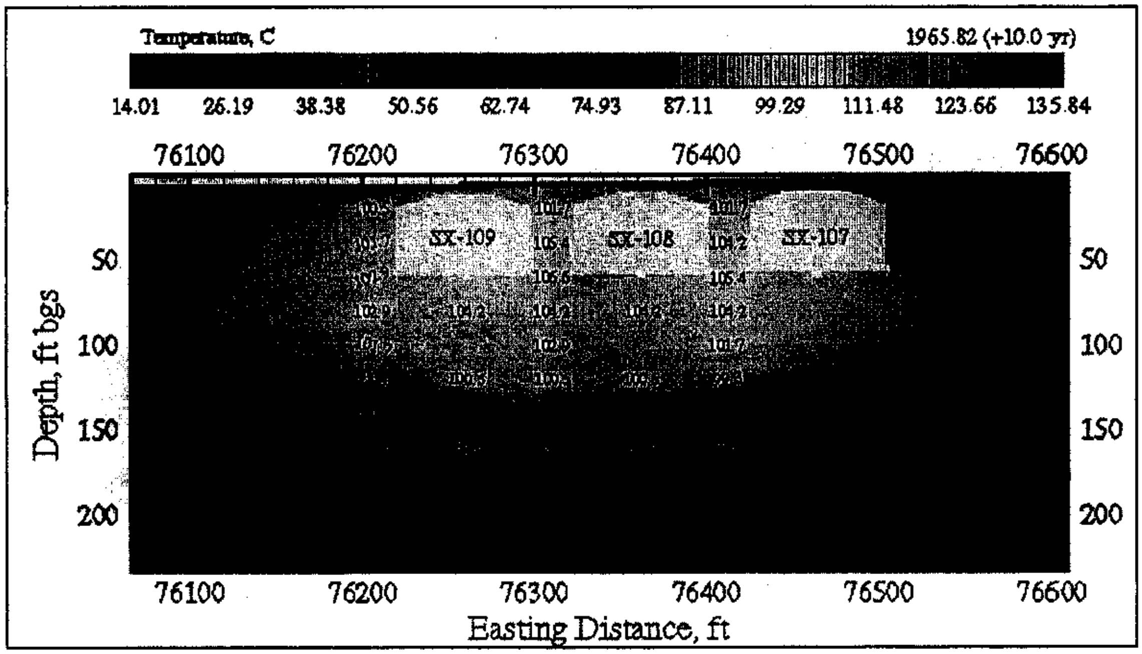

Figure D.7.2.9. Temperature Profile at 1970.82 (+15 yr).

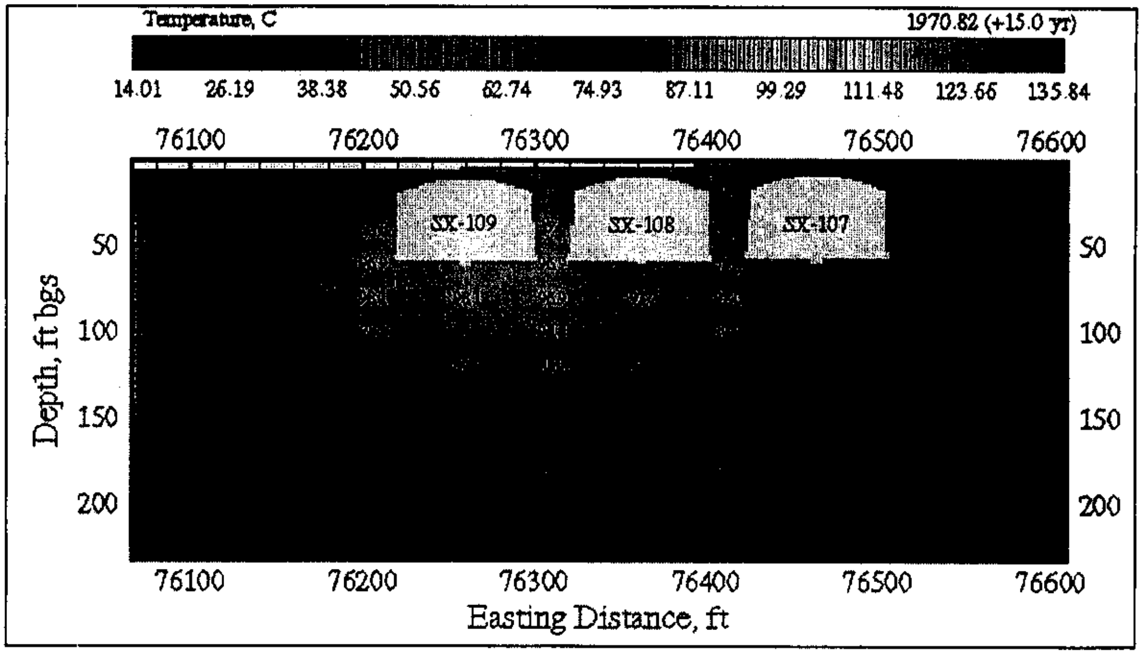

Figure D.7.2.10. Temperature Profile at 1975.82 (+20 yr).

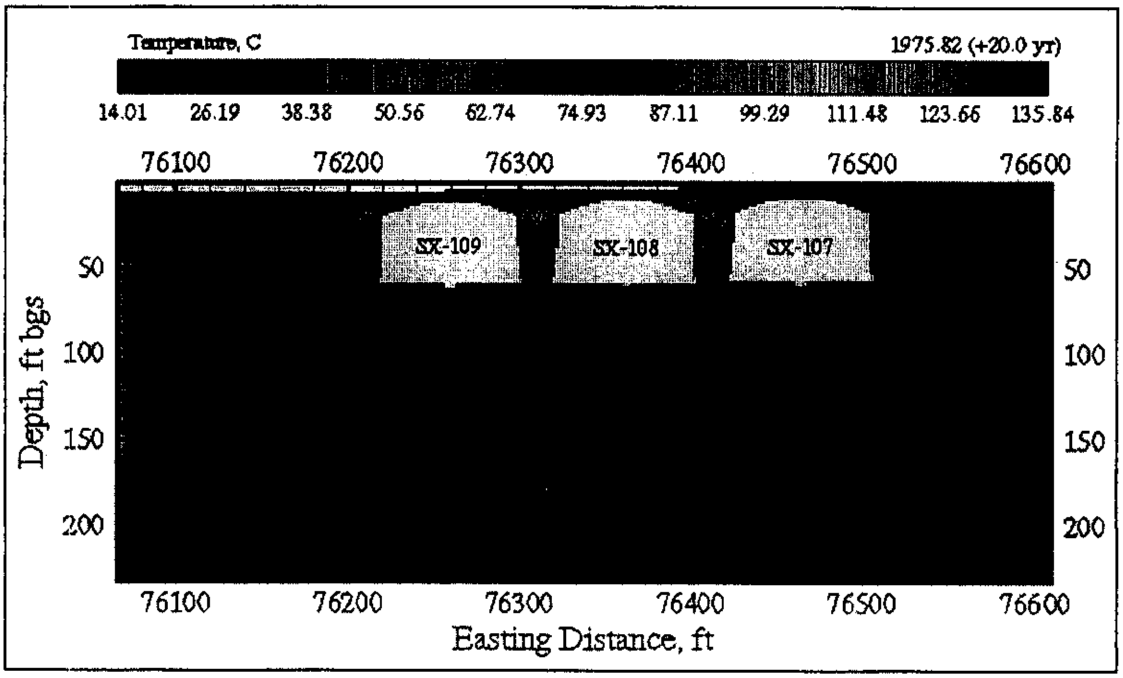

Figure D.7.2.11. Temperature Profile at 1980.82 (+25 yr).

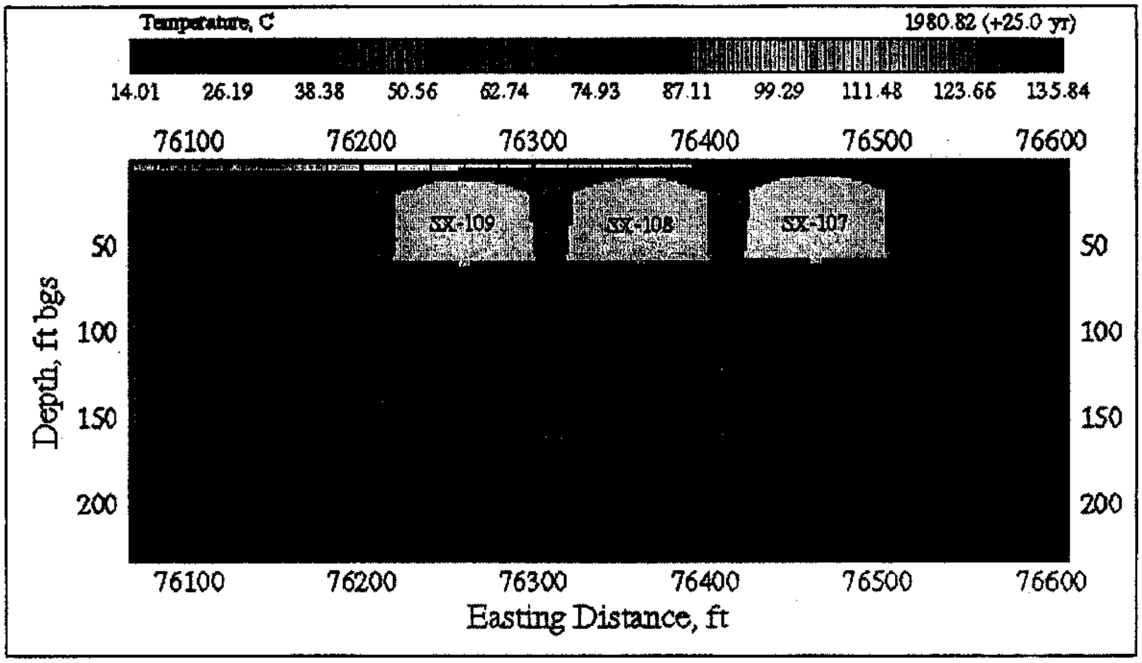

Figure D.7.2.12. Temperature Profile at 1990.82 (+35 yr).

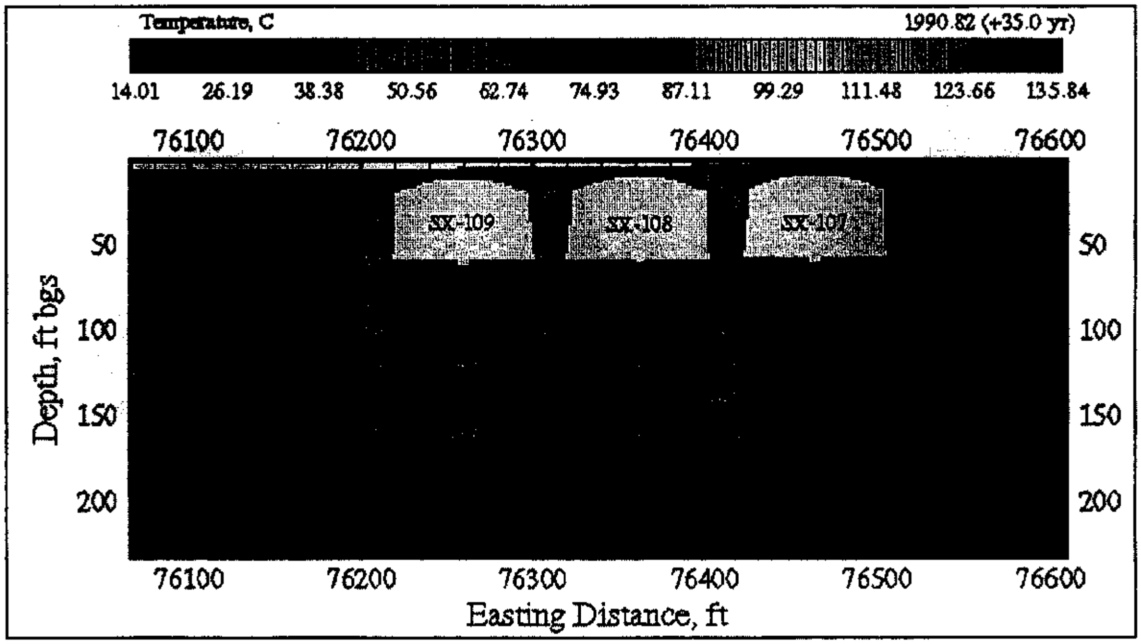

Figure D.7.2.13. Temperature Profile at 2000 (+45 yr).

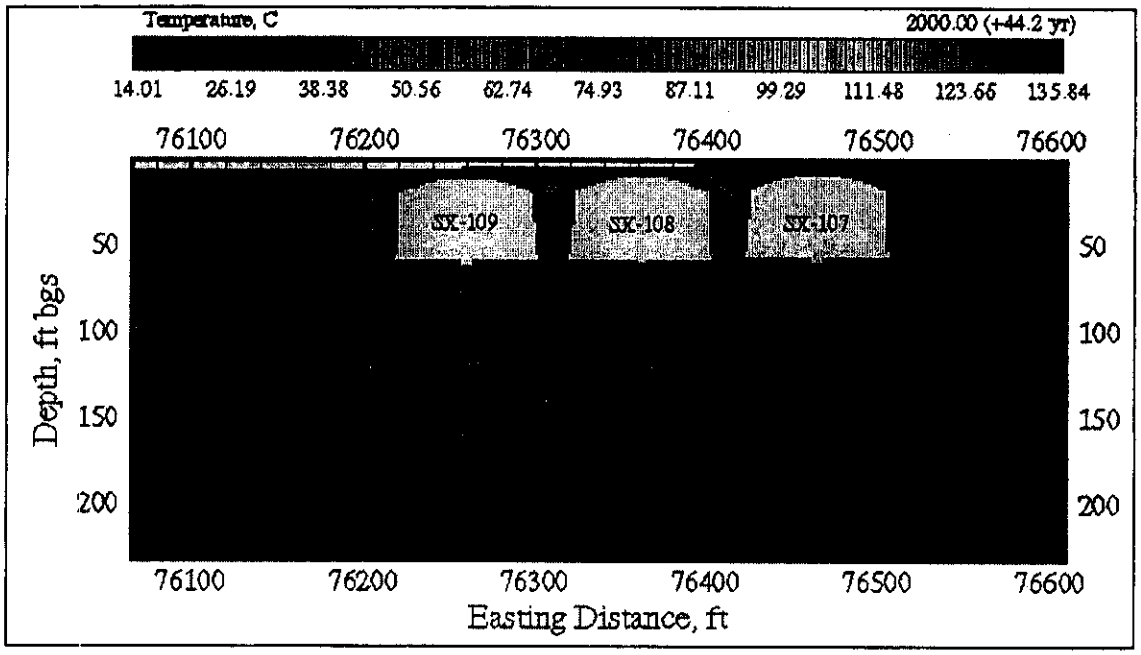

Figure D.7.2.14. Saturation Differential Profile at 1955.92 (+0.1 yr).

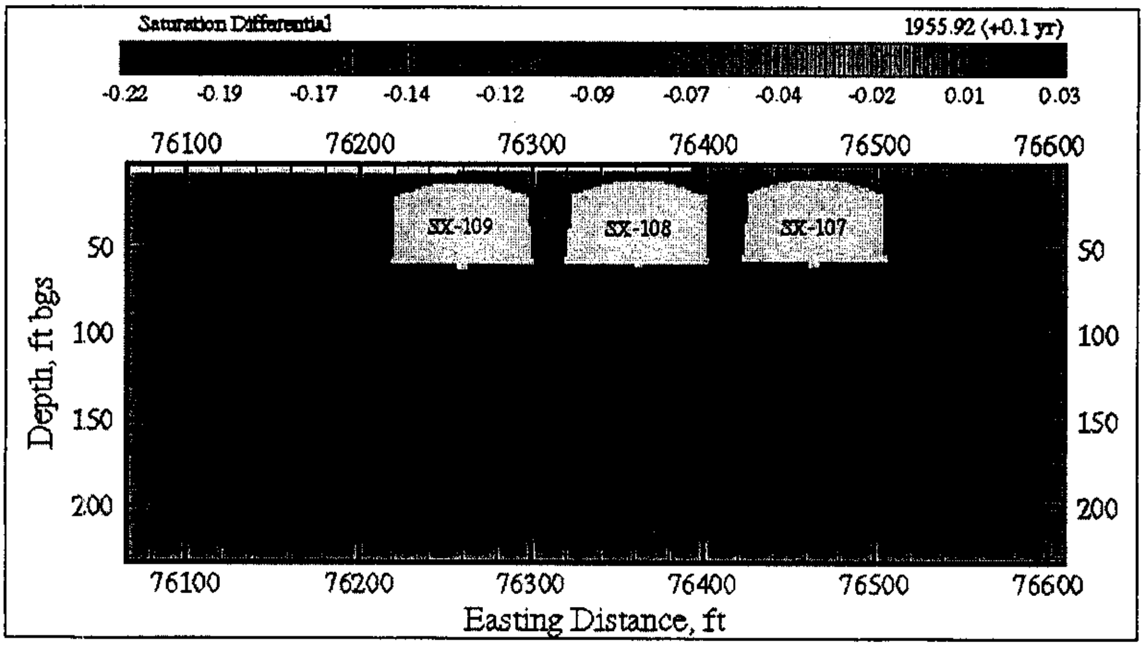

Figure D.7.2.15. Saturation Differential Profile at 1956.32 (+0.5 yr).

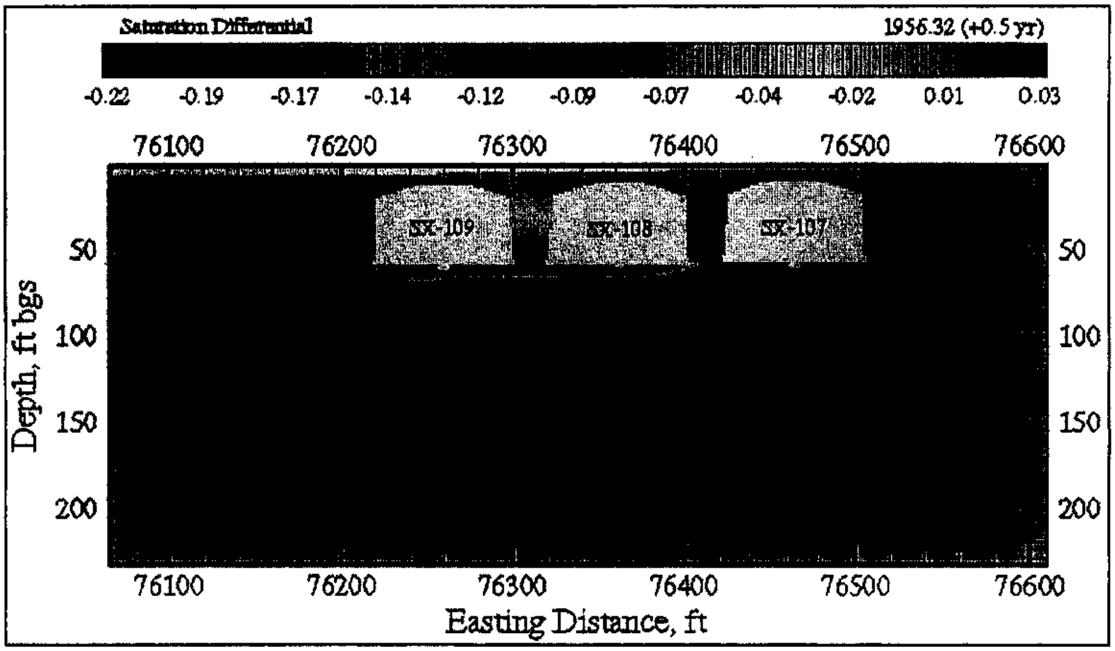

Figure D.7.2.16. Saturation Differential Profile at 1956.82 (+1 yr).

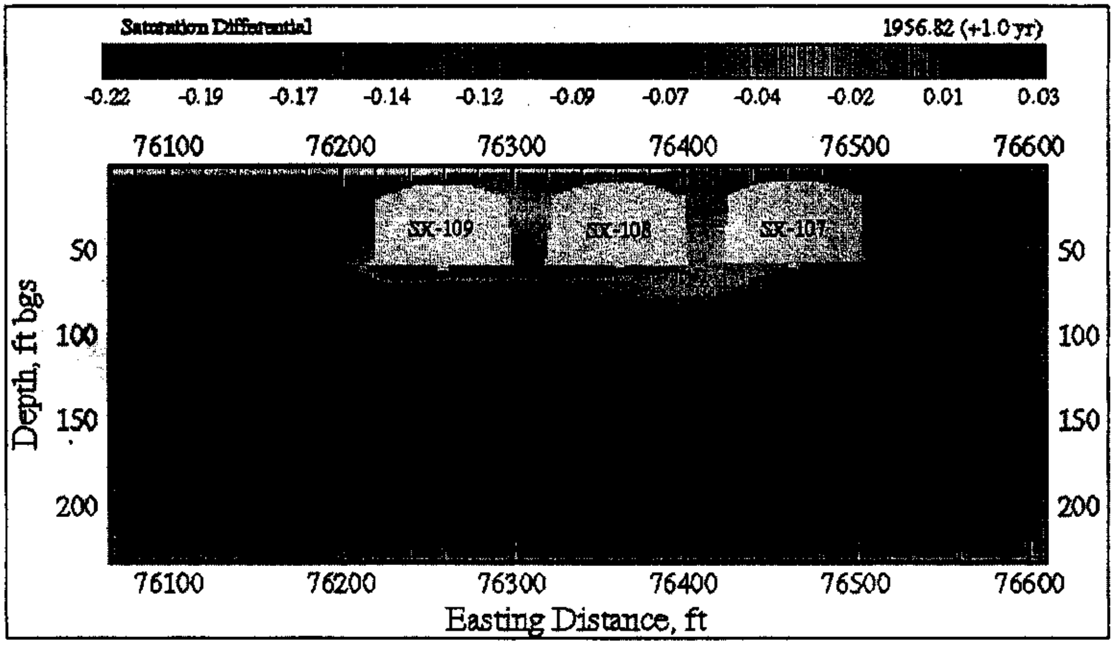

Figure D.7.2.17. Saturation Differential Profile at 1957.82 (+2 yr).

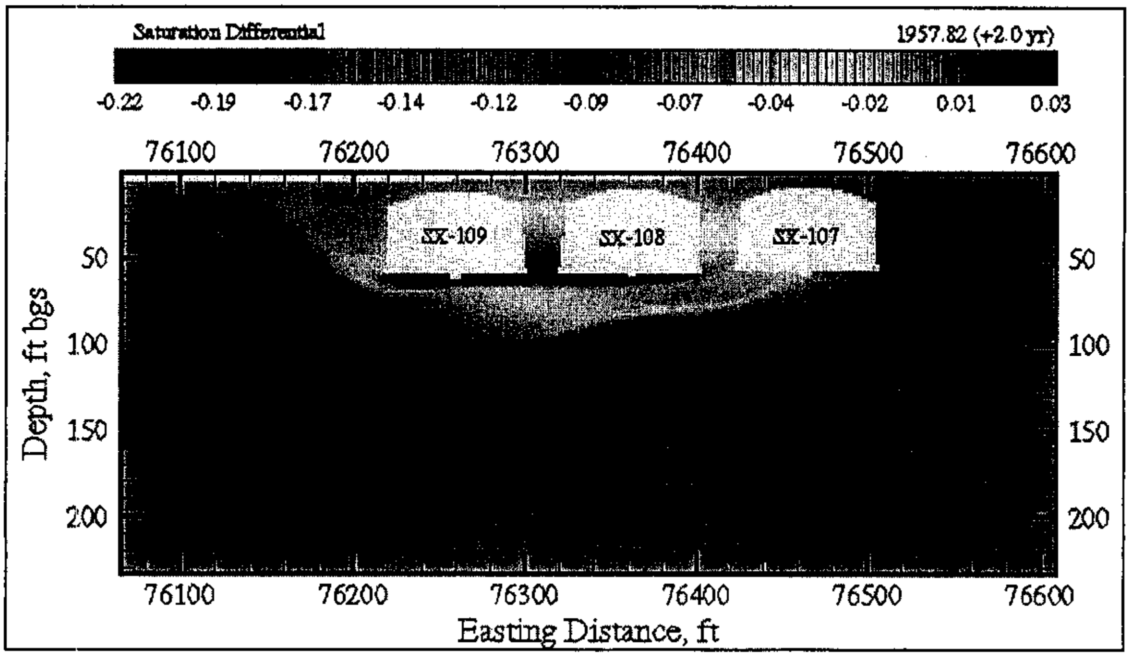

Figure D.7.2.18. Saturation Differential Profile at 1960.82 (+5 yr).

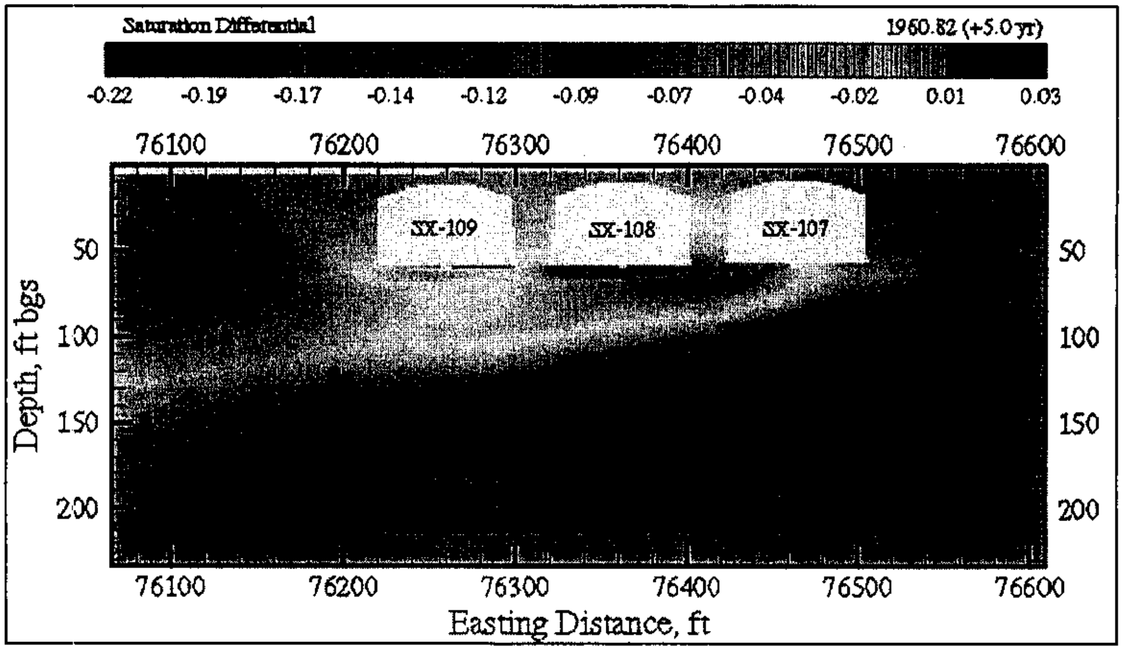

Figure D.7.2.19. Saturation Differential Profile at 1965.82 (+10 yr).

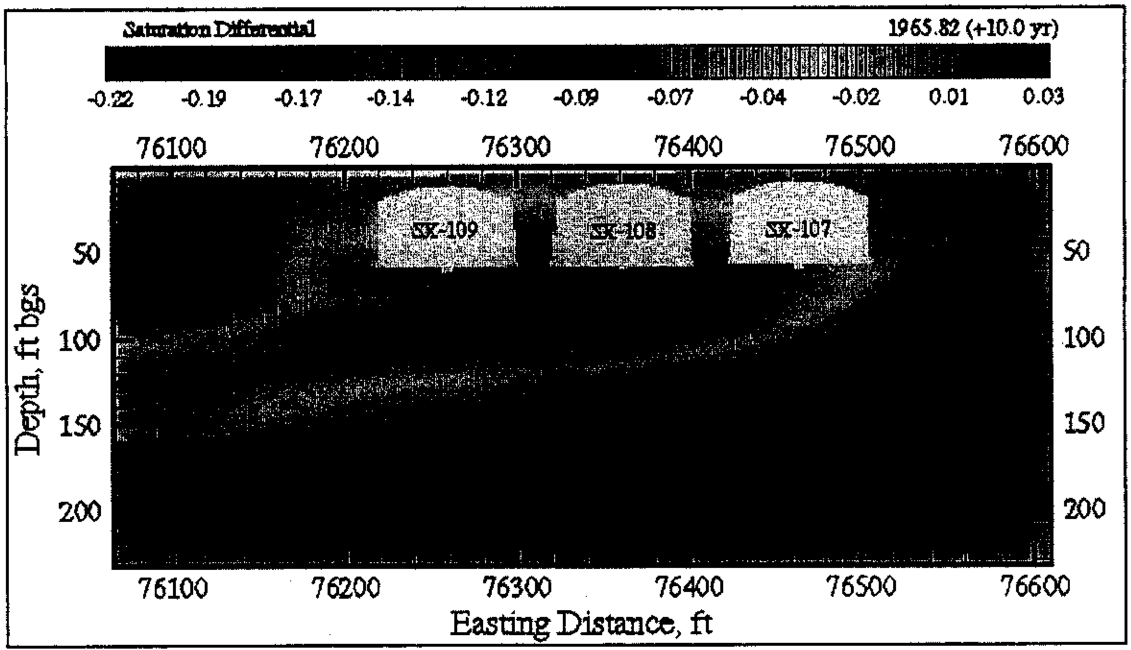

Figure D.7.2.20. Saturation Differential Profile at 1970.82 (+15 yr).

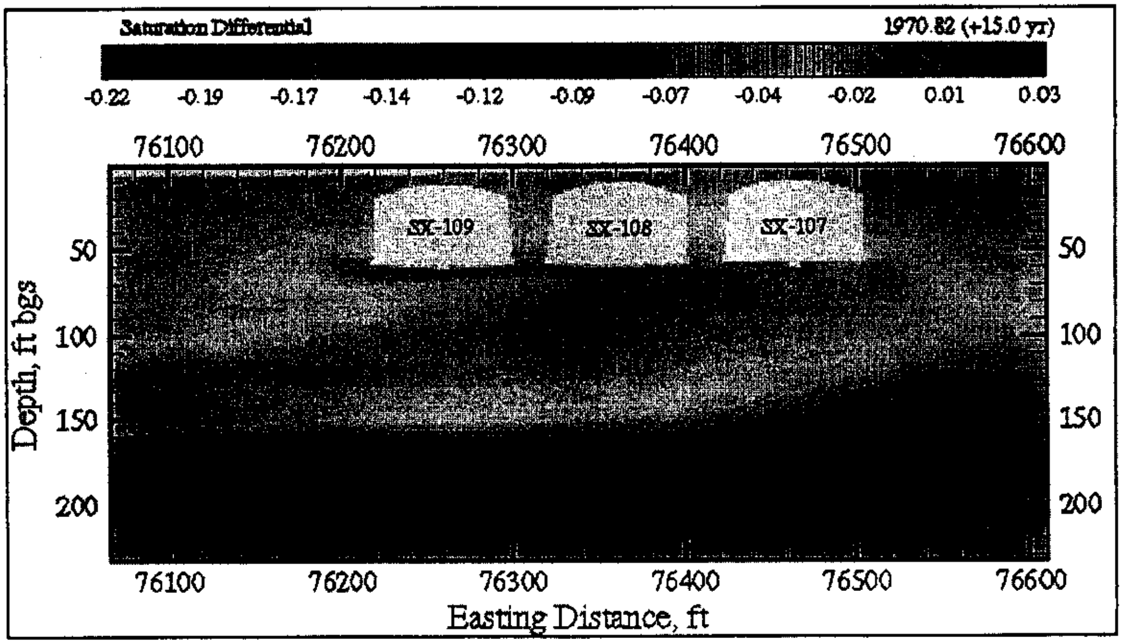

Figure D.7.2.21. Saturation Differential Profile at 1975.82 (+20 yr).

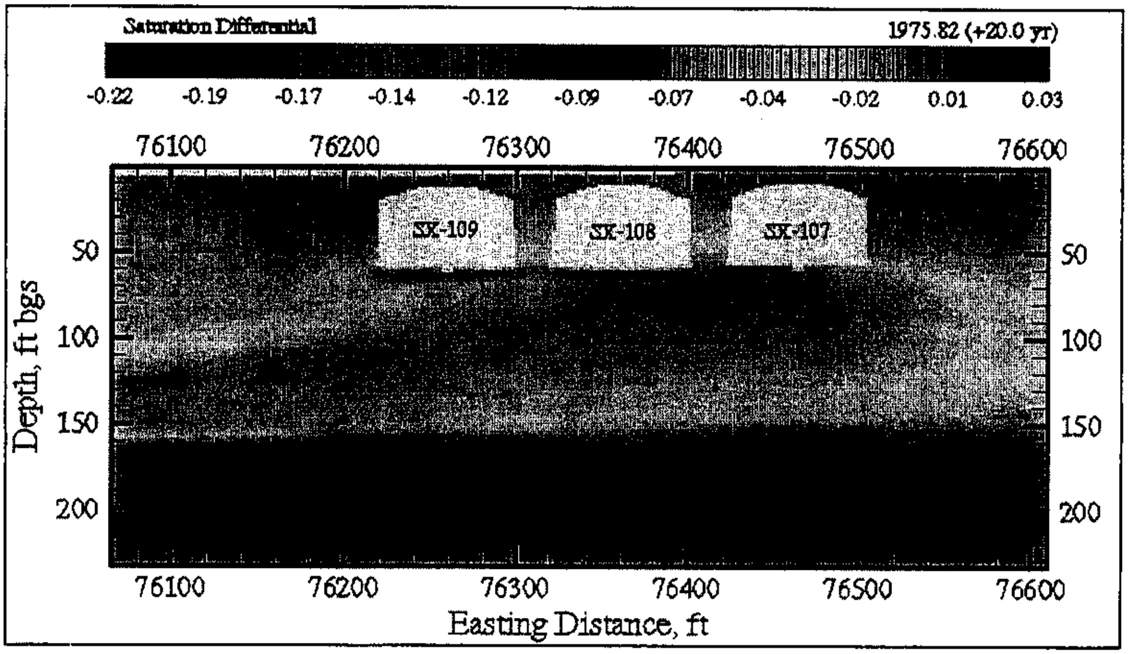

Figure D.7.2.22. Saturation Differential Profile at 1980.82 (+25 yr).

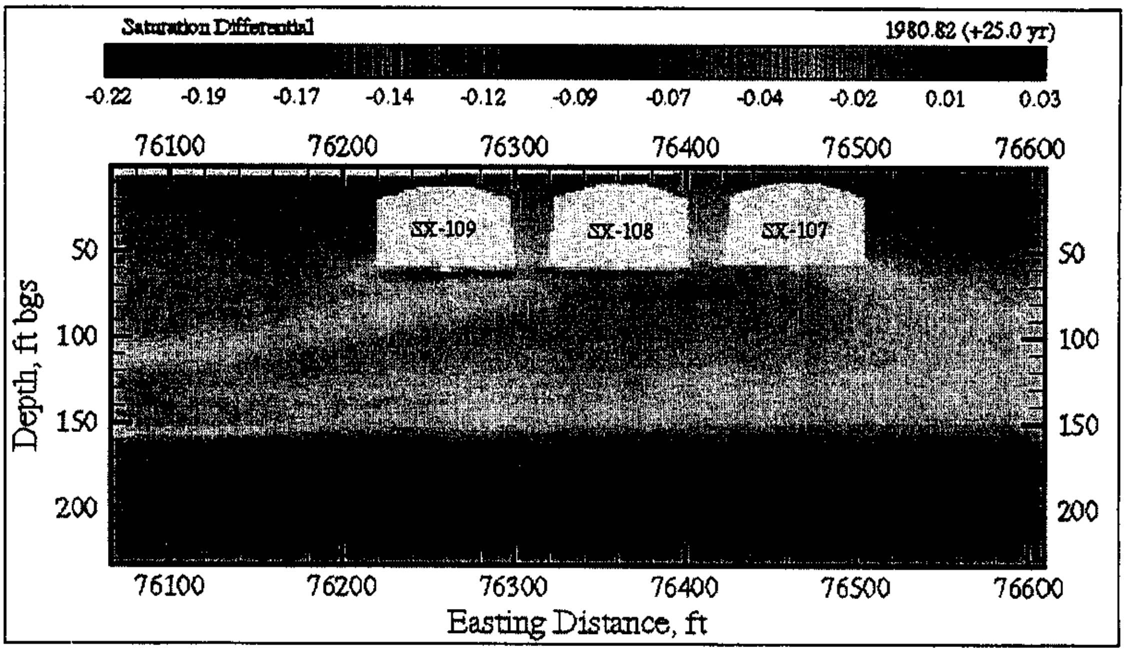

Figure D.7.2.23. Saturation Differential Profile at 1990.82 (+35 yr).

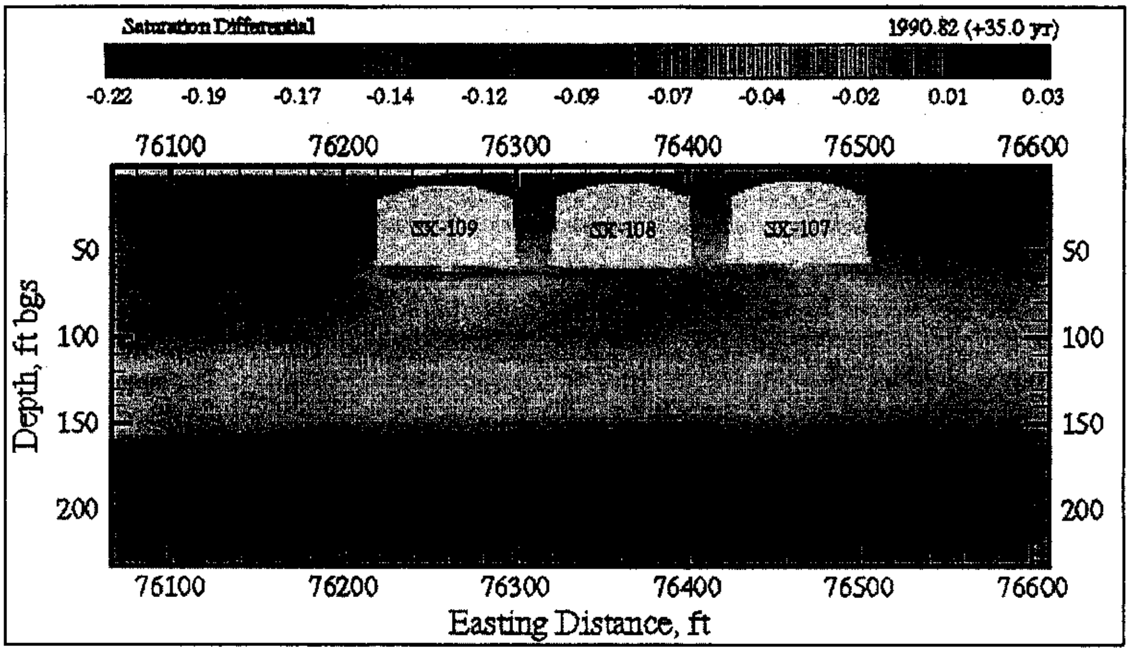

Figure D.7.2.24. Saturation Differential Profile at 2000 (+45 yr).

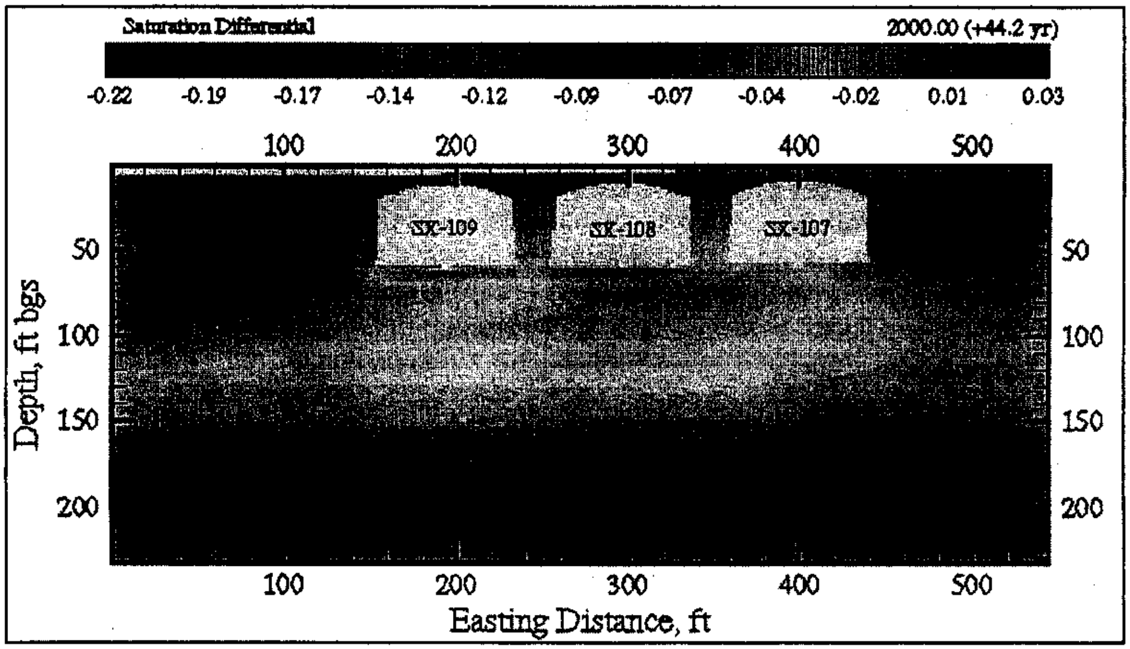

Between mid 1957 and 1961 the surface temperature of tank SX-109 drops linearly from 121 to 60 °C. This temperature drop results in a shift of the thermal environment and soil moisture (Figures D.7.2.6 to D.7.2.7 and D.7.2.17 to D.7.2.18). Most notable is the resaturation of the zone immediately beneath tank SX-109, which occurs via transport of liquid water back to the region under the capillary gradient created during the dryout period. Between 1961 and 1963 the surface temperature of tank SX-109 increases to 140.6 °C, whereas tank SX-108 falls to 104.4 °C. The temperature and saturation differential profiles (Figures D.7.2.8 and D.7.2.19, respectively) in late 1965 show the rapid dryout beneath tank SX-109 with migration of water toward the west. Resaturation occurs beneath tank SX-108 even though the tank surface temperature remains above the atmospheric boiling point (100 °C). After 1963, the surface temperature of tank SX-109 gradually decreases over a period of 10 years to a level that fluctuates between 60 and 70 °C. Tank SX-108 remains at elevated temperatures until 1967 when it drops sharply to 90 °C and then sharply again to below 60 °C near the end of 1973. In the period between late 1962 and late 1968, the sustained tank surface temperatures above 100 °C create a large dryout region and constant temperature region beneath the tanks (Figures D.7.2.19 to D.7.2.20 and D.7.2.8 to D.7.2.9, respectively). In late 1965, the 100 °C temperature region extends to a point roughly 75 ft below the bottom of the tanks. Saturation decreases during this period are greatest within the sloping gravely-sand strata and saturation increases from displaced moisture can be seen deep in the vadose zone.

The 100 °C temperature region that forms beneath and between the tanks comprises three zones of heat transport. In the zone nearest the tank surfaces, soil temperatures rise toward the tanks from 100 °C to the time-dependent tank surface temperature. Soil moisture in this region exists below the residual saturation and strong capillary pressures produce a reduction in the water vapor pressure. Heat transfer in this zone occurs primarily by conduction through the dried-out soil. The second zone is the constant temperature zone, which occurs beyond the dry-conduction zone nearest the tanks. Heat transfer in this region is dominated by counter-current flow of water vapor away from the tanks and liquid water toward the tanks, commonly referred to as the "heat-pipe" effect. Unlike conventional heat pipes, however, heat-pipe type flow regions in geologic media are dynamic, expanding and contracting according to the heat flux, moisture-retention characteristics of the soils, thermal conductivity of the soils, driving temperatures, and hydrologic conditions. A small transition region occurs between the dry-conduction and constant-temperature zones, which contains both conduction and heat-pipe modes of heat transfer. Evaporation of the counter-flow liquid water occurs primarily in this small region. The third heat-transfer zone occurs at the low-temperature perimeter of the constant-temperature zone. Heat transfer in this zone primarily is by conduction through soils of elevated saturation. A small transition region also occurs between the constant-temperature zone and this wet-conduction zone. Condensation of the counter-flow water vapor occurs in this small region.

In the time period between 1968 and 1978 the tank surface temperatures decay to levels between 60 and 70 °C, and after 1978 tank surface temperatures were maintained at 71.1 and 68.9 °C, respectively, for tanks SX-108 and SX-109. During this period, the thermal field and hydrologic conditions beneath the tanks transition from being dominated by heat-pipe type heat transport and counter-current flow to combined conduction/heat-pipe heat transport with weaker counter-current flow (Figures D.7.2.11 through D.7.2.13 and D.7.2.22 through D.7.2.24). With steady tank-surface temperatures and surface recharge the thermal and hydrologic fields approach steady-flow conditions that differ from the hydrologic field under the isothermal assumption. The tank-surface temperatures of 70 °C produce drier soils that extend deep in the vadose zone. Under steady-flow conditions the thermal and hydrologic fields are controlled by the rate of surface recharge, temperature of the meteoric water, tank-surface temperature, and the unconfined aquifer temperature.

The ground surface was assumed to be maintained at 12.7 °C and 30% relative humidity. Under these conditions steep temperature gradients form between the tank domes and ground surface. Water vapor migration in this region is primarily by diffusion through the gas phase with the driving force being controlled by gradients in water-vapor partial pressure. Steep gradients in water-vapor partial pressure above the tank domes, causes water vapor to diffuse vertically toward the ground surface, but the constant temperature assumption of 12.7 °C for the ground surface creates a 100 °C contour within the soil; therefore, a water-vapor-condensation zone. Because of this condensation the amount of water vapor leaving the ground surface is relatively small (less than 2%) compared with the meteoric recharge as shown in Figure D.7.2.25. More realistic boundary conditions at the ground surface would consider allowing the ground-surface temperature to be determined through a convective-radiative heat transfer coefficient to the above-ground air temperature. A more comprehensive analysis at the ground surface, considering time variation in temperature, relative humidity, wind speed, solar insolation, ground-surface albedo, for example, was not warranted because of the constant meteoric recharge assumption.

Figure D.7.2.25. Water-Vapor Flux at the Ground Surface, % of Meteoric Recharge.

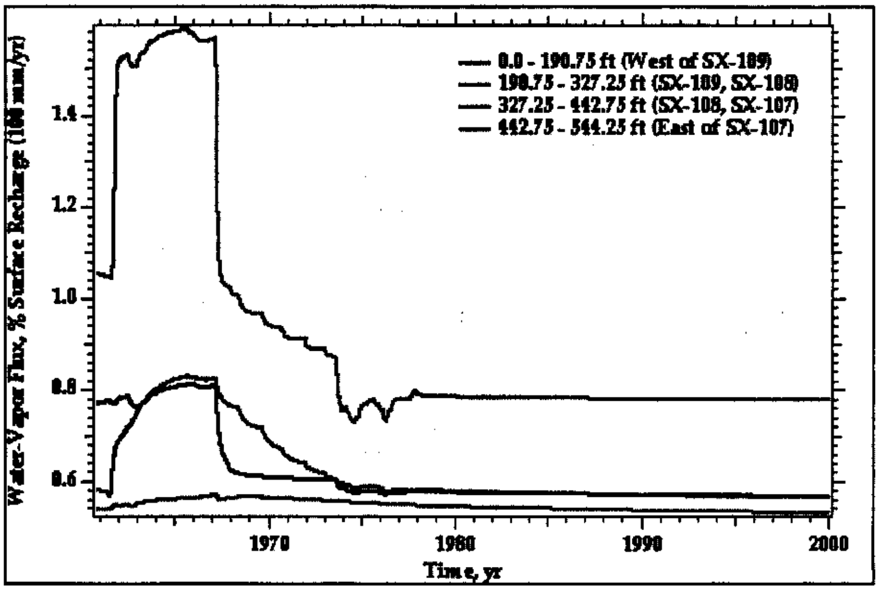

D.7.2.3.2 Comparisons with Field Measurements. Actual thermal and hydrologic conditions in the subsurface surrounding and beneath the WMA S-SX tanks are a function of environmental factors at the ground surface and unconfined aquifer, radiological heat sources of liquids stored in the tanks, past leaks from storage tanks and water lines and operational procedures for the tanks (e.g., ventilation rates, cooling techniques). It is not presumed that the simulations of this investigation will yield accurate representations of the thermal or hydrologic fields in the subsurface at the WMA S-SX. The conceptual models, on which they were founded, lack historical information related to the natural environment and engineered systems and only considered a two-dimensional cross-section through a three-dimensional domain. Two images, however, are provided that compare simulation results for the year 2000 in terms of moisture content and temperature against field measurements taken from monitoring wells within the WMA S-SX. Color-scaled contours of modeled and down-borehole measurements of soil moisture content are shown for comparison at the year 2000 (Figure D.7.2.26). Field measurements of soil moisture were made with neutron probes, which are affected by gamma radiation. Red regions within the boreholes are generally an indication of ^{137}Cs contamination or other gamma emitting radionuclide sources. In general the well measurements show greater variability in soil moisture than the simulated results and the moisture content in the backfill material is generally higher than predicted by the simulation. Both the simulated and field measured results show lower moisture contents in the sloping gravely-sand strata and there is good correspondence between simulated and measured moisture contents for those regions beneath the tanks.

Figure D.7.2.26. Color-Scaled Contours and Well Logs of Moisture Content (2000).

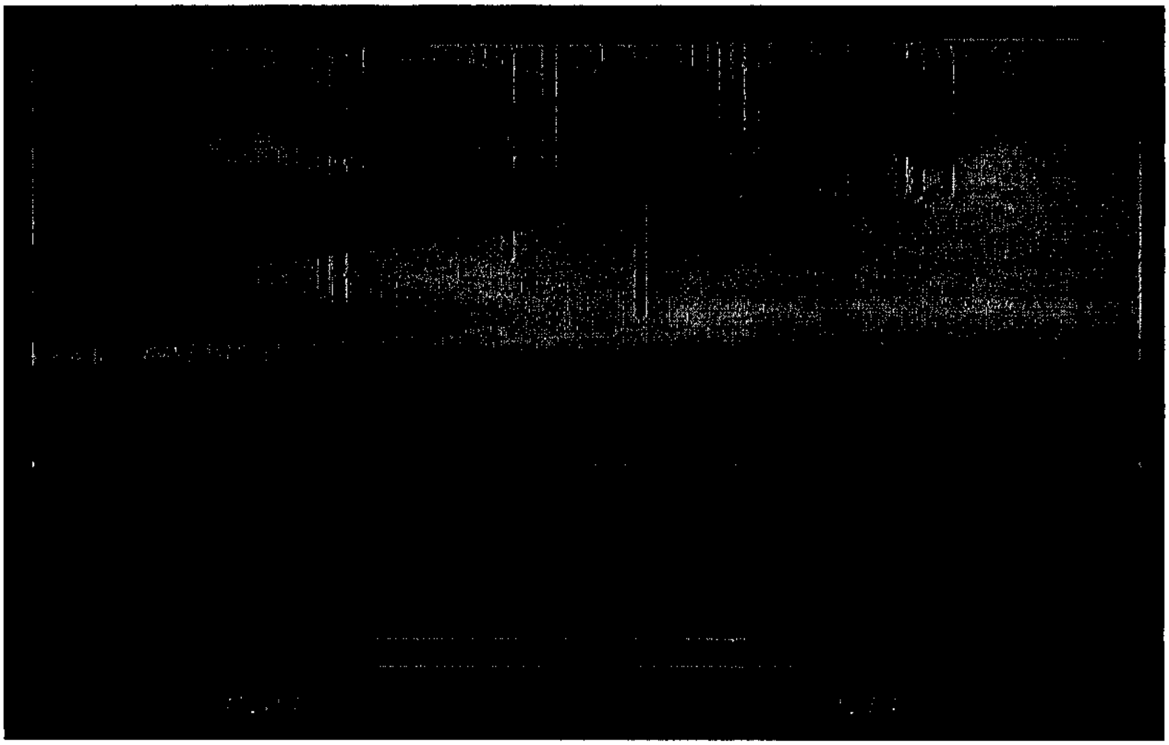

In 2000, temperatures were measured along the length of two boreholes near tanks SX-109 and SX-108: 41-09-39 borehole and the SX-108 slant borehole, respectively. These boreholes are not in the plane of the modeling domain and as such, they are not directly comparable to the simulated temperature contours. However, the projection of these two borehole temperatures onto the modeling results (Figure D.7.2.27) does show a general agreement with the magnitude of predicted temperatures, especially for 41-09-39 borehole. The general discrepancy is that the peak temperatures are observed about 30 feet below the bottom of the tank rather than the predicted peak at the tank bottom. The depth of the observed peak temperature would seem to indicate that this is a residual heat signature from a historic leak of high temperature tank fluid.

Figure D.7.2.27. Color-Scaled Contours and Well Logs of Temperature (2000).

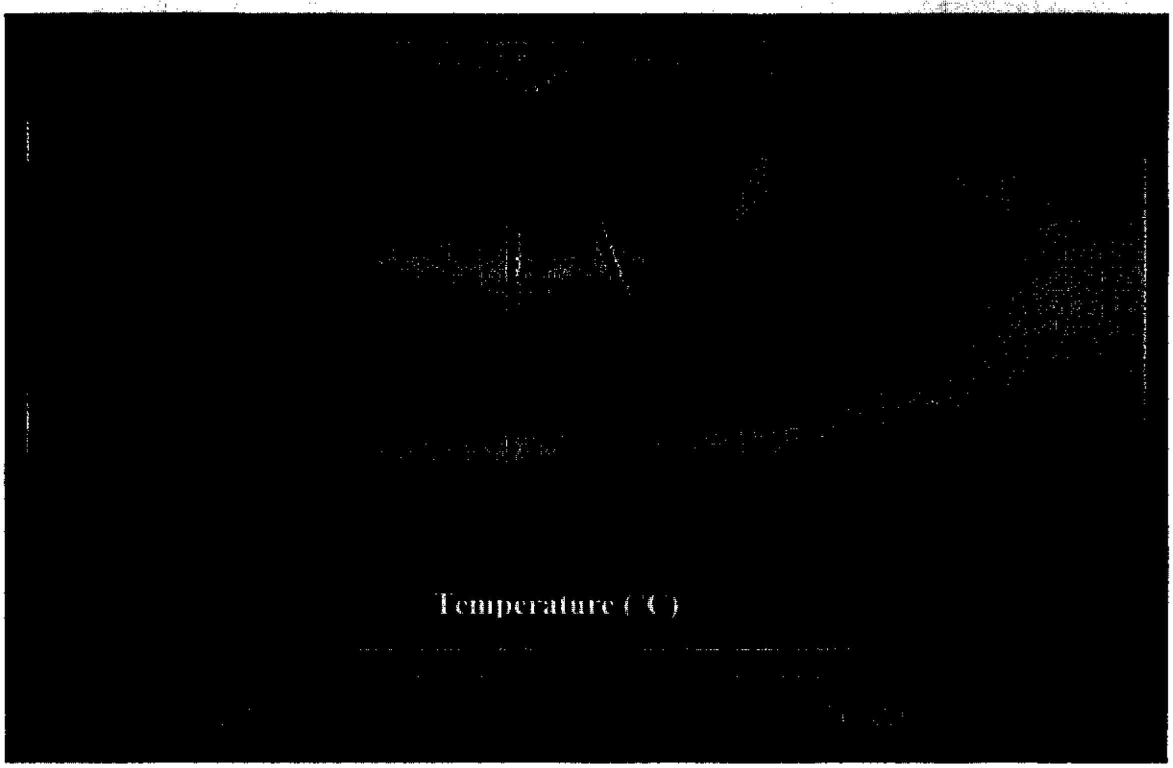

D.7.2.3.3 Solute Transport. Solutes migration through geologic media is governed by the mechanisms of advection, diffusion and hydraulic dispersion, subject to phase partitioning and sorption to the media. The simulations of solute transport in this investigation considered the migration of ^{99}Tc as a nonreactive (i.e., unretarded) species, soluble only in the aqueous phase (i.e., no partitioning into the gas phase). Initial distributions of ^{99}Tc inventory were derived from field measurements and were assumed to represent the distribution at the year 2000. Therefore, simulations of ^{99}Tc migration in this investigation were restricted to the period following the year 2000 and, thus, do not consider solute migration during the known leak events or during the period of heat-pipe conditions in the thermal and hydrologic fields.

The progression of ^{99}Tc migration from 2001 to 2100 is shown for the nonisothermal and isothermal simulation in the color-scaled contours of dissolved ^{99}Tc concentration in Figures D.7.2.28 through D.7.2.38. To enhance the visualization of the plume migration logarithmic color-scaling was used to contour the dissolved concentrations in this series of images. The distribution of dissolved ^{99}Tc in 2000.01 (Figure D.7.2.28) is nearly identical to the initial distribution assigned in 2000 according to the modeling data package (Khaleel et at. 2000). By 2001 (Figure D.7.2.29), however, significant dispersion of the plume has occurred and there is evidence of preferential migration along the sloping gravely-sand strata. Because the ^{99}Tc inventory was initially distributed primarily below this strata, its effect on the lateral migration of ^{99}Tc is limited. The dissolved ^{99}Tc plume migrates rapidly over the first 40 years (Figures D.7.2.30 through D.7.2.33) toward the unconfined aquifer, where it dilutes and is transported laterally toward the WMA S-SX eastern boundary. At 2040 a closure barrier becomes effective, reducing the surface recharge and consequentially slowing the downward migration of ^{99}Tc (Figures D.7.2.33 through D.7.2.38). A plot of ^{99}Tc concentrations at the

WMA S-SX boundary versus time is shown in Figure D.7.2.39 for both the isothermal and nonisothermal simulations. Peak concentrations of ^{99}Tc at the WMA S-SX boundary were predicted to be 1.575 x 10^6 pCi/L at year 2040.3 for the isothermal simulation.

Figure D.7.2.28. Dissolved ^{99}Tc Concentration Profile at 2000.01 (+0.01 yr).

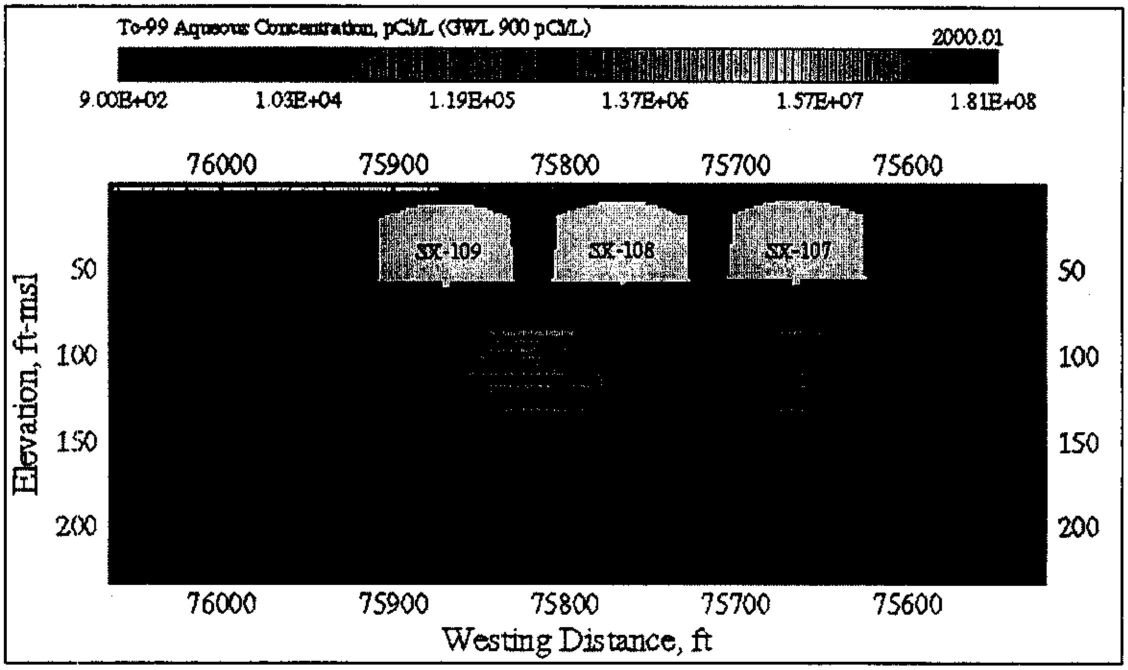

Figure D.7.2.29. Dissolved ^{99}Tc Concentration Profiles at 2001 (+1 yr) (Nonisothermal: Color-Scaled, Isothermal: Black Contour Lines).

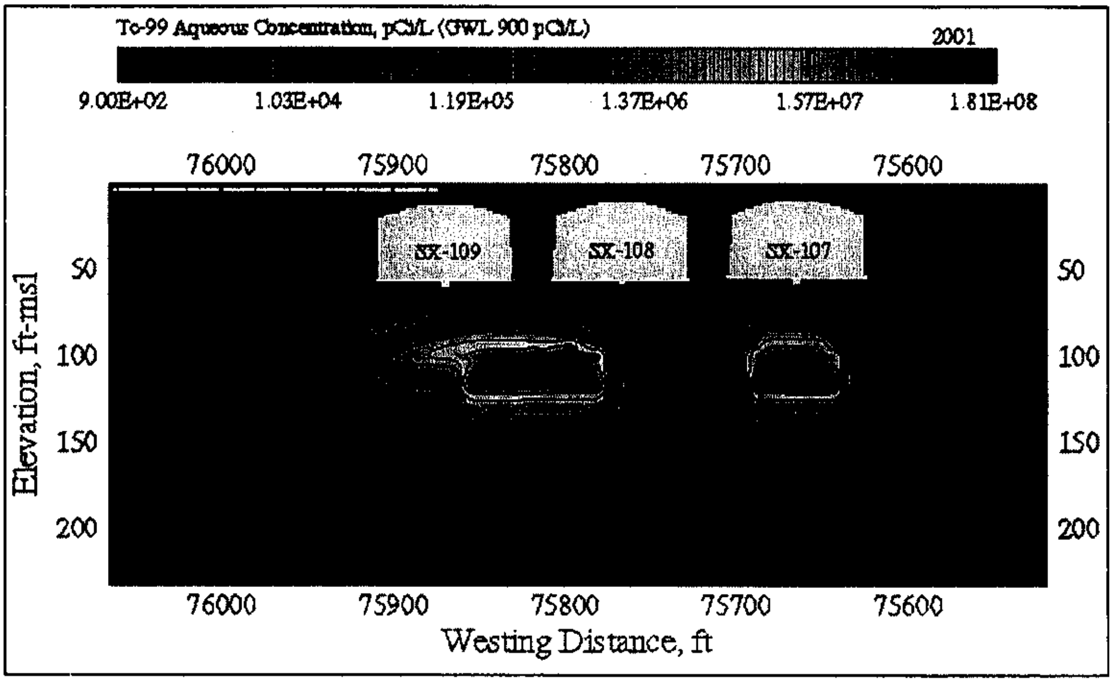

Figure D.7.2.30. Dissolved ^{99}Tc Concentration Profile at 2010 (+10 yr) (Nonisothermal: Color-Scaled, Isothermal: Black Contour Lines).

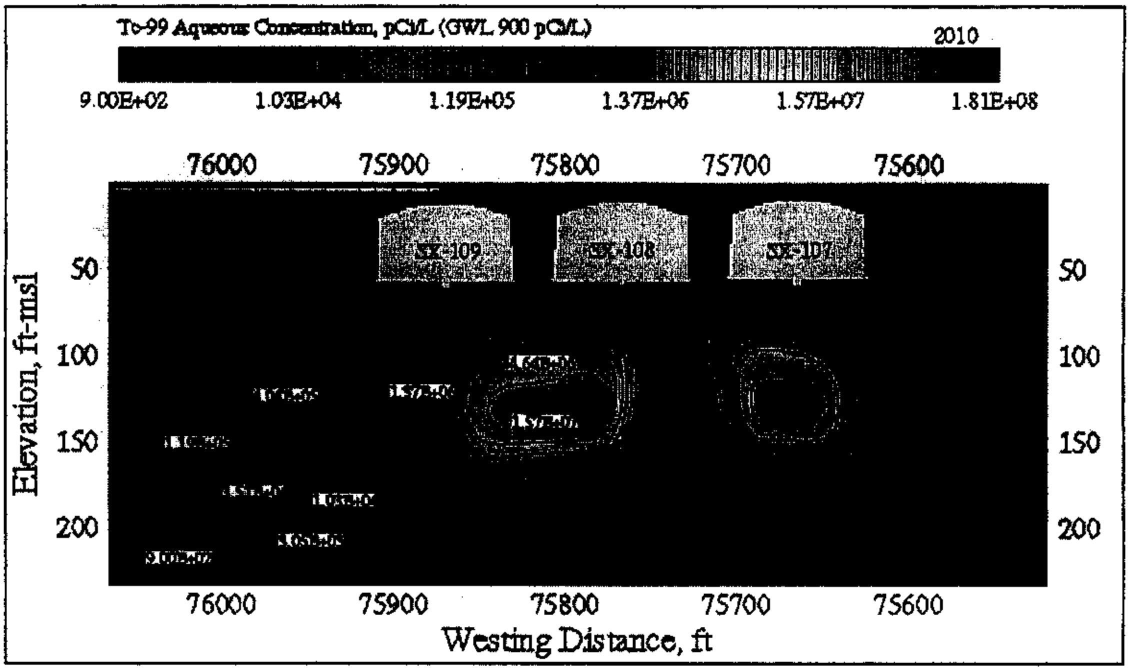

Figure D.7.2.31. Dissolved ^{99}Tc Concentration Profile at 2020 (+20 yr) (Nonisothermal: Color-Scaled, Isothermal: Black Contour Lines).

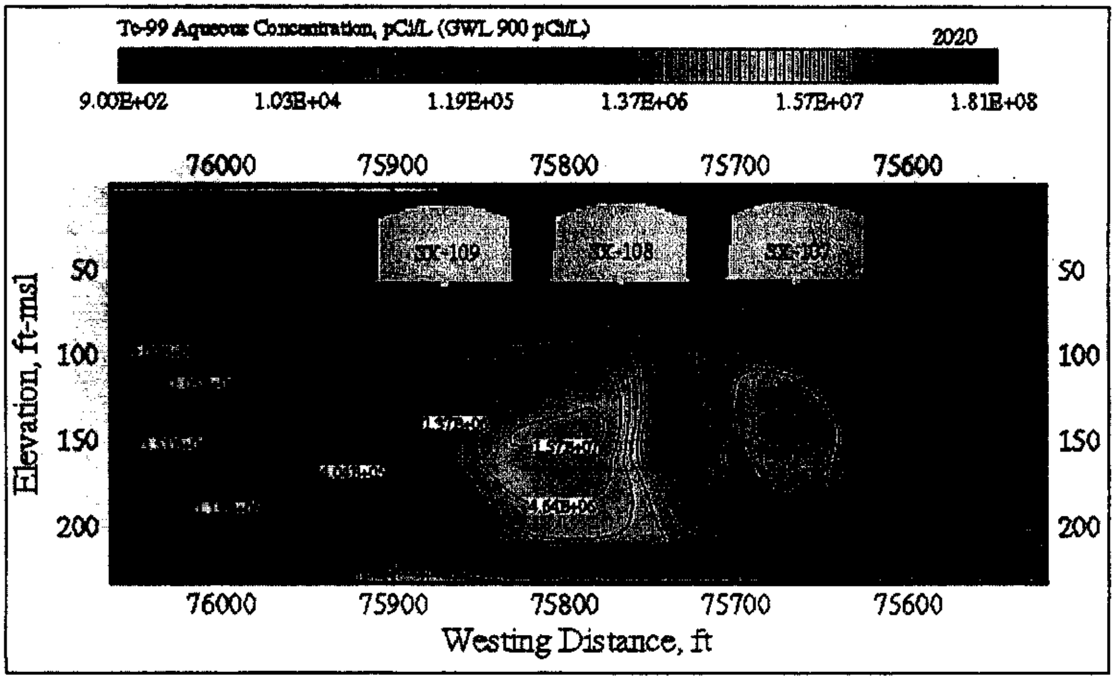

Figure D.7.2.32. Dissolved ^{99}Tc Concentration Profile at 2030 (+30 yr) (Nonisothermal: Color-Scaled, Isothermal: Black Contour Lines).

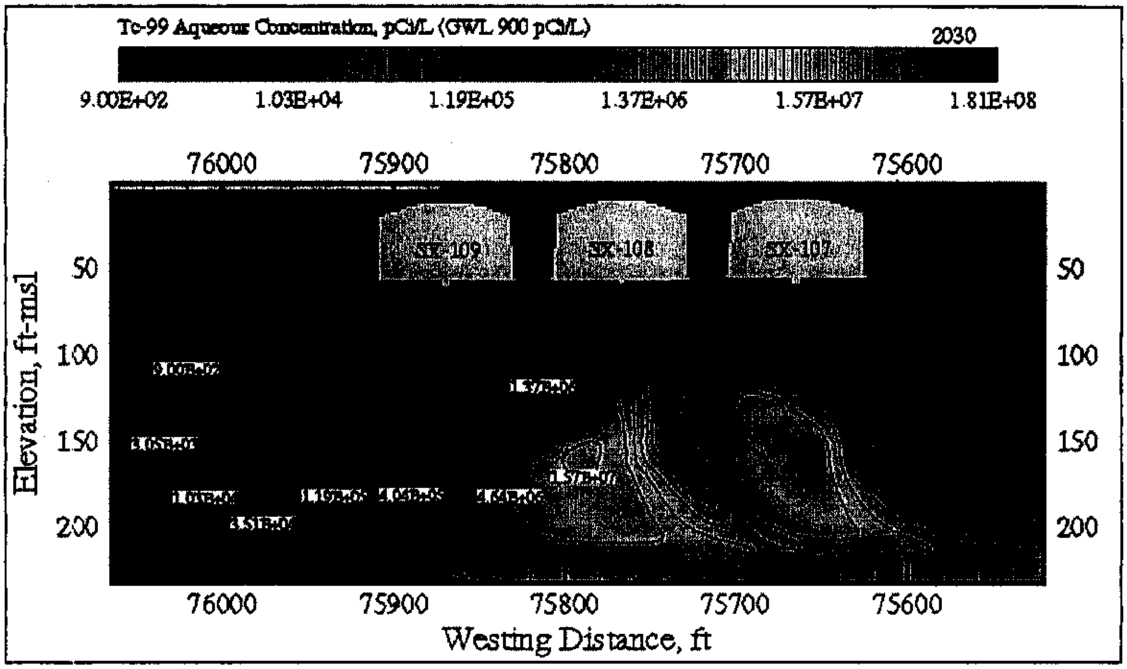

Figure D.7.2.33. Dissolved ^{99}Tc Concentration Profile at 2040 (+40 yr) (Nonisothermal: Color-Scaled, Isothermal: Black Contour Lines).

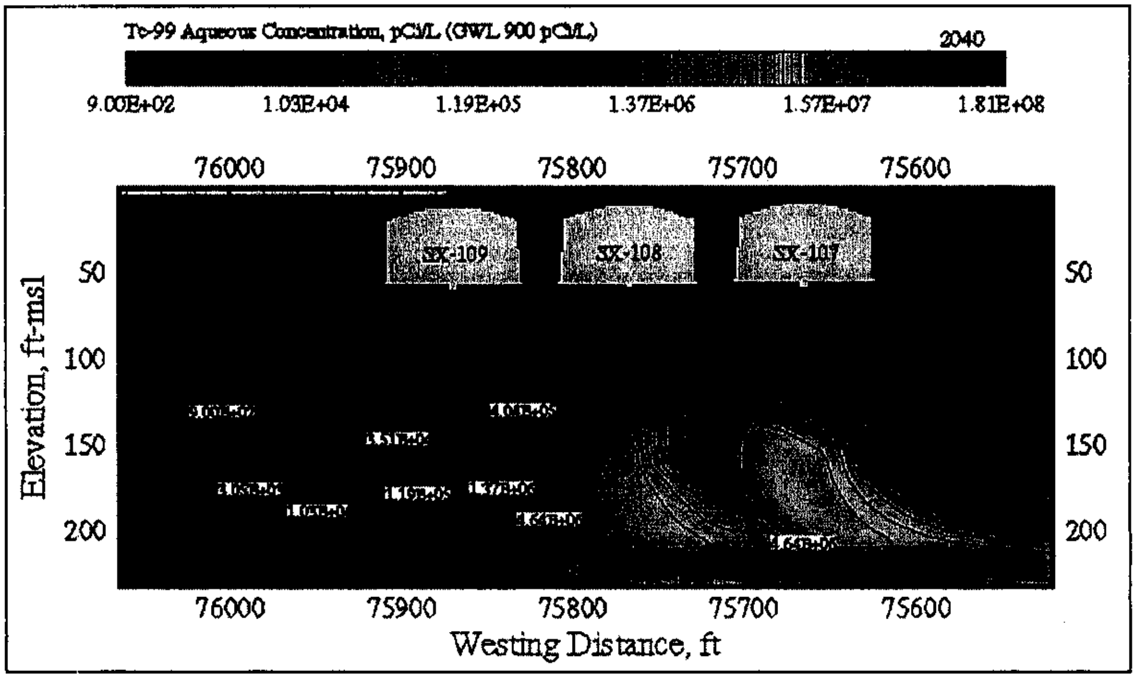

Figure D.7.2.34. Dissolved ^{99}Tc Concentration Profile at 2050 (+50 yr) (Nonisothermal: Color-Scaled, Isothermal: Black Contour Lines).

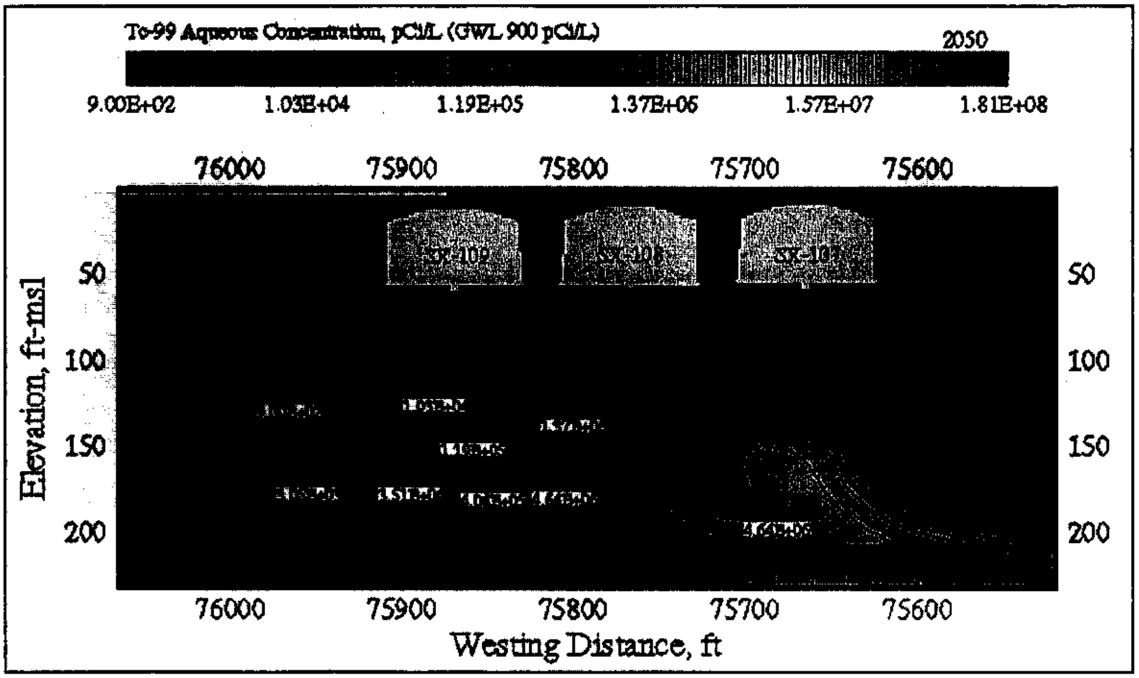

Figure D.7.2.35. Dissolved ^{99}Tc Concentration Profile at 2060 (+60 yr) (Nonisothermal: Color-Scaled, Isothermal: Black Contour Lines).

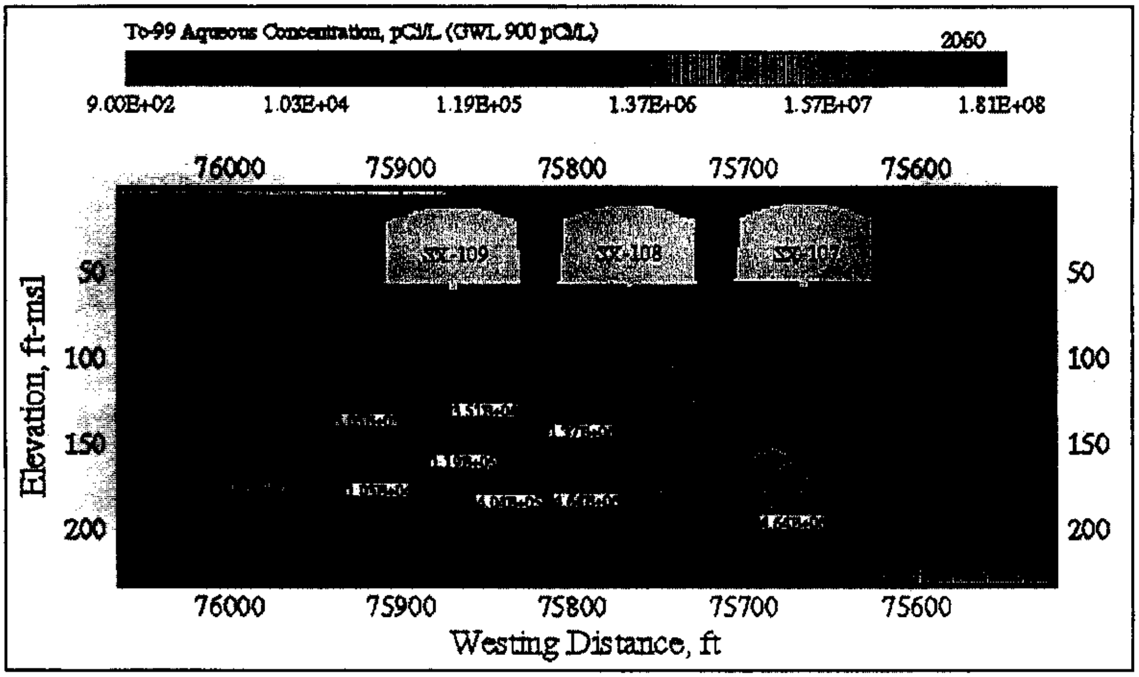

Figure D.7.2.36. Dissolved ^{99}Tc Concentration Profile at 2070 (+70 yr) (Nonisothermal: Color-Scaled, Isothermal: Black Contour Lines).

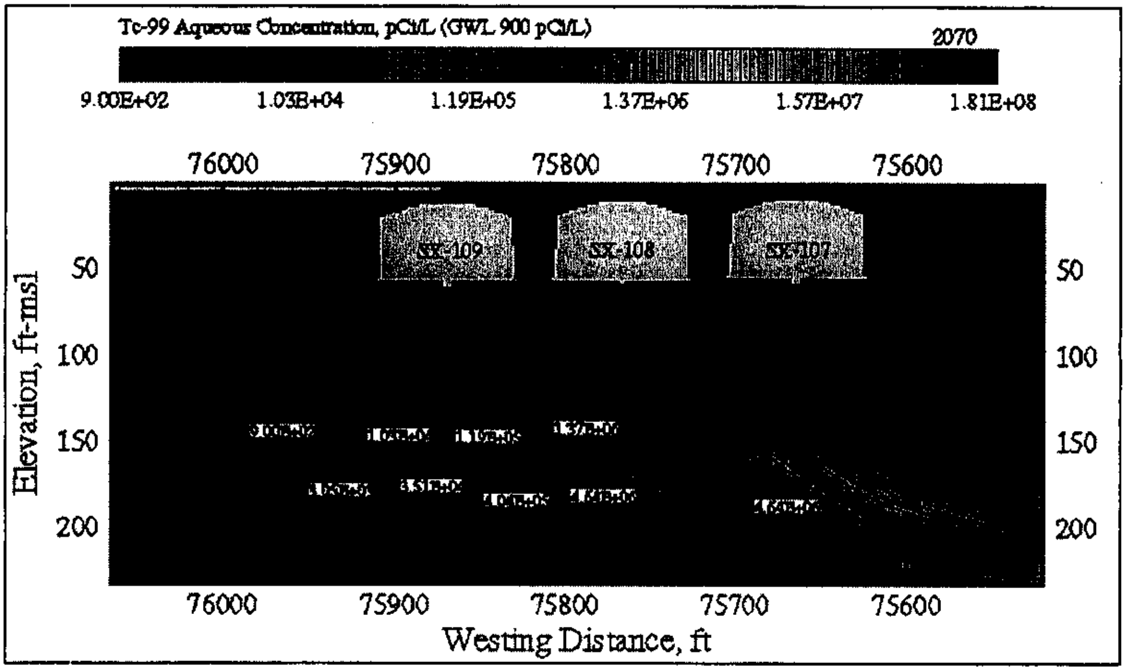

Figure D.7.2.37. Dissolved ^{99}Tc Concentration Profile at 2080 (+80 yr) (Nonisothermal: Color-Scaled, Isothermal: Black Contour Lines).

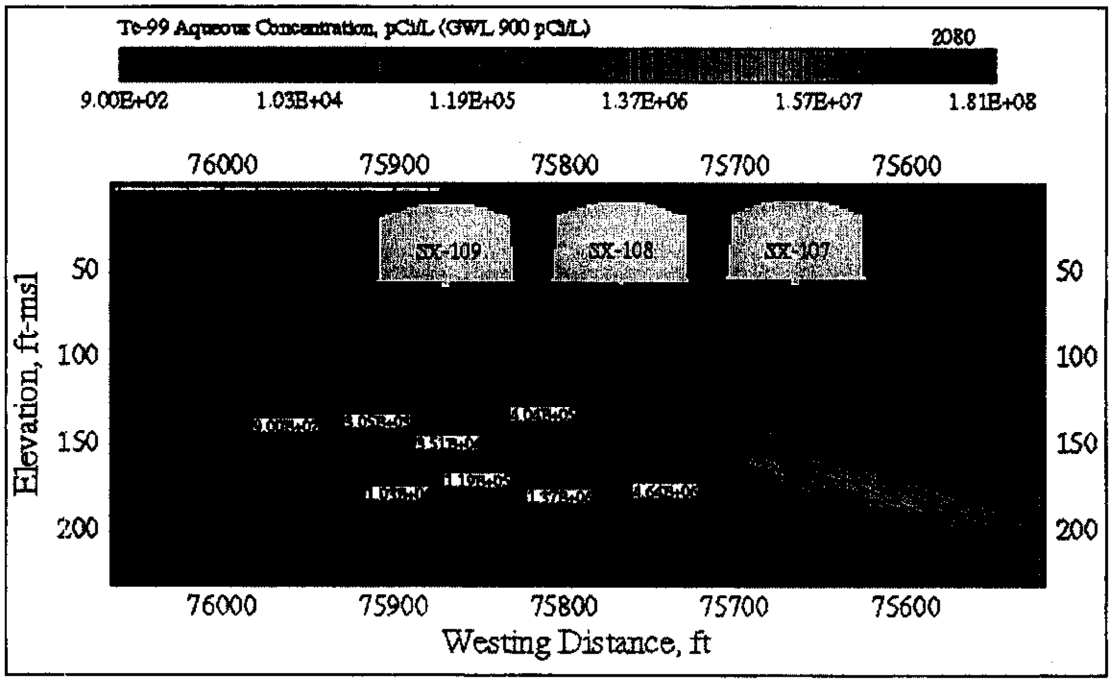

Figure D.7.2.38. Dissolved ^{99}Tc Concentration Profile at 2100 (+100 yr) (Nonisothermal: Color-Scaled, Isothermal: Black Contour Lines).

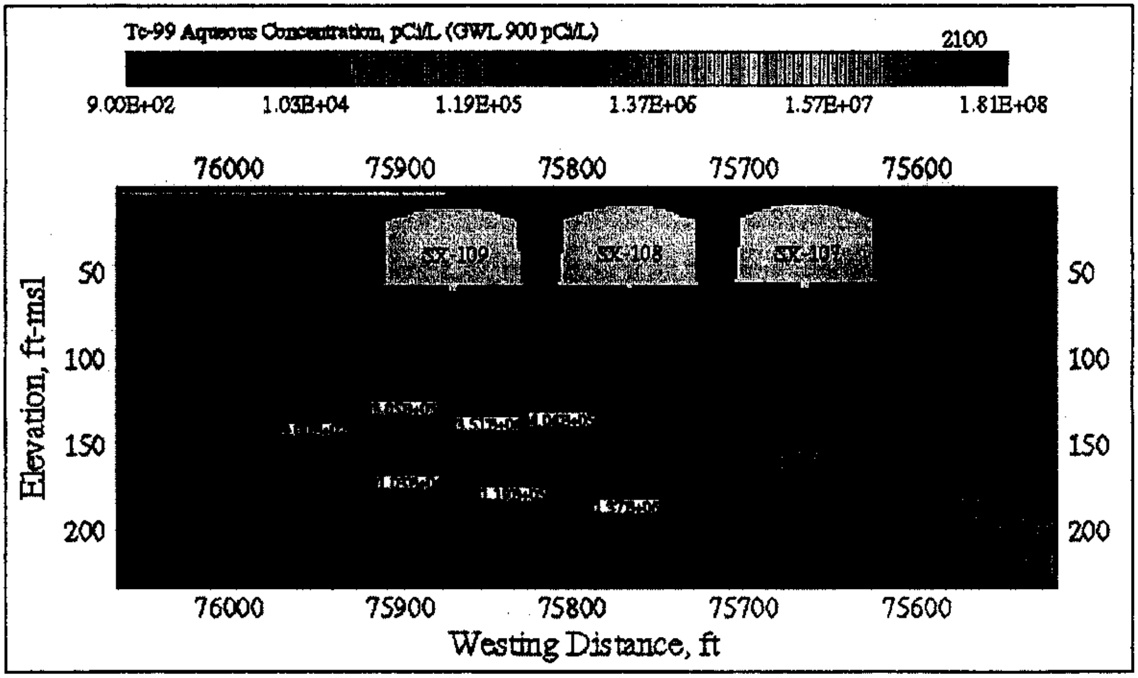

Figure D.7.2.39. Dissolved ^{99}Tc Concentration at the WMA S-SX Boundary.

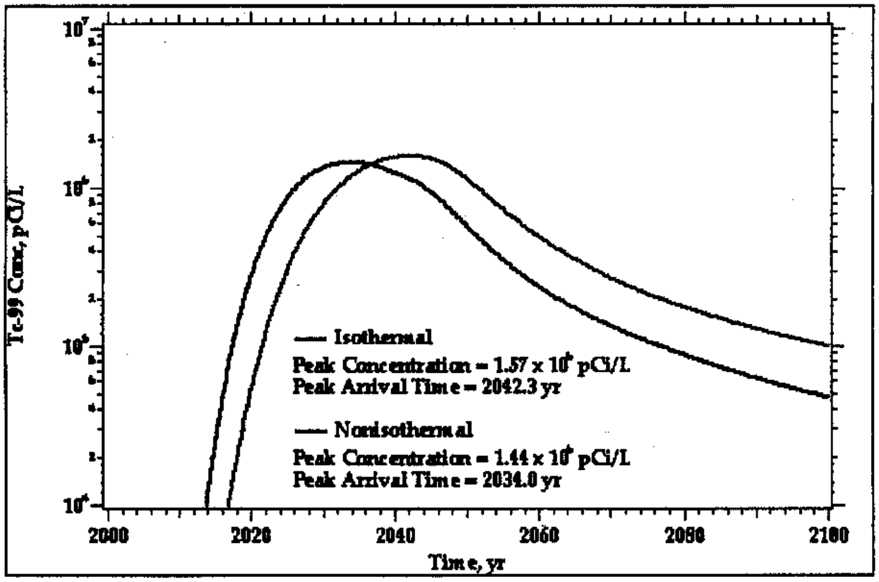

D.7.2.4 Conclusions and Implications

The fundamental implication of this investigation to the future management of the WMA S-SX is that the thermal and hydrologic environment of the subsurface is strongly coupled. Therefore, in order to understand historical behavior and predict future migration of contaminants around and beneath the WMA S-SX tanks, it is crucial to consider this coupling between the thermal and hydrologic conditions. The simulations of ^{99}Tc migration into the future under isothermal and nonisothermal conditions, suggest that the current thermal conditions beneath the tanks do not significantly alter the behavior of this nonreactive contaminant. For investigations that will consider future tanks leaks from retrieval activities (e.g., sluicing, salt-cake dissolution) the implication of this investigation is that the coupled nature of the thermal and hydrologic environments be considered.

Radiological heat sources from previous tank leaks was not considered during these investigations. The strong heat-pipe type flow regimes that developed during the late 1960s and early 1970s beneath tanks SX-108 and SX-109 would tend to concentrate aqueous soluble radionuclides near the water evaporation zone (i.e., the transition region between the dry-conduction zone and the counter-current or constant-temperature zone). Concentration of mobile radionuclides using this mechanism could produce local radiological decay heat sources. The simulation results additionally indicate that the influence of these solute concentrating heat-pipe type flow regimes extended roughly 75 feet beneath tanks SX-108 and SX-109. The implication here is that future investigations may need to address thermal and hydrologic coupling for localized heat generation by radionuclide decay.

This investigation was principally directed at understanding the impact of thermal-hydrological coupling on the transport of mobile radionuclides to the unconfined aquifer. Though this investigation has demonstrated the importance of the coupled effect the simulation results additionally show the critical role of a surface barrier in retarding the downward migration of mobile solutes. The implication is that surface recharge strongly influences downward migration of solutes and surface barriers or other engineered technologies that reduce meteoric recharge will lower peak concentrations and delay peak arrival times of these species. This further suggests that early application of an interim surface barrier would have strong merit. Under constant ground-surface temperature and meteoric recharge conditions, the diffusive flux of water vapor vertically through the ground surface is less than 2% of the meteoric recharge. If the ground-surface temperature had been computed using a radiative-convective heat transfer coefficient the percent of meteoric recharge lost through the ground surface would be higher.

D.7.2.5 References

Agnew, S. F., and R. A. Corbin, 1998, *Analysis of SX Farm Leak Histories--Historical Leak Model (HLM)*, HNF-3233, LA-UR-96-3537, Prepared by Los Alamos National Laboratory, Los Alamos, New Mexico, for U.S. Department of Energy, Richland Operations Office and Project Hanford Management Company, Lockheed Martin Hanford Corporation, Richland, Washington.

Corey, A. T., 1954, "The Interrelation Between Gas and Oil Relative Permeabilities," *Producers Monthly*, November, pp. 38-41.

Gee, G. W., M. J. Fayer, M. L. Rockhold, and M. D. Campbell, 1992, "Variations in Recharge at the Hanford Site," *Northwest Science*, Vol. 60:237-250.

Khaleel, R., T. E. Jones, A. J. Knepp, F. M. Mann, D. A. Myers, P. M. Rogers, R. J. Serne, and M. I. Wood, 2000, *Modeling Data Package for S-SX Field Investigation Report (FIR),* RPP-6296, Rev. 0, CH2M HILL Hanford Group, Inc., Richland, Washington.

Millington, R. J., and J. P. Quirk, 1961, "Permeability of Porous Media," *Nature*, Vol. 183:387-388.

Mualem, Y., 1976, "A New Model for Predicting the Hydraulic Conductivity of Unsaturated Porous Media," *Water Resources Research*, Vol. 12(3):513-522.

Somerton, W. H., J. A. Keese, and S. L. Chu, 1973, "Thermal Behavior of Unconsolidated Oil Sands," Paper SPE-4506, presented at the 48th Annual Fall Meeting of the Society of Petroleum Engineers, San Francisco, California.

Polmann, D. J., 1990, "Application of Stochastic Methods to Transient Flow and Transport in Heterogeneous Unsaturated Soils," Ph.D. Thesis, Massachusetts Institute of Technology, Cambridge, Massachusetts.

Price, W. H., and K. R. Fecht, 1976, *Geology of the 241-SX Tank Farm,* ARH-LD-133, Atlantic Richfield Hanford Company, Richland, Washington.

van Genuchten, M. Th., 1980, "A Closed-Form Equation for Predicting the Hydraulic Conductivity of Unsaturated Soils," *Soil Science Society of America Journal*, Vol. 44:892-898.

Ward, A. L., G. W. Gee, and M. D. White, 1997, *A Comprehensive Analysis of Contaminant Transport in the Vadose Zone Beneath Tank SX-109*, PNNL-11463, Pacific Northwest National Laboratory, Richland, Washington.

White, M. D. and M. Oostrom, 2000a, *STOMP Subsurface Transport Over Multiple Phases, Version 2.0, Theory Guide*, PNNL-12030, Pacific Northwest National Laboratory, Richland, Washington.

White, M. D. and M. Oostrom, 2000b, *STOMP Subsurface Transport Over Multiple Phases, Version 2.0, User's Guide*, PNNL-12034, Pacific Northwest National Laboratory, Richland, Washington.

White, M. D., M. Oostrom, and M. D. Williams, 2001, *FY00 Initial Assessments for S-SX Field Investigation Report (FIR): Simulations of Contaminant Migration with Surface Barriers*, Pacific Northwest National Laboratory, Richland, Washington. (In Press)

D.7.3 ESTIMATION OF TANK SUPERNATANT LIQUID COMPOSITIONS

P. C. Lichtner[1]

[1]Los Alamos National Laboratory, Los Alamos, New Mexico 87545

D.7.3.1 Introduction

Leaks that have occurred from single-shell tanks containing high-level radioactive waste in the 200 Area of the Hanford Site contain high ionic strength fluids that can adversely affect the migration of radionuclides. It is expected that these fluids reacted strongly with the sediments beneath the tanks, very likely altering their sorptive properties. Furthermore, competitive sorption effects for the limited number of sorption sites between radionuclides and cations in the background electrolyte solution leaked from the tanks could enhance the mobility of certain radionuclides.

In order to use quantitative models to describe the movement of radionuclides, which have leaked from many of the single-shell tanks (it has been estimated that 67 out of 149 single-shell tanks have leaked), an estimate of the chemical composition of the fluid is required. Determining the tank leak composition is a highly nontrivial task. Unfortunately, because of the highly radioactive nature of the tank inventory, and because tank inventories varied over time, direct measurements are not available. Thus, indirect approaches must be used to estimate the composition of each tank at the time it was suspected to have leaked.

Tank inventories fluctuated over time depending on their fill histories, heat load, and evaporative loss. Precipitates composed of sodium nitrate and nitrite and alumina among others are likely to have formed in the tanks. Timing of leak events have been estimated based on unaccounted volume losses using the Historical Leak Model (HLM) corroborated with reports of lateral and drywell contamination (Agnew and Corbin 1998). Tank waste inventories can be estimated as functions of time using the Hanford Defined Wastes (HDW) model developed by Agnew (1997). The HDW model takes into account blending and concentration of the wastes over time. Considerable disagreement, however, still exists over the volume of fluid that has leaked from the various tanks and its composition (Agnew and Corbin 1998; Jones et al. 2000). An exception is tank SX-115 for which relatively accurate data exists for leak timing and volume.

Once a best estimate for the tank inventory has been obtained at the time of the leak, it is still necessary to determine the composition of the tank supernate liquid, the most likely phase to have leaked from the tank. Assuming the supernate is in equilibrium with salts precipitated in the tanks, a thermodynamic model is needed to determine the equilibrium phase assemblage consistent with a given tank inventory. The high ionic strength of the supernate liquid characteristic of several of the tanks in the SX tank farm, places severe requirements on thermodynamic models that can be used for this purpose. In this contribution, the Pitzer activity coefficient algorithm as developed for the GMIN computer code (Felmy 1995) and its associated database, is implemented into the reactive transport code FLOTRAN (Lichtner 2001). Equilibration of the tank inventory is carried out using a reaction path simulation from which both the supernate composition and the stable mineral assemblage at equilibrium are determined simultaneously.

D.7.3.2 Modeling Approach

Tank waste compositions estimated using the HDW model represent a combination of contributions from both liquid and solid (saltcake) inventories. Because the liquid phase is considered to be the main fraction of the tank inventory lost during a leak event, it is necessary to obtain an estimate for the liquid composition alone. Direct use of the tank waste inventory itself would lead to an unrealistic estimate of the liquid phase composition, resulting in a solution highly supersaturated with respect to a number of minerals. The composition of the supernate liquid in the tank may be determined by calculating the equilibrium configuration of liquid and solid phases starting with the same total mass balance as the tank waste inventory.

D.7.3.2.1 Reaction Path Formulation. There are two basic approaches available for calculating the composition of the liquid fraction of the tank inventory and the solids with which it is in equilibrium. One approach is to minimize the Gibbs free energy of the system consisting of liquid and solids. This approach is independent of any particular reaction stoichiometry. It involves the free energy of each species at the temperature and pressure of interest, and mass balance and electroneutrality constraints. The result of the minimization process provides the composition of the liquid phase and the number of moles of each solid, which is present in the final equilibrium state. A gas phase may also be present.

An alternative, equivalent approach, is based on the explicit treatment of chemical reactions formulated for a particular, nonunique, reaction stoichiometry. An equilibrium constant for each chemical reaction is required along with species mass conservation relations.

The equivalent procedure to minimizing the Gibbs free energy in the reaction-based approach is to perform a reaction path, or titration, calculation in a closed system. Both of these approaches determine the equilibrium state of a closed system from some initial configuration. Because this equilibrium state is unique and independent of the path the system follows to reach equilibrium (Prigogine and Defay 1954), the two approaches must yield identical results assuming equivalent thermodynamic data in the form of free energies or equilibrium constants, and the same treatment of activity coefficient corrections.

The way in which chemical reactions are incorporated into the two models is an important distinction. In the stoichiometric reaction approach, aqueous species are partitioned into primary and secondary species. Chemical reactions are formulated for secondary species in terms of the primary species that serve as a set of basis species. The secondary species consist of ion pairs, complexes, dissociation products (such as OH^-), and related species. Minerals are treated in a similar fashion by writing reactions containing a single mineral in terms of the chosen set of primary species. Because the equilibrium configuration of a closed system is independent of the particular form of the chemical reactions used to represent the system, in the equilibrium constant approach any set of linearly independent reactions may be used (Prigogine and Defay 1954). Thus so long as a linearly independent set of reactions are provided, any of the primary species may be replaced by any of the secondary species. Only when describing kinetic behavior of the system does reaction stoichiometry play a role.

Reaction path calculations may be carried out using several different approaches. One approach is to formulate the problem in terms of a reaction progress variable and to enforce chemical equilibrium on the system at each step along the reaction path. Another approach is to use real time as the progress variable combined with arbitrary reaction kinetics for solid phases. This latter approach is followed in this report using the computer code FLOTRAN (Lichtner 2001). FLOTRAN incorporates the Pitzer model adapted from GMIN (Felmy 1995) for activity coefficient corrections for high ionic strength fluids. In addition, a Debye-Hückel algorithm is available for more dilute solutions. The solvent species, in this case water, is included in mass balance equations, as is the deviation of the activity of water from unity. This is essential for the highly concentrated solutions that characterize some of the tank waste. Mineral reactions are treated with a transition state pseudo-kinetic rate law. Homogeneous reactions within the aqueous phase, such as ion pairing, complexing, redox reactions, and dissociation of water, are assumed to obey conditions of local chemical equilibrium. All thermodynamic data is read from a single database that must be provided by the user. The database used for the calculations in this report is derived from the EQ3/6 database, version data0.com.V8.R6. The database provides equilibrium constants over a range of temperatures from 0 to 300 °C with pressure at 1 bar, or taken along the saturation curve of pure water for temperatures above 100 °C. Additional databases provided by GMIN are required for the various Pitzer parameters when using the Pitzer activity coefficient algorithm. It should be noted, however, that the GMIN database does not extend below 25 °C and is limited to temperatures less than or equal to 100 °C for many species.

The reaction path formulation has a number of advantages over the free energy minimization approach. In the first place, the reaction path method enables a true kinetic formulation of reaction rates for a system in partial chemical equilibrium. Secondly, many of the objections that have been raised against the stoichiometric formulation (e.g., Harvie et al. 1987) disappear when this approach is combined with a real time, pseudo-kinetic, description of mineral reactions. It then becomes an easy and automatic process to determine the stable equilibrium mineral assemblage. Because it is not possible to know in advance which minerals are present at equilibrium, a sufficient number of possible mineral reactions must be included in the reaction path calculation to resolve the final equilibrium state of the system. Some of these minerals may precipitate during the early stages of the reaction path calculation, but completely dissolve at later times and hence not appear in the final equilibrium state. This approach enables the equilibrium mineral assemblage to be determined "automatically" without the necessity to check whether in fact an absolute minimum in free energy has been achieved within the mineral subspace included in the simulation.

D.7.3.2.2 Pitzer Activity Coefficient Algorithm. For implementation of the Pitzer model for use in the DOE Science and Technology Modeling program, the GMIN activity coefficient algorithm was adapted for use with the stoichiometric chemical reaction formulation common to reactive transport models. The GMIN code is based on minimization of the Gibbs free energy, which, although mathematically equivalent to the stoichiometric reaction approach for equilibrium systems, involves a different set of numerical algorithms for obtaining the equilibrium state of the system. The need for an stoichiometric-based approach in reactive transport models is dictated by the necessity to describe systems in partial equilibrium. In these systems, kinetically controlled mineral reactions and slowly evolving redox reactions, for example, can control the state of the system. Such reactions are especially important for describing the interaction between the Hanford sediments and the tank fluid.

The Pitzer activity coefficient algorithm is based on a virial expansion (Pitzer 1973, 1991), which reduces to the Debye-Hückel formulation at low ionic strength. The virial expansion involves a sum over all possible binary and ternary short-range interaction terms. The expansion coefficients must be determined through extensive experimental work over a range of pressure and temperature conditions. It is generally not possible to extrapolate results beyond the region used for fitting the data. The Pitzer activity coefficients account for electrostatic interaction and ion hydration effects in addition to formation of complexes and ion pairing. In this sense the Pitzer approach differs conceptually from the Debye-Hückel formulation in which only electrostatic and hydration effects are included. In the Debye-Hückel formulation, complexing and ion pairing must be explicitly taken into account. When using a Debye-Hückel activity coefficient algorithm in speciation calculations any of the relevant chemical species that are found in a thermodynamic database are generally employed. Often many of these species are unimportant, but some are essential. The Pitzer model, in contrast, uses a restricted set of aqueous species compared to the Debye-Hückel model. To determine which additional species are necessary to include in any particular chemical system, the user must refer to the original data on which the expansion coefficients in the Pitzer model are based. Otherwise double counting the effect of species interactions on the activity correction could result. For example, the species $NaCl_{(aq)}$ is not considered a valid species in the Pitzer model at moderate temperatures, but is usually included in a Debye-Hückel model—although at low temperatures it probably has little effect within the range of validity of the Debye-Hückel algorithm. On the other hand, strong complexes such as $NaNO_{3(aq)}$ and $NaNO_{2(aq)}$ are required in both models for an accurate representation of the fluid composition. In addition, species which undergo protonation and deprotonation, such as H^+-OH^--H_2O, $CO_{2(aq)}$-CO_3^{2-}-HCO_3^-, Al^{3+}-$Al(OH)_4^-$, Fe^{3+}-$Fe(OH)_4^-$, and $SiO_{2(aq)}$-H_3SiO_4-$H_2SiO_4^{2-}$ generally must be explicitly taken into account. Because the activity coefficient in the Pitzer formulation accounts for aqueous complexing and ion pairing, the greater these effects the smaller the activity coefficient, thereby reducing the activity of the free ion or neutral species.

An immediate consequence of the difference between the Pitzer and Debye-Hückel approaches for incorporating speciation, is the effect this has on computation of mineral solubility and retardation, two important chemical processes for reducing the migration of contaminants. In the Debye-Hückel approach it is necessary to explicitly include those complexes that have a significant contribution to the total aqueous concentration of the species in question to properly account for solubility and retardation. In the Pitzer model, this is handled somewhat differently depending on whether aqueous complexes are explicitly included in the model or whether their presence is adsorbed into activity coefficients. If complexes are not explicitly included, the reduction in retardation of a particular species is taken into account by a reduction in the activity coefficient of that species. Both models, of course, must give the same results within a common range of validity.

To obtain a sense of the accuracy with which the Pitzer activity coefficient formulation can represent mineral solubility at high ionic strength, comparison is given with experimentally measured data for the solubility of $NaNO_{3(s)}$, an important component of tank waste. Using the FLOTRAN code with the GMIN database for Pitzer activity coefficient corrections the results presented in Table D.7.3.1 are obtained. Also listed in the table is the solubility predicted using the Debye-Hückel activity coefficient algorithm. As can be seen from the table, the fit with the Pitzer model is quite good for temperatures above 25 °C. By contrast, the Debye-Hückel model significantly over predicts the solubility at high temperatures and under predicts it at low temperatures. The GMIN database is calibrated for temperatures at 25 °C and above for this system, which explains the spurious increase in solubility at 20 °C obtained from the Pitzer model. GMIN, in fact, failed to converge for temperatures below approximately 18 °C, which illustrates the danger in going outside the range of calibration of the Pitzer expansion coefficients.

Table D.7.3.1. Comparison of the Solubility of $NaNO_3$ as Computed Using FLOTRAN with Pitzer and Debye-Hückel Activity Coefficient Corrections, with Experimental Data Taken From Kirk-Othmer Encyclopedia of Chemical Technology Published by Wiley Interscience.

T[C]	Total Na [Molal]		Experiment [Molal]
	Pitzer	Debye-Hückel	
-17.5	-	-	7.4
0.	-	5.142	8.62
20.	13.919	-	-
25.	10.773	8.838	-
40.	12.158	12.806	12.39
80.	17.401	30.298	17.42
100.	21.213	34.126	-
120.	24.486	32.432	24.80

D.7.3.3 Results

In this section reaction path calculations are presented for the equilibrium state of the tank waste inventory using FLOTRAN combined with the Pitzer algorithm. In what follows, compositions of three tanks in the SX tank farm are evaluated. These are tanks SX-108, SX-109 and SX-115. Not all species possible are considered, but only a selected set which constitutes the dominant species in the tank waste and several minor species for which there exists temperature-dependent thermodynamic data. These species are: Al, Fe, Ca, Ni, K, Na, NO_3, NO_2, Cl, CO_2, S, Cr, and Si. Those species not included in the present analysis are: F, Mn, P, Pb, Pu, Se, Sr, Tc, U, Zr, and organic species. However, incorporation of these species should not affect the major solution properties because of their low concentrations.

D.7.3.3.1 Initial Tank Waste Inventory. Initial conditions for the reaction path simulations were determined from the initial total tank waste inventories, including contributions from both liquid and solid phases. The tank inventory at the time of a leak can only be estimated since there are no direct measurements available. The pH of the liquid portion of the tank waste composition is not known, and because of errors involved in the estimation procedure, the waste composition may not be charge balanced. For these reasons it is necessary to make some additional assumptions to determine the initial pH and to obtain an initially balanced solution.

Jones et al. (2000) arbitrarily set the initial OH^- concentration to 0.1 mol/L and balanced the solution charge on Na^+. An alternative approach to that of Jones et al. (2000) is to use the Na^+ inventory estimated from the HDW model and determine pH by charge balancing on OH^-. This approach has the advantage that it involves only one adjustable parameter (namely the concentration of OH^-), whereas the approach used by Jones et al. (2000) involves two parameters (concentrations of OH^- and NA^+). There seems to be no justifiable reason why the HDW calculated Na^+ concentration should not be used if all the other species concentrations are. This latter approach is followed in this report with the exception of tank SX-108. For this tank it was necessary to use a higher weight percent H_2O than derived from the HDW model by Jones et al. (2000) in order to obtain convergence. The starting solution compositions for tanks SX-108, SX-109, and SX-115 for the reaction path calculations are listed in Table D.7.3.2.

Table D.7.3.2. Initial Tank Waste Inventory for Total Liquid and Solid Contributions Used as Starting Solution in Reaction Path Calculations.

Tank	SX-108	SX-109	SX-115
Temperature [C]	100	100	75
H2O [wt%]	30*(27.11)	31.39	75.07
Species	Total Concentration [mol/L]		
H2O	35.09$^{(a)}$	29.15	44.09
Al(OH)4-	3.361	2.56	0.8258
Fe(OH)4-	0.0072	0.0056	0.00211
Ca++	0.0325	0.0252	0.00950
Ni++	0.00649	0.00504	0.00173
K+	0.0739	0.05763	0.01105
Na+	19.6	15.19	3.593
OH-	5.2502#	3.9645#	0.6172#
NO3-	5.46	4.485	1.197
NO2-	4.42	3.225	0.784
Cl-	0.34	0.2651	0.05071
HCO3-	0.0325	0.0252	0.00955
SO4--	0.0277	0.06775	0.0192
CrO4--	0.4128	0.3211	0.05088
SiO2(aq)	0.0933	0.06561	0.01279
Cs+&	6.51^{e}-5	4.38e-5	8.35e-6

(a) Assumed value—value in parentheses is reported by Jones et al. (2000). #-Value determined by charge balance. &-Value corresponds to radioisotope Cs^{137}.

Note: Values are Taken From Jones et al. (2000), Tables 1a and 1b, Derived from the HDW Model with the Exception of OH that is Determined by Charge Balance. For Tank SX-108 Assumed Weight Fraction for H_2O is Used. Moles of Water are Determined from the Reported H_2O Weight Fraction for Tanks SX-109 and SX-115.

D.7.3.3.2 Equilibrium Tank Supernatant Compositions. To determine the equilibrium configuration for the starting tank inventories listed in Table D.7.3.2, the three tank fluids are reacted with minerals and a limited number of aqueous reactions. Diaspore was taken as a candidate mineral for the stable equilibrium assemblage in the high temperature tank fluid in place of gibbsite, which is often found in low temperature weathering environments. Boehmite was not considered, which is found as a metastable phase in natural systems.

To facilitate convergence, dominant species in solution are chosen as primary species. Thus in place of H^+, Al^{3+}, Fe^{3+}, HCO_3^-, and $SiO_{2(aq)}$, the species OH^-, $Al(OH)_4^-$, $Fe(OH)_4^-$, CO_3^{2-}, and $H_2SiO_4^{2-}$ are chosen as primary species. Mass action equations and kinetic reaction rates are then expressed in terms of these species along with the remaining primary species that are chosen as the free ionic species. Secondary species included in the model calculations are: H^+, HCO_3^-, $CO_{2(aq)}$, $CaCO_{3(aq)}$, Al^{3+}, $NaNO_{3(aq)}$, $NaNO_{2(aq)}$, $SiO_{2(aq)}$, $H_3SiO_4^-$, HSO_4^-, Fe^{3+}, $O_{2(aq)}$, and $NH_{3(aq)}$. The effects of any other ion pairs and complexes must be accounted for by the Pitzer virial expansion coefficients and are incorporated into activity coefficient corrections.

Reaction path results for the equilibrated aqueous solution with starting initial total concentrations given in Table D.7.2.2 using the Pitzer activity coefficient algorithm are presented in Tables D.7.3.3, D.7.3.4, and D.7.3.5 for tanks SX-108, SX-109, and SX-115, respectively. These results should be considered as preliminary. As refinements in thermodynamic data and data for the Pitzer virial expansion become available, including incorporation of properties for additional species, these results can be expected to change in detail, although the gross properties of the supernate composition should be approximately the same. For some species, notably cesium, chromium, and nickel, new data could significantly alter the results presented here.

The tank solution compositions are characterized by the dominant species $NaOH$-$NaNO_3$-$NaNO_2$-$Al(OH)_3$. Tank SX-108 has the most concentrated aqueous solution of the three tanks considered. The aqueous solution is close to saturation with respect to solids $NaNO_3$ and $NaNO_2$, although these solids did not actually precipitate out in the equilibrium state. Tank SX-109 is also close to saturation with respect to these solids, but with a saturation index an order of magnitude less compared to tank SX-108. Ionic strengths ranged from 18 mol/kg-H_2O for tank SX-108, 17 mol/kg-H_2O for tank SX-109, and to 3.54 mol/kg-H_2O for tank SX-115. Computed solution densities ranged from 2.1 g/cm^3 for tank SX-108, 1.65 g/cm^3 for tank SX-109, and to 1.13 g/cm^3 for tank SX-115. The concentration of Na^+ is higher for tanks SX-108 and SX-109 than the value given in Table D.7.3.1 for the solubility of $NaNO_3$, but it should be kept in mind that the solubility is based on equal total concentrations of Na^+ and NO_3^-, which does not apply to the tank inventory. The equilibrium solution compositions were all mildly reducing (Eh = -0.05 to -0.227 V) determined by the redox couple NO_3^- and NO_2^-. The pH ranged from approximately 14.11 for tank SX-108, 14.04 for tank SX-109, and to 12.8 for tank SX-115.

Table D.7.3.3. Final Equilibrium State for Tank SX-108 with Pitzer Activity Corrections. (4 Sheets)

```
Temperature [C]      =  1.0000E+02

H2O mole fraction    =  5.3990E-01, weight fraction =  3.0416E-01

activity of water    =  3.4719E-01

osmotic coefficient =  1.2414E+00

ionic strength       =  1.8021E+01

solution density     =  2.0924     [g/cm^3]

pH =  14.110     pe =  -2.941     Eh = -2.1773E-01  [V]

-----------------------------------------------------------------------

primary       molarity  tot [mol/L]  molality  tot [mol/kg] act.  coef.

species

-----------------------------------------------------------------------

Al(OH)4-     3.2692E+00  3.2692E+00  5.1369E+00  5.1369E+00  1.1722E-01

Fe(OH)4-     1.3991E-08  1.3991E-08  2.1985E-08  2.1985E-08  1.7046E-01

Ca++         6.3214E-06  6.3223E-06  9.9328E-06  9.9342E-06  5.7686E-05

Ni++         1.6286E-15  1.6286E-15  2.5590E-15  2.5590E-15  3.1363E-04

K+           7.3900E-02  7.3900E-02  1.1612E-01  1.1612E-01  1.5791E+00

Na+          1.0922E+01  1.9508E+01  1.7162E+01  3.0653E+01  1.1312E+00

OH-          5.1469E+00  5.1469E+00  8.0873E+00  8.0873E+00  3.0454E+00

NO3-         2.1942E-01  5.4600E+00  3.4478E-01  8.5794E+00  7.1761E+00

NO2-         1.0743E+00  4.4200E+00  1.6881E+00  6.9452E+00  3.5848E+00

Cl-          3.4000E-01  3.4000E-01  5.3425E-01  5.3425E-01  3.4661E-01

CO3--        3.2500E-02  3.2500E-02  5.1068E-02  5.1068E-02  3.5812E-03

SO4--        2.7700E-02  2.7700E-02  4.3525E-02  4.3525E-02  2.1583E-04

CrO4--       4.1280E-01  4.1280E-01  6.4864E-01  6.4864E-01  6.3291E-03

H2SiO4--     4.1714E-05  4.3949E-05  6.5546E-05  6.9057E-05  5.7504E+00
```

Table D.7.3.3. Final Equilibrium State for the Tank SX-108 with Pitzer Activity Corrections. (4 Sheets)

```
Cs+          6.5100E-05  6.5100E-05  1.0229E-04  1.0229E-04  1.4259E+00

H2O          3.5326E+01  3.5326E+01  5.5508E+01  5.5508E+01  1.0000E+00

complex               molarity    molality    act.  coef.  log K

--------------------------------------------------------------------

NaNO3(aq)             5.2406       8.2346      1.3819     -0.62538

NaNO2(aq)             3.3457       5.2571      1.0435      -1.3307

H3SiO4-             2.23366E-06  3.50977E-06 0.60733     -0.39666

HCO3-               4.54187E-08  7.13670E-08 0.24347      -2.1713

SiO2(aq)            1.10656E-09  1.73875E-09 9.70835E-02 -3.5660

CaCO3(aq)           9.00668E-10  1.41523E-09  1.0000       4.1305

NH3(aq)             2.08048E-14  3.26909E-14  1.0000      -13.122

H+                  9.81381E-15  1.54206E-14 0.50319      -12.259

HSO4-               6.54809E-17  1.02891E-16 0.71615      -9.2546

CO2(aq)             1.94029E-17  3.04880E-17  31.416      -8.0386

O2(aq)              3.25117E-25  5.10860E-25  1.0000      -23.515

Al+++               5.00050E-28  7.85734E-28 7.36617E-12 -32.451

Fe+++               6.85462E-35  1.07707E-34 4.02967E-12 -31.370

mineral          volume fraction  concentration rate [mol/dm^3/s]

                                     [mol/L]

--------------------------------------------------------------------

Nepheline             4.9724E-03      9.1810E-02  0.0000E+00

Portlandite           1.0741E-03      3.2494E-02 -3.7969E-21

Ni2SiO4               6.1681E-05      1.4476E-03  0.0000E+00

Trevorite             1.8055E-03      3.6111E-03  0.0000E+00

--------------------------------------------------------------------
```

Table D.7.3.3. Final Equilibrium State for Tank SX-108 with Pitzer Activity Corrections. (4 Sheets)

```
                    mineral saturation indices

mineral                        SI          log K

-----------------------------------------------------------------------

Ni2SiO4                    0.00000E+00    3.59130E+01

Trevorite                  0.00000E+00    3.31103E+01

Nepheline                  0.00000E+00    4.21999E+00

Portlandite                0.00000E+00    6.45896E+00

Diaspore                  -5.45988E-02    1.09772E+00

NaNO2(s)                  -7.06677E-02   -2.14063E+00

NaNO3(s)                  -8.08570E-02   -1.76237E+00

Ni(OH)2                   -3.10092E-01    1.50025E+01

Boehmite                  -3.49459E-01    8.02859E-01

Halite                    -1.01748E+00   -1.57316E+00

Gibbsite                  -1.28256E+00    3.29193E-01

Thenardite                -1.73667E+00    7.14285E-01

Goethite                  -2.33614E+00    7.02211E+00

Calcite                   -3.66061E+00    9.31908E+00

Dawsonite                 -5.01541E+00    4.37532E-01

Analcime                  -5.57853E+00    5.63528E+00

Jadeite                   -5.91453E+00    4.51211E+00

Quartz                    -6.69584E+00   -4.89194E-01

SiO2(am)                  -7.58976E+00   -1.38311E+00

Gypsum                    -1.02746E+01    4.91328E+00

Muscovite                 -1.06158E+01    1.03469E+01

K-Feldspar                -1.09181E+01    7.73998E+00
```

Table D.7.3.3. Final Equilibrium State for Tank SX-108 with Pitzer Activity Corrections. (4 Sheets)

```
Paragonite          -1.14430E+01     7.49495E+00

Kaolinite           -1.46121E+01     5.65275E-01

 gas    log partial pressure  pressure [bars]   log K

-----------------------------------------------------------------------

CO2(g)         -13.05            8.9319E-14     -6.0689

O2(g)          -21.19            6.5234E-22     -20.409
```

Table D.7.3.4. Final Equilibrium State for Tank SX-109 with Pitzer Activity Corrections. (4 Sheets)

```
Temperature [C]       =  1.0000E+02

H2O mole fraction     =  5.5796E-01, weight fraction =  3.2228E-01

activity of water     =  3.6293E-01

osmotic coefficient =  1.2793E+00

ionic strength        =  1.6988E+01

solution density      =  1.6504      [g/cm^3]

pH =   14.039      pe =   -2.834      Eh = -2.0980E-01  [V]

-----------------------------------------------------------------------

primary         molarity   tot [mol/L]  molality  tot [mol/kg] act.  coef.

species

-----------------------------------------------------------------------

Al(OH)4-     2.2929E+00  2.2929E+00  4.3109E+00  4.3109E+00  1.4705E-01

Fe(OH)4-     9.6650E-09  9.6650E-09  1.8171E-08  1.8171E-08  1.9796E-01

Ca++         4.7265E-06  4.7275E-06  8.8864E-06  8.8883E-06  8.1746E-05

Ni++         1.2567E-15  1.2567E-15  2.3628E-15  2.3628E-15  4.4024E-04

K+           5.7630E-02  5.7630E-02  1.0835E-01  1.0835E-01  1.5185E+00

Na+          8.5636E+00  1.5126E+01  1.6101E+01  2.8438E+01  1.1969E+00

OH-          4.0870E+00  4.0870E+00  7.6842E+00  7.6842E+00  2.8466E+00

NO3-         2.3753E-01  4.4850E+00  4.4659E-01  8.4324E+00  5.3257E+00

NO2-         9.1047E-01  3.2250E+00  1.7118E+00  6.0634E+00  2.8753E+00

Cl-          2.6510E-01  2.6510E-01  4.9842E-01  4.9842E-01  3.8201E-01

CO3--        2.5200E-02  2.5200E-02  4.7379E-02  4.7379E-02  4.1075E-03

SO4--        6.7750E-02  6.7750E-02  1.2738E-01  1.2738E-01  3.4202E-04

CrO4--       3.2110E-01  3.2110E-01  6.0371E-01  6.0371E-01  6.7060E-03

H2SiO4--     4.4788E-05  4.6654E-05  8.4207E-05  8.7715E-05  3.6916E+00
```

Table D.7.3.4. Final Equilibrium State for Tank SX-109 with Pitzer Activity Corrections. (4 Sheets)

```
Cs+          4.3770E-05  4.3770E-05  8.2293E-05  8.2293E-05  1.3447E+00

H2O          2.9524E+01  2.9524E+01  5.5508E+01  5.5508E+01  1.0000E+00

complex               molarity    molality    act.  coef.  log K

----------------------------------------------------------------------

NaNO3(aq)             4.2475       7.9858      1.3598     -0.62538

NaNO2(aq)             2.3145       4.3516      1.0178      -1.3307

H3SiO4-             1.86508E-06  3.50659E-06 0.59009     -0.39666

HCO3-               4.65612E-08  8.75413E-08 0.24861      -2.1713

CaCO3(aq)           1.01551E-09  1.90930E-09  1.0000        4.1305

SiO2(aq)            7.95526E-10  1.49569E-09 0.11801      -3.5660

NH3(aq)             1.05388E-14  1.98144E-14  1.0000      -13.122

H+                  9.21028E-15  1.73166E-14 0.52741      -12.259

HSO4-               3.10976E-16  5.84677E-16 0.68791      -9.2546

CO2(aq)             2.78316E-17  5.23271E-17  25.814      -8.0386

O2(aq)              3.79565E-25  7.13632E-25  1.0000      -23.515

Al+++               3.16433E-28  5.94937E-28 1.64618E-11 -32.451

Fe+++               4.76373E-35  8.95645E-35 7.47622E-12 -31.370

mineral           volume  fraction  concentration rate [mol/dm^3/s]

                                       [mol/L]

----------------------------------------------------------------------

Diaspore             3.5992E-03      2.0266E-01  0.0000E+00

Nepheline            3.4907E-03      6.4452E-02  3.7969E-21

Portlandite          8.3286E-04      2.5195E-02  0.0000E+00

Ni2SiO4              4.7563E-05      1.1162E-03  0.0000E+00

Trevorite            1.4028E-03      2.8055E-03  6.0750E-24
```

Table D.7.3.4. Final Equilibrium State for Tank SX-109 with Pitzer Activity Corrections. (4 Sheets)

```
-----------------------------------------------------------------------

              mineral saturation indices

mineral                   SI          log K

-----------------------------------------------------------------------

Ni2SiO4               0.00000E+00    3.59130E+01

Trevorite             0.00000E+00    3.31103E+01

Diaspore              0.00000E+00    1.09772E+00

Nepheline             0.00000E+00    4.21999E+00

Portlandite           0.00000E+00    6.45896E+00

NaNO3(s)             -1.01184E-01   -1.76237E+00

NaNO2(s)             -1.63581E-01   -2.14063E+00

Boehmite             -2.94860E-01    8.02859E-01

Ni(OH)2              -3.00520E-01    1.50025E+01

Halite               -1.00858E+00   -1.57316E+00

Thenardite           -1.07676E+00    7.14285E-01

Gibbsite             -1.20871E+00    3.29193E-01

Goethite             -2.32167E+00    7.02211E+00

Calcite              -3.53056E+00    9.31908E+00

Analcime             -5.53836E+00    5.63528E+00

Quartz               -6.67647E+00   -4.89194E-01

SiO2(am)             -7.57039E+00   -1.38311E+00

Gypsum               -9.46674E+00    4.91328E+00

Muscovite            -1.05118E+01    1.03469E+01

K-Feldspar           -1.09232E+01    7.73998E+00

Kaolinite            -1.44449E+01    5.65275E-01
```

Table D.7.3.4. Final Equilibrium State for Tank SX-109 with Pitzer Activity Corrections. (4 Sheets)

```
 gas    log partial pressure  pressure [bars]   log K

----------------------------------------------------------------------

 CO2(g)        -12.90          1.2596E-13      -6.0689

 O2(g)         -21.04          9.1127E-22      -20.409
```

Table D.7.3.5. Final Equilibrium State for Tank SX-115 with Pitzer Activity Corrections. (4 Sheets)

```
Temperature [C]      =  7.5000E+01

H2O mole fraction    =  8.8313E-01, weight fraction =  7.9297E-01

activity of water    =  8.6911E-01

osmotic coefficient =  1.0601E+00

ionic strength       =  3.5377E+00

solution density     =  1.1326      [g/cm^3]

pH =  12.836     pe = -0.6980     Eh = -4.8214E-02  [V]

-----------------------------------------------------------------------

primary        molarity  tot [mol/L]  molality  tot [mol/kg] act.  coef.

species

-----------------------------------------------------------------------

Al(OH)4-     8.0032E-02  8.0032E-02  8.9114E-02  8.9114E-02  5.7008E-01

Fe(OH)4-     7.5584E-09  7.5584E-09  8.4160E-09  8.4160E-09  5.1622E-01

Ca++         5.1707E-05  5.3061E-05  5.7574E-05  5.9081E-05  1.0552E-02

Ni++         1.3837E-15  1.3837E-15  1.5407E-15  1.5407E-15  2.3441E-02

K+           1.1051E-02  1.1051E-02  1.2305E-02  1.2305E-02  4.8143E-01

Na+          3.0741E+00  3.5930E+00  3.4229E+00  4.0007E+00  7.3812E-01

OH-          1.3084E+00  1.3082E+00  1.4569E+00  1.4566E+00  8.0422E-01

NO3-         7.5052E-01  1.1970E+00  8.3568E-01  1.3328E+00  7.6596E-01

NO2-         7.1149E-01  7.8400E-01  7.9222E-01  8.7296E-01  6.0563E-01

Cl-          5.0710E-02  5.0710E-02  5.6464E-02  5.6464E-02  5.9338E-01

CO3--        9.5493E-03  9.5521E-03  1.0633E-02  1.0636E-02  3.2931E-02

SO4--        1.9200E-02  1.9200E-02  2.1379E-02  2.1379E-02  1.9409E-02

CrO4--       5.0880E-02  5.0880E-02  5.6653E-02  5.6653E-02  2.4721E-02

H2SiO4--     1.2292E-02  1.2498E-02  1.3686E-02  1.3916E-02  4.0374E-02
```

Table D.7.3.5. Final Equilibrium State for Tank SX-115 with Pitzer Activity Corrections. (4 Sheets)

```
Cs+          8.3450E-06  8.3450E-06  9.2920E-06  9.2920E-06  4.5352E-01

H2O          4.9852E+01  4.9852E+01  5.5508E+01  5.5509E+01  1.0000E+00

complex                 molarity    molality    act. coef.  log K

--------------------------------------------------------------------

NaNO3(aq)             0.44648      0.49714       1.0600     -0.48697

NaNO2(aq)             7.25094E-02  8.07371E-02  0.92268     -1.2114

H3SiO4-               2.06453E-04  2.29880E-04  0.46978     -0.57927

HCO3-                 1.43903E-06  1.60232E-06  0.39961     -2.6081

CaCO3(aq)             1.35393E-06  1.50756E-06   1.0000      3.8505

SiO2(aq)              5.28990E-08  5.89015E-08  0.72473     -3.9745

H+                    2.66693E-13  2.96955E-13  0.49070     -12.707

CO2(aq)               9.57401E-14  1.06604E-13   1.9926     -9.0185

HSO4-                 4.43485E-14  4.93808E-14  0.54604     -10.057

NH3(aq)               2.35176E-15  2.61861E-15   1.0000     -13.697

O2(aq)                4.60580E-26  5.12843E-26   1.0000     -25.540

Al+++                 1.87913E-29  2.09236E-29  4.48986E-06 -32.458

Fe+++                 3.36743E-35  3.74953E-35  4.06825E-07 -32.179

mineral             volume fraction  concentration rate [mol/dm^3/s]

                                         [mol/L]

--------------------------------------------------------------------

Diaspore               1.3246E-02      7.4581E-01  0.0000E+00

Portlandite            3.1241E-04      9.4510E-03  0.0000E+00

Ni2SiO4                1.4404E-05      3.3805E-04  0.0000E+00

Trevorite              5.2795E-04      1.0559E-03  0.0000E+00

--------------------------------------------------------------------
```

Table D.7.3.5. Final Equilibrium State for Tank SX-115 with Pitzer Activity Corrections. (4 Sheets)

```
                 mineral saturation indices

 mineral                    SI           log K

------------------------------------------------------------------------

 Ni2SiO4                0.00000E+00   3.58827E+01

 Trevorite              0.00000E+00   3.29227E+01

 Diaspore               0.00000E+00   1.30199E+00

 Portlandite            0.00000E+00   6.07884E+00

 Nepheline             -3.59245E-02   4.12903E+00

 Boehmite              -3.27748E-01   9.74242E-01

 Calcite               -6.88410E-01   8.98377E+00

 Gibbsite              -8.03015E-01   5.59903E-01

 Ni(OH)2               -1.29819E+00   1.50065E+01

 NaNO3(s)              -1.37923E+00  -1.58799E+00

 Goethite              -1.41880E+00   6.95113E+00

 NaNO2(s)              -1.95153E+00  -2.03510E+00

 Thenardite            -2.04069E+00   5.36289E-01

 Analcime              -2.17217E+00   5.55394E+00

 Halite                -2.67820E+00  -1.60582E+00

 Quartz                -4.06685E+00  -6.71646E-01

 Gypsum                -5.00658E+00   4.71372E+00

 SiO2(am)              -5.06146E+00  -1.66625E+00

 Muscovite             -5.43289E+00   1.07564E+01

 K-Feldspar            -5.85629E+00   7.72899E+00

 Kaolinite             -8.79011E+00   6.65214E-01

  gas    log partial pressure  pressure [bars]   log K
```

Table D.7.3.5. Final Equilibrium State for Tank SX-115 with Pitzer Activity Corrections. (4 Sheets)

```
-----------------------------------------------------------------------------

CO2(g)          -10.80            1.5814E-11      -7.1467

O2(g)           -22.20            6.3531E-23      -22.447
```

There are two general observations that can be made regarding the derived supernate compositions. First, molality (mol/kg H_2O) and molarity (mol/L) differ significantly from each other for the high ionic strength fluids because of the reduced amount of H_2O present. Second, species activity may be very different from concentration (molality), in some cases by many orders of magnitude for higher valent species. For example the calculated activity coefficients for tank SX-108 for Ca^{2+} and SO_4^{2-} are 5.7686e-5 and 2.1583e-4, respectively, which could indicate the presence of significant ion pairing not explicitly incorporated in the Pitzer formulation. It is interesting to note that the cesium activity coefficient increases with increasing ionic strength, as can be seen by comparing the results for the different tank compositions. If ion pairing with cesium was important, it is expected that the cesium activity coefficient would decrease rather than increase.

Nepheline ($NaAlSiO_4$) formed in tanks SX-108 and SX-109, and was close to saturation in tank SX-115 but did not precipitate. The mineral diaspore is slightly undersaturated in tank SX-108, but saturated in tanks SX-109 and SX-115. This is presumably because somewhat more nepheline precipitated in tank SX-108 thereby reducing the concentration of aluminum. However, it is also possible that if the HDW calculated weight percent of H_2O could have been used, diaspore would also have been saturated in tank SX-108. Portlandite [$Ca(OH)_2$], and nickel bearing minerals Ni_2SiO_4, and trevorite ($NiFe_2O_4$) precipitated in all three tanks. Other aluminosilicate minerals are undersaturated as a result of the high pH and low silica concentration as demonstrated by the saturation indices presented in the tables, in spite of rather high aluminum concentrations remaining in solution. It is interesting to note that solids $NaNO_{3(s)}$ and $NaNO_{2(s)}$ are approximately saturated in the predicted tanks SX-108 and SX-109 liquid phases, and undersaturated in the tank SX-115 liquid.

The calculations predict that Ni^{2+} completely precipitates from solution in the form of Ni_2SiO_4 and trevorite (although the mineral Ni_2SiO_4 would not be expected to form at these low temperatures). However, this could be an artifact of the lack of nickel complexes, such as $NiOH^-$, which were not included in the calculation because of unavailability of thermodynamic data at elevated temperatures. Chromium remains in solution at its initial value. No solid phases could be found which precipitated out chromium and thermodynamic data for speciation of chromium in different redox states was also not available at elevated temperatures.

The sensitivity of the pH of the final equilibrium state on the initial pH is illustrated in Table D.7.3.6 for tank SX-115. As can be seen from the table, for low initial pH the final pH is roughly the same, controlled primarily by mineral reactions and is insensitive to the initial pH used in the reaction path calculation. The sodium concentration is determined by charge balance, and so must increase as the OH^- concentration increases. This is an important result because it indicates that the final equilibrium state is largely controlled by reaction with solids. It would thus appear to be important to determine the solid composition of the tank waste in order to provide a better estimate of the composition of the liquid phase.

Table D.7.3.6. Sensitivity of Final pH, Eh, and Ionic Strength on the Initial OH- Concentration for Tank SX-115.

Initial OH^- [mol/L]	Initial pH	Final pH	Total Na^+ [mol/L]	Eh [V]	Ionic Strength [mol/kg H_2O]
5.0	13.347	13.381	8.0108	-0.887	5.1449
1.0	12.720	12.943	4.0106	-0.559	3.7552
0.6172	12.494	12.836	3.5930	-0.482	3.5377
0.1	11.739	12.660	3.1087	-0.356	3.2526
0.001	9.7429	12.605	2.9956	-0.316	3.1783
0.00001	7.7441	12.595	2.9768	-0.309	3.1663

The Debye-Hückel activity correction model gave qualitatively similar results as the Pitzer model for the tank SX-115 composition. The predicted equilibrium pH was approximately the same, and with the exception of calcite that formed in the Debye-Hückel model, the same stable mineral assemblage formed. However, the fluid composition was quantitatively different and the amounts of minerals that precipitated was also different between the two activity coefficient models.

Temperature was found to be an important factor in determining the liquid equilibrium concentration. Attempting to perform reaction path calculations at 25 °C led to unrealistically high pH values on the order of 15 or greater.

D.7.3.3.3 Comparison with Jones et al. (2000). Jones et al. (2000) used the computer code ESP, from OLI Systems, to calculate tank supernate compositions. The ESP code is proprietary software, which makes it difficult to obtain a deeper understanding of the algorithms and origin of databases used by the code and to more fully understand its computed results. Felmy (2000) noted certain problems with the ESP database in comparison with the code GMIN when analyzing several different waste forms. In addition to differences in thermodynamic data, there are undoubtedly also differences in the activity coefficient algorithms used by the two codes that could lead to different supernate compositions.

Although the same tank waste inventories are used in this study as in Jones et al. (2000), because of the different approaches used for determining charge balance and the concentration of OH^-, the compositions presented in this study are more concentrated than the results presented by Jones et al. (2000). It should also be noted that there appears to be a discrepancy in overall mass balance in the results presented by Jones et al. (2000), although it is not clear if this was caused by an incorrect labeling of the concentration units as molarity rather than molality.

Calculations were also carried out with FLOTRAN using the prescription for charge balance and OH- concentration suggested by Jones et al. (2000). There were several differences in the results presented by Jones et al. (2000) using the ESP code. Thenardite (Na_2SO_4), goethite (FeOOH), and calcite ($CaCO_3$) were predicted by Jones et al. (2000) to form, but remained undersaturated in the FLOTRAN simulations. In place of $Ni(OH)_2$, FLOTRAN predicted a nickel silicate

(Ni_2SiO_4) and trevorite to form, although as noted above Ni_2SiO_4 is only expected to form at higher temperatures.

D.7.3.3.4 Important Uncertainties. Because of the large uncertainties involved, both in the reaction path calculation itself resulting from uncertainty in thermodynamic data and activity corrections, and in the HDW derived initial tank waste inventory, these calculations can only be viewed at best as rough estimates of the composition of the leaking tank fluid. Limitations exist on the availability of thermodynamic data for minerals and aqueous species, and activity coefficient correlation data for use in the Pitzer model over the range of temperatures needed. In addition, uncertainties arise from the possibility of nucleation kinetics inhibiting mineral reactions even if thermodynamically feasible (such as formation of Ni_2SiO_4 noted above). In this regard, knowledge of the actual minerals that have formed in the tanks would be useful in validating the model predictions. It is emphasized that the final equilibrium state is independent of the kinetic rates used in the real-time reaction path calculations presented here, and therefore these values play no role in the uncertainty of the simulations.

Perhaps the greatest uncertainty in these calculations is the estimate of the initial tank waste inventory. Agnew and Corbin (1998, Table 4), for example, derived waste inventories for several tanks including tank SX-108. The inventory they estimated for tank SX-108 resulted in a significantly lower Na^+ concentration compared to that calculated by Jones et al. (2000), which resulted in a slightly acidic starting pH. The final pH, however, was still above 12 as a result of mineral precipitation reactions. Apparently, Agnew and Corbin (1998) derived their results by averaging predicted inventories from a number of tanks over some period in time (Tom Jones, private communication), whereas Jones et al. (2000) attempted to obtain each specific tank inventory at the most probable time the tank leaked. Much work still remains to be done to resolve discrepancies between different authors and to obtain representative tank supernate compositions that can be used for modeling migration of radionuclides in the vadose zone.

It will be difficult to observe fluids in the vadose zone with compositions directly comparable to the tank fluids because of various physical and chemical effects that could either dilute or concentrate them. Mixing with ambient pore water and infiltrating surface water will result in dilution. Changes in chemical composition can also be expected as a result of interaction of the leaked tank fluid with sediment minerals. Concentration could occur due to evaporative effects caused by the heat released from the high temperature tanks such as tanks SX-108 and SX-109.

Finally, in order to integrate the tank supernate compositions derived here with reactive transport simulations, it is also necessary to provide an equation of state for the fluid density and constitute relation for viscosity as functions of temperature, pressure and composition. There exist equations of state for simplified systems involving NaCl and $NaNO_3$, but not for the multicomponent fluids of enormous complexity, which have leaked from some of the Hanford storage tanks.

D.7.3.4 Conclusions and Implications

The calculations for the supernate tank fluid presented in this contribution suggest that extremely high ionic strength fluids have leaked from several of the tanks in the SX tank farm. The high sodium concentration associated with these fluids could help explain the advanced migration of cesium that has been observed in the vadose zone beneath tank SX-108. Further work and field investigations are required to understand the effect these fluids have had on alteration of the Hanford sediments and their effect on retardation of radionuclides in the vadose zone.

D.7.3.5 References

Agnew, S. F., 1997, *Hanford Tank Chemical and Radionuclide Inventories: HDW Model. Rev. 4,* LA-UR-96-3800, Los Alamos National Laboratory, Los Alamos, New Mexico.

Agnew, S. F., and R. A. Corbin, 1998, *Analysis of SX Farm Leak Histories--Historical Leak Model (HLM)*, HNF-3233, LA-UR-96-3537, Prepared by Los Alamos National Laboratory, Los Alamos, New Mexico, for U.S. Department of Energy Richland Operation Office and Project Hanford Management Company, Lockheed Martin Hanford Corporation, Richland, Washington.

Felmy, A. R., 2000, *Thermodynamic Modeling of Sr/TRU Removal*, BNFL-RPT-037, Rev. 0, PNWD-3044, Pacific Northwest National Laboratory, Richland, Washington.

Felmy, A. R, 1995, "GMIN, A Computerized Chemical Equilibrium Program Using a Constrained Minimization of the Gibbs Free Energy: Summary Report," *Soil Science Society of America*, Special Publication Vol. 42:377-407.

Harvie, C. E., J. P. Greenberg, and J. H. Weare, 1987, "A chemical equilibrium algorithm for highly non-ideal multiphase systems: Free energy minimization," *Geochimica et. Cosmochimica Acta*, Vol. 51:1045-1057.

Jones, T. E., R. A. Watrous, and G. T. Maclean, 2000, *Inventory Estimates for Single-Shell Tank Leaks in S and SX Tank Farms, RPP-6285*, Rev. 0, U.S. Department of Energy, Office of River Protection, Richland, Washington.

Lichtner, P. C., 2001, *FLOTRAN User Manual*, LA-UR-01-2349, Los Alamos National Laboratory, Los Alamos, New Mexico.

Pitzer, K. S., 1973, "Thermodynamics of Electrolytes. I. Theoretical Basis and General Equations," *Journal of Physical Chemistry*, Vol. 77:268-277.

Pitzer, K. S., 1991, *Activity Coefficients in Electrolyte Solutions. 2nd Edition,*" CRC Press, Boca Raton, Florida, p. 542.

Prigogine, I., and R. Defay, 1954, *Chemical Thermodynamics*, Longmans, pp. 543.

Serne, R. J., 2000, *S-SX Sediment Characterization Results and Issues*, Pacific Northwest National Laboratory, Richland, Washington.

D.7.4 EVALUATION OF THE FIELD EXCHANGE CAPACITY OF HANFORD SEDIMENTS WITH IMPLICATIONS FOR ^{137}CS MIGRATION

Carl I. Steefel[1], and Steve B. Yabusaki[2]

[1]Lawrence Livermore National Laboratory, Livermore, California 94550

[2]Pacific Northwest National Laboratory, Richland, Washington 99352

D.7.4.1 Introduction

While the ion exchange parameters extracted from the batch experiments of Zachara et al. (2001) (Section D.3.1) and the column experiments of Carroll et al. (2001) (Section D.3.3) provide an excellent basis for modeling cesium reactive transport under experimental conditions, it remains to be demonstrated that the same ion exchange model is capable of describing cesium transport in the field. The eventual goal of the modeling of the field transport of cesium is twofold. First, to understand the processes taking place at tanks like tank SX-108 where cesium penetration to significant depths is observed, and second, to use this new-found understanding for improved scientifically credible predictions of future behavior. The leak volume and duration at tank SX-108, however, is poorly known, and the interpretation of cesium migration is complicated by the effects of coupled processes like in-tank boiling and subsurface mineral alteration. In contrast, the volume and duration of the tank SX-115 leak is well known. Tank SX-115 was below boiling when the leak occurred in 1965 over a 1-week period and the tank remained below boiling subsequently. A borehole, 299-W23-19, (R. S. Serne, personal communication 2001) was sited within about 2 m of the edge of tank SX-115, close to the location of the largest of three leaks developed below this tank (Raymond and Shdo 1966). Through analysis of water extractable ions, Serne (personal communication 2001) identified a well-defined chromatographic separation of cations in 299-W23-19 borehole that can be attributed to the ion exchange of waste-derived cations. A peak of sodium occurred at shallower depths in the borehole and is clearly separated from calcium and magnesium peaks which occurred at greater depth. Technetium and nitrate, apparently acting as nonreactive tracers, coincided approximately with the calcium and magnesium fronts. Cesium was not detected in the W23-19 borehole, but was encountered in shallow horizontal wells drilled directly below tank SX-115 (Raymond and Shdo 1966).

Although there is little direct interest in sodium, calcium, magnesium, and potassium as contaminants, these cations are very useful in establishing whether the multicomponent ion exchange model developed to describe cesium exchange and transport in the batch and column experiments can be applied to the field. A key question is whether the *effective* exchange capacity of the Hanford sediments is the same as that measured in batch and column experiments, or whether various hydrologic physical processes may have caused a reduction in cesium retardation. By *effective* exchange capacity, we are referring *not* to the CEC determined with conventional analytical methods (e.g., ^{22}Na isotopic dilution), but rather to the effective CEC needed to account for the observed chromatographic separation (if any) of the cations in the field setting. By applying the self-consistent, multicomponent cation exchange model developed for the column experiments (Carroll et al. 2001) to the distribution of the cations sodium, calcium, potassium, magnesium, and cesium below tank SX-115, we can make a direct comparison of the laboratory and field effective exchange capacities.

D.7.4.2 Determination of Ion Exchange Parameters

Ion exchange parameters were determined by fitting CECs and ion selectivity coefficients to both the batch experimental data of Zachara et al. (2001) (Section D.3.1) and to the column data of Carroll et al. (2001) (Section D.3.3). The fitting procedure used a strong weighting of the column experiments so as to favor these results where the batch and column results were in conflict (see discussion in Carroll et al. 2001). The fitting was carried out with the general optimization code PEST used in conjunction with speciation calculations carried out by CRUNCH. In this way, the resulting parameter set is fully compatible with the reactive transport simulations of cesium migration in both the column experiments and the field which were also carried out with CRUNCH. In contrast to the fit of the data presented by Zachara et al. (2001), the fits presented here include both activity coefficient corrections and aqueous complexation as described further below. Equally important, however, was the inclusion of batch experimental data on the Cs-Na, Cs-Ca, and Cs-K binary systems (Zachara et al. 2001) and a Cs-Na-K column experiment (Carroll et al. 2001) in a single global optimization to arrive at a consistent set of numbers that can be used to the describe the multicomponent system.

The selectivity coefficients in Table D.7.4.1 were fit assuming the Gapon activity convention:

$$Cs^{+} + M_{1/m}X \leftrightarrow CsX + \tfrac{1}{m} M \qquad \text{(D.7.4.1)}$$

where M is the exchanging cation (Na^{+}, K^{+}, Ca^{2+}), and m is its charge (Appelo and Postma 1996). The exchange reactions can then be used to write a standard mass action equation for binary Cs-M exchange:

$$K_{M/Cs} = \frac{[M_{1/m}X][Cs^{+}]}{[CsX][M]^{1/m}} \qquad \text{(D.7.4.2)}$$

In agreement with the conclusions of Zachara et al. (2001), multiple exchange sites were needed to capture the large range in the cesium Kd as a function of cesium concentration. We have fitted cesium exchange with a three-site model because it provides a substantially better fit of the Cs-Ca and, to a lesser extent, the Cs-Na exchange data. The three-site model was used because of the improvement it gave in matching the batch data; however, there is no clear physical evidence for more than two distinct sites actually present in the Hanford sediments.

Table D.7.4.1. Cesium Exchange Selectivity Coefficients, Ion Pair Formation Constants, and CECs Derived From Fits of Batch and Column Experiments, with Weighting of Column Exchange Experiments.

Exchange Reaction	Fitted Parameters Log K
$NaX1 + Cs^+ = Na^+ + CsX1$	6.85
$NaX2 + Cs^+ = Na^+ + CsX2$	3.00
$NaX3 + Cs^+ = Na^+ + CsX3$	2.10
$KX1 + Cs^+ = K^+ + CsX1$	4.50
$KX2 + Cs^+ = K^+ + CsX2$	3.77
$KX3 + Cs^+ = K^+ + CsX3$	0.70
$Ca_{0.5}X1 + Cs^+ = 0.5Ca^{2+} + CsX1$	7.13
$Ca_{0.5}X2 + Cs^+ = 0.5Ca^{2+} + CsX2$	6.46
$Ca_{0.5}X3 + Cs^+ = 0.5Ca^{2+} + CsX3$	1.58
Ion Pairs	Effective Log K (fitted)
$NaNO_3(aq) \rightarrow Na^+ + NO_3$-	0.26
$CsNO_3(aq) \rightarrow Cs^+ + NO_3$-	0.50
Bdot parameter (Cs-X)	-8.90E-02
Exchange Site	**CEC (μeq g^{-1})**
Site 1	0.037
Site 2	0.14
Site 3	102

Note: Mg Selectivity Coefficients were Assumed to be the Same as Those for Ca.

We chose to fit the CEC rather than using an independently determined value because there is significant uncertainty in the CEC determined for these Hanford sediments. The highest value for the CEC was determined by cation elution during preliminary washes of the sediment (CEC = 138 μeq/g) (Carroll et al. 2001). Lower values of the CEC were determined by ^{22}Na and ^{45}Ca isotopic equilibria measurements (CEC = 46 ±3 μeq/g) (Zachara et al. 2001; Carroll et al. 2001). More important than the uncertainty associated with the CEC, however, is the fact that CEC determinations for different cations give different values. For describing multicomponent ion exchange in the field, it is essential to arrive at a single set of CEC(s). Except for the low value of 46 μeq/g (this value results in a poor fit of the experimental data at high cesium concentrations), any of the other CEC values could have been used as a constraint in the fitting procedure. This is because the combined fit of CECs and selectivity coefficients is not unique as shown by the strong inverse correlation between selectivity coefficients for a particular site and the CEC of that site. It is the combination of CECs and selectivity coefficients that control the migration rate of the various cations rather than one parameter or another acting by itself.

The important point, therefore, is to use a *combined* set of CECs and selectivity coefficients that match the results of the batch and column experiments.

We used a standard Debye-Hückel formulation for activity coefficients augmented with fitting parameters for ion pair formation to describe solution activities accurately in the highly concentrated and variable Hanford system. Free cation activities were calculated by adjusting the effective log Ks for the ion pairs $CsNO_{3(aq)}$, $Ca(NO_3)_{2(aq)}$, and $NaNO_{3(aq)}$ to match free cation activities determined with the Pitzer approach as implemented in the code GMIN (Felmy 1995). In this approach, the effective log Ks for the ion pairs attempt to capture the effect of *both* the specific ion pair log K in the GMIN database (not the same as the effective log K proposed here) *and* the parameters describing the cation-anion interaction (the interaction parameters) in the Pitzer formulation. This was carried out in practice by treating the GMIN-calculated ion activities at 0.1, 1, and 5 M $NaNO_3$ as data which must be honored in the optimization procedure. Using this approach, we were able to simulate quite closely the species activities (not activity coefficients) calculated with the Pitzer approach up to 5 M $NaNO_3$. It is unclear, however, whether this approach can be extended significantly beyond 5M $NaNO_3$. In terms of ion exchange, however, the most important quantity is the *ratio* of activity corrections (for example, Na^+ to Cs^+) and not the absolute magnitude of the correction.

It was also necessary to include an empirical activity coefficient correction for the various Cs exchange species in order to capture the ionic strength dependence of the exchange. This took the form of a standard "Bdot" correction in the extended Debye-Hückel equation, but was applied only to the exchange species activities:

$$\ln \gamma_{Cs-X} = BI \qquad \text{(D.7.4.3)}$$

D.7.4.3 Multiphase Flow, Heat Transport, and Reactive Transport Simulations of the Tank SX-115 Leak

The tank SX-115 leak and subsequent plume migration through the vadose zone was modeled by coupling the reactive transport code CRUNCH to the multiphase flow and heat transport code NUFT (Nitao 1998). CRUNCH reads in a transient flow, liquid saturation, and temperature fields generated by NUFT. The simulation begins in 1959 when tank SX-115 was constructed and ends in the year 1999 when borehole 299-W23-19 was drilled. NUFT was run for 10,000 years prior to the emplacement of the tank using a constant infiltration rate of 100 mm/yr to obtain a steady-state initial flow field and liquid saturation. A three-dimensional grid was considered to be necessary to capture the potential effects of a dipping gravel layer and the lack of symmetry with respect to the large leak located on the edge of the tank near borehole 299-W23-19. Nineteen and 17 cells of 2.33-m spacing were used in the X and Y direction respectively, while 34 cells of 2-m spacing were used in the Z (vertical) direction. Tank SX-115 was maintained at a constant temperature of 70 °C throughout the period of the simulation (1959-1999). The data of Raymond and Shdo (1966) indicate that three distinct leaks developed below tank SX-115 (Figure D.7.4.1). Although it is not clear that all three leaks occurred during the same 1-week period in 1965, we have assumed that the largest of the leaks developed on the edge of the tank near well 299-W23-19 (the only one we have modeled) and consisted of 22,800 gallons, which 40% of the total 57,000 gallons lost during this period.

Figure D.7.4.1. Distribution of Contamination Below Tank SX-115 (from Raymond and Shdo 1966).

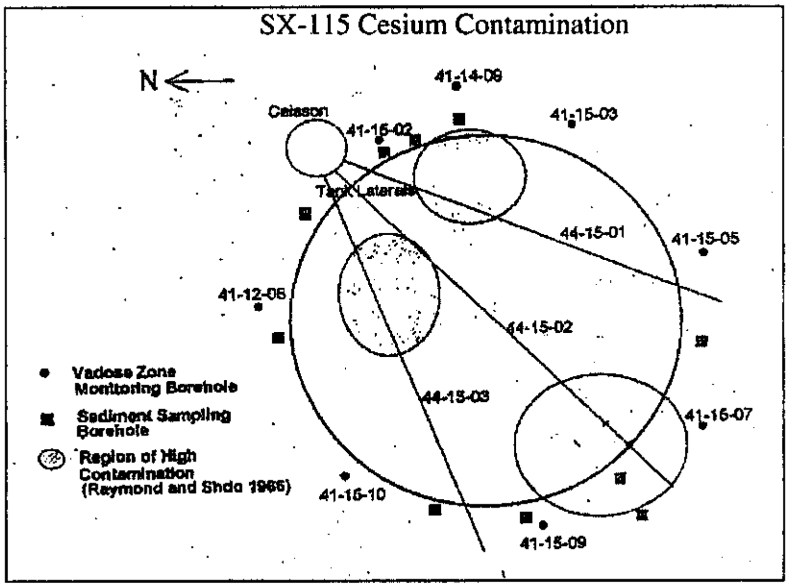
SX-115 Cesium Contamination
N
Caisson
Tank Laterals
41-14-09
41-15-02
41-15-03
44-15-01
41-15-05
41-12-06
44-15-02
44-15-03
41-15-07
41-15-10
41-15-09
● Vadose Zone Monitoring Borehole
■ Sediment Sampling Borehole
Region of High Contamination (Raymond and Shdo 1966)

D.7.4.3.1 Flow and Heat Transport Calculations. Hydrologic parameters used in the simulations are those given in Khaleel et al. (2001). These flow and transport parameters represent effective (upscaled) values for the Hanford vadose zone and are broken out by the strata present at the S and SX tank farms (Table D.7.4.2).

Table D.7.4.2. Composite van Genuchten-Mualem Parameters for Various Strata at the S and SX Tank Farms (Khaleel et al. 2001).

Strata	Porosity	Residual Water Content	α (1/cm)	n	Vertical Ks (cm/s)	Horizontal Ks (cm/s)
Backfill	0.2688	0.0151	0.0197	1.4194	5.15E-04	5.15E-04
Fine sand (upper and lower)	0.3819	010443	0.0117	1.6162	9.88E-05	2.96E-04
Gravelly sand-sandy gravel	0.2126	0.0032	0.0141	1.3730	2.62E-04	7.86E-04
Plio-pleistocene	0.4349	0.0665	0.0085	1.8512	2.40E-04	7.20E-04
Sandy gravel	0.1380	0.0100	0.0210	1.3740	5.60E-04	1.68E-03

The distribution of permeabilities used in the simulations are shown in an X-Z section through tank SX-115 and 299-W23-19 borehole (Figure D.7.4.2). Except for the backfill, all of the strata are assumed to have horizontal conductivities 3 times their vertical conductivity. Based on the shape of cesium contamination detected in horizontal boreholes 10 feet below tank SX-115 (Raymond and Shdo 1966), the assumption of an anistropy ratio of 3:1 appears to be reasonable. A larger anisotropy ratio would have spread the cesium contamination horizontally further than is observed if it can be assumed that the retardation of cesium is approximately the same in the horizontal and vertical directions. The tank is assumed to be impermeable. Boundary conditions for the simulation consisted of no-flow boundaries on the side of the domain and fixed pressure boundary conditions at the bottom (the water table which is assumed to have a fixed depth) and the surface. A constant infiltration rate of 100 mm/yr is assumed at the top of the domain.

Figure D.7.4.2. Distribution of Permeabilities in an X-Z Section Through the Three-Dimensional Model Domain.

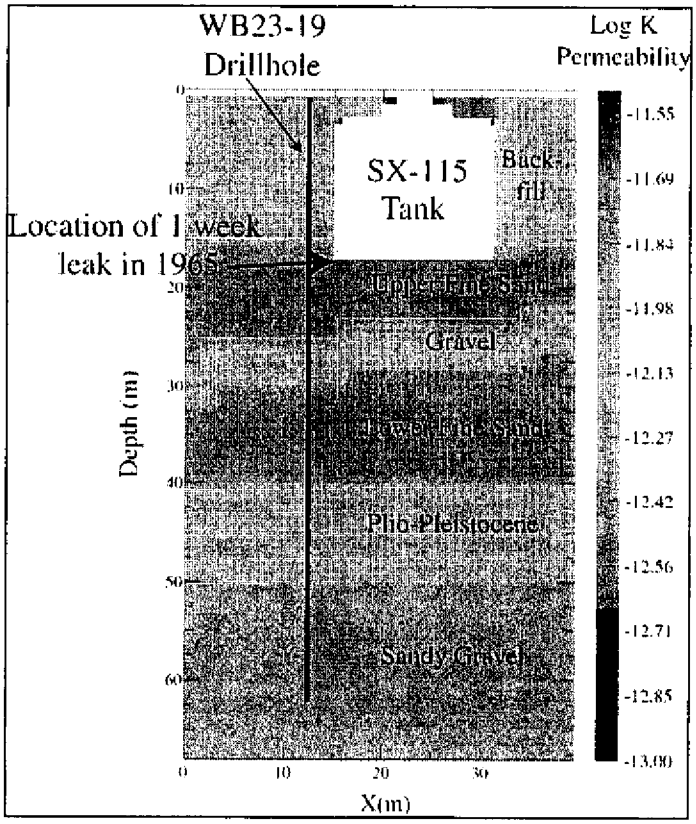

Note: See Table D.7.4.1 for the Various Hydrologic Parameters Used for Each of the Strata. The Upper and Lower Fine Sand Units are Assumed to have the Same Hydrologic Properties.

D.7.4.3.2 Chemical Initial and Boundary Conditions. Much of the point of the modeling exercise described here is to see how well various geochemical parameters taken from batch (Zachara et al. 2001; Section D.3.1) and column experiments (Carroll et al. 2001; Section D.3.3) can be used to describe the field transport of cesium and the other relevant cations. As discussed above, while sodium, calcium, magnesium, and potassium are not themselves significant contaminants, their behavior can be used to evaluate the field exchange capacity of the Hanford sediments. In addition, their behavior can be used as a partial test of the multicomponent ion exchange model. Accordingly, an effort was made to minimize calibration of the model so as to be able to evaluate directly the applicability of the experimental studies to the field.

The cation exchange capacities of the strata were assumed to be those determined by fitting of both batch and column experiments (Table D.7.4.1). While our best estimate of the actual CEC may change with further analysis (now under way), the key point is to use a combined set of CECs and selectivity coefficients that honor the column and batch experiments. With this approach, we are in a good position to make a direct comparison of the laboratory and field cation exchange behavior. The initial composition of the exchangers is calculated by using aqueous concentrations of the cations that give the total masses of magnesium, calcium, and potassium eluted by flushing the Hanford sediment separately with $NaNO_3$ (reported in Carroll et al. 2001). Sodium could not be estimated easily because of the flush with $NaNO_3$, but should be present in lower concentrations on the exchanger than any of the other cations.

The boundary condition at the top of the domain is assumed to be the same as the initial aqueous concentrations given in Table D.7.4.3. While rainwater will be considerably more dilute than these values, it is assumed that the infiltrating water evolves chemically before reaching the stratigraphic level of the Hanford sediments below the tanks. More important is the composition of the fluid leaking from the tank. Lichtner (2001) (Section D.7.3) has presented results based on reaction path modeling of the tank liquors using an approach similar to that employed by Jones et al. (2000). His results for tank SX-115 were used as a "base-case" for the simulations—a variety of runs were then carried out by diluting the "base-case" tank composition of Lichtner (2001). There is some anecdotal evidence at this point (not yet fully documented) that dilution of tank SX-115 did occur immediately before the 1965 leak and may actually have contributed to reopening an older leak.

Table D.7.4.3. Initial Aqueous and Exchange Compositions of the Hanford Sediment Estimated From Column Experiments and Simulations of Tank SX-115 Leak (field estimate).

Chemical component	Aqueous concentration (M)	Exchange concentration 5 M $NaNO_3$ column (eq/g)	Exchange concentration 1 M $NaNO_3$ column (eq/g)	Exchange concentration field estimate (eq/g)
PH	8.0			
$HCO3^-$	5.70E-04			
$NO3^-$	1.00E-06			
Ca^{++}	2.15E-03	8.43E-05	8.34E-05	7.09E-05
Na^+	1.00E-03			
K^+	1.94E-05	1.19E-05	4.8E-06	1.95E-05
Mg^{++}	5.00E-05	2.07E-05	1.78E-05	1.05E-05
Cl^-	6.31E-03			
$SO4^{--}$	1.00E-05			
Cs^+	0.0			

D.7.4.3.3 Model Results-Flow and Temperature. Results presented here represent a preliminary attempt to verify that the ion exchange parameters determined from batch and column experiments can be combined with hydrologic parameters appropriate for the Hanford Formation to describe cesium, sodium, potassium, calcium, and magnesium reactive transport in Hanford sediments. Technetium and nitrate serve as nonreactive tracers that can be used to assess how well the flow regime is captured.

Simulated temperatures and liquid saturations (from NUFT) are shown at a point in time corresponding to the end of the 1-week leak event in 1965 (Figure D.7.4.3). Also shown are streamline plots of the flow field before and during the tank leak. The much discussed "umbrella effect," where infiltration is funneled along the sides of the tank, shows up clearly in the closer spacing of streamlines along the tank edge. Both fluid velocity vectors and streamlines show the effect of the tank leak, with the enhancement in flow rates presumably due to the considerable weight of the fluid in the tank now allowed to penetrate into the vadose zone. The effect of the leak also appears in the temperature and liquid saturation fields.

Figure D.7.4.3. Temperatures, Liquid Saturations, and Streamlines Simulated by NUFT.

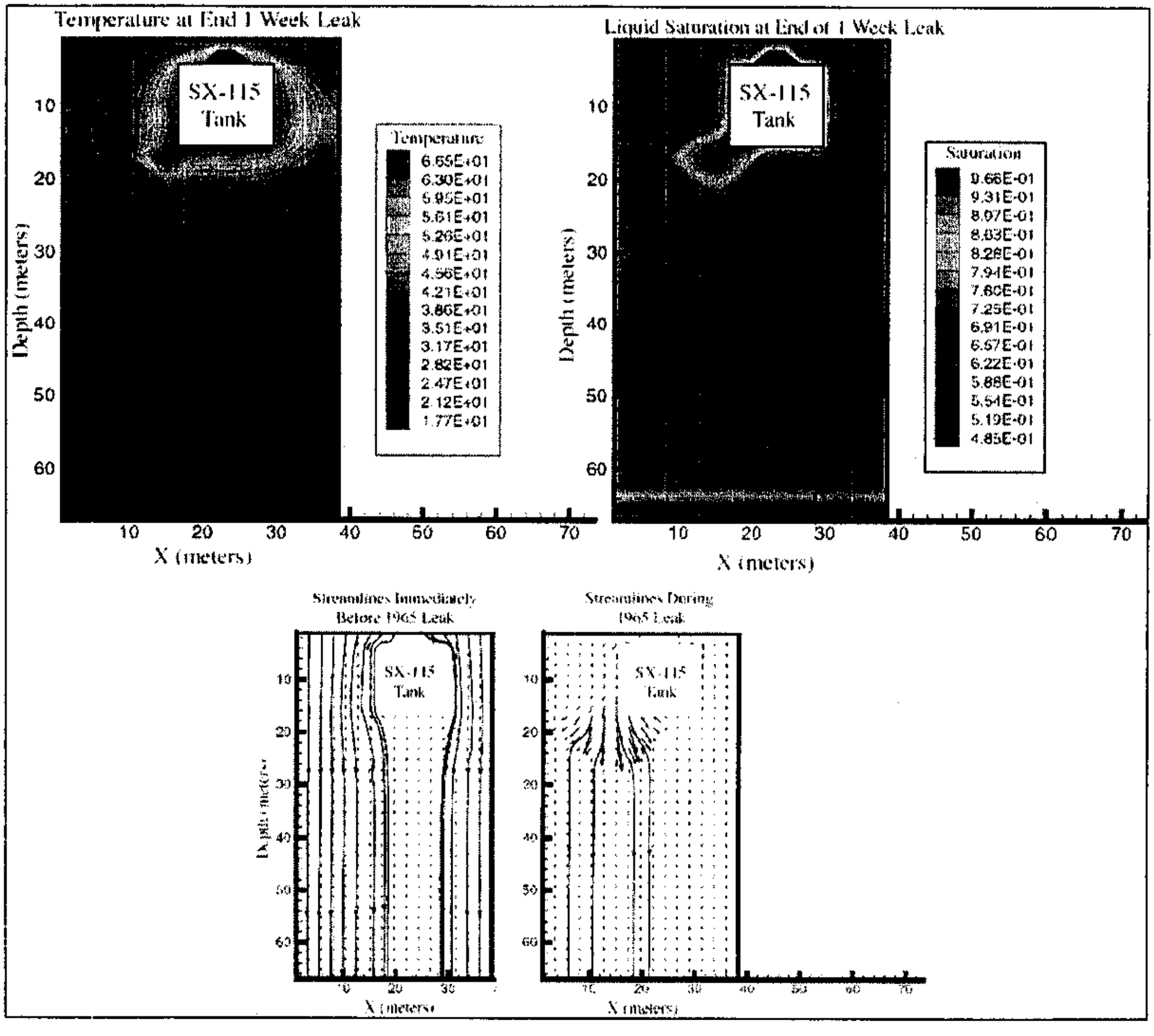

D.7.4.3.4 Model Results-Geochemistry. The simulated spatial distribution of the important chemical components associated with the tank SX-115 leak are shown in a series of X-Z sections cutting through tank SX-115 and 299-W23-19 borehole (Figure D.7.4.4). The results in the year 1999 predict that the nitrate (tracer) plume should have penetrated to a depth of 45 m below the ground surface. Na, in contrast, is noticeably retarded, with the leading edge of the plume occurring at about 39 to 40 m depth. The slightly elevated sodium values (in pale blue) above the main part of the aqueous Na plume is a zone in which sodium is concentrated on exchange sites and is gradually being eluted by the infiltrating ambient rainwater/soil water. Since the infiltrating water is dilute, Na is only slowly eluted, and concentrations in the aqueous phase in this region remain low. Ca and Mg form well-defined plumes at the leading edge of the Na front. K forms a more diffuse plume that straddles the sodium and calcium plumes. Cs is predicted to be strongly retarded, with very little migration occurring beyond the site of the tank leak.

Figure D.7.4.4. Two-Dimensional X-Z Slice Through the Three-Dimensional Model Domain Corresponding to the Year 1999.

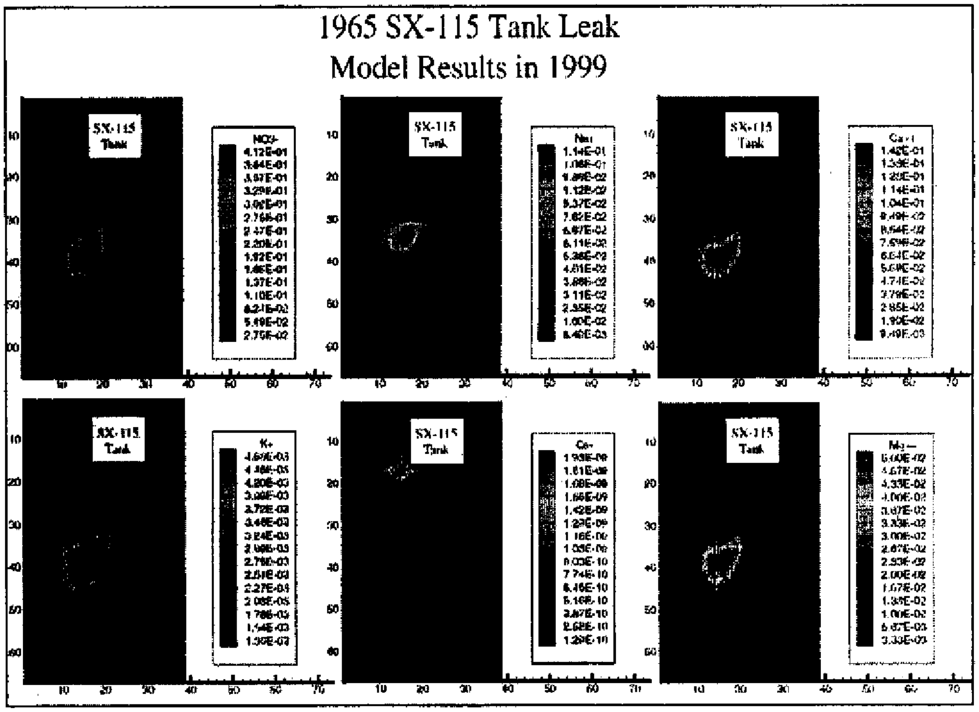

Note: The section cuts through both Tank SX-115 and Well 299-W23-19.

A direct comparison of aqueous geochemical data collected from the 299-W23-19 borehole and the simulations is shown in Figure D.7.4.5. The simulations capture quite closely the leading edge of all the exchange fronts, although the match with the trailing portions of the plumes is not as good. However, the simulations even capture some aspects of the complicated shape of the cation plumes, including the Na "shoulder" above the main part of the Na plume in the aqueous phase. This presumably represents Na being gradually eluted from exchange sites above the main zone of sodium in the aqueous phase. The simulated widths of the Mg, Ca and K plumes, are slightly too broad, although this may be the result of an overly coarse discretization.

The relatively broader shape of the K plume, which shows up clearly in the data, is captured in an approximate fashion by the simulations. Cs, although not detected in significant amounts in the 299-W23-19 borehole, is known to occur very close to the bottom of tank SX-115 (see Figure D.7.4.3 and Raymond and Shdo 1966).

Figure D.7.4.5. Comparison of Three-Dimensional Simulation Results for the Tank SX-115 Leak in 1999 and Geochemical Data for the 299-W23-19 Borehole.

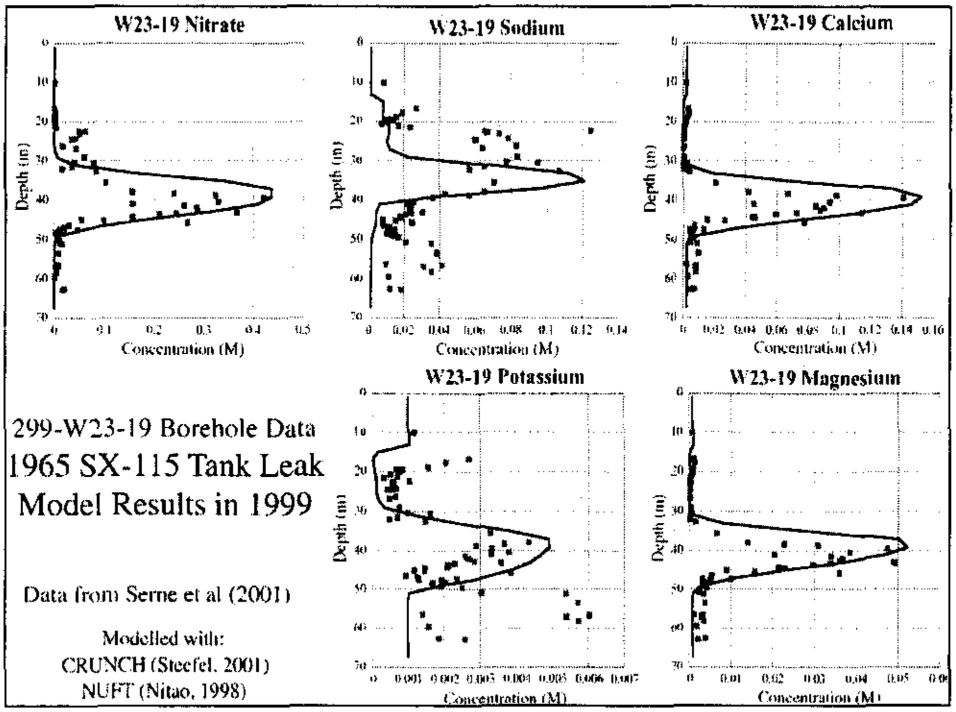

Note: The simulation results do not include any calibration of the experimental (Batch and Column) CECs and ion exchange selectivity coefficients or the independently estimated hydrologic parameters.

It is important to point out that these results do not include any calibration of either the independently estimated hydrologic parameters (taken directly from Khaleel et al. 2001) or the laboratory-determined (batch and column) CECs and ion exchange selectivity coefficients.
In order to match the absolute concentration of Na in the borehole, the composition of the tank leak fluid had to be adjusted (see Table D.7.4.4). The "best fit" value represents a dilution of the estimate provided by Lichtner (2001) (Section D.7.3) by about a factor of 3.5. To obtain a match in the absolute concentrations of Ca, Mg, and K, the initial exchanger compositions had to be adjusted from what they were determined to be in the column experiments (Table D.7.4.3).
The "best fit" from matching the field data indicate a Ca exchange concentration quite close to that estimated from two of the column experiments (about 8×10^{-5} equivalents/g). The exchange concentration of magnesium determined in the column experiments, however, had to be adjusted downward by about a factor of 2 to obtain a match with the field data. Potassium had to be increased by factors ranging 2 to 4 over the values estimated from the column experiments.

Table D.7.4.4. Composition of Tank SX-115 Leak Used in Simulations.

Chemical Component	Base Case (M)	This Report (M)
PH	12.8	10.5
HCO_3^-	9.55E-03	2.70E-03
NO_3^-	1.19E+00	1.21
Ca^{++}	5.30E-05	1.48E-05
Na^+	3.59E+00	1.30
K^+	1.10E-02	4.90E-03
Mg^{++}	5.30E-05	2.37E-05
Cl^-	5.07E-02	1.43E-02
SO_4^{--}	1.92E-02	3.10E-03
Cs^+	8.25E-05	2.24E-05

Note: The "Base Case" represents a simplification of an estimate made by Lichtner (2001), while "This Report" refers to a preliminary "Best Fit" based on matching the field data.

D.7.4.4 Conclusions and Implications

Flow and reactive transport modeling of the tank SX-115 leak indicates that the ion exchange model developed by Zachara et al. (2001) and Carroll et al. (2001) provides an excellent basis for further field simulations of cesium transport. The column experiments provide more direct information on the effect of competing salt concentrations on Cs migration, but the field and modeling study carried out here is very valuable in establishing the effective field exchange capacity of the Hanford sediments. The well-defined chromatographic separation of the cations clearly demonstrates that the effective field CEC is close to the value determined independently in the batch and column experiments. Various hydrologic mechanisms for "bypassing" exchange sites (fast flow pathways or transport-limited sorption in immobile water zones), while not necessarily discounted altogether, do not appear to have had a large effect on the extent of cation exchange.

While there is still significant uncertainty with respect to the appropriate hydrogeologic parameters to be used in the flow and transport simulations, the chromatographic separation of cations that occurs below SX-115 provides a test of the applicability of the cation exchange model which, to some extent, does not depend entirely on knowing these parameters very accurately. This is because the chromatographic separation represents a relative separation of reactive cations and tracers. Whatever detailed flow field resulted in the present location of the tracer plumes, the observation that sodium and cesium are retarded relative to the tracers in the Z (depth) direction implies that the effective exchange capacity of the Hanford sediments had to be reasonably high.

It is likely that a similar exchange capacity applies below such tanks as tank SX-108 where Cs migration is much deeper into the vadose zone than it is at tank SX-115. Therefore, it would appear that the enhanced migration of cesium underneath tank SX-108 is chiefly the result of the very different chemical environment there, although the higher temperatures at tank SX-108 are likely to have produced a substantially different flow regime as well. In keeping with our observations from column experiments (summarized in Carroll et al. 2001), the much higher Na and Cs concentrations in the tank SX-108 leaks would contribute to a substantially lower retardation of Cs than would be expected at tank SX-115. At tank SX-108, for example, there is no retardation of Na relative to nitrate, which makes sense given the very high $NaNO_3$ concentrations there. If the extrapolation of the present ion exchange model and data to the $NaNO_3$ concentrations of SX-108 is valid, then a retardation of Cs that is as low as 2.5 or 3 can be explained by these high $NaNO_3$ concentrations. Other factors, however, are apparently operating at tank SX-108. Perhaps most important is the development of a "heat pipe" that draws flow into the boiling zone developed immediately below the tank. Preliminary simulations of the SX-108 leak indicate that the flow field is far from one-dimensional. During the boiling stage, fluid velocity vectors typically point up into the boiling zone. This "heat pipe" can lead to substantial accumulation of salts (especially $NaNO_3$) below the tank, due in part to the cooling of the fluid, but even more so to the dryout which results. This boiling zone, if it did result in substantial precipitation of salts immediately underneath the tanks, may have an important effect on Cs transport and needs to be carefully considered in assessments of the environmental impact of the tank leaks. While our work to date has shown that Cs will be largely immobile under dilute conditions, infiltration and rewetting of salts could lead again to high concentrations of such cations as Na and thus, potentially, to Cs remobilization.

D.7.4.5 References

Appelo, C. A. J., and D. Postma, 1996, *Geochemistry, Groundwater and Pollution*, A. A Balkema, Rotterdam, p. 536.

Carroll, S., C. I. Steefel, P. Zhao, and S. Roberts, 2001, *Reaction Transport Experiments Investigating the Migration of* ^{137}*Cs in Sediments Beneath the Hanford SX Tank Farm*, FIR Report.

Felmy, A. R., 1995, "GMIN, A Computerized Chemical Equilibrium Program Using a Constrained Minimization of the Gibbs Free Energy: Summary Report," *Chemical Equilibrium and Reaction Models*, SSSA Special Publication 42, Soil Science Society of America, Madison, Wisconsin.

Jones, T. E, R. A. Watrous, and G. T. Maclean, 2000, *Inventory Estimates for Single-Shell Tank Leaks in the S and SX Tank Farms*, RPP-6285, Rev. 0, CH2M HILL Hanford Group, Inc., Richland, Washington.

Khaleel, R., T. E. Jones, A. J. Knepp, F. M. Mann, D. A. Myers, P. M. Rogers, R. J. Serne, and M. I. Wood, 2000, *Modeling Data Package for S-SX Field Investigation Report (FIR)*, RPP-6296, Rev. 0, CH2M HILL Hanford Group, Inc., Richland, Washington.

Lichtner, P. C., 2001, *Estimating Tank Supernatant Liquid Compositions*, FIR report, Los Alamos National Laboratory, Los Alamos, New Mexico.

Nitao, J., 1998, *Reference Manual for the NUFT Flow and Transport Code, Version 2.0*, UCRL-MA-130651, Lawrence Livermore National Laboratory, Livermore, California.

Raymond, J. R., and E. D. Shdo, 1966, *Characterization of Subsurface Contamination in the SX Tank Farm*, BNWL-CC-701, Battelle Northwest Laboratory, Richland, Washington.

Zachara, J. M., S. C. Smith, J. P. McKinley, R. J. Serne, and P. L. Gassman, 2001, "Sorption of Cs^+ to Micaceous Subsurface Sediments from the Hanford Site," *Geochimica et Cosmochimica Acta* (accepted).

D.7.5 CONCLUSIONS OF S&T INVESTIGATIONS OF SIMULATION OF MULTIPHASE FLUID FLOW AND REACTIVE TRANSPORT AT THE SX TANK FARM

D.7.5.1 Nonisothermal Multiphase Fluid Flow

Radiolytic heating during the historical operation of the SX tank farm resulted in years of elevated tank temperatures (up to 200 °C). These temperatures were sufficiently high to significantly alter fluid distribution in the sediments surrounding the tanks. Two sets of modeling analyses, (1) axially symmetric single tank and (2) two-dimensional vertical cross-section multitank, were performed to determine the impact of the tank heat sources on fluid migration by comparing nonisothermal and isothermal modeling results. The hydrologic conceptual model is based on descriptions provided by the River Protection Project (RPP) and will be tested against field observations of temperature and moisture content. Understanding the impact of the heat-induced fluid migration is important when considering travel time of the existing contaminant inventory, and is especially germane in the context of recently measured temperatures in the sediments beneath tank SX-108 that exceed 70 °C. This is a critical consideration for decisions on surface barrier construction and limits on leak loss during tank waste retrieval operations.

Key Findings

- In the SX tank farm vadose zone, tank heat sources have a large impact on liquid saturation and fluxes. In sediments adjacent to these high-heat tanks, pore fluid evaporates into water vapor that is driven away to locations where lower temperatures result in condensation. As the sediments adjacent to the tank dry out, strong capillary forces are induced, drawing more pore fluid to this zone. This liquid-vapor counterflow is predicted to be most significant in the sediments just below the tank bottom (where the tank temperatures are highest) resulting in sediments that are essentially dry.

- When tank temperatures decrease, evaporation decreases; however, capillary forces are still sufficient to draw pore fluids to the dried sediments, rapidly rewetting the sediments. During operational fluctuations in temperature within a tank or between tanks, significant rewetting is predicted to occur over periods as short as a few months.

- In the zone where this liquid-vapor counterflow (also known as the heat pipe effect) is occurring, pore fluids from surrounding sediments are continuously drawn in while water vapor is continuously driven away, allowing salts to accumulate. In particular, highly concentrated sodium solutions as well as the precipitation of sodium minerals are predicted to occur in the sediments adjacent to the high heat tanks. This is a significant finding because very high concentrations of free sodium can substantially reduce cesium sorption, thus causing Cs-137 to migrate with minimal retardation. Furthermore, future rewetting of precipitated sodium salts from natural or artificial recharge could result in sodium concentrations sufficiently high to remobilize previously sorbed cesium.

- The sloping gravel layer in the Hanford formation provides a path away from SX-108 towards SX-109 for fluid migration (natural and heat induced). This underscores the importance of accurately characterizing the geometry and hydrologic parameters of the vadose zone sediments in the SX tank farm.

- An effective surface barrier can significantly control transport to the water table driven by recharge. Timing of the construction is critical as earlier construction will increase travel times, which increases opportunities for mixing, which effectively reduces peak concentrations.

D.7.5.2 Speciation of High-Ionic Strength Tank Fluids

A critical modeling data need is a reasonably representative composition and speciation of the tank fluids at the time of the leaks. The characterized tank fluid species and concentrations are fundamental to the reactive behavior that takes place in the vadose zone sediments. They are complicated by tank fluid that was historically high in temperature (~110 °C) with highly concentrated electrolytes. Significant differences in reactivity and solubility occur at these temperatures compared with thermodynamics at 25 °C. Standard Debye-Huckel activity corrections are inaccurate at these concentrations and ion-specific treatment (e.g., Pitzer ion interaction parameters) is necessary to account for non-ideal, high-ionic strength effects on reactivity. An important requirement under these conditions is the explicit accounting for water as a species since the solution may be less than 70% water.

Very few historical analytical measurements of tank fluids have been identified. Consequently, the principal source of tank fluid composition is from estimates based on process waste stream records, tank transfers, and evaporative losses [e.g., Hanford Defense Waste (HDW) Model]. The objective of these analyses is to examine assumptions underlying the tank fluid speciation calculation, especially as they relate to source term concentrations of critically important chemical components. The analyses specifically address temperature, ionic strength, and mineral precipitation. The resulting speciation of the tank source terms has significant implications for the mobility of some contaminants (e.g., cesium).

Key Findings

- Using tank compositions from the HDW Model as a starting point, charge balancing with OH^- results in higher pH and sodium concentrations as compared to the speciation performed by Jones (2000). At high temperature and ionic strength, the predicted SX-108 free sodium concentrations are sufficiently high to significantly reduce the retardation of cesium in the sediments.

- Mineral solubility exerts significant control over the speciation of the tank fluids. This underscores the importance of correctly identifying the actual mineral phases present in the tanks.

D.7.5.3 Cesium Migration Beneath Hanford Waste Tanks

Mobility of cesium-137 was the galvanizing issue behind the current focus on the Hanford Site Vadose Zone. Considerable resources have been directed at elucidating the process mechanisms that can account for observations of cesium-137 at depth in the SX tank farm. The objective of this analysis is to test the understanding of cesium-137 developed from these studies, in the context of the field situation at SX-108 and SX-115. This can be problematic given the uncertainties in tank leak volumes, rates, and composition, as well as the fact that total cesium can be 4 to 5 times the Cs-137 concentration. However, the tank leak at SX-115 in 1965 was unique because the leak volume (50,000 gallons) and duration (1 week) are constrained by direct observations. At the time of the leak, SX-115 was not a high temperature tank. Coupled with a comprehensive data set from the recently characterized well, W23-19, SX-115 was the logical starting point for modeling cesium migration in a multicomponent reactive system that accounts for competitive cation exchange. The SX-115 analysis provided the basis for the subsequent modeling of cesium migration beneath SX-108.

The analysis of the SX-115 leak was carried out by combining the multisite cation exchange model with modeling of 3D flow and transport using the Hanford hydrostratigraphy and hydrologic parameters as presently known. Although there is little direct interest in sodium, calcium, magnesium, and potassium as contaminants, these cations are very useful in establishing whether the multicomponent ion exchange model developed to describe cesium exchange and transport in the batch and column experiments can be applied to the field. The ability to match the chromatographic pattern of the cations other than cesium provides a test of the self-consistency of the multisite cation exchange.

Key Findings

- Component concentrations in the tank source term developed from the HDW model appear to be consistently high with respect to our interpretation of the leak event and the chemical analyses of the borehole samples.

- After developing a "best fit" dilution of the HDW estimated source term, the multisite cation exchange model developed from laboratory studies provided a reasonable match with the entire suite of cations (cesium, sodium, calcium, potassium, and magnesium) at SX-115. This consistency between field observations and predictions based on laboratory derived cation exchange capacities (CECs) and selectivity coefficients lends strong support for the cation exchange model developed to describe cesium migration at Hanford.

- The analysis suggests that fast pathways and bypassing of immobile zones due to low saturation conditions are unlikely to explain the major chromatographic patterns observed below the leaking SX tank farm.

D.7.5.4 Identification of Critical Data Needs

In the course of these model-building activities, gaps in knowledge and data were identified as well as the applicability of simplifying assumptions. Issues that have been identified:

- **Hydrologic characterization parameters** – At this point in time, no sediments from the SX tank farm have been characterized for soil moisture retention functions. Current parameterizations are based on historical studies of sediments from areas other than the SX tank farm and little effort has been made to adjust these parameterizations in light of the field observations of moisture content. Permeability anisotropy has been shown to significantly impact fluid migration in field experiments; however, mechanistic parameterizations have not been characterized.

- **Tank leaks** – Fluid migration in the Hanford Vadose Zone is sensitive to the rate and duration of recharge (natural and artificial). Unless tank leak rates were very high, it was difficult for them to be detected other than through gamma logging for cesium in the laterals. SX-108 is an example where a chronic, but not obvious leak was probably occurring through the high heat operations in the 1960s. Leak estimates at SX-108 have ranged from a few thousand gallons to over 200,000 gallons based on a variety of estimation approaches.

- **Tank fluid speciation** – Speciation of the tank fluid at the time of the leaks will ultimately dictate the behavior of contaminants that chemically interact with the sediments. Differences in high-ionic strength thermodynamic models and databases need to be understood and updated to achieve consistency in the characterization of the source term being introduced into the sediments.

- **Field and laboratory experiments** – The lack of information on tank composition and speciation is a surprisingly common theme considering the amount of ongoing research that is depending on it. Experimental studies of tank chemistry under high temperature conditions, including the formation of secondary minerals, would provide some needed constraints on the speciation conceptual model.

D.7.5.5 Next Steps

We consider the analyses presented here to be a preliminary step in identifying where additional detail and complexity are needed to assess the appropriate representation of subsurface processes in predictive models of the Hanford Vadose Zone. Subsequent modeling analyses will focus on:

- Three-dimensional, multitank simulations to more realistically identify the impact of multiple tanks and their temperature histories on fluid and contaminant migration to the water table and beyond.

- Developing new estimates of tank leak volumes and rates based on the systematic comparison with observed chemical concentrations, moisture contents and temperatures.

- Linkage of the full multicomponent reactive chemistry system to nonisothermal multiphase fluid flow to determine the potential for highly concentrated salts beneath the tank bottom which could result in cesium mobility during rewetting.

- The reactivity of mineral surfaces exposed to the extreme physical and chemical conditions of the tank fluids.

- Chromium interaction with Fe^{++} released by the dissolution of minerals from the interaction of tank fluid with vadose zone sediments.

D.8.0 VADOSE ZONE FIELD EXPERIMENTS AND INFILTRATION ESTIMATES FOR THE S AND SX TANK FARMS

Tank waste contaminants such as chromate, nitrate, technetium, and tritium, among others, continue to be found in increasing concentrations in groundwaters beneath tank farms and burial grounds at the Hanford Site (e.g., 618-11). Cores collected from beneath leaked tanks in the S and SX tank farms, and others, display complex solute concentration profiles indicative of highly anisotropic hydrologic processes. Vadose zone contaminant distributions in one borehole, often seem in conflict with those from another nearby borehole, or groundwaters that are vertically below. These observations all suggest that water movement through the Hanford vadose zone, and the factors that control it are poorly understood. There is an urgent need for: (1) more information about the transport of contaminants as they move through the vadose zone to the underlying water table, and (2) improved models of water and solute migration with appropriate scale dependencies.

A critical information requirement in assessing the need for corrective actions in the S and SX tank farms is the infiltration rate of meteoric waters. It is well known that the infiltration over vegetated soils near the tank farms increased after the native vegetation was removed from the tank farms and the area was covered by over a meter of gravel. The modeling assessments presented in the body of the report assumed an infiltration rate (100 mm/yr [4 in./yr]) as the basis of their calculations. But, are these rates reasonable? The infiltration rate controls the timing of solute breakthrough from the vadose zone to groundwater. Surface barriers, that reduce the infiltration rate, are one of the most logical corrective actions that could be applied in the tank farms. Credible estimates of recharge are therefore needed for the S and SX tank farms and others in order to estimate travel times to groundwater and the remedial contributions of barriers.

In this Appendix section, we describe hydrologic studies that have been performed in support of the WMA S-SX field investigation. These studies include: (1) field injection experiments at the vadose zone test facility (VZTF) designed to evaluate the influence of fine-textured sediment layers on water movement, and (2) infiltration estimates at the S and SX tank farms using a water-balance approach calibrated against Hanford lysimetry data.

D.8.1 HANFORD VADOSE ZONE TRANSPORT FIELD STUDIES

Glendon W. Gee[1] and Andy L. Ward[1]

[1]Pacific Northwest National Laboratory (PNNL), Richland, Washington 99352

D.8.1.1 Introduction

The scope of the Vadose Zone Transport Field Studies (VZTFS) is to conduct a series of tests at the Hanford Site to evaluate how contaminant plumes move in the vadose zone. This information will be used to improve predictions of vadose zone contaminant transport at tank farms and other waste disposal sites. A series of flow and transport experiments at uncontaminated sites focused on characterizing transport processes and parameters in the Hanford subsurface and generating accurate and reliable databases for testing three-dimensional numerical vadose zone models of flow and transport. The VZTFS plan calls for conducting two flow and transport tests at an uncontaminated site to simulate a near-surface tank leak, followed by two flow and transport tests in deeper Hanford formation sediments. During FY 2000, the first of four field tests was completed using a low ionic strength solution (1000 ppm).

The objectives of the VZTFS are to conduct controlled transport experiments at well-instrumented field sites at Hanford to: (1) identify mechanisms controlling transport processes in soils typical of the hydrogeologic conditions of Hanford's waste disposal sites, (2) reduce uncertainty in conceptual models, (3) develop a detailed and accurate database of hydraulic and transport parameters for validation of three-dimensional numerical models, and (4) identify and evaluate advanced, cost-effective characterization methods with the potential to assess changing conditions in the vadose zone, particularly as surrogates of currently undetectable high-risk contaminants.

A detailed test plan (Ward and Gee 2000) outlines the overall scope of the VZTFS. Activities focus on hydrogeologic investigation and characterization of field sites to address current data gaps in transport of mobile contaminants by making in situ measurements of surrogate parameters using new monitoring technologies.

D.8.1.2 Experimental Approach and Methods

Testing has been approached in two phases: (1) characterization of background site conditions, and (2) process characterization that will occur during and after the actual transport test and will include assessment of the physical and chemical properties affecting the vadose zone transport processes.

A test location was selected at Hanford in the 200 East Area (299-E24-111, also referred to as the Sisson and Lu Site), where an extensive amount of characterization had already been completed (Sisson and Lu 1984; and Fayer et al. 1993, 1995). Ward and Gee (2000) provide details of the site selection process. Figure D.8.1.1 shows the site location.

Figure D.8.1.1. Location of Sisson and Lu Test Site.

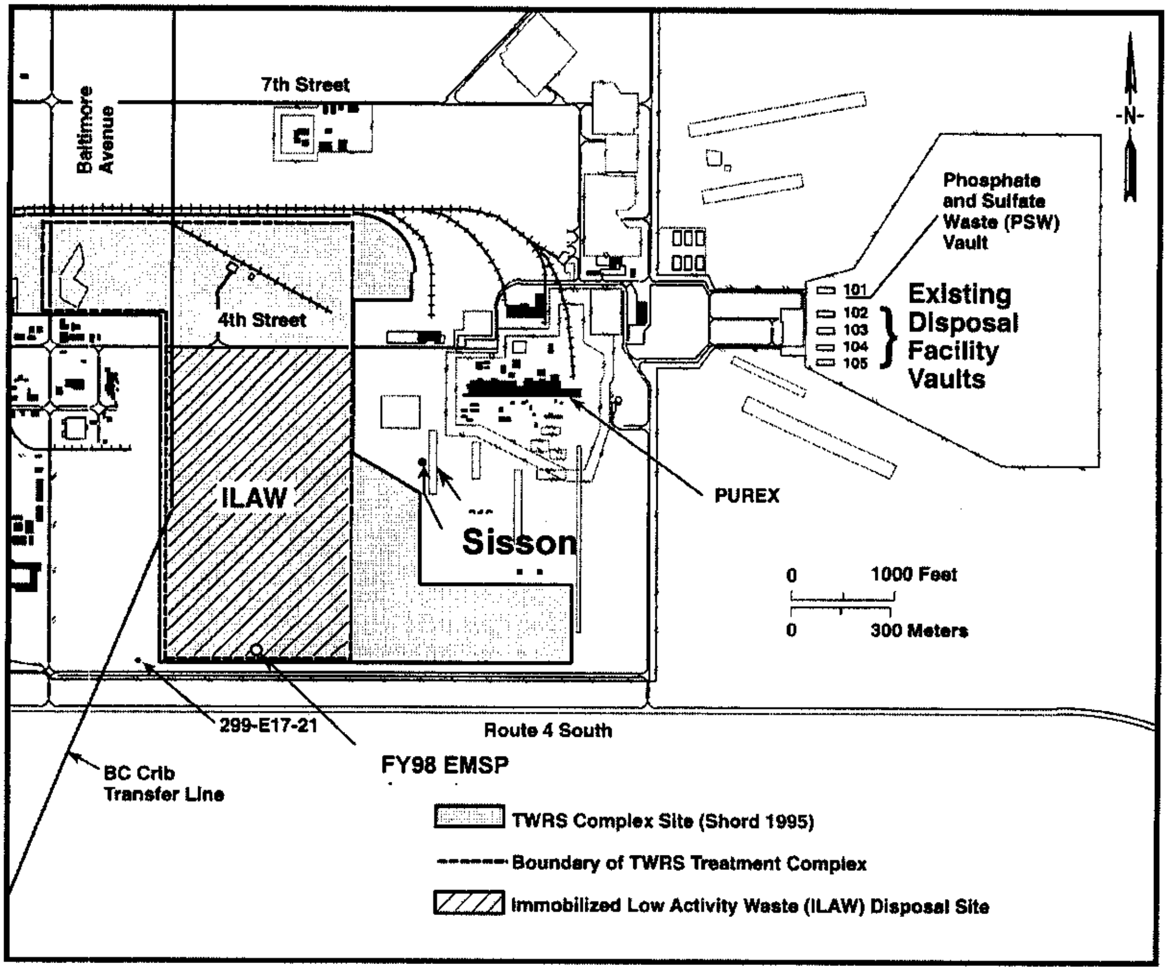
7th Street
Baltimore Avenue
4th Street
ILAW
Sisson
PUREX
Phosphate and Sulfate Waste (PSW) Vault
101
102
103
104
105
Existing Disposal Facility Vaults
-N-
0 1000 Feet
0 300 Meters
299-E17-21
Route 4 South
FY98 EMSP
BC Crib Transfer Line
TWRS Complex Site (Shord 1995)
Boundary of TWRS Treatment Complex
Immobilized Low Activity Waste (ILAW) Disposal Site

Note: The Site is designated as 299-E24-111, experimental Test Well Site in the Hanford Waste Information Data System (WIDS).

The geology at the test site is well characterized. The surface soil at the site is a coarse sand, locally known as a Quincy sand, which is associated with the Quincy soil series. The soil has a high infiltration capacity (greater than 50 mm/h [2 in./hr]) and precipitation infiltrates readily with little or no runoff. The vegetation at the site before the experiment was a mixture of sagebrush and cheatgrass. The shrubs on the site were "grubbed" off in March 1980 and since that time the site has been dominated with a sparse cover of cheatgrass, tumble mustard, and tumbleweed (Fayer et al. 1993). Below the surface soil is the Hanford formation, which extends to about 60 m (200 ft) below the surface. The water table is more than 90 m (295 ft) deep. Therefore, the field injection experiment was conducted in the Hanford formation sediments.

The original field experiment (Sisson and Lu 1984) consisted of a central injection well surrounded by 32 observation wells. The wells are constructed of 15.24-cm (6-in.) diameter steel casing and extend to 18 m (59 ft). The FY 2000 field test included a series of new boreholes and instruments installed by auger and cone penetrometer. A new injection well was installed at the site and vertical electrical resistance tomography (ERT) arrays were emplaced by cone penetrometer. The layout of the FY 2000 field test is illustrated in Figure D.8.1.2, showing a plan view of the locations of access tubes, electrode arrays, and injection and core sampling points.

Figure D.8.1.2. Plan View of FY 2000 Test Site Showing Locations of Access Tubes, Vertical Electrode Arrays, Injection, and Core Sampling Points.

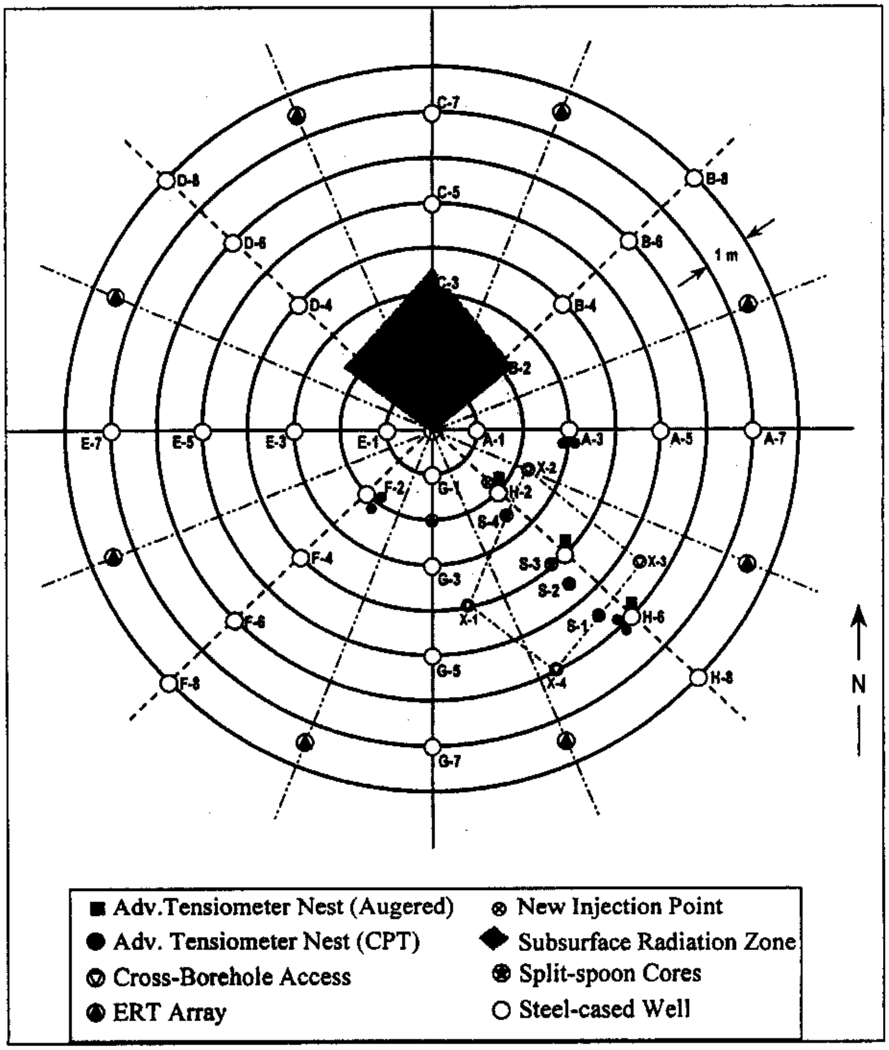
C-7
D-8
B-8
C-5
D-6
B-6
1 m
D-4
C-3
B-4
B-2
E-7
E-5
E-3
E-1
A-1
A-3
A-5
A-7
X-2
F-2
G-1
H-2
S-4
F-4
S-3
X-3
G-3
S-2
X-1
S-1
H-6
F-6
F-8
G-5
X-4
H-8
N
G-7
■ Adv.Tensiometer Nest (Augered)
● Adv. Tensiometer Nest (CPT)
Cross-Borehole Access
ERT Array
⊗ New Injection Point
◆ Subsurface Radiation Zone
Split-spoon Cores
○ Steel-cased Well

More than 20 technologies were screened to identify those that could be used to delineate the moisture and contaminant plume during the field injection tests, either as stand alone technologies or used in conjunction with others. With this objective in mind, a short list of candidate technologies was identified based on the following criteria which included the ability to (1) identify key geologic features controlling water movement with a vertical resolution of 0.1 m (4 in.) or better and a horizontal resolution of 1 m (3.3 ft) or better, (2) locate wetting fronts and a change in water content of 0.01 m^3/m^3 or better with a repeatability of at least 0.01 m^3/m^3, (3) determine the shape and extent of non-gamma-emitting contaminant plumes or their surrogates, and (4) function and produce useful results in environments that are culturally noisy.

The nine technologies selected from the screening process included neutron moisture logging, advanced tensiometry/suction lysimetry; electrical resistance tomography (ERT); crosshole radar tomography (CRT); crosshole seismic tomography; crosshole electromagnetic induction (CEMI); and high-resolution resistivity (HRR). Additional methods included tracers (including isotopes), and coring. The details of each of the nine methods selected and the collaborators who helped deploy the selected methods are listed in the VZTFS test plan (Ward and Gee 2000).

For the FY 2000 study, water content changes were the primary measurement variable. Water content as determined by neutron probe logging was selected as the primary standard upon which the other geophysical methods could be compared. Neutron probes were used in the past to monitor water content at the Sisson and Lu injection site (Sisson and Lu 1984; Fayer et al. 1993 1995). These probes are also used routinely to monitor field water contents at the Hanford Site. Details of the calibration of neutron probes for monitoring water content at the Sisson and Lu site are provided by Fayer et al. (1995).

D.8.1.3 Field Tests and Results

In late April 2000 the site was approved for use and installation of equipment (e.g., electrodes for electrical resistance tomography, cross-borehole ports, and advanced tensiometers) began in early May. Electrode, port, and tensiometer placements were completed before scheduled baseline measurements by all of the geophysical methods before starting water injections.
A total of nine methods were tested: neutron probe logging, electrical resistance tomography (ERT), cross-borehole radar (XBR), seismic (XBS), high-resolution resistivity (HRR), electromagnetic imaging (EMI), and advanced tensiometry (AT). In addition isotopic tracers were deployed during the test and subsequently sampled by soil coring. Soil coring was also used to obtain samples for hydraulic characterization. A schedule was established so that baseline sampling and subsequent data collection from each method could be obtained in the most efficient manner and so that there was minimal interference between methods. For example, XBR and ERT measurement schedules were compatible and these measurements could be made simultaneously with the neutron probe. In contrast, the HRR and EMI measurements could not be taken at the same time so a rather strict schedule was set to ensure collection of the best possible data. Table D.8.1.1 shows the detailed schedule for the FY 2000 test.

After baseline data from all methods were obtained, a series of 5 injections were performed, beginning on June 1, 2000, when 4000 L (1060 gal) of water was metered into the 5-m (16.4-ft) deep injection well over a 6-hour period. Subsequent injections occurred weekly for a period of 5 weeks. The third injection included 1000 ppm bromide and a suite of isotopic tracers. Neutron logging of 32 steel-cased wells (surrounding the injection well) occurred before the initial injection and followed each of the 5 injections within a day, with the exception of the injection that occurred on June 26, 2000. On that day a wildfire burned within about 0.5 km (0.3 mi) of the test site. After the injection, the Hanford Site was closed to traffic due to the fire, so no neutron logging occurred at the test site July 7. Subsequently two more readings of the 32 wells were completed during the month of July. One additional 4000 L (1060 gal) injection was made on September 18. This injection was made to obtain in situ hydrologic properties using a combination of pressure measurements and neutron probe water content measurements at the same depth. Only limited water content measurements were made at a few selected locations and no other geophysical measurements were made after the September injection. Details of the neutron-probe logging are provided in a companion report (Ward and Caldwell 2000).

Water content profiles measured by neutron probe (Figure D.8.1.3) captured the nature of the plume during the course of the injection testing and indicated that water content changes below the 11-m (36-ft) depth were minimal, suggesting that the plume spread laterally along layers of finer sediments which were noted at 6 and 11 m (19.7 ft and 36 ft). The FY 2000 test was simulated using STOMP, a multiphase (unsaturated) flow and transport code developed at PNNL. Conditional simulation of the five injections was made using methods developed by Rockhold et al. (1999). The simulations were conditioned on the initial water contents and the water retention characteristics of Hanford Site soils that are similar but not identical to those soils found at the Sisson and Lu site.

Figure D.8.1.3. Two-Dimensional Cross-Sections of the Water Content Profile Measured by Neutron Probe after Four Injections on June 23, 2000.

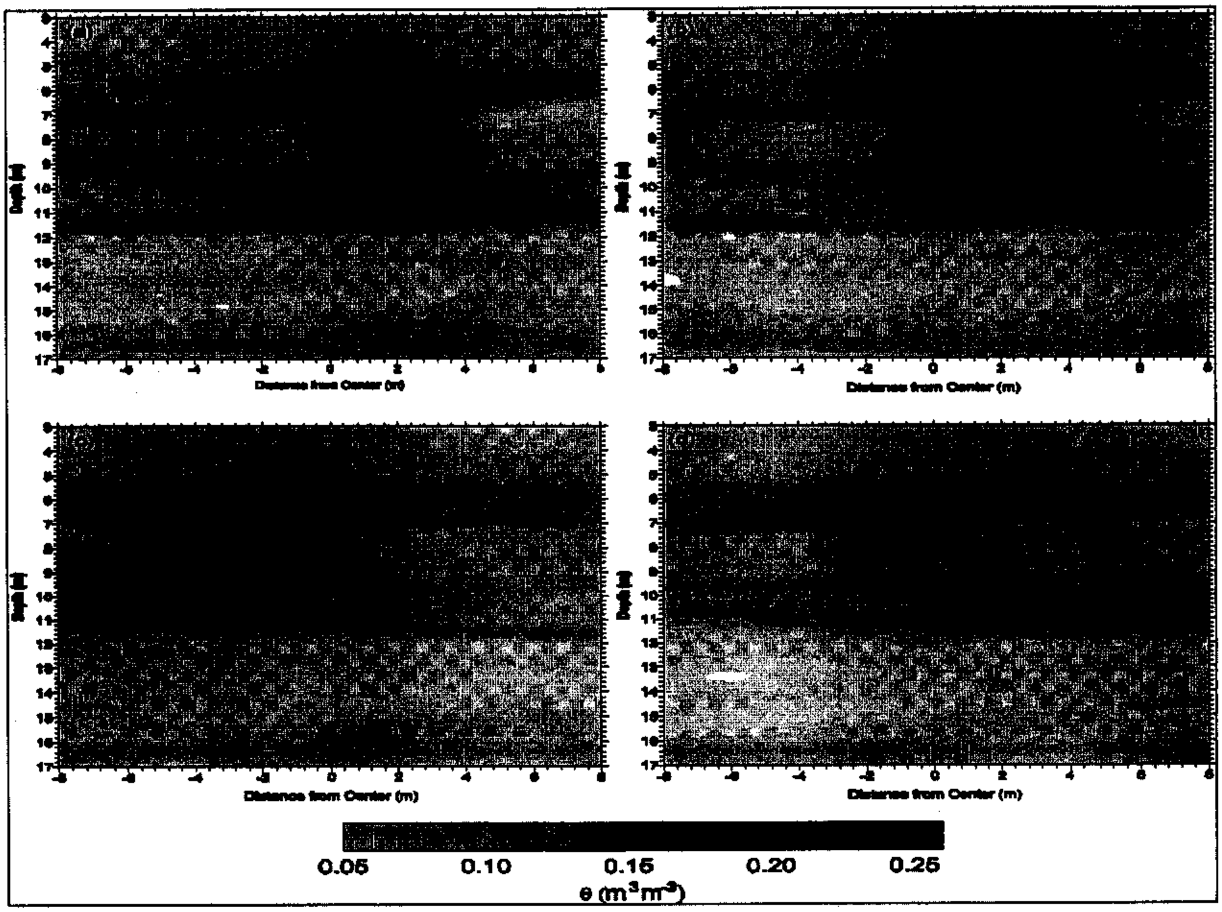

Note: Figures a), b), c) and d) represent cross-sections taken along transects EA, DH, CG and BF, respectively (see Figure D.8.1.2).

Table D.8.1.1. List of FY 2000 Test Activities for the VZTFS project at the 299-E24-111 Experimental Test Well (Sisson and Lu) Site, 200 E Area, Hanford Site, Washington. (2 Sheets)

Date	Action	Method 1	Method 2	Method 3	Method 4	Method 5	Method 6	Method 7	Method 8	Method 9
		Neutron	AT Tens.	ERT	XB Radar	Seismic	EMI	HRR	Isotopes	Coring
05-May	Pre-Leak	Read 35								
06-May		Cross-Calibrate								
09-May				CPT Install (3 day)						
12-May			CPT Install (2 day)							
15-May					CPT Install (2 day)					
19-May										Install/ Inject
20-May			Install Nest (2 day)				Set up/ Read (3 day)			
23-May			Read-continuously	Setup/ Read (3 day)						
25-May					Set/Read					
26-May					Read			Set/Read		
30-May								Read	Sample	Core (S-1)
31-May								Read	Samples	Core (S-1)
01-Jun	1st Leak			Read						
02-Jun		Read 32		Read						
05-Jun							Read (2 day)			
08-Jun	2nd Leak	Read 8								
09-Jun		Read 24								
12-Jun										
13-Jun					Read					
14-Jun				Read	Read					
15-Jun	3rd Leak	Read 8		Read						
16-Jun		Read 24		Read						

Table D.8.1.1. List of FY 2000 Test Activities for the VZTFS project at the 299-E24-111 Experimental Test Well (Sisson and Lu) Site, 200 E Area, Hanford Site, Washington. (2 Sheets)

Date	Action	Method 1	Method 2	Method 3	Method 4	Method 5	Method 6	Method 7	Method 8	Method 9
		Neutron	AT Tens.	ERT	XB Radar	Seismic	EMI	HRR	Isotopes	Coring
19 Jun								Read (6 day)		
21-Jun										
22-Jun	4th Leak	Read 8								
23-Jun		Read 24								
24-Jun										
28-Jun	5th Leak	Read 8/Fire			Read					
06-Jul									Samples	Core (S-2)
07-Jul	Post Leak	Read 32			Read (2 day)				Samples	Core (S-2)
10-Jul				Read (2 day)					Samples	Core (S-3)
13-Jul							Read (2 day)			
14-Jul							Read			
17-Jul		Read 32								
21-Jul									Samples	CPT (WL1)
31-Jul		Read 32								
1-Aug						Read (2 day)				
11-Sep									Samples	CPT (WL2)
12-Sep									Samples	CPT (WL2)
15-Sep			CPT (2 ATs)							
18-Sep	Pulse	Read (5 day)	Read (5 day)							

The results indicate that the model captures the general flow depths and directions of the plume but does not completely describe the extent of the lateral spreading of the plume. Hydraulic property data collected during the testing this past year may be helpful in improving the prediction of the lateral spreading. These estimates will be updated in FY 2001.

D.8.1.4 Conclusions and Implications

The first of two field tests at the 299-E24-111 (Sisson and Lu 1984) injection site in the 200 East Area of the Hanford Site was completed during FY 2000. The results of the injection experiments indicate that lateral flow appears to dominate much of the transport that occurs in Hanford sediments. Sediment layering, even subtle changes in texture can do much to cause lateral spreading of water and contaminants. The observed lateral movement of cesium near tank SX-109 (Price and Randall 1998) may be caused by lithologic control of the hydraulic properties.

All of the geophysical methods deployed in the field experiment were successful to some degree in identifying changes in subsurface water contents (or pressures) as a result of the five injections. Work in FY 2001 is focused on using the most successful geophysical techniques and isotopic tracers. During the FY 2001 field experiment, a high salt concentration (>1M) will be added in the water injections and the salt plume is being tracked with geophysical logging and solution sampling techniques similar to those used in FY 2000.

Summary reports for the FY 2000 tests can be found at the following Universal Resource Locator (URL) address: http://etd.pnl.gov:2080/vadose/contrepts.htm. Analysis of the data is continuing through FY 2001 and a final report describing the FY 2000/2001 testing will be published in September 2001.

D.8.1.5 Acknowledgments

We thank our collaborators: Wes Bratton (Applied Research Associates); Buck Sisson (Idaho National Engineering and Environmental Laboratory); Bill Daily and Abe Ramirez (Lawrence Livermore National Laboratory), Ernie Majer and his staff at Lawrence Berkeley National Laboratory (LBNL); Mike Hoversten (LBNL) and Mike Wilt (CEMI); Jim Fink (Hydrogeophysics Inc.); Mark Conrad (LBNL) and Todd Caldwell (PNNL), Everett Springer and Brent Neuman (Los Alamos National Laboratory); and Mark Rockhold (Oregon State University).

D.8.1.6 References

Fayer, M. J., J. B. Sisson, W. A. Jordan, A. H. Lu, and P. R. Heller, 1993, *Subsurface injection of radioactive tracers: Field experiment for model validation testing*, NUREG/CR-5996. U.S. Nuclear Regulatory Commission, Washington, D.C.

Fayer, M. J., R. E. Lewis, R. E. Engleman, A. L. Pearson, C. J. Murray, J. L. Smoot, R. R. Randall, W. H. Wegener, and A. H. Lu, 1995, *Re-Evaluation of a Subsurface Injection Experiment for Testing of Flow and Transport Models*, PNL-10860, Pacific Northwest National Laboratory, Richland, Washington.

Last, G. V. and D. G. Horton, 2000, *Review of Geophysical Characterization Methods Used at the Hanford Site*, PNNL-13149, Pacific Northwest National Laboratory, Richland, Washington.

Price, R. K., and R. R. Randall, 1998, *Monitoring Results for the SX Single Shell Tank Farm Dry Well Gamma Ray Surveillance Log Surveys*, WMNW/TRS-ES-VZMA-002, Three Rivers Scientific, West Richland, Washington.

Rockhold, M. L., C. J. Murray, and M. J. Fayer, 1999, "Conditional simulation and upscaling of soil properties," In: *Proceedings of the International Workshop on Characterization and Measurement of the Hydraulic Properties of Unsaturated Porous Media*, M. Th. Van Genuchten, F. J. Leij and L. Wu (eds.), pp. 1391–1401. University of California, Riverside.

Sisson, J. B. and A. H. Lu, 1984, *Field Calibration of Computer Models for Application to Buried Liquid Discharges: A Status Report*, RHO-ST-46P, Rockwell Hanford Operations, Richland, Washington.

Ward, A. L. and G. W. Gee, 2000, *Vadose Zone Transport Field Study: Detailed Test Plan for Simulated Leak Tests*, PNNL-13263, Pacific Northwest National Laboratory, Richland, Washington.

D.8.2 ESTIMATION OF NET INFILTRATION OF METEORIC WATER AT THE SX TANK FARM

Glendon W. Gee[1] and Andy L. Ward[1]

[1]Pacific Northwest National Laboratory (PNNL), Richland, Washington 99352

D.8.2.1 Introduction

There is mounting evidence that mobile constituents (e.g., ^{99}Tc, chromate, and nitrate) from tank leaks have reached groundwater (Serne et al. 1997; Johnson and Chou 1998; Hodges 1998; Narbutovskih 1998; Myers et al. 1998) at Hanford Site tank farms. One cause for the transport of mobile constituents to groundwater is deep infiltration of winter rains and episodic snowmelt runoff that leach soil contamination from the vadose zone to the underlying water table.
The accelerated movement of water around and beneath buried tanks can be attributed to bare, gravel surfaces that enhance net infiltration of meteoric water (from winter precipitation and snow melt) (Smoot et al. 1989; Connelly et al. 1992; Ward et al. 1997). The FIR provides insights into mechanisms that control the migration rates of contaminants that leak from tanks into groundwater at the SX tank farm. These observations can be used to assist in mitigating leaks both now and in the future, when tank sluicing and other operations may require additions of water to ruptured or otherwise leaking tanks or to transfer lines. Interest in net infiltration (drainage) rates stems from the assumption that contaminant plumes are largely driven by advective water flowing in the subsurface, gravity drainage being the dominant mechanism for transport of mobile contaminants in the vadose zone.

Simplified calculations, assuming a conservative scenario for transport (e.g., one-dimensional vertical transport of nonreactive contaminants moving through coarse, highly permeable sediments) can be used to illustrate the problem. Assume that a tank leak occurred in 1970 from a tank whose bottom was 60 m (200 ft) from the water table. Typical water contents in coarse Hanford sediments under draining conditions are 7% by volume or less. If the average flux of water around the tank and impacting the tank leak is 70 mm/yr (2.8 in./yr), then the contaminant transport rate for a leak beneath the tank is 1 m/yr (3.3 ft/yr). Thus, in 60 years, the contamination from the tank leak will reach the water table. Under tank farm conditions, the buried tanks create concentrated flow paths adjacent to the tank walls, so pore-water velocities can locally exceed 1 m/yr (3.3 ft/yr), accelerating the flow and reducing the travel time to the water table. If concentrated flow pathways exist or localized recharge zones have developed at some point in the tank farm, the recharge rates can also be accelerated. Support for localized recharge zones have been documented in recent tank farm reports (Hodges 1998; Johnson and Chou 1998; Narbutovskih 1998). While it may be difficult to obtain detailed data on localized flow around tanks, it should be possible to obtain estimates of the net infiltration into a tank farm. For tank farms, we define the net infiltration as synonymous with drainage and equivalent to precipitation minus evaporation. This net infiltration (drainage) then becomes the driving force for most, if not all, of the contaminant migration that occurs at the tank farm. The following analysis is used to estimate drainage rates at the SX tank farm and to predict future drainage rates, assuming that the surface cover does not change substantially until final closure.

D.8.2.2 Water-Balance Analysis

Deep drainage at tank farms and other Hanford waste sites is best analyzed by assessing the complete water balance of the surface soils. Drainage is an integral component of the water balance, which in its simplest form can be written as:

$$D = P - S - ET - RO \qquad \text{(D.8.2.1)}$$

where:

D = drainage
P = precipitation input
S = storage change
ET = evapotranspiration
RO = runoff/run-on.

Three main variables, climate, soils, and vegetation, control the water balance of surface soils. The assessment of net infiltration (drainage) at the tank farms involves the interaction of these three factors. Topography also can affect drainage due to runoff or run-on, but most tank farms are on relatively level ground or are bermed so that runoff or run-on are controlled or minimized.

D.8.2.2.1 Climate. The Hanford Site can be characterized as arid, the dominant climatic features being cool, wet winters coupled with hot, dry summers (Stone et al. 1983; Rickard et al. 1988). While there are no site-specific, long-term weather records for individual tank farms, a reliable source of meteorological data (e.g., precipitation, wind speed, air temperature, humidity, solar radiation) is the Hanford Meteorological Station (HMS), located on the 200 Area plateau between the 200 East and 200 West Areas and within a few kilometers of all of the tank farms. The HMS records have been kept since the late 1940s and thus cover the time period of interest for all tank farm and other 200 Area waste site operations at Hanford. For the past 20 years, precipitation has averaged 184 mm/yr (7.2 in./yr), about 14% above the historical average (Hoitink et al. 2000). During this time, annual precipitation amounts have varied by more than a factor of three, ranging from a record high of 313 mm/yr (12.3 in./yr) in 1995 to a low of 95 mm (3.7 in.) in 1999. While variations in both seasonal and annual precipitation strongly affect drainage rates at the tank farms, the most dominant factor appears to be winter (November through March) precipitation. Winter precipitation during the past 20 years at Hanford has varied from a record high of 224 mm (8.8 in.) in 1997 to a low of 58 mm (2.3 in.) in 1990. Winter months typically have the greatest amount of precipitation (over 62% of the annual average) and the lowest amount of evaporation. Precipitation occurring outside of the winter period appears to contribute little to drainage (Gee et al. 1992; Fayer et al. 1999).

D.8.2.2.2 Soils. All tank farm surfaces consist of coarse-textured backfill materials. At some tank farms (e.g., BY, BX), commercial "top-course" materials (gravelly sands) have been added to cover surface contamination and provide operational stability for worker access. These well-drained sediments hold little water, transmitting it readily to the underlying sediment of the Hanford formation (Tallman et al. 1979). There is very limited characterization data on surface soils at tank farms, but some textural information is available (Smoot et al. 1989). More detailed soil characterization, such as saturated and unsaturated hydraulic conductivity, particle-size analysis, and water-retention characteristics of surface sediments, would be helpful in future assessments of the tank farms.

D.8.2.2.3 Vegetation. All tank-farm surfaces are kept vegetation free. Plants are kept off tank-farm surfaces by application of herbicides and soil sterilants. The control of vegetation is important in the tank farm operations because of concerns about radiation uptake by plants (e.g., radioactive tumbleweeds). Without vegetation, there is no root zone for plant water uptake, and evaporation is the sole mechanism for upward removal of water. In coarse soils, the lack of vegetation greatly increases the potential for drainage.

D.8.2.2.4 Tank Farm Water Balance. Based on the above description of climate, soils, and vegetation, we developed a simple water-balance model for surface soils at the Hanford Site tank farms. The model assumes the following conditions for the tank farms.

(1) Winter precipitation dominates the net infiltration process.

(2) Water runoff and run-on at tank farms are negligible.

(3) Annual water-storage changes are negligible.

(4) Soil texture (e.g., particle-size distribution) controls the amount of water retained in the surface and influences the overall evaporation rate.

(5) The soil surface remains unvegetated (upward water movement is by evaporation only [i.e., no transpiration or water uptake by plants]).

Based on the above assumptions, the surface-water balance can be written as:

$$D = (P_1 + P_2) - (E_1 + E_2) \qquad (D.8.2.2)$$

where

P_1 = winter (November through March) precipitation
P_2 = Non-winter (April through October) precipitation
E_1 = winter evaporation
E_2 = Non-winter evaporation.

Combining terms leads to the following expression:

$$D = P_1 - E_f \qquad (D.8.2.3)$$

where $E_f = (E_1 + E_2) - P_2$ is an evaporation factor.

E_f is dependent upon soil texture and precipitation. Based on an analysis of lysimeter records (Gee et al. 1992; Fayer et al. 1999), we determined the impact of precipitation and soil texture on drainage for a range of surface conditions, ranging from clean, washed gravels to fine-textured silt-loam soils. The following relationship was developed:

$$E_f = E_f^o \text{ for } P_1 > 80 \text{ mm/yr} \qquad (D.8.2.4)$$

$$E_f = E_f{}^{o}[P_1/115]^{0.5}, \text{ for } P_1 \leq 80 \text{ mm/yr} \qquad (D.8.2.5)$$

where $E_f^o = 0.0069 f^3 - 0.43 f^2 + 12.64 f + 25.157$ with f being the % fines (all material less than 53 microns in size).

The performance of this model is shown in Figure D.8.2.1, where the model is applied to a PNNL lysimeter located just north of the 300 Area at the Hanford Site. The PNNL lysimeter has a bare sand surface, is 8 m (26 ft) deep, and has been draining for the past 20 years (Gee 1987; Gee et al. 1992; Tyler et al. 1999). The agreement between modeled and observed drainage is reasonable. It must be kept in mind that the model was not independent of the lysimeter data because the total drainage from the lysimeter was used in fitting the evaporation factor, E_f, for coarse sand. The model was then applied to independent data from the Hanford Solid Waste Landfill (SWL) lysimeter (DynCorp 2000). The SWL lysimeter is a 7-m (23-ft) deep, basin-type lysimeter with a capture area of 85 m^2. Figure D.8.2.2 indicates that drainage has occurred from the SWL landfill since July 1996 (the lysimeter was placed at the bottom of the landfill trench in 1992 and subsequently filled over the next 3 years). Drainage has been collected from this site since July 1996 (DynCorp 2000). Cumulative drainage has been 280 mm (11 in.), averaging 62 mm/yr (2.4 in./yr). Table D.8.2.1 shows the measured annual drainage compared to that predicted by the water-balance model for a 4-year period (i.e., Equation D.8.2.3). It should be noted that annual drainage is predicted within 4 mm (0.16 in.) for all 4 years. Also note that for the calendar year 1997, the winter precipitation of 224 mm (8.8 in.) exceeds the 1997 annual value of 162 mm (6.4 in.). This results from the calculation of winter precipitation (November 1996 through March 1997), which includes a record 162 mm (6.4 in.) from November and December 1996. Fortuitously, the November through December record precipitation is identical to the entire 1997 annual value, illustrating the extreme variability in Hanford climate. The wide variation in the ratio of drainage to total precipitation (last column) reflects the importance of precipitation distribution and supports the concept that winter precipitation and soil texture are more important than total precipitation in determining drainage rates for bare waste sites at Hanford.

Figure D.8.2.1. Twenty-Year Record of Measured and Predicted Drainage From PNNL Lysimeter.

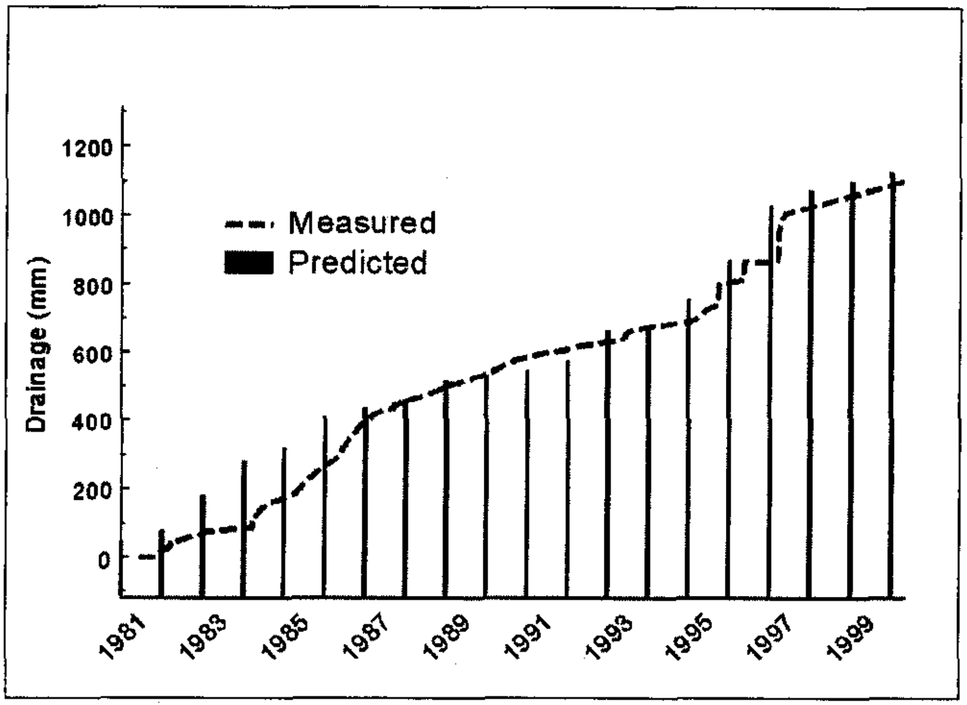

Note: Lysimeter is 8-m (26 ft) deep and sand filled. Predictions are using tank farm water balance model with HMS (Hanford Meteorological Station) climate record and measured soil texture (3% fines).

Figure D.8.2.2. Solid-Waste Landfill Drainage at the Hanford Site.

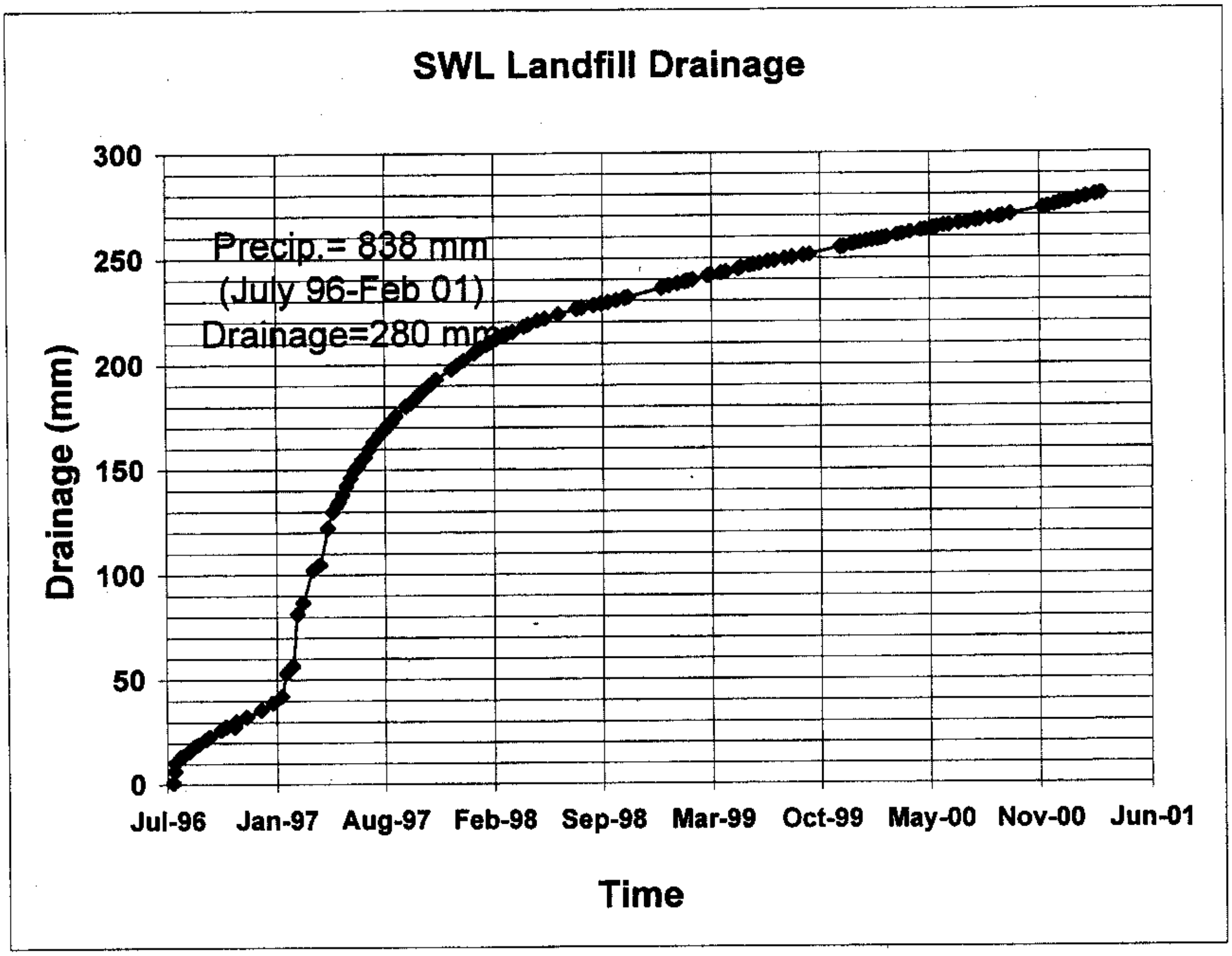

Note: The landfill was closed in 1995 and drainage began in July 1996. The Lysimeter is located below the landfill at a depth of 7 m (23 ft).

Table D.8.2.1. Measured Drainage at the Hanford Solid Waste Landfill Compared to that Predicted by Tank Farm Water Balance Model.

Year	Annual Precipitation (mm)	Winter Precipitation (mm)	Measured Drainage (mm)	Predicted Drainage (mm)	Drainage as % Total Precipitation
1997	162	224	162	158	100
1998	164	107	41	42	25
1999	95	86	22	21	23
2000	205	88	19	23	9

Note that in 1997, the winter precipitation exceeds the annual. This is a result of the differing time period for the two precipitation amounts and the record winter precipitation (November 1996 through March 1997). Uncertainty in the drainage is dependent on uncertainties in the surface texture. Variations in texture (percentage of fines of several percentage points can alter the drainage estimate by 10 to 20 mm/yr (0.4 to 0.8 in./yr) or more, particularly when the percentage of fines is low (less than10). It should also be noted that modest increases in the percentage of fines significantly reduces the drainage. An increase of percent fines from 1 to 7 % reduces the predicted drainage by a factor of nearly three, from 80 to 28 mm/yr (3.1 to 1.1 in./yr). Based on modeling results, Smoot et al. (1989) suggested that adding silt-loam soils to tank-farm surfaces was one means of virtually eliminating net infiltration (drainage).

D.8.2.2.5 Model Predictions. Drainage predictions were developed for several tank farms where textural data were available for surface sediments. Table D.8.2.2 shows the predicted annual drainage, based on surface texture and the past 20-year-climate record. No soil-texture data are currently available for surface sediments of SX tank farm. Assuming that the SX tank farm has a surface texture similar to S tank farm, the estimated average drainage rate for the SX tank farm is 56 mm/yr (2.2 in./yr).

Table D.8.2.2. Predicted Tank Farm Drainage Rates Related to Percent Fines in Surface Sediments and Percentage of Annual Precipitation Based on 20-Year Record.

Site/Soil	% Fines	Drainage (mm.yr)	% Precipitation
AP tank farm	1	80	43
S tank farm	3	56	30
U tank farm	7	28	15
Coarse Gravel	0	98	53
SWL Site	3	56	32
Silt Loam	60	0	0

D.8.2.3 Discussion

Data available from lysimeter studies at Hanford have shown that winter precipitation and surface textures are the dominant controls to waste-site drainage. The calibration data set contained the past 20-year-precipitation record and drainage from lysimeters with surfaces ranging from clean gravels to fine silt loams. Combining these data into a water-balance model has led to a simple expression for predicting drainage at tank farms. Based on the past 20-year record, we predict drainage rates for tank farms ranging from 20 to 80 mm/yr (0.8 to 3.1 in./yr). The model does not account for thermal effects on evaporation due to radiolytically heated tank wastes (i.e., warmer subsurface temperatures could increase the evaporation rates from tank farms, thus decreasing drainage). For this reason, the values reported here may overestimate the true drainage flux.

There have been no measurements of drainage at Hanford tank farms, so verification of the model remains to be completed. The surface-water balance must be modeled in more detail because employing deterministic codes requires hydrologic data such as water-retention characteristics and unsaturated hydraulic conductivities of the surface soil, presently unavailable in any of the tank farms. Examples of deterministic codes include UNSAT-H (Fayer and Gee 1997), HELP (Schroeder et al. 1994), or a transient water-budget model (Simmons and Meyer 2000). Even if hydrologic data were available, it is apparent that calibration is required (Fayer et al. 1992; Fayer and Gee 1997; Simmons and Meyer 2000) for such models to correctly predict drainage at Hanford tank farms.

Several options are available for improving tank-farm drainage predications. First, it is important to continue to maintain the lysimeter records upon which models can be calibrated. Longer records, including additional climatic variations and their impact on drainage, can build confidence in the range over which a drainage model will perform. Second, as a minimum, obtain textural data from surface soils at SX and other tank farms of interest. It also would be helpful, in using more sophisticated methods (as described above), to obtain water-retention and unsaturated-hydraulic-conductivity data for surface soils required for model inputs. Finally, short of installing a large lysimeter facility within a tank farm, it would be useful to obtain a direct measure of the water flux within the tank farm. This could be accomplished by installing small water-flux meters (Gee et al. 2000) within several of the tank farms. These devices measure water-flux rates from less than 10 mm/yr (0.4 in./yr) to more than 10,000 mm/yr (394 in./yr), providing short-term (multiple-year) drainage data upon which numerical models can be calibrated. Such an effort will provide improved predictions of the net infiltration that drives contaminants to groundwater at tank farms at Hanford.

D.8.2.4 Conclusions and Implications

Estimates were made of net infiltration (drainage) of meteoric water at the SX tank farm using a simple water-balance model. The model was based on climatic variables and surface soil textures specific to the Hanford Site. Winter (November through March) precipitation records for the past 20 years were combined with soil-texture data obtained from tank farm soil samples. These data were required to calibrate the water-balance model, which was subsequently used to estimate drainage flux at the SX tank farm. SX tank farm soil texture was assumed to be sandy gravel with 3% fines. When the water-balance model was applied to the SX tank farm, the drainage averaged 56 mm/yr (2.2 in./yr) for the past 20 years and ranged from 5 to 162 mm/yr (0.2 to 6.4 in./yr). The drainage estimate is conservative since it does not include the influence of elevated temperatures in the subsurface (due to radiolytic soil heating). Improvements in the estimates of drainage at the SX tank farm are expected when detailed soil-textural analyses of the SX tank farm surface soil are completed and when direct measurements with water-flux meters are implemented.

D.8.2.5 References

Connelly, M. P., B. H. Ford and J. V. Borghese, 1992, *Hydrogeologic Model for the 200 West Groundwater Aggregate Area,* WHC-SD-EN-TI-014, Rev. 0, Westinghouse Hanford Company, Richland, Washington.

DynCorp, 2000, *Hanford Solid Waste Landfill Closure Plan,* HNF-7173, Rev. 0, DynCorp Tri-Cities Services, Inc., Richland, Washington.

Fayer, M. J., M. L. Rockhold, and M. D. Campbell, 1992, "Hydrologic Modeling of Protective Barriers: Comparison of Field Data and Simulation Results," *Soil Sci. Soc. Am. J.,* 56: 690–700.

Fayer, M. J., and G. W. Gee, 1997, "Hydrologic Model Tests for Landfill Covers Using Field Data." In: *Landfill Capping in the Semi-Arid West, Symposium Proceedings,* T. D. Reynolds and R. C. Morris (eds.), pp. 53–68. Jackson Lake, Wyoming, May 1997. ESRF-019, Environmental Science and Research Foundation, Idaho Falls, Idaho.

Fayer, M. J., E. M. Murphy, J. L. Downs, F. O. Khan, C. W. Lindenmeier, and B. N. Bjornstad, 1999, *Recharge Data Package for the Immobilized Low-Activity Waste 2001 Performance Assessment,* PNNL-13033, Pacific Northwest National Laboratory, Richland, Washington.

Gee, G. W., 1987, *Recharge at the Hanford Site: Status Report,* PNL-6403, Pacific Northwest National Laboratory, Richland, Washington.

Gee, G. W., M. J. Fayer, M. L. Rockhold, and M. D. Campbell, 1992, "Variations in Recharge at the Hanford Site," *Northwest Sci.,* 66:237–250.

Gee, G. W., A. L. Ward, T. Caldwell, and J. Ritter, 2000, "A Simple Water Flux Meter for Coarse Soils," p. 218, *Annual Meeting Abstracts, Minneapolis, Minnesota, November 5-9, 2000, American Society of Agronomy,* Madison, Wisconsin.

Hodges, F. N., 1998, *Results of Phase I Groundwater Quality Assessment for Single-Shell Tank Waste Management Areas S-SX at the Hanford Site*, PNNL-11810, Pacific Northwest National Laboratory, Richland, Washington.

Hoitink, D. J., K. W. Burk, J. V. Ramsdell, 2000, *Hanford Site Climatological Data Summary 1999 With Historical Data,* PNNL-13117, Pacific Northwest National Laboratory, Richland, Washington.

Johnson, V. G., and C. J. Chou, 1998, *Results of Phase I Groundwater Quality Assessment for Single-Shell Tank Waste Management Areas T and TX-TY at the Hanford Site*, PNNL-11809, Pacific Northwest National Laboratory, Richland, Washington.

Myers, D. A., D. L. Parker, G. Gee, V. G. Johnson, G. V. Last, R. J. Serne, and D. J. Moak, 1998, *Findings of the Extension of Borehole 41-09-39, 241-SX Tank Farm,* HNF-2855, Lockheed Martin Hanford Corporation, Richland, Washington.

Narbutovskih, S. M., 1998, *Results of Phase I Groundwater Quality Assessment for Single-Shell Tank Waste Management Areas B-BX-BY at the Hanford Site*, PNNL-11826, Pacific Northwest National Laboratory, Richland, Washington.

Rickard, W. H., L. E. Rogers, B. E. Vaughan, and S. F. Liebetrau, 1988, *Shrub-Steppe: Balance and Change in a Semi-Arid Terrestrial Ecosystem,* p. 8, Elsevier, Amsterdam.

Schroeder, P. R., C. M. Lloyd, and P. A. Zappi, 1994, *The Hydrologic Evaluation of Landfill Performance (HELP) Model. User's Guide for Version 3,* EPA/600/R-94/168a, U.S. Environmental Protection Agency, Cincinnati, Ohio.

Serne, R. J., J. M. Zachara, and D. S. Burke, 1997, *Chemical Information on Tank Supernatants, Cs Adsorption from Tank Liquids onto Hanford Sediments, and Field Observations of Cs Migration from Past Tank Leaks*, PNNL-11495, Pacific Northwest National Laboratory, Richland, Washington.

Simmons, C. S., and P. D. Meyer, 2000, "A Simplified Model for the Transient Water Budget of a Shallow Unsaturated Zone," *Water Resour. Res.,* 36:2835–2844.

Smoot, J. L., J. E. Szecsody, B. Sagar, G. W. Gee, and C. T. Kincaid, 1989, *Simulations of Infiltration of Meteoric Water and Contaminant Plume Movement in the Vadose Zone at Single-Shell Tank 241-T-106 at the Hanford Site*, WHC-EP-0332, Westinghouse Hanford Company, Richland, Washington.

Stone, W. A., J. M. Thorp, O. P. Gifford, and D. J. Hoitink, 1983, *Climatological Summary for the Hanford Area*, PNL-4622, Pacific Northwest National Laboratory, Richland, Washington.

Tallman, A. M., K. R. Fecht, M. C. Marratt, and G. V. Last, 1979, *Geology of the Separations Areas, Hanford Site, South-Central Washington,* RHO-ST-23, Rockwell Hanford Operations, Richland, Washington.

Tyler, S. W., B. R. Scanlon, G. W. Gee and G. B. Allison, 1999, "Water and Solute Transport in Arid Vadose Zones: Innovations in Measurement and Analysis," In: *Vadose Zone Hydrology,* M. B. Parlange and J. W. Hopmans (eds.), pp. 334–373, Oxford Press, New York.

Ward, A. L., G. W. Gee, and M. D. White, 1997, *A Comprehensive Analysis of Contaminant Transport in the Vadose Zone Beneath Tank SX-109,* PNNL-11463, Pacific Northwest National Laboratory, Richland, Washington.

D.8.3 EFFECTS OF ACCELERATED MOVEMENT DUE TO SURFACE TENSION AND CONTACT ANGLE EFFECTS IN HYPERSALINE FLUIDS TRANSPORTED IN UNSATURATED SEDIMENTS

Andy L. Ward[1] and Glendon W. Gee[1]

[1]Pacific Northwest National Laboratory (PNNL), Richland, Washington 99352

D.8.3.1 Introduction

Highly saline fluids have leaked into the ground at the SX tank farm (Serne et al. 1997; Myers et al. 1998). These highly saline fluids have properties quite different from pure water or water from meteoric inputs (rain or snowmelt). Density (e.g., specific gravity) can be in excess of 1.3, relative viscosity greater than 3, surface tension in excess of 100 dynes/cm, and contact angle greater than zero. Meteoric waters added to the subsurface will eventually dilute the tank leak and reduce the impact of the extreme chemistry. However, the fluid properties of the leaked tank liquor must be known to adequately predict the contaminant migration rates in Hanford sediments. During the first 2 years of this EMSP project, efforts were made to evaluate the impact of the salt plume, both in the laboratory and in the field. While these experiments are ongoing, the observations to date can be used to infer the performance of highly saline fluids within the vadose zone.

D.8.3.2 Discussion of High Salt Tests

Both laboratory and field tests were initiated to assess the impact of hypersaline fluids on migration rates in Hanford sediments. In the field, a series of tests were conducted to evaluate the movement of dense fluids in Hanford sediments. Sodium nitrate solution (5 N concentration with a specific gravity of 1.3) was infiltrated into Hanford sediments in the field in the spring of 1999. The highly saline solution rapidly infiltrated, but due to textural layering, the plume was dispersed laterally in all cases, even when the surface tension was altered by use of organic additives. The impacts of density and surface tension were mitigated by layering, which prevented finger formation and deep penetration of the nitrate solution. In the laboratory, coarse sediments from the Hanford formation were placed in cells that were exposed to X-ray Microfocus Tomography (XMT). These tests demonstrated that fingers could develop with hypersaline solutions when coarse Hanford sediments were packed without layering. However, with layering, the fingering was prevented. A theoretical assessment of fingering was conducted using computer models developed by PNNL. The computer code STOMP (White et al. 1995; White and Oostrom 1996) was modified to describe the movement of hypersaline solutions. The modeled finger formed when hypersaline solution with known density and surface tensions were tested in the model. Known hydrologic parameters for a coarse Hanford sediment were also used as model input. Figure D.8.3.1 shows the plume development when water (left) was introduced into the simulated test column compared to the hypersaline solution (right). The model is capable of predicting the finger development. When layered soils are simulated in the model, the finger does not form, qualitatively predicting the observed layer control on fingering that has been observed both in the laboratory and field. The results suggest that layering has a significant impact on the movement of the hyper-saline leak in the SX tank farm. It is very likely that some deep penetration occurred beneath the tank, but the lithology of the subsurface sediments reflects a highly layered system. So it is not surprising that no deep penetration or preferential flow of high salt occurred. At least any deep penetration cannot be attributed solely to surface tension or density effects. This work will continue through the end of FY 2001.

Figure D.8.3.1. Simulated Plume Development in Hanford Sediments Using STOMP.

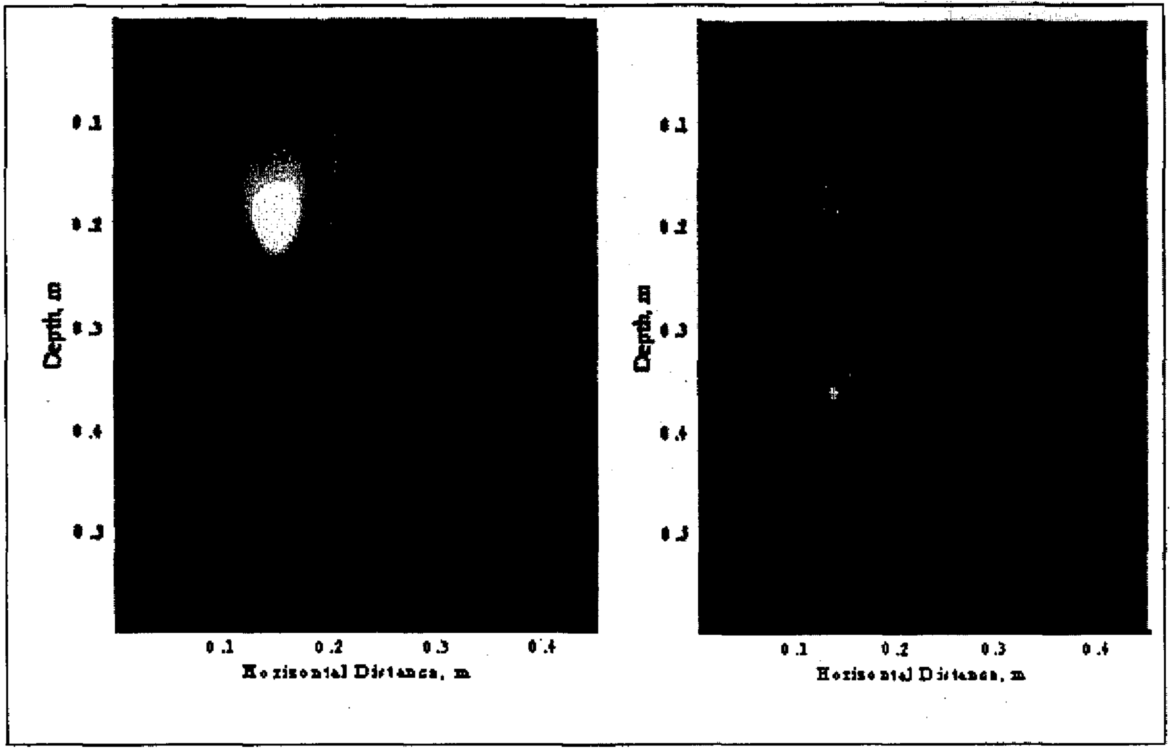

Note: Plot on left is plume developed for low concentration salt system (river water) infiltrating into a 0.6-m (2-ft) deep soil column for a period of 60 minutes. Plume on right is for similar time sequence, but with 5 N $NaNO_3$.

D.8.3.3 Conclusions and Implications

Traditional transport models have failed to provide adequate descriptions of contaminant distributions in the vadose zone of Hanford's tank farms. Tank fluids leaked to the vadose zone are hypersaline with normality at or above 10 and specific gravity ranging from 1.3 to 1.5.
In this study, it is hypothesized that deviation between observed and predicted plume distributions is related to the fluid constitution, its effect on surface tension, equilibrium contact angle, and ultimately on the water-retention function. A thermodynamic model that describes interfacial tension and equilibrium contact angle as functions of aqueous-phase salt concentrations is incorporated into the STOMP numerical simulator and used to predict the infiltration of hypersaline fluids through the vadose zone. Specific wetting-front features, which are absent in the pure-fluid case, are identified and quantified. Laboratory observations and numerical simulations suggest that the elevated surface tensions observed in hypersaline fluids may play a fundamental role in water and contaminant migration at the SX tank farm and wherever these high-salt fluids have leaked into the ground.

D.8.3.4 Acknowledgements

This research was supported by the EMSP through a FY 1999 funded project: "Rapid Migration of Radionuclides Leaked from High-Level Waste Tanks: A Study of Salinity Gradients, Wetted Path Geometis, and Water Vapor Transport" (Ward, Selker, Tyler).

D.8.3.5 References

Myers, D. A., D. L. Parker, G. Gee, V. G. Johnson, G. V. Last, R. J. Serne, and D. J. Moak, 1998, *Findings of the Extension Borehole, 41-09-39, 241-SX Tank Farm,* HNF-2885, Locheed Martin Hanford Corporation, Richland, Washington.

Serne, R. J., J. M. Zachara, and D. S. Burke, 1997, *Chemical Information on Tank Supernatants, Cs Adsorption from Tank Liquids onto Hanford Sediments, and Field Observations of Cs Migration from Past Tank Leaks*, PNNL-11495, Pacific Northwest National Laboratory, Richland, Washington.

White, M. D., M. Oostrom, and R. J. Lenhard, 1995, "Modeling fluid flow and transport in variably saturated porous media with the STOMP simulator. 1. Nonvolatile three-phase model description," *Adv. Water Res.,* 18: 353–364.

White, M. D. and M. D. Oostrom, 1996, *STOMP Subsurface Transport Over Multiple Phases Theory Guide*, PNNL-11217, Pacific Northwest National Laboratory, Richland, Washington.

D.8.4 CONCLUSIONS OF S&T INVESTIGATIONS OF VADOSE ZONE FIELD EXPERIMENTS AND INFILTRATION ESTIMATES FOR THE SX TANK FARM

Hydrologic research efforts that provide additional support to characterization efforts at the SX tank farm include (1) the Vadose Zone Transport Field Study (VZTFS), (2) studies to develop simplified methods for estimating recharge rates at the SX and other tank farms and (3) an EMSP supported study of the hydrologic impacts of highly concentrated salt solutions in Hanford sediments.

VZTFS Studies. VZTFS field studies at the Hanford Site are evaluating the movement of contaminant plumes in the vadose zone in order to better predict the transport of contaminants in tank farms and other waste-disposal sites. The first of four field tests was completed at the 299-E24-111 injection site in the 200 East Area during FY 2000. Five discrete pulses, totaling nearly 19,000 L (5,000 gal), added to injected to the ground during the test. Nine geophysical methods were used in the study, all of which were successful in identifying changes in subsurface water contents. Changes in water content were found to be minimal below 11 m (36 ft), which suggests that lateral flow in shallow soil dominates much of the transport. The two-dimensional numerical model applied to the test site appears to capture the plume's general flow depths and directions, but is deficient in describing the extent of the plume's lateral spreading. It is anticipated that hydraulic property data collected during this testing may help improve future predictions of lateral spreading. The implications of this VZTFS study support the general observations that chemicals such as cesium can move laterally in Hanford sediments, as moves was observed near tank SX-109. The lateral movement of radionuclides is an indication that there is lithologic control of the hydraulic properties, similar to what was observed in our field test.

Simplified Methods for Estimating Recharge. While contaminants such as cesium have been held up in the vadose zone in the SX tank farm, others such as ^{99}Tc, chromate, and nitrate have reached groundwater. It is hypothesized that winter rains and snowmelt runoff, and in some cases water-line leaks, have infiltrated deeply and in specific areas have leached soil contamination from the vadose zone to the underlying water table. Water moves through the soil more rapidly beneath buried tanks because the area is devoid of plants and covered with gravel. The drainage (recharge) rate of meteoric water at the SX tank farm was estimated using a simple water-balance model that was based on the climate and surface soil textures at the Hanford Site. Assessing the complete water balance of the surface soils provides the best way to analyze deep drainage. Three main factors (climate, soils, and vegetation) were evaluated to assess the water balance. Climate studies indicate that most summer precipitation evaporates, leaving winter precipitation as the only significant contributor to water drainage in the soils. The soils around the tank farms are mostly coarse soil and gravel, which allows water to migrate easily under gravity. No vegetation is allowed to grow around the tank farms; therefore, no water is taken up by plants. Winter precipitation records were combined with soil-texture data obtained from tank-farm soil samples. At the SX tank farm, the drainage estimate averaged 56 mm/yr (2.2 in./yr) for the past 20 years and ranged from 5 to 162 mm/yr (0.2 to 6.4 in./yr). This estimate is conservative since it does not include the influence of elevated temperatures in the subsurface because of heating from radioactive wastes in tanks.

Impacts of Highly Concentrated Salt Solutions on Flow Stability in Hanford Sediments. Traditional transport models have not provided adequate descriptions of contaminant distributions in the vadose zone because leaking tank fluids are hypersaline. The properties of these fluids are quite different from meteoric inputs. The effects of these hypersaline solutions needs to be better understood to account for a significant deviation between observed and predicted plume distributions. Preliminary studies suggest that layering has a significant impact on the transport of hyper-saline fluids. Laboratory observations and numerical simulations suggest that the elevated surface tensions observed in hypersaline fluids may play a fundamental role in water and contaminant migration at the Hanford Site.

D.9.0 REFERENCES

Abbasi, S. A., and R. Soni, 1984, "Teratogenic Effects of Chromium(VI) in the Environment as Evidenced by the Impact of larvae of Amphibian *Rand tigrina*: Implications in the Environmental Management of Chromium," *International Journal of Environmental Studies*, Vol. 23:131-137.

Adamson, A. W., 1990, *Physical Chemistry of Surfaces,* John Wiley & Sons, New York.

Agnew, S. F., 1997, *Hanford Tank Chemical and Radionuclide Inventories: HDW Model. Rev. 4*, LA-UR-96-3800, Los Alamos National Laboratory, Los Alamos, New Mexico.

Agnew, S. F., and R. A. Corbin, 1998, *Analysis of SX Farm Leak Histories--Historical Leak Model (HLM)*, HNF-3233, LA-UR-96-3537, Prepared by Los Alamos National Laboratory, Los Alamos, New Mexico, for U.S. Department of Energy, Richland Operations Office and Project Hanford Management Company, Lockheed Martin Hanford Corporation, Richland, Washington.

Ainsworth, C. C., D. C. Girvin, J. M. Zachara, and S. C. Smith, 1989, "CrO_4^{2-} Adsorption on Goethite: Effects of Aluminum Substitution," *Soil Science Society of America Journal*, Vol. 53:411-418.

Ainsworth, C. C., J. M. Zachara, K. Wagnon, and J. P. McKinley, 2001a, "Effect of Hypersaline and High pH Solutions on the Ion Exchange of Cs in Hanford Formation Sediments," *Soil Science Society of America Journal,* (Submitted).

Ainsworth, C. C., J. M. Zachara, J. P. McKinley, and K. Wagnon, 2001b, "Effect of Hyperalkalinity on Hanford Formation Sediments: Base-Induced Mineral Transformations," *Geochimica et Cosmochimica Acta,* (Submitted).

Apelblat, A., and E. Korin, 1998, "The Vapour Pressures of Saturated Aqueous Solutions of Sodium Chloride, Sodium Bromide, Sodium Nitrate, Sodium Nitrite, Potassium Iodide, and Rubidium Chloride at Temperatures from 227 K to 323 K," *Journal of Chemical Thermodynamics,* Vol. 30:59-71.

Appelo, C. A. J., and D. Postma, 1996, *Geochemistry, Groundwater and Pollution*, A. A Balkema, Rotterdam, p. 536.

Baes, C. F., Jr., and R. E. Mesmer, 1986, *The Hydrolysis of Cations*, Robert F. Krieger Publishing Co., Malabar, Florida, p. 489.

Balkwill, D. L., R. H. Reeves, G. R. Drake, J. Y. Reeves, F. H. Crocker, M. Baldwin-King, and D. R. Boone, 1997, "Phylogenetic Characterization of Bacteria in the Subsurface Microbial Culture Collection," *FEMS Microbiology Reviews*, Vol. 20:201-216.

Bargar, J. R., G. E. Brown, Jr., I. Evans, T. Rabedeau, M. Rowen, and J. Rogers, 2001, "A New Hard X-ray XAFS Spectroscopy Facility for Environmental Samples, Including Actinides, at the Stanford Synchrotron Radiation Laboratory," *Proc. 2nd Euroconference and NEA Workshop on Speciation, Techniques, and Facilities for Radioactive Materials at Synchrotron Light Sources*, (In press).

Barnes, C. J., and G. B. Allison, 1988, "Water Movement in the Unsaturated Zone Using Stable Isotopes of Hydrogen and Oxygen," *Journal of Hydrology*, Vol. 100:143-176.

Bartlett, R. J., and B. R. James, 1996, "Chromium," *In* D. L. Sparks et al. (ed.), *Methods of Soil Analysis; Part 3 – Chemical Methods*, pp. 683-701, SSSA Book Series: 5, Soil Science Society of America, Inc. Madison, Wisconsin.

Battistelli, A., C. Calore, and K. Pruess, 1997, "The Simulator TOUGH2/EWASG for Modeling Geothermal Reservoirs with Brines and Non-Condensible Gas," *Geothermics*, Vol. 26:437-464.

Biggar, J. W., and D. R. Nielsen, 1962, "Miscible Displacement: II. Behavior of Tracers," *Soil Science Society of America Proceedings*, Vol. 26:125-128.

Bish, D. L., S. J. Chipera, and P. Snow, 2000, "Mineralogic Studies of Uncontaminated 200-Area tank farm Sediments: Interim Report (PO #401924)," In: *Reports of the Representative Site Workshop on High Level Waste Contaminated Sediments*, Pacific Northwest National Laboratory, Richland, Washington.

Bjornstad B. N., K. R. Fecht, and A. M. Tallman, 1987, *Quaternary Geology of the Pasco Basin, Washington*, Rockwell Hanford Operations, Richland, Washington.

Blum, J. D., and Y. Erel, 1997, "Rb-Sr Isotope Systematics of a Granitic Soil Chronosequence: The Importance of Biotite Weathering," *Geochimica et Cosmochimica Acta*, Vol. 61:3193-3204.

Bond, W. J., and P. J. Wierenga, 1990, "Immobile Water During Solute Transport in Unsaturated Sand Columns," *Water Resources Research*, Vol. 26:2475-2481.

Brigatti, M. F., G. Franchini, C. Lugli, L. Medici, L. Poppi, and E. Turci, 2000a, "Interaction Between Aqueous Chromium Solutions and Layer Silicates," *Applied Geochemistry*, Vol. 15:1307-1316.

Brigatti, M. F., C. Lugli, G. Cibin, A. Marcelli, G. Biuli, E. Paris, A. Mottana, and Z. Wu, 2000b, "Reduction and Sorption of Chromium by Fe(II)-Bearing Phyllosilicates: Chemical Treatments and X-ray Absorption Spectroscopy (XAS) Studies," *Clays and Clay Minerals*, Vol. 48:272-281.

Brockman, F. J., S. W. Li, J. K. Fredrickson, D. B. Ringelberg, T. L. Kieft, C. M. Spadoni, J. P. McKinley, and D. C. White, 1998, "Post-Sampling Changes in Microbial Community Structure and Activity in a Subsurface Paleosol," *Microbial Ecology*, Vol. 36:152-164.

Brockman, F. J., T. L. Kieft, J. K. Fredrickson, B. N. Bjornstad, S. W. Li, W. Spangenburg, and P. E. Long, 1992, "Microbiology of Vadose Zone Palesols in South-Central Washington State," *Microbial Ecology*, Vol. 23:279-301.

Brouwer, E., B. Baeyens, A. Maes, and A. Cremers, 1983, "Cesium and Rubidium Ion Equilibria in Illite Clay," *Journal of Physical Chemistry*, Vol. 87:1213-1219.

Brown, G. E. Jr., V. E. Henrich, W. H. Casey, D. L. Clark, C. Eggleston, A. R. Felmy, D. W. Goodman, M. Gratzel, G. Machiel, M. I. McCarthy, K. H. Nealson, D. A. Sverjensky, M. F. Toney, and J. M. Zachara, 1998, "Metal Oxide Surfaces and Their Interactions with Aqueous Solutions and Microbial Organisms," *Chemical Reviews,* Vol. 99/1:77-174.

Brown, G. E., Jr., G. Calas, G. A. Waychunas, and J. Petiau, 1988, "X-ray Absorption Spectroscopy and its Applications in Mineralogy and Geochemistry," In: *Spectroscopic Methods in Mineralogy and Geology* (F. Hawthorne, ed.), *Reviews in Mineralogy*, Vol. 18, p. 431-512, Mineralogical Society of America, Washington, D.C.

Brown, G. E., Jr., S. A. Chambers, J. E. Amonette, J. R. Rustad, T. Kendelewicz, P. Liu, C. S. Doyle, D. Grolimund, N. S. Foster-Mills, S. A. Joyce, and S. Thevuthasan, 2000, "Interaction of Water and Aqueous Chromium Ions with Iron Oxide Surfaces," In: *American Chemical Society Symposium Series 778, Nuclear Site Remediation - First Accomplishments of the Environmental Management Science Program*, (P. G. Eller and W. R. Heineman, eds.), p. 212-246, American Chemical Society, Columbus, Ohio.

Bruggenwart, M. G. M., and A. Kamphorst, 1979, "Survey of Experimental Information on Cation Exchange in Soil Systems," In: *Soil Chemistry B. Physico-Chemical Models, Elsevier* Scientific Co., G. H. Bolt, ed., New York, pp. 141-192.

Brusseau, M. L., Q. H. Hu, and R. Srivastava, 1997, "Using Flow Interruption to Identify Factors Causing Nonideal Contaminant Transport," *Journal of Contaminant Hydrology*, Vol. 14:39-54.

Buerge, I. J., and S. J. Hug, 1999, "Influence of Mineral Surfaces on Chromium(VI) Reduction by Iron(II)," *Environmental Science and Technology,* Vol. 33:44,285-44,291.

Carroll, S., C. I. Steefel, P. Zhao, and S. Roberts, 2001, *Reaction Transport Experiments Investigating the Migration of* ^{137}*Cs in Sediments Beneath the Hanford SX Tank Farm*, FIR Report.

Comans, R. N. J., and D. E. Hockley, 1992, "Kinetics of Cesium Sorption to Illite," *Geochimica et Cosmochimica Acta*, Vol. 56:1157-1164.

Comans, R. N. J., M. Haller, and P. De Preter, 1991, "Sorption of Cesium on Illite: Non-Equilibrium Behavior and Reversibility," *Geochimica et Cosmochimica Acta*, Vol. 55:433-440.

Connelly, M. P., B. H. Ford, and J. V. Borghese, 1992, *Hydrogeologic Model for the 200 West Groundwater Aggregate Area,* WHC-SD-EN-TI-014, Rev. 0, Westinghouse Hanford Company, Richland, Washington.

Conway, J. G., R. J. Luxmoore, J. M. Matuszek, and R. O. Patt, 1997, *TWRS Vadose Zone Contamination Issue Expert Panel Status Report,* DOE/RL-RL-49, Rev. 0, U.S. Department of Energy, Richland Operations Office, Richland, Washington.

Corey, A. T., 1954, "The Interrelation Between Gas and Oil Relative Permeabilities," *Producers Monthly*, November, pp. 38-41.

Cornell, R. M., 1993, "Adsorption of Cesium on Minerals: A Review," *Journal of Radioanalytical Nuclear Chemistry Articles*, Vol. 171:483-500.

Cornell, R. M., and U. Schwertmann, 1996, "The Iron Oxides. Structure, Properties, Reactions, Occurrence and Uses," BCH Verlagsgesellschaft mbH, D-69451, Weinheim (Federal Republic of Germany).

Craig, H., 1961, "Isotopic Variations in Meteoric Waters," *Science*, Vol. 133:1702-1703.

Crocker, F. H., J. K. Fredrickson, D. C. White, D. B. Ringelberg, and D. L. Balkwill, 2000, "Phylogenetic and Physiological Diversity of *Arthrobacter* Strains Isolated From Unconsolidated Subsurface Sediments," *Microbiology*, Vol. 146:1295-1310.

Daly, M. J., and K. W. Minton, 1995, "Interchromosomal Recombination in the Extremely Radioresistant Bacterium *Deinococcus radiodurans*," *Journal of Bacteriology*, Vol. 177:5495-5505.

Daly, M. J., and K. W. Minton, 1996, "An Alternative Pathway of Recombination of Chromosomal Fragments Precedes recA-dependent Recombination in the Radioresistant Bacterium *Deinococcus radiodurans*," *Journal of Bacteriology*, Vol. 178:4461-4471.

Daly, M. J., L. Ouyang, P. Fuchs, and K. W. Minton, 1994, "*In vivo* Damage and *rec*A-Dependent Repair of Plasmid and Chromosomal DNA in the Radiation-Resistant Bacterium *Deinococcus radiodurans*," *Journal of Bacteriology,* Vol. 176:3508-3517.

Deer W. A., R. A. Howie, and J. Zussman, 1976a, *Rock-Forming Minerals*, Vol. 4, Framework Silicates, John Wiley and Sons, Inc.

Deer W. A., R. A. Howie, and J. Zussman, 1976b, *Rock-Forming Minerals*, Volume 3, Sheet Silicates, Longmans, London.

DOE, 1999, *Groundwater/Vadose Zone Integration Project Science and Technology Summary Description*, DOE/RL-98-48, Vol. III, Rev. 0, U.S. Department of Energy, Richland Operations Office, Richland, Washington.

DOE, 2000, *Groundwater/Vadose Zone Integration Project Science and Technology Summary Description*, DOE/RL-98-48, Vol. III, Rev. 1, U.S. Department of Energy, Richland Operations Office, Richland, Washington.

DOE-RL, 2000, *Groundwater/Vadose Zone Integration Project Science and Technology Summary Description*, DOE/RL-98-48, Vol. III, Rev. 1, U.S. Department of Energy, Richland Operations Office, Richland, Washington.

Doughty, C., and K. Pruess, 1988, "A Semi-Analytical Solution for Heat Pipe Effects Near High Level Nuclear Waste Packages Buried in Partially Saturated Geologic Media," *Int. Journal of Heat and Mass Transfer*, Vol. 31:79-90.

Doyle, C. S., T. Kendelewicz, G. E. Brown, Jr., S. A. Chambers, J. M. Zachara, and C. M. Eggleston, Jr., 2000, "The Effect of Carbonate Coatings on the Reduction of Cr(VI) on the (111) Surface of Magnetite," *Journal of Conference Abstracts*, Vol. 5(2):Goldschmidt Conference, Oxford, United Kingdom.

DynCorp, 2000, *Hanford Solid Waste Landfill Closure Plan*, HNF-7173, Rev. 0, DynCorp Tri-Cities Services, Inc., Richland, Washington.

Eary, L. E., and D. Rai, 1988, "Chromate Removal from Aqueous Wastes by Reduction with Ferrous Iron," *Environmental Science and Technology*, Vol. 22:72-977.

Eary, L. E., and D. Rai, 1989, "Kinetics of Chromate Reduction by Ferrous Ions Derived from Hematite and Biotite at 25 °C," *American Journal of Science*, Vol. 289:180-213.

Eastman, G. Y., 1968, "The Heat Pipe," *Scientific American*, Vol. 218:38-46.

Eng, P. J., M. Newville, M. L. Rivers, and S. R. Sutton, 1999, "Dynamically Figured Kirkpatrick Baez X-ray Micro-Focusing Optics," In: *X-Ray Microfocusing: Applications and Technique* (I. McNulty, ed.), *SPIE Proc.* 3449, p. 145.

Epstein, S., and T. Mayeda, 1953, "Variations of O18 Content of Waters from Natural Sources," *Geochimica et Cosmochimica Acta*, Vol. 4:213-224.

Evans, D. W., J. J. Alberts, and A. I. C. Roy, 1983, "Reversible Ion-Exchange Fixation of Cesium-137 Leading to Mobilization From Reservoir Sediments," *Geochimica et Cosmochimica Acta*, Vol. 47:1041-1049.

Evans, D. W., J. J. Alberts, and R. A. Clark, 1983, "Reversible Ion-Exchange Fixation of Cesium-137 Leading to Mobilization from Reservoir Sediments," *Geochimica et Cosmochimica Acta*, Vol. 47:1041-1049.

Evans, J. C., E. A. Lepel, R. W. Sanders, C. L. Wilkerson, W. Silker, C. W. Thomas, K. H. Abel, and D. R. Robertson, 1983, *Long-Lived Activation Products in Reactor Materials*, NUREG/CR-3474, PNL-4824, National Technical Information Service, Springfield, Virginia, p. 131.

Evans, J. C., E. A. Lepel, R. W. Sanders, C. W. Thomas, and D. E. Roberts, 1988, "Long-Lived Activation Products in Light-Water Reactor Construction Materials: Implications for Decommissioning," *Radioactive Waste Management and the Nuclear Fuel Cycle*, Vol. 11:1-39.

Fayer, M. J., and G. W. Gee, 1997, "Hydrologic Model Tests for Landfill Covers Using Field Data," In: *Landfill Capping in the Semi-Arid West, Symposium Proceedings*, T. D. Reynolds and R. C. Morris (eds.), pp. 53–68, Jackson Lake, Wyoming, May 1997, ESRF-019, Environmental Science and Research Foundation. Idaho Falls, Idaho.

Fayer, M. J., E. M. Murphy, J. L. Downs, F. O. Khan, C. W. Lindenmeier, and B. N. Bjornstad, 1999, *Recharge Data Package for the Immobilized Low-Activity Waste 2001 Performance Assessment,* PNNL-13033, Pacific Northwest National Laboratory, Richland, Washington.

Fayer, M. J., J. B. Sisson, W. A. Jordan, A. H. Lu, and P. R. Heller, 1993, *Subsurface Injection of Radioactive Tracers: Field Experiment for Model Validation Testing,* NUREG/CR-5996. U. S. Nuclear Regulatory Commission, Washington, D.C.

Fayer, M. J., M. L. Rockhold, and M. D. Campbell, 1992, "Hydrologic Modeling of Protective Barriers: Comparison of Field Data and Simulation Results," *Soil Sci. Soc. Am. J.,* 56:690-700.

Fayer, M. J., R. E. Lewis, R. E. Engleman, A. L. Pearson, C. J. Murray, J. L. Smoot, R. R. Randall, W. H. Wegener, and A. H. Lu, 1995, *Re-Evaluation of a Subsurface Injection Experiment for Testing of Flow and Transport Models*, PNL-10860, Pacific Northwest National Laboratory, Richland, Washington.

Felmy, A. R, 1995, "GMIN, A Computerized Chemical Equilibrium Program Using a Constrained Minimization of the Gibbs Free Energy: Summary Report," *Soil Science Society of America*, Special Publication Vol. 42:377-407.

Felmy, A. R., 2000, *Thermodynamic Modeling of Sr/TRU Removal, BNFL-RPT-037, Rev. 0*, PNWD-3044, Pacific Northwest National Laboratory, Richland, Washington.

Fendorf, S. E., and G. Li, 1996, "Kinetics of Chromate Reduction by Ferrous Iron," *Environmental Science and Technology,* Vol. 30:1614-1617.

Fendorf, S. E., B. W. Wielinga, and C. M. Hansel, 2000, "Chromium Transformations in Natural Environments: The Role of Biological and Abiological Processes in Chromium(VI) Reduction," *International Geology Review*, Vol. 42:691-701.

Francis, C. W., and F. S. Brinkley, 1976, "Preferential Sorption of ^{137}Cs to Micaceous Minerals in Contaminated Freshwater Sediment," *Nature*, Vol. 260:511-513.

Fredrickson, J. K., and D. L. Balkwill, 1998, *Sampling and Enumeration Techniques: Techniques in Microbial Ecology*, R. S. Burlage, R. Atlas, D. Stahl, G. Geesey, and G. Sayler, eds, Oxford University Press, New York, 239-254.

Fredrickson, J. K., and T. C. Onstott, 2001, "Biogeochemical and Geological Significance of Subsurface Microbiology," *Subsurface Microbiology and Biogeochemistry,* J. K. Fredrickson and M. Fletcher, Wiley-LISS Inc., New York, pp. 3-38.

Fredrickson, J. K., F. J. Brockman, B. N. Bjornstad, P. E. Long, S. W. Li, J. P. McKinley, J. V. Wright, J. L. Conca, T. L. Kieft, and D. L. Balkwill, 1993, "Microbiological Characteristics of Pristine and Contaminated Deep Vadose Sediments From an Arid Region," *Geomicrobiology Journal,* Vol. 11:95-107.

Fredrickson, J. K., H. M. Kostandarithes, S. W. Li, A. E. Plymale, and M. J. Daly, 2000a, "Reduction of Fe(III), Cr(V), U(VI), and Tc(VII) by *Deinococcus radiodurans* R1," *Applied and Environmental Microbiology*, Vol. 66:2006-2011.

Fredrickson, J. K., J. M. Zachara, D. W. Kennedy, M. C. Duff, Y. A. Gorby, S. W. Li, and K. M. Krupka, 2000b, "Reduction of U(VI) in Goethite (a-FeOOH) Suspensions by a Dissimilatory Metal-Reducing Bacterium," *Geochimica et Cosmochimica Acta,* Vol. 64:3085-3098.

Fredrickson, J. K., S. W. Li, F. J. Brockman, D. L. Haldeman, P. S. Amy, and D. L. Balkwill, 1995, "Time-Dependent Changes in Viable Numbers and Activities of Aerobic Heterotrophic Bacteria in Subsurface Samples," *Journal of Microbiological Methods,* Vol. 21:253-265.

Freeman-Pollard, J. R., J. A. Caggiano, and S. J. Trent, 1994, *Engineering Evaluation of the GAO/RCED-89-157, Tank 241-T-106 Vadose Zone Investigation*, Report No. BHI-00061, Rev. 00, Bechtel Hanford, Inc., Richland, Washington.

Friedman, I., 1953, "Deuterium Content of Natural Water and Other Substances," *Geochimica et Cosmochimica Acta*, Vol. 4:89-103.

Gamerdinger, A. P., and D. I. Kaplan, 2000, "Application of a Continuous-Flow Centrifugation Method for Solute Transport in Disturbed, Unsaturated Sediments and Illustration of Mobile-Immobile Water," *Water Resources Research*, Vol. 36:1747-1755.

Gamerdinger, A. P., and D. I. Kaplan, 2001, "Physical and Chemical Determinants of Colloid Transport and Deposition in Water-Unsaturated Sand and Yucca Mountain Tuff," *Environmental Science and Technology*, (In press).

Gamerdinger, A. P., D. I. Kaplan, D. M. Wellman, and R. J. Serne, 2001a, "Two-Region Flow and Rate-Limited Sorption of Uranium (VI) During Transport in Hanford Groundwater and An Unsaturated Silt Loam," *Water Resources Research*, (In press).

Gamerdinger, A. P., D. I. Kaplan, D. M. Wellman, and R. J. Serne, 2001b, "Two-Region Flow and Decreased Sorption of Uranium (VI) During Transport in Hanford Groundwater and Unsaturated Sands," *Water Resources Research*, (In review).

Gat, J. R., E. Mazor, and Y. Tzur, 1969, "The Stable Isotope Composition of Mineral Waters in the Jordan Rift Valley," *Journal of Hydrology*, Vol. 7:334-352.

Gaudet, J. P., H. Jegat, G. Vachaud, and P. J. Wierenga, 1977, "Solute Transfer, With Exchange Between Mobile and Stagnant Water, Through Unsaturated Sand," *Soil Science Society of America Journal*, Vol. 41:665-671.

Gaye, C. B., and W. M. Edmunds, 1996, "Groundwater Recharge Estimation Using Chloride, Stable Isotopes and Tritium Profiles in the Sands of Northwestern Senegal," *Environmental Geology*, Vol. 27:246-251.

Gee, G. W., 1987, *Recharge at the Hanford Site: Status Report,* PNL-6403, Pacific Northwest National Laboratory, Richland, Washington.

Gee, G. W., A. L. Ward, T. Caldwell, and J. Ritter, 2000, "A Simple Water Flux Meter for Coarse Soils," p. 218, Annual Meeting Abstracts, Minneapolis, Minnesota, November 5-9, 2000, *American Society of Agronom*, Madison, Wisconsin.

Gee, G. W., M. J. Fayer, M. L. Rockhold, and M. D. Campbell, 1992, "Variations in Recharge at the Hanford Site," *Northwest Science,* Vol. 60:237-250.

Haldeman, D. L., P. S. Amy, D. C. White, and D. B. Ringelberg, 1994, "Changes in Bacteria Recoverable From Subsurface Volcanic Rock Samples During Storage at 4 °C," *Applied and Environmental Microbiology*, Vol. 60:2697-2703.

Heald, S. M., D. L. Brewe, E. A. Stern, K. H. Kim, F. C. Brown, D. T. Jiang, E. D. Crozier, and R. A. Gordon, 1999, "XAFS and Micro-XAFS at the PNC-CAT Beamlines," *Journal of Syn. Rad.,* Vol. 6:347-349.

Hearn, P. P., W. C. Steinkampf, D. G. Horton, G. C. Solomon, L. D. White, and J. R. Evans, 1989, "Oxygen-Isotope Composition of Ground Water and Secondary Minerals in Columbia Plateau Basalts: Implications for the Paleohydrology of the Pasco Basin," *Geology*, Vol. 17:606-610.

Hodges, F. N., 1998, *Results of Phase I Groundwater Quality Assessment for Single-Shell Tank Waste Management Areas T and TX-TY at the Hanford Site*, PNNL-11809, Pacific Northwest National Laboratory, Richland, Washington.

Hodges, F. N., 1998, *Results of Phase I Groundwater Quality Assessment for Single-Shell Tank Waste Management Areas S-SX at the Hanford Site*, PNNL-11810, Pacific Northwest National Laboratory, Richland, Washington.

Hodges, F. N., and C. J. Chou, 2000, *Groundwater Quality Assessment for Waste Management Area U; First Determination*, PNNL-13282, Pacific Northwest National Laboratory, Richland, Washington.

Hoitink, D. J., K. W. Burk, J. V. Ramsdell, 2000, *Hanford Site Climatological Data Summary 1999 With Historical Data,* PNNL-13117, Pacific Northwest National Laboratory, Richland, Washington.

Ilton, E. S., and D. R. Veblen, 1994, "Chromium Sorption by Phlogopite and Biotite in Acidic Solutions at 25 °C: Insights from X-ray Photoelectron Spectroscopy and Electron Microscopy," *Geochimica et Cosmochimica Acta,* Vol. 58:2777-2788.

Ilton, E. S., D. R. Veblen, C. O. Moses, and S. P. Raeburn, 1997, "The Catalytic Effect of Sodium and Lithium Ions on Coupled Sorption-Reduction of Chromate at the Biotite Edge-Fluid Interface," *Geochimica et Cosmochimica Acta,* Vol. 61:3543-3563.

Isono, T., 1984, "Density, Viscosity, and Electrolytic Conductivity of Concentrated Aqueous Electrolyte Solutions at Several Temperatures, Alkaline-Earth Chlorides, $LaCl_3$, Na_2SO_4, $NaNO_3$, NaBr, KNO_3, KBr, and $Cd(NO_3)_2$," *Journal of Chemical Engineering Data,* Vol. 29:45-52.

James, B. R., and R. J. Bartlett, 1983, "Behavior of Chromium in Soils. VI. Interactions Between Oxidation-Reduction and Organic Complexation," *Journal of Environmental Quality,* Vol. 12/2:173-176.

Johnson, T. M., and D. J. DePaolo, 1994, "Interpretation of Isotopic Data in Groundwater-Rock Systems: Model Development and Application to Sr Isotopic Data from Yucca Mountain," *Water Resources Research*, Vol. 30:1571-1587.

Johnson, T. M., and D. J. DePaolo, 1997a, "Rapid Exchange Effects on Isotope Ratios in Groundwater Systems, 1. Development of a Transport-Dissolution-Exchange Model," *Water Resources Research*, Vol. 33:187-195.

Johnson, T. M., and D. J. DePaolo, 1997b, "Rapid Exchange Effects on Isotope Ratios in Groundwater Systems, 2. Flow Investigation Using Sr Isotope Ratios," *Water Resources Research*, Vol. 33:197-205.

Johnson, T., R. C. Roback, T. L. McLing, T. D. Bullen, D. J. DePaolo, C. Doughty, R. J. Hunt, R. W. Smith, L. D. Cecil, and M. T. Murrell, 2000, "Groundwater "Fast-Paths" in the Snake River Plain Aquifer: Radiogenic Isotope Ratios as Natural Groundwater Tracers," *Geology*, Vol. 28:871-874.

Johnson, V. G., and C. J. Chou, 1998, *Results of Phase I Groundwater Quality Assessment for Single-Shell Tank Waste Management Areas S-SX at the Hanford Site*, PNNL-11810, Pacific Northwest National Laboratory, Richland, Washington.

Johnson, V. G., and C. J. Chou, 1998, *Results of Phase I Groundwater Quality Assessment for Single-Shell Tank Waste Management Areas T and TX-TY at the Hanford Site*, PNNL-11809, Pacific Northwest National Laboratory, Richland, Washington.

Jones, T. E, R. A. Watrous, and G. T. Maclean, 2000, *Inventory Estimates for Single-Shell Tank Leaks in the S and SX Tank Farms*, RPP-6285, Rev. 0, CH2M HILL Hanford Group, Inc., Richland, Washington.

Kaplan, D. I., and R. J. Serne, 1995, *Distribution Coefficient Values Describing Iodine, Neptunium, Selenium, Tc and Uranium Sorption to Hanford Sediments*, PNL-10379, Pacific Northwest National Laboratory, Richland, Washington.

Kaplan, D. I., K. E. Parker, and I. V. Kutynakov, 1998, *Radionuclide Distribution Coefficients for Sediments Collected from Borehole 299-E17-21: Final Report for Subtask 1a*, PNNL-11966, Pacific Northwest National Laboratory, Richland, Washington.

Kent, D. B., J. A. Davis, L. C. D. Anderson, and B. A. Rea, 1995, "Transport of Chromium and Selenium in a Pristine Sand and Gravel Aquifer: Role of Adsorption Processes," *Water Resources Research*, Vol. 31:1041-1050.

Khaleel, R., and E. J. Freeman, 1995, *Variability and Scaling of Hydraulic Properties for 200 Area Soils, Hanford Site*, WHC-EP-0883, Westinghouse Hanford Company, Richland, Washington.

Khaleel, R., and J. F. Relyea, 1997, "Correcting Laboratory-Measured Moisture Retention Data for Gravels," *Water Resources Research*, Vol. 33:1875-1878.

Khaleel, R., J. F. Relyea, and J. L. Conca, 1995, "Evaluation of van Genuchten - Mualem Relationships to Estimate Unsaturated Hydraulic Conductivity at Low Water Contents," *Water Resources Research*, Vol. 31:2659-2668.

Khaleel, R., T. E. Jones, A. J. Knepp, F. M. Mann, D. A. Myers, P. M. Rogers, R. J. Serne, and M. I. Wood, 2000, *Modeling Data Package for S-SX Field Investigation Report (FIR), River Protection Program*, RPP-6296, Rev. 0, CH2M HILL Hanford Group, Inc., Richland, Washington.

Kieft, T. L., and F. J. Brockman, 2001, "Vadose Zone Microbiology," *Subsurface Microbiology and Biogeochemistry*, J. K. Fredrickson and M. Fletcher, Wiley-LISS Inc., New York, 141-169.

Kieft, T. L., P. S. Amy, F. J. Brockman, J. K. Fredrickson, B. N. Bjornstad, and L. L. Rosacker, 1993, "Microbial Abundance and Activities in Relation to Water Potential in the Vadose Zones of Arid and Semiarid Sites," *Microbial Ecology*, Vol. 26:59-78.

Klobe, W. D., and R. G. Gast, 1970, "Conditions Affecting Cesium Fixation and Sodium Entrapment in Hydrobiotite and Vermiculite," *Soil Science Society of America Proceedings*, Vol. 34:746-750.

Komor, S. C., and D. G. Emerson, 1994, "Movements of Water, Solutes, and Stable Isotopes in the Unsaturated Zones of Two Sand Plains in the Upper Midwest," *Water Resources Research*, Vol. 30:253-267.

Last, G. V. and D. G. Horton, 2000, *Review of Geophysical Characterization Methods Used at the Hanford Site*, PNNL-13149, Pacific Northwest National Laboratory, Richland, Washington.

Le Roux, J., C. I. Rich, and P. H. Ribbe, 1970, "Ion Selectivity by Weathered Micas as Determined by Microprobe Analysis," *Clays and Clay Minerals*, Vol. 18:333-338.

Lederer, C. M., V. S. Shirley, E. Browne, J. M. Dairiki, R. E. Doebler, A. A. Shihab-Elden, L. J. Jardine, J. K. Tuli, and A. B. Buyrn, 1978, *Table of Isotopes, Seventh Edition*, John Wiley & Sons, New York.

Lichtner, P. C, 2001, *FLOTRAN User Manual*, LA-UR-01-2349, Los Alamos National Laboratory, Los Alamos, New Mexico.

Lichtner, P. C., 2001, "Estimating Tank Supernatant Liquid Compositions," LA-UR-01-1403, Los Alamos National Laboratory, Los Alamos, New Mexico.

Lichtner, P. C., 2001, *FLOTRAN User Manual*, LA-UR-01-2349, Los Alamos National Laboratory, Los Alamos, New Mexico.

Liu, D.-C., C. N. Hsu, and C. L. Chung, 1994, "Ion-Exchange and Sorption Kinetics of Cesium and Strontium in Soils," *Applied Radiation Isotope*, Vol. 46:839-846.

Loeppert, R. L., and W. P. Inskeep, 1996, "Iron," In D.L. Sparks et al., ed., *Methods of Soil Analysis; Part 3 – Chemical Methods,* SSSA Book Series: 5, Soil Science Society of America, Inc., Madison, Wisconsin, p. 639-664.

Lomenick, T. F., and T. Tamura, 1965, "Naturally Occurring Fixation of ^{137}Cs on Sediments of Lacustrine Origin," *Soil Science Society of America Proceedings*, Vol. 29:383-387.

Lovley, D. R., 1995, "Microbial Reduction of Iron, Manganese, and Other Metals," *Advances in Agronomy,* Vol. 54:175-231.

Mahiuddin, S., and K. Ismail, 1996, "Temperature and Concentration Dependence of the Viscosity of Aqueous Sodium Nitrate and Sodium Thiosulphate Electrolytic Systems," *Fluid Phase Equilibrium,* Vol. 123:231-243.

Malmstrom, M., and S. Banwart, 1997, "Biotite Dissolution at 25 °C: the pH Dependence of Dissolution Rate and Stoichiometry," *Geochimica et Cosmochimica Acta*, Vol. 61:2779-2799.

Mattimore, V., and J. R. Battista, 1996, "Radioresistance of *Deinococcus radiodurans*: Functions Necessary to Survive Ionizing Radiation are also Necessary to Survive Prolonged Desiccation," *Journal of Bacteriology*, Vol. 178:633-637.

McKinley, J. P., C. J. Zeissler, J. M. Zachara, R. J. Serne, R. M. Lindstrom, H. T. Schaef, and R. D. Orr, 2001, "The Distribution and Retention of ^{137}Cs in Sediments Beneath Leaked Waste Tanks at the Hanford Site, Washington," *Environmental Science and Technology*, (In press).

McKinley, J. P., T. O. Stevens, J. K. Fredrickson, J. M. Zachara, F. S. Colwell, K. B. Wagnon, S. A. Rawson, and B. N. Bjornstad, 1997, "The Biogeochemistry of Anaerobic Lacustrine and Paleosol Sediments within an Aerobic Unconfined Aquifer," *Geomicrobiology Journal*, Vol. 14:23-39.

Melayah, A., L. Bruckler, and T. Bariac, 1996, "Modeling the Transport of Water Stable Isotopes in Unsaturated Soils Under Natural Conditions: 2. Comparison with Field Experiments," *Water Resources Research*, Vol. 32:2055-2065.

Millington, R. J., and J. P. Quirk, 1961, "Permeability of Porous Media," *Nature*, Vol. 183:387-388.

Minton, K. W., 1996, "Repair of Ionizing-Radiation Damage in the Radiation Resistant Bacterium *Deinococcus radiodurans*," *Mutation Research*, Vol. 363:1-7.

Mualem, Y., 1976, "A New Model for Predicting the Hydraulic Conductivity of Unsaturated Porous Media," *Water Resources Research*, Vol. 12(3):513-522.

Murphy, E. M., T. R. Ginn, and J. L. Phillips, 1996, "Geochemical Estimates of Paleorecharge in the Pasco Basin: Evaluation of the Chloride Mass Balance Technique," *Water Resources Research*, Vol. 32:2853-2868.

Myers, D. A., D. L. Parker, G. Gee, V. G. Johnson, G. V. Last, R. J. Serne, and D. J. Moak., 1998, *Findings of the Extension of Borehole 41-09-39, 241-SX Tank Farm,* HNF-2855, Lockheed Martin Hanford Corporation, Richland, Washington.

Narbutovskih, S. M., 1998, *Results of Phase I Groundwater Quality Assessment for Single-Shell Tank Waste Management Areas B-BX-BY at the Hanford Site*, PNNL-11826, Pacific Northwest National Laboratory, Richland, Washington.

Newman, A.C.D., 1987, *Chemistry of Clays and Clay Minerals, Mineralogic Society Monograph No. 6*, John Wiley & Sons.

Nielsen, D. R., and J. W. Biggar, 1961, "Miscible Displacement In Soils: I. Experimental Information," *Soil Science Society of America Proceedings*, Vol. 25:1-5.

Nielsen, D. R., M. T. van Genuchten, and J. W. Biggar, 1986, "Water Flow and Solute Transport Processes in the Unsaturated Zone," *Water Resources Research*, Vol. 22:895-1085.

Nitao, J., 1998, *Reference Manual for the NUFT Flow and Transport Code, Version 2.0*, UCRL-MA-130651, Lawrence Livermore National Laboratory, Livermore, California.

Ogwada, R. A., and D. L. Sparks, 1986, "Kinetics of Ion Exchange on Clay Minerals and Soil: II. Elucidation of Rate-Limiting Steps," *Soil Sciene Society of America Journal*, Vol. 50:1162-1166.

Peterson, M. L., A. F. White, G. E. Brown, Jr., and G. A. Parks, 1997, "Surface Passivation of Magnetite (Fe_3O_4) by Reaction with Aqueous Cr(VI): XAFS and TEM Results," *Environmental Science Technology,* Vol. 31:1573-1576.

Peterson, M. L., G. E. Brown, Jr., and G. A. Parks, 1996, "Direct XAFS Evidence for Heterogeneous Redox at the Aqueous Chromium/Magnetite Interface," *Colloids and Surfaces,* Vol. 107:77-88.

Pettine, M., L. D'Ottone, L. Campanella, F. J. Millero, and R. Passino, 1998, "The Reduction of Cr(VI) by Iron (II) in Aqueous Solutions," *Geochimica et Cosmochimica Acta*, 1509-1519.

Phillips, F. M., 1995, "The Use of Isotopes and Environmental Tracers in Subsurface Hydrology," *Reviews of Geophysics*, Vol. 33:1029-1033.

Piepho, M. G., 1999, *SX Tank Farm Vadose Zone Temperature Sensitivity Study*, HNF-4744, Rev. 0, Fluor Daniel Northwest, Inc., Richland, Washington.

Pitzer, K. S., 1973, "Thermodynamics of Electrolytes. I. Theoretical Basis and General Equations," *Journal of Physical Chemistry*, Vol. 77:268-277.

Pitzer, K. S., 1991, *Activity Coefficients in Electrolyte Solutions. 2nd Edition,*" CRC Press, Boca Raton, Florida, p. 542.

Poinssot, C., B. Baeyens, and M. H. Bradbury, 1999, "Experimental and Modeling Studies of Cesium Sorption on Illite," *Geochimica et Cosmochimica Acta*, Vol. 63:3217-3227.

Polmann, D. J., 1990, "Application of Stochastic Methods to Transient Flow and Transport in Heterogeneous Unsaturated Soils," Ph.D. Thesis, Massachusetts Institute of Technology, Cambridge, Massachusetts.

Price, R. K., and R. R. Randall, 1998, *Monitoring Results for the SX Single Shell Tank Farm Dry Well Gamma Ray Surveillance Log Surveys*, WMNW/TRS-ES-VZMA-002, Three Rivers Scientific, West Richland, Washington.

Price, W. H., and K. R. Fecht, 1976, *Geology of the 241-SX Tank Farm*, ARH-LD-134, Atlantic Richfield Hanford Company, Richland, Washington.

Prigogine, I., and R. Defay, 1954, *Chemical Thermodynamics*, Longmans, p. 543.

Pruess, K., C. Oldenburg, and G. Moridis, 1999, *TOUGH2 User's Guide, Version 2.0*, LBNL-43134, Lawrence Berkeley National Laboratory, Berkeley, California.

Rai, D., and J. M. Zachara, 1986, "Geochemical Behavior of Chromium Species," *EA-4544, Reseach Project 2485-3*, Pacific Northwest National Laboratory, Richland, Washington.

Rai, D., J. M. Zachara, L. E. Eary, D. C. Girvin, D. A. Moore, C. T. Resch, B. M. Sass, and R. L. Schimdt, 1986, "Geochemical Behavior of Chromium Species," *EA-4544*, Electric Power Research Institute, Palo Alto, California.

Raymond, J. R., and E. G. Shdo, 1966, *Characterization of Subsurface Contamination in the SX Tank Farm*, BNWL-CC-701, Battelle-Northwest Laboratory, Richland, Washington.

Richards, L. A., 1931, "Capillary Conduction of Liquids Through Porous Mediums," Physics, Vol. 1:318-333.

Rickard, W. H., L. E. Rogers, B. E. Vaughan, and S. F. Liebetrau, 1988, *Shrub-Steppe: Balance and Change in a Semi-Arid Terrestrial Ecosystem,* p 8, Elsevier, Amsterdam.

Rockhold, M. L., 1999, "Parameterizing Flow and Transport Models for Field-Scale Applications in Heterogeneous, Unsaturated Soils," *Assessment of Non-Point Source Pollution in the Vadose Zone,* Geophysical Monograph 108, pp. 243 - 260, American Geophysical Union, Washington, D.C.

Rockhold, M. L., C. J. Murray, and M. J. Fayer, 1999, "Conditional simulation and upscaling of soil properties," In: *Proceedings of the International Workshop on Characterization and Measurement of the Hydraulic Properties of Unsaturated Porous Media*, M. Th. Van Genuchten, F. J. Leij and L. Wu (eds.), pp. 1391–1401, University of California, Riverside.

Sawhney, B. L., 1970, "Potassium and Cesium Ion Selectivity in Relation to Clay Mineral Structure," *Clays and Clay Minerals*, Vol. 18:47-52.

Schroeder, P. R., C. M. Lloyd, and P. A. Zappi, 1994, *The Hydrologic Evaluation of Landfill Performance (HELP) Model. User's Guide for Version 3,* EPA/600/R-94/168a, U. S. Environmental Protection Agency, Cincinnati, Ohio.

Schwertmann, U., J. Friedl, and H. Stanjek, 1999, "From Fe(III) Ions to Ferrihydrite and then Hematite," *Journal of Colloid Interface Science*, Vol. 209:215-223.

Sedlak, D. L., and P. G. Chan, 1997, "Reduction of Hexavalent Chromium by Ferrous Iron," *Geochimica et Cosmochimica Acta*, 2185-2192.

Serne, R. J., G. V. Last, G. W. Gee, H. T. Schaef, D. C. Lanigan, C. W. Lindenmeir, R. E. Clayton, V. L. LeGore, R. D. Orr, C. F. Brown, D. B. Burke, I. V. Kutnyakov, T. C. Wilson, and D. A Myers, 2001a, *Geologic and Geochemical Data Collected from Vadose Zone Sediments from Borehole SX 41-09-39 in the S/SX Waste Management Area and Preliminary Interpretations*, p. 162, Pacific Northwest National Laboratory, Richland, Washington.

Serne, R. J., H. T. Schaef, B. N. Bjornstad, B. A. Williams, D. C. Lanigan, D. G. Horton, R. E. Clayton, V. L. LeGore, M. J. O'Hara, C. F. Brown, D. E. Parker, I. V. Mitroshkov, G. V. Last, S. C. Smith, C. W. Lindenmeir, J. M. Zachara, and D. B. Burke, 2001b, *Characterization of Uncontaminated Sediments From the Hanford Reservation—RCRA Borehole Core Samples and Composite Samples*, p. 142, Pacific Northwest National Laboratory, Richland, Washington.

Serne, R. J., 2000, "S-SX Sediment Characterization Results and Issues," Pacific Northwest National Laboratory, Richland, Washington.

Serne, R. J., 2001, "S-SX Sediment Characterization Results and Issues," Pacific Northwest National Laboratory, Richland, Washington.

Serne, R. J., H. T. Schaef, B. N. Bjornstad, B. A. Williams, D. C. Lanigan, D. G. Horton, R. E. Clayton, V. L. LeGore, M. J. O'Hara, C. F. Brown, K. E. Parker, I. V. Kutnyakov, J. N. Serne, A. V. Mitroshkov, G. V. Last, S. C. Smith, C. W. Lindenmeier, J. M. Zachara, and D. B. Burke, 2001a, *Characterization of Uncontaminated Sediments from the Hanford Reservation-RCRA Borehole Core and Composite Samples*, PNNL-2001-1, Pacific Northwest National Laboratory, Richland, Washington.

Serne, R. J., G. V. Last , G. W. Gee, H. T. Schaef, D. C. Lanigan, C. W. Lindenmeier, R. E. Clayton, V. L. LeGore, R. D. Orr, M. J. O'Hara, C. F. Brown, D. B. Burke, A. T. Owen, I. V. Kutnyakov, and T. C. Wilson, 2001b, *Geologic and Geochemical Data Collected from Vadose Zone Sediments from Borehole SX 41-09-39 in the S/SX Waste Management Area and Preliminary Interpretations*, PNNL-2001-2, Pacific Northwest National Laboratory, Richland, Washington.

Serne, R. J., H. T. Schaef, B. N. Bjornstad, D. C. Lanigan, G. W. Gee, C. W. Lindenmeier, R. E. Clayton, V. L. LeGore, M. J. O'Hara, C. F. Brown, R. D. Orr, G. V. Last, I. V. Kutnyakov, D. B. Burke, T. C. Wilson, and B. A. Williams, 2001c, *Geologic and Geochemical Data Collected from Vadose Zone Sediments from Borehole 299 W23-19 [SX-115] in the S/SX Waste Management Area and Preliminary Interpretations*, PNNL-2001-3, Pacific Northwest National Laboratory, Richland, Washington.

Serne, R. J., H. T. Schaef, G. V. Last, D. C. Lanigan, C. W. Lindenmeier, R. E. Clayton, V. L. LeGore , M. J. O'Hara, C. F. Brown, R. D. Orr, I. V. Kutnyakov, T. C. Wilson, D. B. Burke, B. A. Williams, and B. N. Bjornstad, 2001d, *Geologic and Geochemical Data Collected from Vadose Zone Sediments from the Slant Borehole under SX-108 in the S/SX Waste Management Area and Preliminary Interpretations*, PNNL-2001-4, Pacific Northwest National Laboratory, Richland, Washington.

Serne, R. J., J. M. Zachara, and D. S. Burke, 1997, *Chemical Information on Tank Supernatants, Cs Adsorption from Tank Liquids onto Hanford Sediments, and Field Observations of Cs Migration from Past Tank Leaks*, PNNL-11495, Pacific Northwest National Laboratory, Richland, Washington.

Simmons, C. S., and P. D. Meyer, 2000, "A Simplified Model for the Transient Water Budget of a Shallow Unsaturated Zone," *Water Resour. Res.*, 36:2835–2844.

Sisson, J. B., and A. H. Lu, 1984, *Field Calibration of Computer Models for Application to Buried Liquid Discharges: A Status Report*, RHO-ST-46P, Rockwell Hanford Operations, Richland, Washington.

Smith, J. T., and R. N. J. Comans, 1996, "Modeling the Diffusive Transport and Remobilization of ^{137}Cs in Sediments: The Effects of Sorption Kinetics and Reversibility," *Geochimica et Cosmochimica Acta*, Vol. 60:995-1004.

Smoot, J. L., and A. H. Lu, 1994, "Interpretation and Modeling of a Subsurface Injection Test, 200 East Area, Hanford, Washington," *In-Situ Remediation: Scientific Basis for Current and Future Technologies*, G. W. Gee and N. R. Wing (eds.), Battelle Press, Richland, Washington.

Smoot, J. L., J. E. Szecsody, B. Sagar, G. W. Gee, and C. T. Kincaid, 1989, *Simulations of Infiltration of Meteoric Water and Contaminant Plume Movement in the Vadose Zone at Single-Shell Tank 241-T-106 at the Hanford Site*, WHC-EP-0332, Westinghouse Hanford Company, Richland, Washington.

Somerton, W. H., J. A. Keese, and S. L. Chu, 1973, "Thermal Behavior of Unconsolidated Oil Sands," Paper SPE-4506, presented at the 48th Annual Fall Meeting of the Society of Petroleum Engineers, San Francisco, California.

Songsheng, J., G. Jingru, J. Shan, L. Chunsheng, C. Anzhi, H. Ming, W. Shaoyong, and L. Shilin, 1997, *Nuclear Instrumental Methods in Physical Research B.*, Vol. 123:405-409.

Sposito, G., 1981, "Cation Exchange In Soils: An Historical and Theoretical Perspective," In Chemistry in the Soil Environment, pp. 13-30, *American Society of Agronomy*, Madison, Wisconsin.

Sposito, G., 1994, "Chemical Equilibria and Kinetics in Soils," Oxford University Press, New York and Oxford.

Steefel, C. I, 2001, "CRUNCH: Software for Modeling Multicomponent-Multidimensional Reactive Transport. 1 ed. User's Manual," Lawrence Livermore National Laboratory (In press).

Stevens, T. O., and J. K. Fredrickson, 1990, "Potential for Microbial Gas Generation in High-Level Radioactive Waste Storage Tanks," Pacific Northwest National Laboratory, Richland, Washington.

Stone, W. A., J. M. Thorp, O. P. Gifford, and D. J. Hoitink, 1983, *Climatological Summary for the Hanford Area*, PNL-4622, Pacific Northwest National Laboratory, Richland, Washington.

Sylvester et al., 2000, "Ferrate Treatment for Removing Chromium from High-Level Radioactive Tank Waste," *Environmental Science and Technology*.

Tallman, A. M., K. R. Fecht, M. C. Marratt, and G. V. Last, 1979, *Geology of the Separations Areas, Hanford Site, South-Central Washington,* RHO-ST-23, Rockwell Hanford Operations, Richland, Washington.

Taylor, R. W., S. Shen, W. F. Bleam, and S. I. Shu, 2000, "Chromate Removal by Dithionite-Reduced Clays: Evidence from Direct X-ray Absorption Near Edge Spectroscopy (XANES) of Chromate Reduction at Clay Surfaces," *Clays and Clay Minerals*, Vol. 48:648-654.

Toride, N., F. J. Leij, and M. Th. van Genuchten, 1999, "The CXTFIT Code for Estimating Transport Parameters From Laboratory or Field Tracer Experiments," *Research Report No. 137*, U.S. Salinity Laboratory, USDA.

Toso, J. P., and R. H. Velasco, 2001, "Describing the Observed Vertical Transport of Radiocesium in Specific Soils with Three Time-Dependent Models," *Journal of Environmental Radioactivity*, Vol. 53:133-144.

Tyler, S. W., B. R. Scanlon, G. W. Gee and G. B. Allison, 1999, "Water and Solute Transport in Arid Vadose Zones: Innovations in Measurement and Analysis," In: *Vadose Zone Hydrology,* M. B. Parlange and J. W. Hopmans (eds.), pp. 334–373. Oxford Press, New York.

van Genuchten, M. Th., 1980, "A Closed-Form Equation for Predicting the Hydraulic Conductivity of Unsaturated Soils," *Soil Science Society of America Journal*, Vol. 44:892-898.

Vennemann, T. W., and J. R. O'Neil, 1993, "A Simple and Inexpensive Method of Hydrogen Isotope and Water Analyses of Minerals and Rocks Based on Zinc Reagent," *Chemical Geology*, Vol. 103:227-234.

Ward, A. L., and G. W. Gee, 2000, *Vadose Zone Transport Field Study: Detailed Test Plan for Simulated Leak Tests*, PNNL-13263, Pacific Northwest National Laboratory, Richland, Washington.

Ward, A. L., and G. W. Gee, 2000, *Vadose Zone Transport Field Study: Detailed Test Plan for Simulated Leak Tests*, PNNL-13263, Pacific Northwest National Laboratory, Richland, Washington.

Ward, A. L., G. W. Gee, and M. D. White, 1997, *A Comprehensive Analysis of Contaminant Transport in the Vadose Zone Beneath Tank SX-109*, PNNL-11463, Pacific Northwest National Laboratory, Richland, Washington.

Watrous, R. A., and D. W. Wootan, 1997, *Activity of Fuel Batches Processed Through Hanford Separations Plants, 1944 Through 1989*, HNF-SD-WM-TI-794, Lockheed Martin Hanford Corporation, Richland, Washington.

WHC, 1992, *Tank 241-SX-108 Leak Assessment*, WHC-MR-0300, Richland, Washington.

White, A. F., A. E. Blum, M. S. Schulz, T. D. Bullen, J. W. Harden, and M. L. Peterson, 1996, "Chemical Weathering Rates of a Soil Chronosequence on Granitic Alluvium: I. Quantification of Mineralogical and Surface Area Changes and Calcualtion of Primary Silicate Reaction Rates," *Geochimica et Cosmochimica Acta*, Vol. 60:2533-2550.

White, M. D., and M. D. Oostrom, 1996, *STOMP Subsurface Transport Over Multiple Phases Theory Guide,* PNNL-11217, Pacific Northwest National Laboratory, Richland, Washington.

White, M. D., and M. Oostrom, 2000a, *STOMP Subsurface Transport Over Multiple Phases, Version 2.0, Theory Guide,* PNNL-12030, Pacific Northwest National Laboratory, Richland, Washington.

White, M. D., and M. Oostrom, 2000b, *STOMP, Subsurface Transport Over Multiple Phases, Version 2.0, User's Guide*, PNNL-12034, Pacific Northwest National Laboratory, Richland, Washington.

White, M. D., M. Oostrom, and R. J. Lenhard, 1995, "Modeling fluid flow and transport in variably saturated porous media with the STOMP simulator. 1. Nonvolatile three-phase model description," *Adv. Water Res.*, 18:353–364.

White, M. D., M. Oostrom, and M. D. Williams, 2001, *FY00 Initial Assessments for S-SX Field Investigation Report (FIR): Simulations of Contaminant Migration with Surface Barriers*, Pacific Northwest National Laboratory, Richland, Washington, (In Press)

Wildung, R. E., Y. A. Gorby, K. M. Krupka, N. J. Hess, S. W. Li, A. E. Plymale, J. P. McKinley, and J. K. Fredrickson, 2000, "Effect of Electron Donor and Solution Chemistry on the Products of the Dissimilatory Reduction of Technetium by *Shewanella putrefaciens*," *Applied and Environmental Microbiology*, Vol. 66:2451-2460.

Zachara, J. M., C. C. Ainsworth, C. E. Cowan, and C. T. Resch, 1989, "Adsorption of Chromate by Subsurface Soil Horizons" *Soil Science Society of America Journal,* Vol. 53/2:418-428.

Zachara, J. M., C. E. Cowan, R. L. Schmidt, and C. C. Ainsworth, 1988, "Chromate Adsorption by Kaolinite," *Clay and Clay Minerals,* Vol. 36:317-326.

Zachara, J. M., D. C. Girvin, R. L. Schmidt, and C. T. Resch, 1987, "Chromate Adsorption on Amorphous Iron Oxyhydroxide in the Presence of Major Groundwater Ions," *Environmental Science and Technology*, Vol. 21:589-94.

Zachara, J. M., S. C. Smith, J. P. McKinley, R. J. Serne, and P. L. Gassman, 2001, "Sorption of Cs^+ to Micaceous Subsurface Sediments from the Hanford Site," *Geochimica et Cosmochimica Acta*, (Accepted).

Zeissler, C. J., R. M. Lindstrom, and J. P. McKinley, 2001, "Radioactive particle analysis by digital autoradiography," *Journal of Radioanalytical and Nuclear Chemistry*, Vol. 248, No. 2, 407-412.

APPENDIX E

IMPACT ASSESSMENT APPROACH AND RESULTS

This page intentionally left blank.

CONTENTS

E.1.0 INTRODUCTION E-1

E.2.0 MODELING APPROACH E-2
- E.2.1 NUMERICAL CASES CONSIDERED E-7
- E.2.2 RECHARGE ESTIMATES AND VADOSE ZONE FLOW AND TRANSPORT PARAMETERS E-9
  - E.2.2.1 Recharge Estimates E-9
  - E.2.2.2 Vadose Zone Flow and Transport Parameters E-9
  - E.2.2.3 Stochastic Model for Macroscopic Anisotropy E-10
  - E.2.2.4 Clastic Dike Infilling Material Properties E-12
  - E.2.2.5 Enhanced Density and Viscosity Estimates E-12
  - E.2.2.6 Effective Transport Parameters E-12
- E.2.3 GROUNDWATER FLOW AND TRANSPORT E-14
  - E.2.3.1 Flow and Transport Parameters E-14
  - E.2.3.2 Unit Dose Factors E-17
- E.2.4 CONTAMINANT INVENTORY E-17
  - E.2.4.1 Basis for Inventory Estimates E-17
  - E.2.4.2 Inventory Distributions E-21
  - E.2.4.3 Inventory Assignment E-22

E.3.0 HUMAN HEALTH RISK AND DOSE ESTIMATION APPROACH E-29
- E.3.1 RECEPTOR SCENARIO RATIONALE E-30
  - E.3.1.1 Residential Exposure Scenario (MTCA Method B) E-31
  - E.3.1.2 Industrial Exposure Scenario (MTCA Method C) E-31
  - E.3.1.3 Industrial Worker Scenario E-32
  - E.3.1.4 Residential Farmer Scenario E-33
  - E.3.1.5 Recreational Shoreline User Scenario E-34
- E.3.2 TANK WASTE CONSTITUENTS OF POTENTIAL CONCERN E-34
  - E.3.2.1 Rationale for Excluding Contaminants of Potential Concern E-34
  - E.3.2.2 Contaminants of Potential Concern for Risk Assessment E-35
- E.3.3 ESTIMATING TOTAL INCREMENTAL LIFETIME CANCER RISK AND HAZARD INDEX E-36
- E.3.4 DOSE METHODOLOGY E-36

E.4.0 VADOSE ZONE MODELING RESULTS E-38
- E.4.1 BASE CASE, NO ACTION ALTERNATIVE (CASE 1) E-38
- E.4.2 BARRIER ALTERNATIVE AND NO WATER-LINE LEAKS CASE (CASE 2) E-43
- E.4.3 NO BARRIER AND 25,000 GALLON WATER-LINE LEAK CASE (CASE 3) E-44
- E.4.4 NO BARRIER AND CLASTIC DIKES CASE (CASE 4) E-51
- E.4.5 NONUNIFORM INVENTORY DISTRIBUTION AND NO BARRIER CASE (CASE 5) E-52
- E.4.6 NONUNIFORM INVENTORY DISTRIBUTION AND BARRIER CASE (CASE 6) E-53

E.4.7 LOCATION OF INVENTORY DISTRIBUTION AND NO BARRIER CASE (CASE 7) E-54
E.4.8 DENSITY AND VISCOSITY EFFECTS CASE (CASE 8) E-55
E.4.9 BASE CASE WITH 50 MM/YR METEORIC RECHARGE CASE (CASE 9) E-56
E.4.10 BASE CASE WITH 30 MM/YR METEORIC RECHARGE (CASE 10) E-59
E.4.11 BASE CASE WITH 10 MM/YR METEORIC RECHARGE (CASE 11) E-61
E.4.12 ALTERNATE INVENTORY DISTRIBUTION CASE (CASE 12) E-64
E.4.13 NO BARRIER AND 200,000 GAL WATER-LINE LEAK CASE (CASE 13) E-65
E.4.14 THREE-DIMENSIONAL SIMULATIONS E-72
E.4.15 SOLUTE MASS BALANCE E-73

E.5.0 STREAMTUBE MODELING RESULTS E-75

E.6.0 HUMAN HEALTH RISK AND DOSE RESULTS E-81
E.6.1 BASE CASE, NO ACTION ALTERNATIVE (CASE 1) E-82
E.6.2 BARRIER ALTERNATIVE AND NO WATER-LINE LEAKS CASE (CASE 2) E-85
E.6.3 BASE CASE WITH 50 MM/YR METEORIC RECHARGE (CASE 9) E-88
E.6.4 BASE CASE WITH 30 MM/YR METEORIC RECHARGE (CASE 10) E-91
E.6.5 BASE CASE WITH 10 MM/YR METEORIC RECHARGE (CASE 11) E-94

E.7.0 REFERENCES E-97

ATTACHMENTS

E1 VADOSE ZONE INVENTORY ESTIMATES E1-i
E2 INVENTORY DISTRIBUTIONS E2-i
E3 VADOSE ZONE AND UNCONFINED AQUIFER MODELING RESULTS E3-i
E4 SOLUTE TRANSPORT TIME SEQUENCES E4-i
E5 RECHARGE SENSITIVITY MODELING RESULTS E5-i

FIGURES

E.1. Location Map of Single-Shell Tank WMA S-SX and Surrounding Facilities in the 200 West Area....E-3
E.2. Cross-Section SX-DD'....E-4
E.3. Cross-Section SX-FF'....E-4
E.4. Cross-Section S-CC'....E-5
E.5. VAM3D-Generated Steady State Hydraulic Head Distribution for the Hanford Site, Following Simulation for 1,000 Years....E-15
E.6. VAM3D-Generated Pathline Distribution at Steady State, Following Simulation for 1,000 Years....E-16
E.7. Material Property Distribution for the Upper Three Elemental Layers for VAM3D Sitewide Groundwater Model....E-18
E.8. Case 1 Aqueous-Phase Saturation at 2000 (steady-flow conditions) for Cross-Section SX-DD'....E-40
E.9. Case 1 Aqueous-Phase Saturation at 2050 (0.1 mm/yr) for Cross-Section SX-DD'.....E-41
E.10. Case 1 Aqueous-Phase Saturation at 2540 (0.1 mm/yr) for Cross-Section SX-DD'.....E-42
E.11. Case 1 Aqueous-Phase Saturation at 3000 (3.5 mm/yr) for Cross-Section SX-DD'.....E-42
E.12. Case 3 Aqueous-Phase Saturation at 2000 plus 5 days for Cross-Section SX-FF'.......E-46
E.13. Case 3 Aqueous-Phase Saturation at 2000 plus 10 days for Cross-Section SX-FF'.....E-46
E.14. Case 3 Aqueous-Phase Saturation at 2000 plus 25 days for Cross-Section SX-FF'.....E-47
E.15. Case 3 Aqueous-Phase Saturation at 2000 plus 50 days for Cross-Section SX-FF'.....E-47
E.16. Case 3 Aqueous-Phase Saturation at 2000 plus 183 days for Cross-Section SX-FF'...E-48
E.17. Case 3 Aqueous-Phase Saturation at 2000 plus 365 days for Cross-Section SX-FF'...E-48
E.18. Case 3 Technetium-99 Aqueous Concentration at 2001 for Cross-Section SX-FF'.....E-49
E.19. Case 3 Technetium-99 Aqueous Concentration at 2040 for Cross-Section SX-FF'.....E-50
E.20. Case 9 Aqueous-Phase Saturation at 2000 (50 mm/yr) for Cross-Section SX-DD'......E-58
E.21. Case 10 Aqueous-Phase Saturation at 2000 (30 mm/yr) for Cross-Section SX-DD'....E-61
E.22. Case 11 Aqueous-Phase Saturation at 2000 (50 mm/yr) for Cross-Section SX-DD'....E-63
E.23. Case 13 Aqueous-Phase Saturation at 2000 plus 5 days for Cross-Section SX-FF'.....E-66
E.24. Case 13 Aqueous-Phase Saturation at 2000 plus 10 days for Cross-Section SX-FF'...E-67
E.25. Case 13 Aqueous-Phase Saturation at 2000 plus 25 days for Cross-Section SX-FF'...E-67
E.26. Case 13 Aqueous-Phase Saturation at 2000 plus 50 days for Cross-Section SX-FF'...E-68
E.27. Case 13 Aqueous-Phase Saturation at 2000 plus 183 days for Cross-Section SX-FF'....E-68
E.28. Case 13 Aqueous-Phase Saturation at 2000 plus 365 days for Cross-Section SX-FF'....E-69
E.29. Case 13 Technetium-99 Aqueous Concentration at 2001 for Cross-Section SX-FF'...E-71
E.30. Case 13 Technetium-99 Aqueous Concentration at 2040 for Cross-Section SX-FF'...E-71
E.31. Translation Geometry....E-77
E.32. Case 1 Industrial Worker ILCR Versus Time at WMA S-SX Boundary....E-83
E.33. Case 1 Industrial Worker ILCR Versus Time at Compliance Points Between the WMA S-SX Boundary and the Columbia River....E-83
E.34. Case 2 Industrial Worker ILCR Versus Time at WMA S-SX Boundary....E-85
E.35. Case 2 Industrial Worker ILCR Versus Time at Compliance Points Between the WMA S-SX Boundary and the Columbia River....E-86
E.36. Case 9 Industrial Worker ILCR Versus Time at WMA S-SX Boundary....E-88

E.37. Case 9 Industrial Worker ILCR Versus Time at Compliance Points Between the WMA S-SX Boundary and the Columbia River E-89
E.38. Case 10 Industrial Worker ILCR Versus Time at WMA S-SX Boundary E-91
E.39. Case 10 Industrial Worker ILCR Versus Time at Compliance Points Between the WMA S-SX Boundary and the Columbia River E-92
E.40. Case 11 Industrial Worker ILCR Versus Time at WMA S-SX Boundary E-94
E.41. Case 11 Industrial Worker ILCR Versus Time at Compliance Points Between the WMA S-SX Boundary and the Columbia River E-95

TABLES

E.1. Timeline Estimates for Emplacement of Interim and Closure Barriers at the S and SX Tank Farms and Corresponding Recharge Estimates E-9
E.2. Composite van Genuchten-Mualem Parameters for Various Strata at the S and SX Tank Farms E-10
E.3. Macroscopic Anisotropy Parameters Based on Polmann (1990) Equations for Various Strata at the S and SX Tank Farms E-12
E.4. Effective Hydraulic Parameters for Clastic Dike Infilling Materials E-12
E.5. Effective Parameter Estimates, $E[\rho_b K_d]$, for Cesium-137 for the Product of Bulk Density (g/cm^3) and K_d (cm^3/g) at WMA S-SX E-13
E.6. Non-Reactive Macrodispersivity Estimates for Various Strata at the S and SX Tank Farms E-14
E.7. Hydraulic Properties for Various Material Types for Site-wide VAM3D Groundwater Model E-19
E.8. Transport Parameters for the Site-wide Groundwater Model E-20
E.9. Unit Dose Factors for Cesium-137 and Technetium-99 ....E-20
E.10. Initial Inventory Distribution Schedule E-27
E.11. Unit Risk Factors for the Industrial Worker, Residential Farmer, and Recreational Shoreline User Scenarios E-33
E.12. Basis for Scaled Groundwater Concentrations E-36
E.13. Industrial Worker Scenario Groundwater Unit Dose Factors E-37
E.14. Peak Concentrations and Arrival Times at the First Compliance Point (i.e., WMA S-SX Boundary) for Case 1 ....E-39
E.15. Case 1 Mean Aqueous-Phase Saturation E-43
E.16. Peak Concentrations and Arrival Times at the First Compliance Point (i.e., WMA S-SX Boundary) for Case 2 ....E-44
E.17. Peak Concentrations and Arrival Times at the First Compliance Point (i.e., WMA S-SX Boundary) for Case 3 ....E-50
E.18. Peak Concentrations and Arrival Times at the First Compliance Point (i.e., WMA S-SX Boundary) for Case 4 ....E-51
E.19. Peak Concentrations and Arrival Times at the First Compliance Point (i.e., WMA S-SX Boundary) for Case 5 ....E-52
E.20. Peak Concentrations and Arrival Times at the First Compliance Point (i.e., WMA S-SX Boundary) for Case 6 ....E-54
E.21. Peak Concentrations and Arrival Times at the First Compliance Point (i.e., WMA S-SX Boundary) for Case 7 ....E-55
E.22. Peak Concentrations and Arrival Times at the First Compliance Point (i.e., WMA S-SX Boundary) for Case 8 ....E-56
E.23. Peak Concentrations and Arrival Times at the First Compliance Point (i.e., WMA S-SX Boundary) for Case 9 ....E-57
E.24. Case 9 Mean Aqueous-Phase Saturation E-58
E.25. Peak Concentrations and Arrival Times at the First Compliance Point (i.e., WMA S-SX Boundary) for Case 10 ....E-60
E.26. Case 10 Mean Aqueous-Phase Saturation E-61
E.27. Peak Concentrations and Arrival Times at the First Compliance Point (i.e., WMA S-SX Boundary) for Case 11 ....E-62

E.28. Case 11 Mean Aqueous-Phase Saturation E-64
E.29. Peak Concentrations and Arrival Times at the First Compliance Point (i.e., WMA S-SX Boundary) for Case 12 .... E-65
E.30. Peak Concentrations and Arrival Times at the First Compliance Point (i.e., WMA S-SX Boundary) for Case 13 .... E-70
E.31. Solute Mass Balance Errors E-74
E.32. Distances and Travel Times from WMA S-SX E-75
E.33. Streamtube Characteristics E-76
E.34. Streamtube Analysis Summary for Technetium-99 .... E-79
E.35. Streamtube Analysis Summary for Chromium E-79
E.36. Streamtube Analysis Summary for Nitrate E-80
E.37. Human Health Risk and Dose Assessment Cases E-81
E.38. Peak Long-Term Human Health Impacts for Case 1 .... E-84
E.39. Peak Long-Term Human Health Impacts for Case 2 .... E-87
E.40. Peak Long-Term Human Health Impacts for Case 9 .... E-90
E.41. Peak Long-Term Human Health Impacts for Case 10 .... E-93
E.42. Peak Long-Term Human Health Impacts for Case 11 .... E-96

LIST OF TERMS

BTC	breakthrough curve
CoPCs	contaminants of potential concern
DOE	U.S. Department of Energy
Ecology	Washington State Department of Ecology
EPA	U.S. Environmental Protection Agency
HSRAM	Hanford Site Risk Assessment Methodology
ILCR	incremental lifetime cancer risk
MTCA	Model Toxics Control Act
TWRS EIS	Tank Waste Remediation System Environmental Impact Statement
WMA	waste management area

This page intentionally left blank.

E.1.0 INTRODUCTION

A series of numerical simulations are conducted to evaluate the performance of interim corrective measures such as surface barriers in reducing long-term human health risks from potential groundwater contamination at waste management area (WMA) S-SX. The specific objectives of the numerical assessment are to: (1) quantify the risks posed by past tank releases to the groundwater if no interim corrective measures are implemented, and (2) determine to what degree implementation of selected interim corrective measures would decrease the risks posed by past tank releases. The assessments focus specifically on impacts to groundwater resources (i.e., the concentration of contaminants in groundwater) and long-term risk to human health (associated with groundwater use). The evaluations consider the extent of contamination presently within the vadose zone, contaminant movement through the vadose zone to the saturated zone (groundwater), contaminant movement in the groundwater to points of compliance, and the types of assumed human receptor activities at the points of compliance. The impact assessment results present several key evaluations for decision-maker input that may impact current operations and future decisions on tank retrieval and closure.

E.2.0 MODELING APPROACH

Both base case (existing tank farm conditions) and engineered alternatives for the interim corrective measures are considered. The focus for the contaminant transport modeling is chemicals (i.e., nitrate and chromium) and long-lived radionuclides (i.e., technetium-99) that are environmentally mobile. The postulated conceptual model utilizes the recently collected data on technetium-99 and other constituents from borehole 41-09-39, borehole 299-W23-19 near tank SX-115, and the MACTEC-ERS cesium-137 plume maps (Goodman 2000).

For simulations with barriers, it is assumed that an interim barrier is in place by the year 2010. It is also assumed that for all simulations, as part of tank farm closure, a closure barrier is in place by the year 2040. Placing a barrier is expected to significantly reduce infiltration of meteoric water and therefore arrival of contaminants at the water table. The modeling considers the estimated inventories of contaminants within the vadose zone and calculates the associated risk (i.e., exceeding the drinking water standards [40 CFR 141] at the compliance point). Inventory estimates are considered to be a critical factor in calculations, and uncertainties in inventories are considered. It is assumed that no tank leaks will occur in the future. It is also assumed that, as part of 'good housekeeping,' water-line leaks from existing piping will be addressed and resolved. However, as discussed later, as part of sensitivity analysis, simulations are run to evaluate long-term effects of water-line leaks in the vicinity of tank SX-115.
The umbrella structure of the tank and shedding of water are simulated. Sediments adjacent to the tanks attain elevated water contents and, while remaining unsaturated, they develop what is known as moisture-dependent anisotropy. Such effects are simulated in the model. Numerical results are obtained for compliance at the WMA boundary, 200 West fence boundary, exclusion boundary beyond the 200 Areas, and the Columbia River. Except for the 200 West fence boundary, these boundaries are based on DOE-RL (2000). Instead of the 200 West fence boundary, DOE-RL (2000) refers to the 200 Areas boundary. However, since the 200 Areas and the exclusion boundaries are relatively close the 200 Areas boundary is replaced by the 200 West fence boundary. Streamtube/analytical models are used to route computed contaminant concentrations at the water table to compliance points.

Two-dimensional cross-sectional models are used to model vadose zone flow and transport. Three representative (west-east) cross-sectional models for the S and SX tank farms (Figure E.1) are considered:

- Cross-section through tanks SX-107, SX-108, and SX-109
- Cross-section through tanks SX-113, SX-114, and S-115
- Cross-section through tanks S-104, S-105, and S-106.

Note that, in this appendix and elsewhere in the main text (Section 4.0), the three cross-sections are labeled in two ways. For example, the row containing tanks SX-107, SX-108, and SX-109 is often labeled as cross-section SX-DD'. Similarly, cross-section SX-FF' refers to the row containing tanks SX-113, SX-114, and SX–115 and cross-section S-CC' refers to the row containing tanks S-104, S-105, and S-106. Figures E.2 through E.4 show the three geologic cross-sections.

Figure E.1. Location Map of Single-Shell Tank WMA S-SX and Surrounding Facilities in the 200 West Area

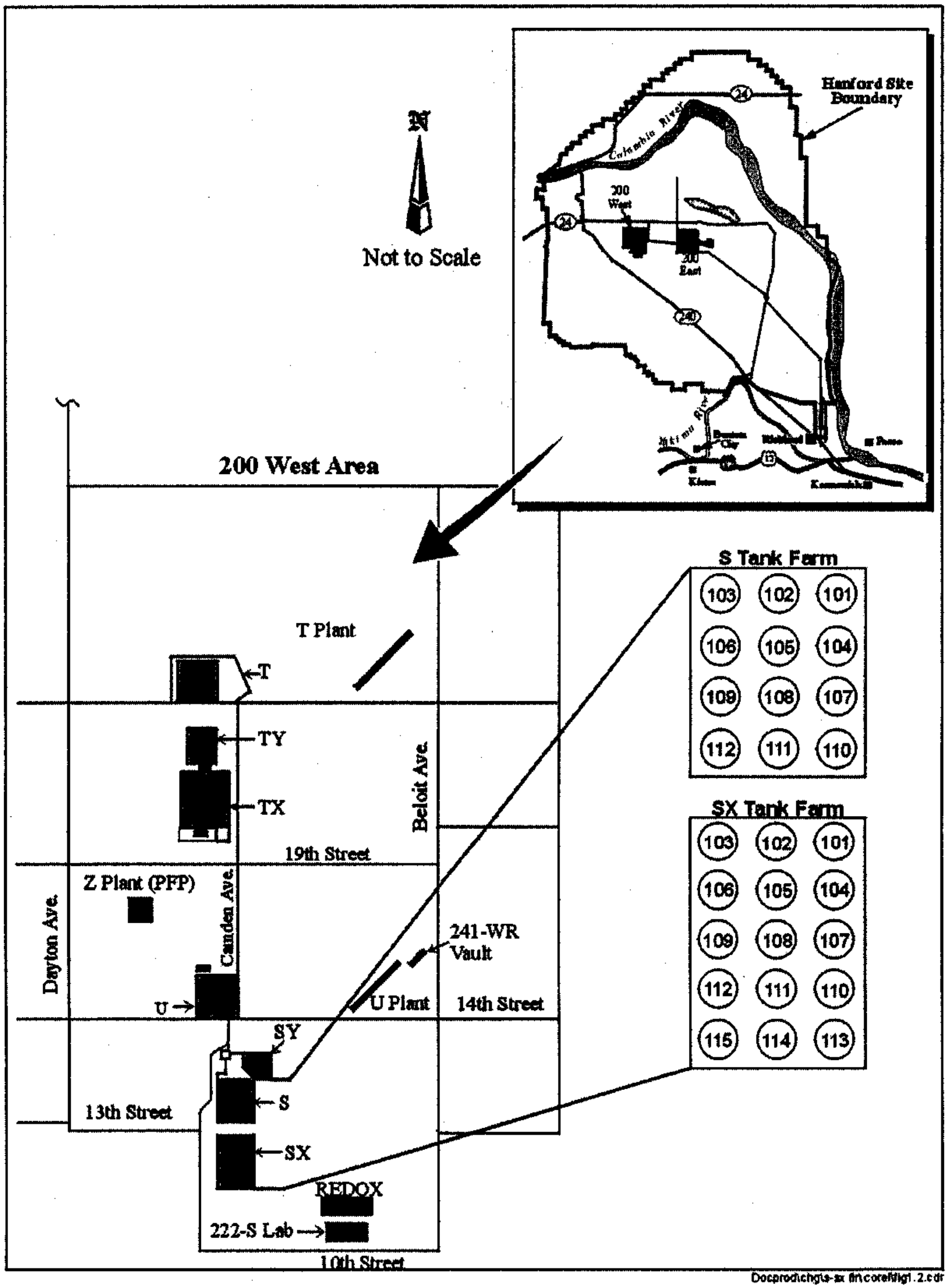
Hanford Site Boundary
24
Columbia River
200 West
200 East
240
Yakima River
Kiona
N
Not to Scale
200 West Area
T Plant
T
TY
TX
Beloit Ave.
19th Street
Z Plant (PFP)
Camden Ave.
Dayton Ave.
241-WR Vault
U
U Plant
14th Street
SY
S
13th Street
SX
REDOX
222-S Lab
10th Street
S Tank Farm
103
102
101
106
105
104
109
108
107
112
111
110
SX Tank Farm
103
102
101
106
105
104
109
108
107
112
111
110
115
114
113

Docprod\chg\s-sx fir\core\fig1.2.cdr

Figure E.2. Cross-Section SX-DD'

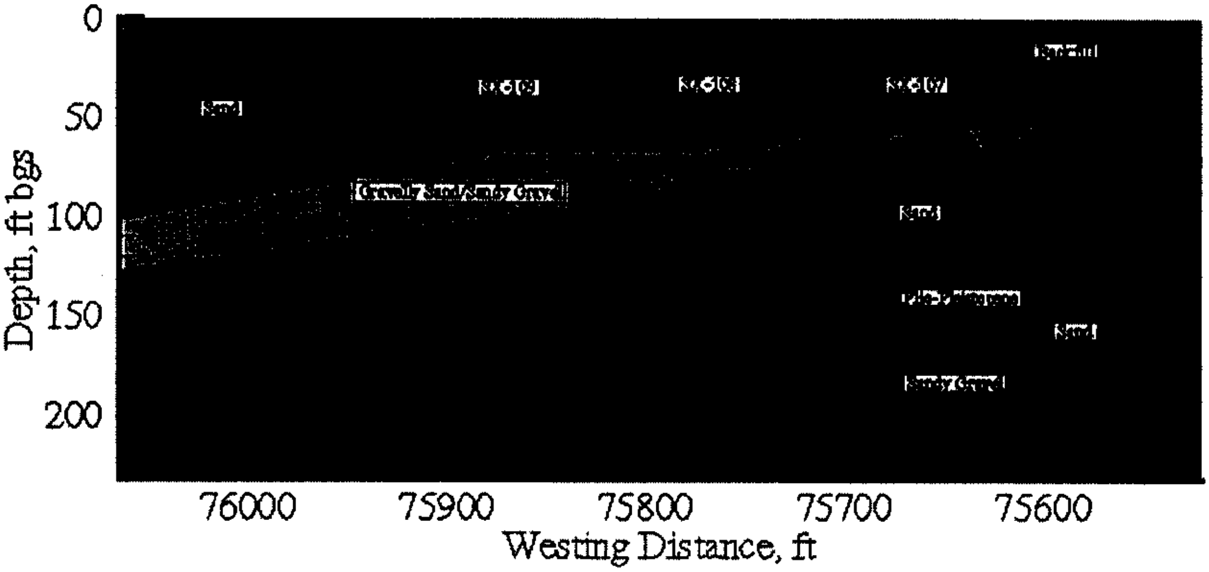

Figure E.3. Cross-Section SX-FF'

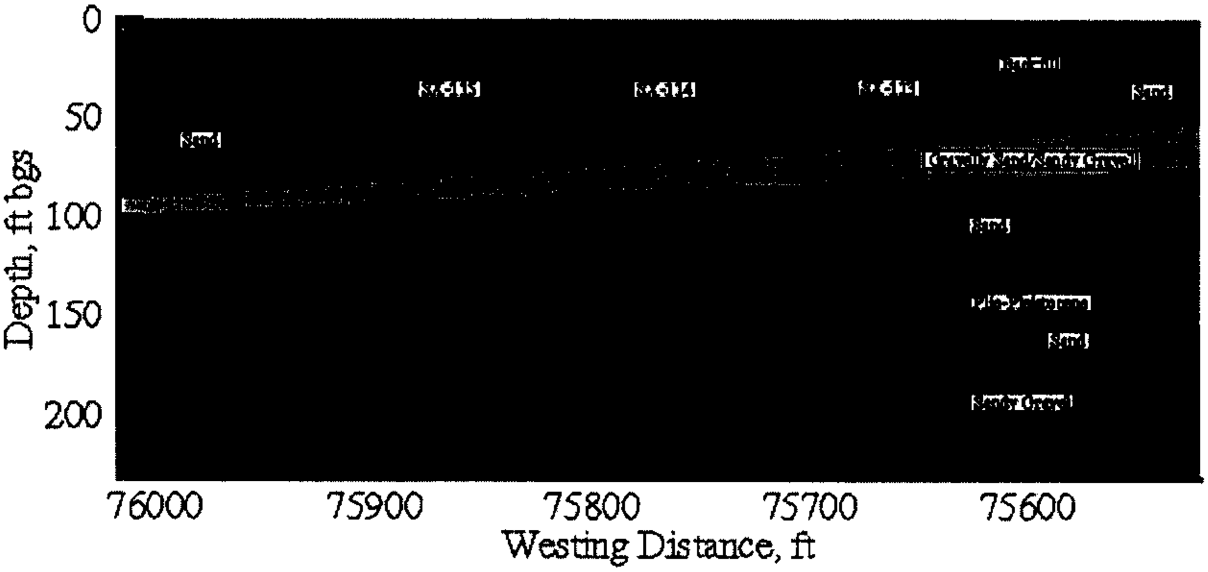

Figure E.4. Cross-Section S-CC'

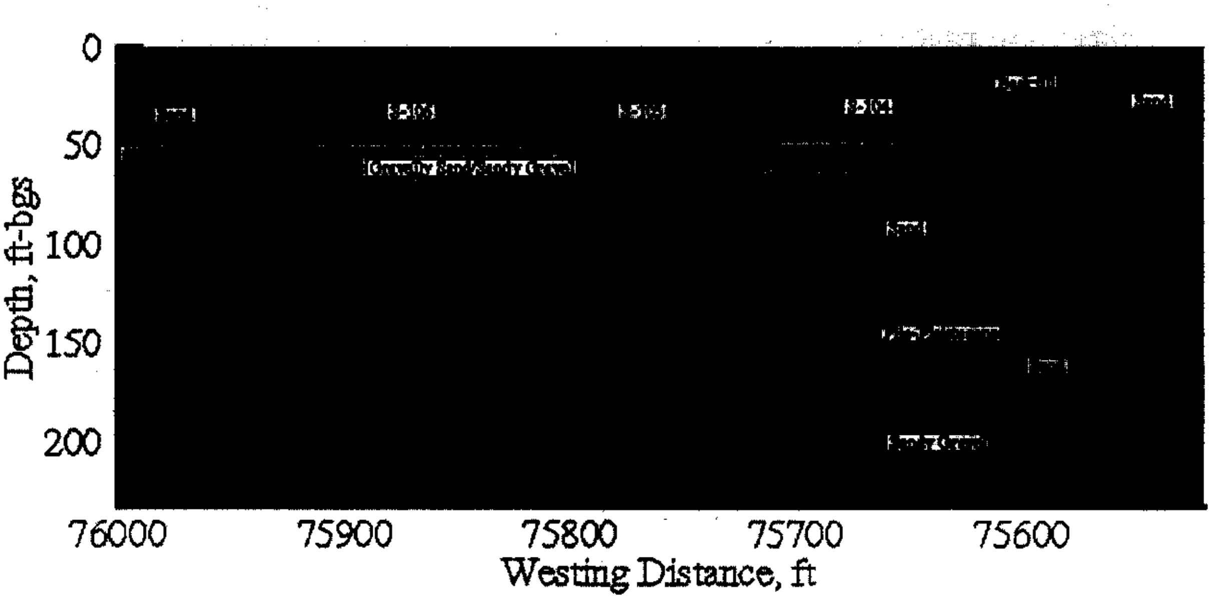

Simulation of flow and transport through each cross-section generates a breakthrough curve (BTC) at the water table. The temporal and spatial distribution for each of these BTCs is recognized and the principle of superposition is used to generate a composite BTC at the compliance boundary. An analytical/streamline approach is used to route the BTCs through the unconfined aquifer to the compliance boundary. The BTCs are converted into dose estimates using appropriate factors.

Fluid flow within the vadose zone is described by Richards' equation, whereas the contaminant transport is described by the conventional advective-dispersive transport equation with an equilibrium linear sorption coefficient (K_d) formulation. Detailed stratigraphic cross-sectional model data are based on information in *Subsurface Physical Conditions Description of the S-SX Waste Management Area* (Johnson et al. 1999), *Geology of the 241-S Tank Farm* (Price and Fecht 1976a), and *Geology of the 241-SX Tank Farm* (Price and Fecht 1976b). The model includes the effects of dipping strata. The enhanced spreading at the fine-grained/coarse-grained interfaces and the increased downdip movement of the plume along these interfaces are included in the model.

Data on laboratory measurements for moisture retention, particle-size distribution, saturated and unsaturated hydraulic conductivity, and bulk density for individual stratum are based on data on 200 East and 200 West Area soils (Khaleel et al. 2000). For each stratum defined by the stratigraphic cross-sectional model, the small-scale laboratory measurements are upscaled to obtain equivalent horizontal and vertical unsaturated hydraulic conductivities as a function of mean tension (Khaleel et al. 2000). Upscaling of unsaturated hydraulic conductivities (K's) leads to development of macroscopic anisotropies (as a function of mean tension) for each layer. An averaging of van Genuchten parameters (θ_r, θ_s, α, and n) (van Genuchten 1980) is used to define a moisture retention curve for each stratum.

In case multiple samples are not available for each stratum, data from other sites in the WMA S-SX vicinity are used. Attempts are made to use hydraulic properties that were obtained using both laboratory-measured moisture retention and unsaturated hydraulic conductivity. This is primarily to avoid extrapolating the unsaturated conductivities (van Genuchten 1980; Mualem 1976) to the dry end, based on saturated conductivity estimate (Khaleel et al. 1995). Also, to reflect field conditions, the laboratory data are corrected for the presence of any gravel fraction in the sediment samples (Khaleel and Relyea 1997).

As with flow modeling, each stratum is modeled with different transport parameters (i.e., bulk density, diffusivity, and dispersivity). As discussed earlier, contaminant mobility is quantified by sorption coefficients. A highly disturbed geochemical environment exists in the WMA S-SX vadose zone. The zones exist because chemistry of some leaked fluids radically differs from water and could change the soil water geochemical regime as migration occurs. The available database suggests that the most severe changes have occurred in soils underlying and near tanks SX-107, SX-108, and SX-109. While there is uncertainty about the sorption coefficient of cesium-137 and how it changes with concentration of competing ions, there is no doubt the sorption coefficient of technetium-99 is close to 0 mL/g in Hanford Site sediments. The low sorption coefficient coupled with a long half-life (2.03×10^5 years) allows technetium-99 to migrate over long distances in both the vadose zone and groundwater, posing a threat to groundwater quality for a long time.

Initial Conditions

Initial conditions are needed for moisture content (or pressure head) and contaminant concentration. For simulations not considering a barrier, initial conditions for pressure head (and moisture content) are established by allowing the vadose zone to equilibrate with an infiltration rate representative of natural infiltration for tank farm conditions. The data on infiltration rates with and without barriers are included in Section E.2.2.1. Initial conditions for contaminant concentration are provided as part of inventory estimates for cesium-137, technetium-99, nitrate, and chromium.

Model Setup and Boundary Conditions

A two-dimensional (west-east) vertical (x-z) slice of the flow domain is used for modeling flow and transport. The simulation domain extends horizontally to include the WMA S-SX boundaries and the water table, which is located about 65 m (213 ft) below ground surface. The geologic strata are assumed continuous but not of constant thickness. A variable grid spacing is used to model features such as the presence of clastic dikes between tanks. Sloped interfaces for geologic units are included based on information in Johnson et al. (1999), Price and Fecht (1976a), and Price and Fecht (1976b).

For flow modeling, Neumann boundary conditions are prescribed at the surface with the flux equal to the recharge rate estimate. For transport modeling, a zero flux boundary is prescribed at the surface for cesium-137, technetium-99, nitrate, and chromium. The western and eastern boundaries are assigned no-flux boundaries for both flow and transport. The water table boundary is prescribed by water table elevations and the unconfined aquifer hydraulic gradient. No-flux boundaries are used for the lower boundary.

To account for the residual effects of tank leaks, the variable density and viscosity of the leaked fluid are considered. The increased fluid density effects are expected to enhance the vertical mobility of both the fluid and the contaminant. The density effect can elongate the plume vertically and tends to decrease the lateral spreading caused by stratigraphic variations in material properties and moisture-dependent anisotropy.

Clastic dikes are included in the modeling as a sensitivity analysis. Clastic dikes occur in many locations in the 200 West Area and have been hypothesized as potential pathways for vertical transport that could explain the deep migration of contaminants at the SX tank farm. Preliminary data on clastic dike infilling materials are based on *Far-Field Hydrology Data Package for Immobilized Low-Activity Tank Waste Performance Assessment* (Khaleel 1999). Detailed inputs for various flow and transport parameters are presented later.

E.2.1 NUMERICAL CASES CONSIDERED

The following simulation runs (Cases 1 through 13) are considered for two-dimensional simulations. Note that Cases 1 through 4 consider a spatially uniform distribution of the inventory for the three cross-sections. Cases 5, 6, and 7 consider a nonuniform distribution of the same inventory. Case 7 considers a different location of the inventory within the two-dimensional cross-section. Cases 3 and 13 consider different volumes for water-line leaks, whereas Cases 9 through 11 consider varying estimates of natural recharge. Note that for Cases 3 and 13, the three-dimensional water-line leak was modeled as a point source of water spread over a circular area between two tanks. The circular leak area was translated for the two-dimensional simulations using a unit computational grid width and assuming that the center of the leak area was situated on the center line between tanks. Details are given in Section E.4.0. The simulations are run for a period of compliance of 1,000 years. Note that each of the 13 cases summarized below involves three cross-sectional runs.

- **Case 1: Base Case, No Action Alternative**. Flow and transport runs for cross-sections through tanks SX-107, SX-108, and SX-109; tanks SX-113, SX-114, and SX-115; and tanks S-104, S-105, and S-106 considering natural infiltration *only*, *no* water-line leak, *no* interim barrier, and a closure barrier by the year 2040.

- **Case 2: Barrier Alternative and No Water-Line Leak.** Flow and transport runs for cross-sections through tanks SX-107, SX-108, and SX-109; tanks SX-113, SX-114, and SX-115; and tanks S-104, S-105, and S-106 considering placement of an interim barrier by 2010; a closure barrier by 2040 (i.e., the interim barrier replaced by the closure barrier); and *no* water-line leak.

- **Case 3: No Barrier and 25,000 gal Water-Line Leak.** Flow and transport runs for cross-sections through tanks SX-107, SX-108, and SX-109; tanks SX-113, SX-114, and SX-115; and tanks S-104, S-105, and S-106 considering natural infiltration, water-line leak (25,000 gal) for tank SX-115 *only*, and *no* barrier until closure.

- **Case 4: No Interim Barrier and Clastic Dikes.** Flow and transport runs for cross-sections through tanks SX-107, SX-108, and SX-109; tanks SX-113, SX-114, and

SX-115; and tanks S-104, S-105, and S-106 considering natural infiltration, clastic dikes midway between tanks SX-108 and SX-109, and *no* interim barrier until closure.

- **Case 5: Nonuniform Inventory Distribution and No Barrier.** Flow and transport runs for cross-sections through tanks SX-107, SX-108, and SX-109; tanks SX-113, SX-114, and SX-115; and tanks S-104, S-105, and S-106 considering natural infiltration *only*; *no* water-line leak; *no* barrier until closure; and a higher distribution of inventory at a few locations (e.g., a few nodes, with a high concentration, either at the same depth or at different depths).

- **Case 6: Nonuniform Inventory Distribution and Barrier.** Flow and transport runs for cross-sections through tanks SX-107, SX-108, and SX-109; tanks SX-113, SX-114, and SX-115; and tanks S-104, S-105, and S-106 considering barrier infiltration (interim barrier replaced at closure); *no* water-line leak; and a higher distribution of inventory at a few locations (e.g., a few nodes, with a high concentration, either at the same depth or at different depths).

- **Case 7: Displaced-Nonuniform Inventory Distribution and No Barrier.** Flow and transport runs for cross-sections through tanks SX-107, SX-108, and SX-109; tanks SX-113, SX-114, and SX-115; and tanks S-104, S-105, and S-106 considering natural infiltration *only*, *no* water-line leak, *no* barrier until closure, and an inventory location close to the water table.

- **Case 8: Density and Viscosity Effects.** Flow and transport runs for cross-sections through tanks SX-107, SX-108, and SX-109; tanks SX-113, SX-114, and SX-115; and tanks S-104, S-105, and S-106 considering natural infiltration *only*, *no* water-line leak, enhanced density and viscosity, and *no* barrier until closure.

- **Case 9: Base Case with 50 mm/yr Meteoric Recharge.** Flow and transport runs for cross-sections through tanks SX-107, SX-108, and SX-109; tanks SX-113, SX-114, and SX-115; and tanks S-104, S-105, and S-106 considering natural infiltration (50 mm/yr) *only*, *no* water-line leak, *no* interim barrier, and a closure barrier by the year 2040.

- **Case 10: Base Case with 30 mm/yr Meteoric Recharge.** Flow and transport runs for cross-sections through tanks SX-107, SX-108, and SX-109; tanks SX-113, SX-114, and SX-115; and tanks S-104, S-105, S-106 considering natural infiltration (30 mm/yr) *only*, *no* water-line leak, *no* interim barrier, and a closure barrier by the year 2040.

- **Case 11: Base Case with 10 mm/yr Meteoric Recharge.** Flow and transport runs for cross-sections through tanks SX-107, SX-108, and SX-109; tanks SX-113, SX-114, and SX-115; and tanks S-104, S-105, S-106 considering natural infiltration (10 mm/yr) *only*, *no* water-line leak, *no* interim barrier, and a closure barrier by the year 2040.

- **Case 12: Alternate Inventory Distribution and No Barrier.** Flow and transport runs for cross-sections through tanks SX-107, SX-108, and SX-109; tanks SX-113, SX-114, and SX-115; and tanks S-104, S-105, and S-106 considering natural infiltration (100 mm/yr) *only*, *no* water-line leak, *no* interim barrier, a closure barrier by the year 2040, and an alternate inventory distribution.

- **Case 13: No Barrier and 200,000 gal Water-Line Leak.** Flow and transport runs for cross-sections through tanks SX-107, SX-108, and SX-109; tanks SX-113, SX-114, and SX-115; and tanks S-104, S-105, and S-106 considering natural infiltration (100 mm/yr), water-line leak (200,000 gal) for tank SX-115 *only*, and *no* barrier until closure.

In addition to the preceding two-dimensional simulations, a fully three-dimensional simulation (see Section E.4.14) is also considered. However, the risk calculations are all based on two-dimensional simulation results. The three-dimensional simulation is performed as a check on the two-dimensional analysis.

E.2.2 RECHARGE ESTIMATES AND VADOSE ZONE FLOW AND TRANSPORT PARAMETERS

Modeling inputs for recharge estimates and effective (upscaled) flow and transport parameters are presented in this section. The effective parameters are based on laboratory measurements of moisture retention, saturated and unsaturated hydraulic conductivity, and bulk density for sediment samples in the 200 Areas.

E.2.2.1 Recharge Estimates

The S and SX tank farm surfaces are covered with gravel to prevent vegetation growth and provide radiation shielding for site workers. Bare gravel surfaces, however, enhance net infiltration of meteoric water compared to undisturbed naturally-vegetated surfaces. Infiltration is further enhanced in the tank farms by the effect of percolating water being diverted by an impermeable, sloping surface of the tank domes. The basis for recharge estimates (Table E.1) for field investigation report modeling is presented in the main text (Section 3.1.2).

Table E.1. Timeline Estimates for Emplacement of Interim and Closure Barriers at the S and SX Tank Farms and Corresponding Recharge Estimates

Condition Simulated	Recharge Estimate (mm/yr)
No barrier [2000-2010]	100
Interim barrier [2010-2040]	0.5
Closure barrier (1st 500 yrs) [2040-2540]	0.1
Degraded closure barrier (post 500 yrs) [2540-3000]	3.5

E.2.2.2 Vadose Zone Flow and Transport Parameters

This section provides effective (upscaled) values of flow and transport parameters for the vadose zone. Specific flow parameters include moisture retention and saturated and unsaturated hydraulic conductivity. Transport parameters include bulk density, diffusivity, sorption coefficients, and macrodispersivity. Details on deriving the effective (upscaled) parameters are addressed in *Modeling Data Package for S-SX Field Investigation Report (FIR)* (Khaleel et al. 2000).

Table E.2 lists composite, fitted van Genuchten-Mualem (van Genuchten 1980; van Genuchten et al. 1991) parameters for various strata at the S and SX tank farms. Again, note that the material type numbers noted in Table E.2 (and in Tables E.3, E.5, and E.6) are identical to those indicated in the modeling data package (Appendix B of Khaleel et al. 2000). Estimates for the equivalent horizontal and vertical hydraulic conductivities are presented in Section E.2.2.3.

Table E.2. Composite van Genuchten-Mualem Parameters for Various Strata at the S and SX Tank Farms

Strata/Material Type	Number of Samples	θ_s	θ_r	α (1/cm)	n	ℓ	Fitted K_s (cm/s)
Backfill (1)	10	0.1380	0.0100	0.0210	1.3740	0.5	5.60E-04
Sand (2)	12	0.3819	0.0443	0.0117	1.6162	0.5	9.88E-05
Gravelly sand/sandy gravel (3)	11	0.2126	0.0032	0.0141	1.3730	0.5	2.62E-04
Plio-Pleistocene (4)	4	0.4349	0.0665	0.0085	1.8512	0.5	2.40E-04
Sandy gravel (5)	10	0.1380	0.0100	0.0210	1.3740	0.5	5.60E-04

Source: Khaleel et al. (2000).

E.2.2.3 Stochastic Model for Macroscopic Anisotropy

Variable, tension-dependent anisotropy provides a framework for upscaling small-scale, laboratory measurements to the effective (upscaled) properties for the large-scale tank farm vadose zone. A stochastic model (Polmann 1990) is used to evaluate tension-dependent anisotropy for sediments at the WMA S-SX; details are in Appendix C of Khaleel et al. (2000). The following is a brief description of the variable anisotropy model used in the field investigation report modeling.

Yeh et al. (1985) analyze steady unsaturated flow through heterogeneous porous media using a stochastic model; parameters such as hydraulic conductivity are treated as random variables rather than as deterministic quantities. The Gardner (1958) relationship is used in Yeh et al. (1985) to describe unsaturated hydraulic conductivity (K) as a function of saturated hydraulic conductivity (K_s) and tension (ψ), that is,

$$K(\psi) = K_s \exp(-\beta\psi) \tag{E.1}$$

where:

β = fitting parameter.

Equation E.1 can be written as

$$\ln K(\psi) = \ln K_s - \beta\psi \tag{E.2}$$

Equation E.2 is referred to as the log-linear model, because lnK is linearly related to ψ through the constant slope β. However, such a constant slope is often inadequate in describing $\ln K(\psi)$ over ranges of tension of practical interest for field applications. As an alternative, the slope β can be approximated locally by straight lines over a fixed range of tension. The $\ln K_s$ in Equation E.2 can then be derived by extrapolating the local slopes back to zero tension.

Using a linear correlation model between the log-conductivity zero-tension intercept and β, Polmann (1990) presents a generalized model that accounts for the cross-correlation of the local soil property (i.e., $\ln K_s$ and β) residual fluctuations. Compared to uncorrelated $\ln K_s$ and β model, partial correlation of the properties is shown to have a significant impact on the magnitude of the effective parameters derived from the stochastic theory. The Polmann (1990) equations for deriving the effective parameters are as follows.

$$\begin{aligned}
&< LnK > = < LnK_s > - A < \psi > - \sigma^2_{LnKs}\lambda[p - p^2 < \psi > - \zeta^2 < \psi >]/(1 + A\lambda) \\
&\sigma^2_{LnK} = \sigma^2_{LnKs}[(1 - p < \psi >)^2 + \zeta^2 < \psi >^2]/(1 + A\lambda) \\
&K_h^{eq} = \exp[< LnK > + (\sigma^2_{LnK}/2)] \\
&K_v^{eq} = \exp[< LnK > - (\sigma^2_{LnK}/2)]
\end{aligned} \tag{E.3}$$

where:

σ^2_{LnK} = variance of log unsaturated conductivity (which depends on mean tension)
$<\psi>$ = mean tension
σ^2_{LnKs} = variance of $\ln K_s$
$<LnK_s>$ =mean of $\ln K_s$
p = slope of the β versus $\ln K_s$ regression line
ζ = $\sigma_\delta/\sigma_{\ln Ks}$
σ_δ = standard deviation of the residuals in the β versus $\ln K_s$ regression
A = mean slope, β, for $\ln K_s$ vs. ψ
λ = vertical correlation lengths for $\ln K_s$ (assumed to be same as that of β)
K_h^{eq} = equivalent unsaturated horizontal conductivity
K_v^{eq} = equivalent unsaturated vertical conductivity.

E.2.2.3.1 Macroscopic Anisotropy Parameters. Table E.3 lists the variable, macroscopic anisotropy parameter estimates for various strata at WMA S-SX. Details on derivation of the parameter estimates are included elsewhere (Appendix C of Khaleel et al. 2000).

Table E.3. Macroscopic Anisotropy Parameters Based on Polmann (1990) Equations for Various Strata at the S and SX Tank Farms

Strata/Material Type	Number of Samples	$\langle LnK_s \rangle$	$\sigma^2_{LnK_s}$	p	ζ	λ (cm)	A
Backfill (1)	10	-15.76	3.56	-1.1E-4	1.84E-4	30	0.00371
Sand (2)	12	-14.6	1.50	-7.2E-4	6.55E-4	50	0.00620
Gravelly sand/sandy gravel (3)	11	-14.85	1.94	-2.6E-4	2.50E-4	30	0.00368
Plio-Pleistocene (4)	4	-10.43	1.01	2.4E-3	9.34E-4	50	0.0104
Sandy gravel (5)	10	-15.76	3.56	-1.1E-4	1.84E-4	30	0.00371

E.2.2.4 Clastic Dike Infilling Material Properties

Data on physical and hydraulic parameters are needed for clastic dike infilling materials to model their effects on flow and contaminant transport. Data on bulk density, particle-size distribution, moisture retention, saturated and unsaturated hydraulic conductivities for clastic dike infilling materials are included in Appendix C of Khaleel et al. (2000). Table E.4 provides the effective parameters.

Table E.4. Effective Hydraulic Parameters for Clastic Dike Infilling Materials

Material	θ_s (cm^3/cm^3)	θ_r (cm^3/cm^3)	α (1/cm)	n (-)	Saturated Hydraulic Conductivity (cm/s)
Clastic dike	0.4348	0.04675	0.07343	1.7115	1.20E-03

E.2.2.5 Enhanced Density and Viscosity Estimates

Numerical simulation cases in Section E.2.1 identify one run with enhanced density and viscosity estimates for the leaked fluid. The impact of fluid properties (density and viscosity) on contaminant migration is investigated by considering a fluid specific gravity of 1.4 (Ward et al. 1997).

E.2.2.6 Effective Transport Parameters

Effective transport parameter (bulk density, diffusivity, and dispersivity) estimates are presented in this section. Because of natural variability, the transport parameters are all spatially variable. The purpose is again, similar to the flow parameters, to evaluate the effect of such variability on the large-scale transport process.

E.2.2.6.1 Bulk Density and Sorption Coefficient. Both bulk density (ρ_b) and sorption coefficient estimates are needed to calculate retardation factors for different species. The effective, large-scale estimate for the product [$\rho_b K_d$] is the average of the product of small-scale laboratory measurements for bulk density and sorption coefficient (Gelhar 1993). Table E.5 provides the effective, large-scale estimates for cesium-137. The average ρ_b, $E[\rho_b]$ (Table E.5) estimates are based on data in Khaleel et al. (2000) for the five strata and clastic dike samples. The sorption coefficient estimates (Table E.5) for cesium-137 are based on *Data from Geochemical Data Package for the Immobilized Low-Activity Waste Performance Assessment* (Kaplan and Serne 1999) for undisturbed sediments. No other species are included, because the sorption coefficients for technetium-99, chromium, and nitrate are estimated to be zero. Calculations (Table E.5) for $E[\rho_b]$ and $E[\rho_b K_d]$ include correction for the gravel fraction.

Table E.5. Effective Parameter Estimates, $E[\rho_b K_d]$, for Cesium-137 for the Product of Bulk Density (g/cm^3) and K_d (cm^3/g) at WMA S-SX

Strata/Material Type	K_d	$E[\rho_b]$	$E[\rho_b K_d]$
Backfill (1)	500	1.94	971
Sand (2)	500	1.76	864
Gravelly sand/sandy gravel (3)	500	2.07	600
Plio-Pleistocene (4)	500	1.65	814
Sandy gravel (5)	500	2.13	488
Clastic dike	500	1.52	759

E.2.2.6.2 Diffusivity. It is assumed that the effective, large-scale diffusion coefficients for all strata at the S and SX tank farms are a function of volumetric moisture content, θ, and can be expressed using the empirical relation from "Permeability of Porous Solids" (Millington and Quirk 1961):

$$D_e(\theta) = D_0 \frac{\theta^{10/3}}{\theta_s^2} \tag{E.4}$$

where:

$D_e(\theta)$ = effective diffusion coefficient of an ionic species
D_0 = effective diffusion coefficient for the same species in free water.

The molecular diffusion coefficient for all species in pore water is assumed to be 2.5×10^{-5} cm^2/sec (Kincaid et al.1995).

E.2.2.6.3 Macrodispersivity. An extended review is provided in Appendix C of Khaleel et al. (2000) on the rationale for vadose zone macrodispersivity estimates. Macrodispersivity estimates are needed for both reactive (cesium-137) and non-reactive (i.e., technetium-99, chromium, and nitrate) species.

E.2.2.6.3.1 Macrodispersivity Estimates for Non-Reactive Species. Macrodispersivity estimates for non-reactive species (i.e., technetium-99, chromium, and nitrate) are listed in Table E.6. Details on the basis for the estimates are provided in Appendix C of

Khaleel et al. (2000). Macrodispersivities for clastic dike sediments are assumed to be same as those for the Plio-Pleistocene unit.

Table E.6. Non-Reactive Macrodispersivity Estimates for Various Strata at the S and SX Tank Farms

Strata/Material Type	A_L (cm)	A_T (cm)
Backfill (1)	~150	15
Sand (2)	~150	15
Gravelly sand (3)	~100	10
Plio-Pleistocene (4)	~50	5
Sandy gravel (5)	~150	15

E.2.2.6.3.2 Heterogeneous Sorption Enhanced Macrodispersivities for the Reactive Species. As expected, the net effect of sorption is to retard the velocity of the contaminant. Because sorption for specific contaminants may be a function of soil properties, as the soil properties experience spatial variability, the sorption also varies (Gelhar 1993; Talbott and Gelhar 1994).

Stochastic analysis results for macrodispersivity enhancement for the five strata are presented in Table C-7 of Khaleel et al. (2000) for the reactive species (i.e., cesium-137). Note that the unsaturated conductivities were evaluated at -100 cm via the fitted van Genuchten-Mualem relation. The macrodispersivity enhancement ranged from about 1.07 for backfill sediments to about 2.35 for Plio-Pleistocene unit sediments. No dispersivity enhancement is assumed for the clastic dike sediments.

E.2.3 GROUNDWATER FLOW AND TRANSPORT

The preceding section provides vadose zone flow and transport parameters. This section includes flow and transport parameters for the unconfined aquifer. Also included are the unit dose conversion factors.

E.2.3.1 Flow and Transport Parameters

Instead of the Hanford Site-wide groundwater model, an analytical/streamtube approach is used to model groundwater flow and transport. However, as indicated in the following sections, flow and transport information needed for the analytical/streamtube model is based on the VAM3D Site-wide groundwater model (Law et al. 1996).

Figure E.5 shows the VAM3D-generated water table map at steady state, following simulation for 1,000 years. Figure E.5 can be used to generate streamlines/pathlines. Figure E.6 shows a streamline/pathline originating from the S and SX tank farms.

Figure E.5. VAM3D-Generated Steady State Hydraulic Head Distribution for the Hanford Site, Following Simulation for 1,000 Years

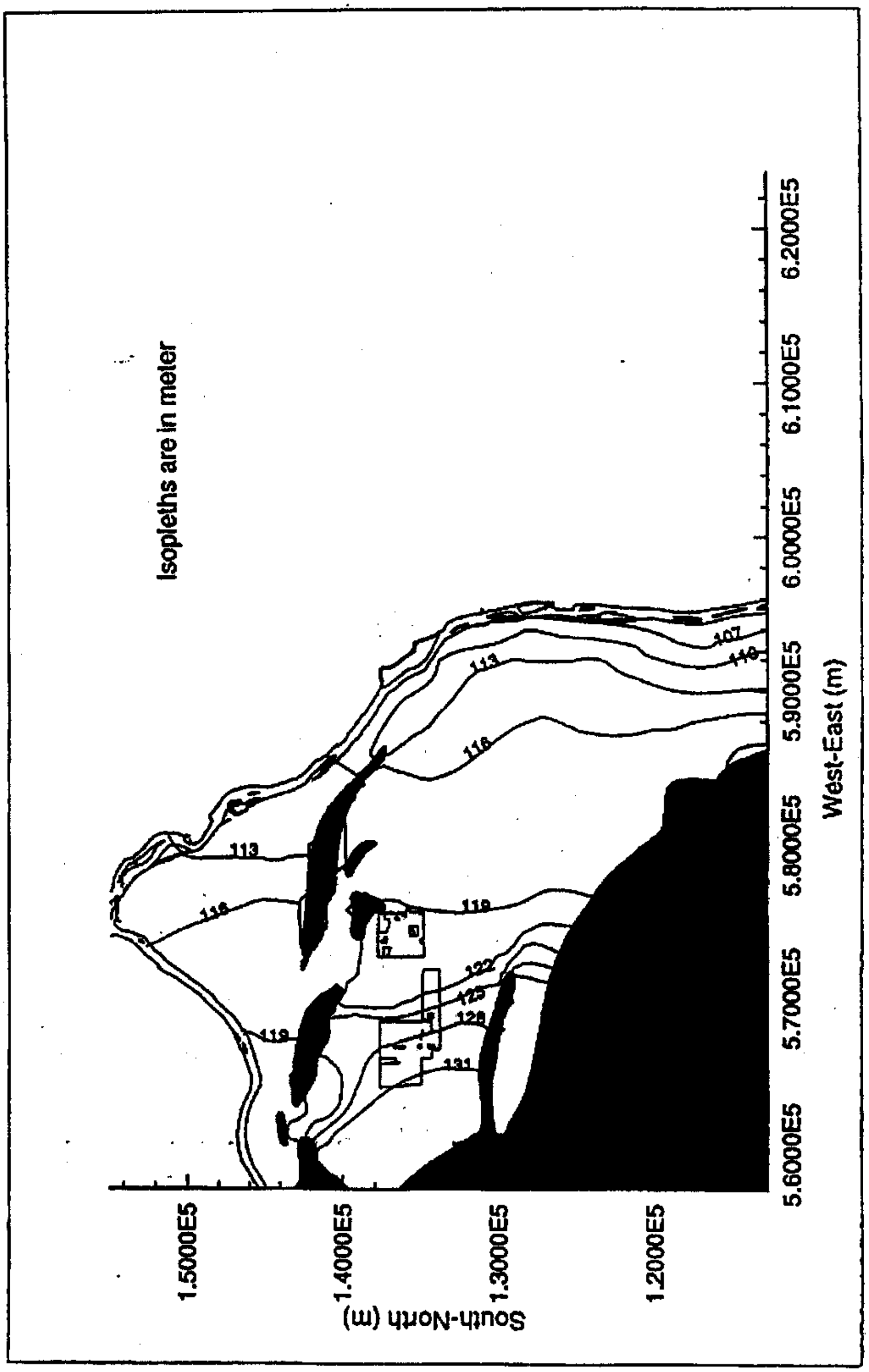
Isopleths are in meter
107
110
113
116
113
116
119
119
122
125
128
131
1.5000E5
1.4000E5
1.3000E5
1.2000E5
South-North (m)
5.6000E5
5.7000E5
5.8000E5
5.9000E5
6.0000E5
6.1000E5
6.2000E5
West-East (m)

Source: Lu 1996.

Figure E.6. VAM3D-Generated Pathline Distribution at Steady State, Following Simulation for 1,000 Years

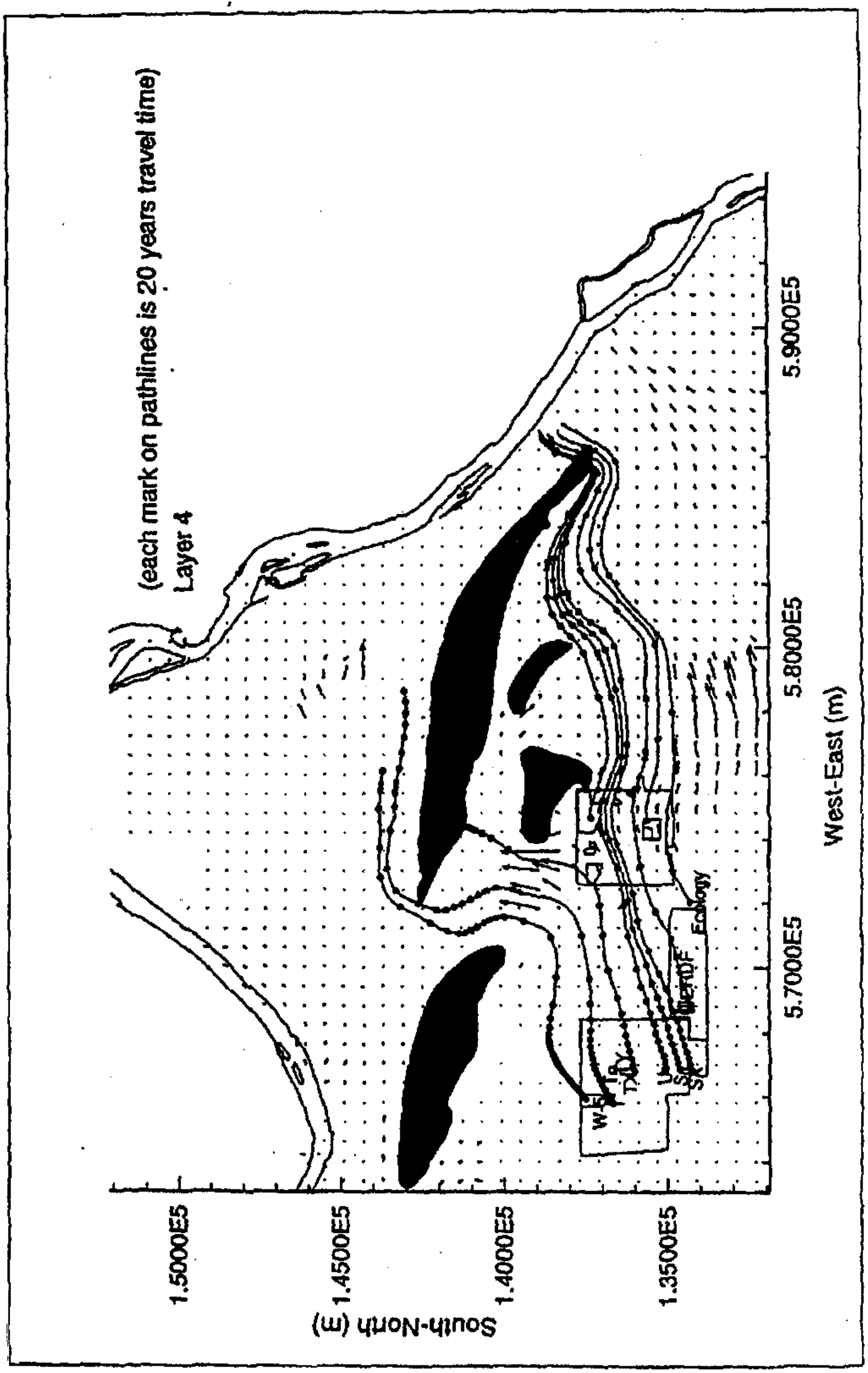
(each mark on pathlines is 20 years travel time)
Layer 4
1.5000E5
1.4500E5
1.4000E5
1.3500E5
South-North (m)
5.7000E5
5.8000E5
5.9000E5
West-East (m)
Ecology

Source: Lu 1996.

Information on groundwater velocity distribution is needed for the analytical/streamtube model. Figure E.7 prescribes the material property numbers for various regions within the flow domain of the Site-wide model. Darcy's law, combined with Figure E.5 and Table E.7, which provides the saturated hydraulic conductivity and porosity for each material type, are used to perform necessary velocity calculations. Other parameters needed for groundwater transport modeling are listed in Table E.8. Note that a small vertical macrodispersivity of 10 mm is used based on the limited vertical mixing observed in stratified aquifers such as those in the 200 Areas (van der Kamp et al. 1994); the other macrodispersivities are the same as those used in the Site-wide model (Law et al. 1996).

E.2.3.2 Unit Dose Factors

Table E.9 lists the unit dose factors needed to convert cesium-137 and technetium-99 concentrations in groundwater to a radiation dose. Table E.9 is based on a drinking water consumption scenario of 730 L/yr.

E.2.4 CONTAMINANT INVENTORY

This section provides details on the basis for vadose zone contaminant inventory estimates and their distributions. Also included are details on how various inventory distributions are implemented in the numerical model.

E.2.4.1 Basis for Inventory Estimates

Vadose zone inventory estimates for the four species (i.e., cesium-137, technetium-99, chromium, and nitrate) are primarily based on *Estimation of SX-Farm Vadose Zone Cs-137 Inventories from Geostatistical Analysis of Drywell and Soil Core Data* (Goodman 2000) and the recently collected borehole data. The Goodman (2000) estimates are used to assign inventory estimates for cesium-137 and the borehole data are used to assign estimates for the mobile species (i.e., technetium-99, chromium, and nitrate).

Goodman (2000) presents kriging analysis of cesium-137 inventory estimates in the vadose zone under the SX farm tanks based on measurements in the drywells, laterals, and borehole 41-09-39 soil cores. The details on inventory used in modeling are presented in *Inventory Estimates for Single-Shell Tank Leaks in S and SX Tank Farms* (Jones 2000) and Khaleel et al. (2000), and are included in Attachment E1. For technetium-99, chromium, and nitrate, the inventory estimates are scaled with respect to measured concentrations in boreholes. Note that data in Attachment E1 are decayed as of January 1, 2000. The decay coefficient for cesium-137 is 0.0231 yr^{-1} (i.e., half-life is 30 years).

Results of laboratory analyses of samples from borehole 41-09-39 provide the basis for inventory estimates for the mobile species under tanks SX-107, SX-108, and SX-109. Concentration measurements for samples from borehole 299-W23-19 southwest of tank SX-115 serve as the basis for estimates for the mobile species under tanks SX-113, SX-115, and S-104. Tank S-104 inventory estimates for cesium-137 are based on data from *Tank Summary Data Report for Tank S-104* (DOE-GJPO 1997). Tank SX-115 inventory estimates for cesium-137 are based on data from *Characterization of Subsurface Contamination in the SX Farm* (Raymond and Shdo 1966).

Figure E.7. Material Property Distribution for the Upper Three Elemental Layers for VAM3D Sitewide Groundwater Model

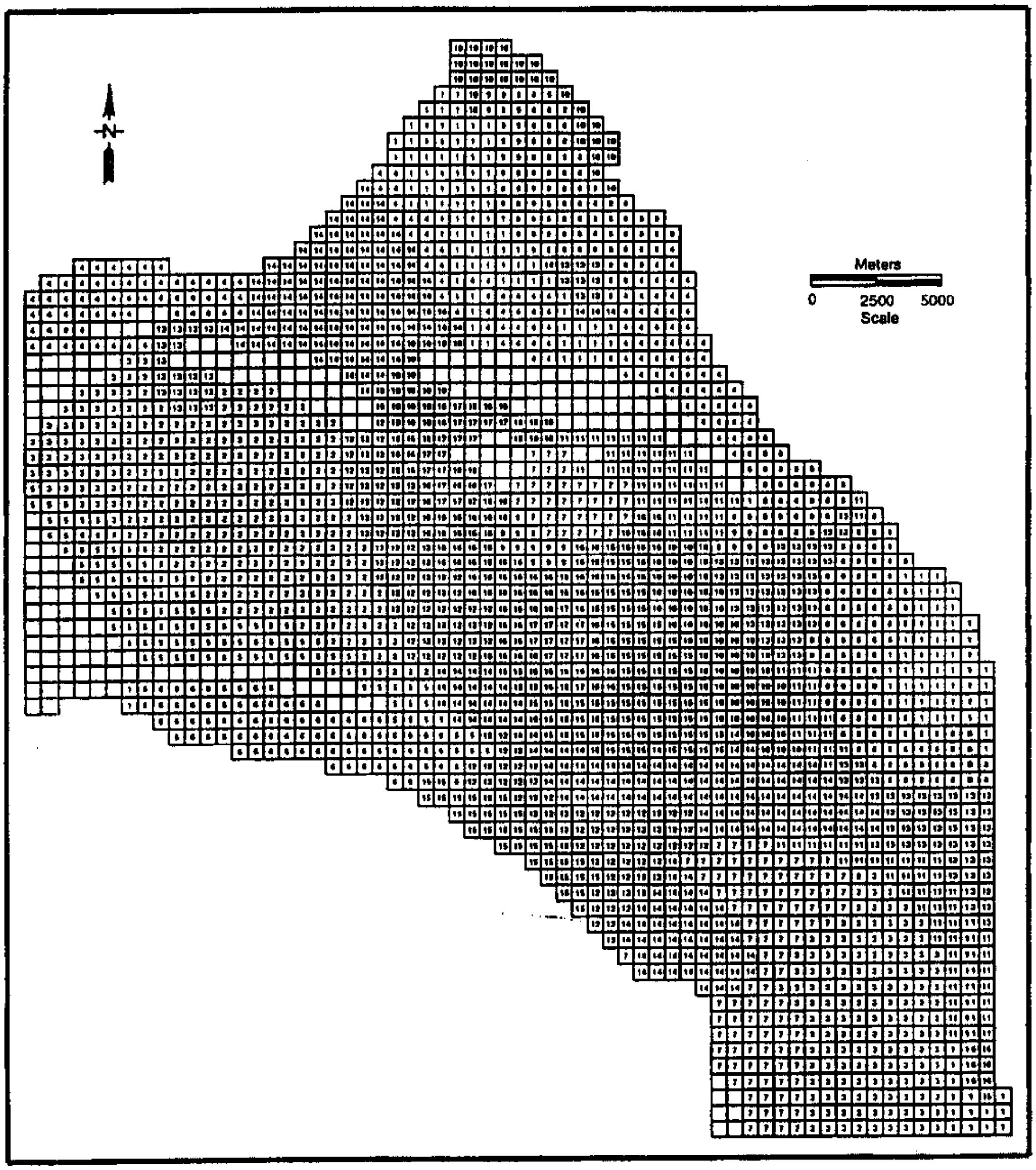
N
Meters
0
2500
5000
Scale

Source: Law et al. 1996.

Table E.7. Hydraulic Properties for Various Material Types for Site-wide VAM3D Groundwater Model

Zone	K_{xx} (m/y)	K_{yy} (m/y)	K_{zz} (m/y)	S_s (1/m)	Porosity (Percent)
1	.800E+03	.800E+03	.800E+02	.100E-05	10
2	.190E+04	.190E+04	.190E+03	.100E-05	25
3	.500E+04	.500E+04	.500E+03	.100E-05	10
4	.650E+04	.650E+04	.650E+03	.100E-05	10
5	.140E+05	.140E+05	.140E+04	.100E-05	25
6	.720E+05	.720E+05	.720E+04	.100E-05	25
7	.260E+05	.260E+05	.260E+04	.100E-05	10
8	.300E+05	.300E+05	.300E+04	.100E-05	25
9	.430E+05	.430E+05	.430E+04	.100E-05	25
10	.055E+06	.055E+06	.055E+05	.100E-05	25
11	.770E+05	.770E+05	.770E+04	.100E-05	25
12	.899E+05	.899E+05	.899E+04	.100E-05	25
13	.140E+06	.140E+06	.140E+05	.100E-05	25
14	.300E+06	.300E+06	.300E+05	.100E-05	25
15	.750E+06	.750E+06	.750E+05	.100E-05	25
16	.113E+07	.113E+07	.113E+06	.100E-05	25
17	.183E+07	.183E+07	.183E+06	.100E-05	25
18	.213E+07	.213E+07	.213E+06	.100E-05	25

K_{xx} = Hydraulic conductivity in the North-South direction
K_{yy} = Hydraulic conductivity in the East-West direction
K_{zz} = Hydraulic conductivity in the vertical direction
S_s = Specific storage
m/y = meters per year
1/m = 1 per meter

Source: Law et al. (1996).

Table E.8. Transport Parameters for the Site-wide Groundwater Model

Parameter	Estimate
Longitudinal macrodispersivity, cm	3050
Lateral macrodispersivity, cm	305
Vertical macrodispersivity	10
Diffusion coefficient, cm^2/sec	2.5×10^{-5}
Cs-137 sorption coefficient, cm^3/g	500
Cs-137 decay coefficient, 1/yr	0.0231

Table E.9. Unit Dose Factors for Cesium-137 and Technetium-99

Radionuclide	Dose factor*
Cs-137	0.0365
Tc-99	0.00107

*Units are mrem per pCi/L of concentration in the groundwater.
Source: Rittmann (1999).

E.2.4.2 Inventory Distributions

Because of significant uncertainties with inventory estimates, several distributions were considered. These included (1) uniform, (2) nonuniform, (3) displaced-nonuniform, and (4) an alternate distribution.

E.2.4.2.1 Uniform Distribution. For uniform distribution, the total inventory is assigned to discrete vadose zones, each having different values based on inventory variability. For uniform inventory distribution, the assigned inventory is uniformly distributed within each zone. For the cross-section with tanks SX-107, SX-108, and SX-109 (Figure E.1) the uniform distribution combines, by depth of each zone, the inventory noted in Attachment E1 under both tanks SX-108 and SX-109. The total inventory under both tanks is then distributed in the lateral direction across the two tanks (including the space between the tanks) by depths noted in Attachment E1. Note that both concentration and mass are honored in distributing the inventory in the lateral direction for each depth. For tank SX-107, the inventory is distributed across the diameter of that tank only.

For the cross-section with tanks SX-113, SX-114, and SX-115 (Figure E.1), the individual inventory for tanks SX-113 and SX-115 is distributed in the lateral direction across the tank diameter by depths noted in Attachment E1.

For the cross-section with tank S-104 (Figure E.1), the inventory is distributed uniformly in the lateral direction across the tank diameter by depths noted in Attachment E1.

E.2.4.2.2 Nonuniform Distribution. For nonuniform distribution, the distribution of inventory, by depth, is maintained. However, the inventory within each zone in the lateral direction is nonuniformly distributed but maintains the same mass of inventory as in the uniform distribution. The nonuniform inventory distribution cases are run *only* for the three mobile species.

For the cross-section with tanks SX-107, SX-108, and SX-109, two nonuniform distributions are generated; one for tanks SX-109 and SX-108 and the other for tank SX-107. For tanks SX-109 and SX-108, the nonuniform distribution combines, by depth, the inventory noted in Attachment E1 for tanks SX-109 and SX-108. The total inventory for both tanks is distributed in the lateral direction within the space between tanks SX-109 and SX-108 by depths noted in Attachment E1. For tank SX-107, the total inventory for each depth is distributed in the lateral direction within one-half the space *only* between tanks SX-107 and SX-108, beginning on the western edge of tank SX-107.

For the cross-section with tanks SX-113, SX-114, and SX-115, two nonuniform distributions are generated; one for tank SX-113 and the other for tank SX-115. For tank SX-113, the inventory for each depth is distributed in the lateral direction within one-half the space *only* between tanks SX-113 and SX-114, beginning on the western edge of tank SX-113. Similarly, for tank SX-115 the inventory for each depth is distributed in the lateral direction within one-half the space *only* between tanks SX-114 and SX-115, beginning on the eastern edge of tank SX-115.

For the cross-section with tank S-104, the inventory is distributed in the lateral direction within one-half the space *only* between tanks S-104 and S-105, beginning on the western edge of tank S-104.

E.2.4.2.3 Displaced-Nonuniform Distribution. To examine sensitivity (for mobile species only) relative to depth, a run considers location of the inventory close to the water table. A depth translation of the inventory data in Attachment E1 is used for the *nonuniform* distribution of the inventory for the three mobile species. The peak inventories, as noted in Attachment E1, are positioned within the Ringold Formation at about 50.3 m (165 ft) below ground surface; all other inventory locations are relative to this peak location.

E.2.4.2.4 Alternate Distribution. To further evaluate uncertainty in the lateral extent of the inventory, an alternate distribution was considered. The alternate distribution uses the tank diameters to define the radial extent of the contaminants.

E.2.4.3 Inventory Assignment

This section presents details on how the Attachment E1 inventory estimates were implemented numerically in STOMP (White and Oostrom 2000a, 2000b) calculations. As discussed in Section E.2.4.2, four different inventory distributions were investigated: uniform, nonuniform, displaced-nonuniform, and an alternate. Inventory distributions were one of two types: variable diameter or fixed diameter. Variable-diameter distributions honored both the concentration and total solute mass reported for a depth. In contrast, fixed-diameter distributions only honored the total solute mass reported for a depth. The uniform distribution was of the variable-diameter type, whereas the nonuniform, displaced-nonuniform, and alternate were fixed-diameter type distributions.

The uniform distribution most closely represented the inventory distributions (Attachment E1) and comprised of a series of concentric stacked disks. In the uniform distribution, the solute concentration within each disk equaled the Attachment E1 value, and the disk diameter was sized to honor the total solute mass for a particular depth. Therefore, the uniform distribution consisted of a series of concentric disks of varying concentration and diameter with depth. The nonuniform distribution comprised of a series of concentric stacked disks of equal diameter. This distribution honored the total solute mass reported in Attachment E1 for the depth, but altered the concentration according to the disk diameter. As the nonuniform distributions were used to investigate concentrating solute mass within the high flux regions between tanks, solute concentrations were generally higher than those reported Attachment E1. The displaced distribution was similar to the nonuniform distribution but displaced toward the water table. The alternate distribution was a fixed-diameter distribution that used the tank diameters to define the radial extent of solute. The algorithms used to develop variable-diameter and fixed diameter distributions differ and will be described in the sections that follow.

E.2.4.3.1 Variable-Diameter Distribution. The variable-diameter distribution honors both the concentration values and inventory mass at each depth by varying the distribution area as a function of depth. The first step in creating a variable-diameter distribution was to vertically interpolate Attachment E1 values on to the computational grid. The concentration and total solute mass are reported (Attachment E1) at discrete depths or in depth bins for each combination of tank (i.e., S-104, SX-107, SX-108, SX-109, SX-113, and SX-115) and solute species (i.e., cesium-137, technetium-99, nitrate, and chromium). The cesium-137 data are reported in contiguous depth bins of 9.84 ft for all 6 tanks. The technetium-99, nitrate, and chromium data are reported in disjointed depth bins of 1 ft for tanks SX-107, SX-108, and SX-109 and at discrete depths for tanks S-104, SX-113, and SX-115. Prior to translating to the computational grid, the discrete data were converted into contiguous binned data by using node-centered discretization (i.e., each discrete depth was converted to a depth bin with the discrete depth centered in depth bin). This discretization yielded depth bins that varied in height with elevation.

After converting those data reported as discrete depths to depth bins, the solute concentrations and inventory integrals were translated to the computational grid using an overlapping approach for each combination of tank and solute specie. The computational grids used vertical spacings of 0.4572 m (1.5 ft), compared with the inventory depth bins that varied in height from 0.1524 m (0.5 ft) to 3.7338 m (12.25 ft). For these sets of dimensions, three domain overlapping conditions occurred:

- Computational grid totally within the inventory depth bin
- Computational grid partially within the inventory depth bin
- Depth bin totally within the computational grid.

For the first two conditions, a fraction of the inventory in the depth bin was assigned to the grid horizon based on the fraction of overlap. For example, if a 0.4572 m (1.5 ft) grid cell was completely enclosed by a 1.242 m (4.075 ft) depth bin, then 36.81% of the inventory integral would be located in the grid horizon. For the third condition the entire inventory integral for the depth bin would be located in the grid horizon. The overlapping approach, described above, distributes the inventory vertically across the computational domain according to Attachment E1 data and exactly preserves the total inventory for each tank and specie combination.

The horizontal distribution of inventory depended on whether the inventory was variable- or fixed-diameter type. As discussed earlier, the variable-diameter distribution honored both the inventory concentration and total mass reported in Attachment E1, whereas the fixed-diameter distribution only honored the total mass and computed the concentration needed to distribute that inventory mass over a declared region (e.g., the region between two tanks).
The variable-diameter inventory distribution honored both the inventory concentration and total mass at each grid horizon by spreading the inventory over horizon-dependent surface area. When developed the variable-diameter distribution resembles a series of stacked disks of varying diameters, which when translated to two-dimensions resulted in a series of stacked rectangles of varying width but having the same height as in the two-dimensional cross-section.

Note that the inventory concentration was specified as sediment concentrations (e.g., pCi/g) and not as aqueous concentrations. The first step in computing a variable-diameter distribution was to convert the inventory concentration and integral into a surface area, according to Equation E.5.

$$A_{horz}^{3D} = \frac{I_{horz}^{3D}}{C_{horz}\, z_{horz}\, \bar{\rho}_b^{3D}{}_{horz}} \qquad \text{(E.5)}$$

where:

A_{horz}^{3D} = surface area (m^2) for the grid horizon (three-dimensional domain)
$\bar{\rho}_b^{3D}{}_{horz}$ = average soil bulk density (kg/m^3) for the grid horizon (three-dimensional domain)
I_{horz}^{3D} = total solute mass (Ci or µg) for the grid horizon (three-dimensional domain)
C_{horz} = solute concentration for the grid horizon (Ci/kg soil or µg/kg soil)
z_{horz} = height of the grid horizon (m).

The surface area (three-dimensional domain) was converted to a surface area per unit width for the grid horizon (two-dimensional cross-section) according to Equation E.6.

$$A_{horz}^{2D} = \sqrt{\frac{4A_{horz}^{3D}}{\pi}} \qquad \text{(E.6)}$$

where:

A_{horz}^{2D} = surface area per unit width (m^2/m) for the grid horizon (two-dimensional cross-section).

Note that 'per unit width' appears because the numerical simulations are based on two-dimensional cross-sectional models.

Assuming that the average soil bulk density for the grid horizon (three-dimensional domain) is equal to that for the two-dimensional cross-section, then the total inventory mass per unit width is computed according to Equation E.7.

$$I_{horz}^{2D} = A_{horz}^{2D}\, C_{horz}\, z_{horz}\, \bar{\rho}_b^{2D}{}_{horz} \qquad \text{(E.7)}$$

where:

I_{horz}^{2D} = solute inventory per unit width (Ci/m or µg/m) for the grid horizon (two-dimensional cross-section)

$\bar{\rho}_b^{2D}{}_{horz}$ = average soil bulk density (kg/m^3) for the grid horizon (two-dimensional cross-section).

To compute number of grid cells (nodes) over which the solute was distributed, the product of the solute concentration for the grid horizon was multiplied by the node length, height, and bulk density and integrated outward from the grid cell that contains the distribution centroid. For each grid horizon, the inventory was distributed over an odd number of grid cells centered on the distribution centroid (e.g., tank centroid). The solute concentration on the two outer grid cells was adjusted to yield an integrated inventory for the grid horizon that honors the grid-horizon total mass described above. This scheme is expressed mathematically as shown in Equation E.8.

$$I^{2D}_{horz} = \sum_{i=2}^{n-1} C_{horz}\,\Delta x^i\,\Delta z^i\,\rho_b^i + \hat{C}\left[\left(\Delta x^1\,\Delta z^1\,\rho_b^1\right) + \left(\Delta x^n\,\Delta z^n\,\rho_b^n\right)\right] \qquad \text{(E.8)}$$

where:

n = odd number of node indices centered around the distribution centroid
Δx = node length (m)
Δz^i = node height (m)
ρ_b^i = node bulk density (kg/m^3)
$\hat{C}$ = solute concentration assigned to the two outer most nodes.

The inventory distribution procedure described above worked for cases where the average soil bulk density was known over the distribution area. Because of the heterogeneous nature of the sediments, the average soil bulk density was unknown. Therefore, the actual calculation procedure followed the modified form expressed by Equations E.9 through E.12.

$$\tilde{A}^{3D}_{horz} = \frac{I^{3D}_{horz}}{C_{horz}\,z_{horz}} \qquad \text{(E.9)}$$

$$\tilde{A}^{2D}_{horz} = \sqrt{\frac{4\,\tilde{A}^{3D}_{horz}}{\pi}} \qquad \text{(E.10)}$$

$$\tilde{I}^{2D}_{horz} = \tilde{A}^{2D}_{horz}\,C_{horz}\,z_{horz} \qquad \text{(E.11)}$$

$$\tilde{I}^{2D}_{horz} = \sum_{i=2}^{n-1} C_{horz}\,\Delta x^i\,\Delta z^i\sqrt{\rho_b^i} + \hat{C}\left[\left(\Delta x^1\,\Delta z^1\sqrt{\rho_b^1}\right) + \left(\Delta x^n\,\Delta z^n\sqrt{\rho_b^n}\right)\right] \qquad \text{(E.12)}$$

where:

$\tilde{A}^{3D}_{horz}$ = surface area per unit bulk density (m^2/[kg/m^3]) for the grid horizon (three-dimensional domain)

$\tilde{A}^{2D}_{horz}$ = surface area per unit width per unit square root bulk density (m^2/m (kg/m^3)$^{1/2}$) for the grid horizon (two-dimensional cross-section)

$\tilde{I}^{2D}_{horz}$ = solute inventory per unit width per unit square root bulk density (Ci/m (kg/m^3)$^{1/2}$ or μg/m (kg/m^3)$^{1/2}$) for the grid horizon (two-dimensional cross-section).

E.2.4.3.2 Variable-Diameter Distribution. The fixed-diameter distribution only honors the Attachment E1 inventory total mass at each depth using a declared distribution area. Solute concentration is computed according to the inventory total mass and distribution area. As with the variable-diameter distribution, the first step in computing the fixed-diameter distribution was to vertically interpolate the Attachment E1 total masses on to the computational grid. This interpolation procedure was identical to that for the variable-diameter distribution. The horizontal distribution of inventory was based on the user declared distribution surface area (i.e., radius for a circular distribution) and the inventory total mass for the depth bin. The concentration within this disk was then computed according to Equation E.13.

$$C_{horz} = \frac{I_{horz}^{3D}}{A_{horz}^{3D}\, z_{horz}\, \bar{\rho}_b^{3D}{}_{horz}} \tag{E.13}$$

where:

A_{horz}^{3D} = surface area (m^2) for the grid horizon (three-dimensional domain)
$\bar{\rho}_b^{3D}{}_{horz}$ = average soil bulk density (kg/m^3) for the grid horizon (three-dimensional domain)
I_{horz}^{3D} = solute inventory (Ci or μg) for the grid horizon (three-dimensional domain)
C_{horz} = solute concentration for the grid horizon (Ci/kg soil or μg/kg soil)
z_{horz} = height of the grid horizon (m).

To determine the number of grid cells over which the inventory was distributed the three-dimensional surface area was converted to a surface area per unit width, according to Equation E.14.

$$A_{horz}^{2D} = \sqrt{\frac{4\, A_{horz}^{3D}}{\pi}} \tag{E.14}$$

where:

A_{horz}^{2D} = surface area per unit width (m^2/m) for the grid horizon (two-dimensional cross-section).

For each grid horizon, the inventory was distributed over an odd number of grid cells centered on the distribution centroid (e.g., tank centroid) with a length equal to the surface area per unit width. The solute concentrations on the two outer grid cells were adjusted honor the inventory total mass. This scheme is expressed mathematically as shown in Equation E.15.

$$\hat{C} = \frac{I_{horz}^{2D} - \sum_{i=2}^{n-1} C_{horz}\, \Delta x^i\, \Delta z^i\, \rho_b^i}{\left[\left(\Delta x^1\, \Delta z^1\, \rho_b^1\right) + \left(\Delta x^n\, \Delta z^n\, \rho_b^n\right)\right]} \tag{E.15}$$

where:

n = odd number of node indices centered around the distribution centroid
Δx =node length (m)

Δz^i = node height (m)
ρ_b^i = node bulk density (kg/m^3)
$\hat{C}$ = solute concentration assigned to the two outer-most nodes.

E.2.4.3.3 Inventory Distribution Maps. Color-scaled images of the initial inventories, expressed as aqueous concentration for the twelve combinations of solute specie and cross-section, are shown for the uniform distribution in Attachment E2, Figures E2.1 through E2.12, for the nonuniform distribution in Figures E2.13 through E2.24, and for the translated-nonuniform distribution in Figures E2.25 through E2.36, and for the alternate distribution in Figures E2.37 through E2.48. The relationship between initial inventory distribution and simulation cases is shown in Table E.10.

Table E.10. Initial Inventory Distribution Schedule

Simulation Case	Inventory Distribution	Figures*
1	Uniform	E2.1 through E2.12
2	Uniform	E2.1 through E2.12
3	Uniform	E2.1 through E2.12
4	Uniform	E2.1 through E2.12
5	Nonuniform	E2.13 through E2.24
6	Nonuniform	E2.13 through E2.24
7	Displaced nonuniform	E2.25 through E2.36
8	Uniform	E2.1 through E2.12
9	Uniform	E2.1 through E2.12
10	Uniform	E2.1 through E2.12
11	Uniform	E2.1 through E2.12
12	Alternate	E2.37 through E2.48
13	Uniform	E2.1 through E2.12

*All figures are located in Attachment E2.

Specie inventories provided in the modeling data package were expressed in soil concentration (e.g., µg/g soil, pCi/g soil). These concentrations were converted to aqueous-phase concentrations based on the soil bulk density (i.e., from particle density and porosity) and the initial saturation, according to Equation E.16.

$$C_\ell = \frac{C_s \rho_s (1 - n_T) y_\ell}{s_\ell n_D} \qquad (E.16)$$

where:

C_ℓ = aqueous-phase concentration
C_s = soil concentration
ρ_s = soil particle density
n_T = total porosity
y_ℓ = equilibrium fraction of solute in the aqueous phase
s_ℓ = aqueous-phase saturation
n_D = diffusive porosity.

Except for density-dependent Case 8 run, the nitrate solute specie was considered a passive scalar for all simulations; therefore, aqueous-phase properties were independent of its concentration and no precipitation of the solute was considered.

E.3.0 HUMAN HEALTH RISK AND DOSE ESTIMATION APPROACH

This section presents the approach used to estimate human health risk (risk) and dose associated with exposure to contaminants of concern from past leaks and releases from WMA S-SX.

Risk is used herein to refer to the following:

- Incremental lifetime cancer risk (ILCR), which can occur from exposure to carcinogenic chemicals and radionuclides
- Hazard index, which is a measure of the potential for toxic health effects from exposure to noncarcinogenic chemicals.

Dose is the measure of radioactivity potentially received in a human body.

The interim measures under consideration for WMA S-SX address mitigation of groundwater impacts. The exposure pathways for this risk assessment therefore are based on the groundwater exposure medium. The exposure scenarios used for this assessment are as follows:

- Industrial
- Residential
- Industrial worker
- Residential farmer
- Recreational shoreline user.

Risk associated with the use of groundwater from a hypothetical water supply well was estimated at several downgradient points of compliance over a 1,000-year timeframe. Groundwater contaminant concentration estimates were based on the results of the contaminant transport analysis presented in Sections E.4.0 and E.5.0.

The risk assessment for this WMA S-SX field investigation report is qualitative at this stage in the corrective action process even though substantial site-specific data have been generated. Qualitative WMA risk evaluations have been performed at the Hanford Site using historical process and characterization data (DOE-RL 1995c; DOE-RL 1996). These qualitative risk evaluations have been used to initially evaluate the applicability and relative effectiveness of interim measures (e.g., eliminate leaking water lines and replace well caps). The risk assessment presented herein also relies on historical process and characterization data but is supplemented with additional site-specific data collected under the *Resource Conservation and Recovery Act of 1976* corrective action program as described in Appendices A and B. The results of this risk assessment are used to support evaluation of potential interim measures or interim corrective measures and to determine the need for additional WMA-specific characterization data.

Procedures for the approach and assumptions necessary to calculate human health risk are described in the following:

- "The Model Toxics Control Act Cleanup Regulation" (WAC 173-340), which implements "Model Toxics Control Act" (MTCA) requirements

- *Hanford Site Risk Assessment Methodology* (DOE-RL 1995b; HSRAM), which is the risk assessment methodology that the U.S. Department of Energy (DOE), Washington State Department of Ecology (Ecology), and the U.S. Environmental Protection Agency (EPA) have agreed to use to support Hanford Site cleanup decisions.

The WAC 173-340 implementing regulations define exposure scenarios and input parameters for two types of site uses: unrestricted (MTCA Method B) and industrial (MTCA Method C). Both the Method B and C exposure scenarios include potential consumption of groundwater. The Method B exposure scenario essentially assumes residential use; the scenario has been used in risk assessments of the Hanford Site 100 Areas to represent unrestricted land use (DOE-RL 1995a). The Method C exposure scenario has not been applied for site-specific decisions at the Hanford Site.

Under MTCA, risk assessment requirements for nonradioactive contaminants stipulate that carcinogenic risks shall be less than 10^{-6} (10^{-5} for multiple contaminants) for Method B and 10^{-5} for Method C. Also, concentrations of individual noncarcinogenic contaminants that pose acute or chronic toxic effects to human health shall not exceed a hazard quotient of 1.0. The MTCA risk criteria apply only to nonradioactive contaminants. The EPA guidance indicates that action is generally warranted when the cumulative carcinogenic risk is greater than 10^{-4} or the cumulative noncarcinogenic hazard index exceeds 1.0. Carcinogenic risks below 10^{-6} or hazard indices less than 1.0 are regarded as 'points of departure' below which no action is required. DOE orders require that groundwater protection standards be consistent with federal and Washington State requirements (i.e., EPA and Ecology requirements).

E.3.1 RECEPTOR SCENARIO RATIONALE

Current land use planning assumptions are documented in *Final Hanford Comprehensive Land-Use Plan Environmental Impact Statement* (DOE 1999), which provides an evaluation of several land uses for the Hanford Site for the next 50 years. That environmental impact statement and associated "Hanford Comprehensive Land-Use Plan Environmental Impact Statement (HCP EIS), Hanford Site, Richland, Washington; Record of Decision (ROD)" (64 FR 61615) identify 'industrial-exclusive use' as the planned use for the 200 Areas Central Plateau, an area that encompasses the 200 East and 200 West Areas. Ecology is evaluating how the DOE land-use planning efforts fit within the Ecology cleanup framework. Ecology has not yet agreed to an industrial use scenario. Therefore, multiple exposure scenarios are considered in the WMA S-SX risk assessment to account for the uncertainty of long-term Hanford Site land use.

As shown in *Phase 1 RCRA Facility Investigation/Corrective Measures Study Work Plan for Single-Shell Tank Waste Management Areas* (DOE-RL 2000), DOE and Ecology have agreed to use MTCA Methods B and C in the corrective action program. MTCA Methods B and C risks are calculated based on equations and parameters specified in the MTCA protocol for establishing groundwater cleanup levels (WAC 173-340-720). Risk is calculated for the residential farmer, industrial worker, and recreational shoreline user exposure scenarios based on the HSRAM. Estimates of risk based on the three HSRAM exposure scenarios are provided in this assessment to allow for comparison to risks cited in *Tank Waste Remediation System, Hanford Site, Richland, Washington, Final Environmental Impact Statement* (DOE and

Ecology 1996; TWRS EIS) and *Retrieval Performance Evaluation Methodology for the AX Tank Farm* (DOE-RL 1999b). Risk calculations for the three HSRAM-based scenarios use groundwater pathway unit risk factors adapted without modification directly from the TWRS EIS.

E.3.1.1 Residential Exposure Scenario (MTCA Method B)

The MTCA cleanup standards are applicable only to nonradioactive constituents. Under the Method B groundwater cleanup level protocol, exposure to hazardous and carcinogenic chemicals is based solely on ingestion of drinking water (with an inhalation correction factor used for volatile chemicals). Method B exposures for noncarcinogenic health effects are based on a drinking water intake rate of 1 L/day (0.2 gal/day) and an average body weight of 16 kg (35 lb) (WAC 173-340-720(3)(a)(ii)(A)). Method B exposures for carcinogenic health effects are based on a drinking water intake rate of 2 L/day (0.5 gal/day), an average body weight of 70 kg (150 lb), an exposure duration of 30 years, and a lifetime of 75 years (WAC 173-340-720(3)(a)(ii)(B)). Oral reference doses (mg/kg-day) and oral slope factors (kg-day/mg) developed by the EPA are applied to convert the exposures to the health effect appropriate for each constituent.

Four hypothetical receptor locations identified by DOE and Ecology (DOE-RL 2000) as the points of compliance for which potential risk will be calculated are as follows:

- Downgradient WMA boundary
- Downgradient boundary of the 200 West Area
- Downgradient boundary of the 200 Area exclusion zone as defined by the Hanford Future Site Uses Working Group (FSUWG 1992)
- Downgradient at the Columbia River shoreline.

The Method B risk is calculated at all four points of compliance. Note that for the WMA S-SX boundary, risk is calculated at three separate locations corresponding to the three cross-sections (S-CC', SX-DD', SX-FF') considered in the contaminant transport analysis.

E.3.1.2 Industrial Exposure Scenario (MTCA Method C)

As in the MTCA Method B residential exposure scenario, the MTCA Method C industrial exposure scenario is applicable only to nonradioactive constituents. Under the Method C groundwater cleanup level protocol, exposure to hazardous and carcinogenic chemicals is based solely on ingestion of drinking water (with an inhalation correction factor used for volatile chemicals). Method C exposures for noncarcinogenic health effects are based on a drinking water intake rate of 2 L/day (0.5 gal/day) and an average body weight of 70 kg (150 lb) (WAC 173-340-720(4)(b)(ii)(A)). Method C exposures for carcinogenic health effects are based on a drinking water intake rate of 2 L/day (0.5 gal/day), an average body weight of 70 kg (150 lb), an exposure duration of 30 years, and a lifetime of 75 years (WAC 173-340-720(4)(b)(ii)(B)). Oral reference doses (mg/kg-day) and oral slope factors (kg-day/mg) developed by the EPA are applied to convert the exposures to the health effect appropriate for each constituent.

Method C risk is calculated for the same four points of compliance as defined for the Method B calculations in Section E.3.1.1.

E.3.1.3 Industrial Worker Scenario

An industrial worker scenario consistent with the scenario described in HSRAM is used to represent potential exposure to workers in a commercial or industrial setting. The receptors are adult employees assumed to work at a location for 20 years. A body weight of 70 kg (150 lb) and a lifetime of 70 years are assumed. The scenario involves mainly indoor activities, although outdoor activities (e.g., soil contact) also are included. The groundwater exposure pathways for this scenario include drinking water ingestion (1 L/day [0.2 gal/day]), dermal absorption during showering, shower-water ingestion, and inhalation. These exposures would not be continuous because the worker would go home at the end of each workday (i.e., after 8 hours). The scenario is intended to represent nonremediation workers assumed to wear no protective clothing.

Industrial worker risk is evaluated using a unit risk factor approach consistent with that used for the TWRS EIS and DOE-RL (1999b) analyses. This approach involves calculating risk as the product of the groundwater concentration and the unit risk factor. The basic expression for risk using an unit risk factor approach is:

$$R_{x,y,t} = \sum C^{i}_{x,y,t} \cdot URF^{i}_{S} \qquad \text{(E.17)}$$

Where:

$R_{x,y,t}$ = risk at point of compliance x,y,t

$C^{i}_{x,y,t}$ = groundwater concentration at point of compliance x,y,t for contaminant i

URF^{i}_{S} = groundwater unit risk factor for contaminant i and receptor scenario S

x,y = horizontal location coordinates

t = time.

The summation in Equation E.17 represents addition of the contributions from all constituents. The unit risk factors used for the three HSRAM-based exposure scenarios are shown in Table E.11. These unit risk factors are for the groundwater pathway and are taken from the risk analysis presented in the TWRS EIS. These unit risk factors were also used in DOE-RL (1999).

Industrial worker risk is calculated for the same four points of compliance as defined in Section E.3.1.1.

Table E.11. Unit Risk Factors for the Industrial Worker, Residential Farmer, and Recreational Shoreline User Scenarios

Contaminant of Concern	Units	Industrial Worker[a]	Residential Farmer[b]	Recreational Shoreline User[c]
C-14	ILCR per Ci/mL	5.23E+06	6.06E+08	8.70E+05
Se-79	ILCR per Ci/mL	3.22E+07	2.87E+08	5.36E+06
Tc-99	ILCR per Ci/mL	7.11E+06	2.61E+08	1.18E+06
I-129	ILCR per Ci/mL	9.33E+08	1.29E+10	1.55E+08
Cr	HQ per g/mL	3.31E+06	1.14E+07	3.47E+05
F	HQ per g/mL	1.65E+05	1.61E+06	2.27E+04
Hg	HQ per g/mL	3.85E+07	8.36E+08	4.85E+06
NO_3	HQ per g/mL	6.20E+03	7.59E+06	8.52E+02
NO_2	HQ per g/mL	9.92E+03	3.73E+04	1.36E+03
EDTA	HQ per g/mL	7.61E+06	1.47E+09	1.05E+06

[a] Source = TWRS EIS, Appendix D, Tables D.2.1.21 and D.2.1.23 (groundwater pathway).
[b] Source = TWRS EIS, Appendix D, Tables D.2.1.18 and D.2.1.20 (groundwater pathway).
[c] Source = TWRS EIS, Appendix D, Tables D.2.1.24 and D.2.1.26 (groundwater pathway).

ILCR = incremental lifetime cancer risk.
HQ = hazard quotient.

E.3.1.4 Residential Farmer Scenario

A residential farmer scenario is used to represent exposures associated with the use of the land for residential and agricultural purposes. This scenario is a slight modification to the residential scenario described in HSRAM; it includes all of the exposure pathways for the residential scenario plus most of the food ingestion pathways described in the HSRAM agriculture scenario. The residential farmer scenario includes using groundwater for drinking water (ingestion rate of 2 L/day [0.5 gal/day]) and other domestic uses as well as for irrigation to produce and consume animals, vegetables, and fruit products. The exposures are assumed to be continuous and include occasional shoreline related recreational activities, which includes contact with surface water sediments. A composite adult is used as the receptor for some of the exposure pathways. The composite adult is evaluated using child parameters for 6 years and adult parameters for 24 years, with total exposure duration of 30 years. Body weights of 16 kg (35 lb) for a child and 70 kg (150 lb) for an adult and a lifetime of 70 years are assumed.

Residential farmer risk is evaluated using a unit risk factor approach as discussed for the industrial worker scenario in Section E.3.1.3. The unit risk factors used are shown in Table E.11.

Residential farmer risks are calculated for the same four points of compliance as defined in Section E.3.1.1.

E.3.1.5 Recreational Shoreline User Scenario

A recreational shoreline user scenario consistent with the scenario described in the HSRAM is used to represent exposure to contamination in groundwater seeps along the Columbia River shoreline from recreational swimming, boating, and other shoreline activities. The scenario involves outdoor activities and occurs only in an area within 400 m (0.25 mi) of the river shoreline. These exposures would not be continuous but would occur for 14 days a year for 30 years. Exposure to both adults and children are taken into account using the same composite adult as described in the residential farmer scenario in Section E.3.1.4.

Recreational shoreline user risk is evaluated using a unit risk factor approach as described in the industrial worker scenario in Section E.3.1.3. The unit risk factors used are shown in Table E.11. Recreational shoreline user risks are calculated only at the downgradient Columbia River shoreline point of compliance that is defined in Section E.3.1.1.

The recreational land user scenario is not included in the WMA S-SX risk assessment because this receptor does not have access to the groundwater pathways.

E.3.2 TANK WASTE CONSTITUENTS OF POTENTIAL CONCERN

Determination of the constituents of potential concern (CoPCs) to be used in the WMA S-SX risk assessment starts with the estimated inventory released from the tank farm system to the environment. That estimated inventory is provided in *Inventory Estimates for SST Leaks in S and SX Tank Farms* (Jones et al. 2000). The CoPCs listed in the Jones et al. 2000 estimate include the analytes listed in the model cited in *Hanford Defined Wastes: Chemical and Radionuclide Compositions* (Agnew 1997). The following sections provide the rationale used to exclude some of these CoPCs to calculate human health risk and dose in the WMA S-SX risk assessment. Because not all of the constituents associated with the released tank waste will migrate to the groundwater, the contaminants of concern in a groundwater pathway must be selected. The rationale for making this constituents selection is provided in the following sections.

E.3.2.1 Rationale for Excluding Contaminants of Potential Concern

Following are the criteria used to exclude CoPCs from consideration in the WMA S-SX risk assessment.

- Constituents with distribution coefficients (K_d) equal or greater than 0.6. *Composite Analysis for Low-Level Waste disposal in the 200 Area Plateau of the Hanford Site* (Kincaid et al. 1998) provides reference to distribution coefficient selection used in previous studies and for past tank leaks. *Hanford Immobilized Low-Activity Tank Waste Disposal Performance Assessment* (DOE-RL 1999a), along with Kincaid et al. (1998), provides rationale for selection of CoPCs for risk calculations. Numerical modeling results provided in the TWRS EIS indicate that constituents with distribution coefficients equal to or greater than one take over 1,000 years to reach the vadose zone/saturated zone interface. Numerical modeling of past tank leaks for concurrent S tank farm retrieval performance evaluation (Thompson 2001) and for DOE-RL (1999b) indicate that within 1,000 years constituents with distribution coefficients equal to or greater than 0.6 would not reach the underlying aquifer or would reach the underlying aquifer at very low concentrations (less than 3.0×10^{-2} pCi/L) that would not contribute to significant human health risks (less than 4.0×10^{-8} ILCR for the residential farmer scenario) using base case recharge estimates as shown in Table 3.1.

CoPCs eliminated because of the distribution coefficient criterion are aluminum, iron, bismuth, lantharium, zirconium, lead, nickel, strontium, manganese, calcium, plutonium (total), nickel-59, nickel-63, cobalt-60, strontium-90, yttrium-90, zirconium-93, niobium-93m, cadmium-113m, antimony-125, tin-126, cesium-134, cesium-137, barium-137, samarium-151, europium-152, europium-154, and europium-155, radium-226, radium-228, plutonium series, americium series, curium series, uranium series, and thorium-232.

- Low-activity radionuclides present in low concentrations and with short half-lives if they have decayed for at least five half-lives. A decay time of 5 half-lives is sufficient for decay of 96.9% of the radionuclide activity and results in a reduced level of potential risk (EPA 1995). Based on numerical modeling results provided in the TWRS EIS, constituents with distribution coefficients of 0 take 150 years to reach the vadose zone/saturated zone interface.

  CoPCs eliminated because of the half-life criterion are ruthenium-106 and tritium.

- Constituents without documented human health risk or toxicity factors. The basis for these factors is documented in the *Integrated Risk Information System* (EPA 2000a) or the *User's Guide: Radionuclide Carcinogenicity* (EPA 2000b) databases. A constituent lacking a toxicity reference dose or a carcinogenic slope factor is eliminated.

  CoPCs eliminated because of the health effects criterion are carbonate, chloride, calcium, hydroxide, potassium, phosphate, sulfate, silica, and sodium.

Although several organic chemicals are listed in the Agnew (1997) model, only EDTA (ethylenediaminetetraacetic acid) was carried forward because it is the only constituent that has a reference dose. All others were not listed in the Integrated Risk Information System.

In addition, field data was used for revising the risk-producing contaminants of potential concern (Section 3.3.5) that met the criteria in Section 4.3.2.1, but were determined to have inventories associated with below background levels or very small inventories in the vadose zone. The field data assisted in eliminating the uranium series isotopes (see Section 3.3.5) that appears to be overestimated in Jones et al. (2000).

E.3.2.2 Contaminants of Potential Concern for Risk Assessment

The CoPCs to be used in the WMA S-SX risk assessment after applying the exclusion criteria described in Section E.3.2.1 are:

- **Chemicals**: chromium, fluoride, mercury, nitrate, nitrite, and EDTA
- **Radionuclides**: carbon-14; selenium-79; technetium-99; and iodine-129.

E.3.3 ESTIMATING TOTAL INCREMENTAL LIFETIME CANCER RISK AND HAZARD INDEX

The total ILCR for a particular receptor scenario at a particular point in time and space is expressed as the sum of the ILCR calculated for the individual carcinogenic chemical and radionuclide CoPCs. Note that because none of the chemical CoPCs identified in Section E.3.2.2 is classified as carcinogenic, ILCR values for this assessment are based only on radionuclide exposures. Although hexavalent chromium is classified as carcinogenic by inhalation, carcinogenic impacts from hexavalent chromium would apply only for airborne releases from a facility, or for suspension of surface contamination. Because groundwater is the only exposure medium considered in this assessment, neither of these exposure routes applies and hexavalent chromium is treated as an ingestion toxicant. As for the total ILCR, the total hazard index is expressed as the sum of the hazard quotients calculated for the individual noncarcinogenic chemical CoPCs. Total ILCR and hazard index values are calculated for each receptor scenario and point of compliance for the 1,000-year period of analysis used in the contaminant transport simulations.

Risks for CoPCs included in the contaminant transport analysis (i.e., technetium-99, nitrate, and chromium) are based on the modeled groundwater concentrations. Risks for CoPCs not included in the contaminant transport analysis are based on scaled groundwater concentrations. Scaling is performed by multiplying the non-modeled CoPC source inventories (as reported in Jones et al. 2000) by the ratio of the modeled groundwater concentration to source inventory for one of the modeled CoPCs. The basis for the scaling calculations is shown in Table E.12.

Table E.12. Basis for Scaled Groundwater Concentrations

Simulated CoPC	Non-simulated CoPC Ratioed from Simulated CoPC
Tc-99	C-14, Se-79, I-129
Cr	None
NO_3	NO_2, Hg, F, EDTA

CoPC = constituent of potential concern.

E.3.4 DOSE METHODOLOGY

Radionuclide doses are calculated as the product of the groundwater concentration and a unit dose factor. The unit dose factors used are groundwater pathway unit dose factors provided in Kincaid et al. (1998). Unit dose factors are shown in Table E.13. Dose calculations are performed only for the industrial worker exposure scenario. Exposure pathways and parameters associated with this scenario are described in Section E.3.1.3.

Table E.13. Industrial Worker Scenario Groundwater Unit Dose Factors

Constituent	Unit	Unit Dose Factor
C-14	(mrem/yr)/(pCi/L)	5.22E-04
Se-79	(mrem/yr)/(pCi/L)	2.17E-03
Tc-99	(mrem/yr)/(pCi/L)	3.65E-04
I-129	(mrem/yr)/(pCi/L)	6.90E-02

Source = Kincaid et al. (1998).

Industrial worker dose is calculated at the four points of compliance as defined in Section E.3.1.1.

E.4.0 VADOSE ZONE MODELING RESULTS

All simulations reported herein were performed using the STOMP simulator (White and Oostrom 2000a, 2000b). Detailed discussion on the numerical implementation for STOMP and simulation results are presented in *FY00 Initial Assessments for S-SX Field Investigation Report (FIR): Simulations of Contaminant Migration with Surface Barriers* (White et al. 2001). Results presented in the following sections are essentially based on White et al. (2001).

In this section, reporting of modeling results are focused on key flow and transport behavior, mass balance errors, and BTCs at the first compliance point (i.e., WMA S-SX boundary) for the 13 cases for two-dimensional simulations (Section E.2.1). The simulated peak aqueous concentration, time to peak concentration, and the maximum aqueous initial concentration values for the two-dimensional simulations are summarized. The maximum aqueous initial concentration values (based on the inventory estimates in Section E.2.4.3) are presented for comparison with the simulated peak aqueous concentration.

Note that the simulated BTCs and the plume maps for various cases are presented in Attachments E3 and E4, respectively, whereas the results of the recharge sensitivity runs are presented in Attachment E5. Translation of these results to the down-gradient compliance points and streamtube modeling results are described in Section E.5.0. Note that, as a check on the two-dimensional analysis, results of a three-dimensional simulation are presented in this section. However, the risk calculations are all based on two-dimensional simulation results. Also, note that the three cross-sections are labeled in two ways. For example, the row containing tanks SX-107, SX-108, and SX-109 is often labeled as cross-section SX-DD'. Similarly, cross-section SX-FF' refers to the row containing tanks SX-113, SX-114, and SX-115, and cross-section S-CC' refers to the row containing tanks S-104, S-105, and S-106.

E.4.1 BASE CASE, NO ACTION ALTERNATIVE (CASE 1)

The base case suite of simulations, Case 1, investigated solute transport through three cross-sections in WMA S-SX considering natural surface infiltration, with no water-line leaks and no interim surface barriers but with a closure barrier by the year 2040. These simulations were initialized using a steady-flow solution defined by a surface recharge rate of 100 mm/yr and a hydraulic gradient in the unconfined aquifer. Inventories of the four contaminant species were initialized using the uniform distribution pattern. Plot-file output for these simulations was generated at the years 2000, 2010, 2020, 2030, 2040, 2050, 2060, 2070, 2080, 2090, 2100, 2540, and 3000 and include values for the aqueous saturation (θ/θ_s where θ = aqueous moisture content and θ_s = saturated moisture content), aqueous pressure, aqueous moisture content, and concentrations for the four solute species. The moisture content field for these simulations remains unchanged from the initial steady-flow field until the year 2040, when the closure barrier becomes effective.

Solute BTCs at the first compliance point for the three cross-sections (S-CC', SX-DD', and SX-FF') are shown in Attachment E3, Figures E3.1 through E3.9, for the three solute species (technetium-99, chromium, and nitrate), respectively. Aqueous fluxes at the water table for the three cross-sections (S-CC', SX-DD', and SX-FF') are shown in Figures E3.10 through E3.12, respectively. No cesium-137 was transported to the first compliance point for any of the simulated cross-sections. This is true for Case 1 as well as for all the other simulated cases.

Breakthrough times and aqueous concentrations at the first compliance point are shown in Table E.14, along with the maximum initial aqueous concentrations. Area-weighted averages (across the three cross-sections) of the solute BTCs were generated for the three solute species and are shown in Attachment E3, Figures E3.13 through E3.15 for technetium-99, chromium, and nitrate, respectively. Comparison of the peak inventory and peak arrival concentrations generally shows an order of magnitude reduction in concentration as the solute migrates through the vadose zone and across the unconfined aquifer within the WMA. Arrival times show a weak dependence on the cross-section geology.

Table E.14. Peak Concentrations and Arrival Times at the First Compliance Point (i.e., WMA S-SX Boundary) for Case 1

Parameter	S-CC'	SX-DD'	SX-FF'
	Tc-99		
Arrival Time	2032.9 yr	2050.3 yr	2032.6 yr
Peak Conc.	1.379×10^5 pCi/L	1.233×10^6 pCi/L	2.869×10^5 pCi/L
Max. Initial Conc.*	4.491×10^6 pCi/L	9.480×10^7 pCi/L	5.074×10^6 pCi/L
	Cr		
Arrival Time	2050.3 yr	2053.0 yr	2051.7 yr
Peak Conc.	2.818×10^3 µg/L	1.032×10^5 µg/L	4.538×10^3 µg/L
Max. Initial Conc.	6.456×10^4 µg/L	1.244×10^7 µg/L	1.089×10^5 µg/L
	NO_3		
Arrival Time	2032.9 yr	2050.3 yr	2032.9 yr
Peak Conc.	8.461×10^5 µg/L	3.349×10^6 µg/L	1.013×10^6 µg/L
Max. Initial Conc.	3.254×10^7 µg/L	4.448×10^8 µg/L	3.616×10^7 µg/L

*Maximum initial concentration is based on inventory data (Section E.2.4.3) and listed for comparison with the simulated peak concentration at the compliance boundary.

Color-scaled images of solute concentrations for the three mobile species (technetium-99, chromium, and nitrate) and three cross-sections (S-CC', SX-DD', and SX-FF') are shown as a series of time sequences in Attachment E4, Figures E4.1 through E4.63. The aqueous concentrations of the solutes are color valued using exponential scaling from the drinking water standard for the specie to the maximum initial inventory concentration, where the standards are 900 pCi/L for technetium-99, 50 µg/L for chromium, and 45,000 µg/L for nitrate. Note the differences in time sequences for cross-section SX-DD' (Figures E4.1 through E4.21); the initial inventory was spread across the region between tanks SX-108 and SX-109 and centered beneath tank SX-107. Although differences are noticeable in the plume located between tanks SX-109 and SX-108 with the plume beneath tank SX-107, the overall rate of migration toward the groundwater is nearly identical. The initial inventory beneath tank SX-107 shows a slight delay in arrival times. The initial inventory distribution for chromium was located beneath the tanks.

The time sequence for chromium, depicted in Figures E4.8 through E4.14, shows an initial upward movement of the solute toward the tank bottoms. This migration occurred, in part, by diffusion, but was additionally aided by the divergent flow of recharge water in the region between tanks at the tank bottom depth. Again, for all cross-sections and solutes, the migration is principally toward the groundwater. Small variations in solute migration direction are noted in cross-section SX-DD' from the sloped gravelly sand strata, but none significantly alter the breakthrough concentrations at the WMA S-SX boundary, located on the lower right-hand corner of the domain.

The aqueous saturation field is dependent on the surface recharge, impermeable structures (e.g., single-shell tanks), various strata and their hydrologic parameters. The steady-flow saturation field for cross-section SX-DD' (tanks SX-107, SX-108, and SX-109) with 100 mm/yr of meteoric recharge is shown in Figure E.8. This field shows the impact of the tanks on the aqueous saturation, where higher than ambient saturations occur above and between the tanks and lower than ambient saturations occur just below the tanks. By 2040 a closure barrier was assumed to be active, which lowered the meteoric recharge from 100 mm/yr to 0.1 mm/yr.

Figure E.8. Case 1 Aqueous-Phase Saturation at 2000 (steady-flow conditions) for Cross-Section SX-DD'

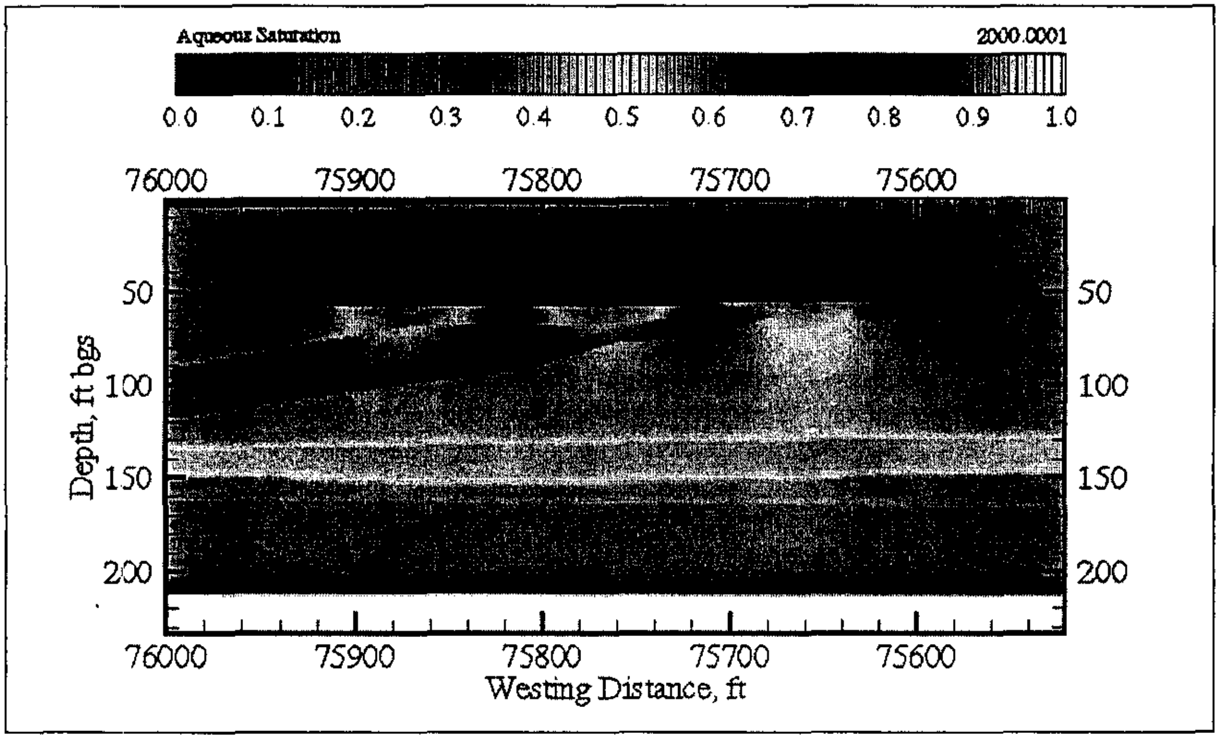

The aqueous saturation field dried in response to the change in surface recharge, as shown in Figure E.9 for the year 2050. The impact of the impermeable tanks on the aqueous saturation was reduced at lower surface recharge, as shown by comparing Figures E.8 and E.9. The closure barrier was assumed to remain effective for 500 years, at which point it degrades, allowing meteoric recharge to increase to 3.5 mm/yr. In the 500-year period between 2040 and 2540, the aqueous saturation field continued to slowly dry reaching a minimum average level at 2540, as shown in Figure E.10. In the 460-year period between 2540 and 3000, the aqueous saturation field wetted, in response to the increased meteoric recharge of 3.5 mm/yr for the degraded surface barrier. The aqueous saturation at year 3000 is shown in Figure E.11. The closure barrier was assumed to decrease the meteoric recharge from 100 mm/yr to 0.1 mm/yr for 500 years and then degrade to 3.5 mm/yr for the next 460 years. These variations in surface recharge had the greatest impact on aqueous saturation in the region between tanks within the backfill material and the soils immediately below the bottom level of the tanks.

The Plio-Pleistocene unit soil showed the least change in aqueous saturation with change in the surface recharge. The regions directly beneath the tanks additionally showed lower variability in aqueous saturation.

Figure E.9. Case 1 Aqueous-Phase Saturation at 2050 (0.1 mm/yr) for Cross-Section SX-DD'

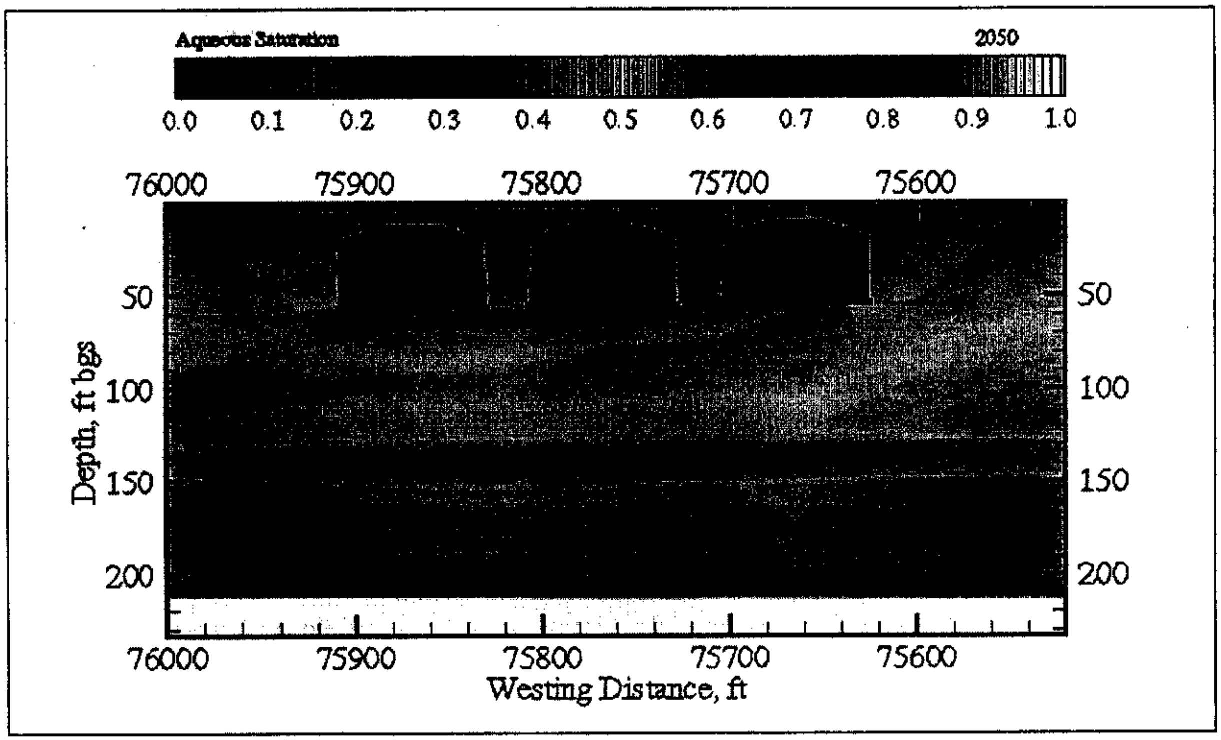

Figure E.10. Case 1 Aqueous-Phase Saturation at 2540 (0.1 mm/yr) for Cross-Section SX-DD'

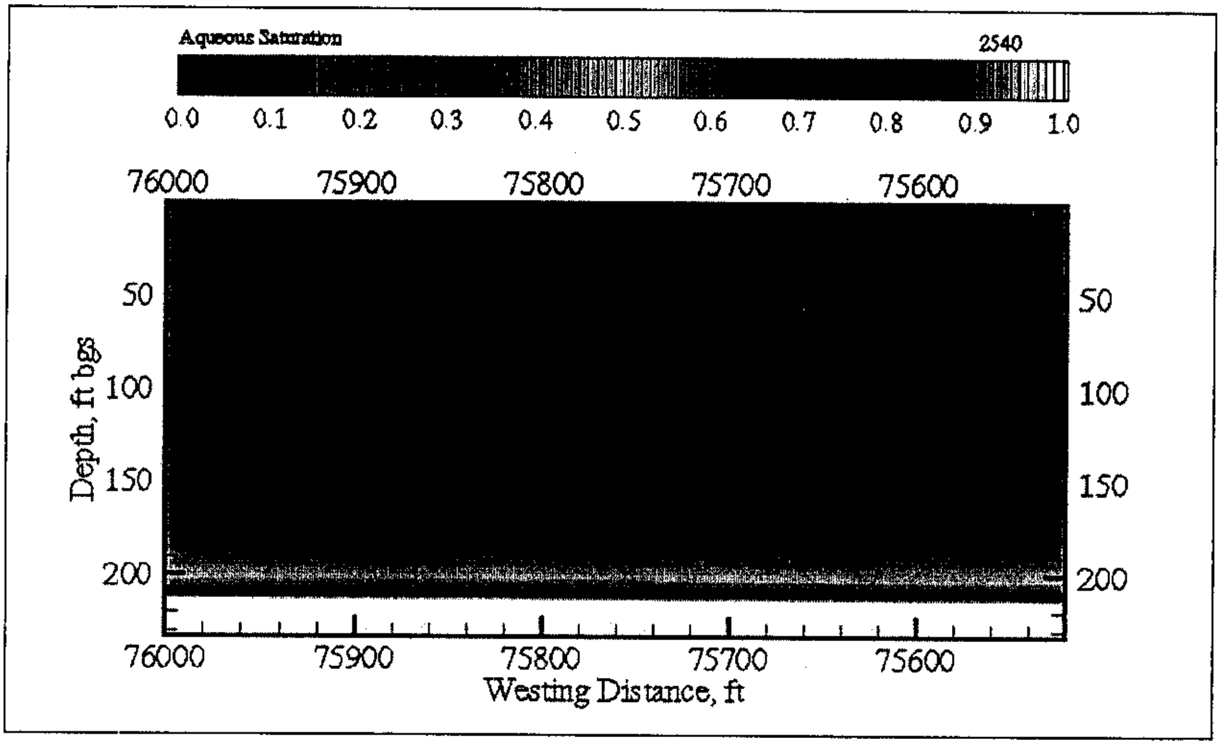

Figure E.11. Case 1 Aqueous-Phase Saturation at 3000 (3.5 mm/yr) for Cross-Section SX-DD'

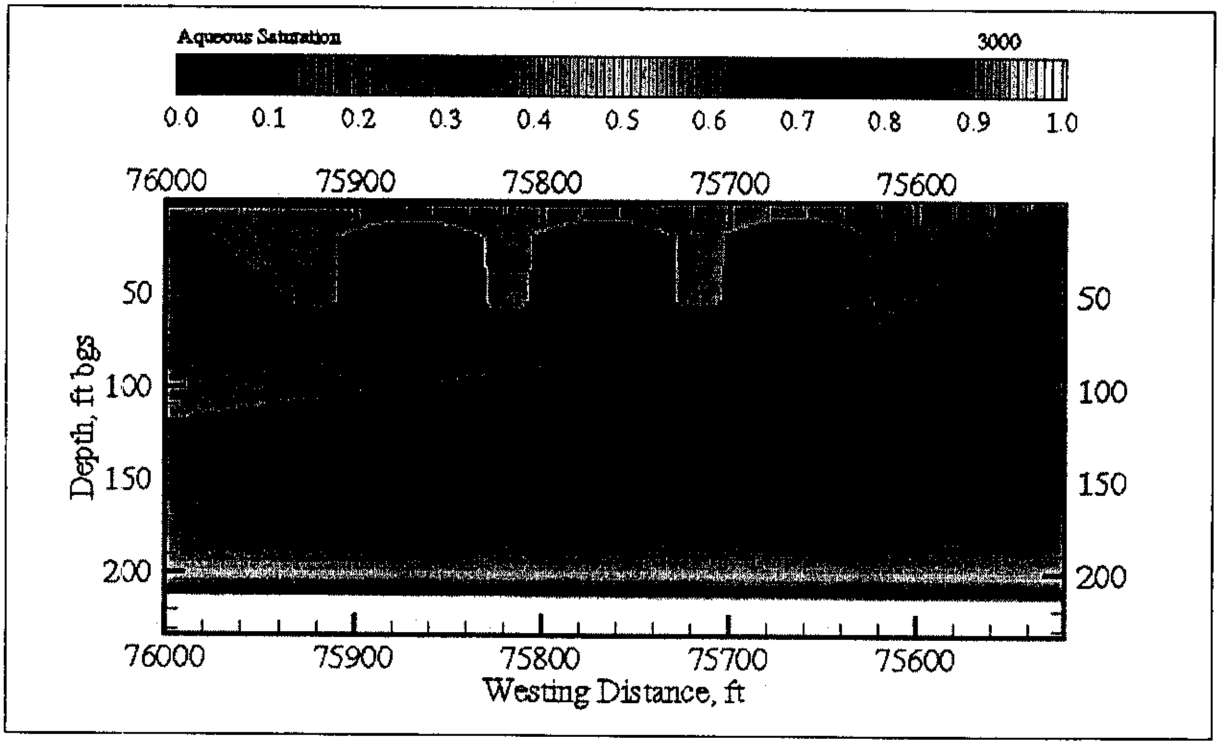

The water table level showed little variation with the rate of surface recharge; therefore, the mean aqueous saturation in the cross-section gives a general indication of the effect of surface recharge on the hydrologic environment. Mean aqueous phase saturations at selected times during the simulation period are shown in Table E.15 for the three cross-sections (S-CC', SX-DD', and SX-FF'). As expected, the mean saturations follow the trends in surface recharge (i.e., higher mean saturations at higher surface recharge), but the rate of change in mean saturation is slow, as is evidenced by the gradual decrease in saturation during transition from 100 to 0.1 mm/yr in 2040 until the next rate change in 2540. In contrast, the aqueous flow field changes nearly immediately to variations in the surface recharge. The saturation values in Table E.15 show little variation between cross-sections.

Table E.15. Case 1 Mean Aqueous-Phase Saturation

Year	Meteoric Recharge	S-CC'	SX-DD'	SX-FF'
2000	100 mm/yr	0.5481	0.5471	0.5396
2040	100 to 0.1 mm/yr	0.5481	0.5471	0.5396
2050	0.1 mm/yr	0.4987	0.4988	0.4908
2060	0.1 mm/yr	0.4691	0.4962	0.4618
2070	0.1 mm/yr	0.4513	0.4516	0.4445
2080	0.1 mm/yr	0.4393	0.4396	0.4327
2090	0.1 mm/yr	0.4304	0.4307	0.4240
2100	0.1 mm/yr	0.4234	0.4237	0.4172
2540	0.1 to 3.5 mm/yr	0.3625	0.3623	0.3576
3000	3.5 mm/yr	0.4115	0.4106	0.4060

E.4.2 BARRIER ALTERNATIVE AND NO WATER-LINE LEAKS CASE (CASE 2)

The barrier alternative and no water-line leaks suite of simulations, Case 2, investigated solute transport through three cross-sections in WMA S-SX considering natural surface infiltration, with no water-line leaks and closure barrier by the year 2040. This suite of simulations differs from Case 1 simulations in that an interim surface barrier was implemented between the years 2010 and 2040. These simulations were initialized using a steady-flow solution defined by the surface recharge rate of 100 mm/yr and a hydraulic gradient in the unconfined aquifer. Inventories of the four contaminant species were initialized using the uniform distribution pattern. Plot-file output for these simulations was generated at the years 2000, 2010, 2040, 2540, and 3000 and include values for the aqueous saturation, aqueous pressure, aqueous moisture content, and concentrations for the four solute species. The moisture content field for these simulations remains unchanged from the initial steady-flow.

Solute BTCs at the first compliance point for the three cross-sections (S-CC', SX-DD', and SX-FF') are shown in Attachment E3, Figures E3.16 through E3.24 for the three solute species (technetium-99, chromium, and nitrate), respectively. Aqueous flux at the water table for the three cross-sections (S-CC', SX-DD', and SX-FF') are shown in Figures E3.25 through E3.27, respectively. Breakthrough times and aqueous concentrations at the first compliance point are shown in Table E.16, along with the maximum initial aqueous concentrations. Area-weighted averages (across the three cross-sections) of the solute BTCs were generated for the three solute species and are shown in Attachment E3, Figures E3.28 through E3.30 for technetium-99, chromium, and nitrate, respectively.

Table E.16. Peak Concentrations and Arrival Times at the First Compliance Point (i.e., WMA S-SX Boundary) for Case 2

Parameter	S-CC'	SX-DD'	SX-FF'
Tc-99			
Arrival Time	2028.3 yr	2059.7 yr	2028.3 yr
Peak Conc.	9.207×10^4 pCi/L	1.839×10^5 pCi/L	2.020×10^5 pCi/L
Max. Initial Conc.*	4.491×10^6 pCi/L	9.480×10^7 pCi/L	5.074×10^6 pCi/L
Cr			
Arrival Time	2053.3 yr	2072.3 yr	2049.3 yr
Peak Conc.	5.169×10^2 µg/L	9.623×10^3 µg/L	8.621×10^2 µg/L
Max. Initial Conc.	6.456×10^4 µg/L	1.244×10^7 µg/L	1.089×10^5 µg/L
NO_3			
Arrival Time	2028.0 yr	2052.0 yr	2027.7 yr
Peak Conc.	5.739×10^5 µg/L	5.466×10^5 µg/L	6.845×10^5 µg/L
Max. Initial Conc.	3.254×10^7 µg/L	4.448×10^8 µg/L	3.616×10^7 µg/L

*Maximum initial concentration is based on inventory data (Section E.2.4.3) and listed for comparison with the simulated peak concentration at the compliance boundary.

Results indicate that the interim surface barrier reduces solute concentrations at the compliance points but has negligible impact on the peak concentration arrival times at the first compliance point. The impact of the interim surface barrier on lower peak concentrations is most effected by the initial inventory distribution. Inventory distributions having concentrations of solute mass nearer the water table were less impacted by the interim barrier compared against the inventory mass located higher in the vadose zone. For example, the technetium-99 inventory for cross-section S-CC' is generally deeper than that for chromium, and the interim barrier reduced its peak concentration by 33%; whereas the reduction in peak concentration for chromium was 82%. Concentrations at the first compliance point at year 3000 were always higher for the interim barrier simulation compared against the Case 1 simulation, which indicates that a major impact of the interim barrier is a smoothing of the breakthrough concentrations at the compliance points.

E.4.3 NO BARRIER AND 25,000 GALLON WATER-LINE LEAK CASE (CASE 3)

The no barrier and 25,000 gallon water-line leak suite of simulations, Case 3, investigated solute transport through one cross-section in the S and SX tank farms considering natural surface infiltration and a closure barrier by the year 2040. This suite of simulations differs from the

Case 1 simulations in that a water-line leak occurs for tank SX-115 in cross-section SX-FF'. The water-line leak was modeled as a point source of water (25,000 gal over a 5-day period) spread over a 15 ft radius between tanks SX-114 and SX-115. The 15 ft radius leak area was translated to the two-dimensional simulation by using a computational grid width of 1 ft and assuming that the center of the circular leak area was situated on the center line between tanks. This approach results in a two-dimensional water-line leak of 1,061 gal over a 5-day period. These simulations were initialized using a steady-flow solution defined by the surface recharge rate of 100 mm/yr and a hydraulic gradient in the unconfined aquifer. Inventories of the four contaminant species were initialized using the uniform distribution pattern. Plot-file output for these simulations was generated at the years 2000, 2000.0137, 2000.0274, 2000.0685, 2000.137, 2000.5, 2001, 2040, 2540, and 3000 and include values for the aqueous saturation, aqueous pressure, aqueous moisture content, and concentrations for the four solute species.

The flow environment following the leak event is shown in a series of color-scaled images of aqueous saturation at 5, 10, 25, 50, 183, and 365 days after the leak in Figures E.12 through E.17, respectively. After 5 days (Figure E.12), the 25,000 gal leak has completely saturated the backfill material between tanks SX-114 and SX-115, with a portion of the saturated zone extending above the tank dome. After 10 days, the leak-water has descended into the undisturbed soils beneath the tanks (Figure E.13), with the peak front sitting above the coarser grained gravelly-sand strata. At 25 and 50 days (Figures E.14 and E.15), the leak has passed through the gravelly-sand strata, continued to migrate downward and diffuse laterally, but showed little migration down the sloped coarser-grained strata. Between 50 days and 1 year, the downward migration of the leak-water plume has slowed (Figures E.16 and E.17), and the aqueous saturation between tanks SX-114 and SX-115 has returned to within a few percent of the steady-flow conditions.

Solute BTCs at the first compliance point for cross-section SX-FF' are shown in Attachment E3, Figures E3.37 through E3.39, for the three solute species (technetium-99, chromium, and nitrate), respectively. Aqueous flux at the water table for cross-section SX-FF' is shown in Figure E3.42. Times and aqueous concentrations for the BTC peaks at the first compliance boundary are shown in Table E.17. Area-weighted averages of the solute BTCs were generated for the three solute species, as shown in Attachment E3, Figures E3.43 through E3.45 for technetium-99, chromium, and nitrate, respectively. These results indicate that although the water-line leak was sufficient to completely saturate the soil between the tanks, it had negligible impact on solute concentration and arrival times at the first compliance point. The rapid dispersion of the saturated water plume beneath the tanks and the homogenizing influence of the Plio-Pleistocene unit were the primary factors influencing the water-line leak.

Figure E.12. Case 3 Aqueous-Phase Saturation at 2000 plus 5 days for Cross-Section SX-FF'

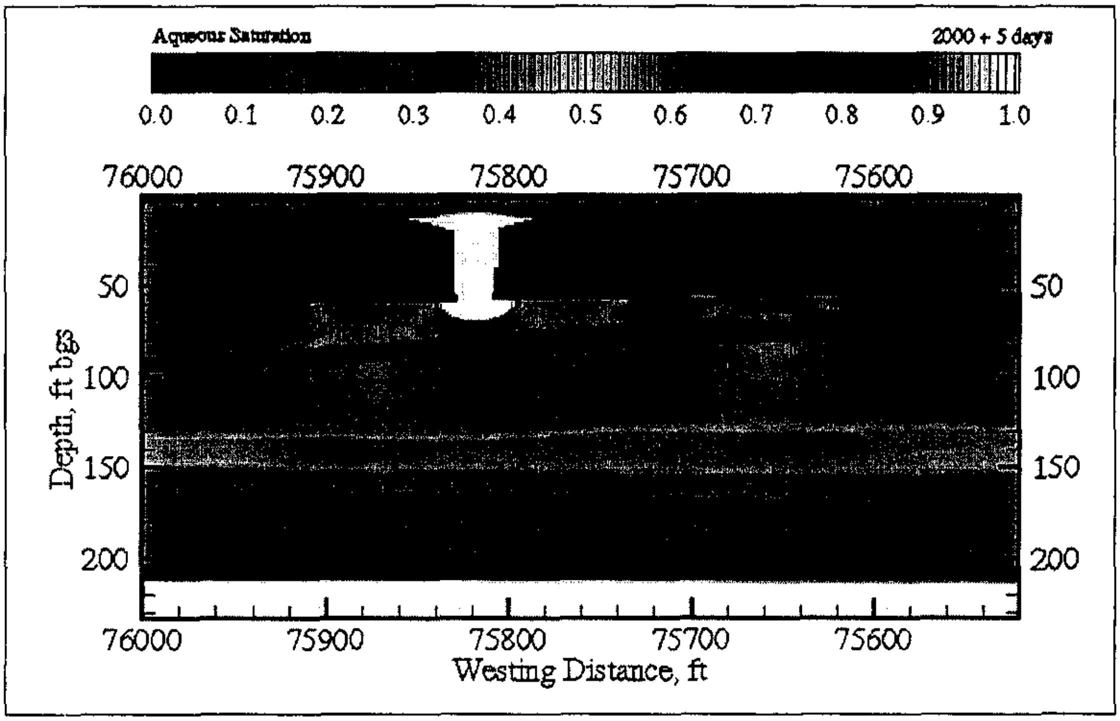

Figure E.13. Case 3 Aqueous-Phase Saturation at 2000 plus 10 days for Cross-Section SX-FF'

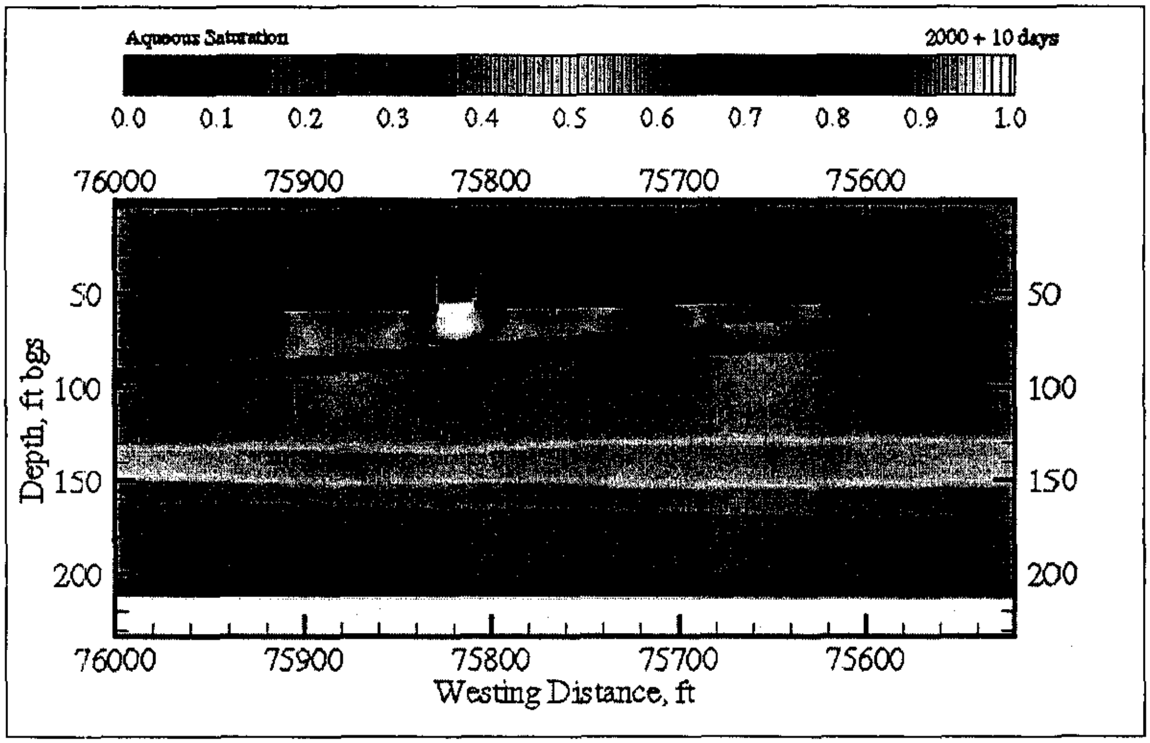

Figure E.14. Case 3 Aqueous-Phase Saturation at 2000 plus 25 days for Cross-Section SX-FF'

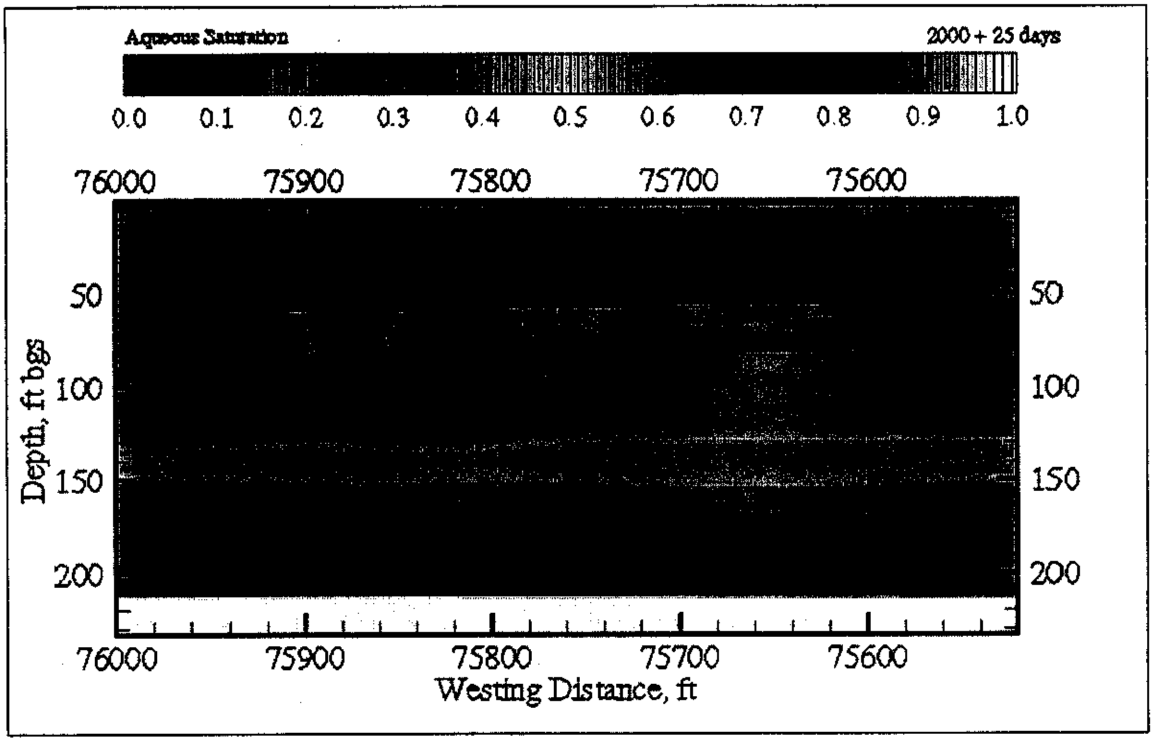

Figure E.15. Case 3 Aqueous-Phase Saturation at 2000 plus 50 days for Cross-Section SX-FF'

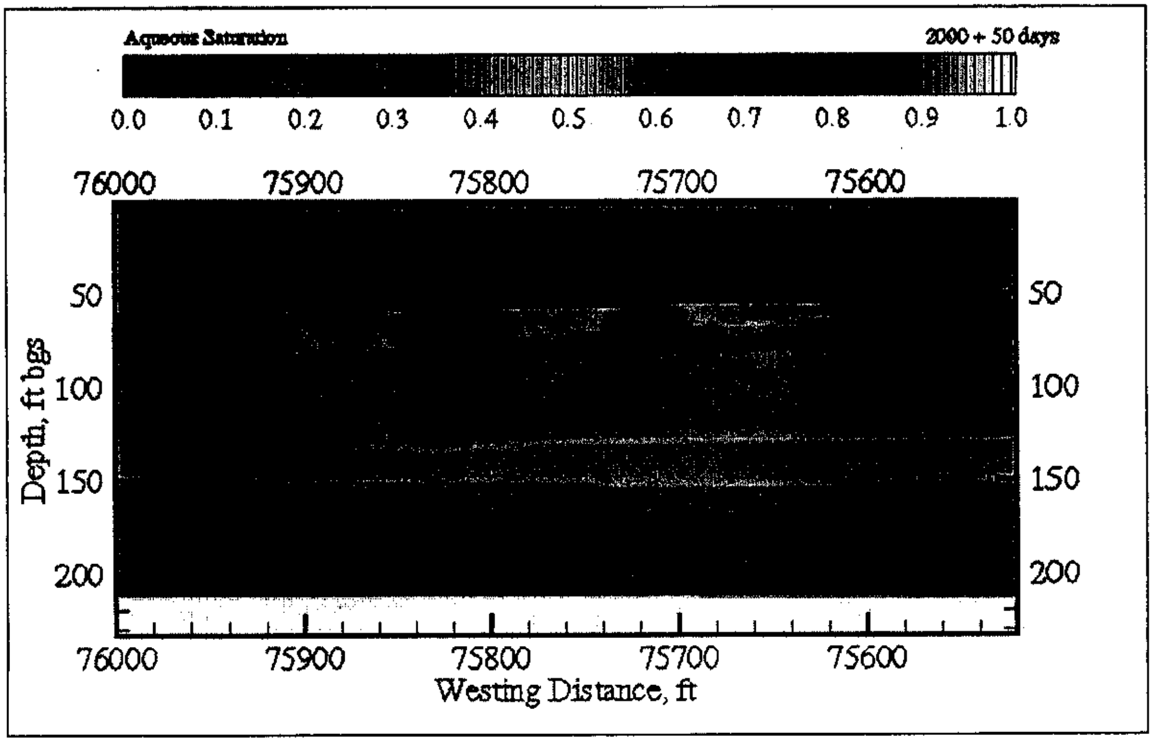

Figure E.16. Case 3 Aqueous-Phase Saturation at
2000 plus 183 days for Cross-Section SX-FF'

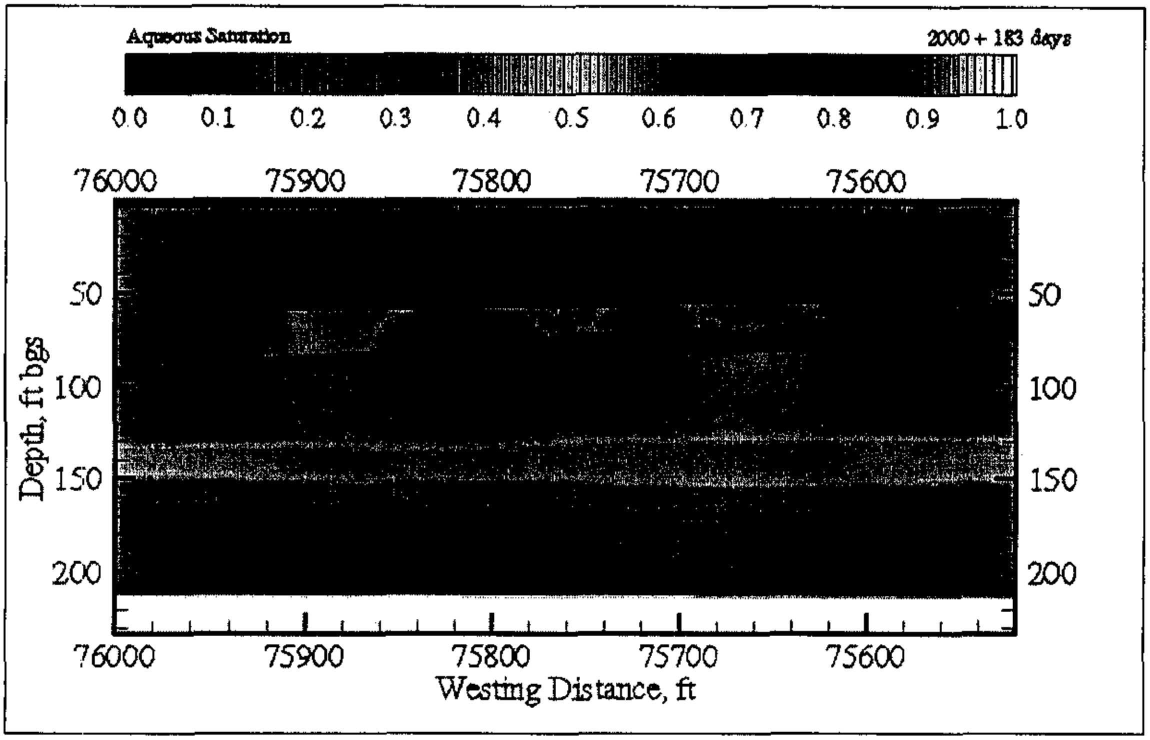

Figure E.17. Case 3 Aqueous-Phase Saturation at
2000 plus 365 days for Cross-Section SX-FF'

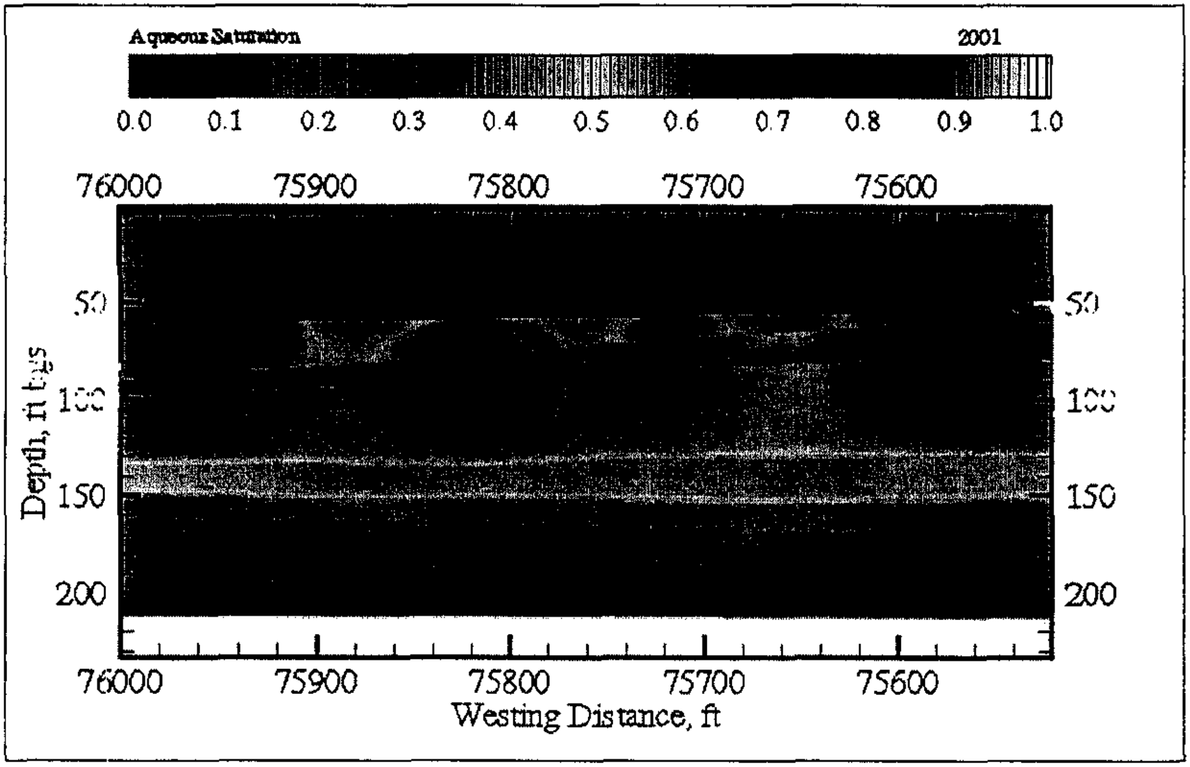

The impact on the transport of contaminants of the 25,000 gal leak event is shown by comparing the distribution of technetium-99 at 2001 and 2040 (Figures E.18 and E.19). By 2001, the flow field (Figure E.17) has nearly returned to steady-flow conditions leaving the distribution of technetium-99 unaltered from its initial inventory distribution, but for diffusion and reduced concentrations in the region immediately below the tank bottom between tanks SX-114 and SX-115 (Figure E.18). The distribution of technetium-99 in 2040, however, shows general downward migration toward the water table and laterally in the groundwater. These images indicate that the water-line leak event has significantly less impact on the migration of the mobile contaminant than the meteoric recharge over a 40-year period.

Figure E.18. Case 3 Technetium-99 Aqueous Concentration at 2001 for Cross-Section SX-FF'

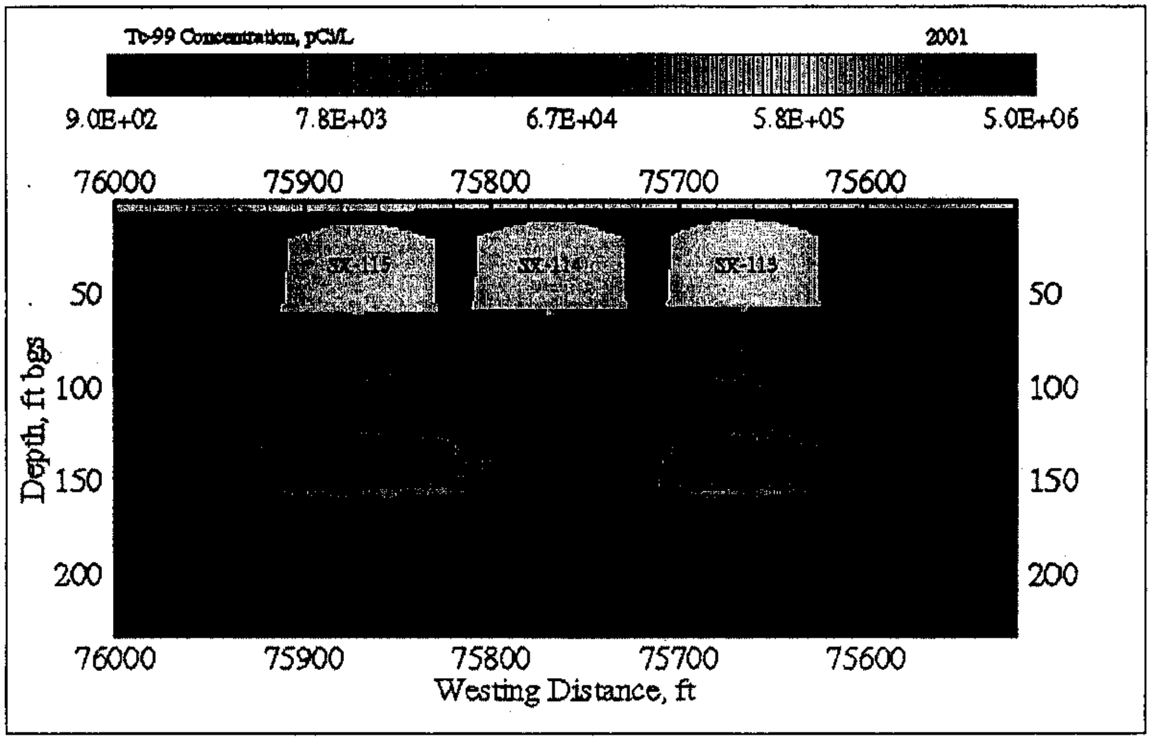

Figure E.19. Case 3 Technetium-99 Aqueous Concentration at 2040 for Cross-Section SX-FF'

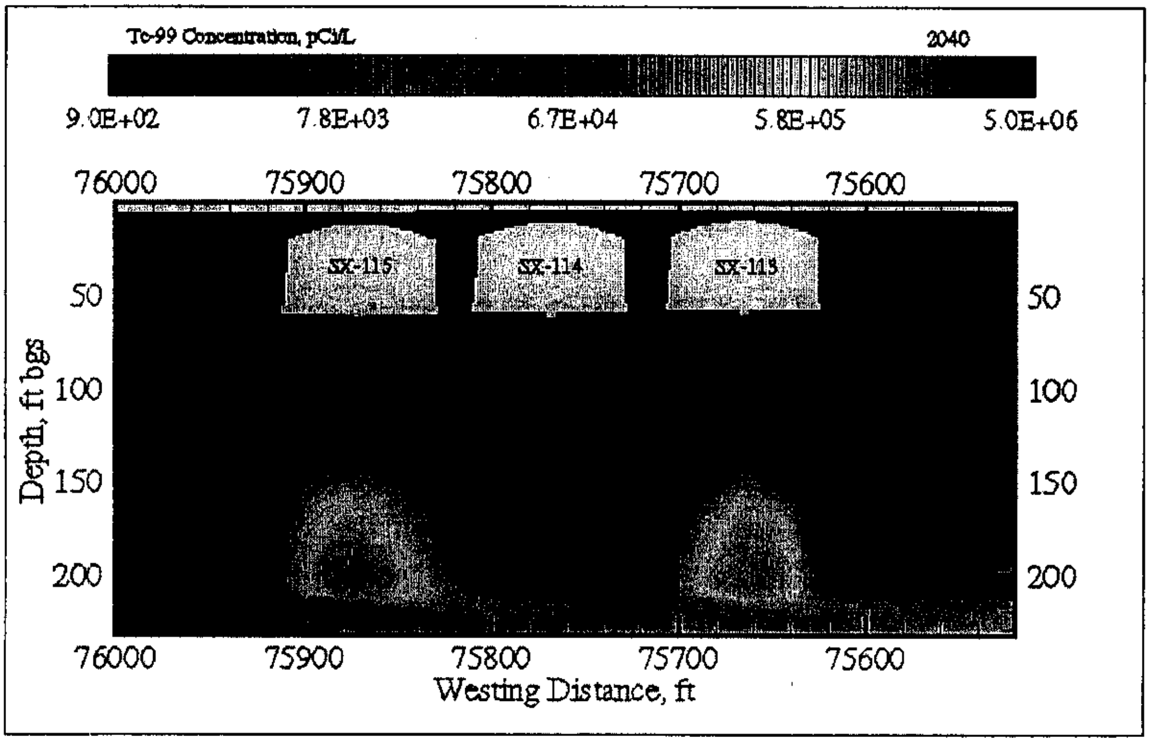

Table E.17. Peak Concentrations and Arrival Times at the First Compliance Point (i.e., WMA S-SX Boundary) for Case 3

Parameter	SX-FF'
Tc-99	
Arrival Time	2031.2 yr
Peak Conc.	2.862×10^5 pCi/L
Max Initial Conc.*	5.074×10^6 pCi/L
Cr	
Arrival Time	2051.3 yr
Peak Conc.	4.565×10^3 µg/L
Max. Initial Conc.	1.089×10^5 µg/L
NO_3	
Arrival Time	2031.9 yr
Peak Conc.	1.018×10^6 µg/L
Max Initial Conc.	3.616×10^7 µg/L

*Maximum initial concentration is based on inventory data (Section E.2.4.3) and listed for comparison with the simulated peak concentration at the compliance boundary.

E.4.4 NO BARRIER AND CLASTIC DIKES CASE (CASE 4)

The no barrier and clastic dikes suite of simulations, Case 4, investigated solute transport through one cross-section in the S and SX tank farms considering natural surface infiltration and a closure barrier by the year 2040. This suite of simulations differs from the Case 1 simulations in that a clastic dike occurs midway between tanks SX-108 and SX-109 in cross-section SX-DD'. The clastic dike was modeled as a vertical feature having hydrologic properties of its infilling material (Table E.4). The computational grid was refined in the horizontal direction in the region around the clastic dike. These simulations were initialized using a steady-flow solution defined by the upper surface recharge rate of 100 mm/yr and a hydraulic gradient in the unconfined aquifer. Inventories of the four contaminant species were initialized using the uniform distribution pattern. Plot-file output for these simulations was generated at the years 2000, 2040, 2540, and 3000 and include values for the aqueous saturation, aqueous pressure, aqueous moisture content, and concentrations for the four solute species.

Solute BTCs at the first compliance point for cross-section SX-DD' are shown in Attachment E3, Figures E3.49 through E3.51 for the three solute species (technetium-99, chromium, and nitrate), respectively. Aqueous flux at the water table for cross-section SX-DD' is shown in Figures E3.56. Times and aqueous concentrations for the BTC peaks at the first compliance boundary are shown in Table E.18. Area-weighted averages of the solute BTCs were generated for the three solute species, as shown in Attachment E3, Figures E3.58 through E3.60 for technetium-99, chromium, and nitrate, respectively. These results indicate that the clastic dike has a negligible impact on solute peak concentrations and arrival times at the first compliance point. This result is due in part to the location of the clastic dike outside of initial inventory distribution and the negligible impact of the dike on the response of the flow system.

Table E.18. Peak Concentrations and Arrival Times at the First Compliance Point (i.e., WMA S-SX Boundary) for Case 4

Parameter	SX-DD'
Tc-99	
Arrival Time	2050.3 yr
Peak Conc.	1.227×10^6 pCi/L
Max Initial Conc.*	9.480×10^7 pCi/L
Cr	
Arrival Time	2053.3 yr
Peak Conc.	1.022×10^5 μg/L
Max Initial Conc.	1.244×10^7 μg/L
NO_3	
Arrival Time	2050.7 yr
Peak Conc.	3.320×10^6 μg/L
Max Initial Conc.	4.448×10^8 μg/L

*Maximum initial concentration is based on inventory data (Section E.2.4.3) and listed for comparison with the simulated peak concentration at the compliance boundary.

E.4.5 NONUNIFORM INVENTORY DISTRIBUTION AND NO BARRIER CASE (CASE 5)

The nonuniform inventory distribution and no barrier suite of simulations, Case 5, investigated solute transport through three cross-sections in the S and SX tank farms considering natural surface infiltration, with no water-line leaks and closure barrier by the year 2040. This suite of simulations differs from the Case 1 simulations in that a nonuniform distribution was used for the initial inventory; where the inventory distribution by depth was maintained, but concentrated between tanks (Section E.2.4.2.2). These simulations were initialized using a steady-flow solution defined by the surface recharge rate of 100 mm/yr and a hydraulic gradient in the unconfined aquifer. Inventories of the four contaminant species were initialized using the nonuniform distribution pattern. Plot-file output for these simulations was generated at the years 2000, 2010, 2040, 2540, and 3000 and include values for the aqueous saturation, aqueous pressure, aqueous moisture content, and concentrations for the four solute species. The moisture content field for these simulations remains unchanged from the initial steady-flow field until the year 2040, when the closure barrier becomes effective.

Solute BTCs at the first compliance point for the three cross-sections (S-CC', SX-DD', and SX-FF') are shown in Attachment E3, Figures E3.61 through E3.69 for the three solute species (technetium-99, chromium, and nitrate), respectively. Aqueous flux at the water table for the three cross-sections (S-CC', SX-DD', and SX-FF') are shown in Figures E3.70 through E3.72, respectively. Times and aqueous concentrations for the BTC peaks at the first compliance boundary are shown in Table E.19. Area-weighted averages (across the three cross-sections) of the solute BTCs were generated for the three solute species and are shown in Attachment E3, Figures E3.73 through E3.75 for technetium-99, chromium, and nitrate, respectively.

Table E.19. Peak Concentrations and Arrival Times at the First Compliance Point (i.e., WMA S-SX Boundary) for Case 5

Parameter	S-CC'	SX-DD'	SX-FF'
	Tc-99		
Arrival Time	2031.9 yr	2048.7 yr	2030.9 yr
Peak Conc.	1.779×10^6 pCi/L	5.428×10^6 pCi/L	2.627×10^6 pCi/L
Max Initial Conc.*	6.262×10^8 pCi/L	2.033×10^9 pCi/L	4.425×10^8 pCi/L
	Cr		
Arrival Time	2050.3 yr	2051.3 yr	2049.3 yr
Peak Conc.	3.872×10^4 µg/L	4.485×10^5 µg/L	3.615×10^4 µg/L
Max. Initial Conc.	1.710×10^7 µg/L	1.074×10^8 µg/L	7.290×10^6 µg/L
	NO_3		
Arrival Time	2031.6 yr	2049.0 yr	2029.6 yr
Peak Conc.	7.915×10^6 µg/L	7.635×10^6 µg/L	4.382×10^6 µg/L
Max. Initial Conc.	2.711×10^9 µg/L	2.159×10^9 µg/L	7.048×10^8 µg/L

*Maximum initial concentration is based on inventory data (Section E.2.4.3) and listed for comparison with the simulated peak concentration at the compliance boundary.

As indicated by the figures and Table E.19, the nonuniform distribution of initial inventory has negligible impact on arrival times of peak concentrations at the WMA S-SX boundary. This result agrees with other observations, in that peak arrival times at the WMA S-SX boundary were most strongly correlated with the initial depth of the peak concentration. The nonuniform distribution had initial aqueous concentrations that were between 4.85 and 264 times greater than corresponding values for the uniform distribution; whereas, the resulting peak concentrations at the WMA S-SX boundary were only 2.27 to 13.7 times greater than the corresponding values for the uniform distribution. The nonuniform distribution, therefore, resulted in greater dilution of the contaminant concentrations in migrating to the first compliance point from the initial inventory distribution.

E.4.6 NONUNIFORM INVENTORY DISTRIBUTION AND BARRIER CASE (CASE 6)

The nonuniform inventory distribution and barrier suite of simulations, Case 6, investigated solute transport through three cross-sections in the S and SX tank farms considering natural surface infiltration, an interim barrier, with no water-line leaks and closure barrier by the year 2040. This suite of simulations differs from the Case 1 simulations in that an interim surface barrier was implemented between the years 2010 and 2400, and a nonuniform distribution was used for the initial inventory; where the inventory distribution by depth was maintained, but concentrated between tanks (Section E.2.4.2.2). These simulations were initialized using a steady-flow solution defined by the upper surface recharge rate of 100 mm/yr and a hydraulic gradient in the unconfined aquifer. Inventories of the four contaminant species were initialized using the uniform distribution pattern. Plot-file output for these simulations was generated at the years 2000, 2010, 2040, 2540, and 3000 and include values for the aqueous saturation, aqueous pressure, aqueous moisture content, and concentrations for the four solute species. The moisture content field for these simulations remains unchanged from the initial steady-flow field until the year 2010, when the interim barrier becomes effective.

Solute BTCs at the first compliance point for the three cross-sections (S-CC', SX-DD', and SX-FF') are shown in Attachment E3, Figures E3.76 through E3.84, for the three solute species (technetium-99, chromium, and nitrate), respectively. Aqueous flux at the water table for the three cross-sections (S-CC', SX-DD', and SX-FF') are shown in Figures E3.85 through E3.87, respectively. Times and aqueous concentrations for the BTC peaks at the first compliance boundary are shown in Table E.20. Area-weighted averages (across the three cross-sections) of the solute BTCs were generated for the three solute species, as shown in Attachment E3, Figures E3.88 through E3.90 for technetium-99, chromium, and nitrate, respectively. Compared against the simulations for the nonuniform inventory distribution and no interim barrier case (Case 5), these results reflect those found for uniform inventory distributions with and without an interim barrier. As expected, the interim barrier has the greatest impact on reducing peak concentrations at the WMA S-SX boundary for those inventory distributions with solute mass located higher in the vadose zone (i.e., chromium).

Table E.20. Peak Concentrations and Arrival Times at the First Compliance Point (i.e., WMA S-SX Boundary) for Case 6

Parameter	S-CC'	SX-DD'	SX-FF'
Tc-99			
Arrival Time	2027.7 yr	2054.7 yr	2027.3 yr
Peak Conc.	1.236×10^6 pCi/L	8.669×10^5 pCi/L	2.000×10^6 pCi/L
Max. Initial Conc.*	6.262×10^8 pCi/L	2.033×10^9 pCi/L	4.425×10^8 pCi/L
Cr			
Arrival Time	2050.3 yr	2063.0 yr	2044.0 yr
Peak Conc.	6.607×10^3 µg/L	4.786×10^4 µg/L	7.732×10^3 µg/L
Max. Initial Conc.	1.710×10^7 µg/L	1.074×10^8 µg/L	7.290×10^6 µg/L
NO_3			
Arrival Time	2027.3 yr	2050.0 yr	2026.0 yr
Peak Conc.	5.648×10^6 µg/L	1.291×10^6 µg/L	3.339×10^6 µg/L
Max. Initial Conc.	2.711×10^9 µg/L	2.159×10^9 µg/L	7.048×10^8 µg/L

*Maximum initial concentration is based on inventory data (Section E.2.4.3) and listed for comparison with the simulated peak concentration at the compliance boundary.

E.4.7 LOCATION OF INVENTORY DISTRIBUTION AND NO BARRIER CASE (CASE 7)

The location of inventory distribution and no barrier suite of simulations, Case 7, investigated solute transport through three cross-sections in the S and SX tank farms considering natural surface infiltration, with no water-line leaks and closure barrier by the year 2040, and an inventory location close to the water table. This suite of simulations differs from the Case 1 simulations in that a displaced-nonuniform distribution was used for the initial inventory; where the inventory distribution by depth was maintained, but concentrated between tanks and shifted toward the water table (Section E.2.4.2.3). These simulations were initialized using a steady-flow solution defined by the upper surface recharge rate of 100 mm/yr and a hydraulic gradient in the unconfined aquifer. Plot-file output for these simulations was generated at the years 2000, 2010, 2040, 2540, and 3000 and include values for the aqueous saturation, aqueous pressure, aqueous moisture content, and concentrations for the four solute species. The moisture content field for these simulations remains unchanged from the initial steady-flow field until the year 2040, when the closure barrier becomes effective.

Solute BTCs at the first compliance point for the three cross-sections (S-CC', SX-DD', and SX-FF') are shown in Attachment E3, Figures E3.91 through E3.99, for the three solute species (technetium-99, chromium, and nitrate), respectively. Aqueous flux at the water table for the three cross-sections (S-CC', SX-DD', and SX-FF') are shown in Attachment E3, Figures E3.100 through E3.102, respectively. Times and aqueous concentrations for the BTC peaks at the first compliance boundary are shown in Table E.21. Area-weighted averages (across the three